Central Iowa Expo Pavement Test Sections: Pavement and Foundation Construction Testing and Performance Monitoring

FEBRUARY 2018

Final Report

CENTER FOR
CEER
EARTHWORKS ENGINEERING
RESEARCH

IOWA STATE UNIVERSITY
Institute for Transportation

Sponsored by
Iowa Department of Transportation
(InTrans Project 14-493)
Iowa Highway Research Board
(IHRB Project TR-671)
Federal Highway Administration

About the Center for Earthworks Engineering Research

The mission of the Center for Earthworks Engineering Research (CEER) at Iowa State University is to be the nation's premier institution for developing fundamental knowledge of earth mechanics, and creating innovative technologies, sensors, and systems to enable rapid, high quality, environmentally friendly, and economical construction of roadways, aviation runways, railroad embankments, dams, structural foundations, fortifications constructed from earth materials, and related geotechnical applications.

Disclaimer Notice

The contents of this report reflect the views of the authors, who are responsible for the facts and the accuracy of the information presented herein. The opinions, findings and conclusions expressed in this publication are those of the authors and not necessarily those of the sponsors.

The sponsors assume no liability for the contents or use of the information contained in this document. This report does not constitute a standard, specification, or regulation.

The sponsors do not endorse products or manufacturers. Trademarks or manufacturers' names appear in this report only because they are considered essential to the objective of the document.

ISU Non-Discrimination Statement

Iowa State University does not discriminate on the basis of race, color, age, ethnicity, religion, national origin, pregnancy, sexual orientation, gender identity, genetic information, sex, marital status, disability, or status as a U.S. veteran. Inquiries regarding non-discrimination policies may be directed to Office of Equal Opportunity, Title IX/ADA Coordinator, and Affirmative Action Officer, 3350 Beardshear Hall, Ames, Iowa 50011, 515-294-7612, email eooffice@iastate.edu.

Iowa Department of Transportation Statements

Federal and state laws prohibit employment and/or public accommodation discrimination on the basis of age, color, creed, disability, gender identity, national origin, pregnancy, race, religion, sex, sexual orientation or veteran's status. If you believe you have been discriminated against, please contact the Iowa Civil Rights Commission at 800-457-4416 or the Iowa Department of Transportation affirmative action officer. If you need accommodations because of a disability to access the Iowa Department of Transportation's services, contact the agency's affirmative action officer at 800-262-0003.

The preparation of this report was financed in part through funds provided by the Iowa Department of Transportation through its "Second Revised Agreement for the Management of Research Conducted by Iowa State University for the Iowa Department of Transportation" and its amendments.

The opinions, findings, and conclusions expressed in this publication are those of the authors and not necessarily those of the Iowa Department of Transportation or the U.S. Department of Transportation.

Technical Report Documentation Page

1. Report No.	2. Government Accession No.	3. Recipient's Catalog No.
IHRB Project TR-671		

4. Title and Subtitle	5. Report Date
Central Iowa Expo Pavement Test Sections: Pavement and Foundation Construction Testing and Performance Monitoring	February 2018
	6. Performing Organization Code

7. Author(s)	8. Performing Organization Report No.
David White (orcid.org/0000-0003-0802-1167), Pavana Vennapusa (orcid.org/0000-0001-9529-394X), Peter Becker (orcid.org/0000-0003-0283-8248), Jesus Rodriguez (orcid.org/0000-0002-6793-3249), Yang Zhang (orcid.org/0000-0002-1150-5595), and Christianna White (orcid.org/0000-0002-9354-8635)	InTrans Project 14-493

9. Performing Organization Name and Address	10. Work Unit No. (TRAIS)
Center for Earthworks Engineering Research Iowa State University 2711 South Loop Drive, Suite 4700 Ames, IA 50010-8664	**11. Contract or Grant No.**

12. Sponsoring Organization Name and Address		13. Type of Report and Period Covered
Iowa Highway Research Board Iowa Department of Transportation 800 Lincoln Way Ames, IA 50010	Federal Highway Administration U.S. Department of Transportation 1200 New Jersey Avenue SE Washington, DC 20590	Final Report
		14. Sponsoring Agency Code SPR TR-671

15. Supplementary Notes

Visit www.ceer.iastate.edu for color pdfs of this and other research reports.

16. Abstract

The Central Iowa Expo facility located in Boone, Iowa, needed to be reconstructed in 2012 to provide an improved pavement foundation for pavement with hot mix asphalt (HMA) and portland cement concrete (PCC). This rework created a unique opportunity to conduct pavement foundation research using a range of stabilization construction and testing technologies on about 4.8 miles of roadway. The Iowa Department of Transportation (DOT) initiated a research project to build the pavement foundation layer (Phase I), construction of the pavement layers (Phase II), and performance monitoring of the pavement systems (Phase III). During Phase I, 16 test sections were constructed, that used woven and non-woven geotextiles and geogrids at subgrade/subbase interfaces; 4 in. and 6 in. geocells in the subbase layer + non-woven geosynthetics at subgrade/subbase interfaces; portland cement (PC) and fly ash stabilization of subgrades; PC stabilization of recycled subbase; PC + fiber stabilization of recycled subbase with polypropylene fibers and monofilament-polypropylene fibers; mechanical stabilization (mixing subgrade with existing subbase); and high-energy impact compaction. A series of laboratory tests were conducted to characterize the soils, determine compaction characteristics, unconfined compressive strength tests on chemical stabilized samples, and freeze-thaw durability. In situ strength and stiffness-based test measurements were performed during construction (in July 2012), about three months after construction (in October 2012), seven months after construction (in January 2012) during frozen condition, and about nine to ten months after construction (in April/May 2013) during spring-thaw. During Phase II, asphalt compaction was monitored using intelligent compaction technology along with in situ point testing. Phase III monitoring involved testing on the asphalt layer, conducting ground penetrating radar testing to evaluate layer thicknesses and moisture conditions over time. This project generated significant information regarding the mechanistic properties for pavement foundation support for a range of foundation improvement/stabilization methods. The test sections at this facility are unique in terms of the range of technologies used and for the fact that the performance data particularly isolates the influence of the seasonal changes without any loading. Some significant lessons learned from this project and the limitations of the findings are identified in this report.

17. Key Words	18. Distribution Statement
falling weight deflectometer—HMA paving—in situ testing—intelligent compaction—low volume roads—soil stabilization	No restrictions.

19. Security Classification (of this report)	20. Security Classification (of this page)	21. No. of Pages	22. Price
Unclassified.	Unclassified.	353	NA

Form DOT F 1700.7 (8-72) **Reproduction of completed page authorized**

CENTRAL IOWA EXPO PAVEMENT TEST SECTIONS: PAVEMENT AND FOUNDATION CONSTRUCTION TESTING AND PERFORMANCE MONITORING

Final Report
February 2018

Principal Investigator
David J. White, Professor and Former Director
Center for Earthworks Engineering Research, Iowa State University

Co-Principal Investigator
Pavana K. R. Vennapusa, Research Assistant Professor and Former Assistant Director
Center for Earthworks Engineering Research, Iowa State University

Authors
David White, Pavana Vennapusa,
Peter Becker, Jesus Rodriguez, Yang Zhang, and Christianna White

Sponsored by
Iowa Highway Research Board
(IHRB Project TR-671),
Iowa Department of Transportation,
and Federal Highway Administration

Preparation of this report was financed in part
through funds provided by the Iowa Department of Transportation
through its research management agreement with the
Institute for Transportation
(InTrans Project 14-493)

A report from
Center for Earthworks Engineering Research (CEER)
Iowa State University
2711 South Loop Drive, Suite 4700
Ames, IA 50010-8664
Phone: 515-294-8103 / Fax: 515-294-0467
www.intrans.iastate.edu

TABLE OF CONTENTS

LIST OF FIGURES

LIST OF TABLES

ACKNOWLEDGMENTS

This project was sponsored by the Iowa Highway Research Board and the Iowa Department of Transportation (DOT) using Federal Highway Administration state planning and research funds.

Numerous people from the Iowa DOT, the Central Iowa Expo, the Boone County Engineering Office, Foth Engineering Alliance, JB Holland Construction, and CEER assisted during field and laboratory testing and provided access to the project site. All of their efforts were greatly appreciated.

EXECUTIVE SUMMARY

The Central Iowa Expo facility located in Boone, Iowa, needed to be reconstructed in 2012 to provide an improved pavement foundation for pavement with hot mix asphalt (HMA) and portland cement concrete (PCC). This rework created a unique opportunity to conduct pavement foundation research using a range of stabilization construction and testing technologies on about 4.8 miles of roadway. The Iowa Department of Transportation (DOT) initiated a research project to build the pavement foundation layer (Phase I), construction of the pavement layers (phase II), and performance monitoring of the pavement systems (Phase III).

Phase I: Pavement Foundation Construction and Testing

Phase I construction occurred in May–July 2012. The project site consists of thirteen roads oriented in the North-South direction (denoted as 1st St. to 13th St.) and three roads oriented in the East-West direction (denoted as South Ave., Central Ave., and North Ave.). Re-construction occurred on all roads except 13th St, which was paved with HMA earlier in 2012. Construction of test sections required removing the existing deteriorated chip seal surface and subbase, and 6 to 12 in. of subgrade. The subgrade consisted primarily of wet soils classified as lean clay (CL) or A-6(5). Ground water was at depths of 3 to 6 ft below original grade across the site, and at about 12 ft or greater near drainage features.

Sixteen test sections were constructed on the North-South roads that used woven and non-woven geotextiles at subgrade/subbase interfaces; triaxial and biaxial geogrids at subgrade/subbase interfaces; 4 in. and 6 in. geocells in the subbase layer + non-woven geosynthetics at subgrade/subbase interfaces; portland cement (PC) and fly ash stabilization of subgrades; PC stabilization of recycled subbase; PC + fiber stabilization of recycled subbase with polypropylene fibers and monofilament-polypropylene fibers; mechanical stabilization (mixing subgrade with existing subbase); and high-energy impact compaction. Triaxial and biaxial geogrids were used at subgrade/subbase interfaces at select locations on East-West roads. All North-South test sections except one were topped with a nominal 6 in. of modified subbase material (MSB) classified as GP-GM or A-1-a (7% fines content); the 6 in. geocell section required 7 in. of MSB. All East-West test sections were topped with a nominal 9 in. of MSB material. Crushed limestone was used in the MSB layer on all North-South roads, and a mixture of recycled concrete and recycled asphalt was used in the MSB layer on all East-West roads. Six North-South test sections (6th St., 7th St., and 9th St.) and the East-West test sections consisted of 6 in. of recycled subbase material classified as SM or A-1-a (14% fines content) between the subbase and subgrade layers.

A series of laboratory tests were conducted to characterize the soils, determine compaction characteristics, unconfined compressive strength tests on chemical stabilized samples, and freeze-thaw durability. In situ strength and stiffness based test measurements were performed during construction (in July 2012), about three months after construction (in October 2012), seven months after construction (in January 2012) during frozen condition, and about nine to ten months after construction (in April/May 2013) during spring-thaw. Strength based test measurement included dynamic cone penetrometer (DCP), and stiffness based measurements

included light weight deflectometer (LWD), falling weight deflectometer (FWD), and roller-integrated compaction monitoring (RICM) or intelligent compaction (IC). Field permeability of the aggregate base material was assessed in several test section using a gas permeameter test (GPT) device. Traditional nuclear density gauge testing was also conducted during subgrade and subbase layer construction, and the results are compared with the strength-stiffness based test measurements. In addition, earth pressure sensor arrays were also installed in the foundation layers at different depths to monitor ground stresses for different loading conditions.

Significant findings from the Phase I testing were as follows:

- Cost, average stiffness values, and uniformity were reported for all of the pavement foundation sections. Analysis of this data is useful to optimize pavement foundation design.
- Comparison between LWD and FWD measurements indicated that both provided statistically related moduli measurement values, but LWD measurements do not always show influence of stiff underlying layers as measured with the FWD. The measurement influence depth is greater for the FWD compared to the LWD, because of the higher stresses that can applied with the FWD.
- The RICM values (CMV and MDP* measured with Caterpillar IC roller and CCV measured with Sakai roller) provided near-continuous electronic records of ground stiffness and showed variations between the test sections and locations of lower stiffness materials within sections. The CMV and CCV values correlated better with FWD values than MDP* values. CMV values correlated better to FWD values than LWD values.
- The QC/QA nuclear density testing showed that this approach to quality assessment can lead to shortcomings (including lack of reproducibility and infrequent testing) and does not capture the wide range in stiffness values measured from the other devices.
- Shortly after construction and after spring thaw, test sections with mechanical stabilization (TS-MS) with in situ mixing of recycled aggregate with existing subgrade versus over excavation (TS-OE) and replacement produced comparatively higher elastic moduli values than control (TS-C) sections. There was no statistical evidence to suggest that TS-OE pavement foundation performed better than the TS-MS pavement foundation, or vice versa, after construction. However, after spring-thaw, results showed that the TS-OE pavement foundation performed better than the TS-MS foundation.
- Laboratory freeze-thaw testing showed that the mechanically stabilized subgrade used in this study exhibits strength and stiffness behavior similar to the on-site recycled material at optimum environmental conditions. During thaw-weakening conditions, the mechanically stabilized subgrade exhibits strength and stiffness behavior similar to the subgrade.
- Average FWD composite elastic moduli values from each test section during October 2012 (i.e., never-frozen) ranged from 37 MPa to 507 MPa. Test sections with Portland cement (PC) stabilized subgrade, fly ash stabilized subgrade, or PC stabilized reclaimed gravel subbase produced the highest moduli values. Test sections with mechanically stabilized subgrade, compacted subgrade, or untreated reclaimed gravel subbase produced comparatively higher moduli values than control test sections with no subgrade compaction or other treatment.

- Average FWD composite elastic moduli during April 2013 (i.e., thaw-weakened) ranged from 11 MPa to 159 MPa. All test sections experienced reductions in moduli values as conditions transitioned from never-frozen to thaw-weakened (by about 2 to 9 times on average). Test sections with PC stabilized subgrade or PC stabilized reclaimed gravel subbase produced the highest moduli values. Test sections with fly ash stabilized subgrade or untreated reclaimed gravel subbase produced relatively high moduli values as well.
- Correlations between thaw-weakened and never-frozen elastic moduli values suggest that PC stabilized pavement foundations are less susceptible to thaw-weakening than untreated pavement foundations or fly ash stabilized pavement foundations.
- Elastic moduli values determined from FWD in never-frozen condition showed statistically significant relationships with both subbase and subgrade layer penetration index (PI) values from DCP tests at that time. But, FWD elastic moduli values after thawing showed strong correlation with the subgrade PI, but not with the subbase layer PI at that time. This emphasizes the importance of subgrade support on composite response as measured from the top of the subbase layer.
- Laboratory freeze-thaw durability tests showed that subgrade stabilized with self-cementing fly ash exhibits improvements with increasing fly ash content up to 15% with decreasing level of frost-heave and thaw-weakening susceptibility. Greater improvement was related to shorter fly ash set time. Subgrade and subbase stabilized with cement showed low to negligible frost susceptibility. For subbase, the addition of fibers increased the pre-test and post-test (saturated) CBR values slightly. Comparatively, the addition of cement reduced the heave rates and increased the CBR values significantly. Results also indicated that curing time and compaction delay influence the freeze-thaw performance of chemically stabilized soils.
- To achieve very low thaw-weakening susceptibility, the heave rate must be controlled to less than 4 mm/day per ASTM D5918. The current ASTM classification does not distinguish classifications with CBR values greater than 20. A proposed classification for chemically stabilized soils identifies thaw-susceptibility as negligible for post-test CBR values ≥ 100. The advantage of this rating is it provides additional criteria for rating freeze-thaw susceptibility for stabilized soils with post-test CBR values greater than 20. It is difficult to predict the post-tests CBR values from the pre-test measurements for chemically stabilized soils due to time-dependent strength gain and supports the need to perform the freeze-thaw tests and monitoring the influence of curing time for stabilized soils.
- In situ gas permeameter tests (GPTs) were conducted to rapidly determine field saturated hydraulic conductivity of granular base layer and its relationship with different foundation support conditions and gradation of the subbase. Testing was focused on three test sections, where the subbase layer was compacted with a vibrator smooth drum roller. Aggregate degradation from over-compaction varied between sections and appears to be linked to the foundation support condition. The section with the highest support values (i.e, high CBR and elastic moduli values) consisted of cement stabilized subgrade, but it showed the highest degradation of the aggregate subbase and the lowest hydraulic conductivity. The control section (with only granular subbase over uncompacted subgrade) yielded the lowest support values, but the highest hydraulic conductivity. The

geogrid reinforced aggregate section provided comparatively better support conditions than the control section and intermediate hydraulic conductivity values.

Phases II and III: Pavement Construction and Performance Monitoring Testing

Pavement construction occurred in June-July 2013. All test sections oriented in the North-South direction, except on the 6th street, were paved with nominal 4 in. of asphalt base course layer and a nominal 2 in. of asphalt surface course layer. The asphalt layer mixes comprised of different combinations of either warm mix or hot mix binder and either low or high absorption aggregate. Evaluation of the asphalt layers as a function of the mix type was beyond the scope of this study. All test section with asphalt pavement layers were compacted using a Hamm HD+ 120 VV dual smooth-drum vibratory roller equipped with RICM technology (referred to as HMV value). The 6th street north-south sections and all east-west roadways were paved with 6 in. of PCC. A geosynthetic composite drainage layer was installed directly beneath the PCC layer in 6th St. South section for comparison of drainage with the 6th St. North section without the geocomposite. A geocomposite layer was also installed on 11th St. North section (stabilized with PC in subgrade) directly beneath the asphalt layer, along with a control section without for comparison of drainage performance between the two sections.

All test sections were mapped with the Hamm roller prior to paving to compare with measurements obtained on the asphalt base and surface course layers, to assess the significant of support layer conditions on the surface layer compaction properties. Asphalt temperature was monitored with the Hamm roller during compaction, and the mat temperature was independently measured at different times and locations for comparison with the roller measured temperature values. Asphalt density was monitored with nuclear gauge at multiple compaction passes and were correlated with the roller measurements.

Shortly after paving was completed, performance monitoring testing was conducted from Fall 2013 to Fall 2016. This testing included FWD testing on the pavement layer in Fall 2013 and after spring thaw in Spring 2014, and ground penetrating radar (GPR) measurements to evaluate thickness of the asphalt layer and moisture conditions of the base layer. In addition, foundation layer temperatures were monitored in a test section with asphalt surface layer versus temperatures in a test section with PCC surface layer down to a depth of about 5 ft below surface over the entire monitoring period.

Many highway agencies currently use FWD testing as part of routine testing of pavements in situ. Different agencies use different back- or forward-calculation procedures to determine layer moduli values. Many agencies also rely on empirical relationships in determining the design moduli values. This study attempted to point out the statistical uncertainties associated with the values determined from the different procedures (AASHTO and Hogg forward calculation and ERIDA backcalculation) and empirical relationships.

Significant findings from the Phases II and III testing were as follows:

- In general, HMV values during asphalt pavement construction were higher when placing asphalt over stiff pavement foundations. All HMV measurements correlated with statistical significance to HMV measurements obtained on the foundation layer.
- For asphalt construction over softer pavement foundations, HMV increased with each additional pavement layer. For asphalt construction over stiff foundations, in general, the pavement foundation HMV was greater than base course HMV, and base course HMV was less than surface course HMV.
- Asphalt pavement surface temperature measurements from the roller temperature sensors were in agreement with thermal camera temperatures at higher temperatures (greater than 87.4 °C), but tended to underestimate pavement surface temperatures at lower temperatures (< 87.4 °C).
- Asphalt pavement relative compaction from neither nuclear density gauge tests nor pavements cores correlated with HMV measurements. However, falling weight deflectometer (FWD) measurements strongly correlate with HMV measurements.
- Based on multivariable analyses, RICM systems can potentially be used as QC for asphalt pavement layer modulus, provided that the composite modulus of the pavement foundation is a known target value.
- Comparison of three different forward and back-calculation procedures for FWD data analysis has indicated significant differences in the estimated moduli values for the asphalt, base, and subgrade layers. Standard errors of the estimated values were in the range of 13 MPa for subgrade, over 120 MPa for base layer, and over 3,000 MPa for asphalt layer.
- Numerous regression relationships have been documented in the literature between DCP test measurements and moduli values and are summarized herein. Upper and lower bounds are presented based on the available relationships. The bounds suggest that the predicted moduli values can have an error of ± 50 to 335 MPa if DCP penetration resistance (PR) values are between 2 and 10 mm/blow, and ± 10 to 50 MPa if PR value is > 10 mm/blow.
- New relationships between PR and moduli values calculated from three forward and back calculation methods for a PR range of 2 and 78 mm/blow are presented herein. PR values determined from the weakest 75 mm of the subgrade showed slightly higher R^2 values when compared to PR values for the top 300 mm of the subgrade.
- The relationships presented in this study indicated that for if PR data between 2 to 78 mm are considered, the SE of the estimate ranged from 24 to 60 MPa, depending on the modulus calculation method. The SE of the estimate decreased to < 20 MPa, when PR data from only subgrade are considered.
- A new database of dielectric properties of subgrade and base layer materials and chemically stabilized subgrade materials at different moisture contents are provided in this study. Results indicated that the dielectric properties are sensitive to moisture content, as expected, and are sensitive to curing times for chemically stabilized soil due to the hydration process. PC and FA stabilized subgrade materials produced lower dielectric values than unstabilized subgrade materials.
- GPR surveys conducted during frozen condition did not properly differentiate variations in the foundation layers because of similar dielectric properties of those materials in a frozen condition. This was verified by conducting a simple laboratory box study with compacted pavement and foundation layers in frozen and unfrozen conditions.

- The estimated asphalt thicknesses using the actual measured dielectric properties from the GS3 device values produced an average error of about 11%. The estimated values asphalt thicknesses were close to the 1:1 line when compared with the measured values, when dielectric properties backcalculated from GPR were used. The average error reduced to about 3.7% with that process and the errors are similar to reported by others in the literature with air-coupled GPR antennas.
- Comparison between asphalt thickness measured using the MIT gauge and GPR indicated that the MIT gauge measurements were on average about 9% higher than estimated with GPR.
- GPR data was used to estimate volumetric moisture content of the granular subbase material. Results indicated that on average, the volumetric moisture contents in the subbase layer varied from about 6 to 25%. The variations are attributed to material segregation and degradation, and variations in aggregate gradations and permeability between the test sections, as documented in the Phase I portion of this study with GPT measurements.
- Air and surface temperatures were used to estimate the seasonal frost penetrations in accordance with three simplified empirical models and the modified Berggren equations in this study. The estimated results were compared to in situ measurements to evaluate the accuracy of these models. These comparisons showed that the frost penetration depth estimates from the three empirical models did not match well the measured frost penetration depths. When using tested values for moisture contents and dry unit weights, calculations with the modified Berggren equation provided more accurate results of predicted frost penetrations than using default soil property values. However, the n-factor used in the estimations was found to have a significant influence on the accuracy of estimations, although it is difficult to precisely determine the value of *n* at every specific location.

Significant Lessons Learned, Limitations, and Recommendations

This project generated significant and important information regarding the mechanistic properties for pavement foundation support for a range of foundation improvement/ stabilization methods. The test sections at the Central Iowa Expo facility are unique in terms of the range of technologies used and for the fact that the performance data particularly isolates the influence of the seasonal changes without any loading. Some significant lessons learned from this project and the limitations of the findings are identified below, to identify the path forward for the Iowa DOT with implementation of the findings into the design and construction practice and future research/testing on these test sections.

Traditional nuclear gauge moisture-density testing has played an important role in earthwork quality assessment specifications in the U.S. for decades. This form of QC/QA can be effective, but has shortcomings due to regulations, test reproducibility, limited test frequency, and only serving as a surrogate to strength and stiffness design requirements. Results from this study showed that all the QC agent test results met the target moisture and density criteria, while the QA agent results are much more variable on both accounts. At this point, one could only

speculate about these differences. It is clear though that the nuclear density testing does not indicate the wide stiffness variations resulting from treatments and materials.

The distinct advantage of the strength/stiffness related measurements used at this site (i.e., DCP, FWD, and LWD) is that they identified the variations in support values between different stabilization sections. While these measurements were critical in identifying the relative differences in the strength/stiffness properties between the test sections, they all produced different measurement values that can potentially be used to estimate the mechanistic input parameters used in the pavement design process. However, the following limitations of these test measurements must be realized:

Thus far, however, there is no supporting evidence that these measurements can be reliably used to predict the key mechanistic input parameters used in design (i.e., resilient modulus (Mr) and modulus of subgrade reaction (k-value)) with high statistical confidence.

Empirical relationships have been published between DCP or CBR measurements and Mr and k-values, but all these relationships produce significantly different numbers and therefore present significant uncertainty in selecting an appropriate value in design. Local or regional correlations can be more reliable, but can be very time consuming to generate.

In situ Mr is commonly predicted from non-destructive surrogate tests including the FWD or LWD, but the elastic moduli values calculated from these test devices based on elastic deformations are often confused with resilient modulus values which is based on resilient (i.e., recoverable) deformations. One of the major limitations of these non-destructive surrogate tests is the lack of a conditioning stage prior to testing. During pavement construction, pavement foundation materials are subjected to relatively high loads from construction traffic and compaction equipment. In response to these loads, aggregate particles rearrange themselves resulting in higher density and stiffness. For this reason, it is important to apply conditioning load cycles prior to testing to determine in situ resilient modulus. Once surface paving is complete, the pavement foundation below is confined by the overlying pavement layers. The response of a pavement foundation to subsequent repeated traffic loading is both nonlinear and stress-dependent and therefore the effect of confinement is an important condition to consider in a field based Mr test.

FWD testing provides an estimate of the modulus of the asphalt layer, but is not the same as the stress and frequency dependent dynamic modulus value used in the design for the asphalt layer.

The results documented herein demonstrated the importance of support conditions on the overall composite response at the surface under loading. Improved support at the subgrade level with cement stabilization provided the best response to loading at the surface, followed by cement stabilization at the granular base layer level. The geosynthetic stabilized test sections, although did not show as high of moduli values as cement stabilized test sections, past experience has showed that geosynthetic reinforcement can provide better resistance against permanent deformation/rutting under traffic loading than sections without reinforcement. This aspect was not evaluated at this site and must be evaluated in future testing.

- Although cement stabilization method provided improved support conditions than in sections without stabilization, stabilization did not improve uniformity. The coefficient of variation of moduli values in the cement stabilized sections were higher than in the sections without stabilization, and this is related to lack of construction process control with the stabilization process.

Based on the lessons learned and the limitations identified above, the following are recommended for considerations by the Iowa DOT for future testing and evaluation at this site:

- Evaluate new in situ testing technologies that provide a direct measurement of the M_r and *k*-values of the foundation layers, and stress and frequency dependent dynamic modulus of the asphalt layers. The objective of such testing and evaluation should be to generate typical foundation input parameter values that can be used in future design by the Iowa DOT.
- Evaluate the test sections over the long-term (10+ years) and/or with accelerated pavement testing (trafficking or accelerated loading) to evaluate the influence of the foundation layers on the permanent deformation behavior at the surface.
- Evaluate the condition of the temperature monitoring sensors and continue the monitoring to generate frost-depth penetration data over longer period.

CHAPTER 1: INTRODUCTION

Problem Statement

The Central Iowa Expo facility located in Boone, Iowa, needed to be reconstructed in 2012 to provide an improved pavement foundation for eventual pavement with hot mix asphalt (HMA) and portland cement concrete (PCC). This rework created a unique opportunity to conduct pavement foundation research using a range of technologies on 4.8 miles of roadway. The Iowa Department of Transportation (DOT) initiated a research project to build the pavement foundation systems (Phase I), construction the pavement layers (phase II), and monitor performance of the pavement system (Phase III).

This report covers the research tasks as part of the Phase I pavement foundation construction and testing. Results from Phases II and III are discussed in separate reports.

Objectives

The primary research objectives for the Phase I project were to:

- conduct full-scale field studies to assess pavement foundation compaction using intelligent compaction and high energy impact compaction technology,
- build full-scale field test sections consisting of geosynthetics, chemical stabilizers, and recycling of existing materials that will allow long-term performance monitoring,
- develop recommendations with respect to conducting the Phase II pavement studies to demonstrate various pavement technologies.
- develop local experience with stiffness based quality assurance (QA) and quality control (QC) measurement technologies to assist with near-term implementation; and
- increase the range of stabilization technologies to be considered for future pavement foundation design to optimize the pavement system;

The primary research objectives for the Phase III monitoring project were to monitor:

a. Seasonal changes (within a year and over time) in foundation layer support conditions,
b. Seasonal changes (within a year and over time) in subbase layer permeability,
c. Seasonal temperature changes in foundation layers (document number of F/T cycles),
d. Seasonal changes in in-ground stresses under loading,
e. Surface layer distresses over time (crack mapping and elevation changes),
f. Moisture changes in subbase and subgrade layers seasonally and over time,
g. Micro-mechanical changes in stabilized subgrade over time,
h. Seasonal water table changes, and
i. Loss of support/erosion
j. Weather information monitoring

Phase I Project Scope

The project was constructed in Boone, Iowa during May–July 2012. The project site consists of 4.8 miles of roadway with thirteen roads oriented in the North-South direction (denoted as 1st St. to 13th St.) and three roads oriented in the East-West direction (denoted as South Ave., Central Ave., and North Ave.). Re-construction occurred on all roads except 13th St, which was paved with HMA earlier in 2012. Construction of test sections required removing the existing chip seal surface and subbase, and 6 to 12 in. of subgrade. The subgrade consisted primarily of wet soils classified as lean clay (CL) or A-6(5). Pore water pressure measurements from cone penetration tests (CPTs) indicated ground water elevations at depths of about 3 to 6 ft below original grade across the site, and at about 12 ft or greater near drainage features.

Sixteen test sections were constructed on the North-South roads that used woven and non-woven geotextiles at subgrade/subbase interfaces; triaxial and biaxial geogrids at subgrade/subbase interfaces; 4 in. and 6 in. geocells in the subbase layer + non-woven geosynthetics at subgrade/subbase interfaces; portland cement (PC) and fly ash stabilization of subgrades; PC stabilization of recycled subbase; PC + fiber stabilization of recycled subbase with polypropylene fibers and monofilament-polypropylene fibers; mechanical stabilization (mixing subgrade with existing subbase); and high-energy impact compaction. Triaxial and biaxial geogrids were used at subgrade/subbase interfaces at select locations on East-West roads.

All North-South test sections except one were topped with a nominal 6 in. of modified subbase material (MSB) classified as GP-GM or A-1-a (7% fines content); the 6 in. geocell section required 7 in. of MSB. All East-West test sections were topped with a nominal 9 in. of MSB material. Crushed limestone was used in the MSB layer on all North-South roads, and a mixture of recycled concrete and recycled asphalt was used in the MSB layer on all East-West roads. Six North-South test sections (6th St., 7th St., and 9th St.) and the East-West test sections consisted of 6 in. of recycled subbase material classified as SM or A-1-a (14% fines content) between the subbase and subgrade layers.

In situ strength and stiffness based test measurements were performed during construction (in July 2012), about three months after construction (in October 2012), seven months after construction (in January 2012) during frozen condition, and about nine to ten months after construction (in April/May 2013) during spring-thaw. Strength based test measurement included dynamic cone penetrometer (DCP), and stiffness based measurements included light weight deflectometer (LWD), falling weight deflectometer (FWD), and roller-integrated compaction monitoring (RICM) or intelligent compaction (IC). Traditional nuclear density gauge testing was also conducted during subgrade and subbase layer construction, and the results are compared with the strength-stiffness based test measurements. In addition, earth pressure sensor arrays were also installed in the foundation layers at different depths to monitor ground stresses for different loading conditions.

Phases II and III Project Scope

Pavement construction at the site occurred in June-July 2013. All test sections oriented in the North-South direction, except on the 6th street were paved with nominal 4 in. of asphalt base course layer and a nominal 2 in. of asphalt surface course layer. The asphalt layer mixes comprised of different combinations of either warm mix or hot mix binder and either low or high absorption aggregate. Evaluation of the asphalt layers as a function of the mix type is beyond the scope of this study. All test section with asphalt pavement layers were compacted using a Hamm HD+ 120 VV dual smooth-drum vibratory roller equipped with RICM technology (referred to as HMV value). The 6th street north-south sections and all east-west roadways were paved with 6 in. of PCC. A geosynthetic composite drainage layer was installed directly beneath the PCC layer in 6th St. South section for comparison of drainage with the 6th St. North section without the geocomposite. A geocomposite layer was also installed on 11th St. North section (stabilized with PC in subgrade) directly beneath the asphalt layer, along with a control section without for comparison of drainage performance between the two sections.

All test sections were mapped with the Hamm roller prior to paving to compare with measurements obtained on the asphalt base and surface course layers, to assess the significant of support layer conditions on the surface layer compaction properties. Asphalt temperature was monitored with the Hamm roller during compaction, and the mat temperature was independently measured at different times and locations for comparison with the roller measured temperature values. Asphalt density was monitored with nuclear gauge at multiple compaction passes and were correlated with the roller measurements.

Shortly after paving was completed, performance monitoring testing was conducted from Fall 2013 to Fall 2016. This testing included FWD testing on the pavement layer in Fall 2013 and after spring thaw in Spring 2014, and ground penetrating radar (GPR) measurements to evaluate thickness of the asphalt layer and moisture conditions of the base layer. In addition, foundation layer temperatures were monitored in a test section with asphalt surface layer versus temperatures in a test section with PCC surface layer down to a depth of about 5 ft below surface over the entire monitoring period.

Many highway agencies currently use FWD testing as part of routine testing of pavements in situ. Different agencies use different back- or forward-calculation procedures to determine layer moduli values. Many agencies also rely on empirical relationships in determining the design moduli values. This study attempted to point out the statistical uncertainties associated with the values determined from the different procedures (AASHTO and Hogg forward calculation and ERIDA backcalculation) and empirical relationships.

Report Organization

The report is organized into ten chapters and an Appendix. Chapter 2 of this report provides background for the selected pavement foundation treatments. Chapter 3 summarizes the experimental test methods used in this study. Chapter 4 summarizes the index material properties including laboratory performance characterization tests. Chapter 5 presents the overall site

conditions and research plan. Chapter 6 describes the construction methods for each of the pavement foundation tests sections and the field QA/QC test results. Chapter 7 presents analysis results comparing the different pavement foundation properties. Chapter 8 provides results from pavement construction. Chapters 9 and 10 presents results from performance monitoring after pavement construction. Chapter 11 summarizes key findings and conclusions from this study along with lessons learned and recommendations for future work.

CHAPTER 2: BACKGROUND

Subgrade soils in Iowa generally rate from fair to poor with the majority of soils classifying as A-4 to A-7-6 (according to AASHTO classification). These soils can exhibit low bearing strength, high volumetric instability, and freeze/thaw durability problems. Stabilization offers opportunities to improve these soil conditions. One of the objectives of this study is to investigate the use of different stabilization methods in subgrade and subbase layers to optimize pavement foundation design by measuring in situ engineering properties over time with a special focus on freeze/thaw performance. This chapter provides a brief background of the stabilization methods and the stiffness based quality control and quality assurance technologies that are used on this project.

Geomaterials Stabilization Methods

Chemical Stabilization

Numerous studies have been conducted over the past several decades on chemical stabilization process. Review of literature indicates that admixtures used in the chemical stabilization process are typically either active or passive. Active chemical admixtures that are commonly used include portland cement, fly ash, lime, and passive chemical admixtures include bitumen, plant processed bio-fuel co-products with varying lignin contents and lignosulfates, and polymer emulsions.

General information published in the literature for selecting stabilizer based on soil grain-size characteristics and Atterberg limits are shown in Figure 1 to Figure 3 and Table 1. ASTM class C self-cementing fly ash has been used on a limited scale in Iowa to treat unstable/wet subgrades. Using self-cementing fly ash for soil stabilization provide environmental incentives in terms of using a waste product, cost savings relative to other chemical stabilizers, and availability at several power plants across Iowa (White et al. 2005). The characteristics of fly ash can vary significantly between different plants due to variations in the coal used and various operating conditions in the plant. Laboratory mix design is recommended when using fly ash for stabilization.

Chemical stabilization process in the field typically involves application of stabilizer to loose soil, mixing the stabilizer with a soil reclaimer and moisture-conditioning the mixture, and compacting the mixture within a specified time (typically less than 1 to 2 hours). Compaction time is critical and is dependent on the chemical admixture set time and must be determined using laboratory testing.

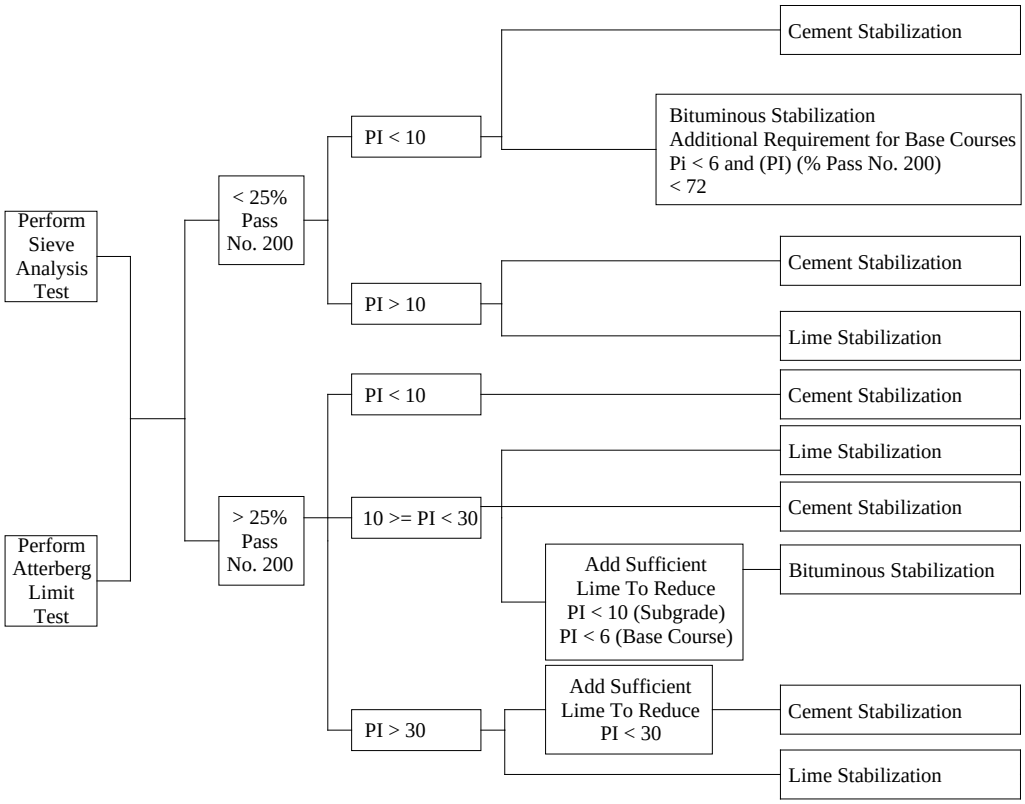

Figure 1. Chart for selection of stabilizer (Chu et al. 1955)

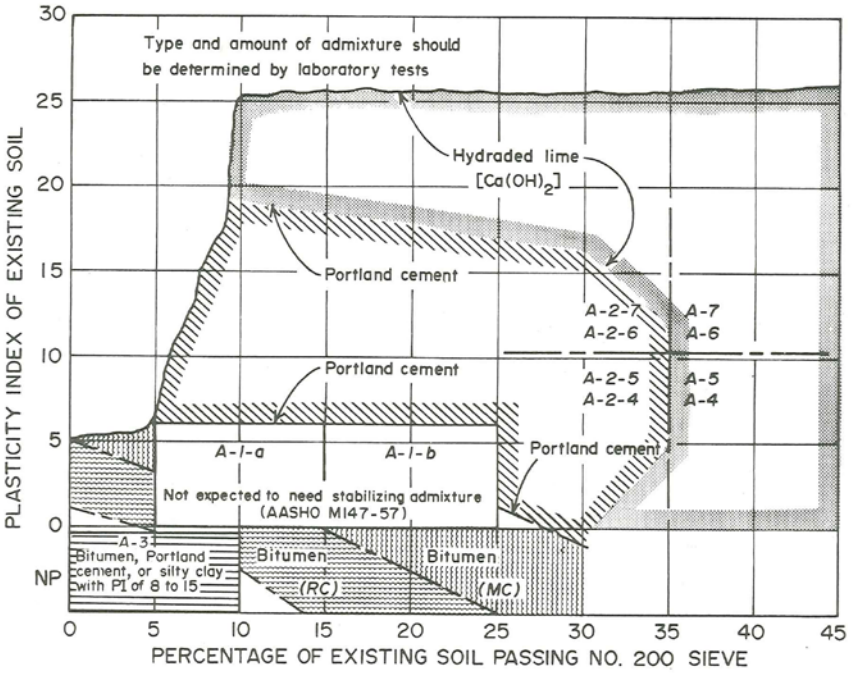

Figure 2. Chart for selection of stabilizer (Terrel et al. 1979)

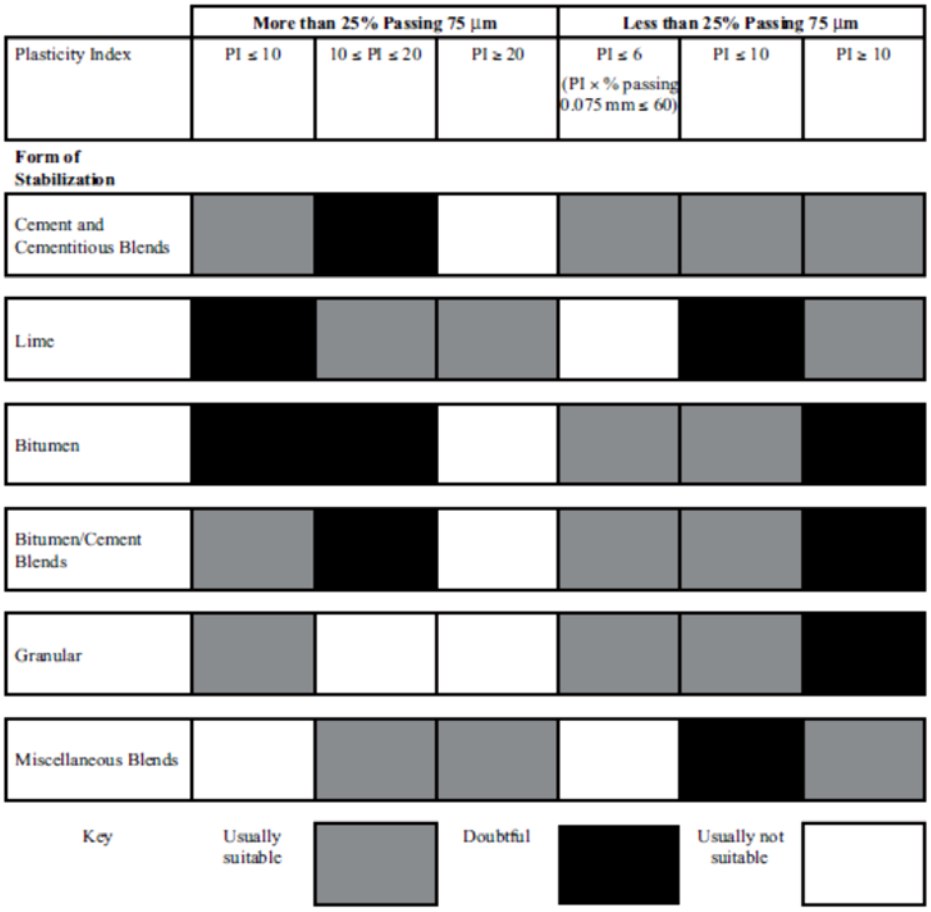

Should be taken as a broad guideline only.

Note: The above forms of stabilization may be used in combination, for example, using lime stabilization to dry out materials and reduce their plasticity, making them suitable for other methods of stabilization.

Figure 3. Guide to selecting stabilization method (Originally from Austroads 1998 and modified by Hicks 2002)

Table 1. Recommended cement contents for different soil types (PCA 1995)

AASHTO soil classification	Unified soil classification	Normal range of cement requirements		Cement content for moisture-density test, % by weight	Cement contents for wet-dry and freeze-thaw tests, % by weight
		% by volume	% by weight		
A-1-a	GW, GP, GM, SW, SP, SM	5-7	3-5	5	3-5-7
A-1-b	GM, GP, SM, SP	7-9	5-8	6	6-4-8
A-2	GM, GC, SM, SC	7-10	5-9	7	5-7-9
A-3	SP	8-12	7-11	9	7-9-11
A-4	CL, ML	8-12	7-12	10	8-10-12
A-5	ML, MH, CH	8-12	8-13	10	8-10-12
A-6	CL, CH	10-14	9-15	12	10-12-14
A-7	MH, CH	10-14	10-16	13	11-13-15

Durability of chemically stabilized materials to freeze-thaw cycles has been studied by many researchers in laboratory setting. The testing involves either determining loss of material during freeze thaw cycles and/or measuring unconfined compressive strength/California bearing ratio (CBR) after a certain number of freeze thaw cycles. Previous research indicated that portland cement stabilized materials generally show superior performance than any other chemical stabilizer (e.g., Parsons and Milburn 2003, Henry et al. 2005). A few studies indicated improvements with non-traditional stabilizers such as Soil-Sement (polymer emulsion) products (e.g., Collins 2011). Mixed information was found with fly ash stabilized fine-grained and coarse-grained soils. For e.g., Berg (1998) studied freeze-thaw performances of reclaimed hydrated fly ash activated aggregate materials, and found that the materials did not survive over ten laboratory freeze-thaw cycles. The percentage fly ash additive levels in these materials varied from about 15% to 20%. However, some field studies documented therein showed that these materials did perform well, even though they break down during the freeze-thaw action. Results presented by Bin-Shafique et al. (2010) were similar to Berg (1998), in terms of performance of fly ash stabilized soils. Bin-Shafique et al. (2010) indicated that fly ash stabilized soils lost up to 40% of the strength due to freeze-thaw cycles, although they did not experience significant strength loss during wet-dry cycles. The swell potential of the stabilized expansive soil was greater due to freeze-thaw cycles. However, even after the strength loss, the fly ash stabilized mixture had about three times more strength than an unstabilized soil. Khoury and Zaman (2007) investigated the effect of freeze-thaw cycles on cement kiln dust (CKD), class C fly ash, and fluidized bed ash (FBA) stabilized aggregates. Results indicated that the resilient modulus values of these mixtures decreased with increasing freeze thaw cycles. Comparisons with no stabilizer were not provided in that study. It is mentioned therein that CKD stabilized base materials deteriorated faster than fly ash and FBA stabilized base materials.

Stabilization of aggregates, sand, and silt soils using foamed asphalt also showed good performance on unpaved roadways (Castedo and Wood 1983, Collings et al. 2004, Kendall et al. 2001). The foamed asphalt is produced by a process in which water is injected into the hot bitumen resulting in immediate foaming. The foam expands to approximately 15 times its original volume forming foam with high surface area and low viscosity, and is mixed with aggregate in its foamed state (Kendall et al. 2001 and Muthen 1998). Foamed asphalt can offer a cheaper means of mixing asphalt/bitumen into soils compared to emulsified asphalt. Information of freeze-thaw durability of these mixtures is not well documented in the literature. White et al. (2007) conducted field full depth reclamation of granular shoulders with foamed asphalt, which indicated increase in CBR of the stabilized layer shortly after stabilization but started rutting after one year. Freeze-thaw testing indicated that the material can expand by about 18%, but the percent loss during freeze-thaw was however not significant.

A recent Iowa DOT research study (TR-582) by Gopalakrishnan et al. (2010) conducted a laboratory study investigating the use of ethanol based liquid type bio-fuel by-products with high and low lignin contents. Their study results indicated that the by-products are effective in stabilizing Iowa Class 10 soils (CL or A-6(8)) with excellent resistance to moisture degradation. By-products with high lignin content performed better than with low lignin content. The authors of that study indicated that additional research is warranted to evaluate the freeze-thaw durability of the stabilized soils.

Use of lignosulfonates to treated unpaved gravel roads is documented in the literature (Cook 2002 and Bushman et al. 2005). Lignosulfonates are the glue found mainly in trees. During the pulping process, lignosulfonates are removed from the pulp and flushed into tanks or lagoons. The chemicals added during the pulping process determine whether it is a calcium, sodium, or ammonium lignosulfonate. The liquid is typically sold in a 50% suspended solid solution (Cook 2002). Previous research documented mixed performance information on lignosulfonate stabilized granular materials. Cook (2002) reported good performance results based on studies conducted in New York on shoulder material with no signs of erosion or distress after two years. In contrary, Bolander (1999) reported that lignosulfonates have poor durability to wet-dry and freeze-thaw cycle. White et al. (2007) studied performance of stabilized granular shoulders with polymer and soybean oil by-product materials. Results from their study did not show considerable improvement, but recommended needing additional durability testing.

Table 2 shows typical elastic moduli for geomaterials that are chemically stabilized with hydrated lime, PC, and asphalt.

Table 2. Typical elastic moduli for chemically stabilized geomaterials (SHRP 1993)

Material Type	Unconfined Compressive Strength, UCS (psi)	Elastic Modulus, E (psi)
Hydrated Lime Stabilized	< 250	5,000 – 100,000
	250 – 500	10,000 – 150,000
	> 500	15,000 – 200,000
Asphalt Stabilized	< 300	10,000 – 300,000
	300 – 800	25,000 – 800,000
	> 800	50,000 – 1,500,000
Portland cement Stabilized	< 750	50,000 – 1,500,000
	750 – 1,250	100,000 – 3,000,000
	> 1,250	150,000 – 4,000,000

Mechanical Stabilization (Blending)

Mechanical stabilization by mixing/blending coarse-grained granular materials with wet fine grained subgrade soils and compaction can provide a stable working platform and foundation layer under pavements (Christopher et al. 2005). The mechanically stabilized layer can potentially exhibit lower plasticity, lower frost-heave potential, and higher drainage characteristics compared to subgrade soils (Kettle and McCabe 1985, Rollings and Rollings 1996). Based on laboratory testing, Kettle and McCabe (1985) found that the magnitude of reduction in frost-heave is related to the coarse-aggregate content and the type of aggregate used in the mechanically stabilized layer. Further, support capacity of a mechanically stabilized layer is influenced by the degree of saturation and the percentage of clay-particles present in the mixture (Hopkins et al. 1995). Therefore, post-construction changes in saturation (in part due to freeze-thaw) must be considered in properly understanding the long-term performance of a mechanically stabilized layer. Hopkins et al. (1995) indicated that a soil-aggregate mixture must be designed to have a Kentucky California bearing ratio ≥10 in soaked condition but cautioned

that this limiting condition must be viewed as very approximate. Freeze-thaw durability of mechanically stabilized (by blending) materials is not well documented in the literature.

Geosynthetic Stabilization

Geosynthetics have been used in roadway foundation layers for separation, filtration, lateral drainage, and reinforcement purposes (Berg et al. 2000). The mechanisms by which geosynthetics provide reinforcement when placed at the subbase and subgrade interface include lateral restraint or confinement of aggregate material, and increase in bearing capacity. Previous research has documented the following benefits of using geosynthetics in roadways (Berg et al. 2000, Giroud and Han 2004a, Giroud and Han 2004b, Powell et al. 1999):

- Reduction of the intensity of stress on the subgrade.
- Increase the bearing capacity of the subgrade.
- Preventing the subgrade fines from pumping into the base.
- Preventing contamination of the base materials allowing for more open graded, free-draining aggregates.
- Reducing the depth of excavation required for the removal of unsuitable subgrade materials.
- Reducing the thickness of the aggregate layer required to stabilize the subgrade.
- Minimize disturbance of the subgrade during construction.
- Minimize maintenance and extend the life of the pavement.
- Prevents development and growth of local shear zones and allows the subgrade to support stresses close to the plastic limit while acting as if it is still in the elastic limit.

Two types of geosynthetics are commonly used: geotextiles and geogrids. There are two types of geotextiles (woven and non-woven) and both act primarily as separation layers between strata to prevent the upward migration of fine-grained particles from the subgrade into aggregate layers. The non-woven geotextiles can also provide lateral drainage. Polymer geogrids act primarily as reinforcement by providing lateral restraint or confinement of aggregate layers above subgrade. Some pictures of geotextiles and geogrids are shown in Figure 4 and Figure 5, respectively.

Figure 4. Woven geotextile (left) and non-woven geotextile (right) placed at subgrade/aggregate layer interface

Figure 5. Triaxial (left) and biaxial (right) polymer geogrids placed on the subgrade

Giroud and Han (2004a) presented a theoretical method to predict rutting behavior of unpaved roadways by calibrating the method using experimental results. In this method, the subgrade is assumed as saturated, has low permeability, and behaves in an undrained manner. The following equation was developed for calculating gravel layer thickness:

$$h = \frac{0.868 + (0.661 - 1.006J^2)\left(\frac{r}{h}\right)^{1.5}}{f_E} \log N \; X \left[\sqrt{\frac{P/(\pi r^2)}{mN_c f_C CBR_{sg}}} - 1\right] r \quad (1)$$

where, h = required base course thickness (m); J = geogrid aperture stability modulus (mN/^{o}); N = number of axel passages; P = wheel load (kN); r = radius of equivalent tire contact area (m); *m* = bearing capacity mobilization coefficient; N_c = bearing capacity factor; f_c = factor equal to 30 kPa; and CBR_{sg} = CBR of subgrade soil. For unreinforced unpaved roads, J = 0 and N_c = 3.14. For geotextile-reinforced unpaved roads, J = 0 and N_c = 5.14. For geogrid-reinforced unpaved roads, J > 0 and N_c = 5.71. The bearing capacity mobilization coefficient, *m*, is calculated using the following equation:

$$m = \left(\frac{s}{f_s}\right)\left\{1 - \xi \exp\left[-\omega\left(\frac{r}{h}\right)^n\right]\right\} \quad (2)$$

where, s = rut depth (mm); and f_s = factor equal to 75 mm rut depth. ζ, ω, and n are parameters equal to 0.9, 1.0, and 2, respectively, based on the experimental data used for calibration. The bearing capacity mobilization coefficient, m, cannot be greater than unity. If m > 1, the base course thickness must be increased or a smaller allowable rut depth is selected.

To calculate the required base course thickness for specific site conditions, the second equation is first used to calculate m using an assumed base course thickness and then the base course thickness h is calculated using the first equation and is compared to the assumed h value. The process is repeated until the assumed base course thickness value in the first step equals the calculated value in the second step.

The limitations of this method are the following:

- The method was validated for Tensar biaxial geogrids and geotextiles products only.
- Only aperture stability modulus of less than or equal to 0.8 mN/^{o} can be used.
- Tensioned membrane effect is not taken into account.

A recent Iowa DOT study (TR-531) on granular shoulder material stabilization indicated that rut depths measured in field compared well with rut depths predicted using the Giroud and Han (2004) method (White et al. 2007).

Henry (1996) provided a literature review of using geotextiles to mitigate frost effects in soils, by using them as capillary barriers and drainage layers. It is indicated therein that soil particle size distribution, wettability, and for some products the material thickness influence will influence the performance. Hoover et al. (1981) evaluated frost-heave properties of geosynthetic (spun-bounded polyethylene and polypropylene material) reinforced silty clay soil. Their results

indicated that sample with two layers of geosynthetic heaved much less than sample with one and no geosynthetic. It was hypothesized that capillary barrier and reinforcement are possible reasons for reduced heave.

Geocell Reinforcement

Geocells are three-dimensional, honeycomb-shaped soil-reinforcing geosynthetics composed of polymeric materials and are primarily used for confinement of granular material. Geocells are placed at grade, in-filled with granular material, and compacted. The cellular structures of the geocells provide lateral and vertical confinement and tensioned membrane effect, thereby increasing the bearing capacity and providing a wider stress distribution (Rea and Mitchell 1978). As a result, rutting or permanent deformations under traffic loading can be reduced. Typically, the geocell-base/subbase system is underlain by a geotextile to separate the infilled base/subbase material from the subgrade.

US Army Corps of Engineers first studied the use of geocells to reinforce unpaved roads with poorly graded sand soils in the 1970s (Webster 1979). Yuu et al. (2008) and Pokharel (2010) summarized previous experimental (lab and field) and analytical studies conducted using geocells. Some key aspects of geocell reinforcement that have been studied include (Pokharel 2010): (a) influence of geometric ratio (i.e., height to diameter) of geocell, (b) failure mechanisms, (c) properties of geocell, (d) effectiveness of geocell, (e) loading area, position, and type, (f) infill density, and (h) type and size of geocell. A design methodology to estimate required base layer thickness over unreinforced or geosynthetic-reinforced layers was proposed by Giroud and Han (2004). This design methodology was extended for geocell reinforcement by Pokharel (2010). Several studies (Bathurst and Karpurapu, 1993; Latha and Murthy, 2007, Mengelt et al., 2000; Pokharel, 2010) have investigated the shear strength and stiffness properties of geocell reinforced geomaterials in laboratory environments, but only limited studies (Webster, 1979; Webster, 1981; White et al., 2011a) have assessed performance in situ. Freeze-thaw durability performance of geocells will primarily depend on the permeability characteristics of the infill granular material, but studies on the durability performance of geocells are not well documented. Henry et al. (2005) built test sections in Vermont (Figure 6), but conclusive results related to freeze-thaw durability in those sections was not provided.

Figure 6. Geocells placed over non-woven geotextile on a test section in Vermont (Henry et al. 2005)

Fiber Reinforcement

Previous research studies (e.g., Gray and Ohashi 1983, Consoli et al. 1998, Santoni and Webster 2001, Kaniraj and Havanagi 2001, Consoli et al. 2003, Newman and White 2008) on discrete fiber reinforced natural and chemically stabilized soils have generally shown improvements in soil shear strength, bearing capacity, ductility, toughness, and resistance to rutting. Gray and Ohashi (1983) reported that the failure mechanism of a fiber-reinforced soil depends on the acting average effective stress. Failure occurs through slippage of fibers up to a critical stress and as the stresses increase, failure is governed by the tensile strength of the fiber element (Consoli et al. 2011). Santoni and Webster (2001) reported that in unconfined compressive strength tests, the fiber reinforced soil yielder higher shear strengths due to development of tension in the fibers with increasing strains. Consoli et al. (2003) indicated that the fiber content, orientation of fibers with respect to the shear surface, and the elastic modulus of the fibers influences the contribution of the reinforcement to the shear strength. In Iowa loess, Hoover et al. (1982) found that inclusion of fibers decreased freeze-thaw volumetric changes on the order of 40% compared to soil with no fibers.

Improvement of engineering properties from fiber reinforcement depends on the fiber material type (e.g., polypropylene or polyetheylene), fiber type (e.g., fibrillated or monofilament), fiber length, fiber aspect ratio (i.e., length to diameter), fiber content, fiber orientation, and original geomaterial properties. Fiber reinforcement that is used in conjunction with chemical stabilization offsets the brittle behavior induced by chemical stabilization in favor of ductile behavior; which is characterized by increased toughness (i.e., the ability to endure stresses at

high strains) (Consoli et al., 1998; Consoli, et al., 2009; Consoli, et al., 2010; Consoli et al., 2011). There have been several laboratory and theoretical studies into fiber-reinforced geomaterials (Al-Refeai, 1991; Andrawes et al., 1980; Benson and Khire, 1994; Fletcher and Humphries, 1991; Freitag, 1986; Gray and Ohashi, 1983; Michalowski and Čermák, 2003; Sadek et al., 2010), however there are limited field studies (Grogan and Johnson, 1994; Newman and White, 2008; Santoni and Webster, 2002). Pictures of construction from an airfield construction project in Australia are shown in Figure 7.

Santoni and Webster (2002) evaluated the efficacy of polypropylene fibers in various lengths for stabilization of sandy soil. Their study indicated that increasing fiber contents from 0.6 to 1.0 percent (by dru weight of soil) significantly increases the engineering properties of the sandy soil. Fiber lengths greater than 2 in. were not found to significantly improve soil properties and proved more difficult to work with in both laboratory and field experiments. In their study, fibrillated fibers yielded better results over tape, monofilament, and mesh fibers. Their field observations indicated that it was necessary to treat a fiber stabilized soil surface using emulsion to prevent fiber pullout from traffic.

Figure 7. Polypropylene fibers (left) and distribution of fibers and mixing with cement (right) (Newman and White 2008)

High-Energy Impact Roller Compaction

Application of high-energy impact roller (IR) compaction technology to earthwork and stabilization projects in Iowa has been limited primarily to concrete pavement recycling projects, but is recently seeing increased interest. IR is essentially a non-circular-shaped, tow-behind solid steel compactor that typically varies in weight from about 9 to 15 tons. Picture of an IR manufactured by Impact Roller Technology company in Plattsmouth, Nebraska is shown in Figure 8.

The dynamic impact compaction energy is transferred to the soil by means of the lifting and falling motion of the non-circular rotating mass. The type of roller depends on the soil type and moisture regime and depth of treatment needed. The rollers are pulled at relatively high speeds (typically about 6 to 8 mph) to generate a high-impact force that reportedly can densify material

to depths greater than 6 ft, which is significantly deeper than conventional static or vibratory rollers (Clegg and Berrangé 1971). One disadvantage of this technology is that the high-impact forces disturb (i.e., loosen) the top 0.25 to 1.5 ft of the surface so the top layer needs additional compaction with conventional rollers. The vibrations caused by the impact rollers and their effect on nearby structures (e.g., underground utilities/pipe lines or nearby building structures) are important to consider with this technology. Some case studies indicated that the vibration effect is minimal beyond 30 to 45 ft from the impact source (Bouazza and Avalle 2006).

The range of applications of IR is broad and includes the following:

- In situ densification of existing fill, collapsible sands, landfill waste, chemically-stabilized soils, mine haul roads, and bulk earthwork
- Thick lift compaction
- Existing pavement rubblization to create a new subbase
- Construction of water storage and channel banks in the agricultural sector

Figure 8. High energy impact compaction (HEIC) roller manufactured by Impact Roller Technology in Plattsmouth, Nebraska

Stiffness-Based QA/QC Methods

Stiffness based quality control (QC) and quality assurance (QA) in situ tests provide performance data which can be input into mechanistic and mechanistic-empirical pavement designs. This section discusses the stiffness based QC and QA in situ tests that are used in this project: light weight deflectometer, falling weight deflectometer, dynamic cone penetrometer, and roller-integrated compaction monitoring.

Light Weight Deflectometer and Falling Weight Deflectometer

The light weight deflectometer (LWD) and the falling weight deflectometer (FWD) are dynamic load in situ tests that are used to determine elastic modulus. Elastic moduli are calculated from the Boussinesq solution for homogeneous, elastic half-space (Boussinesq, 1883). LWD tests apply lower applied contact stresses (about 30 psi or less) than FWD testing (up to 150 psi). FWD tests are often performed with an array of deflection sensors spaced away from the loading source to develop deflection basin data to assess the stiffness/modulus of the subsurface layers down to a depth of about 6 ft.

FWD equipment is trailer-mounted and pulled with a suitable vehicle. LWD devices come in an enclosed box and can be carried in a truck. Although the methodology of the LWD and FWD tests is similar, different manufacturers use different type of measurement sensors to measure deflections (e.g., geophones, accelerometers, or seismometers). For LWD testing, some devices assume a constant load while some devices use a load cell to measure the applied load. These differences between device configurations affect the modulus value. LWDs are generally setup with 8 in. or 12 in. diameter plates, while FWDs are generally setup with 12 in. and 18 in. diameter plates. The modulus values are affected by the plate diameter and applied contact stresses. Additional information about factors affecting the dynamic modulus values is documented in Vennapusa and White (2009).

Deflection basin data can be useful in comparing FWD measurements over time. Example data from Salour and Erlingsson (2012) are shown in Figure 9, which shows low values during the thawing period and recovery after thawing.

Dynamic Cone Penetrometer

The dynamic cone penetrometer (DCP) is an intrusive test which involves driving a cone tip into the soil by lifting an 17.6 lb sliding hammer to 22.6 in. drop height and then releasing it. The total penetration for a given number of blows is then measured and recorded as mm/blow. Based on the measurements, CBR or shear strength of soil layers down to about 3 ft can be determined. ASTM D6951 provides correlations between California Bearing Ratio (CBR) and mm/blow for different soil types. Correlations between DCP and undrained shear strength and modulus are documented in the literature.

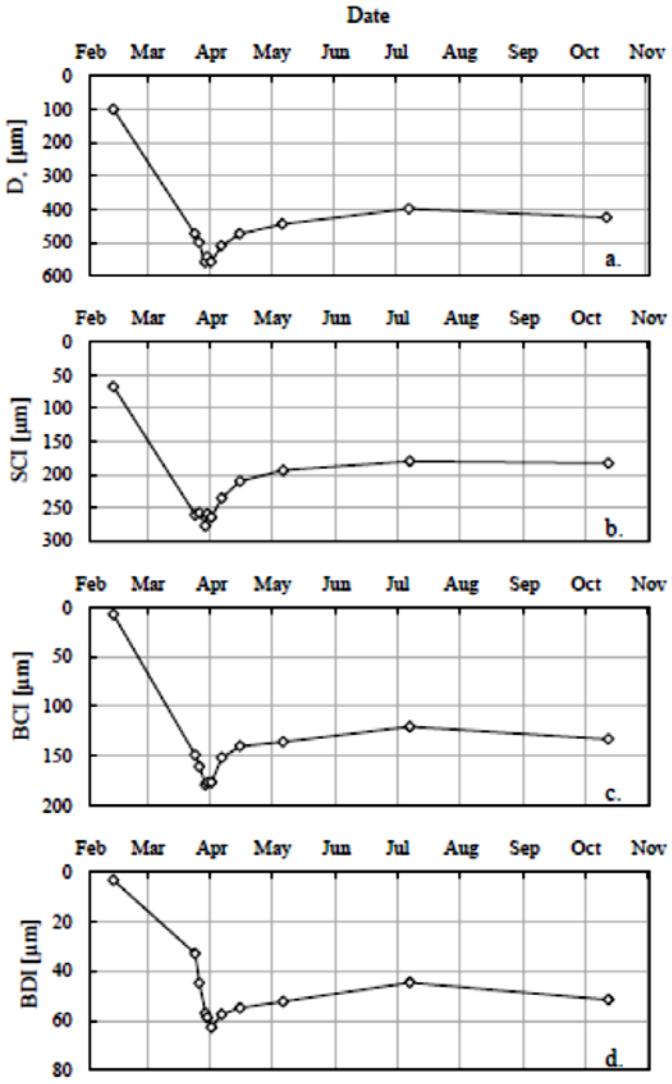

Figure 9. Variation in FWD deflection basin parameters over an year (lowest point in all graphs depicting the thawing time) from a low volume road site in Southern Sweden (Salour and Erlingsson 2012)

Roller Integrated Compaction Monitoring

Roller-integrated compaction monitoring (RICM) (or also referred to as intelligent compaction or continuous compaction control) refer to sensor measurements integrated into compaction machines. This technology allows recording and color-coded real time display of integrated measurement parameter values on rollers virtually over 100% of the compacted area, including roller operation parameters, position (based on global positioning system (GPS) measurements), and roller-ground interaction parameter values. Several manufacturers currently offer RICM technologies on smooth drum vibratory roller configurations for compaction or mapping of granular materials and non-vibratory roller configurations for non-granular materials (Figure 10).

The compaction measurement values (noted next to the manufacturer names in Figure 10) vary between the manufacturers and technologies. These current technologies calculate: (1) an index value based on a ratio of selected frequency harmonics for a set time interval for vibratory compaction, (2) ground stiffness or dynamic elastic modulus based on a drum-ground interaction model for vibratory compaction, or (3) a measurement of rolling resistance calculation from machine drive power for vibratory and non-vibratory compaction (White et al. 2011b). Research over the past three decades on this technology indicated that these measurements generally correlate well with modulus or stiffness based measurements (such as FWD or LWD modulus) than with dry density or CBR measurements (White et al. 2011b). This technology can be used on gravel/base/subgrade layers to detect areas of concern to apply appropriate stabilization to improve the conditions.

Figure 10. Pictures of various roller manufacturers, roller configurations, and display software's with RICM technology (note that this does not represent a complete list)

CHAPTER 3: TEST METHODS AND ANALYSIS

Laboratory Testing

Index Properties and Soil Classification

Particle-size analysis tests were conducted on soil samples collected from field in accordance with ASTM D422-63. Atterberg limits tests (i.e., liquid limit—LL, plastic limit—PL, and plasticity index—PI) were performed in accordance with ASTM D4318-10 using the dry preparation method. Using the results from particle size analysis and Atterberg limits tests, the samples were classified using the unified soil classification system (USCS) in accordance with ASTM D2487-10 and American Association of State Highway and Transportation Officials (AASHTO) classification system in accordance with ASTM D3282-09.

Moisture-Density Relationship

Laboratory Proctor compaction tests were performed in accordance with ASTM D698-10. Proctor methods were performed based on the material gradations. An automated, calibrated mechanical rammer was used to perform these tests. Proctor tests on stabilized materials (with fly ash and cement) were conducted on samples mellowed for about 30 min.

Unconfined Compressive Strength

Unconfined compressive strengths were determined for soils stabilized with cementitious material. All soils were compacted into cylindrical specimens under standard Proctor energy following 30 min compaction time delay. Soils with gradations meeting the criteria for method A of ASTM D698 were compacted into 2 in. diameter by 2 in. high cylindrical specimens. Soils with gradations meeting the criteria method B of ASTM D698 were compacted into 4 in. diameter by 4.584 in. high cylindrical specimens. Samples were immediately extruded from their molds, sealed in clear plastic wrap and aluminum foil, and placed in an oven set to 100° F for 7 days to cure. Samples that could not maintain their shapes after compaction (i.e., cohesionless samples) were not extruded from their molds until 24 hours after compaction before sealing and placement into the oven. After samples had cured at 100° F for 7 days, unconfined compressive strength test were conducted using a strain rate of approximately 1% per minute. Select samples were vacuum saturated in accordance with Dempsey and Thompson (1973) prior to testing.

Freeze/Thaw Testing

ASTM D5918-96 “Standard Test Methods for Frost Heave and Thaw Weakening Susceptibility of Soils” is the index test for estimating the relative degree of frost-susceptibility of soils used in pavement systems. Johnson (2012) fabricated the laboratory equipment used in this study for conducting freeze-thaw tests (Figure 11). Six-inch samples are fully saturated before they are put into the freezer, then they are connected to Mariotte water supplies that maintain the water pressure. Two disks that connect to the water bath are applied to control the temperatures at the

top and bottom. Lasers are set above the samples to measure the heave values during testing, and the computer program records the outputs of thermocouples, pressure transducers, and lasers. The entire freeze-thaw process takes around 120 hours, and includes two 8-hour freezing cycles (Table 1).

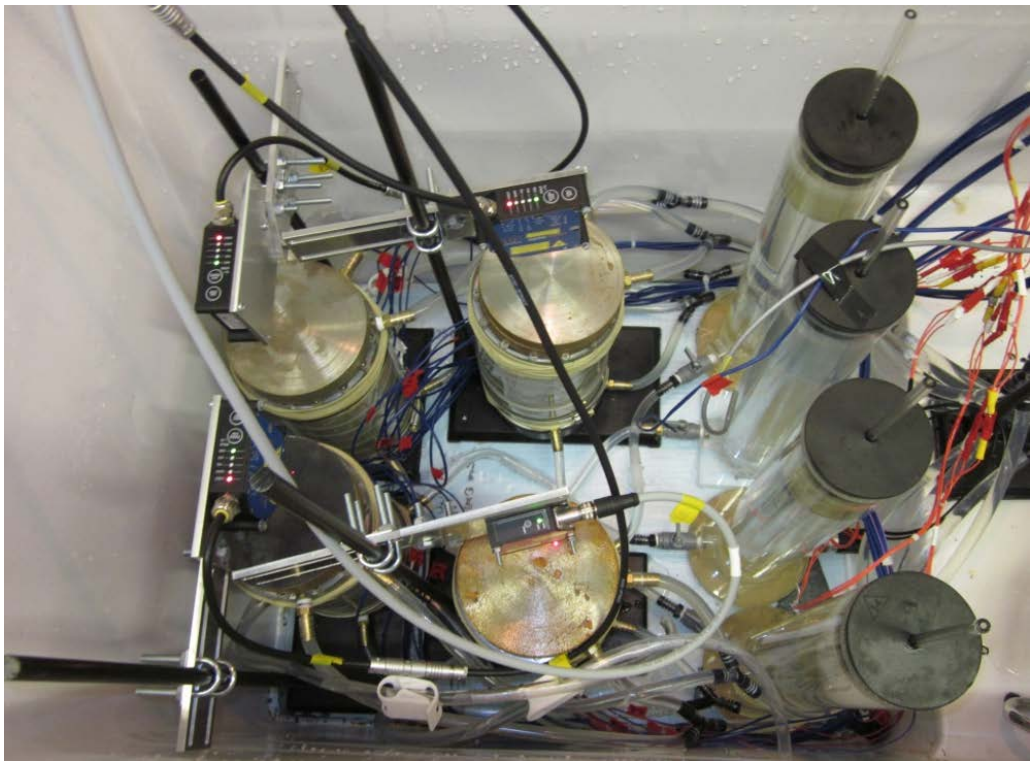

Figure 11. Freeze-thaw test assembly in the freezer (Zhang 2013)

Table 3. Freezing schedule based on computer program settings (Zhang 2013)

Day	Elapsed Time, hr	Top Plate Temperature, °C	Bottom Plate Temperature, °C	Comments
1	0	3	3	24-hr conditioning
2	24	3	3	First 8-hr freeze
	32	12	0	Freeze to bottom
3	48	12	3	First thaw
	64	3	3	—
4	72	3	3	Second 8-hr freeze
	80	12	0	Freeze to bottom
5	96	12	3	Second thaw
	112 to 120	3	3	—

Field Testing

Light Weight Deflectometer

LWD tests were conducted using a Zorn LWD setup with an 11.81 in. diameter plate and a 27.9 in. drop height (Figure 12). The tests were conducted by performing three seating drops and three loading drops, per ASTM E2835-11. Elastic modulus values were determined using Eq. 1:

$$E = \frac{(1-\eta^2)\sigma_0 r}{D_0} \times F \quad (1)$$

where: E = elastic modulus (psi), D_0 = measured deflection under the plate (in.), η = Poisson's ratio (assumed as 0.4), σ_0 = applied stress (psi), r = radius of the plate (in.), and F = shape factor depending on stress distribution (assumed as 8/3 for testing on granular materials (see Vennapusa and White 2009). In this report, LWD modulus values obtained on granular subbase layers are presented as $E_{SB\text{-}LWD}$.

Figure 12. Zorn light weight deflectometer

Falling Weight Deflectometer

FWD tests were conducted using a Kuab FWD setup with an 11.81 in. diameter loading plate by applying one seating drop and four loading drops (Figure 13). The applied loads varied from about 5,000 to 15,000 lb in the four loading drops. The actual applied forces were recorded using a load cell, and deflections were recorded using seismometers mounted on the device, per ASTM D4694-09. Elastic modulus values from the FWD tests ($E_{SB\text{-}FWD}$) were determined using Eq. 1. The loading plate used in the test is a segmented (four-part) plate. According to the manufacturer, the segmented plate results in a uniform stress distribution. Therefore, F = 2 was used in determination of $E_{SB\text{-}FWD}$.

To compare $E_{SB\text{-}FWD}$ from different test locations at the same applied contact stress, the deflection values at each test location were normalized to a 14,000 lb load.

Figure 13. Kuab falling weight deflectometer

Dynamic Cone Penetrometer

DCP tests were conducted in accordance with ASTM D6951-03 (Figure 14). The tests involve dropping a 17.6 lb hammer from a height of 22.6 in. and measuring the resulting penetration depth. California bearing ratio (CBR) values were determined using either Eq. 2 or 3, as appropriate, where the penetration index (PI) is in units of mm/blow.

$$CBR = \frac{292}{PI^{1.12}} \text{ for all soils with CBR} > 10 \quad (2)$$

$$CBR = 1/(0.017019\ DPI)^2 \text{ when CBR} < 10 \text{ on CL soils} \quad (3)$$

Figure 15 shows a sample DCP-CBR profile and cumulative blows with a depth profile that illustrates the procedure used to determine layer depths and calculate the CBR of subbase layers. In this report, CBR values of different layers are presented as follows:

- Existing granular subbase layer – CBR_{SB}
- Crushed limestone MSB layer – $CBR_{C\text{-}MSB}$
- Recycled MSB layer – $CBR_{R\text{-}MSB}$
- Reclaimed subbase layer – CBR_{RSB}
- Mechanically stabilized subgrade layer – CBR_{MSS}
- Subgrade layer – CBR_{SG}

Figure 14. Dynamic cone penetrometer

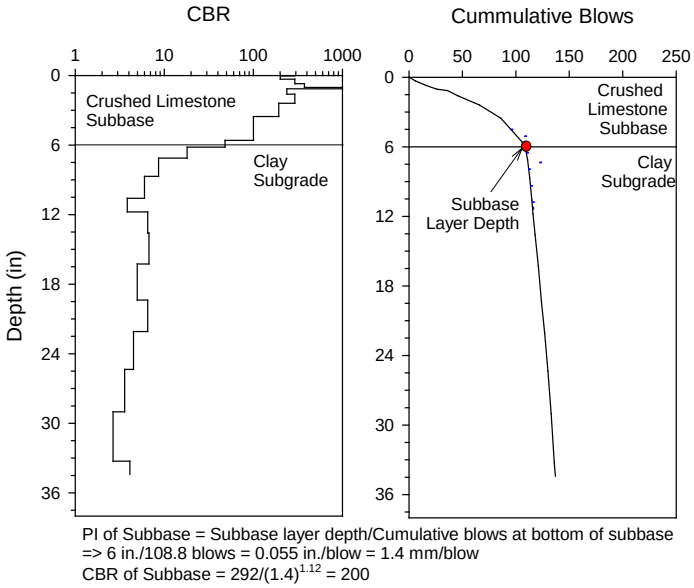

Figure 15. Example of DCP-CBR and cumulative blows with depth profiles and procedure followed to determine CBR for each layer

Roller-Integrated Compaction Monitoring (RICM) Systems

Roller-integrated compaction monitoring (RICM) (i.e., intelligent compaction or continuous compaction control) is the recording and color-coded, real-time display of integrated measurement parameter values on rollers including roller operation parameters, position, roller-ground interaction parameter values, and/or temperature. Intelligent Compaction (IC) technologies consist of machine-integrated sensors and control systems that provide a record of drum-soil interaction and automatically adjust vibration amplitude and/or frequency and/or speed using drum feedback during the compaction process. Without the automatic feedback system, the technology is commonly referred to as continuous compaction control (CCC). Although most RICM technologies are vibratory-based systems applied to self-propelled smooth drum rollers, RICM technologies have also been applied to vibratory double drum asphalt compactors and self-propelled padfoot machines.

Four rollers equipped with different RICM systems were used on this project and were all operated in the CCC mode of operation:

- Caterpillar CS683 (Figure 16) vibratory smooth drum roller equipped with compaction meter value (CMV) and machine drive power (MDP) measurement technologies.
- Caterpillar CS74 (Figure 16) vibratory smooth drum roller equipped with CMV and MDP measurement technologies.
- Sakai SV610D (Figure 18) vibratory smooth drum roller equipped with compaction control value (CCV) measurement technology.
- Hamm HD120VV (Figure 19) vibratory double smooth drum roller equipped with CMV measurement technology.

(a) (b)

Figure 16. (a) Caterpillar CS683 vibratory smooth drum roller, (b) Caterpillar on-board display monitor

(a) (b)

Figure 17. (a) Caterpillar CS74 vibratory smooth drum roller, (b) Caterpillar on-board display monitor

(a) (b)

Figure 18. (a) Sakai SV610D vibratory smooth drum roller, (b) Sakai on-board display monitor

(a) (b)

Figure 19. (a) Hamm HD120VV vibratory smooth drum roller, (b) Hamm on-board display monitor

CMV is a dimensionless compaction parameter developed by Geodynamik that depends on roller dimensions, (i.e., drum diameter and weight) and roller operation parameters (e.g., frequency, amplitude, speed), and is determined using the dynamic roller response (Sandström 1994). CMV is calculated using Eq. 4:

$$\mathrm{CMV} = \mathrm{C} \cdot \frac{\mathrm{A}_{2\Omega}}{\mathrm{A}_{\Omega}} \tag{4}$$

where: C = constant (300), $A_{2\Omega}$ = the acceleration of the first harmonic component of the vibration, and A_{Ω} = the acceleration of the fundamental component of the vibration (Sandström and Pettersson 2004). To differentiate CMV obtained from the CS683, CS74, and HD120 rollers, the values are presented as CMV_{CS683}, CMV_{CS74}, and CMV_{HD120}, respectively.

CCV measurement system was developed by Sakai and is similar to CMV. However, it is calculated using the acceleration data from first sub-harmonic ($A_{0.5\Omega}$), fundamental (A_{Ω}), and higher-order harmonics ($A_{1.5\Omega}$, $A_{2\Omega}$, $A_{2.5\Omega}$, $A_{3\Omega}$). According to the manufacturer, as the ground stiffness increases and roller drum starts to enter into a "jumping" motion, vibration accelerations at various frequency components are developed (Scherocman et al. 2007). CCV is calculated using Eq. 5, using

$$\mathrm{CCV} = \left[\frac{\mathrm{A}_{0.5\Omega} + \mathrm{A}_{1.5\Omega} + \mathrm{A}_{2\Omega} + \mathrm{A}_{2.5\Omega} + \mathrm{A}_{3\Omega}}{\mathrm{A}_{0.5\Omega} + \mathrm{A}_{\Omega}} \right] \times 100 \tag{5}$$

Caterpillar's MDP technology relates mechanical performance of the roller during compaction to the properties of the compacted soil. Detailed background information on the MDP system is provided by White et al. (2005b). Controlled field studies documented by White and Thompson (2008), Thompson and White (2008), and Vennapusa et al. (2009) verified that MDP values are empirically related to soil compaction characteristics (e.g., density, stiffness, and strength). MDP is calculated using Eq. 6:

$$\mathrm{MDP} = \mathrm{P_g} - \mathrm{Wv}\left(\sin\alpha + \frac{\mathrm{A}'}{\mathrm{g}} \right) - \left(\mathrm{mv} + \mathrm{b} \right) \tag{6}$$

where: MDP = machine drive power (lb-ft/s), P_g = gross power needed to move the machine (lb-ft/s), W = roller weight (lb), A' = machine acceleration (ft/sec^2), g = acceleration of gravity (ft/s^2), α = slope angle (roller pitch from a sensor), *v* = roller velocity (ft/s), and m (lb-ft/ft) and b (lb-ft/s) = machine internal loss coefficients specific to a particular machine (White et al. 2005).

MDP is a relative value referencing the material properties of the calibration surface, which is generally a hard compacted surface (MDP = 0 lb-ft/s). Positive MDP values therefore indicate material that is less compact than the calibration surface, while negative MDP values indicate material that is more compacted than the calibration surface (i.e., less roller drum sinkage). The

MDP values obtained from the machine were recalculated to range between 1 and 150, and these re-scaled values are referred to as MDP*. While the original MDP values decrease in increasing compaction, the MDP* values increase with increasing compaction. To differentiate MDP* obtained from the CS683 and CS74 rollers, the values are presented as MDP^*_{CS683} and MDP^*_{CS74}, respectively.

In-ground Earth Pressure Cells

Earth pressure cells (EPC) with measurement ranges between 0 and 600 kPa (Figure 20) were used to measure the increase in in situ vertical stresses. The EPCs in this study were semiconductor-type sensors manufactured by Geokon (3500 series). They are made of two stainless steel plates welded together around their periphery and separated by a narrow gap filled with de-aired hydraulic fluid.

The array of EPCs in this study comprised 7 EPCs installed between 0 and 4 ft. below the surface of the subgrade. EPCs were installed beneath the 6th St South test section. Each EPC was placed and levelled on top of a mound of silica sand (Figure 9b) and then backfilled with silica sand (Figure 9c). The GPS coordinates for each EPC were measured following placement (Figure 9d).

The deepest most EPC was installed first by excavating a level pit to about 4 ft. below the surface of the subgrade. Following EPC placement, the pit was backfilled with an approximately 6 in. to 12 in. thick lift of compacted, natural subgrade over which another EPC was placed. Alternating layers of EPCs and lifts of compacted, natural subgrade were placed until the surface of the subgrade was reach. Test section construction required that the subbase layer above subgrade be mixed in place with a reclaimer which could potential damage EPCs placed at or near the surface of the subgrade. For this reason, the shallowest EPC (i.e., subgrade surface) was installed after the test section subbase layer had been mixed and compacted by the contractor.

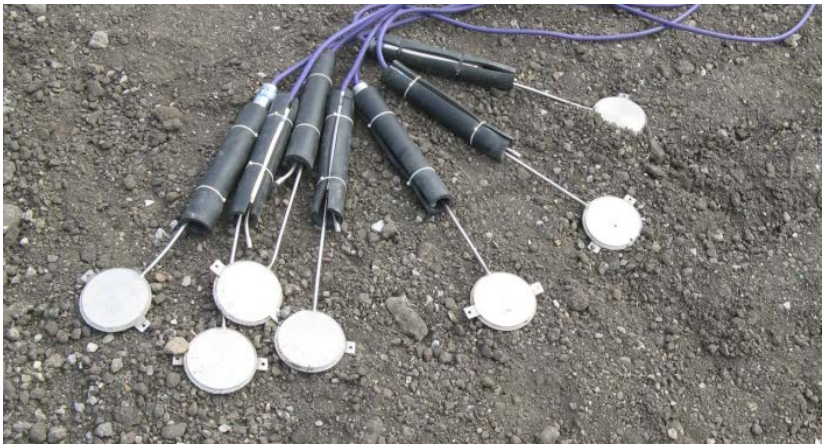

Figure 20. Earth pressure cells (EPC)

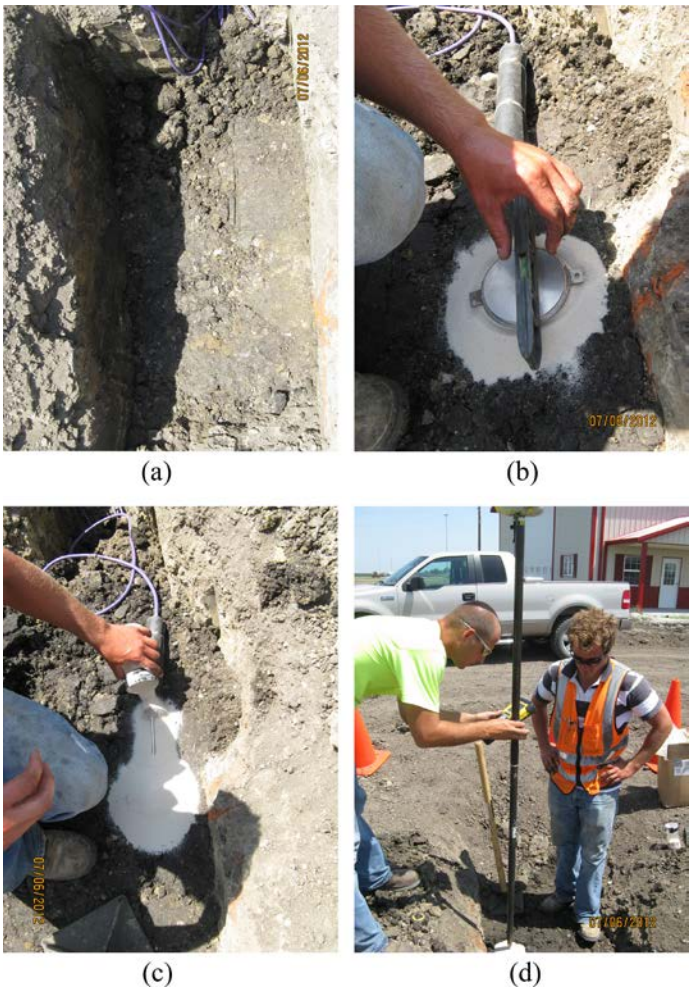

Figure 21. EPC installation on 6th St. South: (a) excavation; (b) level placement on top of silica sand; (c) backfilling with silica sand; and (d) measurement of actual elevation using RTK-GPS

In Situ Permeability

Two different in situ permeameter test devices were used in the evaluation of the permeability of the granular subbase materials. Details about the two devices are provided below.

Air Permeameter Test

The air permeability test (APT) device weights about 40 lbs and consists of a contact ring, differential pressure gauges, precision orifice, and a programmable digital display (Figure 22). A compressed gas source is connected to the device and acts as the permeant. Air was used as the permeant in this study. The device is described in detail in White et al. (2014). The test involves control and measurement of gas pressure on the inlet and outlet sides of a precision orifice and calculation of gas flow rate to determine the saturated hydraulic conductivity (K_{sat}). A detailed description of the derivation of K_{sat} is provided in White et al. (2007). The K_{sat} is derived by

expanding Darcy's Law considering the compressibility of gas, viscosity of gas, and gas flow under partially saturated conditions. K_{sat} was calculated using Equation 7:

$$K_{sat} = 2834.65 \times \left[\frac{2\mu_{gas} Q P_1}{r\, G_o \left(P_1^{\,2} - P_2^{\,2} \right)} \right] \times \frac{\rho\, g}{\mu_{water} \left(1 - S_e\right)^2 \left(1 - S_e^{((2+\lambda)/\lambda)}\right)} \qquad (7)$$

where, Ksat = saturated hydraulic conductivity (ft/day); μgas = dynamic viscosity of the gas = 1.83E-05 PaS for air; Q = volumetric flow rate (cm3/s); P1 = absolute gas pressure on the soil surface (Pa) = Po(g) x 9.81 + 101325; Po(g) = gauge pressure at the orifice outlet (mm of H20); P2 = atmospheric pressure = 101325 Pa; r = radius at the outlet (4.45 cm); Go= Geometric factor (dimensionless factor, see White et al. 2007), Se = effective water saturation [Se = (S – Sr)/(1-Sr)]; λ = Brooks-Corey pore size distribution index; Sr = residual water saturation; S = water saturation; ρ = density of water (g/sm3); g = acceleration due to gravity (cm/s2); and μwater = absolute viscosity of water = 0.01 gm/cm-s.

For the results presented in this study, λ is assumed as 0.3 and S_r is assumed as 1% in the calculations. S was determined assuming a constant dry unit weight of 120 pcf (based on laboratory Proctor testing on crushed limestone subbase material), specific gravity of 2.70, and an average moisture content of 1% based on measurements from a few locations (varied between 0.1% to 1.5. A parametric study by White et al. (2014) indicated that λ and S_r values have negligible influence on K_{sat} for S < 20%. $P_{o(g)}$ and Q values have the maximum influence on K_{sat} values and are measured during the test.

Figure 22. In situ APT setup for determination of saturated hydraulic conductivity

Mn/DOT Permeameter

Mn/DOT permeameter test (MPT) was originally developed by Clyne et al. (2001). The test device shown in Figure 23 was fabricated at Iowa State University, based on the design provided

in Clyne et al. (2001). The MPT procedure involved scraping loose material from the test surface (Figure 24a), excavating an approximately 5 in. diameter by 4 in. deep hole using confining base plate with a 5 in. diameter hole as a guide (Figure 24b), and then performing a constant-head permeability test. Material excavated from the hole was collected for moisture content and grain size analyses. Water was allowed to drain out of the MPT internal reservoir and into the hole (Figure 24c) such that a constant total head of approximately 2 in. was maintained in the hole (Figure 24d). Flow volume into the hole was measured at intervals ranging from 20 seconds to 2 minutes depending on apparent flow rate out of the hole. K_{sat} was calculated using Equation 8.

$$K_{sat} = \frac{2834.65 \times CQ}{2\pi H^2 \left(1 + \frac{C}{2}\left(\frac{a}{H}\right)^2\right)} \tag{8}$$

where, K_{sat} = saturated hydraulic conductivity (ft/day); C = shape factor = $0.02(H/a)^{2/3}$; Q = flow rate (cm^3/s); H = total head within hole (cm); and a = radius of hole (cm).

Figure 23. In situ MPT setup for determination of saturated hydraulic conductivity

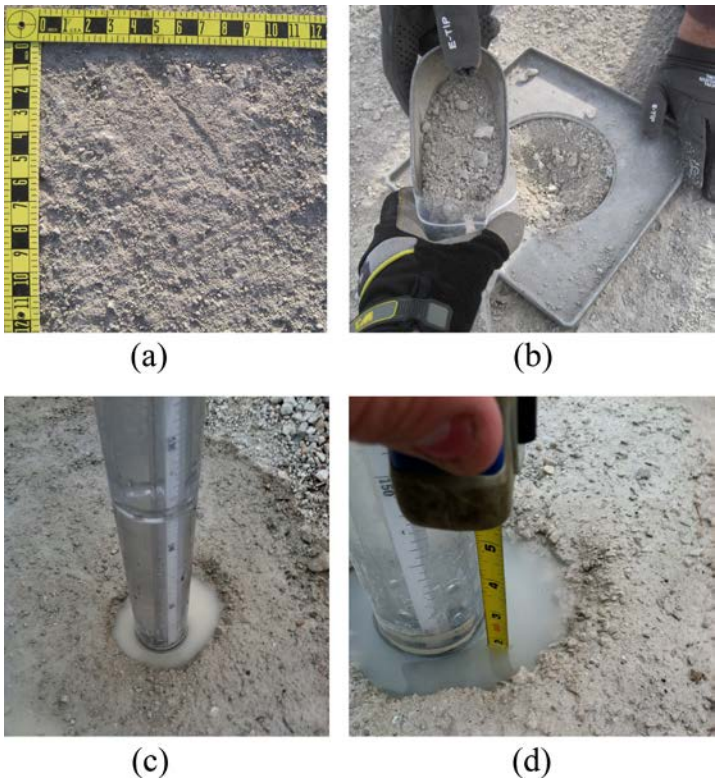

Figure 24. MPT testing included (a) clearing the test surface, (b) excavating a hole for testing, (c) using the testing apparatus to release water into the hole; and (c) maintaining a constant head of approximately 2 in.

Statistical Data Analysis

CBR values of the MSB layer (CBR_{MSB}) and the immediate underlying stabilized and unstabalized layers ($CBR_{Underlying\ Layer}$) determined from DCP test results were compared with $E_{SB\text{-}FWD}$ measurements (which represents composite dynamic stiffness) obtained at the surface. A multiple regression analysis was performed by incorporating CBR_{MSB} and $CBR_{Underlying\ Layer}$ into a multivariate linear regression model to predict $E_{SB\text{-}FWD}$, as shown in Eq. 9:

$$E_{SB\text{-}FWD} = b_0 + b_1 (CBR_{MSB}) + b_2 (CBR_{Underlying\ Layer}) \quad (9)$$

where b_0, b_1, and b_2 are regression coefficients. The statistical significance of each parameter was assessed using the p-value and t-value statistics (p-value < 0.05 and t-value > 2 are considered as statistically significant). The purpose of this multiple regression analysis was to assess the relative influence of subgrade and gravel layers on the surface FWD measurements using Eqs. 10 and 11:

$$\text{Influence of MSB (\%)} = \frac{b_1}{b_1 + b_2} \times 100 \quad (10)$$

$$\text{Influence of the Underlying layer (\%)} = \frac{b_2}{b_1 + b_2} \times 100 \quad (11)$$

CHAPTER 4: MATERIAL PROPERTIES

Different subbase and subgrade geomaterials, geosynthetics, and chemical stabilizers were used on this project. This chapter provides a summary of the material properties and results from laboratory testing.

Pavement Foundation Materials

Four geomaterials were used in construction of the test sections—crushed limestone modified subbase (MSB), recycled MSB, reclaimed subbase (reclaimed from existing granular subbase layer), and natural subgrade. The crushed limestone material was imported from Martin Marietta Quarry in Ames and recycled material was imported from Mannats in Ames. The recycled material consisted of a mixture of recycled asphalt and concrete. Table 4 summarizes gradation, plasticity, and compaction properties for the three four materials. Figure 25 shows grain size distribution curves for the four geomaterials and Figure 26 shows standard proctor curves for the four geomaterials.

Table 4. Summary of gradation, plasticity, and compaction properties for geomaterials

Parameter	Crushed Limestone MSB	Recycled PCC MSB	Reclaimed Subbase	Subgrade
Specific Gravity	2.75 (Assumed)	2.60 (Assumed)	2.60 (Assumed)	2.70 (Assumed)
Gravel Content (%) (>4.75 mm)	65.2	61.3	37.2	5.3
Sand Content (%) (4.75 – 75 μm)	58.1	34.0	48.4	39.7
Silt + Clay content (%) (<75μm)	7.1	4.7	14.4	55.0
D_{10} (mm)	0.3	0.3	0.02	0.12
D_{30} (mm)	3.6	2.6	0.45	0.01
D_{60} (mm)	10.1	11.6	4.0	-
Coefficient of Uniformity, C_u	33.7	39.7	160	-
Coefficient of Curvature, C_c	4.3	2.0	2.0	-
Liquid Limit, LL (%)	NP	NP	NP	33
Plasticity Index, PI (%)				15
AASHTO	A-1-a	A-1-a	A-1-a	A-6(5)
USCS Group Symbol	GP-GM	GW	SM	CL
USCS Group Name	Poorly graded gravel with silt and sand	Well graded gravel	Silty sand with gravel	Sandy lean clay
Maximum Dry Unit Weight, $\gamma_{d,max}$ (pcf)	136.2	116.6	124.7	115.8
Optimum Moisture Content, w_{opt} (%)	8.9	11.1	7.9	13.5

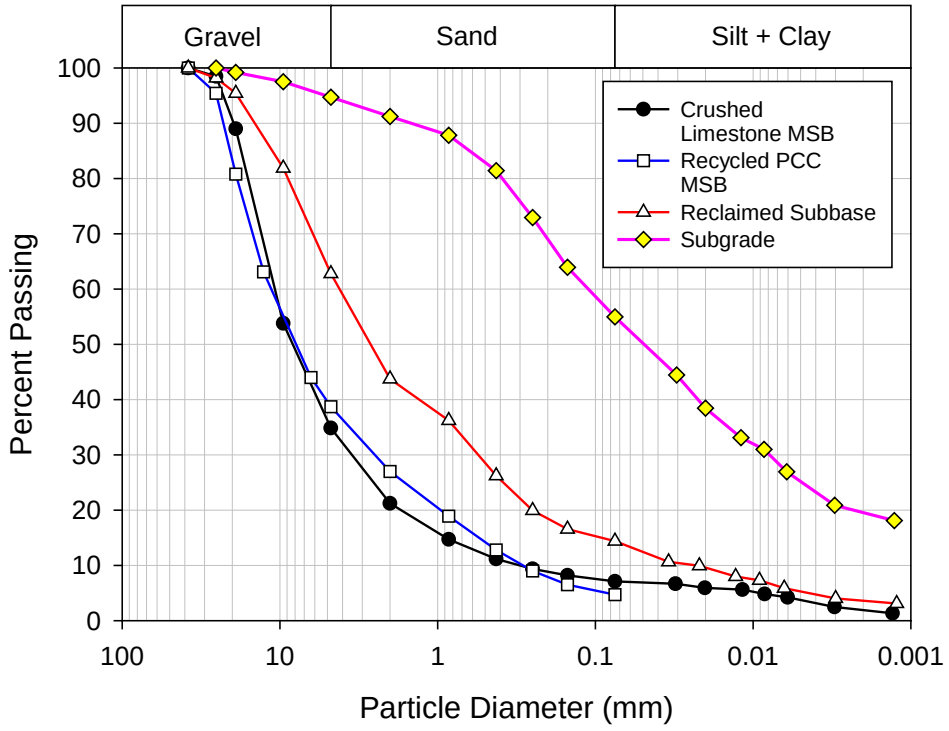

Figure 25. Grain size distribution curves from particle size analysis on geomaterials

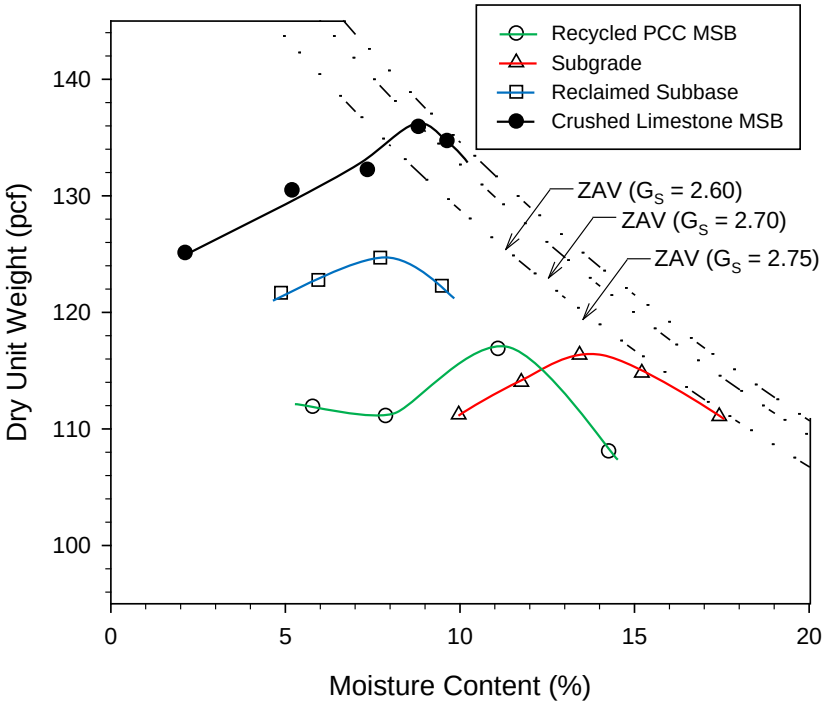

Figure 26. Moisture-dry unit weight relationships from standard Proctor tests on geomaterials

Stabilization/Reinforcement Materials

Geosynthetics

Four geosynthetic materials—4 in. and 6 in. high geocells, woven and NW geotextiles, biaxial and triaxial polymer geogrids—were used in this study.

Geocell sections were composed of individual cells that were approximately rhomboidal in shape. The sides of each cell had perforations for drainage. Table 5 summarizes the key features and properties of the geocells. Per AASHTO M 288, the NW geotextile classified as a Class II geotextile and the woven geotextile classified as a Class I geotextile. Table 6 summarizes the key features and properties for the geotextiles. Biaxial polymer geogrids had rectangular shaped aperture openings and triaxial polymer geogrids had triangular shaped aperture openings. Table 7 summarizes the key features and properties of the polymer geogrids.

Table 5. Summary features of geocell products (from manufacturer)

Feature	4 in. geocell	6 in. geocell
Manufacturer	Strata Systems, Inc.	
Product ID	StrataWeb™ 20 (4 in. depth)	StrataWeb™ 20 (6 in. depth)
Material Description	Virgin, non-thermally degraded high-density-polyethylene	
Minimum Polymer Density (ASTM D 1505)	58.7 lb./ft.^{3}	
Environmental Stress Crack Resistance (ASTM D 5397)	>400 hours	
Carbon Black Content (ASTM D 1603)	Minimum 1.5% (by weight)	
Nominal Sheet Thickness Before Texturing (ASTM D 5199)	50 mil (± 5%)	
Nominal Sheet Thickness Before Texturing (ASTM D 5199)	60 mil (± 5%)	
Rhomboidal texturing surface density	140 to 200 per in.^{2}	
Cell Cross-Sectional Dimensions (Expanded)	10.2 in. x 8.8 in.	
Cell Area (Expanded)	44.8 in.^{2}	
Cell Height	4 in.	6 in.
Section Size (Expanded)	8.4 ft. x 21.4 ft.	
Seam Peel Strength	320 lb.	480 lb.
Section Weight	57 lb.	86 lb.

Table 6. Summary features of geotextile fabric products (from manufacturer)

Feature	NW Geotextile	Woven Geotextile
Manufacturer	Propex, Inc.	
Product ID	GEOTEX 601	GEOTEX 350ST
Material description	Polypropylene staple fiber, needlepunched	Woven silt film geotextile
Geotextile Class (AASHTO M 288)	Class II	Class I
Section Size	15 ft. x 300 ft.	
Grab Tensile Strength (ASTM D 4632)	160 lb.	350 lb.
Ultimate Tensile Strength (ASTM D 4595)	Not available	4,500 lb./ft.
Tensile Strength at 2% Strain (ASTM D 4595)	Not available	540 lb./ft.
Tensile Strength at 5% Strain (ASTM D 4595)	Not available	1,360 lb./ft.
Elongation (ASTM D-4632)	50%	12%
Puncture (ASTM D 4833)	85 lb.	180 lb.
CBR Puncture (ASTM D 6241)	410 lb.	1000 lb.
Mullen Burst (ASTM D 3786)	280 psi	1000 psi
Trapezoidal Tear (ASTM D 4533)	60 lb.	150 lb.
UV Resistance (ASTM D 4355)	70% Retained at 500 hours.	
Apparent Opening Size (ASTM D 4491)	70 US Std. Sieve	30 US Std. Sieve
Permittivity (ASTM D 4491)	1.30 s^{-1}	0.52 s^{-1}
Permeability (ASTM D 4491)	Not available	0.05 cm/s
Water Flow Rate (ASTM D 4491)	110 gpm/$ft.^2$	40 gpm/ft^2

Table 7. Summary features of polymer geogrid products (from manufacturer)

Feature	Biaxial Polymer Geogrid	Triaxial Polymer Geogrid
Manufacturer	Tensar Earth Technologies, Inc.	
Product ID	BX4100	TX130S
Material	Polypropylene	Polypropylene
Section Size	13.1 ft. x 246 ft.	
Aperture Shape	Rectangular	Triangular
Aperture Dimensions	1.3 in. x 1.3 in.	*
Aperture Area	1.69 $in.^2$	1.09 $in.^2$
Rib Length	1.3 in.	1.3 in.
Minimum Rib Thickness	0.03 in.	0.02 in.
Ultimate Tensile Strength (ASTM D 4595)	880 lb./ft.	*
Tensile Strength at 2% Strain (ASTM D 4595)	270 lb./ft.	*
Tensile Strength at 5% Strain (ASTM D 4595)	550 lb./ft.	*
Junction Efficiency (GRI-GG2-B7)	93%	
Flexural Stiffness (ASTM D 5732)	250,000 mg-cm	*
Aperture Stability**	0.28 m-N/deg	0.03 m-N/deg
Resistance to Installation Damage in Clayey Sand (SC) (ASTM D 6637)	90%	*
Resistance to Installation Damage in well graded sand (SW) (ASTM D 6637)	83%	*
Resistance to Installation Damage in poorly graded gravel (GP) (ASTM D 6637)	70%	*
Radial Stiffness at Low (0.5%) Strain (ASTM D 6637)	*	15,075 lb./ft.
Resistance to long Term Degradation (EPA 9090)	100%	
Resistance to UV Degradation (ASTM D 4365)	100%	

*Data not available
**In accordance with U.S. Army corps of Engineers Methodology for measurement of Torsional Rigidity

Fibers

Two types of discrete fibers were used in this study, which included black monofilament polypropylene (MF-PP) fibers and white fibrillated polypropylene (PP) micro-fibers (Figure 27). The MF-PP fibers were 1 in. long by 0.1 in. wide monofilament strips of polypropylene. The PP fibers were 3/4 in. long, 0.004 in. diameter strands of polypropylene. Table 8 summarizes key features and properties for the fibers.

(a) (b)

Figure 27. (a) Black MF-PP fibers, and (b) white fibrillated PP fibers

Table 8. Summary features of fiber products (from manufacturers)

Feature	Fibrillated Polypropylene (PP) Fibers	Monofilament Polypropylene (MF-PP) Fibers
Manufacturer	Fiber Reinforced Soils, LLC	Euclid Chemical Company
Product ID	Geofibers 3610BF	PSI Fiberstrand™ 100
Description	Discrete, fibrillated fibers	Monofilament polypropylene micro-fiber
Material	Polypropylene	Polypropylene
Fiber Length	1 in.	0.75 in.
Fiber Width	0.1 in.	0.004 in. (Diameter)
Fiber Depth	0.004 in.	
Fiber Aspect Ratio (Length to Diameter)	177	188
Specific Gravity (ASTM D 762)	0.91	0.91
Water Absorption	Negligible	
Carbon Black Content (ASTM D 1603)	0.6%	*
Tensile Strength (ASTM D 2256)	40,000 psi	*
Tensile Elongation (ASTM D 2256)	15%	*
Young's Modulus (ASTM D 3822)	600,000 psi	*
Melting Point	*	320 °F
Electrical and Thermal Conductivity	*	Low
Acid and Alkali Resistance	*	Excellent

*Data not available

Fly Ash

Fly ash (FA) was imported from three sources across Iowa—Ames power plant, Muscatine power plant, and Port Neal power plant. Each FA classified as type C per ASTM C618. Diffractograms for the three FA materials are shown in Figure 28. Key compositional values from X-ray fluorescence (XRF) analysis and ASTM C618 classification are provided in Table 9.

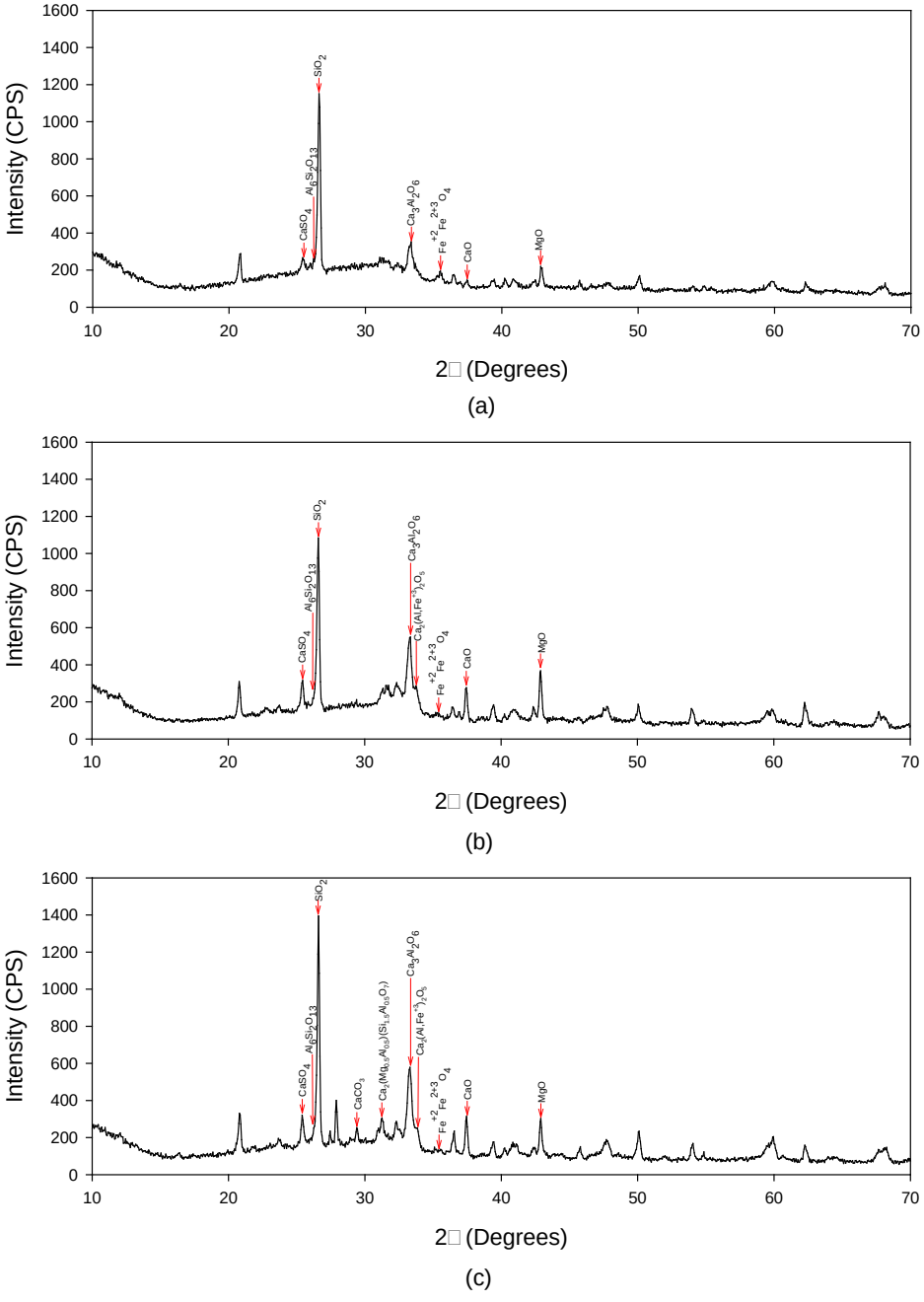

Figure 28. Diffractograms for (a) Muscatine FA, (b) Ames FA, and (c) Port Neal FA

Table 9. XRF chemical assays and classifications for FA materials

Chemical composition and other properties	Port Neal	Ames	Riverside
$SiO_2 + Al_2O_3 + Fe_2O_3$, %	61.22	56.16	64.25
CaO, %	25.3	26.4	22.9
SO_3, %	2.25	2.53	2.14
Moisture Content, %	0.2	0.1	0.2
Loss on ignition, %	1.0	1.5	0.4
ASTM C 618 Class	C	C	C
Final Set Time (minutes)	6	19	170

Set times for the FA materials are shown in Figure 29. Results indicated that the Muscatine FA material had longer set times (107 min initial and 170 min final) than Ames FA (4 min initial and 19 min final) and Port Neal FA (3 min initial and 6 min final). The set time gives an indication of the rate at which the cementation reaction products form in the FA that cements soil particles together and provides a basis for setting the compaction schedule.

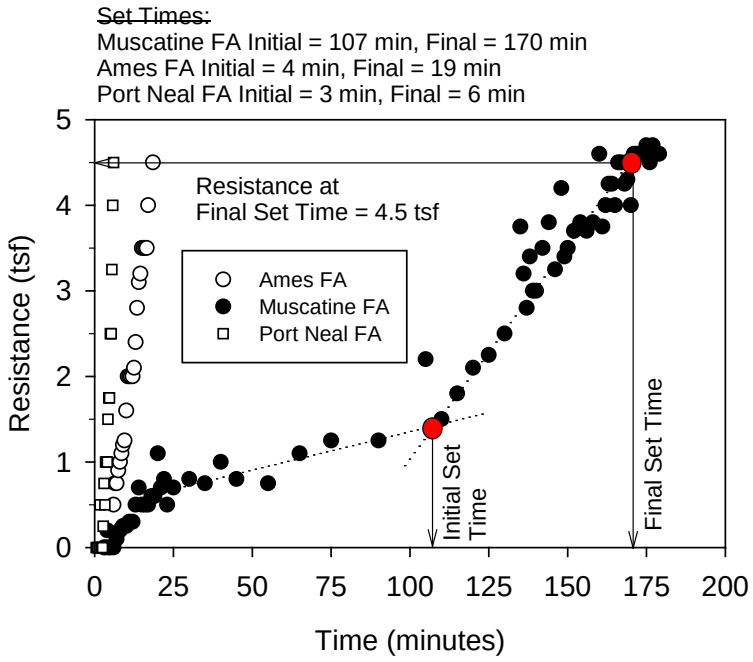

Figure 29. Set times for FA materials

Portland Cement

Type I/II Portland cement (PC) were used in this study for stabilized subgrade and reclaimed subbase materials.

Laboratory Durability Tests

Freeze-thaw and CBR tests were conducted on a total of 36 materials comprising unstabilized and stabilized materials. Table 10 provides a summary of the frost-heave and thaw-weakening susceptibility ratings for all materials. The unstabilized soils tested in this study (SM, CL, and ML) exhibited frost-heaves of 11.43 to 19.1 mm/day and post-test CBR of 0.5% to 8.8% resulting in high to very high frost susceptibility and medium to very high thaw-weakening susceptibility. The finding in grain size distribution indicated that the freeze-thaw susceptibility might be influenced by the fine contents of soils.

For all tests, the CBR pre-test values ranged from 2.8% to over 200%. The unstabilized subgrade is rated as very high thaw-weakening susceptibility based on the post-test CBR of 1.4%. The unstabilized recycled subbase resulted in a medium rating for thaw-weakening susceptibility with a post-test CBR of 8.8%.

Subgrade stabilized with fly ash yielded variable results, but generally showed improvement in post-test CBR and lower heave rates with increasing fly ash. Both the 15% Port Neal and Ames fly ash stabilized subgrade (based on dry weight of soil) reached the very low to negligible thaw-weakening susceptibility rating. Increasing the fly ash content to 20% resulted in slightly higher heave rates with medium to low frost-heave susceptibility for two fly ashes. The fly ash source was identified as a factor in the freeze-thaw susceptibility rating. Comparing the set time of the three fly ash specimens with the frost susceptibility rating shows that shorter set times resulted in reduced frost-heave and thaw-weakening for the 7-day curing duration. Tests performed on loess (ML) specimens stabilized with 15% Ames fly ash showed that curing up to 180 days before testing improved the freeze-thaw performance by both reducing the heave rate and increasing the post-test CBR.

For cement stabilized materials, heave rates for the subgrade specimens were close to 0 mm/day for both the 5% and 10% cement additional rates. For the recycled subbase, frost susceptibility decreased as the cement content increased; however, there was little improvement at 2.5% cement content. For all cement contents, the post-test CBR values were about four times lower than the pre-test CBR values.

Fibers were added to the recycled base (SM) at rates of 0.2%, 0.4%, and 0.6% (based on dry weight of soil). Results showed improvement in both reduced heave rate and increased CBR values. For this set of experiments, the post-test CBR values were all higher than the pre-test CBR values. This finding suggests that the freeze-thaw action and associated stress development in the fibers contributed to the increase in CBR values. The frost susceptibility ratings based on heave ranged from medium to high for all six combinations of fibers. At 0.6% fibers, the heave rate was reduced from about 15 mm/day to about 7 mm/day. The finding with respect to frost heave differs from Hoover's (1982) conclusions, but the finding with respect to thaw-weakening matches to the conclusion reported by Gullu and Khudir (2014).

Table 10. Summary of frost-heave and thaw-weakening tests results.

Soil	Stabilizer	Heave rate (mm/d)	Post-test CBR (%)	Pre-test CBR (%)	Frost-heave susceptibility	Thaw-weakening susceptibility
Subgrade	No stabilizer	11.43	1.4	2.8	High	Very high
	5% Ames fly ash	8.40	6.6	15.5	High	Medium
	10% Ames fly ash	6.60	9.6	44.6	Medium	Medium
	15% Ames fly ash	6.87	20.1	73.2	Medium	Negligible
	20% Ames fly ash	7.85	10.2	18.2	Medium	Low
	5% Muscatine fly ash	9.88	2.9	—	High	High
	10% Muscatine fly ash	12.32	2.6	—	High	High
	5% Port Neal fly ash	6.61	5.7	—	Medium	Medium
	10% Port Neal fly ash	8.21	11.2	15.0	High	Low
	15% Port Neal fly ash	1.96	16.9	25.8	Very low	Very low
	20% Port Neal fly ash	3.16	17.9	—	Low	Very low
	5% cement	0.02	165.8	37.3	Negligible	Negligible
	10% cement	0.07	>200.0	94.5	Negligible	Negligible
Recycled subbase	No stabilizer	15.63	8.8	4.6	High	Medium
	2.5% cement	12.70	12.8	95.6	High	Low
	3.75% cement	2.09	35.1	127.0	Low	Negligible
	5.0% cement	3.35	56.7	208.9	Low	Negligible
	7.5% cement	1.64	43.4	>200.0	Very low	Negligible
	0.2% PP	12.11	11.4	4.6	High	Low
	0.4% PP	12.75	7.8	7.3	High	Medium
	0.6% PP	6.25	16.3	5.8	Medium	Very low
	0.2% MF	10.34	12.1	4.1	High	Low
	0.4% MF	9.90	14.8	7.9	High	Low
	0.6% MF	6.94	18.4	8.6	Medium	Very low
	0.2% PP + 3.75% cement	1.31	58.2	185.5	Very low	Negligible
	0.2% PP + 3.75% cement (12-hr compaction delay)	3.83	20.3	—	Low	Negligible
	0.4% PP + 3.75% cement	0.18	127.4	>200.0	Negligible	Negligible
	0.4% PP + 3.75% cement (12-hr compaction delay)	2.98	19.8	—	Low	Negligible
	0.6% PP + 3.75% cement	1.48	120.1	>200.0	Very low	Very low
	0.2% MF+ 3.75% cement	0.75	190.5	184.9	Negligible	Negligible
	0.4% MF+ 3.75% cement	1.43	203.2	143.1	Very low	Negligible
	0.6% MF+ 3.75% cement	1.00	177.0	158.7	Negligible	Negligible
Western Iowa loess	No stabilizer	19.1	0.5	—	Very high	Very high
	15% Ames fly ash 7 days curing	14.10	7.1	—	High	Medium
	15% Ames fly ash 90 days curing	11.83	8.7	—	High	Medium
	15% Ames fly ash 180 days curing	8.27	32.0	—	High	Negligible

Note: — = data not available

Adding cement to the recycled subbase-fiber mixtures significantly reduced the heave rates. The frost susceptibility classifications of all the cement + fiber stabilized recycled subbase (no

compaction delay) ranged from very low to negligible levels. When the 0.2% PP + 3.75% cement and 0.4% PP + 3.75% cement stabilized recycled subbase specimens with a 12-hour compaction delay were tested, the frost susceptibility increased from very low or negligible to low. The addition of 3.75% cement into the fiber-soil mixtures reduced the thaw weakening susceptibility to negligible, even with the 12-hr compaction delay. The possible reason to explain these results might be cement improved the compressive strength while fibers improved the tensile strength. This finding matches to the conclusion reported by Gullu and Khudir (2014), which was fibers plus chemical stabilization can provide better freeze-thaw performance than fibers alone.

Figure 30 shows the heave rate values and ASTM D 5918 frost susceptibility classifications for all tests. Comparing 7-day and 90-day curing, thaw-weakening susceptibility of 15% fly ash stabilized loess decreased from medium to negligible. Based on these results, the improvements from longer curing times for fly ash stabilization was limited to strength improvement, and did not show significant improvement for controlling frost-heave. Figure 31 shows the corresponding CBR values and thaw-weakening susceptibility ratings for all tests.

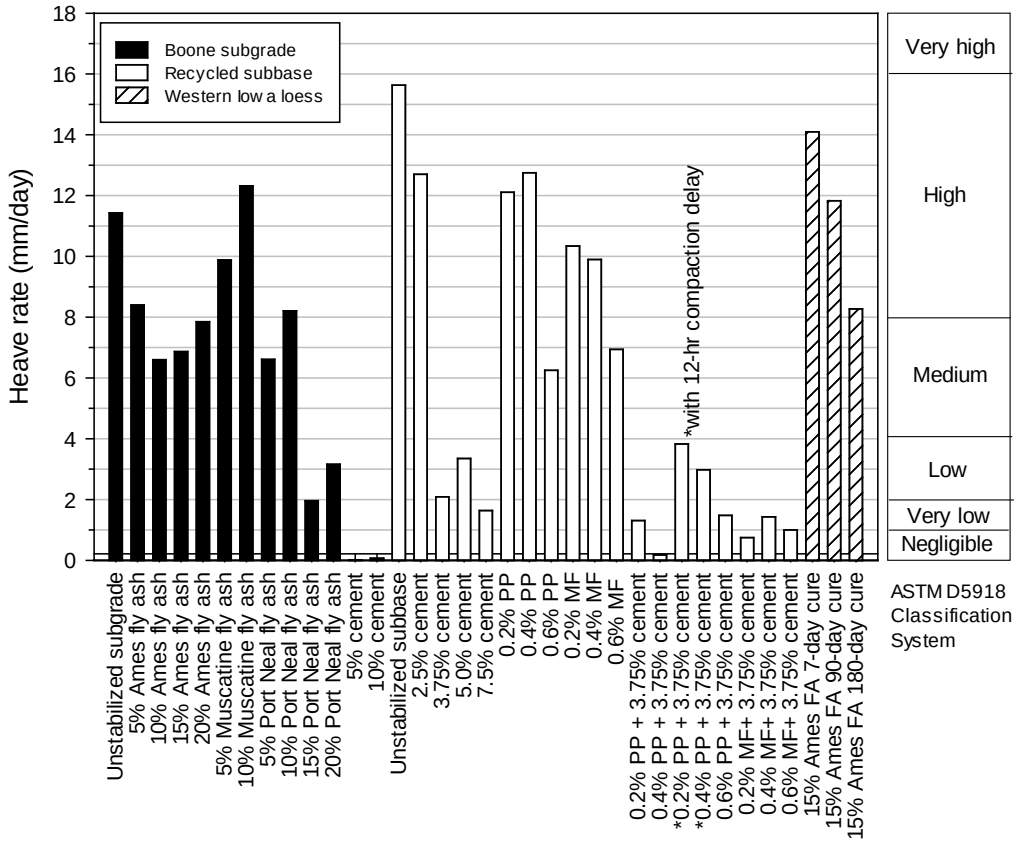

Figure 30. Comparison of frost-heave rates of all tested materials

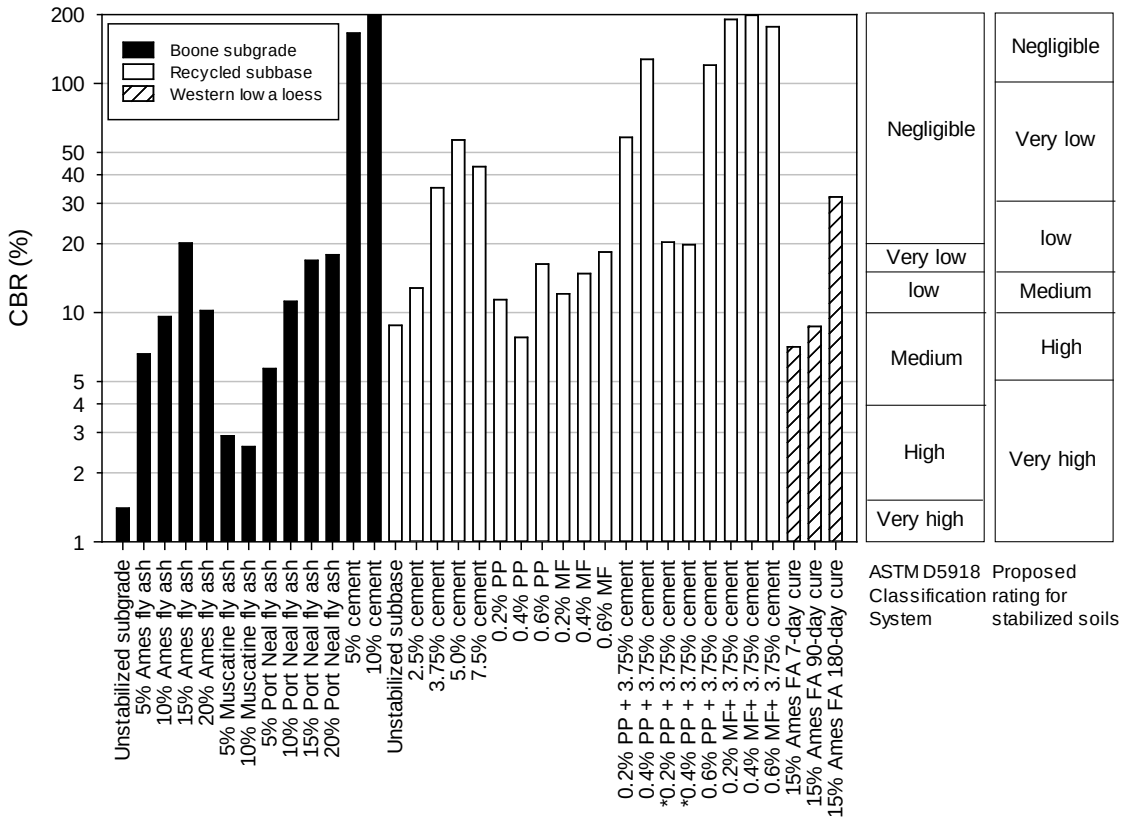

Figure 31. Post-test CBR values and corresponding frost susceptibility ratings based on ASTM and the results from this study

Relationships between frost-heave rates and CBR values are shown in Figure 32. Very low thaw-weakening susceptibility is achieved when the heave rate is less than 4 mm/day. Frost susceptibility based on frost-heave cannot predict thaw-weakening susceptibility.

Based on the ASTM D5918 frost susceptibility classification method and data from this research, an alternative thaw-weakening susceptibility classification rating is presented in Table 11. The boundary values were adjusted to reflect differences in post-CBR and heave rates for the stabilized materials. The current ASTM classification does not distinguish classifications with CBR values greater than 20. The alternative classification proposed herein identified thaw-susceptibility as negligible for post-test CBR values ≥ 100. Figure 33 shows a side-by-side comparison of the ASTM rating and the rating proposed herein for stabilized soils. The advantage of the proposed rating criteria is that it allows for more refined classification of stabilized soils.

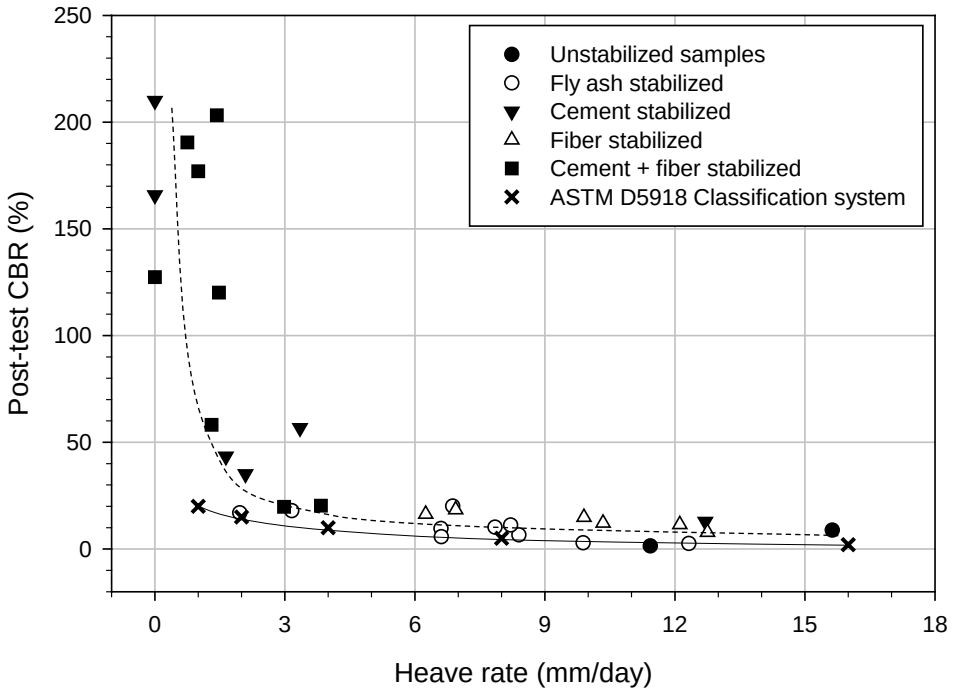

Figure 32. Relationships between Post-test CBR and measured heave rates with comparison to the ASTM D5918 criteria

Table 11. Proposed frost-heave and thaw-weakening susceptibility classification for stabilized soils based on data from this study.

Frost/thaw-weakening susceptibility classification	2nd 8-hr heave rate (mm/d)	CBR after thaw (%)
Negligible	<1	>100
Very low	1 to 2	100 to 30
Low	2 to 4	30 to 15
Medium	4 to 8	15 to 10
High	8 to 16	10 to 5
Very high	>16	<5

Figure 33 shows yet another perspective of evaluating pre and post-test CBR values for stabilized soils. Five materials, the 5% and 10% cement stabilized subgrade and the 3.75% cement with 0.2%, 0.4%, and 0.6% MF fiber stabilized specimens, presented time dependent strength gain. Freeze-thaw softening or no stiffness changes occurred for the other tested materials. Plotting the results in terms of pre and post-test CBR values shows it is difficult to predict the post-test CBR values from the pre-test measurements and supports the need to perform the freeze-thaw tests and evaluate the influence of curing time for stabilized soils.

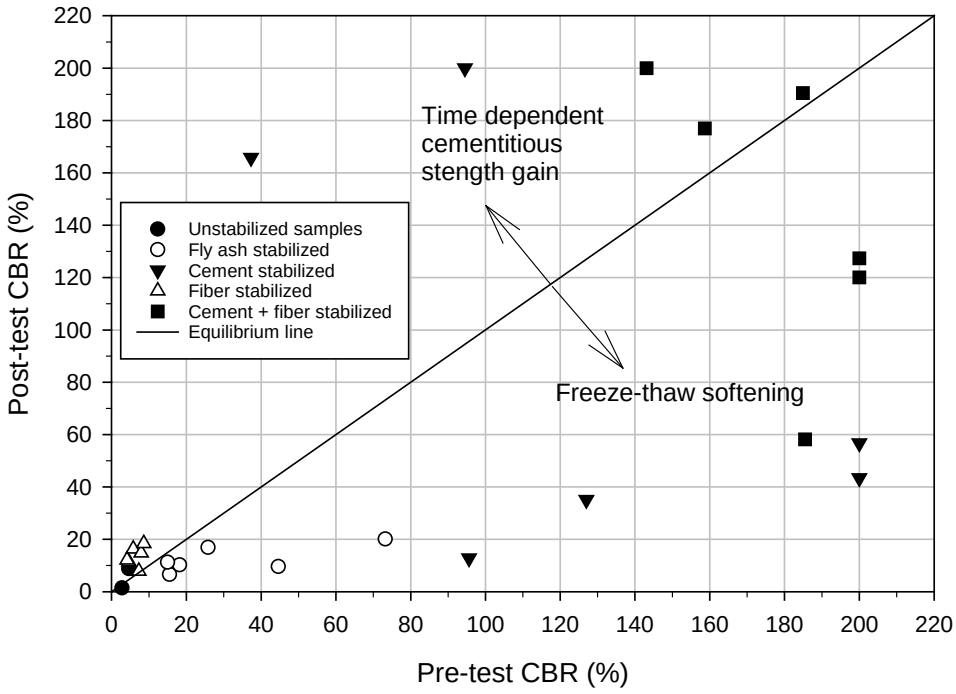

Figure 33. Comparison between pre and post-test CBR values showing the influence of time dependent strength gain for cement and cement + fiber stabilized specimens

CHAPTER 5: SITE DESCRIPTION AND TEST SECTION LAYOUT

The Central Iowa Expo (CIE) site is a 72 acre area just north of the US 30/Iowa Highway 17 interchange in Boone County, Iowa (Figure 34). The CIE site has been hosting Farm Progress shows bi-annually since 2008. This chapter presents an overview of the site conditions with historical aerial imagery of t he CIE site since 1994, subsurface conditions from soil survey information, geotechnical explorations, and field testing conducted prior to 2012 construction, and the designed test section layout for foundation layer stabilization.

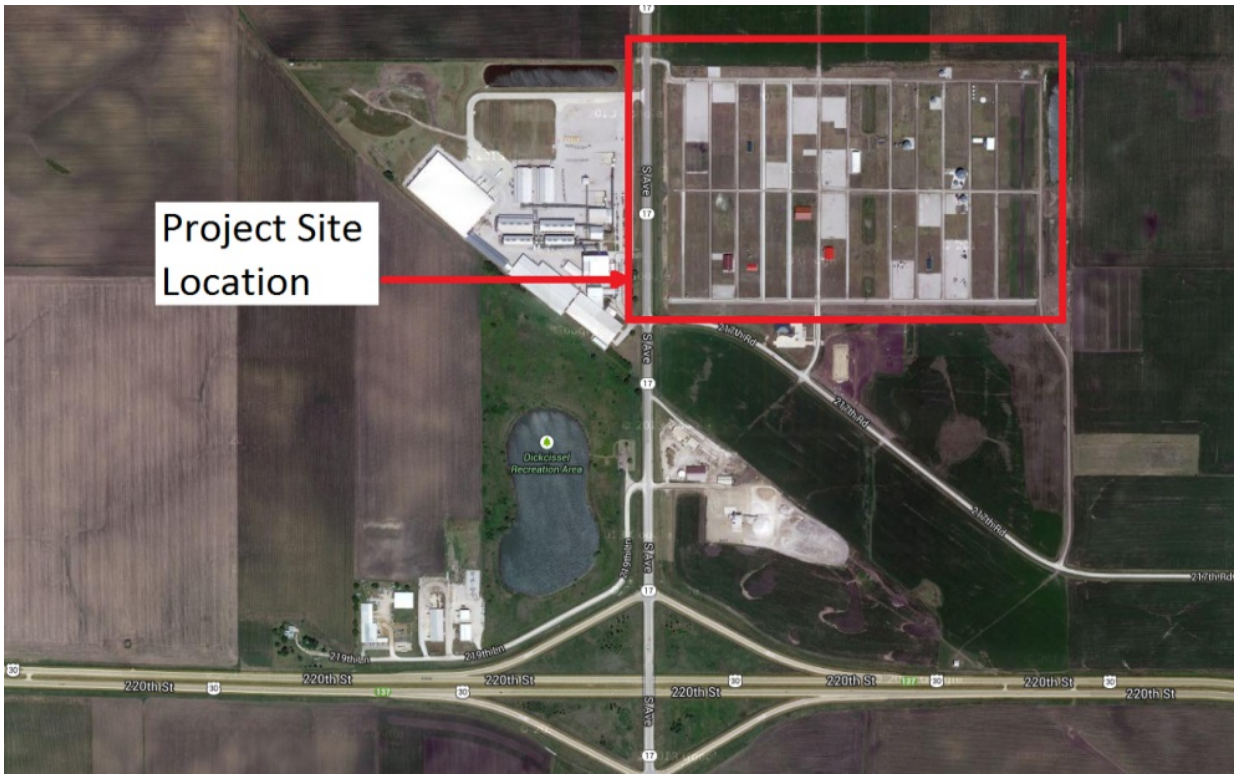

Figure 34. Aerial imagery of CIE site in Boone County, IA

Site Conditions

Historical aerial imagery of the project site at selected time intervals from 1994 to 2012 is shown in Figure 35. As can be seen in the images, grading in the north-west portion of the site began in 1994. More grading work was performed in 2007/2008 to create a 4.8 mile grid network of 12 roads oriented in North-South direction (denoted as 1st St. to 13th St. from West to East) and three roads oriented in East-West direction (denoted as South Ave., Central Ave., and North Ave.) (Figure 36). In this report, sections on each North-South road located north and south of Central Ave. are referred to as North sections and South sections, respectively.

Project drawings from 2007/2008 construction indicate that the East-West and North-South roads were topped with asphalt chipseal coating (over a nominal 6 in. granular subbase and

natural subgrade). Geogrid was installed at the interfaces of granular subbase and natural subgrade on all East-West roads and 6th St.

North Ave. and South Ave. were 24 ft. wide, and Central Ave. and 6th St. were 28 ft. wide. These roads were shaped as inverted crowns with nominal 2.0% slopes towards the centerline, where storm sewers were located at about 4 ft below grade. The remaining North-South roads were 18 ft wide, also with inverted crowns with 2.0% slopes towards the centerline.

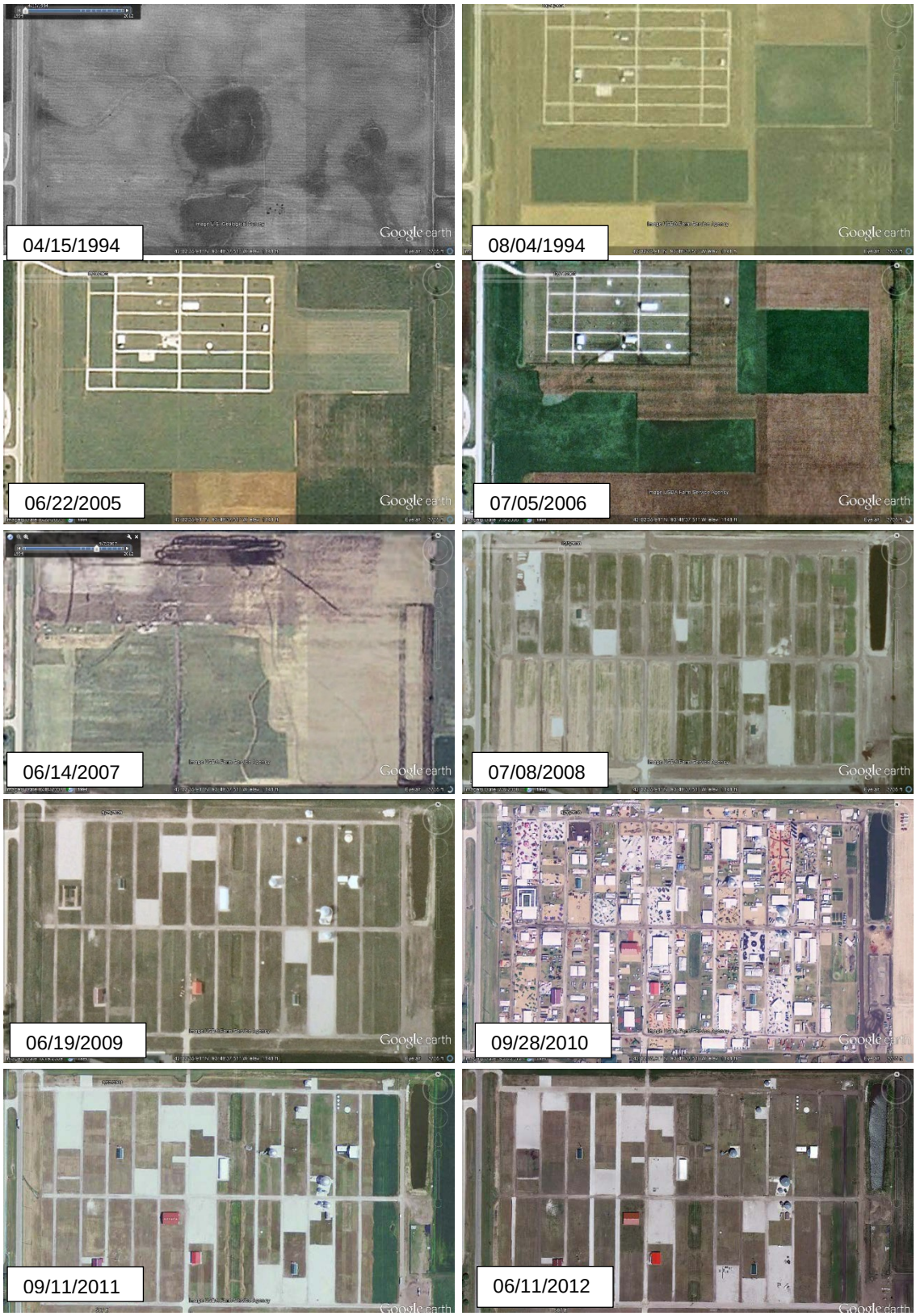

Figure 35. Historical aerial imagery from 1994 to 2012 of the CIE site

Figure 36. North-south and east-west road layout at the CIE site (aerial image from June 2012)

Field observations in April 2012 indicated that the existing roads were in poor condition with potholes, rutting, and water ponding (Figure 37). Test pits were conducted on South Ave. to observe subsurface soil conditions and obtain soil samples for preliminary testing (Figure 38). Figure 39 shows the foundation layer cross-section based on test pit observations, which consisted of an asphalt chipseal at the surface underlain by about 8 in. of granular subbase (classified as SM and A-1-a) and 12 in. of brow-gray sandy lean clay (classified as CL, A-6(5)) fill or reworked subgrade. Biaxial polymer geogrid was present at the granular subbase and subgrade interface.

Figure 37. Conditions of South Ave. in April 2012

Figure 38. Pavement foundation layer profile from test pit observations on South Ave. (April 2012)

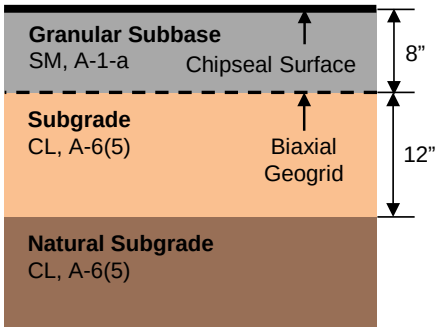

Figure 39. Existing roadway cross-section (prior to 2012 construction) on South Ave.

Subsurface Conditions

NRCS Soil Survey Information

The site is located within the Iowa's Des Moines Lobe, which typically consists of sandy lean clay glacial till deposits with random zones of high sand and/or silt content. Soils identified in the Natural Resources Conservation Service (NRCS) soil survey map (NRCS 2013) are shown in Figure 40. Summary of soil properties are provided in Table 12. Atterberg limits of the soils from NRCS (2013) are overlaid on the plasticity chart in Figure 41, which indicate the on-site soils are predominantly classified as CL. Based on soil coloring (i.e., grayish redoximorphic features), NRCS (2013) indicated that the depth to groundwater table ranges between 0 to 4 ft. of the surface in all soils expect the Okoboji mucky silt loam (identified with symbol 90). The depth to groundwater table in Okoboji mucky silt loam is > 6.5 ft.

Figure 40. NRCS soil survey map of CIE site (numbers indicate soil map unit symbol) (NRCS 2013)

Table 12. Summary of surficial soils from USDA soil survey (NRCS 2013)

Soil map unit symbol	Name	Acres	Percent Coverage	LL	PI	AASHTO
55	Nicollet loam	17.8	24.6	37.5	17.5	A-6
90	Okoboji mucky silt loam	5.2	7.2	75	20	A-7
95	Harps loam	22.4	31.1	37.5	17.5	Not available
107	Webster silty clay loam	6.5	9.0	47.5	22.5	A-7
138	Clarion loam	12.9	17.9	32.5	10	A-4
507	Canisteo silty clay loam	7.3	10.2	45	17.5	A-7

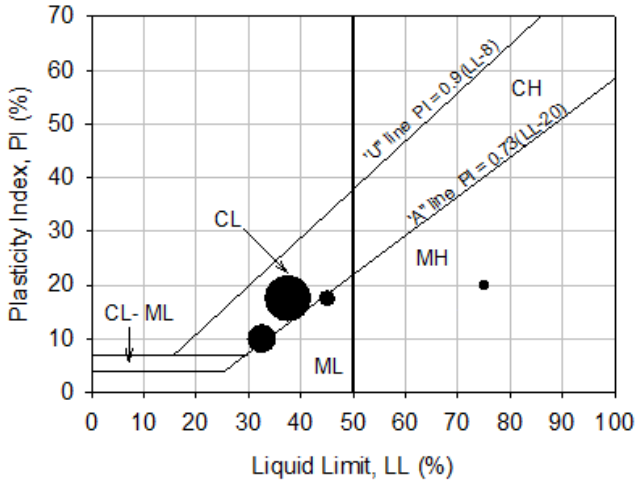

Figure 41. Atterberg limits of soils from NRCS soil survey overlaid on the plasticity chart

Soil Borings – 2007

Geotech Engineering and Observation (GEO) conducted soil borings on the site in June 2007 prior to grading work on the site during 2007/2008. The Geotechnical Exploration Report (Brocka and Casteel 2007) submitted for the project indicated cut-and-fill construction on the site on the order of 9 ft. or less on the site as part of the 2007/2008 construction, to achieve the desired final grades. Twenty soil borings were conducted across the site down to about 15 to 20 ft. below exiting grades. The soils borings indicated topsoil or possible reworked soils (classified as CL) at the surface. Below the surficial soils, medium stiff to stiff, brown to gray-brown sandy lean clay (CL) glacial till soils were encountered. In one of the borings, a layer of lean to fat clay (CL/CH) glacial till was encountered beneath the topsoil. Some of the borings indicated interbedded sand seams/layers at random depths in the glacial till. Stiff to very stiff dark gray sandy lean clay (CL) was encountered beneath the brown to gray-brown sandy lean clay. Shortly after the borings were completed, groundwater accumulation was observed at about 3.5 to 12.5 ft. below existing grades in fifteen of the borings, and no groundwater accumulation was

observed in five of the borings. Piezometers were installed in five borings for long-term groundwater monitoring. Twenty-five days after the completion of drilling, groundwater was observed at depths of about 4 to 5 ft. in five borings.

Pre-Construction In Situ Testing – 2012

Geotechnical Services, Inc. (GSI) performed eight piezocone penetration tests (CPTu) to a depth of about 20 ft. below existing grade at eight locations across the project site, in general accordance with ASTM D5778 (Thomas and Lustig 2012). The CPTu locations are provided in Appendix A. CPTu profiles from two selected locations are shown in Figure 42 and Figure 43. Profiles from all test locations are included in Appendix A. The profiles consist of tip resistance (q_t), frictional resistance (f_s), pore pressure (p_w), and soil behavior type. Soil behavior types were determined based on soil classification chart developed by Robertson and Campanella (1986).

Soil classifications from CPTu soundings generally indicated cohesive clay and silty clay soils. Sand seams existed between approximately 8 ft to 10 ft below the ground surface in the south eastern portion of the site (CPTu #1 and CPTu #4) and in the north central portion of the site (CPTu #5). A lower strength zone existed at a depth ranging from approximately 10 to 14.5 ft below the ground surface to termination over the eastern half of the site (CPTu #1, CPTu #2, CPTu #3, and CPTu #4). Interbedded sand deposits existed at depths ranging from approximately 12 ft. to 15.5 ft. below the ground surface to termination over the western half of the site (CPTu #6, CPTu #7, and CPTu #8). CPT p_w measurements indicated groundwater elevations at the time of testing at depths of about 3 to 6 ft. below original grade across the site, and at about 12 ft or greater near drainage features.

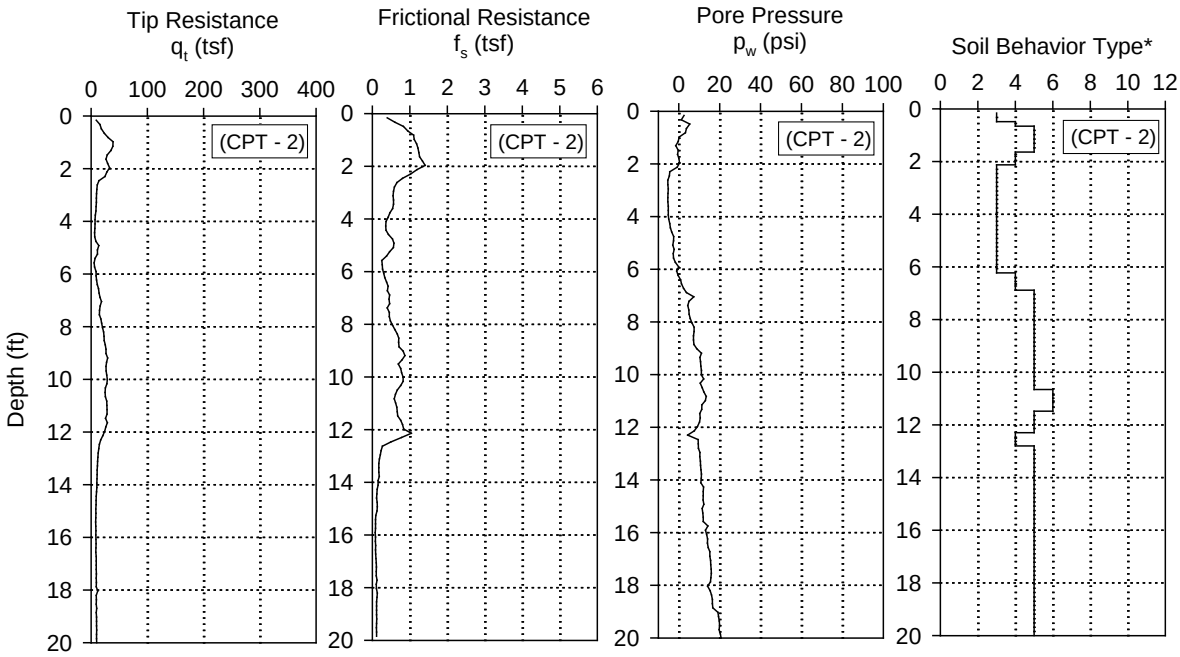

*Soil Behavior Type (Robertson and Campanella 1986): 1 - sensitive fine grained, 2 - organic material, 3 - clay, 4 - silty clay to clay, 5 - clayey silt to silty clay, 6 - sandy silt to clayey sitl, 7 - silty sand to sandy silt, 8 - sand to silty sand, 9 - sand, 10 - gravelly sand to sand, 11 - very stiff fine grained, 12 - sand to clayey sand

Figure 42. CPT results from test location 2 on 12th St. South

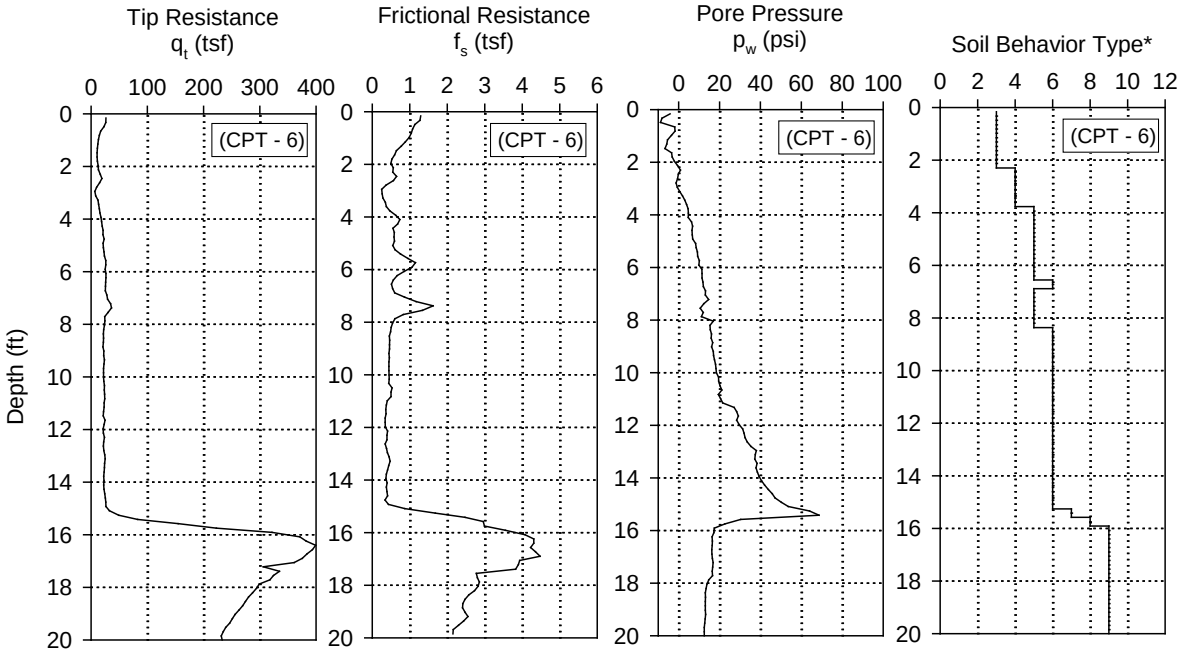

*Soil Behavior Type (Robertson and Campanella 1986): 1 - sensitive fine grained, 2 - organic material, 3 - clay, 4 - silty clay to clay, 5 - clayey silt to silty clay, 6 - sandy silt to clayey sitl, 7 - silty sand to sandy silt, 8 - sand to silty sand, 9 - sand, 10 - gravelly sand to sand, 11 - very stiff fine grained, 12 - sand to clayey sand

Figure 43. CPT results from test location 6 on North Ave. just north of 2nd St. North

FWD, LWD, and DCP tests were conducted on all north-south road sections. Two FWD and LWD tests, and one DCP test were conducted in the north and south sections of each street. The purpose of this testing was to generate baseline information for comparison with post-construction foundation layer properties.

A summary of the $E_{SB\text{-}FWD}$ (determined from 14,000 lb load), $E_{SB\text{-}LWD}$ (determined from 1,597 lb load), CBR of subbase (CBR_{SB}), and CBR of subgrade (CBR_{SG} for top 12 in. of subgrade) results with average and coefficient of variation (COV) of these measurements are provided in Table 13. Average $E_{SB\text{-}FWD}$ and average $E_{SB\text{-}LWD}$ for each section are shown in Figure 44 and Figure 45, respectively. Similarly, CBR_{SB} and CBR_{SG} for each section are shown in Figure 46 and Figure 47, respectively. An example DCP-CBR and cumulative blows profile from 1st St. South section is shown in Figure 48.

The site showed variable foundation layer conditions stiffness and strength characteristics across the site. FWD testing indicated that the average $E_{SB\text{-}FWD}$ based on testing on all North-South roads was about 6,528 psi with a coefficient of variation (COV) of about 46%. Similarly, average $E_{SB\text{-}LWD}$ was about 15,309 psi with a COV of about 45%. Average CBR_{SB} was about 59% with a COV of about 51% and average CBR_{SG} was about 9.1 with a COV of about 64%.

Table 13. Summary of pre-construction FWD, LWD, and DCP test results

Road	Road Section	$E_{SB\text{-}FWD}$, psi (COV %)	$E_{SB\text{-}LWD}$, psi (COV %)	CBR_{SB}*	CBR_{SG}*
1st St.	North	4,146 (6)	6,869 (2)	43	14
	South	5,987 (9)	12,026 (35)	71	10
2nd St.	North	6,513 (53)	15,534 (45)	47	3.9
	South	4,710 (14)	18,543 (74)	62	4.4
3rd St.	North	5,099 (21)	14,960 (18)	25	7.1
	South	3,218 (15)	7,172 (21)	49	1.2
4th St.	North	5,239 (8)	11,198 (14)	43	7.6
	South	5,349 (25)	12,438 (6)	6	6.1
5th St.	North	3,832 (26)	8,522 (17)	50	12
	South	5,480 (13)	12,833 (17)	63	3.5
6th St.	North	8,926 (20)	20,306 (11)	65	26
	South	9,561 (34)	13,196 (10)	76	7.9
7th St.	North	4,547 (46)	10,897 (27)	50	4.7
	South	9,258 (62)	16,911 (16)	42	13
8th St.	North	3,294 (14)	10,490 (21)	17	1.5
	South	10,305 (21)	14,183 (23)	59	15
9th St.	North	6,486 (6)	14,912 (8)	50	13
	South	6,836 (3)	20,415 (15)	51	5.8
10th St.	North	4,746 (23)	9,366 (9)	49	3.9
	South	14,186 (2)	23,919 (12)	156	13
11th St.	North	6,092 (4)	11,518 (10)	65	12
	South	11,427 (—*)	18,790 (—*)	113	4.5
12th St.	North	7,539 (47)	10,349 (40)	77	18
	South	6,348 (19)	15,406 (6)	79	13

*only one test

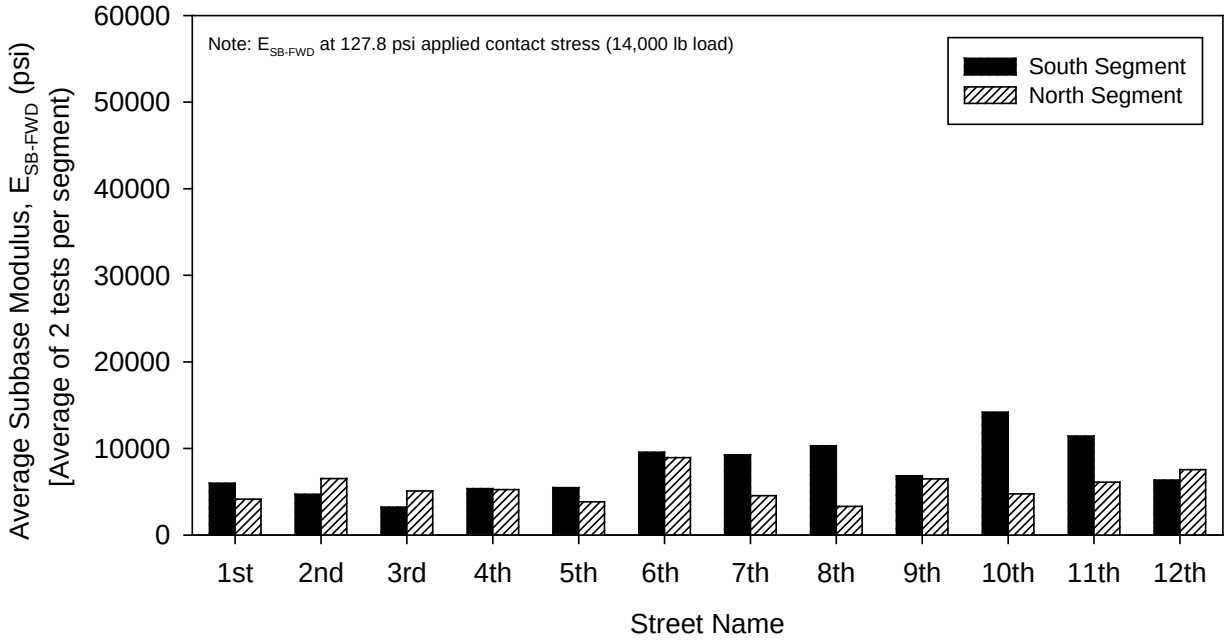

Figure 44. Average pre-construction FWD modulus by road section

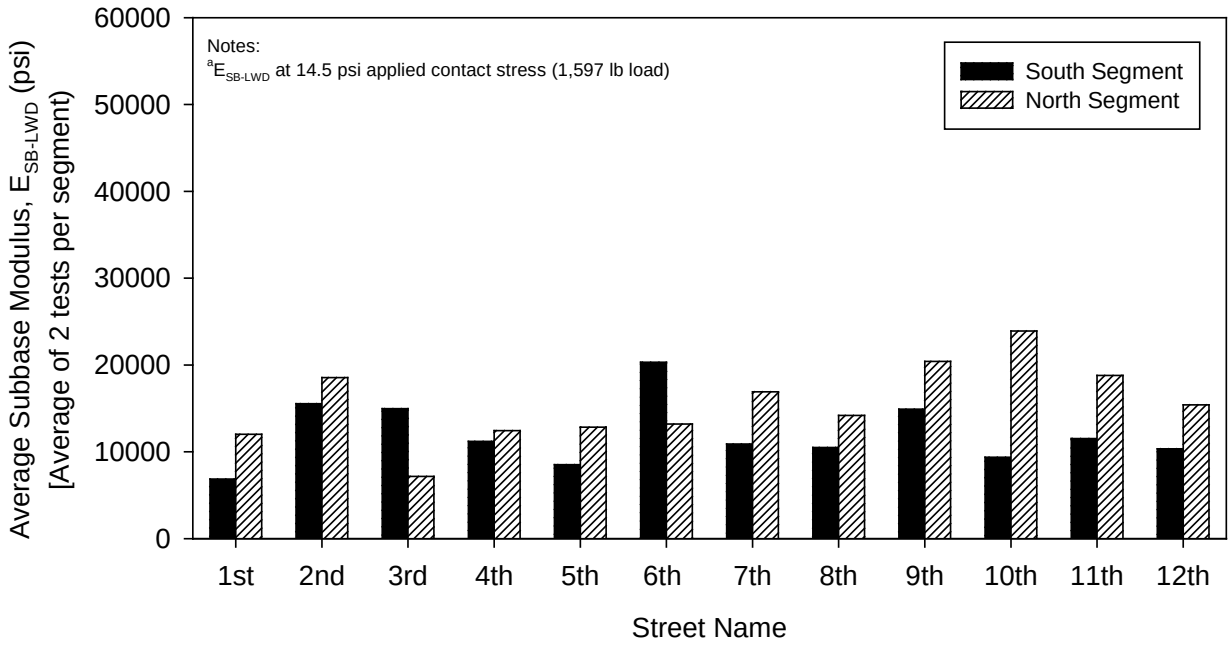

Figure 45. Average pre-construction LWD modulus by road section

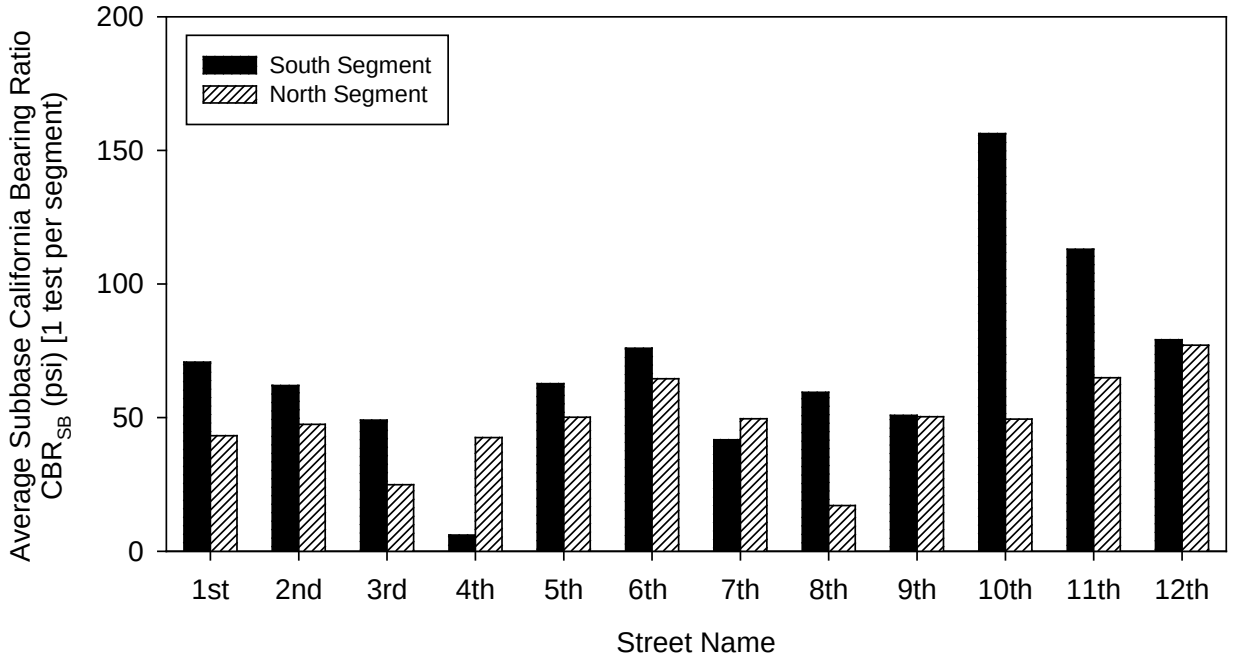

Figure 46. Pre-construction subbase CBR by road section

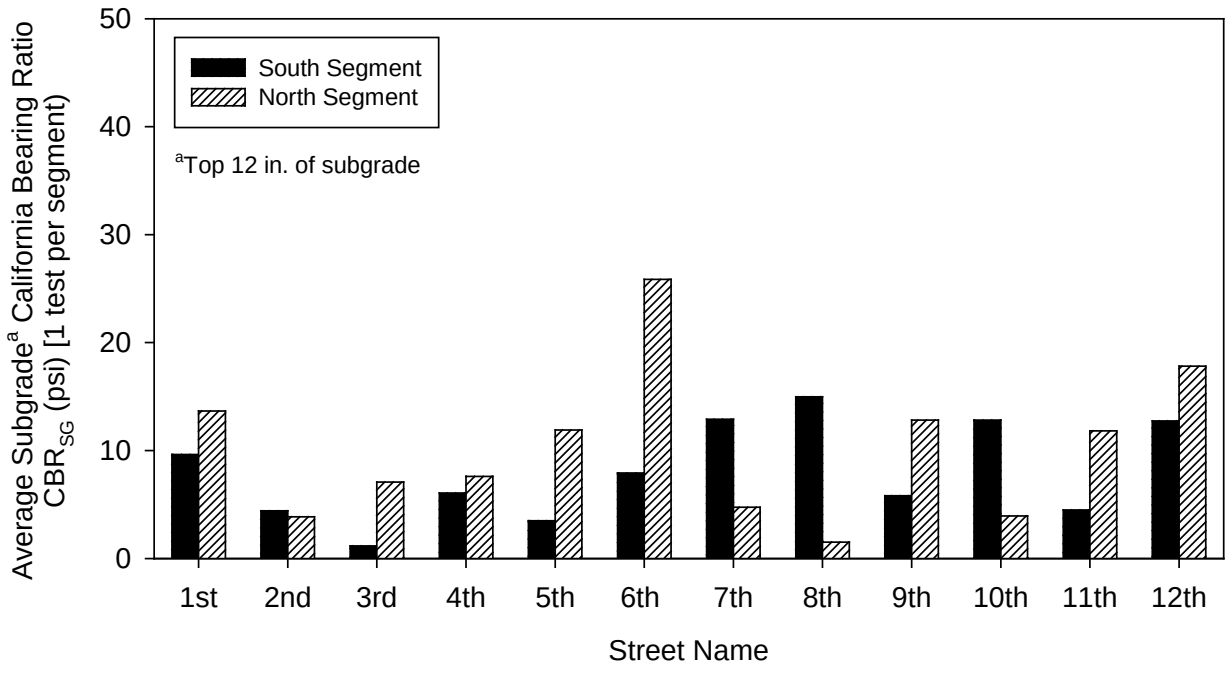

Figure 47. Pre-construction subgrade (top 12 in.) CBR by road section

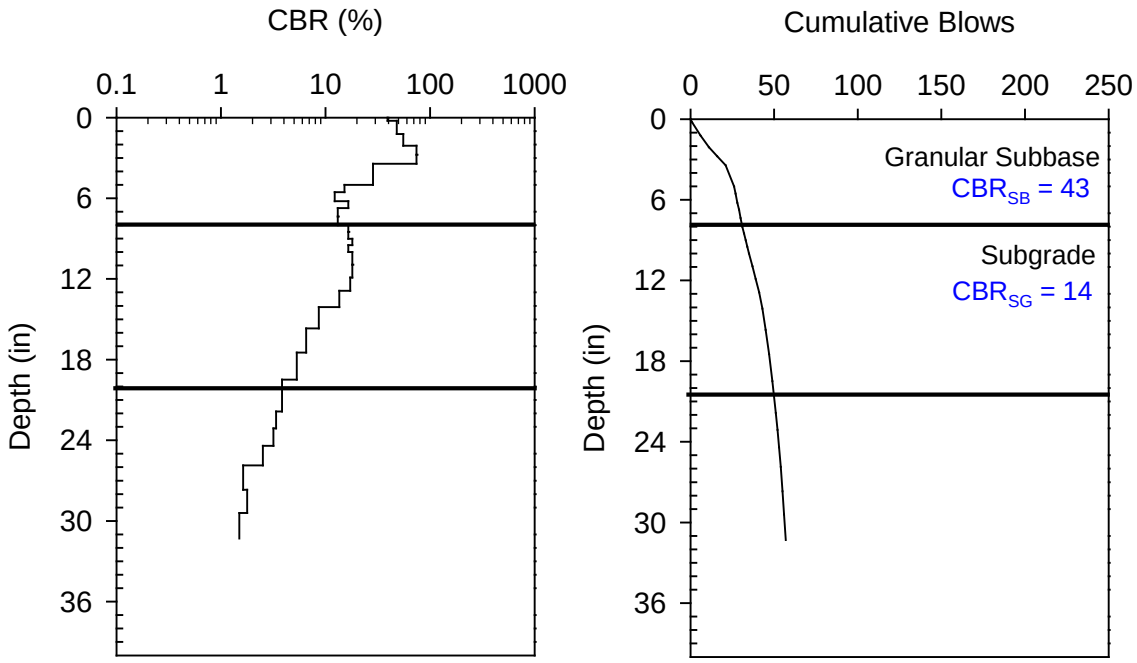

Figure 48. Example DCP-CBR and cumulative blows profiles (from 1st St. South) showing pre-construction conditions and CBR values for subbase and subgrade layers

Test Section Layout and Construction

The Iowa DOT in partnership with Iowa State University designed sixteen test sections along the North-South and East-West road sections with different stabilization technologies (Table 10). These technologies included:

- woven and NW geotextiles at subgrade/subbase interfaces,
- triaxial and biaxial geogrids at subgrade/subbase interfaces,
- 4 in. and 6 in. geocells in the subbase layer + non-woven geosynthetics at subgrade/subbase interfaces,
- PC stabilization of subgrades,
- FA stabilization of subgrades,
- PC stabilization of reclaimed subbase (reclaimed from existing granular subbase layer on-site),
- PC + fiber stabilization of reclaimed subbase with black PP fibers,
- PC + fiber stabilization of reclaimed subbase with white MF-PP fibers,
- mechanical stabilization (mixing subgrade with reclaimed subbase);
- reclaimed subbase between MSB and subgrade; and
- high-energy impact compaction.

Table 14. Summary of foundation layer design profiles for all test sections

Street	Section	Station	Foundation Layer Profile[a] (above existing/natural subgrade)	
1st St.	North	107+14.00 to 113+88.00	6 in. (5.5 in. actual) MSB[b]	12 in. compacted subgrade[c]
	South	100+12.00 to 106+86.00		
2nd St.	North	207+14.00 to 213+88.00	6 in. (6.1 in. actual) MSB[b]	12 in. mechanically stabilized subgrade
	South	200+12.00 to 206+86.00		
3rd St.	North	307+14.00 to 313+88.00	2 in. MSB[b]	4 in. geocell reinforced MSB, NW geotextile
	South	300+12.00 to 306+04.00	1 in. MSB[b]	6 in. geocell reinforced MSB, NW geotextile
	South	306+04.00 to 306+86.00		6 in. geocell reinforced MSB (no geotextile)
4th St.	North	407+14.00 to 413+88.00	6 in. (7.0 in. actual) MSB[b]	NW geotextile
	South	400+12.00 to 406+86.00		woven geotextile
5th St.	North	507+14.00 to 513+88.00	6 in. (6.1 in. actual) MSB[b]	triaxial geogrid
	South	500+12.00 to 506+86.00	6 in. (5.8 in. actual) MSB[b]	biaxial geogrid
6th St.	North	4026+93.49 to 4032.85.49	6 in. (4.5 to 5 in. actual) MSB[b]	6 in. reclaimed subbase + 5% (5.6% actual) PC + 0.4% (0.5% actual) PP fibers
		4032+85.49 to 4033+67.49		6 in. reclaimed subbase + 0.4% (0.5% actual) PP fibers
	South	4020+82.30 to 4026+65.49	6 in. (4.5 to 5 in. actual) MSB[b]	6 in. reclaimed subbase subbase + 5% (5.5% actual) PC + 0.4% (0.5% actual) MF-PP fibers
		4020+21.30 to 4020+82.30		6 in. reclaimed subbase subbase + 0.4% (0.4% actual) MF-PP fibers
7th St.	North	707+14.00 to 713+88.00	6 in. (5.5 in. actual) MSB[b]	6 in. reclaimed subbase + 5% (6.2% actual) PC
	South	700+12.00 to 706+86.00		6 in. reclaimed subbase + 5% (5.2% actual) PC
8th St.	North	807+14.00 to 813+88.00	6 in. (6.0 in. actual) MSB[b]	Compacted subgrade[d]
	South	800+12.00 to 806+86.00		
9th St.	North	907+14.00 to 913+88.00	6 in. (6.0 in. actual) MSB[b]	6 in. reclaimed subbase
	South	900+12.00 to 906+86.00		
10th St.	North	1007+14.00 to 1013+88.00	6 in. (5.5 in. actual) MSB[b]	12 in. compacted subgrade[c]
	South	1000+12.00 to 1006+86.00		—
11th St.	North	1107+14.00 to 1113+88.00	6 in. (6.0 in. actual) MSB[b]	12 in. 10% (11.4% actual) PC stabilized subgrade
	South	1100+12.00 to 1106+86.00		12 in. 20% (22.3% actual) Port Neal FA stabilized subgrade
12th St.	North	1207+14.00 to 1213+88.00	6 in. (6.0 in. actual) MSB[b]	12 in. 15% (15.8% actual) Ames FA stabilized subgrade
	South	1200+12.00 to 1204+46.00	6 in. (5.7 in. actual) MSB[b]	12 in. 10% (10% actual) Port Neal FA stabilized subgrade
	South	1204+46.00 to 1206+86.00	6 in. (6.0 in. actual) MSB[b]	12 in. 10% (10% actual) Muscatine FA stabilized subgrade
North Ave.	West[e]	3000+02.50 to 3002+02.50	9 in. MSB[f]	6 in. reclaimed subbase, biaxial geogrid
	West[e]	3002+02.50 to 3004+02.50		6 in. reclaimed subbase, triaxial geogrid
	East[e]	3004+02.50 to 3023+38.14		6 in. reclaimed subbase
South Ave.	West[e]	1001+00.00 to 1003+00.00	9 in. MSB[f]	6 in. reclaimed subbase, biaxial geogrid
		1003+00.00 to 1005+00.00		6 in. reclaimed subbase, biaxial geogrid
		1005+00.00 to 1009+06.08		6 in. reclaimed subbase
South Ave.	East[e]	1009+94.00 to 1011+94.00	9 in. MSB[f]	6 in. reclaimed subbase, biaxial geogrid
		1011+94.00 to 1013+94.00		6 in. reclaimed subbase, biaxial geogrid
		1013+94.00 to 1023+39.91		6 in. reclaimed subbase
Central Ave.	East/West	2000+01.43 to 2023+39.59	9 in. MSB[f]	6 in. reclaimed subbase

[a]thicknesses provided are nominal unless indicated as actual in parenthesis (actual measurements were obtained from test pits); [b]crushed limestone; [c] Existing subgrade scarified, moisture conditioned, and compacted; [d] The original subbase layer topped with chipseal was compacted with high-energy impact roller and the subbase layer was excavated down to about 6 in. below final grade and replaced with MSB; [e]with reference to 6th St.; [f]mixture of recycled PCC and asphalt

Construction of the test sections required removing the existing chip seal surface, granular subbase, existing biaxial geogrid, and 6 to 12 in. of subgrade. The existing granular subbase material was stockpiled on-site for use as reclaimed subbase on some of the test sections.

Details of construction and results from in situ testing during construction are provided separately for each test section in the next chapter. In brief, all North-South test sections except one were topped with a nominal 6 in. of crushed limestone MSB (GP-GM or A-1-a with 7% fines content); the 6 in. geocell section required 7 in. of crushed limestone MSB. All East-West roads were topped with 9 in. of recycled MSB (GW or A-1-a with 5% fines content). 6th St., 7th St., 9th St. and all East-West test sections consisted of 6 in. of reclaimed subbase material (SM or A-1-a 1 with 4% fines content) between crushed limesonte MSB and subgrade layers.

The final MSB layer elevation on all the roads were at about 6 in. below the previous chipseal surface elevation (constructed during 2007/2008), to accommodate pavement layer during Phase II construction. The roadway widths and shape were same as previous with inverted crowns with 2.0% slopes towards the centerline. Additional grading was performed prior to paving and is discussed in the Phase II report.

CHAPTER 6: TEST SECTION CONSTRUCTION AND TESTING

This chapter documents construction observations and field test results on each test section. In brief, the following testing was conducted at different times during and after construction of test sections:

- July 2012 – during construction: DCPs in test sections constructed using chemical stabilizers), and DCPs and RICM using Caterpillar CS583 in mechanically stabilized subgrade test section.
- July 2012 – shortly after construction: FWDs, LWDs, and RICM (using Caterpillar CS683 roller) in each test section.
- October 2012 – about three months after construction: DCPs, FWDs, and RICM (using Sakai and Hamm rollers) in each test section.
- February 2013 (frozen condition) – about seven months after construction: FWDs in each test section.
- April/May 2013 (sprig-thaw condition) – about nine to ten months after construction: DCPs, FWDs, and RICM (using Caterpillar CS74 and CS683 rollers) in each test section.

Results from July 2012, October 2012, and April/May 2013 are presented in this chapter. Comparison of results between test sections along with results from February 2013 are provided in the next chapter.

1st North-South: Compacted Subgrade (Control)

Construction Observations

Control test sections with compacted subgrade was constructed on 1st St. North and South. The pavement foundation profile on the test sections are shown in Figure 49. First, the existing subbase layer was excavated down to the subgrade elevation. Then the top 12 in. of subgrade was pulverized using a soil reclaimer (Figure 50a,b) and was compacting using a padfoot roller followed by a smooth drum roller (Figure 50c,d). A 6 in. thick layer of crushed limestone MSB was placed and compacted over the subgrade (Figure 50e,f).

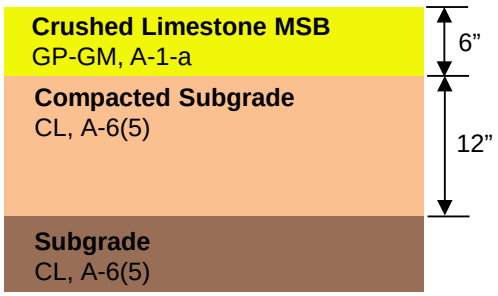

Figure 49. Pavement foundation profile on 1st St. North and South test sections

(a) (b)

(c) (d)

(e) (f)

Figure 50. Construction operations on 1st St.: (a) pulverizing top 12 in. of subgrade, (b) pulverized subgrade layer, (c) compaction of subgrade using smooth drum roller after padfoot roller, (d) compacted subgrade layer, (e) and (f) placement of MSB layer

As-Constructed Test Results

RICM values (MDP*, CMV, and elevation) on compacted crushed limestone MSB layer are shown in Figure 51. RICM measurements were obtained in low amplitude mode (a = 0.85 mm, f = 30 Hz). FWD and LWD modulus measurements obtained from 20 test locations along 1st St. are also shown in Figure 51.

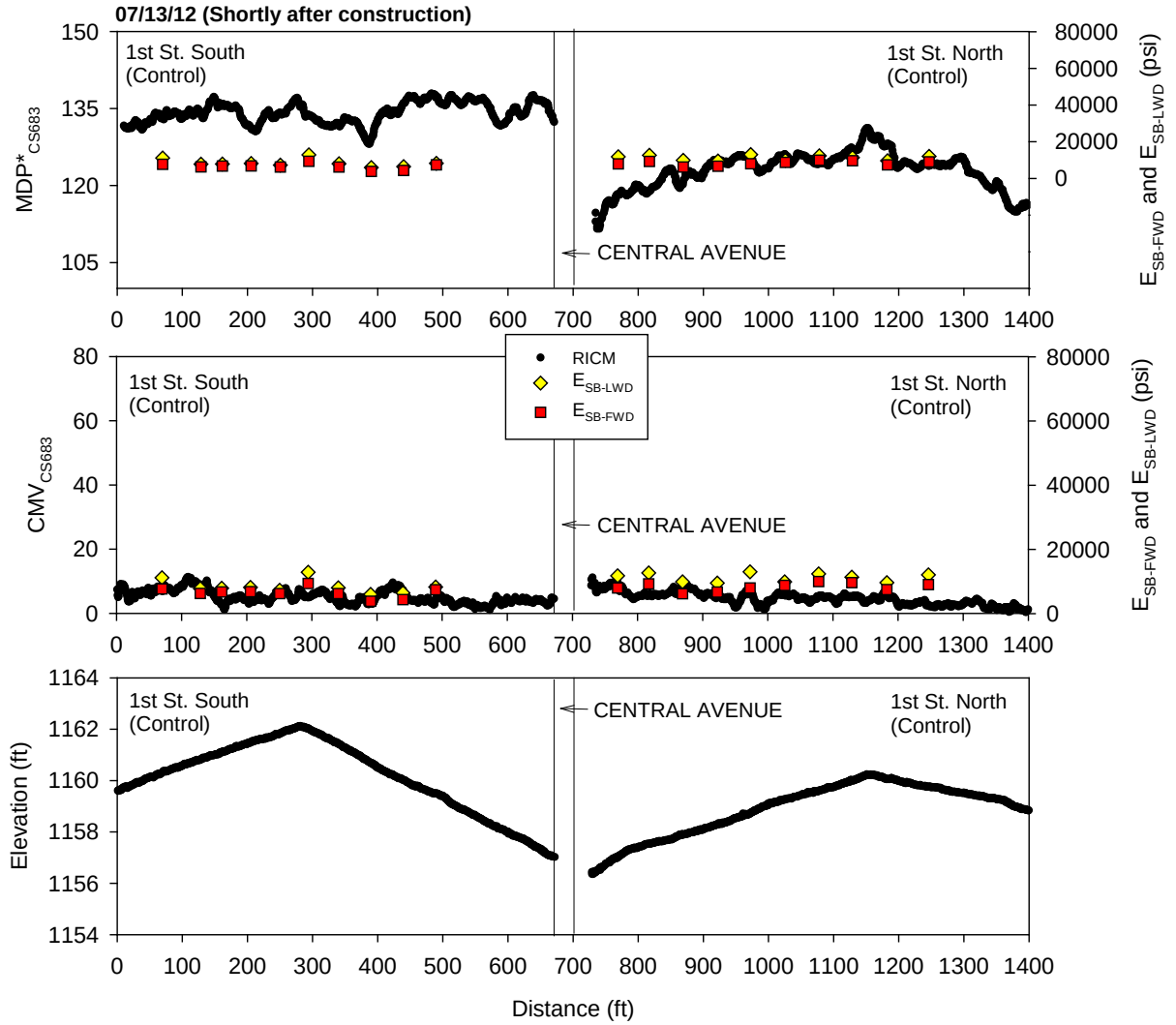

Figure 51. CS683 RICM, LWD, and FWD modulus measurements on 1st St. shortly after construction (July 2012)

Performance Monitoring Results

CCV results obtained in low amplitude mode (a = 0.63 mm, f = 33 Hz) in comparison with $E_{SB\text{-}FWD}$ from October 2012 (about three months after construction) are shown in Figure 52. MDP* and CMV results from the CS683 machine obtained in low amplitude mode (a = 0.85 mm, f = 30 Hz)) in comparison with $E_{SB\text{-}FWD}$ from April 2013 (during spring-thaw) are shown in Figure 53.

Similarly, results from the CS74 machine obtained in low amplitude mode (a = 0.97 mm, f = 28 Hz) are shown in Figure 54. MDP* and CMV results obtained from the CS683 machine from July 2012 and April 2013 are compared in Figure 55.

DCP-CBR and cumulative blows profiles from different testing times are shown in Figure 56 and Figure 57. Average CBR_{MSB} and CBR_{SG} for each test section are shown in Figure 58. Average $E_{SB\text{-}FWD}$ for each test section are shown in Figure 59.

CBR_{MSB} and CBR_{SG} showed lower values in May 2013 during spring-thaw compared to measurements in October 2012 and April 2013. $E_{SB\text{-}FWD,}$ MDP*, and CMV measurements were lower in April 2013 than in July and October 2012.

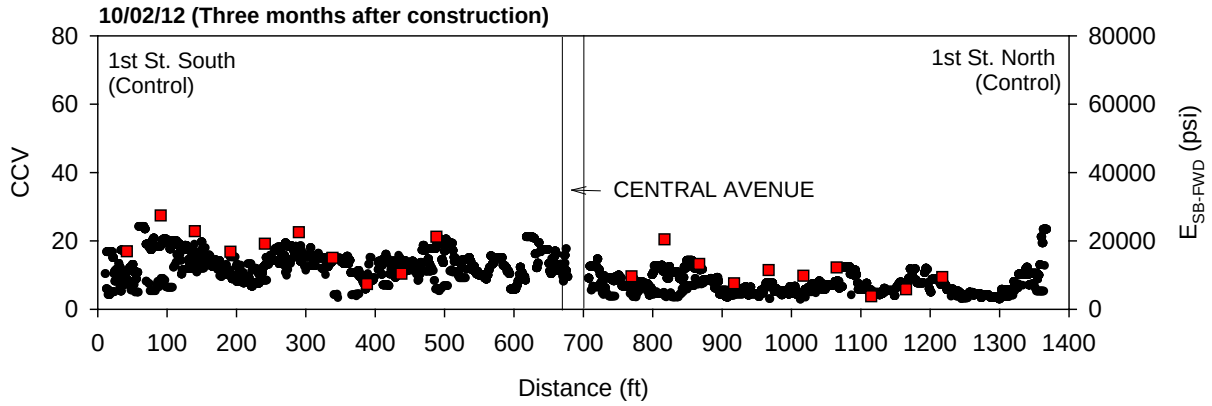

Figure 52. Sakai CCV and FWD modulus measurements on 1st St. three months after construction (October 2012)

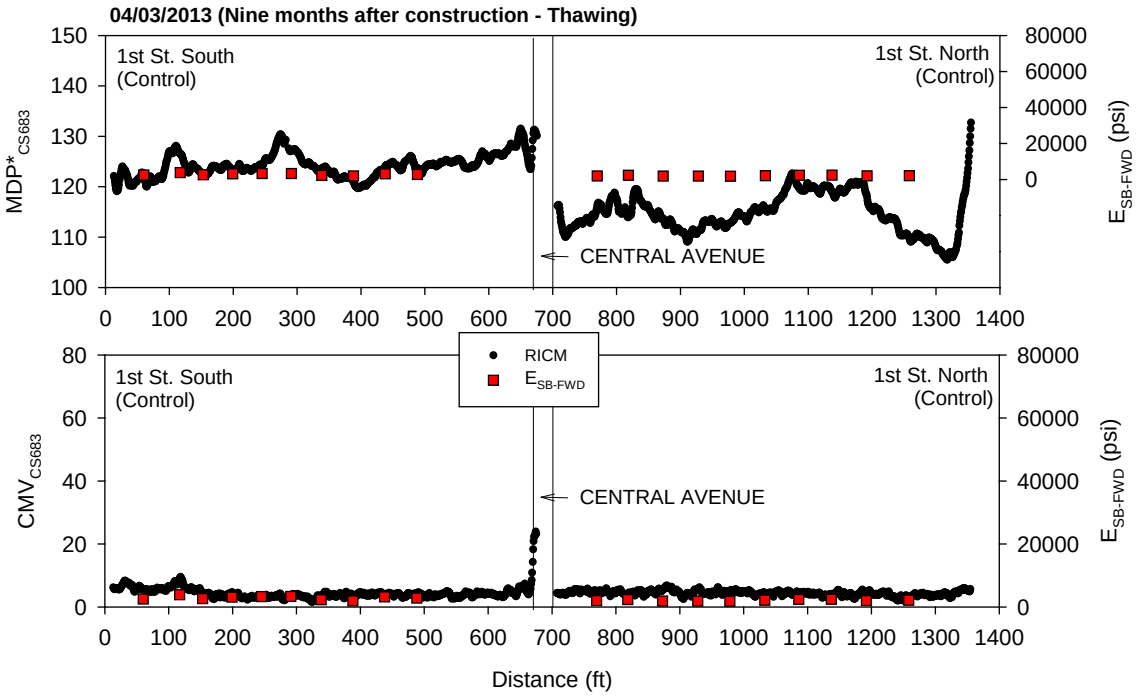

Figure 53. CS683 RICM and FWD modulus measurements on 1st St. nine months after construction during thawing (April 2013)

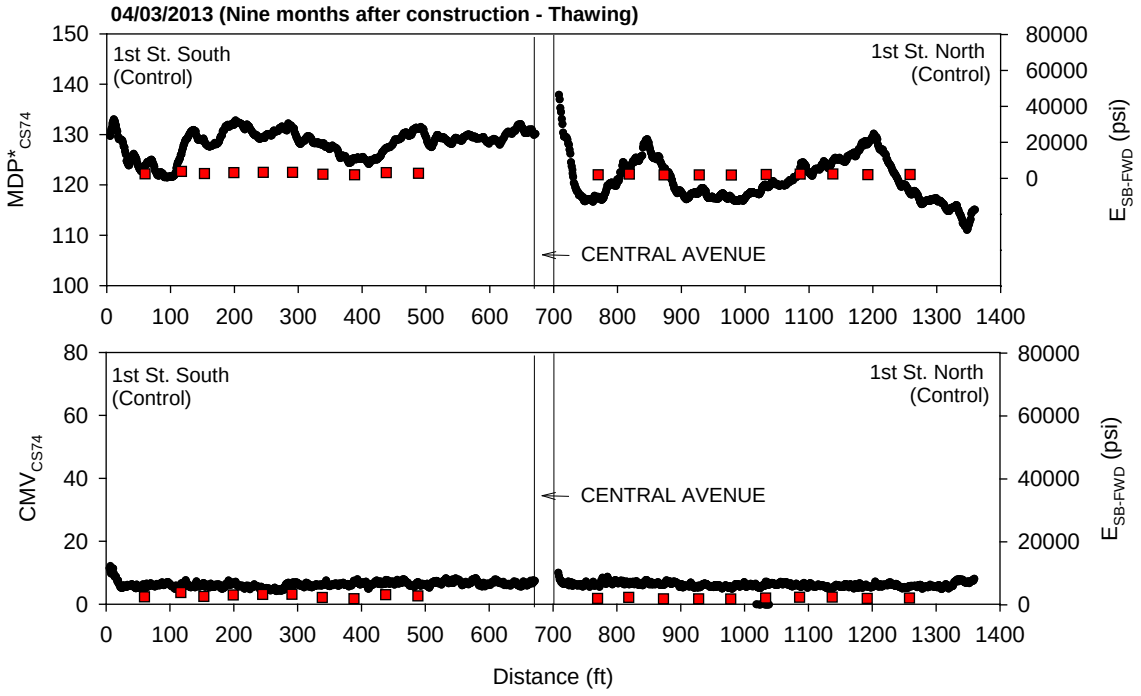

Figure 54. CS74 RICM and FWD modulus measurements on 1st St. nine months after construction during thawing (April 2013)

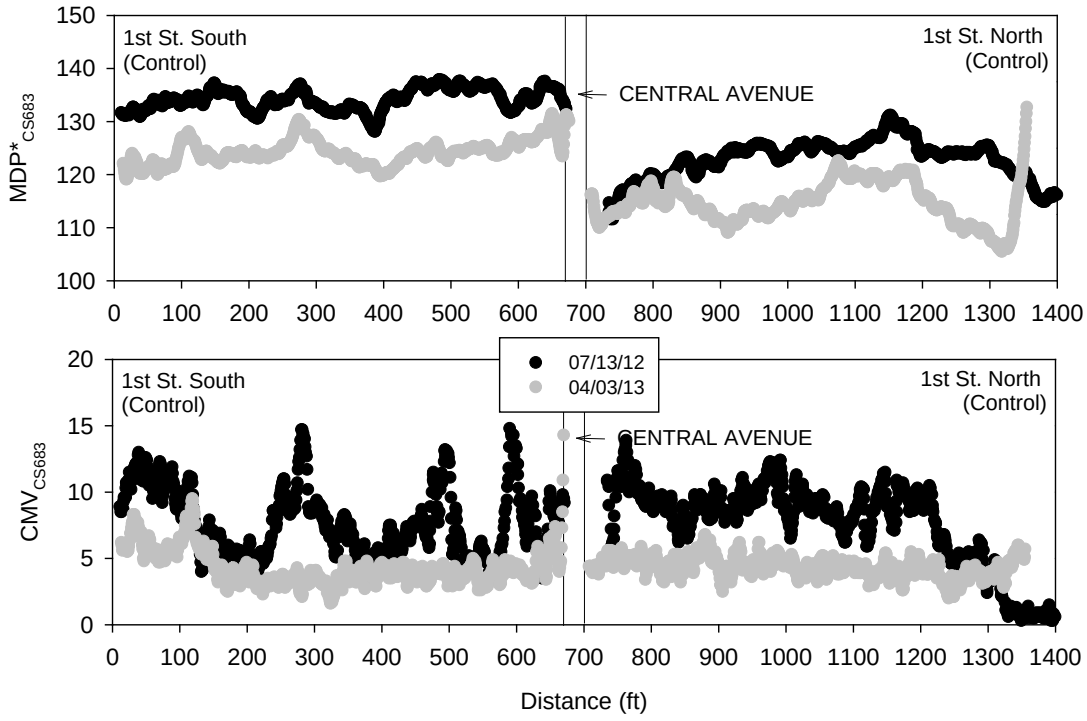

Figure 55. Comparison between CS683 RICM measurements on 1st St. shortly after construction and nine months after construction during thawing

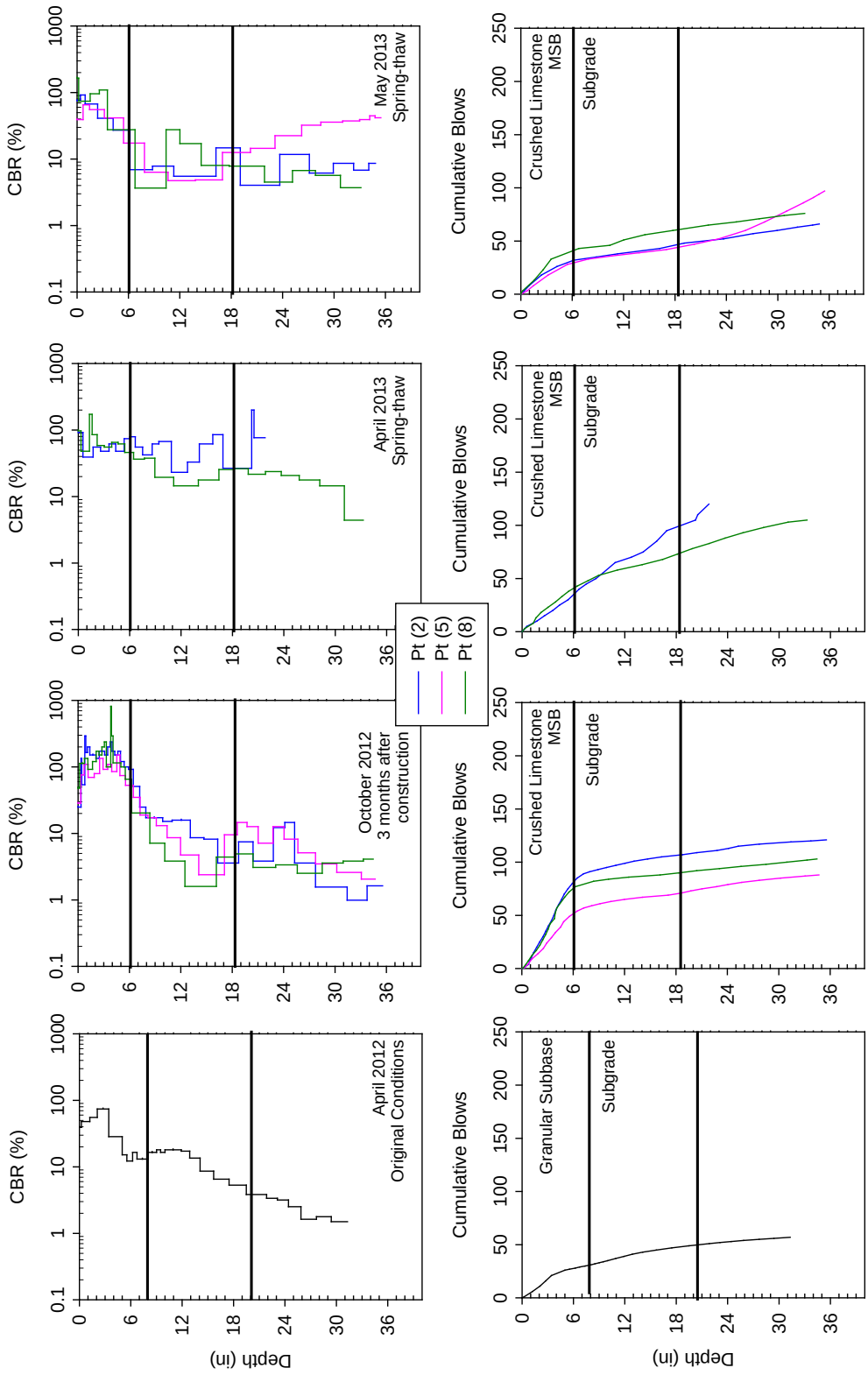

Figure 56. DCP test results from 1st St. South from different testing times

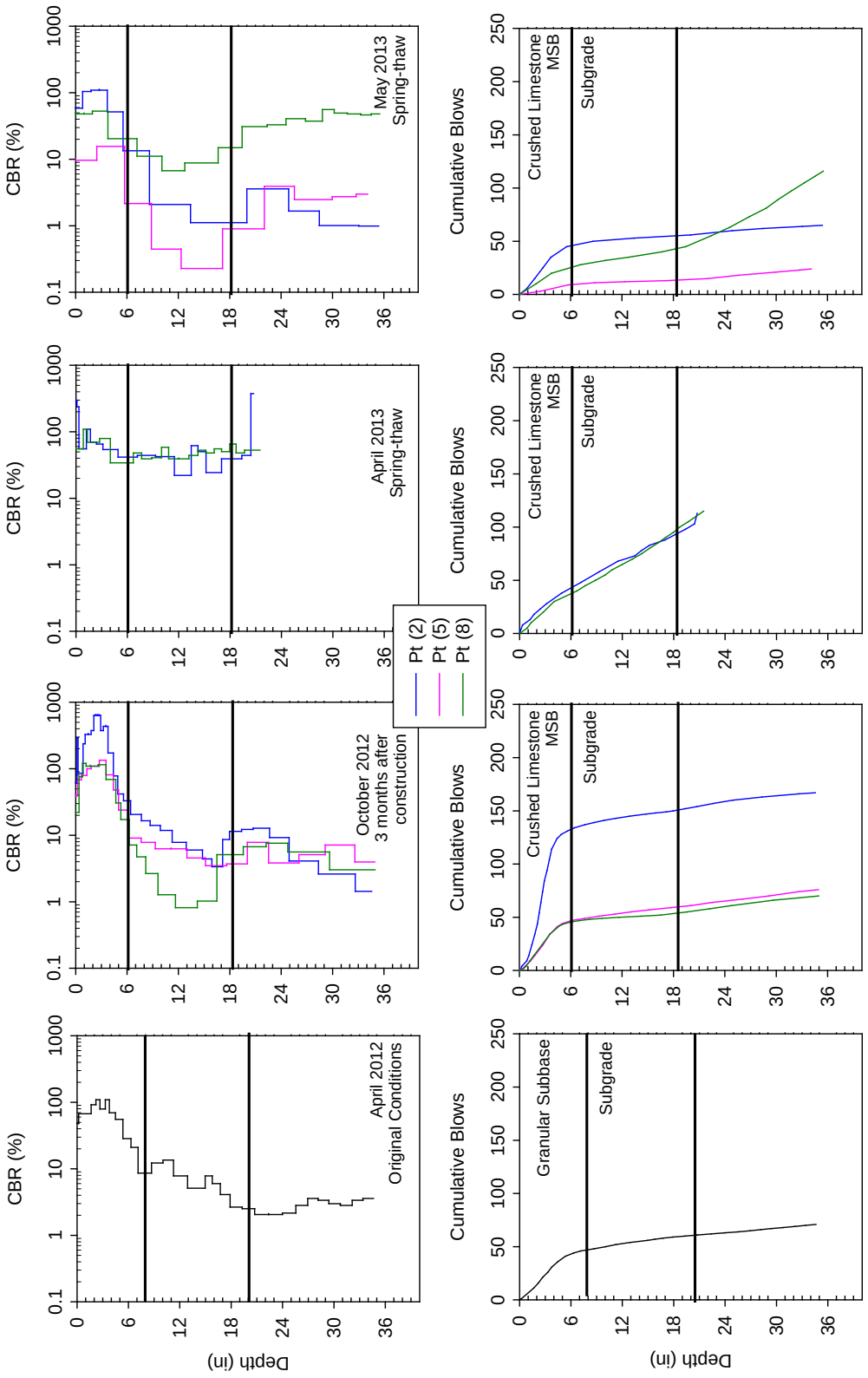

Figure 57. DCP test results from 1nd St. North from different testing times

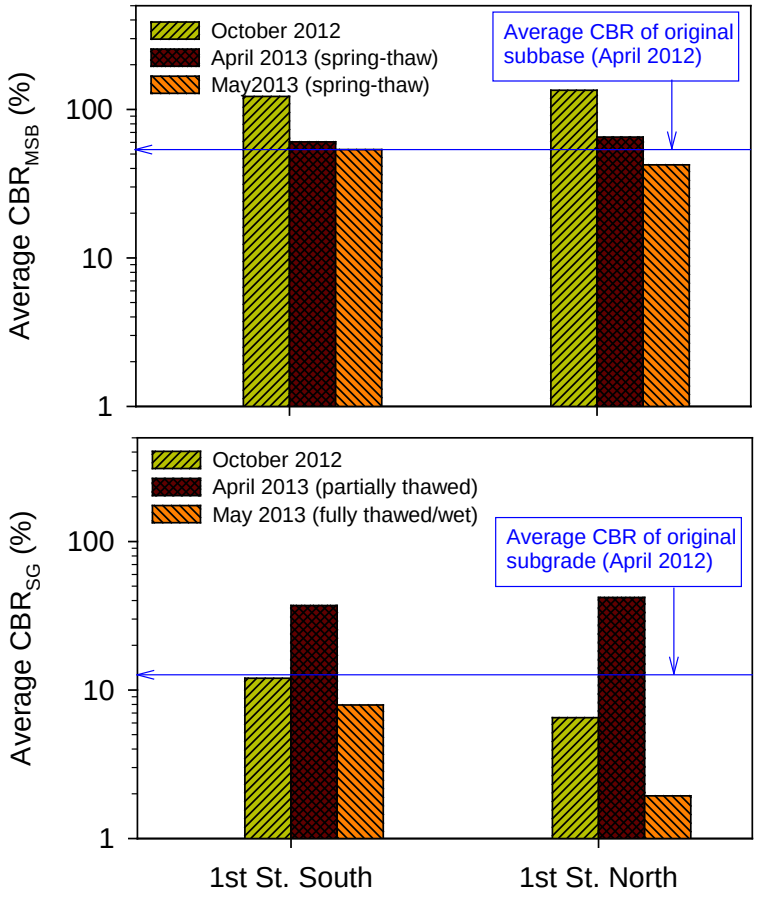

Figure 58. Average CBR (based on 2 to 3 tests) of MSB and subgrade layers on 1st St. South and North

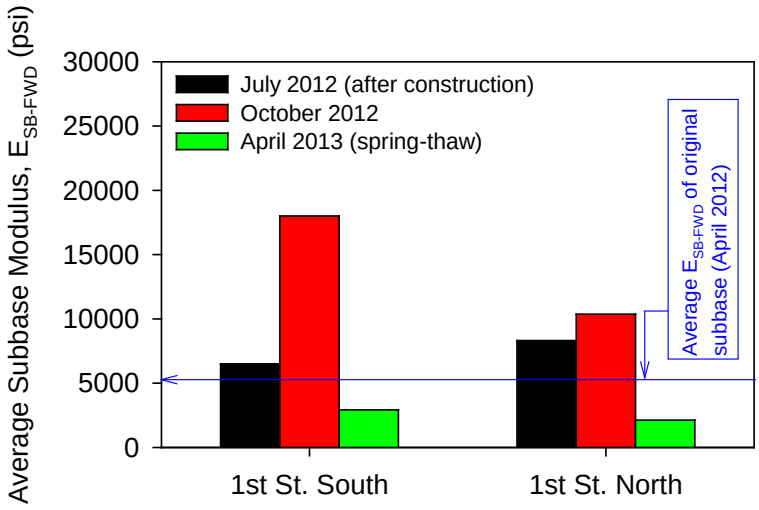

Figure 59. Average FWD subbase modulus (based on 10 tests) on 1st St. South and North sections

2nd North-South: 12 inch Mechanically Stabilized Subgrade

Construction Observations

Test sections with mechanically stabilized subgrade between the MSB and the unstabilized subgrade layers were constructed on 2nd St North and South. The pavement foundation profile in the test sections is shown in Figure 60. The existing subbase layer was scarified (Figure 61a) and excavated down to the subgrade elevation (Figure 61b). About 6 in. of reclaimed subbase layer was loosely placed on the subgrade (Figure 61c) and was mixed with the underlying subgrade using a soil reclaimer (Figure 61d) to create a mechanically stabilized subgrade layer. The stabilized layer was compacted using the CS683 vibratory smooth drum roller equipped with RICM (Figure 61e). A 6 in. thick layer of crushed limestone MSB was placed and compacted over the stabilized subgrade layer (Figure 61f). A picture of the final compacted surface is shown in Figure 62.

Soil samples of the stabilized subgrade layer were obtained from six random locations along 2nd St. for laboratory testing. Gradation curves of the mechanically stabilized subgrade samples in comparison with subgrade, reclaimed subbase, and crushed limestone MSB materials are shown in Figure 63. The mechanically stabilized subgrade material was classified as clayey sand (SC) according to the USCS soil classification system and A-2-6 according to the AASHTO soil classification system (average fines content of about 33%).

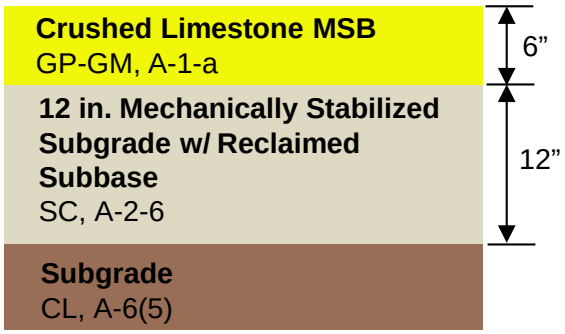

Figure 60. Pavement foundation profile on 2nd St. North and South test sections

(a) (b)

(c) (d)

(e) (f)

Figure 61. Construction operations on 2nd St.: (a) scarifying existing subbase layer, (b) excavating existing subbase layer, (c) replacing 6 in. of reclaimed subbase layer, (d) mixing reclaimed subbase and subgrade layers, (e) compaction of mechanically stabilized layer, and (f) placement of crushed limestone MSB layer

Figure 62. 2nd St. after placement and compaction of crushed limestone modified subbase layer

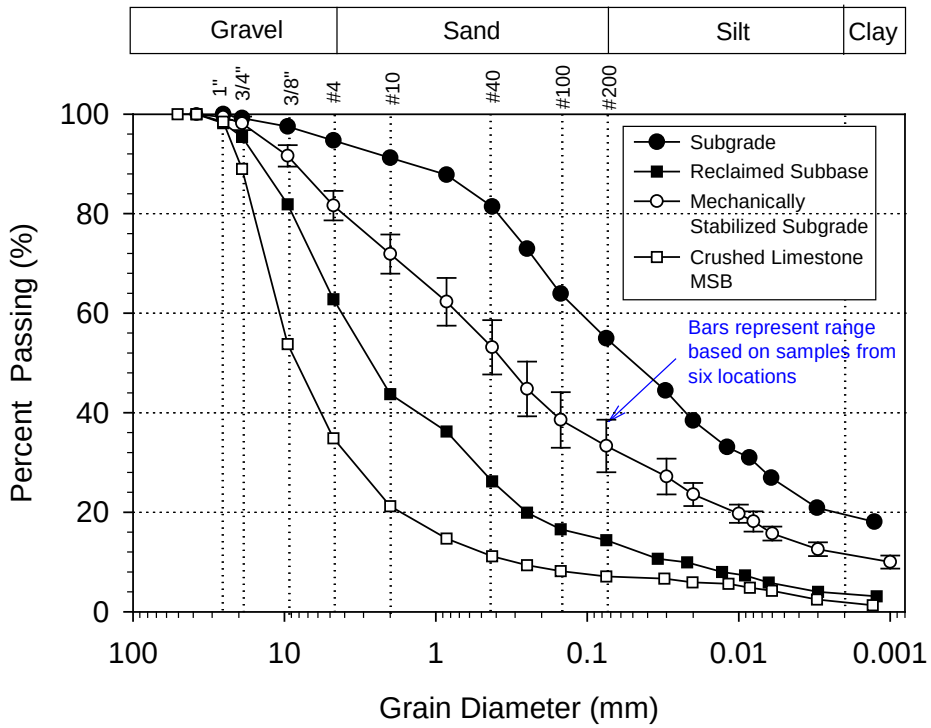

Figure 63. Grain-size distribution curves for subgrade, reclaimed subbase, mechanically stabilized subgrade, and crushed limestone MSB materials

As-Constructed Test Results

The mechanically stabilized subgrade layer was compacted using the RICM roller in three roller lanes (namely east, middle, and west lanes). Compaction was performed using low amplitude (a = 0.9 mm, f = 30 Hz) and high amplitude (a = 1.8 mm, f = 30 Hz) settings. LWD and DCP tests were conducted at 0 pass and after 6 passes.

Linear plots of RICM data, i.e., MDP^*_{CS683}, CMV_{CS683}, elevation, and change in elevation (ΔElevation), obtained on the west, middle, and east lanes for six roller passes are shown in Figure 64, Figure 65, and Figure 66, respectively. The ΔElevation values were calculated using pass 1 elevation data as reference. Change in average (per pass) MDP^*_{CS683}, CMV_{CS683}, and elevation with increasing passes are shown in Figure 67.

Average LWD modulus (based on 3 to 10 measurements) and CBR (based on 10 measurements) of the mechanically stabilized subgrade layer (CBR_{MSS}) before and after compaction (6 passes) are also shown in Figure 67. DCP-CBR and cumulative blows with depth profiles for 2nd St. South and North are shown in Figure 68 and Figure 69, respectively.

MDP^*_{CS683} results from multiple compaction passes indicate that the measurements are repeatable and generally increased with compaction passes. CMV_{CS683} values were low (< 10) and did not change considerably with increasing passes. Elevation values generally showed a decreasing trend with increasing pass.

FWD and LWD testing and RICM measurements using the CS683 roller were conducted on the MSB layer shortly after construction (July 2012). RICM values (MDP^*_{CS683}, CMV_{CS683}, and elevation) obtained in low amplitude mode (a = 0.85 mm, f = 30 Hz) on 2nd St. are shown in Figure 70. FWD and LWD modulus measurements obtained from 20 locations along 2nd St. are also presented in Figure 70, as comparison with the RICM measurements.

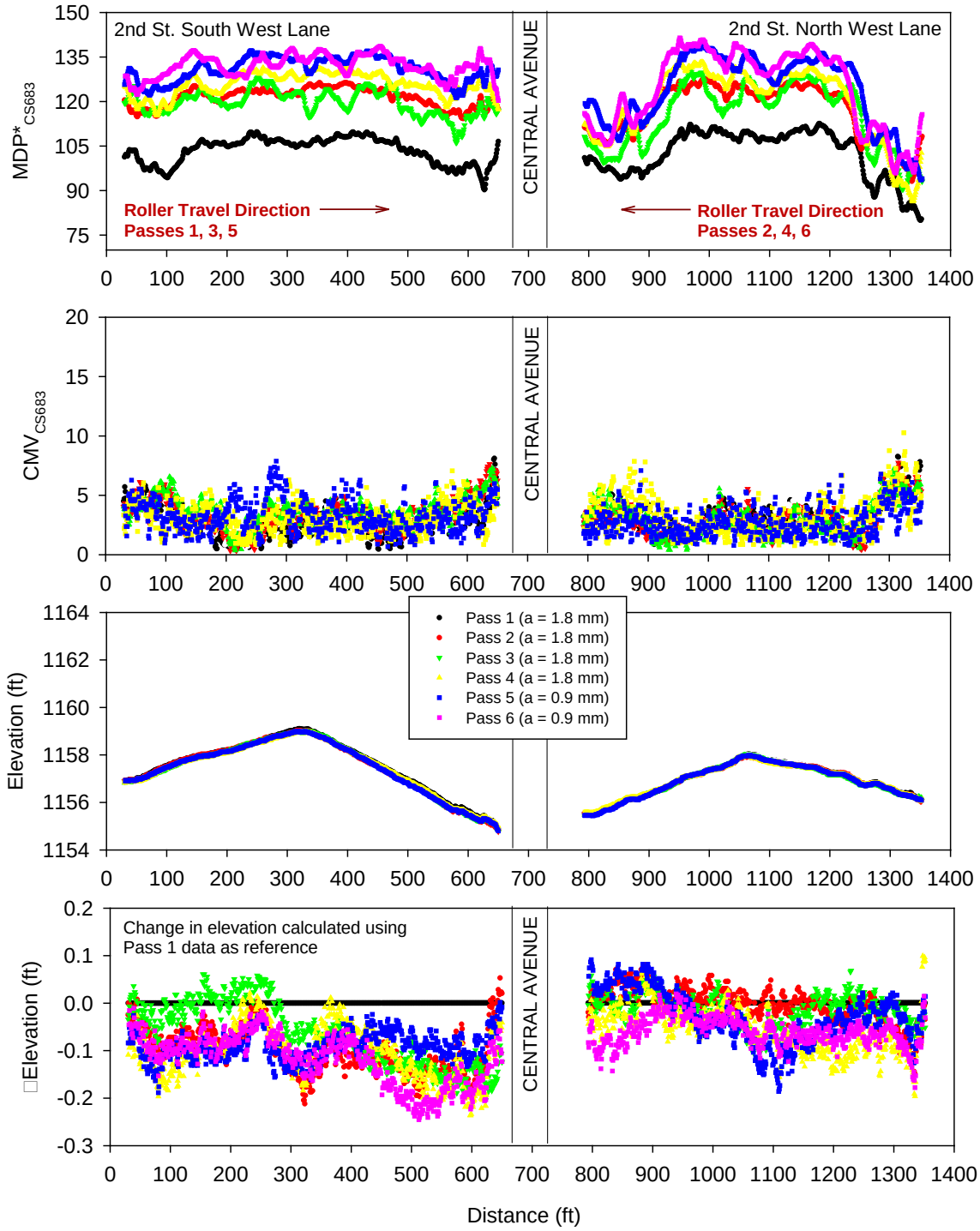

Figure 64. Plots of MDP*, CMV, elevation, and change in elevation on west lane from the RICM roller during compaction of the mechanically stabilized layer

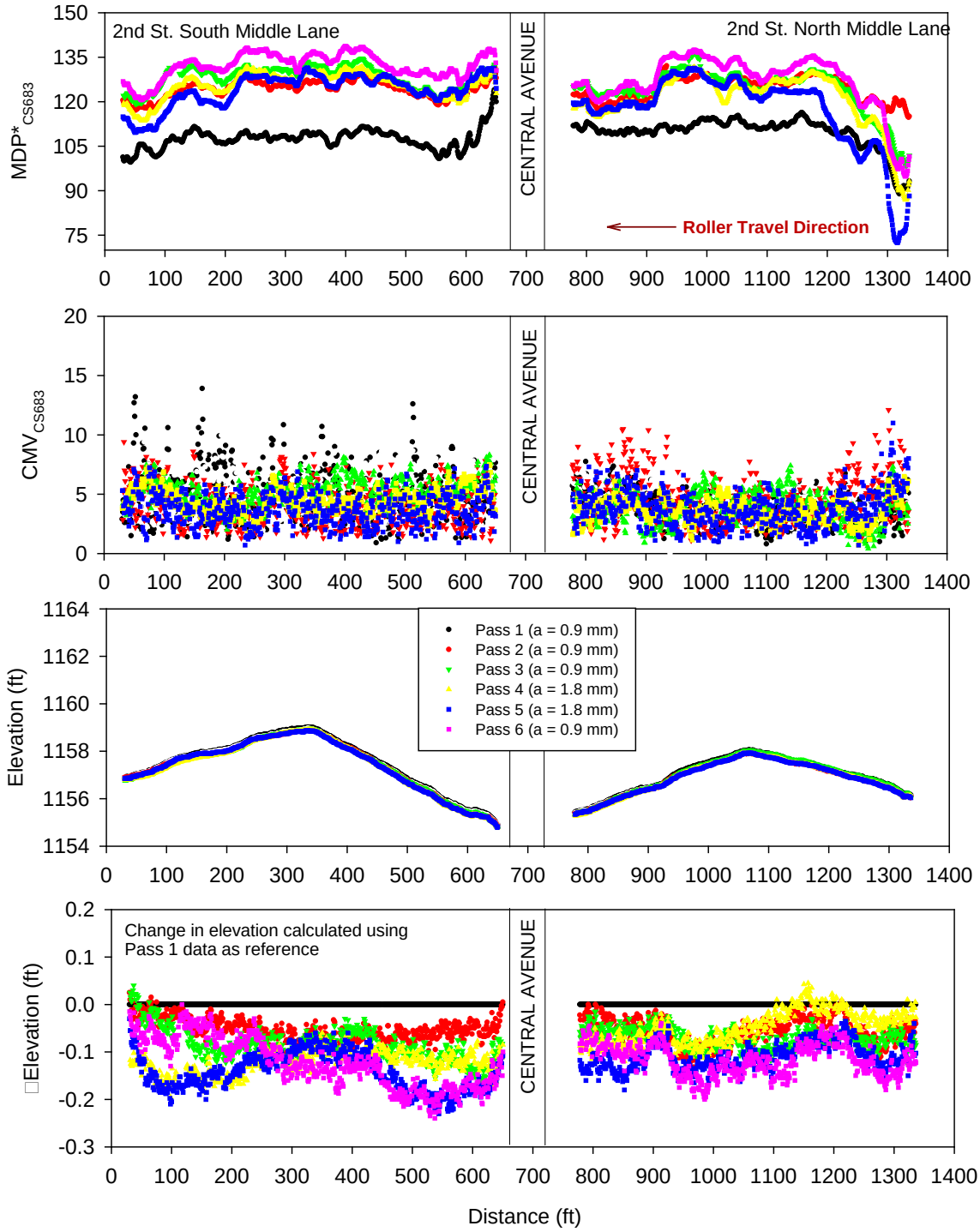

Figure 65. Plots of MDP*, CMV, elevation, and change in elevation on middle lane from the RICM roller during compaction of the mechanically stabilized layer

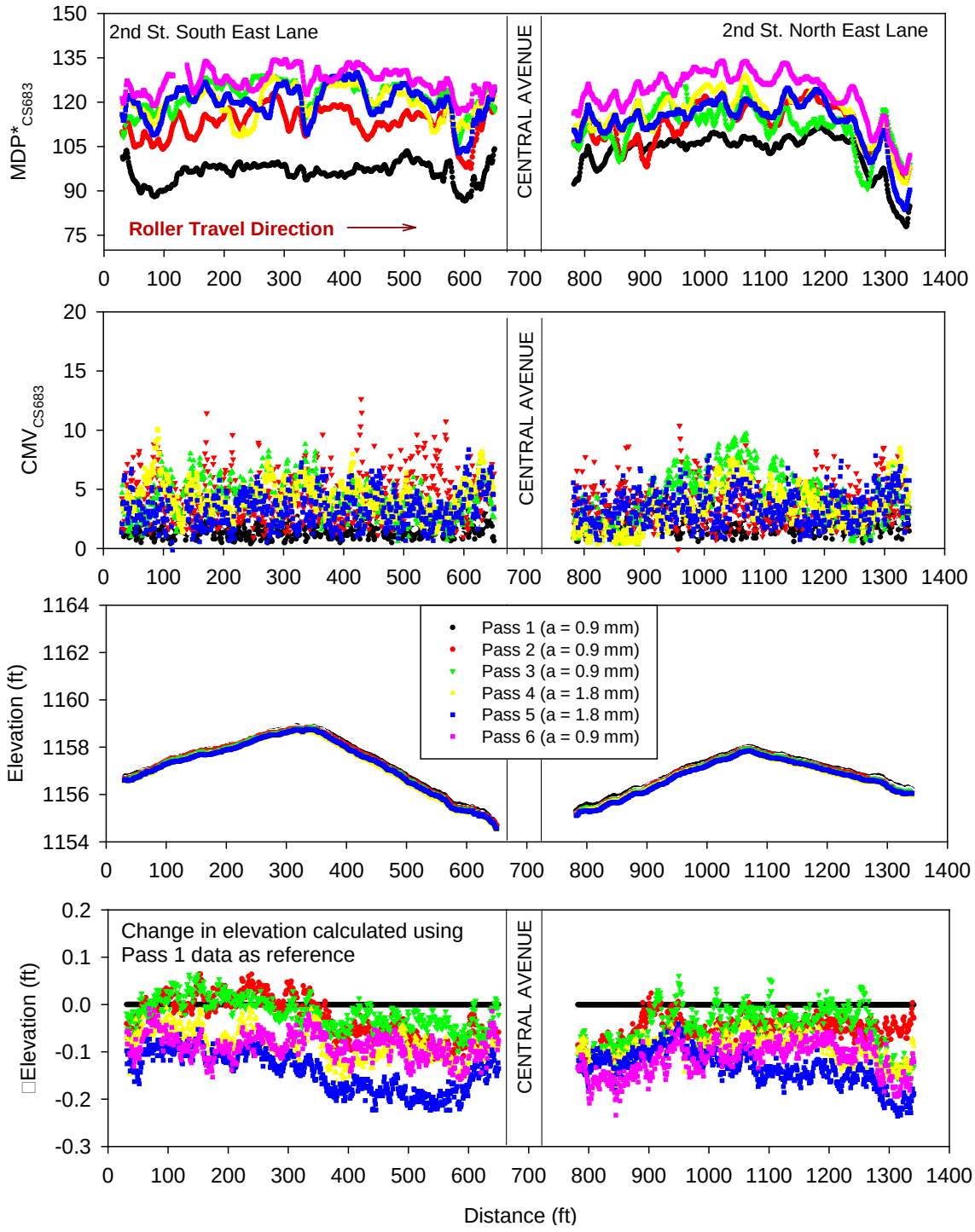

Figure 66. Plots of MDP*, CMV, elevation, and change in elevation on east lane from the RICM roller during compaction of the mechanically stabilized layer

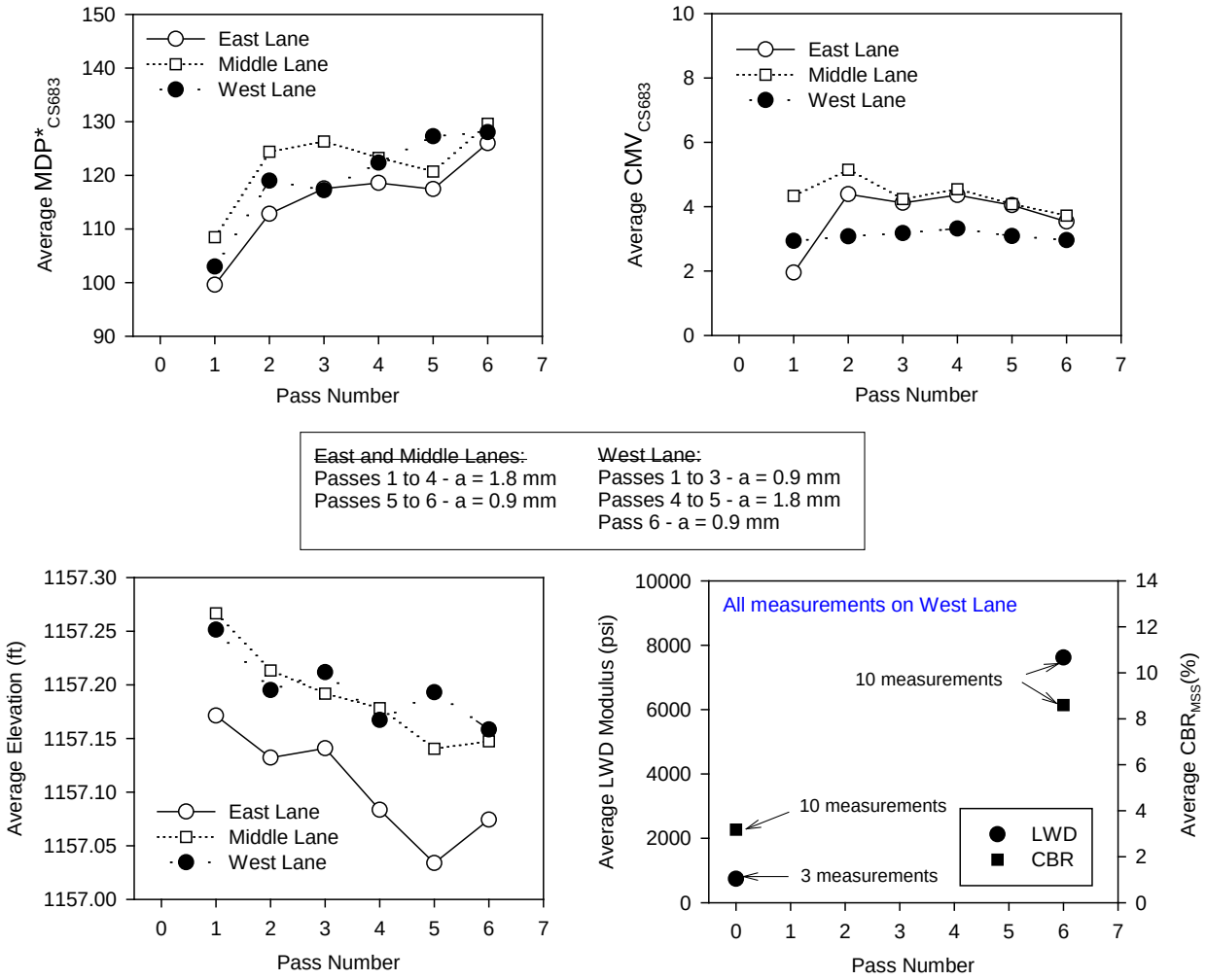

Figure 67. Change in average MDP*, CMV, elevation, LWD modulus, and CBR with increasing passes on the mechanically stabilized layer

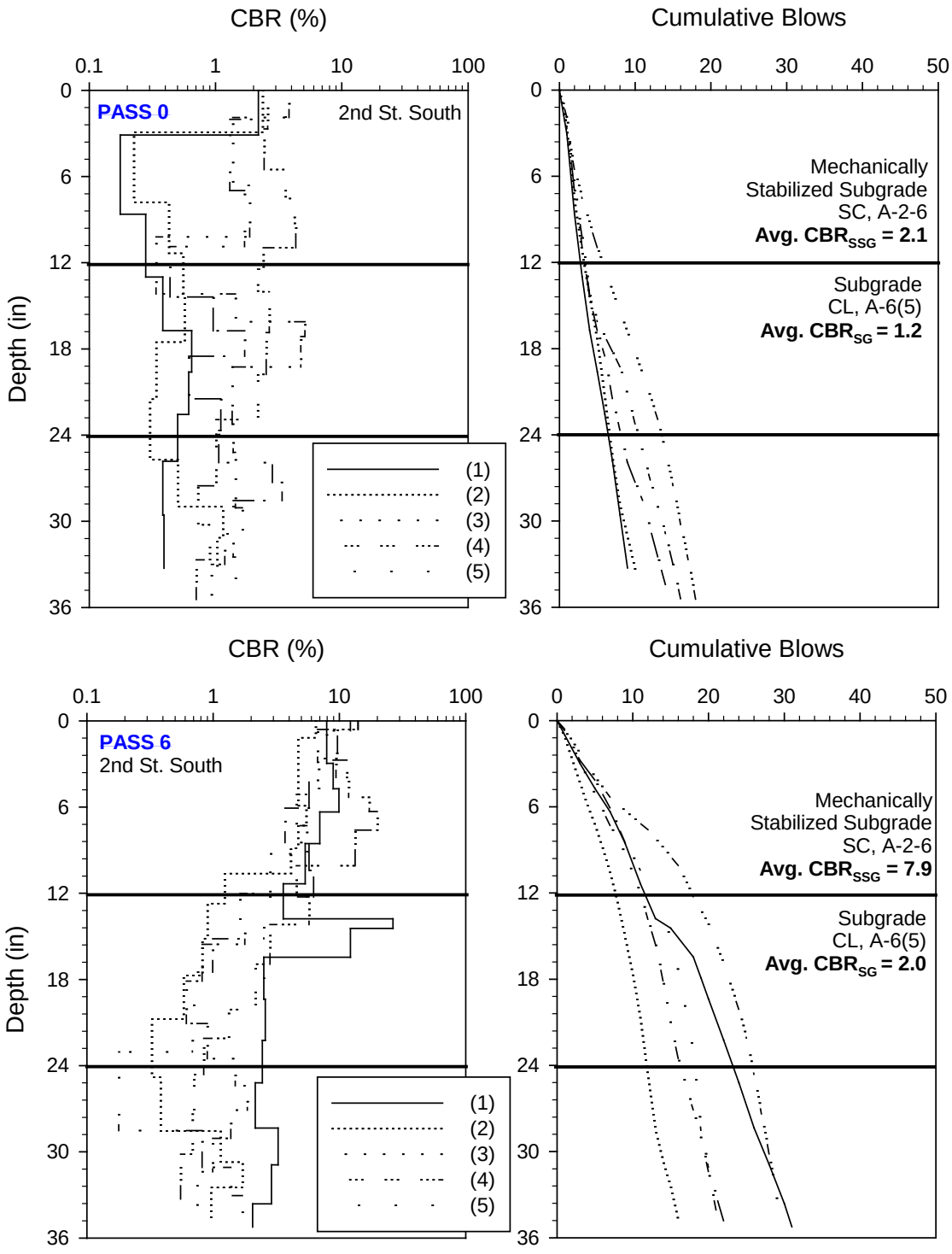

Figure 68. DCP-CBR and cumulative blows with depth profiles at five test locations from 2nd St. South at pass 0 and after pass 6

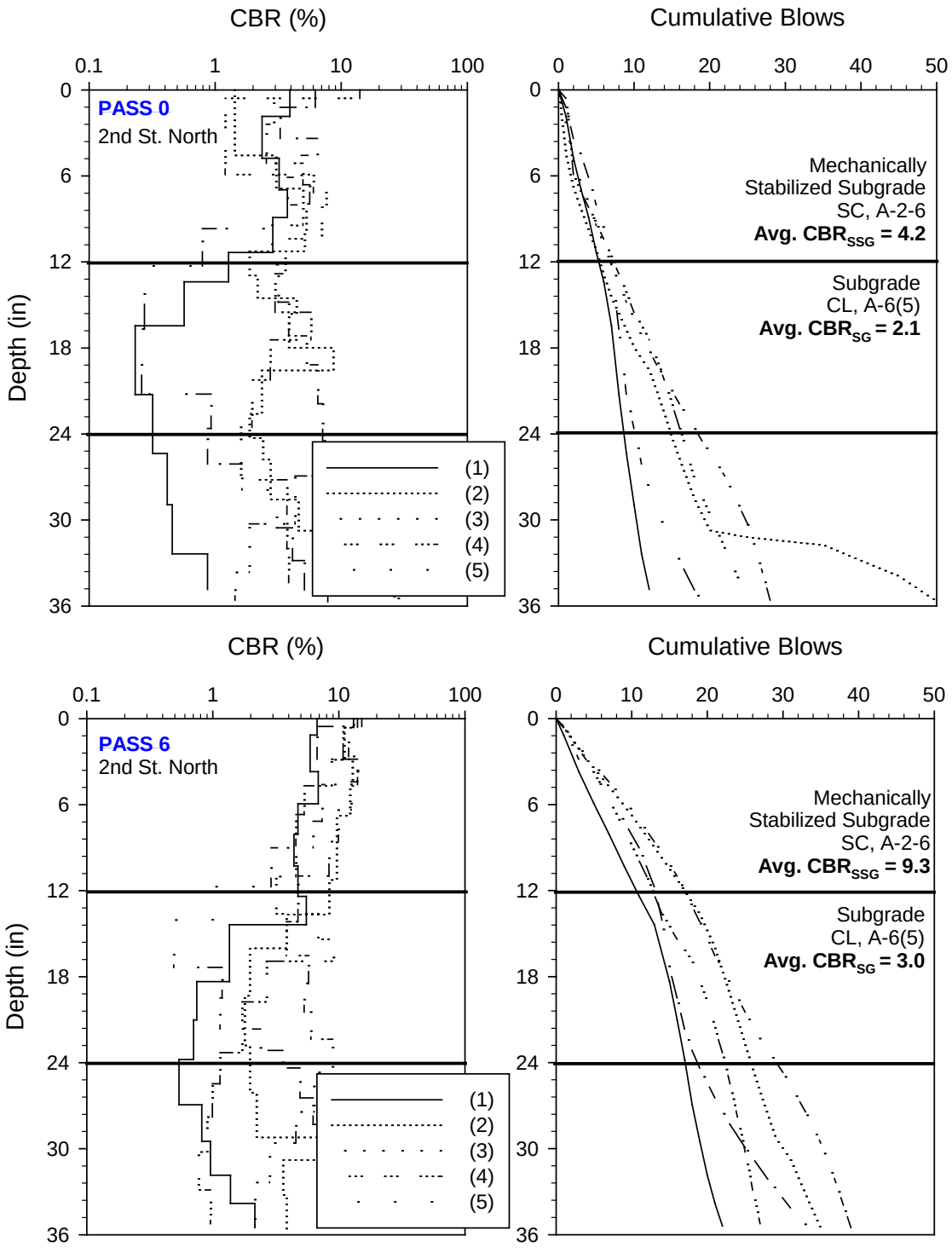

Figure 69. DCP-CBR and cumulative blows with depth profiles at five test locations from 2nd St. North at pass 0 and after pass 6

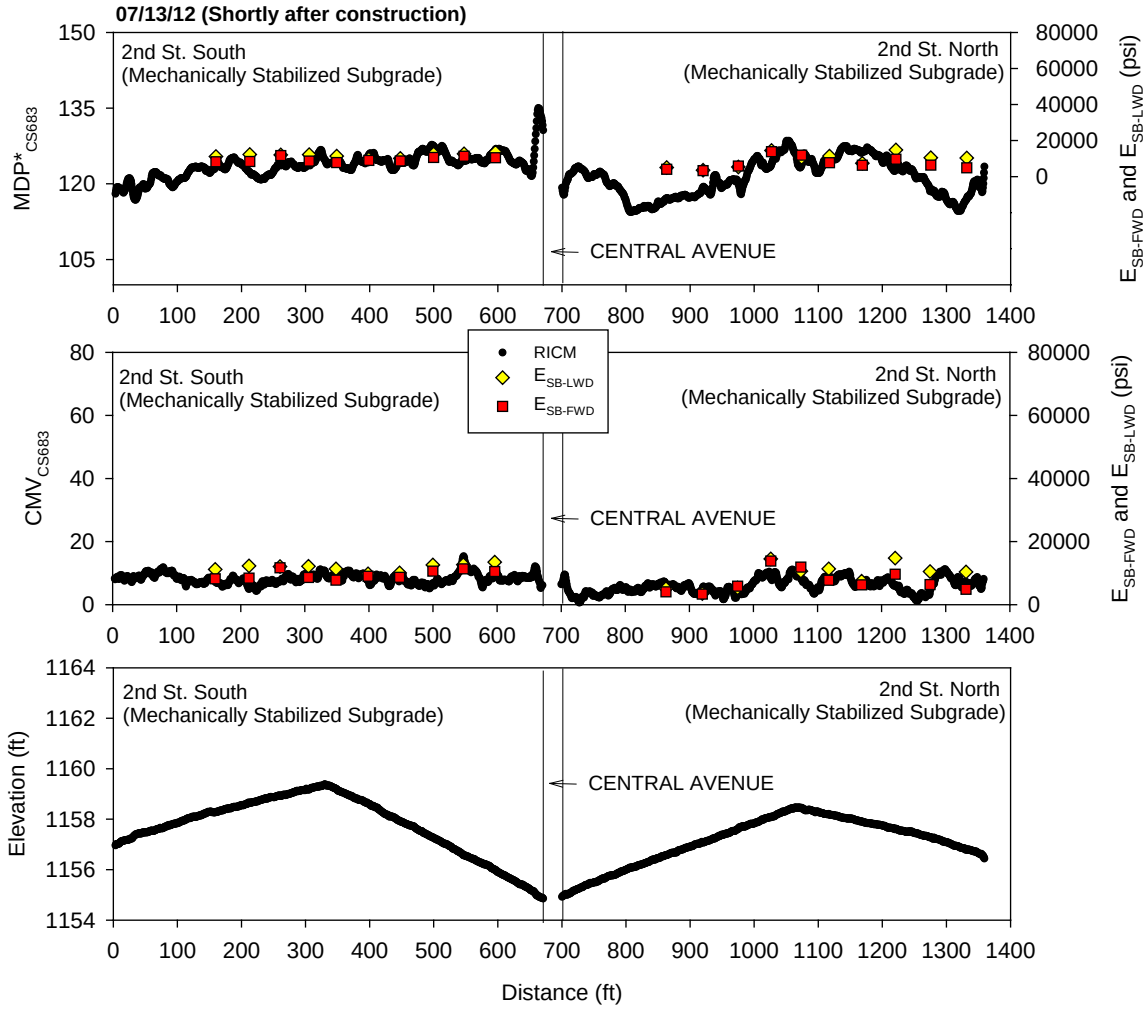

Figure 70. CS683 RICM, LWD, and FWD modulus measurements on 2nd St. shortly after construction (July 2012)

Performance Monitoring Results

CCV results obtained in low amplitude mode (a = 0.63 mm, f = 33 Hz) in comparison with $E_{SB\text{-}FWD}$ from October 2012 (about three months after construction) are shown in Figure 71. MDP^*_{CS683} and CMV_{CS683} results in comparison with $E_{SB\text{-}FWD}$ from April 2013 (during thawing about nine months after construction) are shown in Figure 72. Similarly, results from the CS74 machine obtained in low amplitude mode (a = 0.97 mm, f = 28 Hz) are shown in Figure 73. MDP^*_{CS683} and CMV_{CS683} results obtained from July 2012 and April 2013 are compared in Figure 74.

DCP-CBR and cumulative blows profiles from different testing times are shown in Figure 75 and Figure 76. Average CBR_{MSB} and CBR_{SG} for each test section are shown in Figure 77. Average $E_{SB\text{-}FWD}$ for each test section are shown in Figure 78.

CBR in the surface MSB layer and the underlying stabilized and unstabilized subgrade layers were lower in May 2013 than in October 2012 and April 2013. The subgrade and the stabilized subgrade layers were likely in partially thawed/frozen condition in April 2013. $E_{SB\text{-}FWD}$, MDP*, and CMV measurements were lower in April 2013 than in July and October 2012.

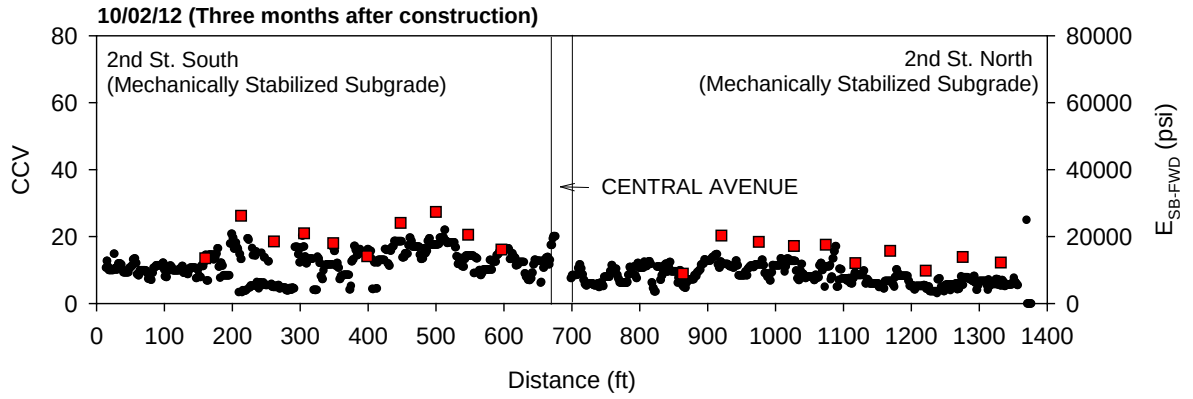

Figure 71. Sakai CCV and FWD modulus measurements on 2nd St. three months after construction (October 2012)

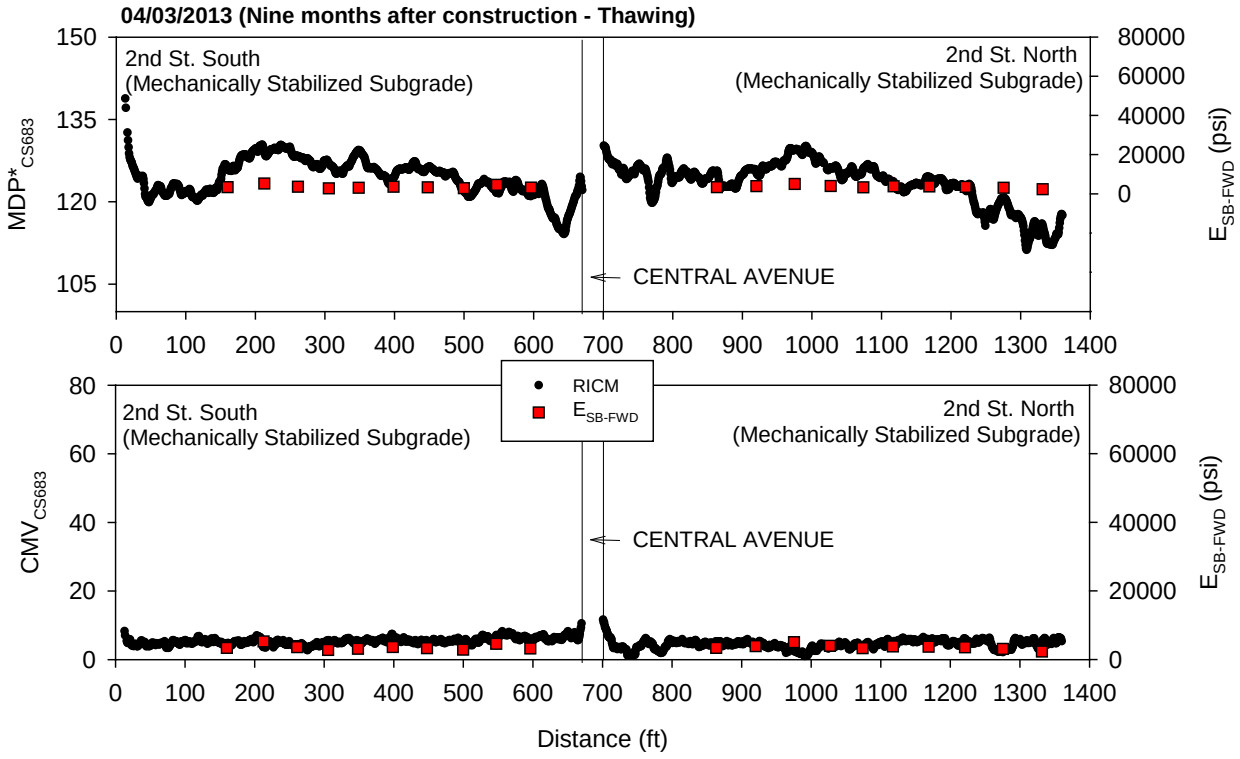

Figure 72. CS683 RICM and FWD modulus measurements on 2nd St. nine months after construction during thawing (April 2013)

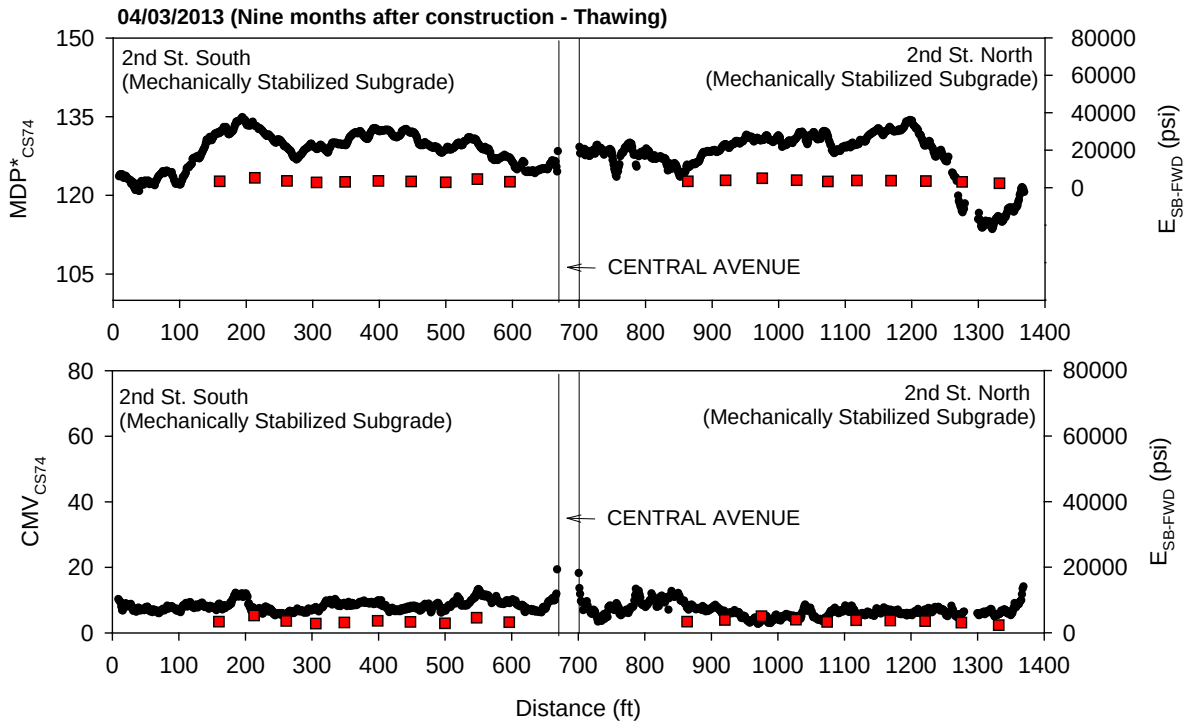

Figure 73. CS74 RICM and FWD modulus measurements on 2nd St. nine months after construction during thawing (April 2013)

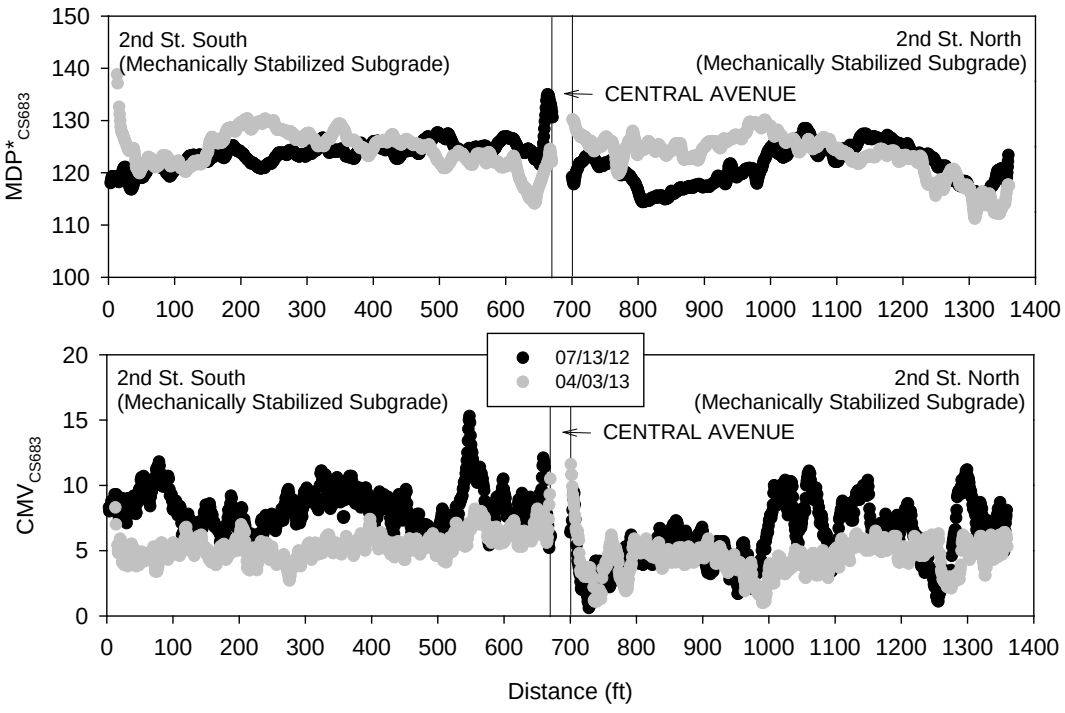

Figure 74. Comparison between CS683 RICM measurements on 2nd St. shortly after construction and nine months after construction during thawing

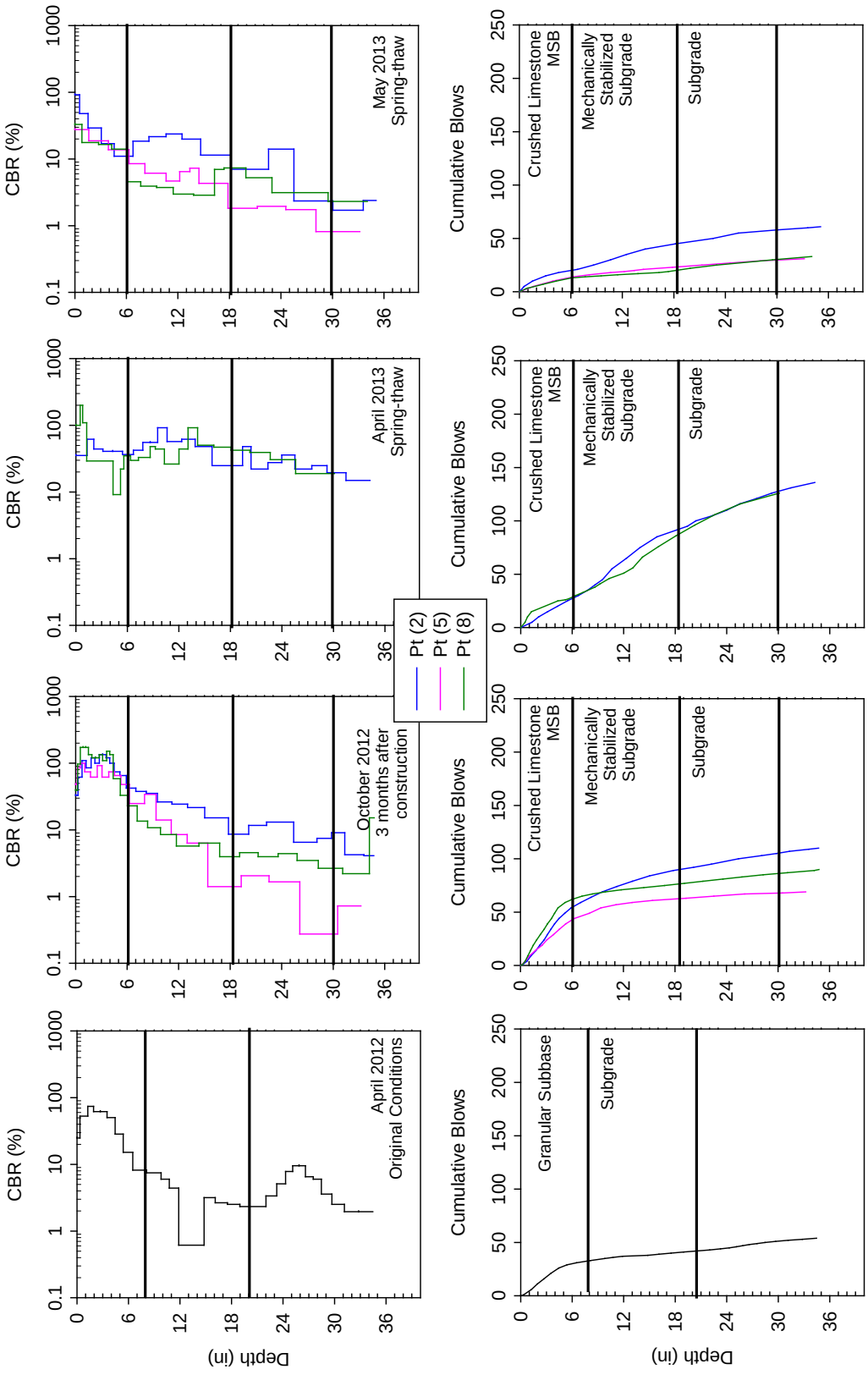

Figure 75. DCP test results from 2nd St. South from different testing times

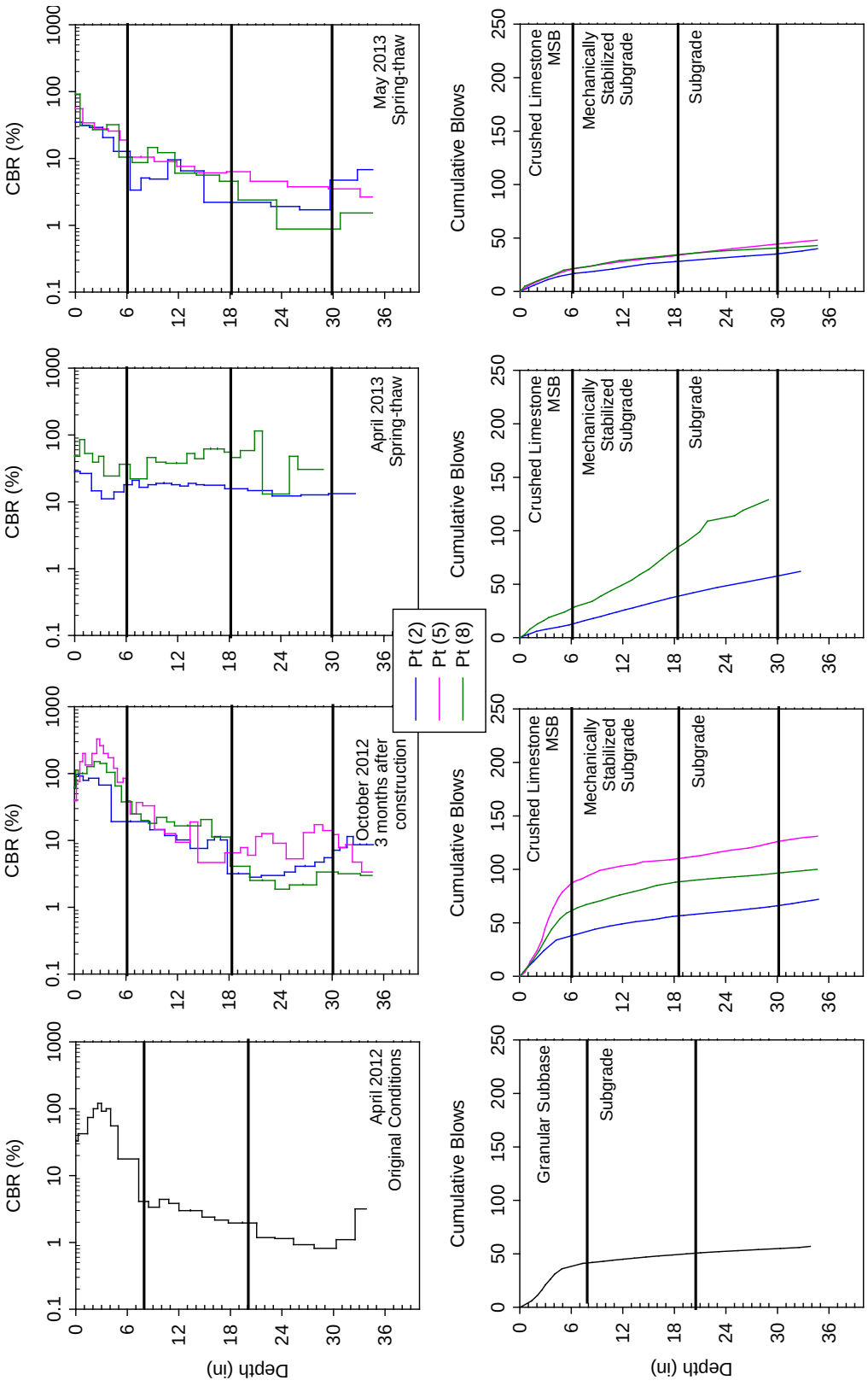

Figure 76. DCP test results from 2nd St. North from different testing times

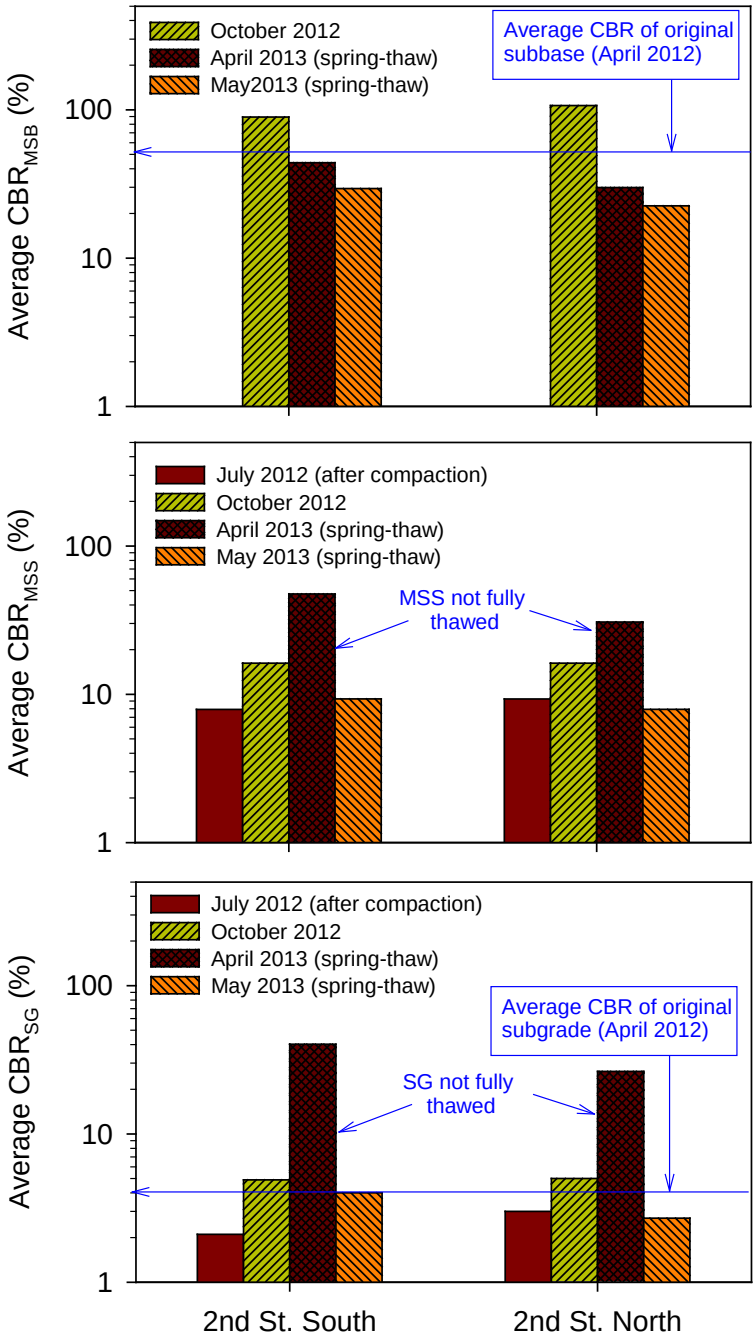

Figure 77. Average CBR (based on 3 to 5 tests) of subbase, mechanically stabilized layer, and unstabilized subgrade layers on 2nd St. South and North

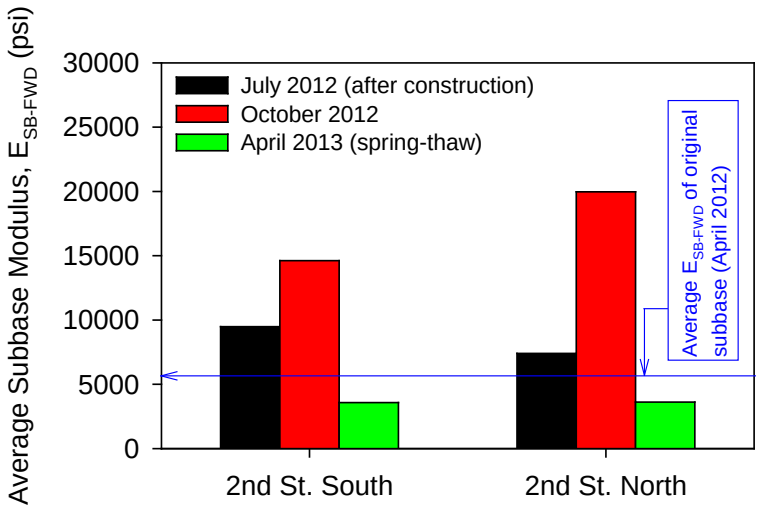

Figure 78. Average FWD subbase modulus (based on 10 tests) on 2nd St. South and North sections

3rd North-South: 4 and 6 inch Geocell + Geotextile

Construction Observations

Test sections were constructed with 4 in. high geocells on 3rd St. North and with 6 in. high geocells on 3rd St. South. The pavement foundation profiles for the two test sections are shown in Figure 79. The existing granular subbase layer was first excavated down to the subgrade level (Figure 80). A non-woven geotextile was placed over the subgrade to act as a separation barrier (Figure 81a). The geocell strips were stretched by staking the edges with short pieces of rebar (Figure 81b). Adjacent geocell strips were initially attached using 5 in. long staples or zip ties. This approached resulted in variability in the geocell opening widths and relatively slow speed of construction. Later, a pneumatic hog ring tool was used to staple adjacent geocell strips (Figure 81c) which expedited the construction process and helped achieve more uniform geocell openings. After the geocells were installed, crushed limestone MSB was placed with a skid steer (Figure 81d,e, and f) and compacted using a smooth drum vibratory roller. The design subbase layer thickness was 6 in. in the 4 in. geocell section and about 7 in. in the 6 in. geocell section.

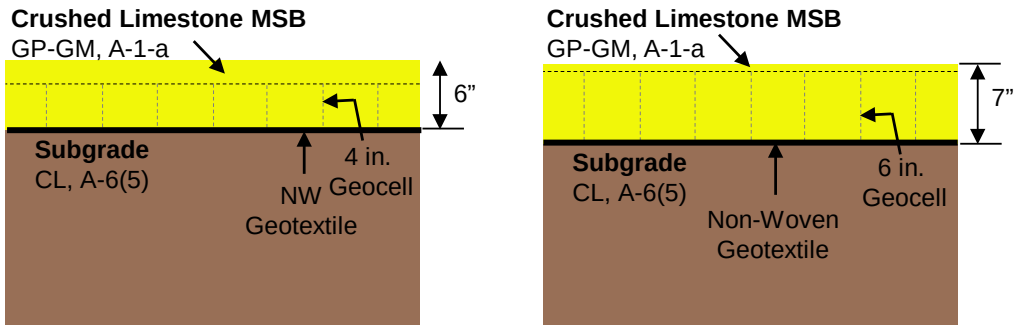

(a) (b)

Figure 79. Pavement foundation profiles with (a) 4 in. geocells on 3rd St. North, and (b) 6 in. geocells on 3rd St. South

Figure 80. Removal of existing granular subbase on 3rd St.

(a) (b)

(c) (d)

(e) (f)

Figure 81. Geocell installation and crushed limestone MSB layer construction: (a) installation of non-woven geotextile over subgrade; (b) stretching geocells over non-woven geotextile using short rebars; (c) attaching adjacent geocell strips using pneumatic hog ring tool; (d) placement of MSB in geocells; (e) MSB in geocells; and (f) 3rd St. after compaction of MSB layer

As-Constructed Test Results

RICM values (MDP*, CMV, and elevation) along 3rd St. on compacted crushed limestone MSB layer are shown in Figure 82. RICM measurements were obtained in low amplitude mode (a = 0.85 mm, f = 30 Hz). FWD and LWD modulus measurements obtained from 20 test locations along 3rd St. are also presented in Figure 82.

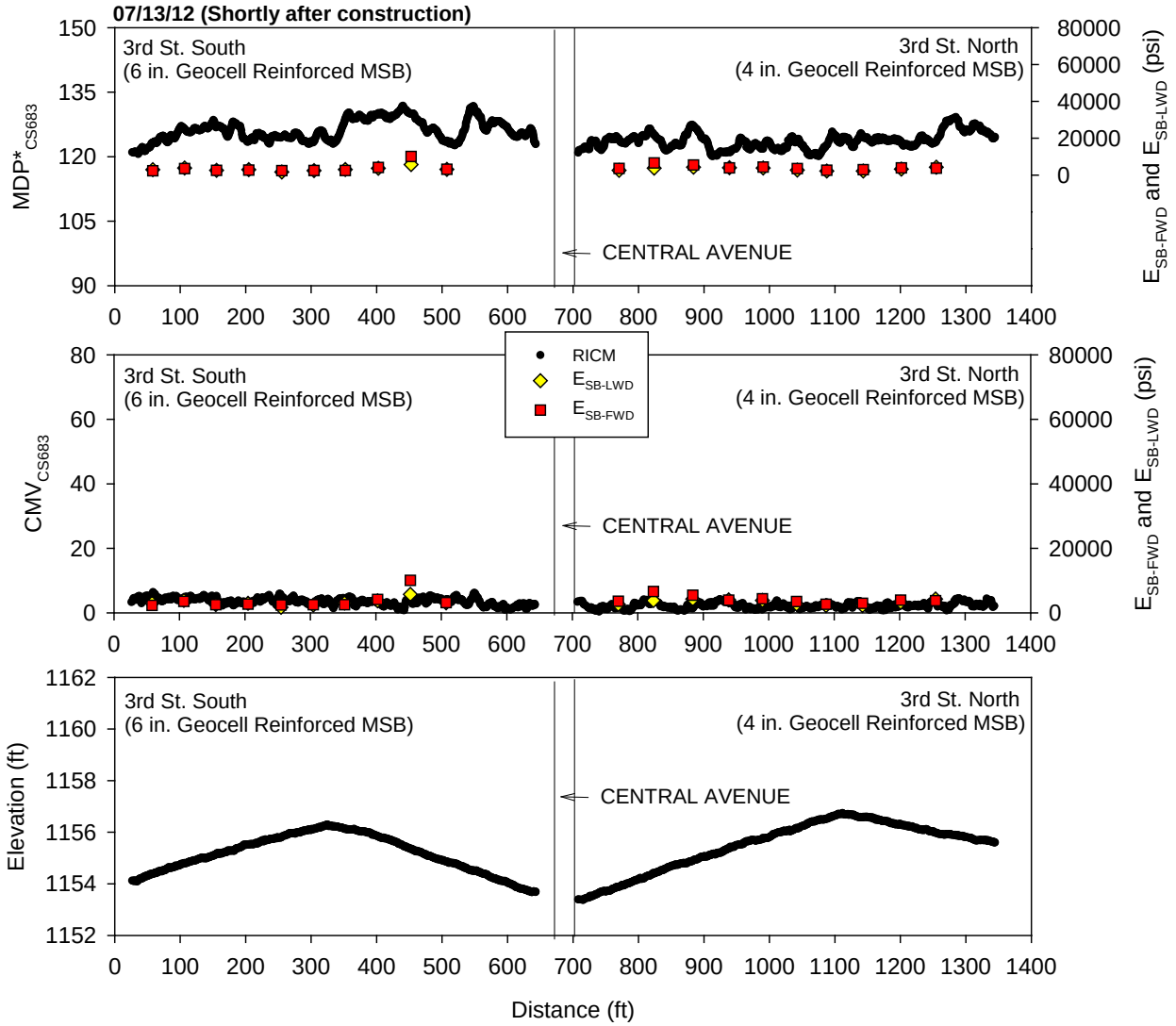

Figure 82. RICM, LWD, and FWD measurements on 3rd St. shortly after construction (July 2012)

Performance Monitoring Results

CCV results obtained in low amplitude mode (a = 0.63 mm, f = 33 Hz) in comparison with $E_{SB\text{-}FWD}$ from October 2012 (about three months after construction) are shown in Figure 83.

MDP^*_{CS683} and CMV_{CS683} results in comparison with $E_{SB\text{-}FWD}$ from April 2013 (during spring-thaw) are shown in Figure 84. Similarly, results from the CS74 machine are shown in Figure 85. MDP^*_{CS683} and CMV_{CS683} from July 2012 and April 2013 are compared in Figure 86.

DCP-CBR and cumulative blows profiles from different testing times are shown in Figure 87 and Figure 88. Average CBR_{MSB} and CBR_{SG} for each test section are shown in Figure 89. Average $E_{SB\text{-}FWD}$ for each test section are shown in Figure 90.

$E_{SB\text{-}FWD}$ showed slightly lower values in April 2013 during spring-thaw than in July and October 2012. No significant differences were observed in CBR_{MSB} on 3rd St. North between different testing times, but the values on 3rd St. South were lower during spring-thaw in April 2013 than in October 2012. No significant differences were observed in CMV and MDP* measurements between July 2012 and April 2013.

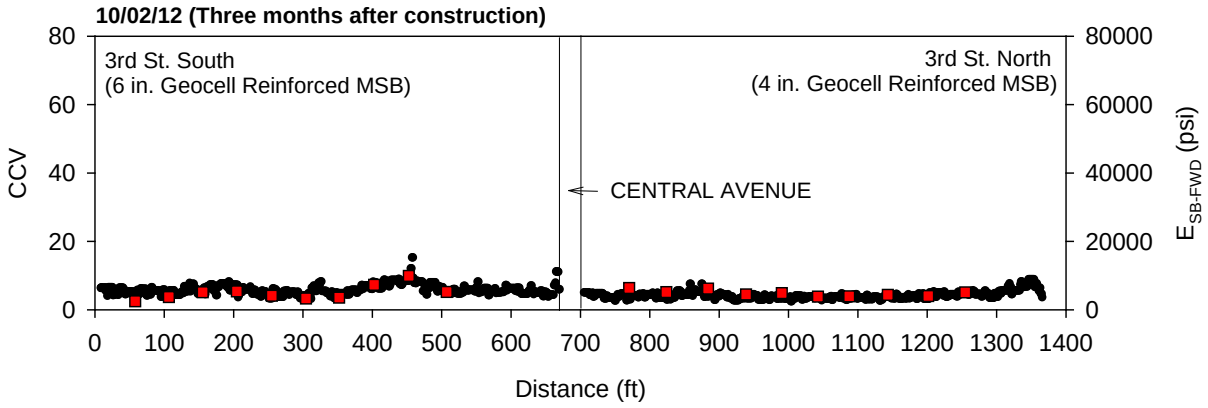

Figure 83. Sakai CCV and FWD modulus measurements on 3rd St. three months after construction (October 2012)

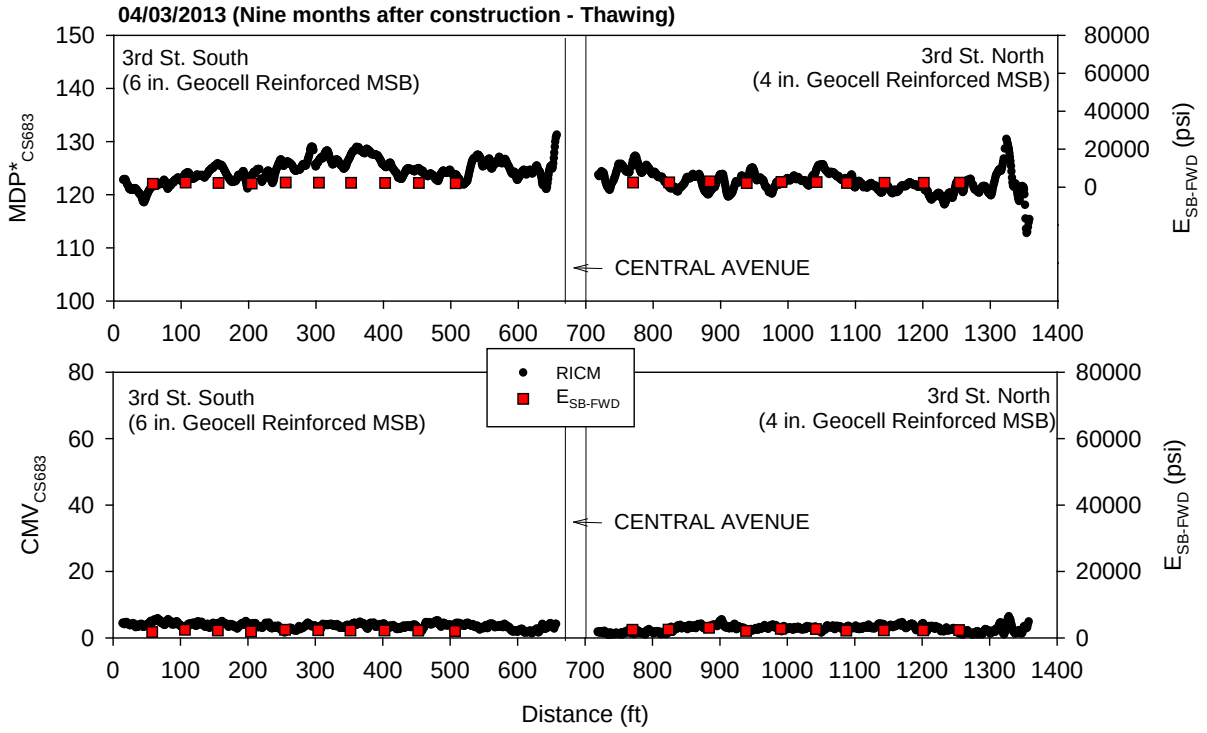

Figure 84. CS683 RICM and FWD modulus measurements on 3rd St. nine months after construction during thawing (April 2013)

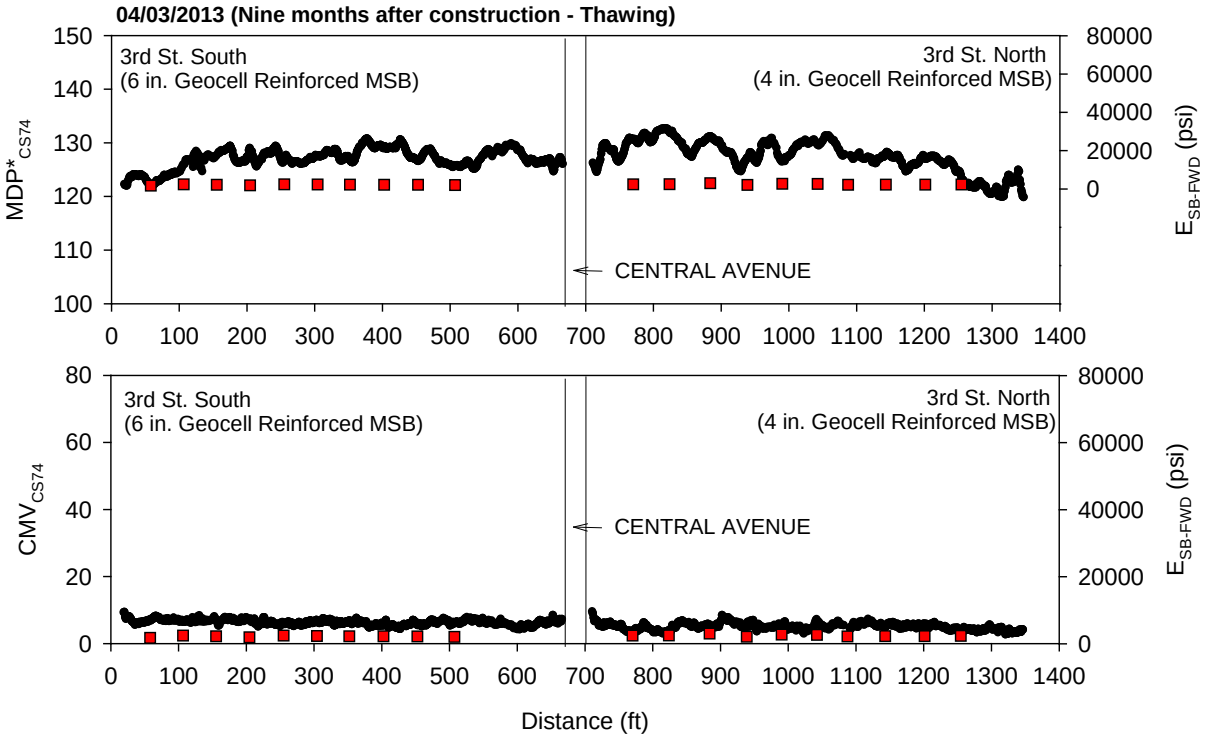

Figure 85. CS74 RICM and FWD modulus measurements on 3rd St. nine months after construction during thawing (April 2013)

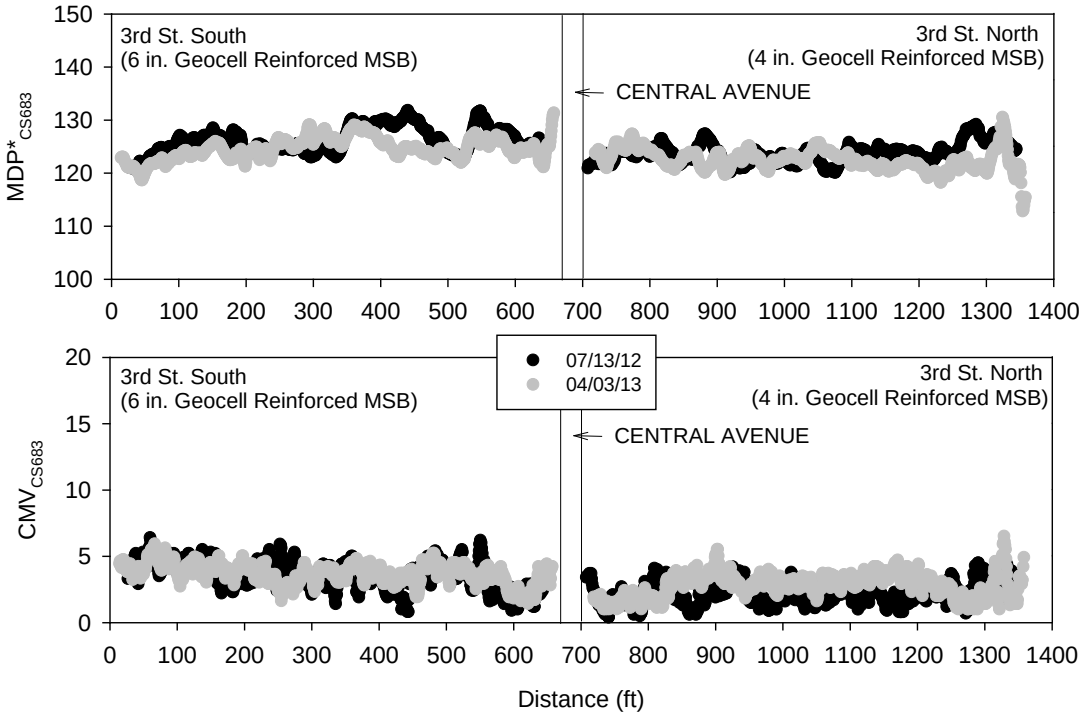

Figure 86. Comparison between CS683 RICM measurements on 3rd St. shortly after construction and nine months after construction during thawing

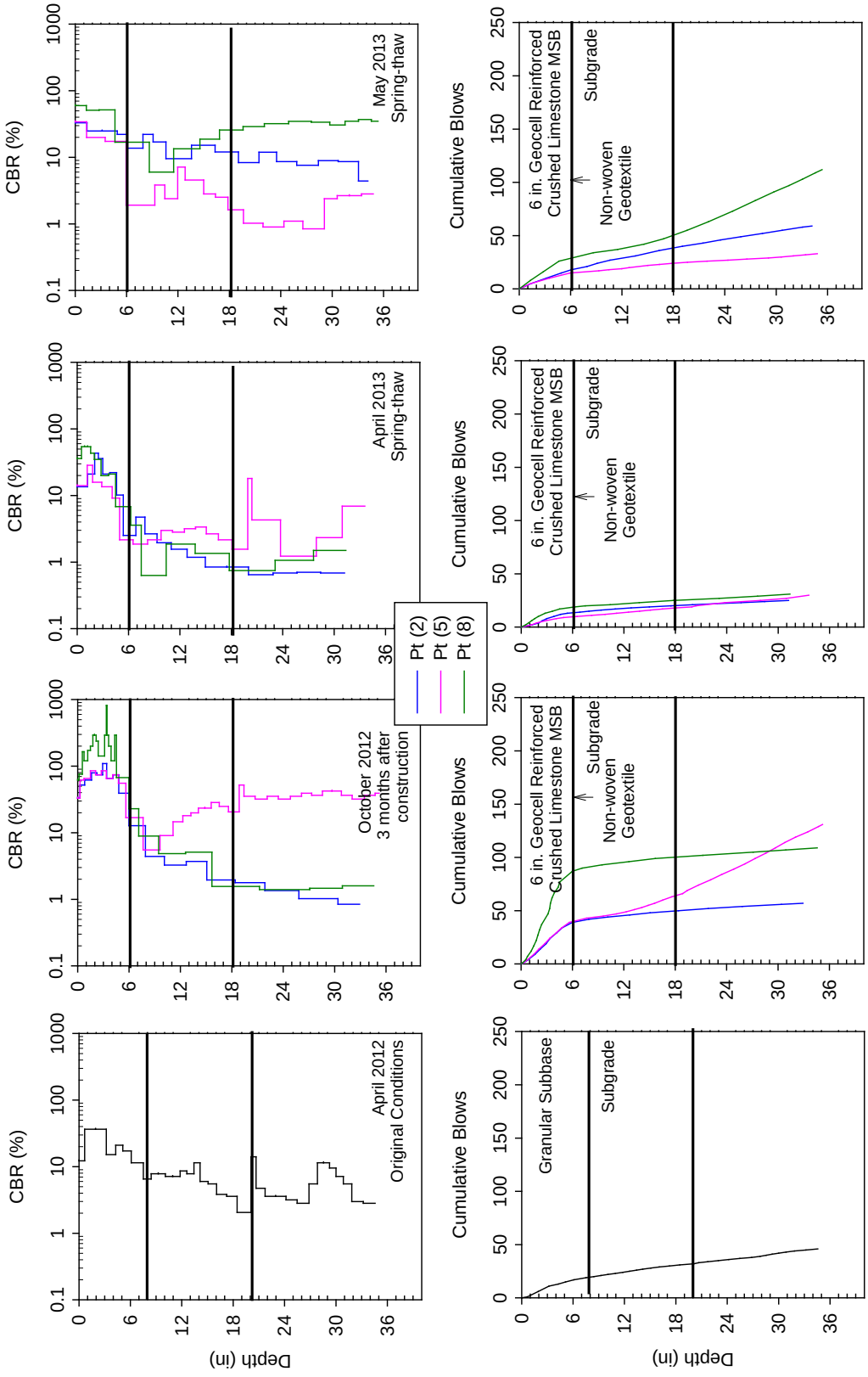

Figure 87. DCP test results from 3rd St. South from different testing times

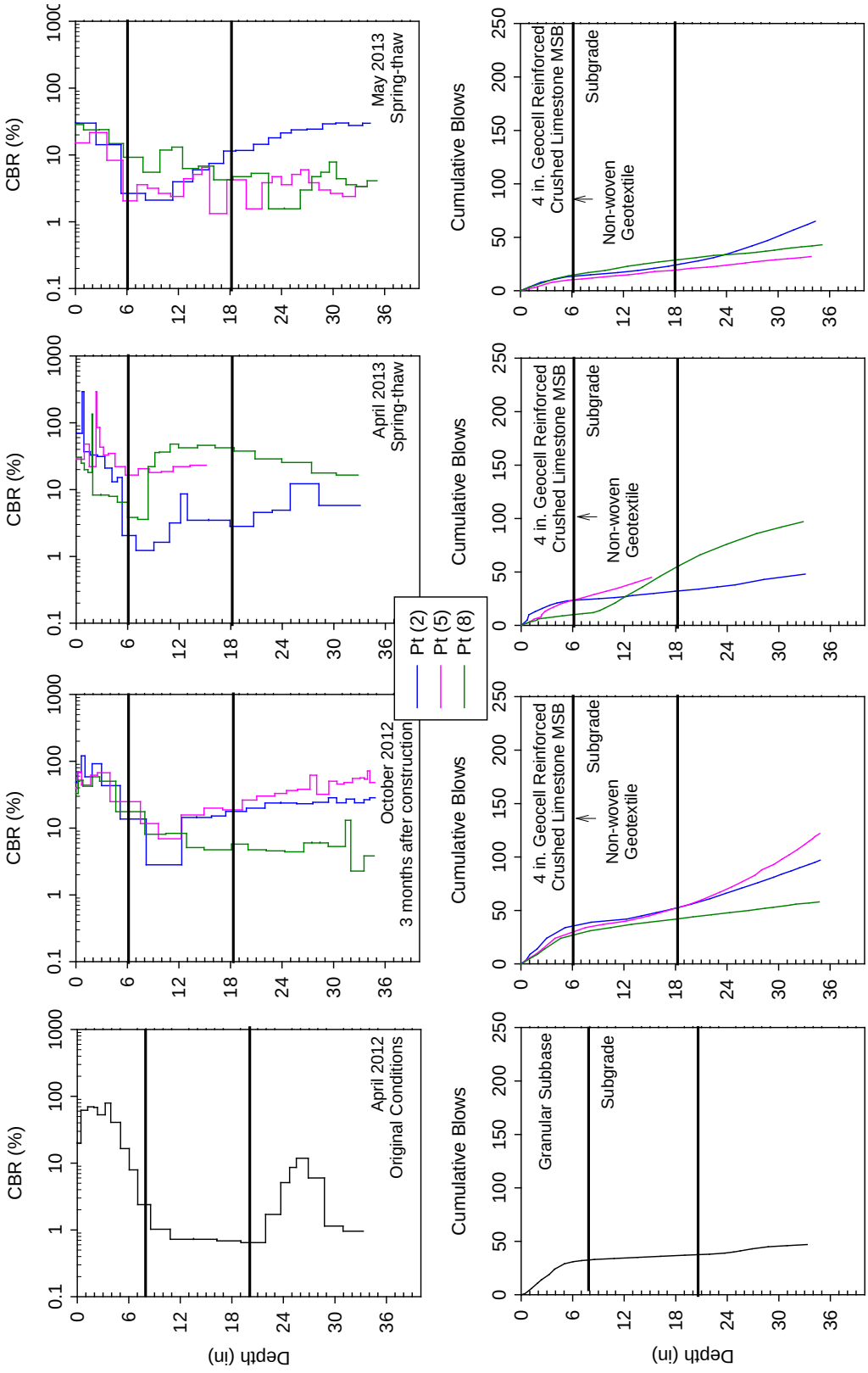

Figure 88. DCP test results from 3rd St. North from different testing times

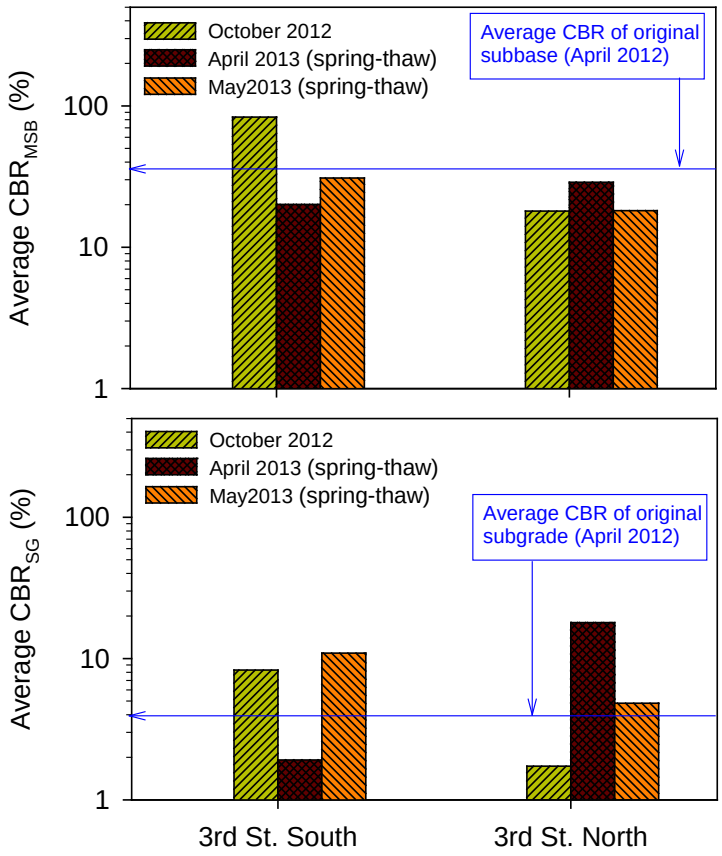

Figure 89. Average CBR (based on 3 tests) of geocell reinforced MSB and subgrade layers on 3rd St. South and North

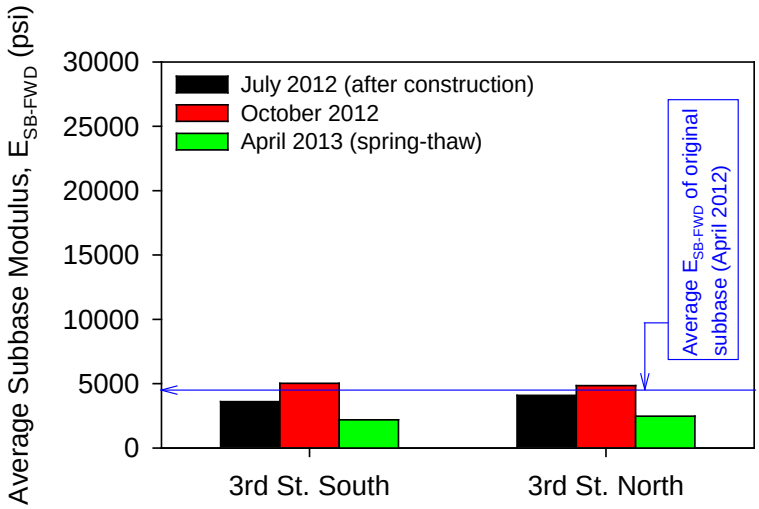

Figure 90. Average FWD subbase modulus (based on 10 tests) on 3rd St. South and North sections

4th North-South: Non-woven and Woven Geotextile

Construction Observations

Test sections were constructed with non-woven geotextile on 4th St. North and with woven geotextile on 4th St. South, by placing the geotextiles at the subgrade and MSB layer interface. The pavement foundation profiles are shown in Figure 91. The existing granular subbase layer was first excavated down to the subgrade level (Figure 92). Geotextiles were then placed over the subgrade (Figure 93a,b). A 6 in. thick crushed limestone MSB was placed over the geotextile (Figure 93c,d,e,f) and compacted using a smooth drum vibratory roller.

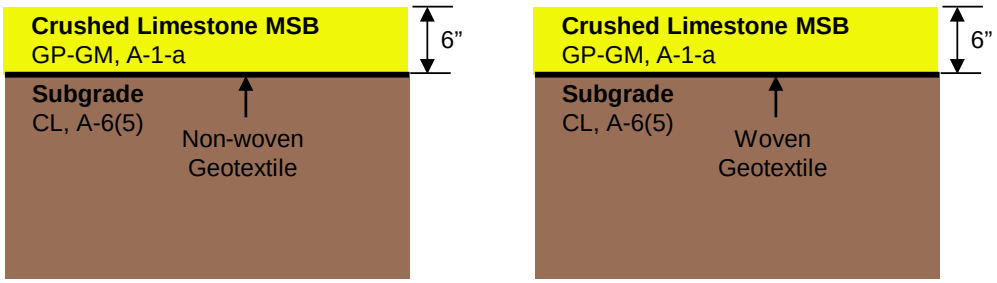

(a) (b)

Figure 91. Pavement foundation profiles with (a) non-woven geotextile on 4th St. North, and (b) woven geotextile on 4th St. South

Figure 92. Removal of existing granular subbase and excavating to subgrade elevation on 4th St.

(a) (b)

(c) (d)

(e) (f)

Figure 93. Geotextile installation and crushed limestone MSB layer construction: (a) woven geotextile over subgrade; (b) non-woven geotextile over subgrade; (c) MSB layer placement over woven geotextile; (d) MSB layer placement over non-woven geotextile; (e) MSB layer spreading using motor grader; and (f) 4th St. after compaction of MSB layer

As-Constructed Test Results

RICM values (MDP*, CMV, and elevation) along 4th St. on compacted crushed limestone MSB layer are shown in Figure 94. RICM measurements were obtained in low amplitude mode (a = 0.85 mm, f = 30 Hz). FWD and LWD modulus measurements obtained from 20 test locations along 4th St. are also presented in Figure 94.

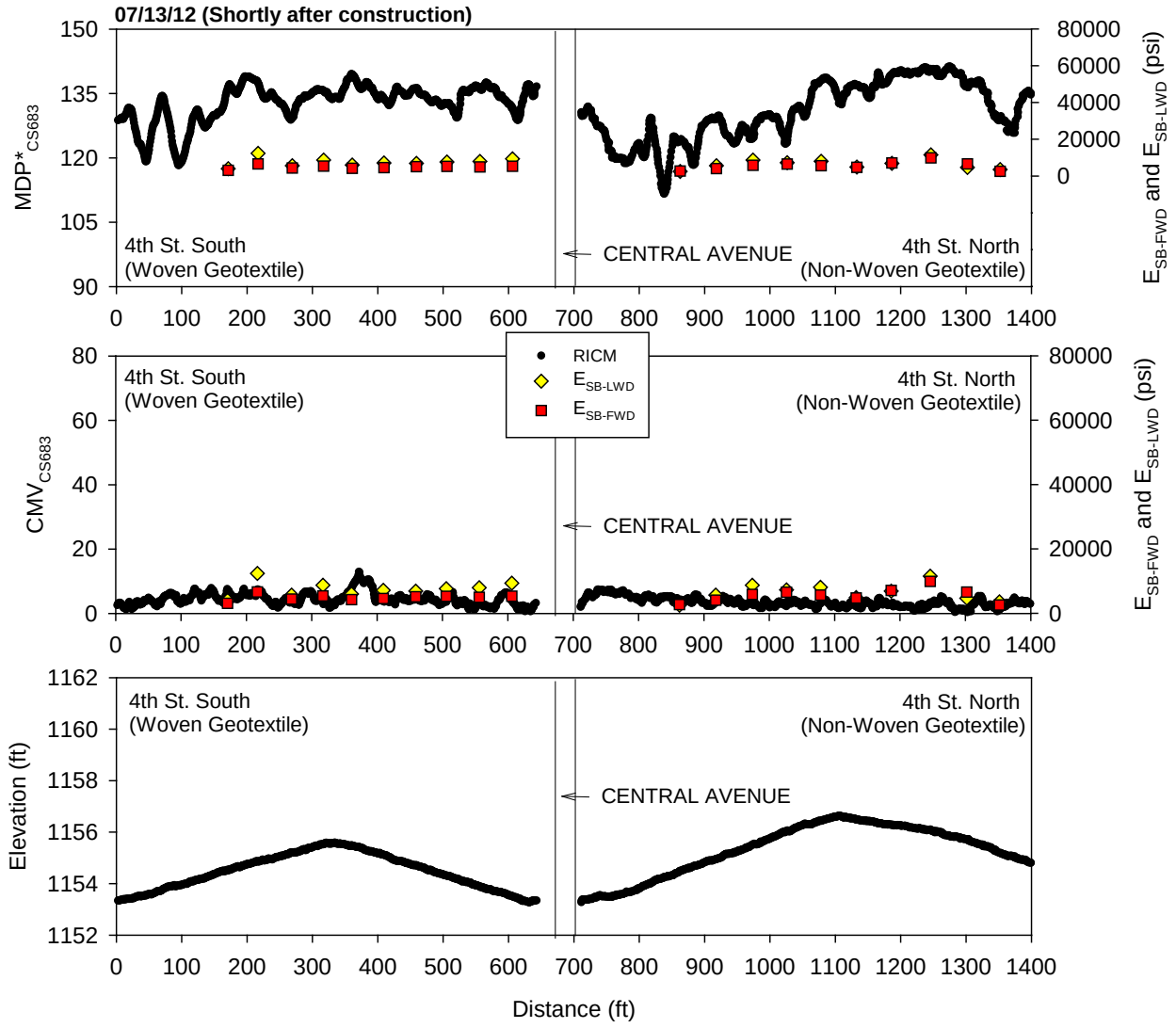

Figure 94. RICM, LWD, and FWD measurements on 4th St. shortly after construction (July 2012)

Performance Monitoring Results

CCV results obtained in low amplitude mode (a = 0.63 mm, f = 33 Hz) in comparison with $E_{SB\text{-}FWD}$ from October 2012 (about three months after construction) are shown in Figure 95. MDP^*_{CS683} and CMV_{CS683} results in comparison with $E_{SB\text{-}FWD}$ from April 2013 (during spring-

thaw) are shown in Figure 96. Similarly, results from the CS74 machine are shown in Figure 97. MDP^*_{CS683} and CMV_{CS683} from July 2012 and April 2013 are compared in Figure 98.

DCP-CBR and cumulative blows profiles from different testing times are shown in Figure 99 and Figure 100. Average CBR_{MSB} and CBR_{SG} for each test section are shown in Figure 101. Average $E_{SB\text{-}FWD}$ for each test section are shown in Figure 102.

$E_{SB\text{-}FWD}$ showed lower values in April 2013 during spring-thaw than in July and October 2012. CBR_{MSB} values were lower during spring-thaw in April 2013 than in October 2012, but increased in May 2013. CMV and MDP* measurements were generally lower in April 2013 than in July 2012.

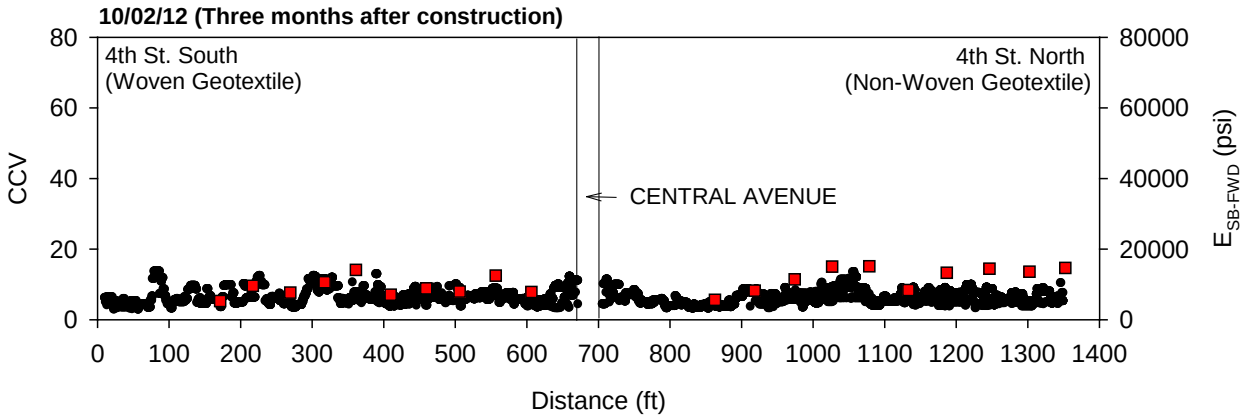

Figure 95. Sakai CCV and FWD modulus measurements on 4th St. three months after construction (October 2012)

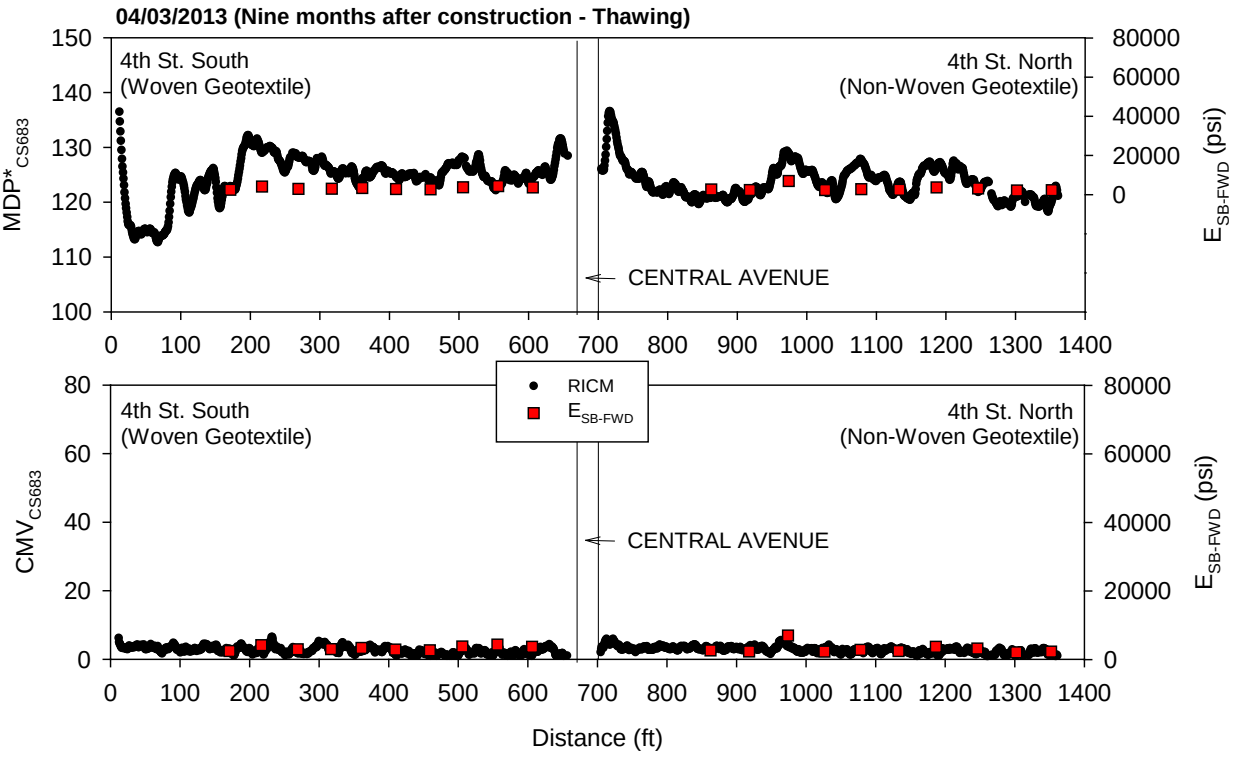

Figure 96. CS683 RICM and FWD modulus measurements on 4th St. nine months after construction during thawing (April 2013)

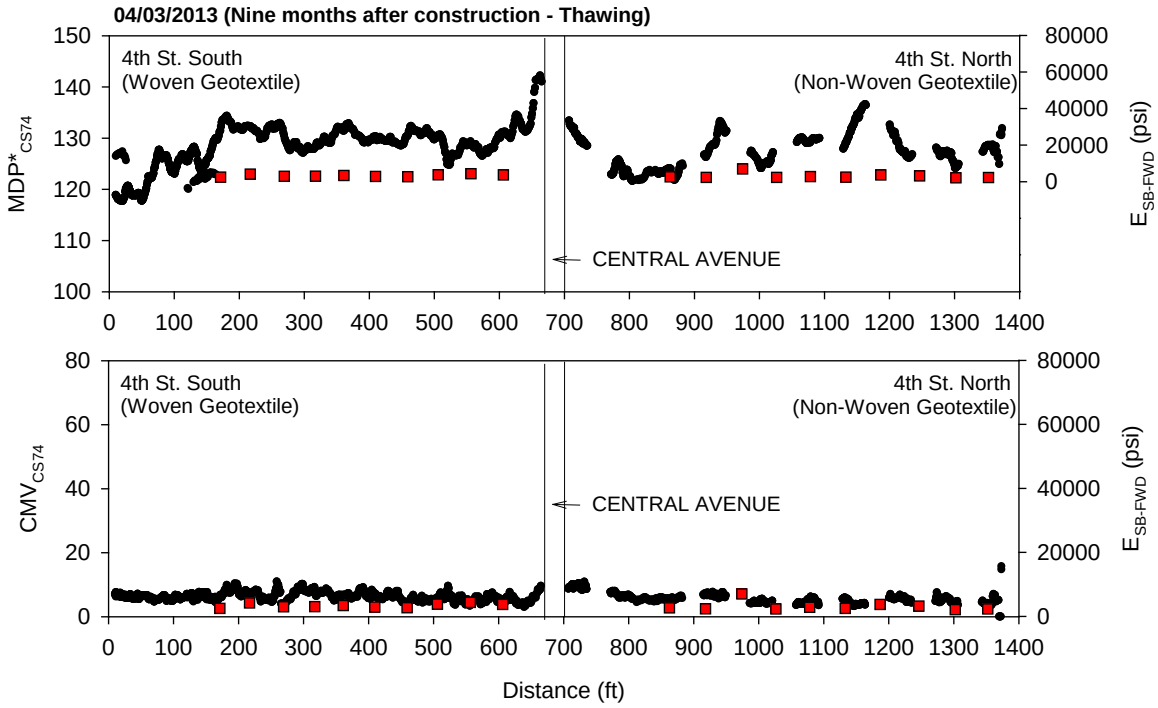

Figure 97. CS74 RICM and FWD modulus measurements on 4th St. nine months after construction during thawing (April 2013)

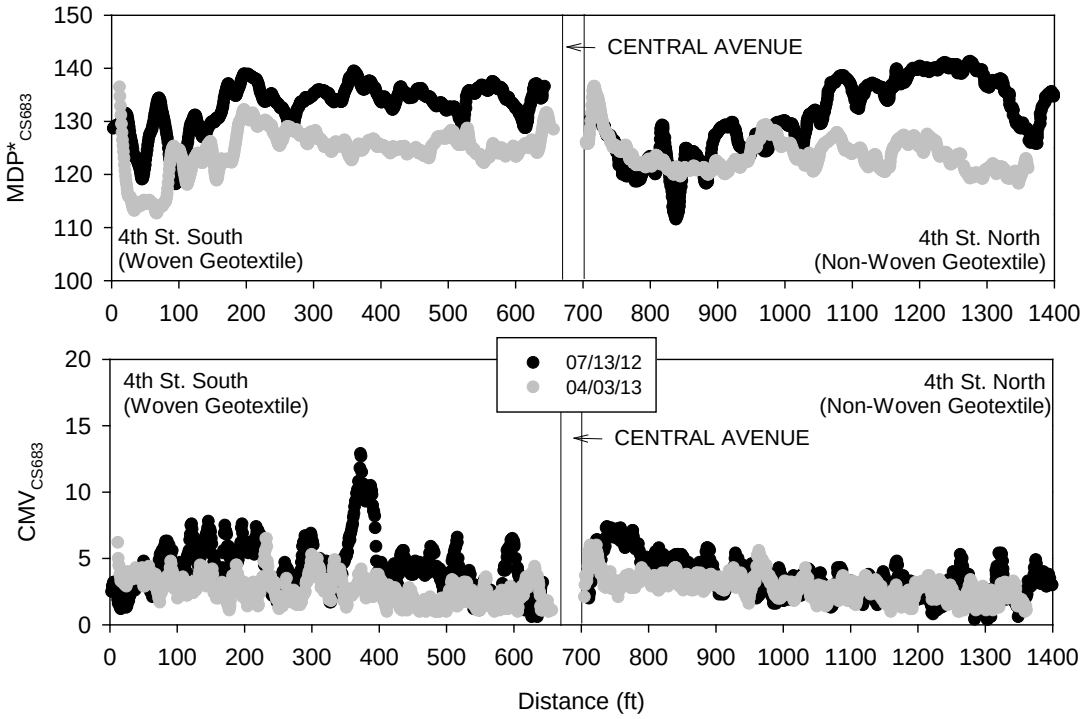

Figure 98. Comparison between CS683 RICM measurements on 4th St. shortly after construction and nine months after construction during thawing

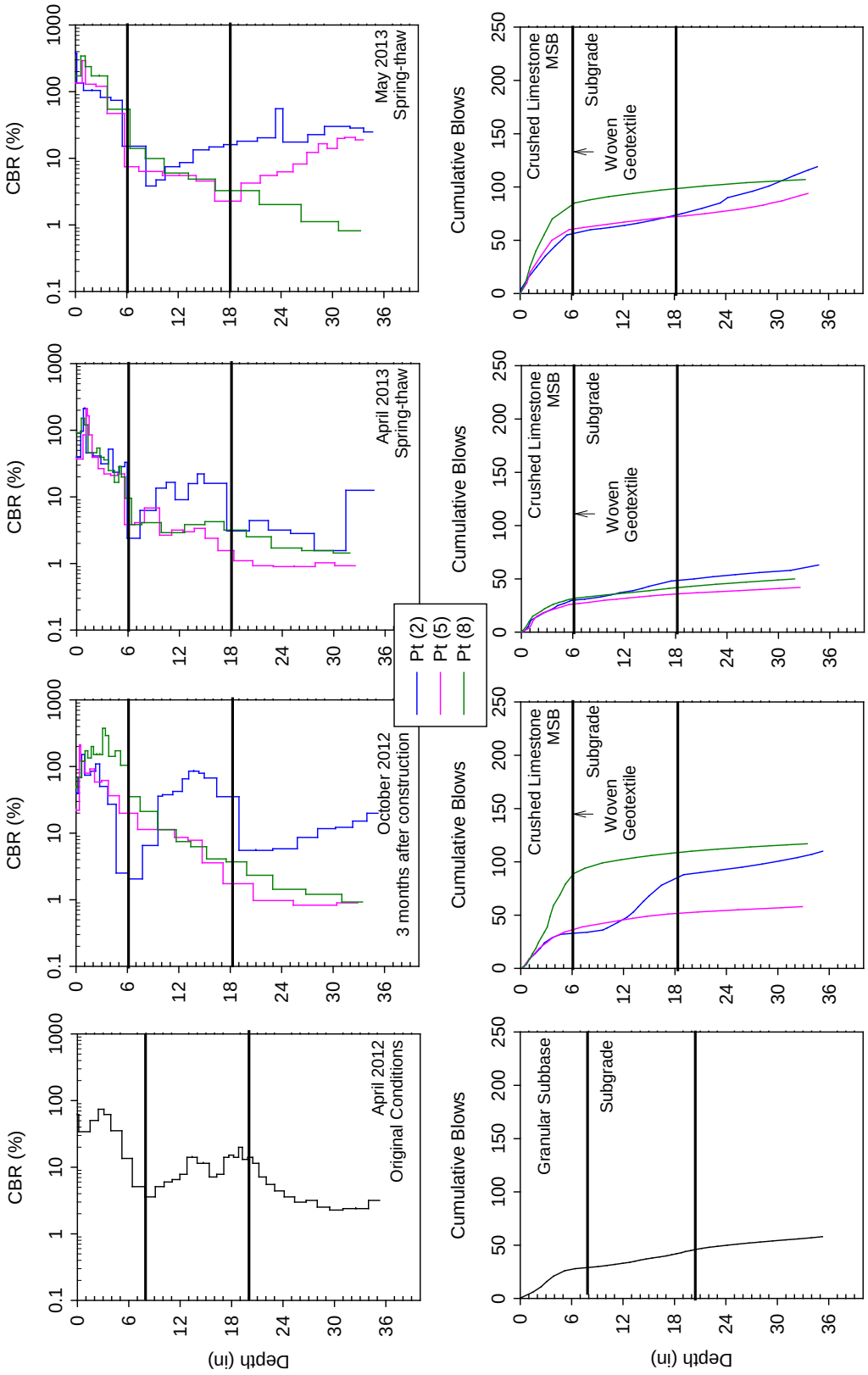

Figure 99. DCP test results from 4th St. South from different testing times

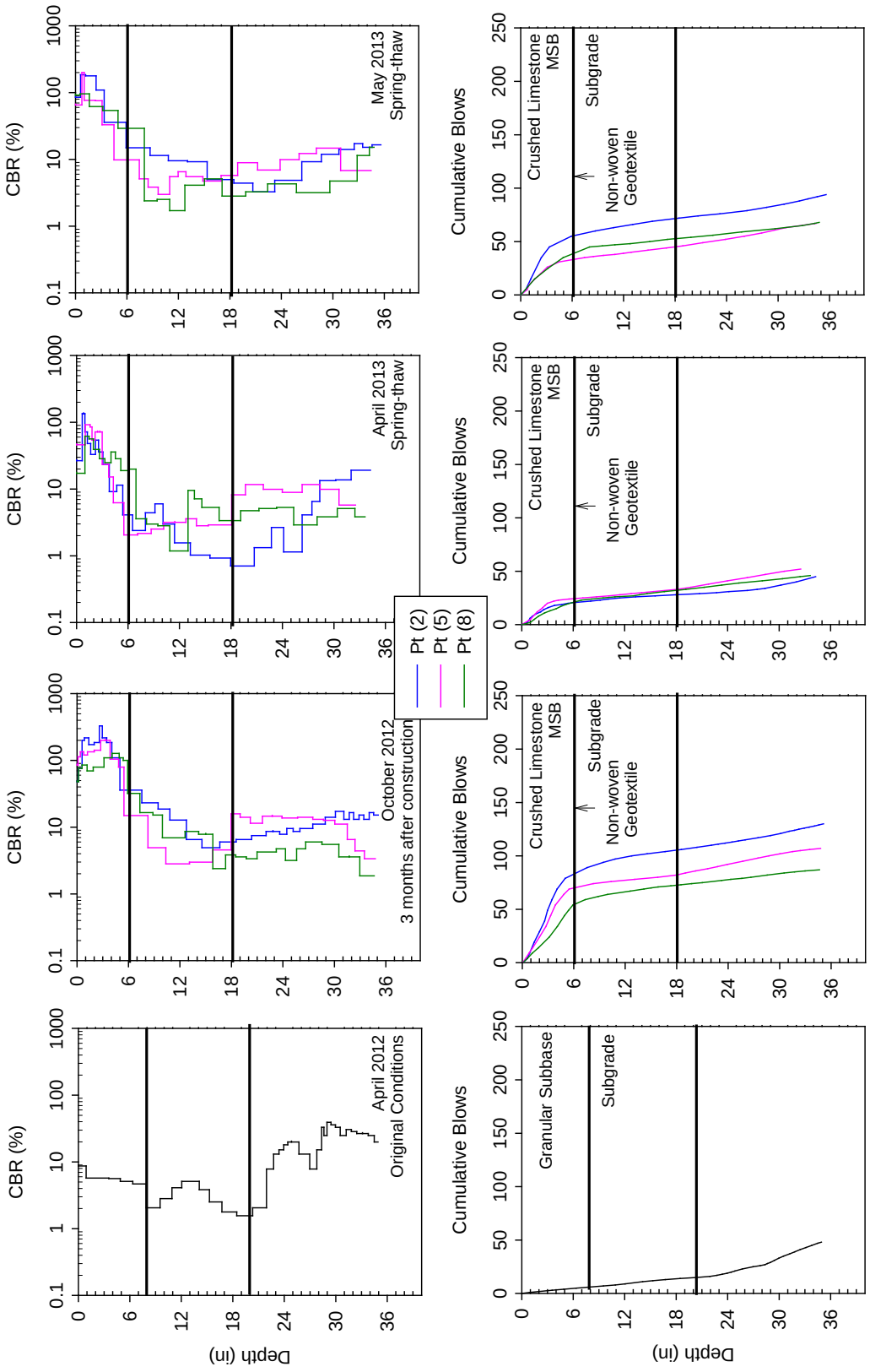

Figure 100. DCP test results from 4th St. North from different testing times

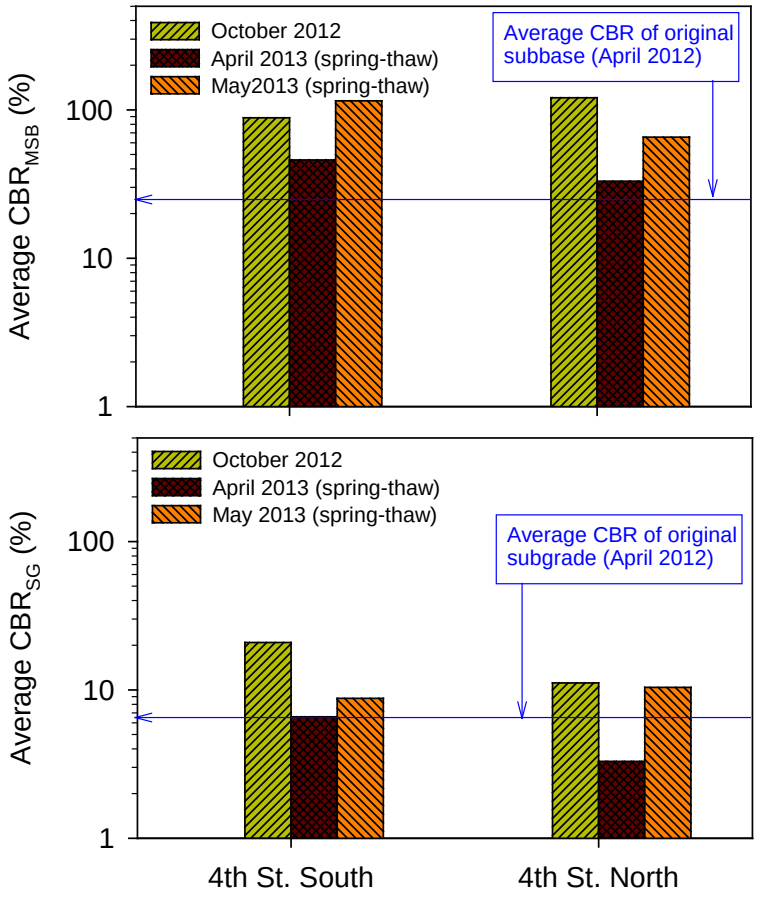

Figure 101. Average CBR (based on 3 tests) of MSB and subgrade layers on 4th St. South and North

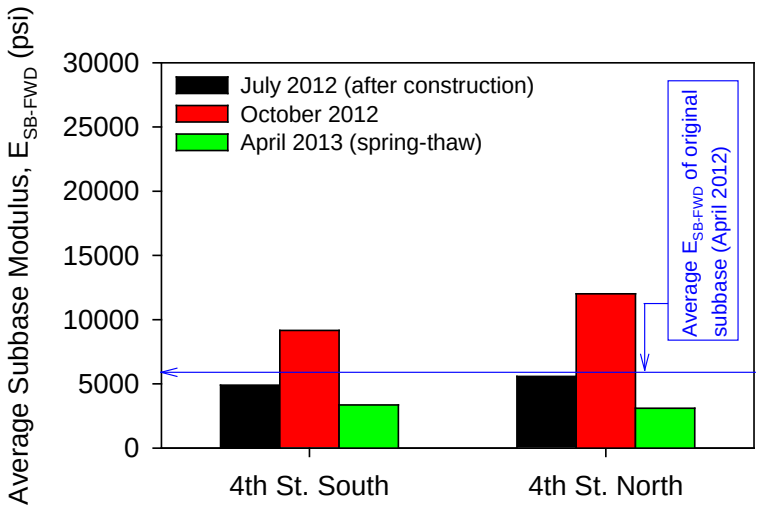

Figure 102. Average FWD subbase modulus (based on 10 tests) on 4th St. South and North sections

5th North-South: Triaxial and Biaxial Geogrid

Construction Observations

Test sections were constructed with triaxial geogrid on 5th St. North and with biaxial geogrid on 5th St. South, by placing the geogrids at the subgrade and MSB layer interface. The pavement foundation profiles are shown in Figure 103. The existing granular subbase layer was first excavated down to the subgrade level (Figure 104). Geogrids were then placed over the subgrade (Figure 105a,b). A 6 in. thick crushed limestone MSB was placed over the geogrids (Figure 106c,d,e,f) and compacted using a smooth drum vibratory roller.

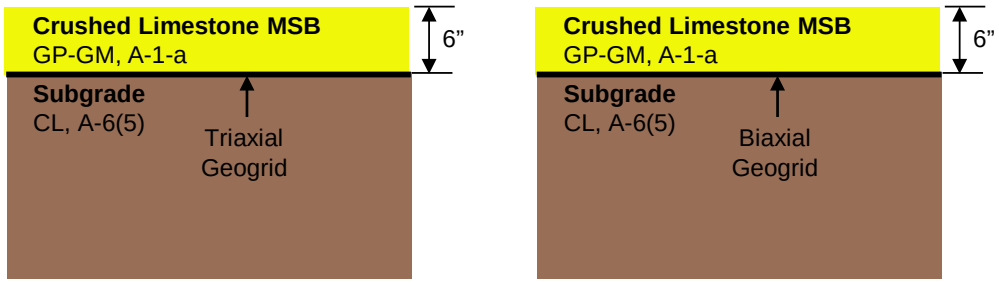

(a) (b)

Figure 103. Pavement foundation profiles with (a) triaxial geogrid on 5th St. North, and (b) biaxial geogrid on 4th St. South

Figure 104. Removal of existing granular subbase and excavating to subgrade elevation on 5th St.

(a) (b)

(c) (d)

(e) (f)

Figure 105. Geogrid installation and crushed limestone MSB layer construction: (a) biaxial geogrid over subgrade; (b) triaxial geogrid over subgrade; (c) MSB layer placement over biaxial geogrid; (d) MSB layer placement over triaxial geogrid; (e) MSB layer spreading using motor grader; and (f) 5th St. after compaction of MSB layer

As-Constructed Test Results

RICM values (MDP*, CMV, and elevation) along 5th St. on compacted crushed limestone MSB layer are shown in Figure 106. RICM measurements were obtained in low amplitude mode (a = 0.85 mm, f = 30 Hz). FWD and LWD modulus measurements obtained from 20 test locations along 5th St. are also presented in Figure 106.

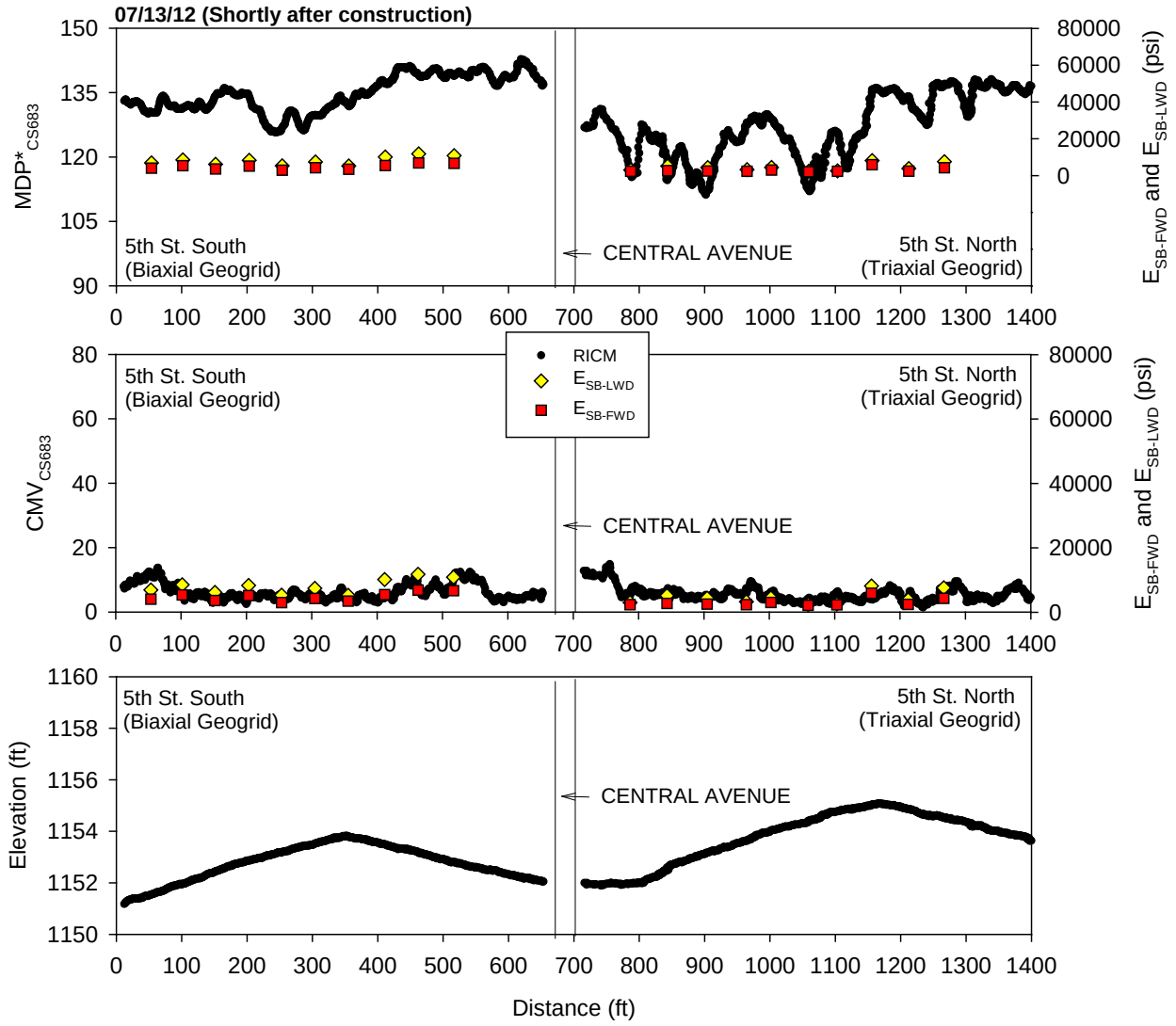

Figure 106. RICM, LWD, and FWD measurements on 5th St. shortly after construction (July 2012)

Performance Monitoring Results

CCV results obtained in low amplitude mode (a = 0.63 mm, f = 33 Hz) in comparison with $E_{SB\text{-}FWD}$ from October 2012 (about three months after construction) are shown in Figure 107. MDP^*_{CS683} and CMV_{CS683} results in comparison with $E_{SB\text{-}FWD}$ from April 2013 (during spring-

thaw) are shown in Figure 108. Similarly, results from the CS74 machine are shown in Figure 109. MDP^*_{CS683} and CMV_{CS683} from July 2012 and April 2013 are compared in Figure 110.

DCP-CBR and cumulative blows profiles from different testing times are shown in Figure 111 and Figure 112. Average CBR_{MSB} and CBR_{SG} for each test section are shown in Figure 113. Average $E_{SB\text{-}FWD}$ for each test section are shown in Figure 114.

$E_{SB\text{-}FWD}$ showed lower values in April 2013 during spring-thaw than in July and October 2012. CBR_{MSB} values were lower during spring-thaw in April 2013 than in October 2012, but increased in May 2013. No significant changes were observed in CBR_{SG}. CMV and MDP* measurements were generally lower in April 2013 than in July 2012.

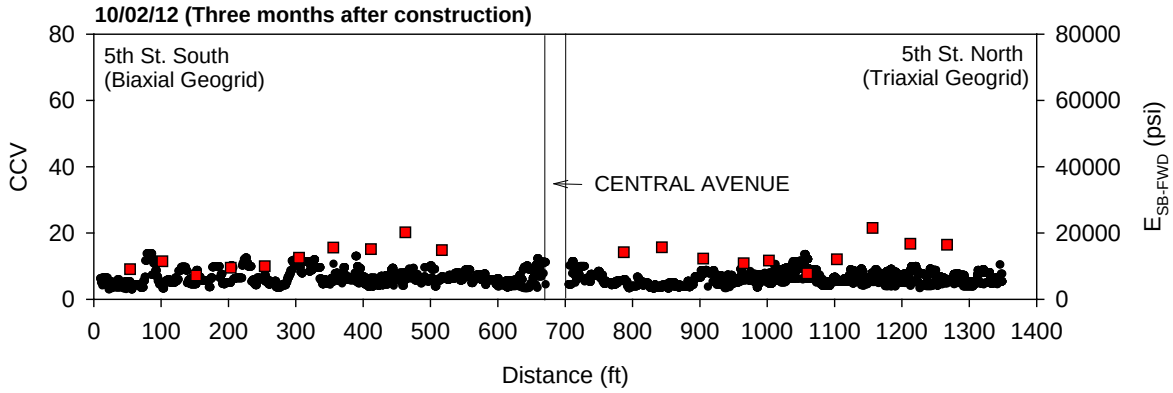

Figure 107. Sakai CCV and FWD modulus measurements on 5th St. three months after construction (October 2012)

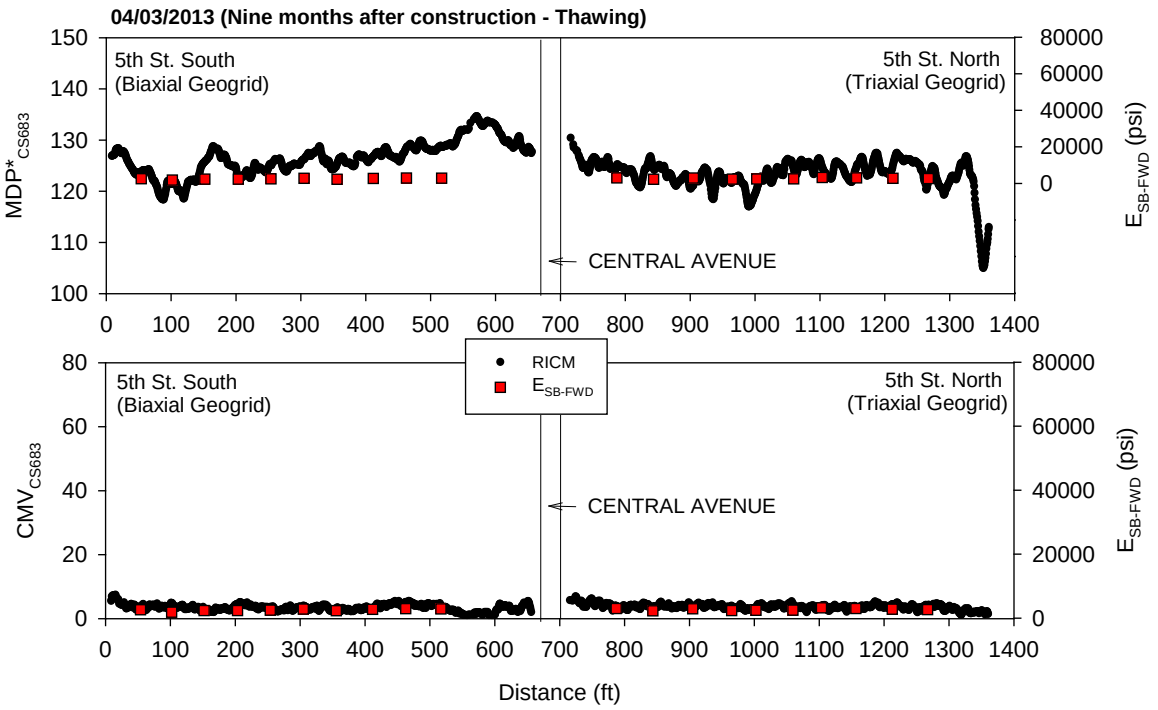

Figure 108. CS683 RICM and FWD modulus measurements on 5th St. nine months after construction during thawing (April 2013)

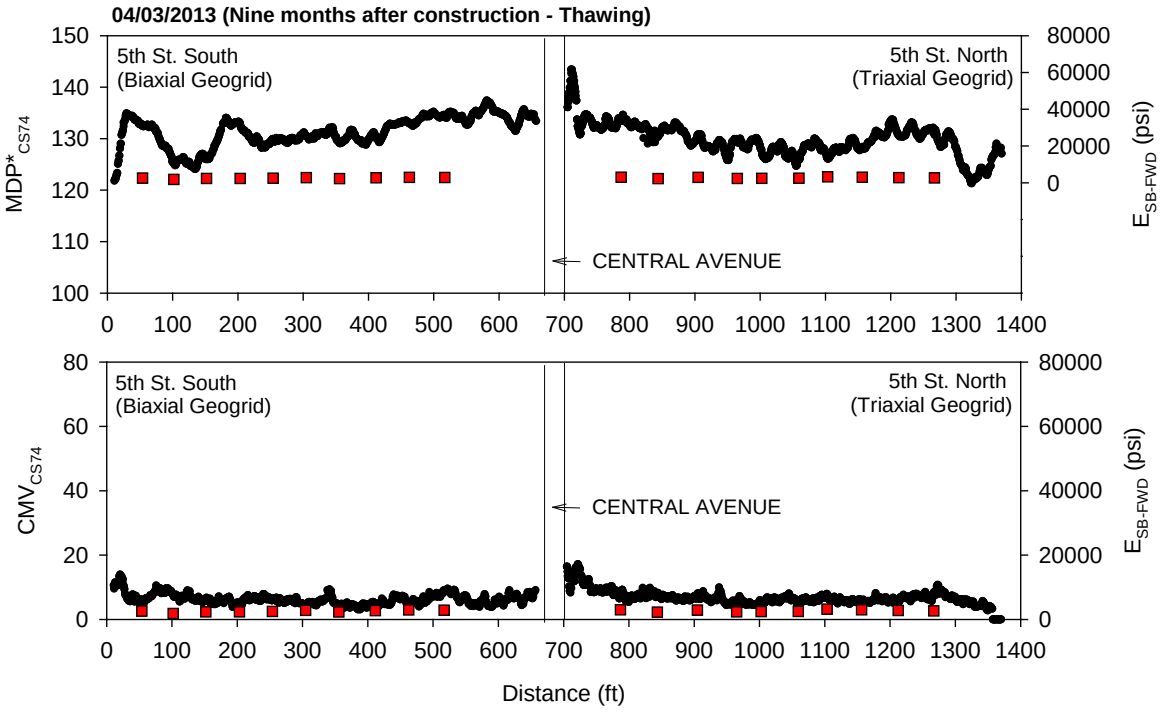

Figure 109. CS74 RICM and FWD modulus measurements on 5th St. nine months after construction during thawing (April 2013)

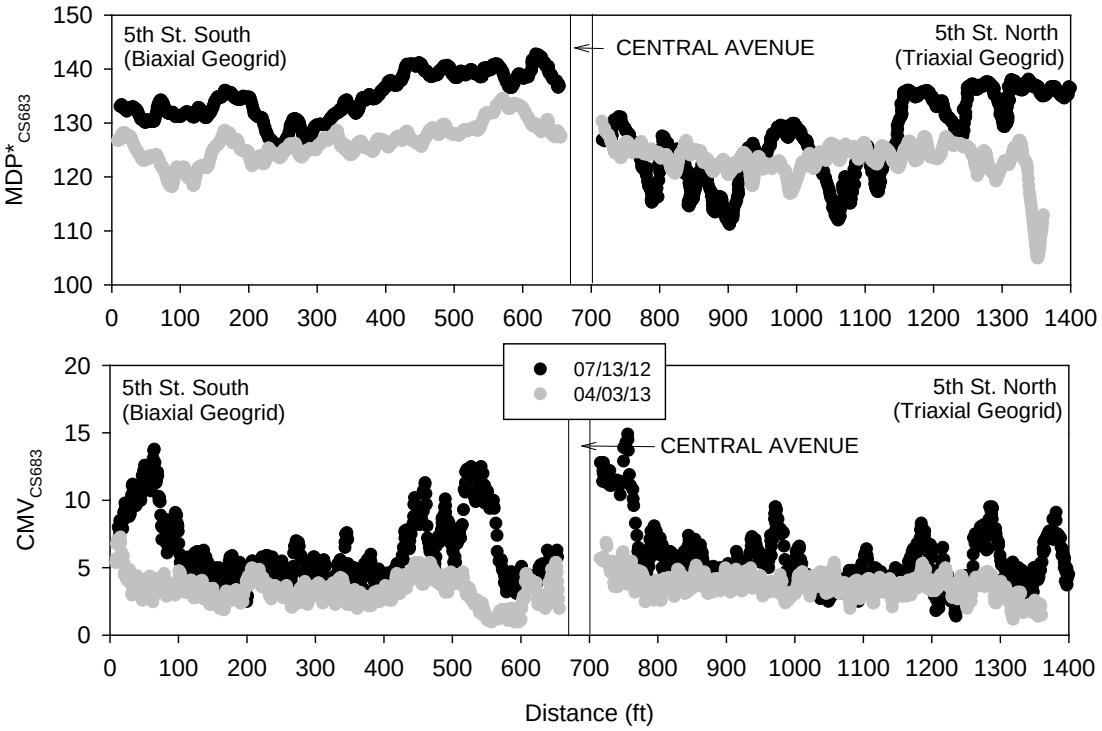

Figure 110. Comparison between CS683 RICM measurements on 5th St. shortly after construction and nine months after construction during thawing

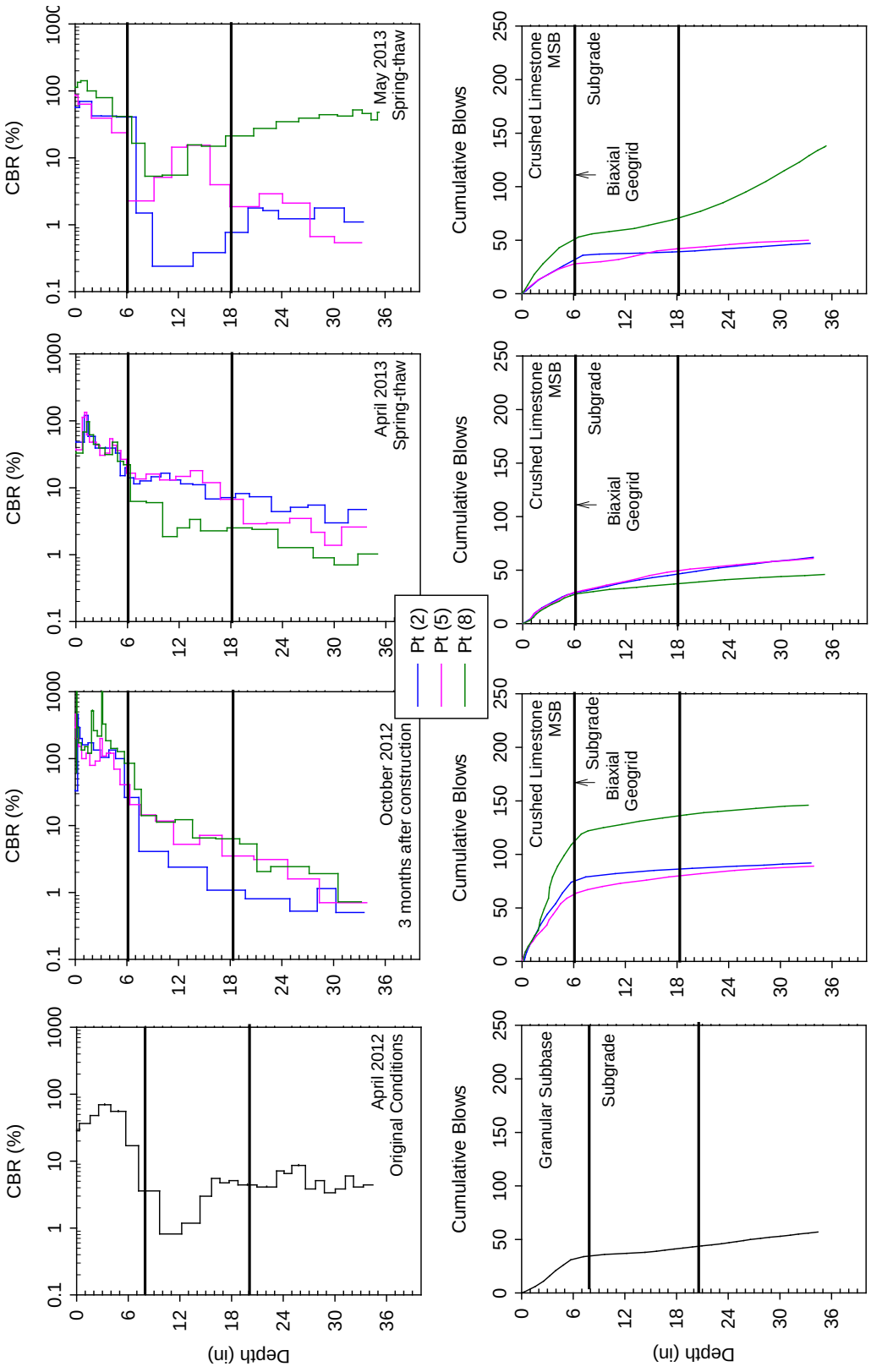

Figure 111. DCP test results from 5th St. South from different testing times

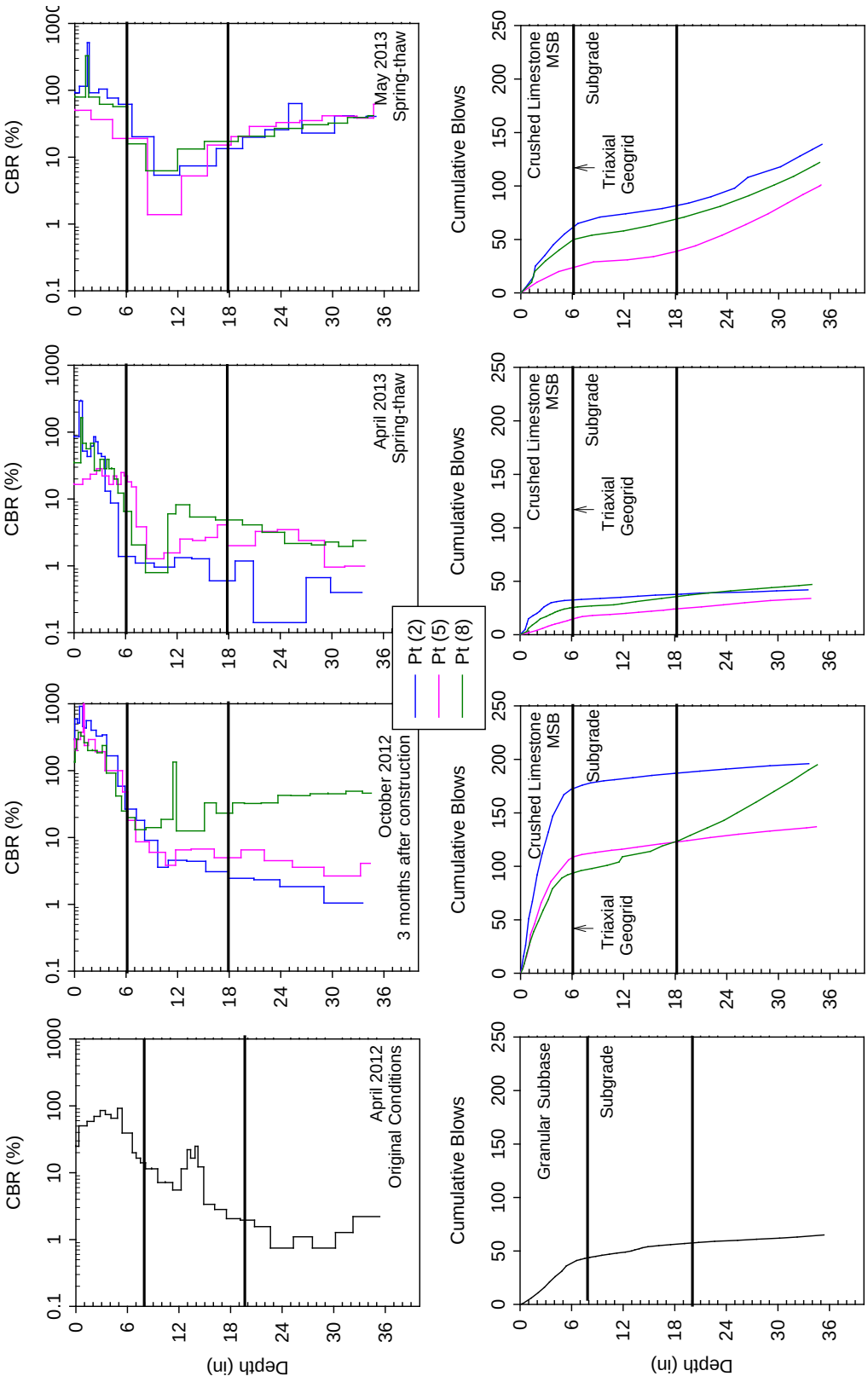

Figure 112. DCP test results from 5th St. North from different testing times

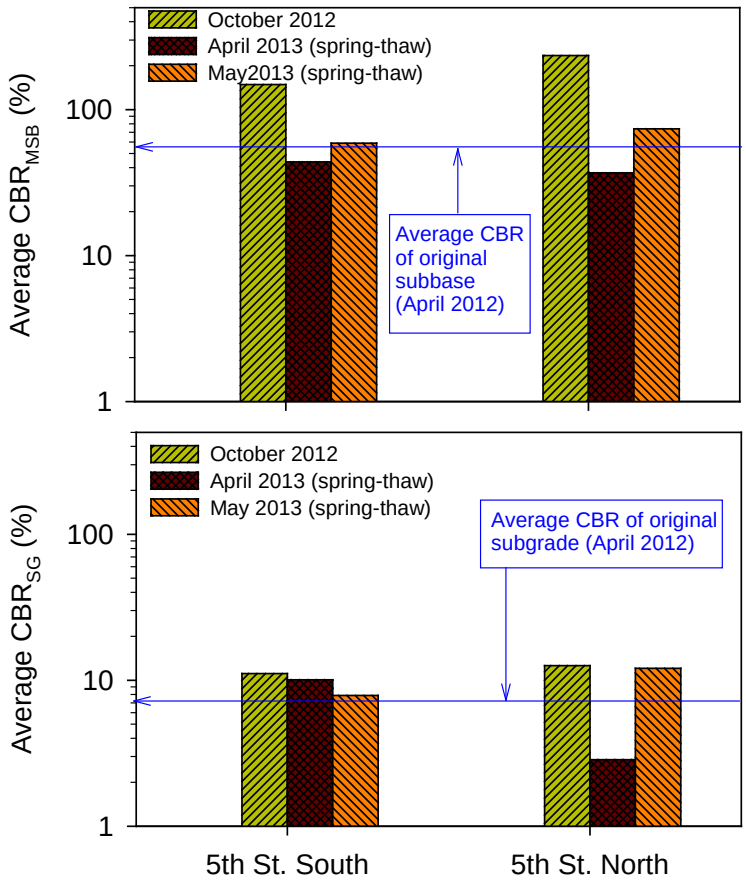

Figure 113. Average CBR (based on 3 tests) of MSB and subgrade layers on 5th St. South and North

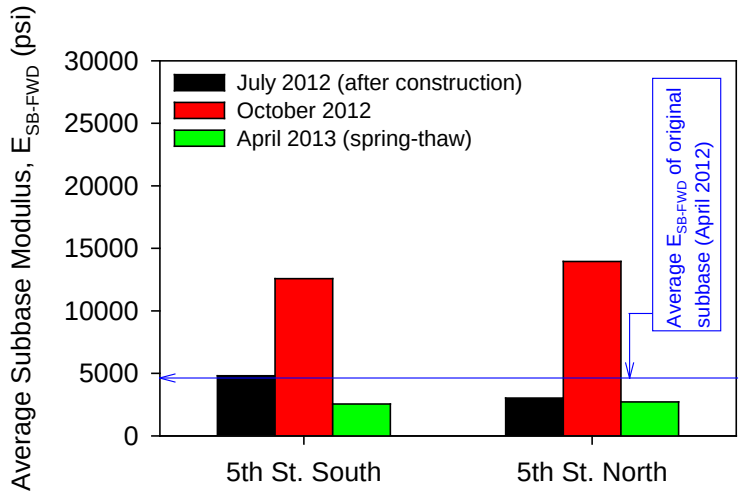

Figure 114. Average FWD subbase modulus (based on 10 tests) on 5th St. South and North sections

6th North-South: Bottom 6 inch Subbase + 5% Cement Stabilization and Fibers

Construction Observations

PC stabilization with fiber reinforced reclaimed subbase layer was conducted on 6th St. North and South test sections. MF-PP black fibers were used on 6th St. South and PP white fibers were used on 6th St. North. About 60 ft on the south end of 6th St. South and about 80 ft on the north end of 6th St. North included only fiber reinforcement without PC stabilization in the subbase layer. The pavement foundation profiles are shown in Figure 115. The construction process involved: (1) excavating the existing subbase and subgrade material down to the desired elevation and loosely placing the reclaimed subbase material over the subgrade (Figure 116a,b), (2) distributing a target 0.4% fibers on the subbase layer using a straw blower (Figure 116c,d); (3) mixing the subbase material with fibers using a soil reclaimer (Figure 116e,f); (4) distributing a target 5% cement on the subbase-fiber mixture (Figure 117a); (5) mixing and moisture conditioning the mixture by injecting water into the mixing drum (Figure 117b); and (f) compacting the stabilized layer with a vibratory padfoot roller immediately behind the reclaimer (Figure 117b). Note that the PC and fiber contents are based on dry weight of the soil. Close-up views of the subbase material after mixing with PC and fibers are shown in Figure 117c,d. Within one to three days of curing, a 6 in. crushed limestone MSB layer was placed over the stabilized subbase layers and compacted using a vibratory smooth drum roller.

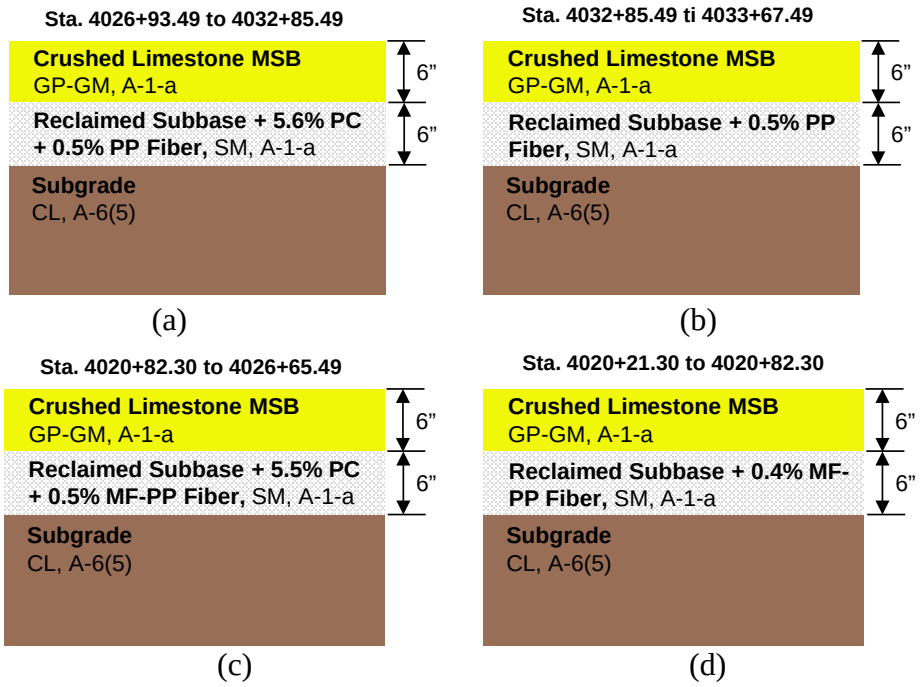

Figure 115. Pavement foundation profiles with (a) PC + PP fiber stabilized reclaimed subbase on 6th St. North; (b) PP fiber stabilized reclaimed subbase on 6th St. N; (c) PC + MF-PP fiber stabilized reclaimed subbase on 6th St. S; and (d) MF-PP fiber stabilized reclaimed subbase on 6th St. S

(a) (b)

(c) (d)

(e) (f)

Figure 116. PC + Fiber stabilized subbase layer construction: (a) scarification of existing subbase; (b) stockpiling of existing subbase after removing biaxial geogrid beneath the existing subbase lyaer; (c) placing white PP fiber with a straw blower; (d) mixing white PP fiber with subbase; (e) placing black MF-PP fiber with a straw blower; and (f) mixing black MF-PP fibers with subbase

(a) (b)

(c) (d)

(e)

Figure 117. PC and fiber mixing: (a) placement of PC on fiber reinforced subbase layer; (b) moisture conditioning and mixing PC with fiber reinforced subbase; (c) PC + PP stabilized subbase; (d) PC + MF-PP stabilized subbase; and (e) 6th St. after placement of crushed limestone MSB layer

As-Constructed Test Results

RICM values (MDP*, CMV, and elevation) along 6th St. on compacted crushed limestone MSB layer are shown in Figure 118. RICM measurements were obtained in low amplitude mode (a = 0.85 mm, f = 30 Hz). FWD and LWD modulus measurements obtained from 20 test locations along 6th St. are also presented in Figure 118.

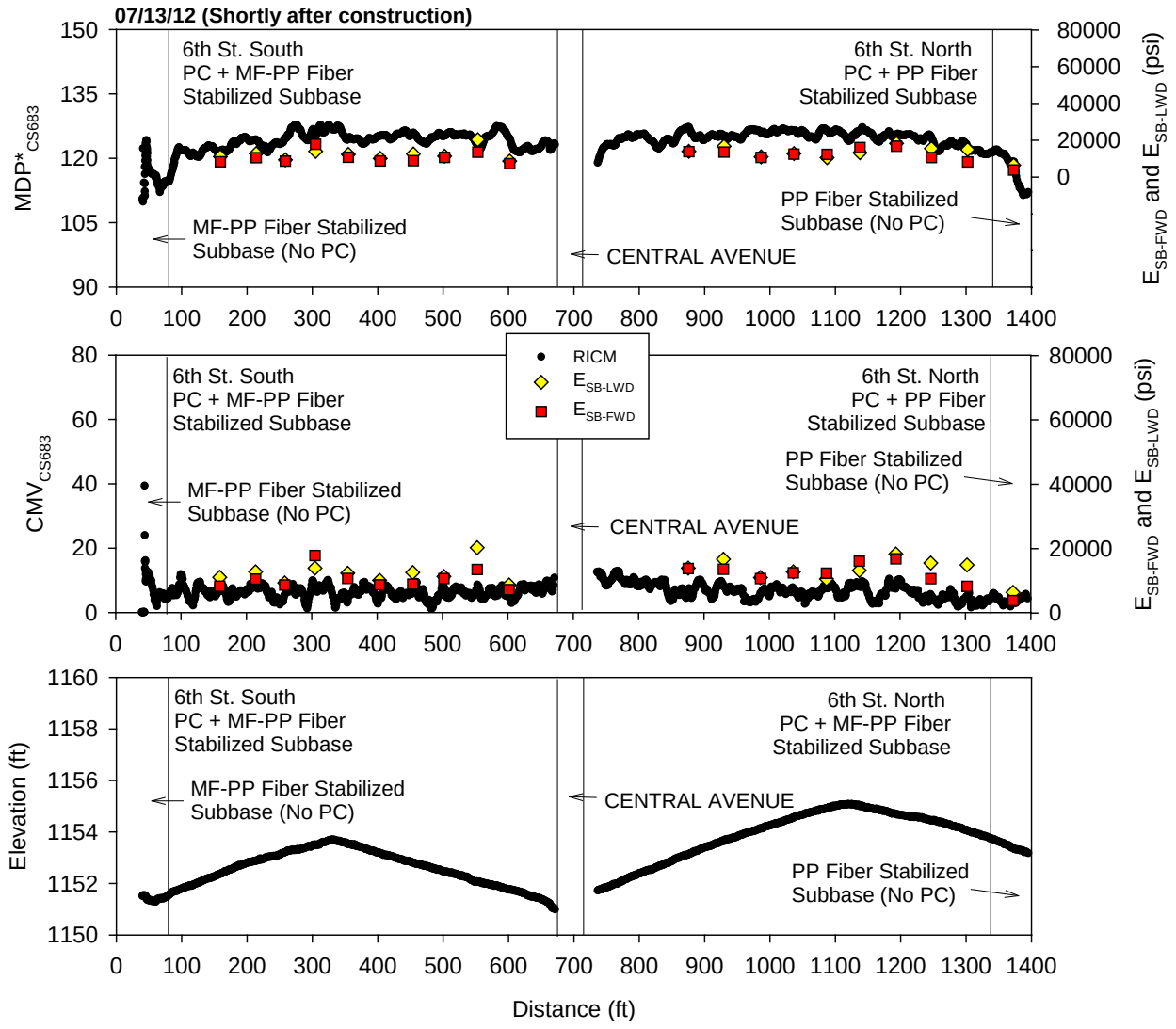

Figure 118. RICM, LWD, and FWD measurements on 6th St. shortly after construction (July 2012)

Performance Monitoring Results

CCV results obtained in low amplitude mode (a = 0.63 mm, f = 33 Hz) in comparison with $E_{SB\text{-}FWD}$ from October 2012 (about three months after construction) are shown in Figure 119. MDP^*_{CS683} and CMV_{CS683} results in comparison with $E_{SB\text{-}FWD}$ from April 2013 (during spring-

thaw) are shown in Figure 120. Similarly, results from the CS74 machine are shown in Figure 121. MDP^*_{CS683} and CMV_{CS683} from July 2012 and April 2013 are compared in Figure 122.

DCP-CBR and cumulative blows profiles from different testing times are shown in Figure 122 and Figure 100. Average CBR_{MSB}, $CBR_{PC\text{-}Fiber\ Subbase}$ and CBR_{SG} for each test section are shown in Figure 101. Average $E_{SB\text{-}FWD}$ for each test section are shown in Figure 102.

$E_{SB\text{-}FWD}$ obtained on both 6th St. North and South showed lower values in April 2013 during spring-thaw than in October 2012, but were higher than values obtained shortly after construction in July 2012. CBR_{MSB} and $CBR_{PC\text{-}Fiber\ Subbase}$ layers also showed similar trend. This trend is also confirmed by RICM measurements with higher values in April 2013 than in July 2012.

$E_{SB\text{-}FWD}$ values on PP fibers only section were lower than PC + PP fibers section on 6th St. North at all testing times. On average, the $E_{SB\text{-}FWD}$ was about 6 times lower in April 2013 in the PP fibers only section than in PC + PP fibers section. DCP tests indicated lower CBR values in the MSB layer and the stabilized subbase layer in the fiber only sections compared to PC + fiber sections, on 6th St. North and South. No significant differences were observed between the PC + MF-PP fiber and the PC + PP fiber sections in terms of $E_{SB\text{-}FWD}$ and CBR values.

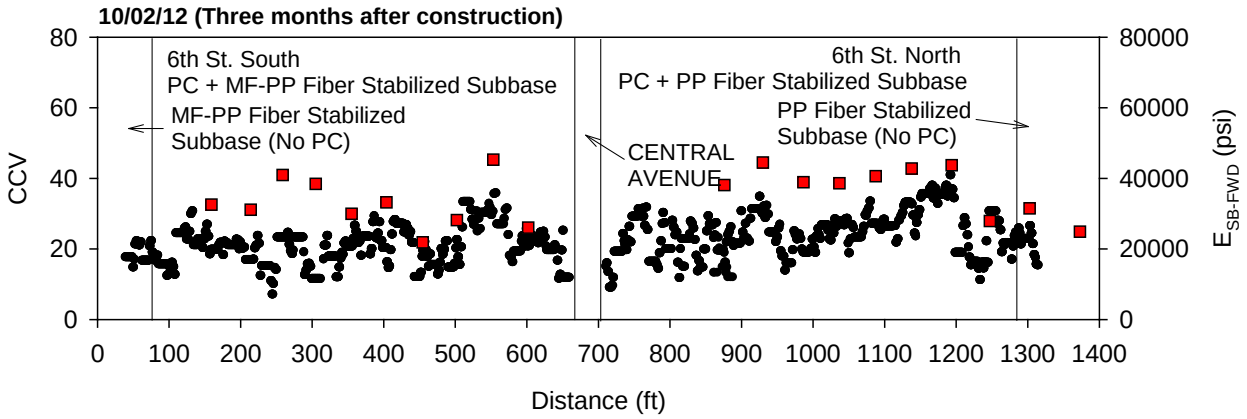

Figure 119. Sakai CCV and FWD modulus measurements on 6th St. three months after construction (October 2012)

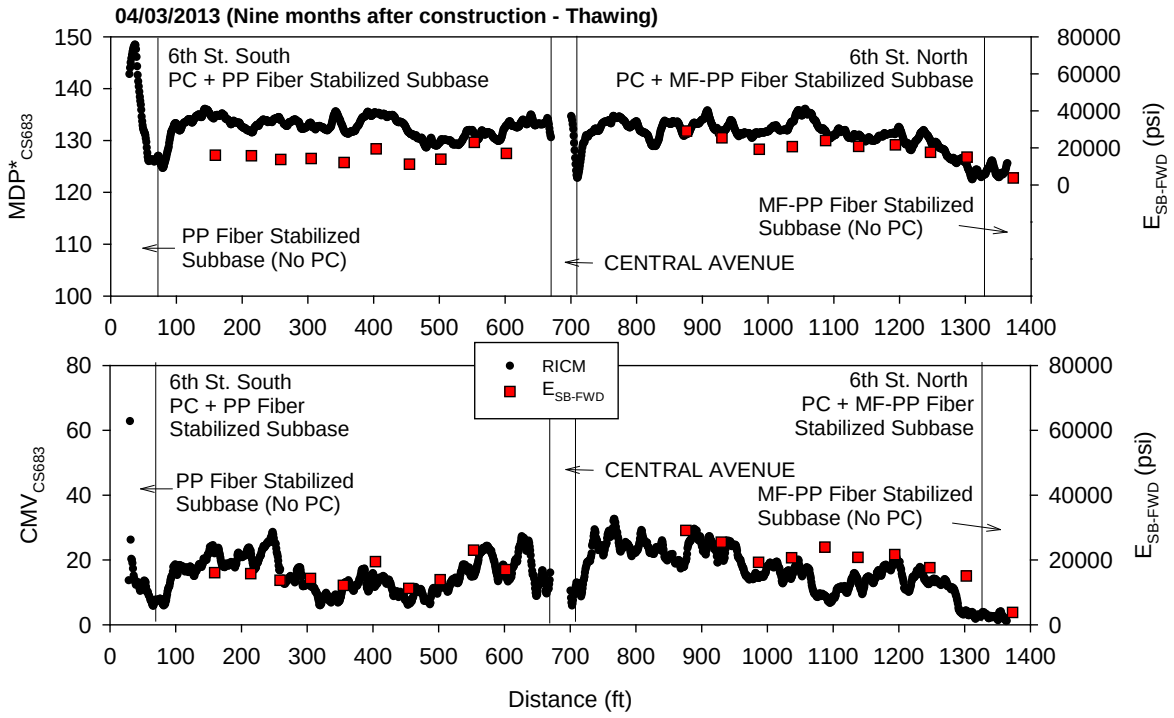

Figure 120. CS683 RICM and FWD modulus measurements on 6th St. nine months after construction during thawing (April 2013)

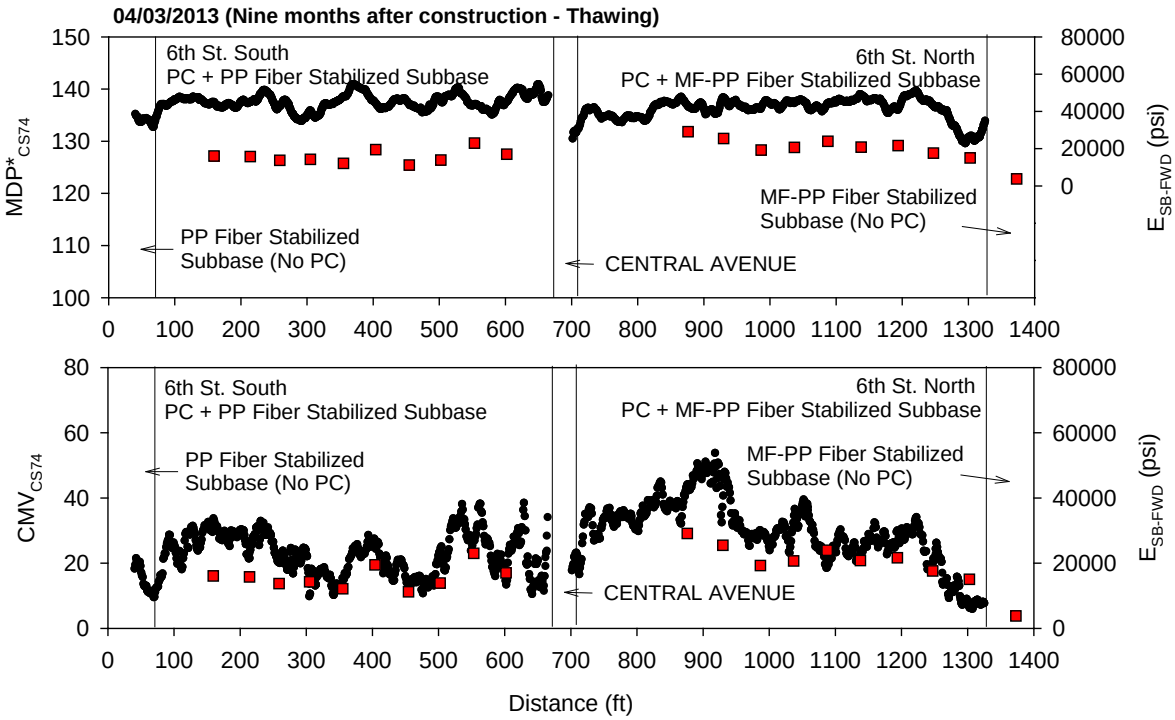

Figure 121. CS74 RICM and FWD modulus measurements on 6th St. nine months after construction during thawing (April 2013)

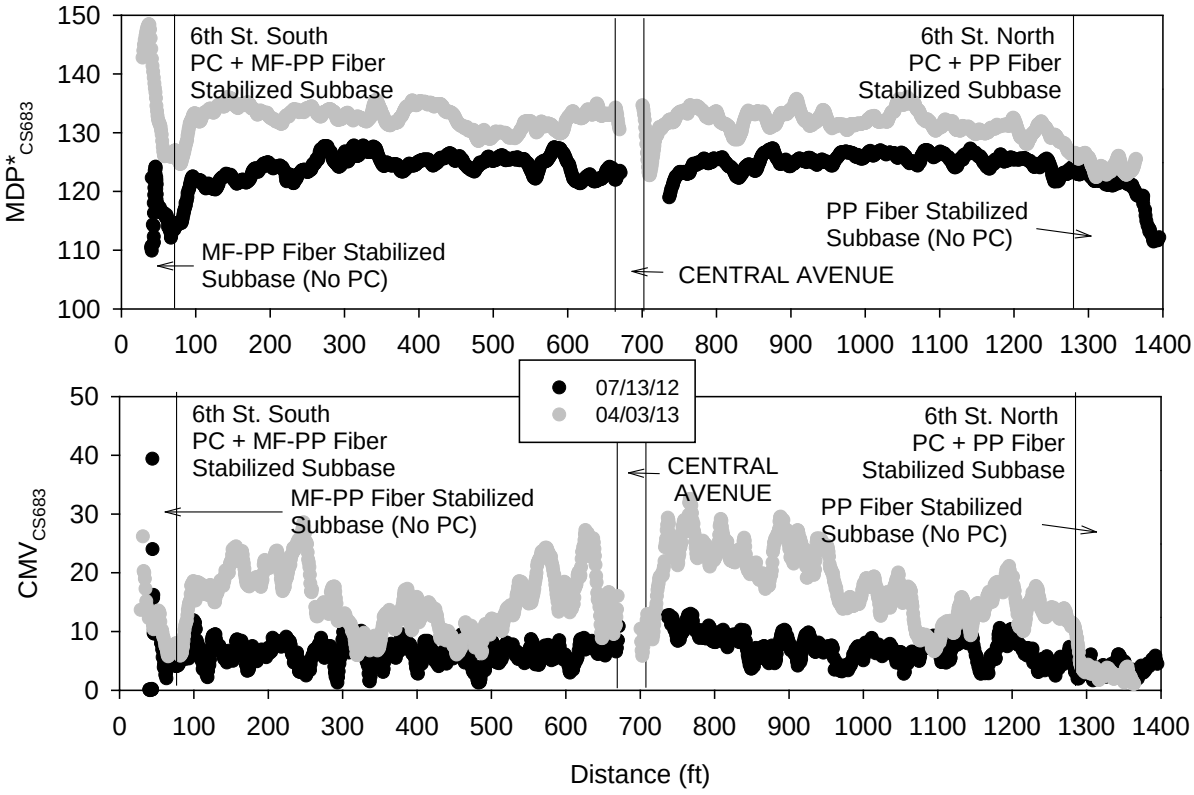

Figure 122. Comparison between CS683 RICM measurements on 6th St. shortly after construction and nine months after construction during thawing

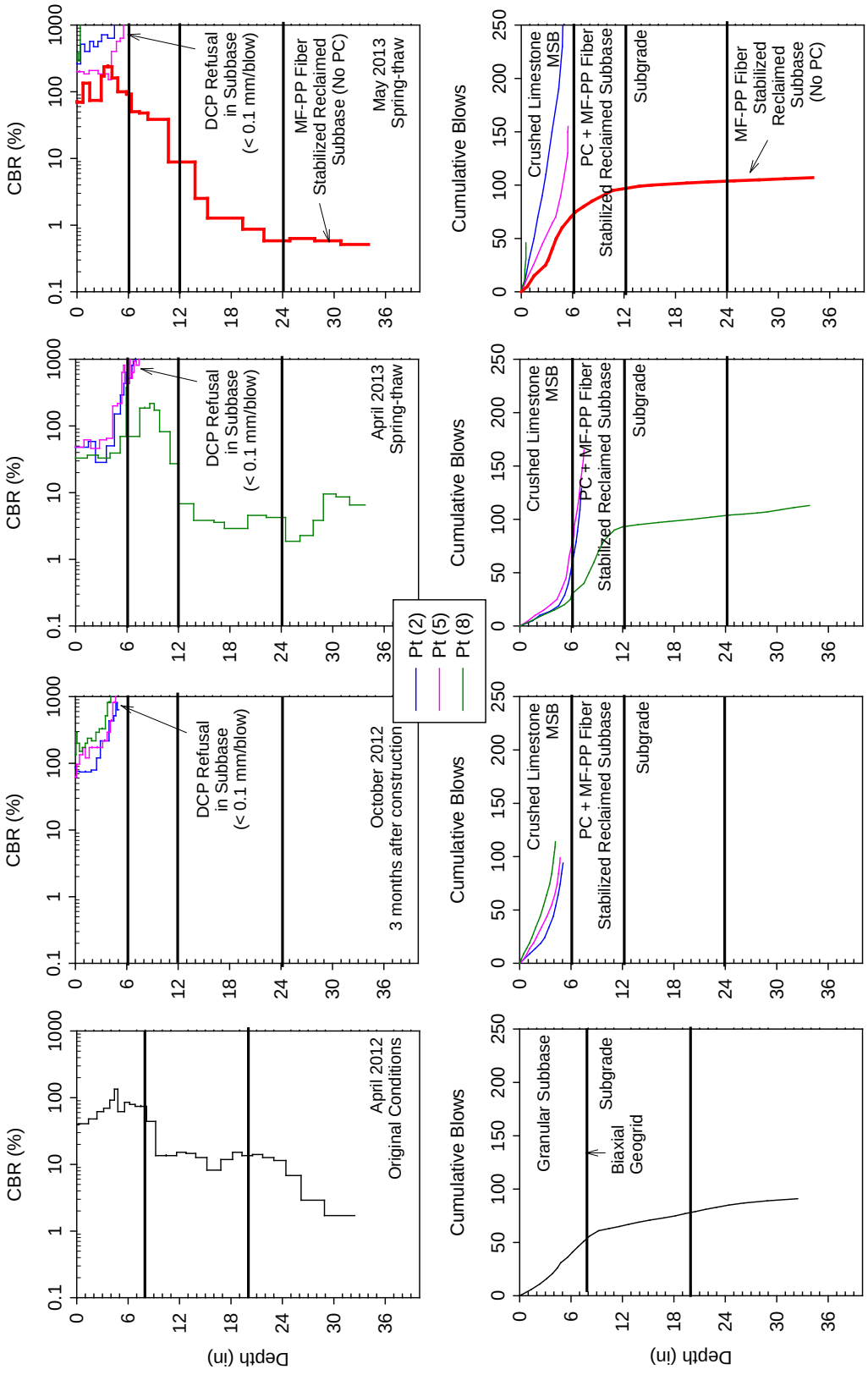

Figure 123. DCP test results from 6th St. South from different testing times

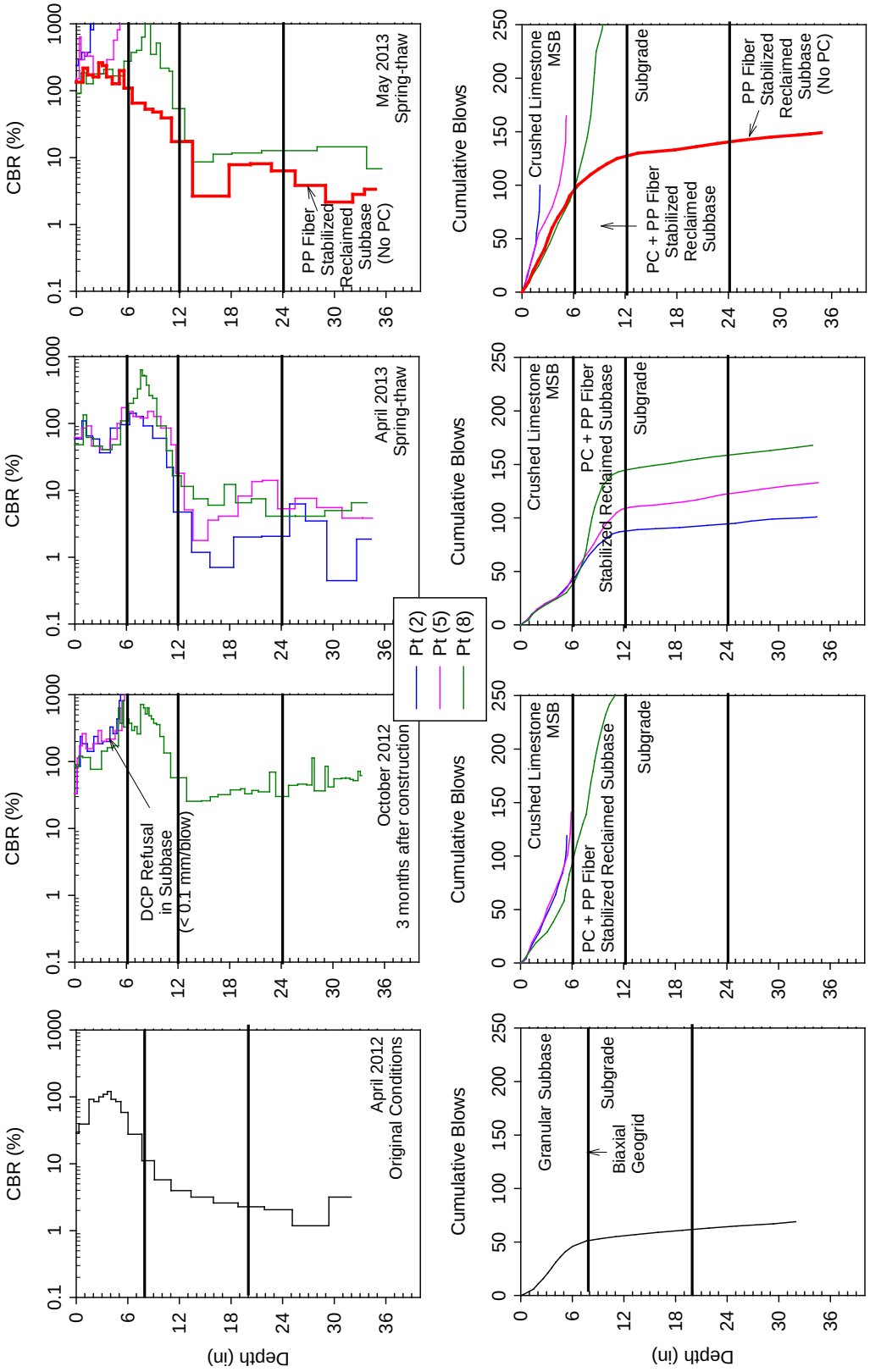

Figure 124. DCP test results from 6th St. North from different testing times

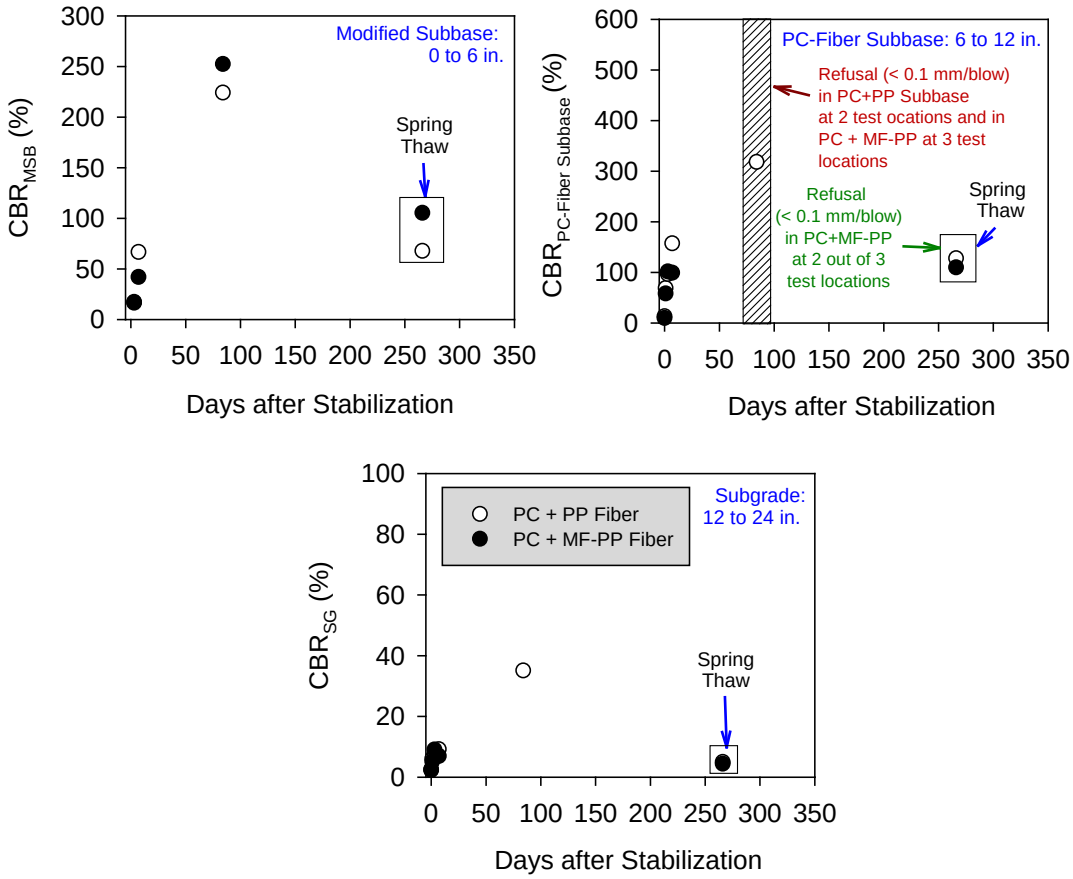

Figure 125. Average CBR (based on 3 tests) of MSB, stabilized subbase, and unstabilized subgrade on 6th St. South and North

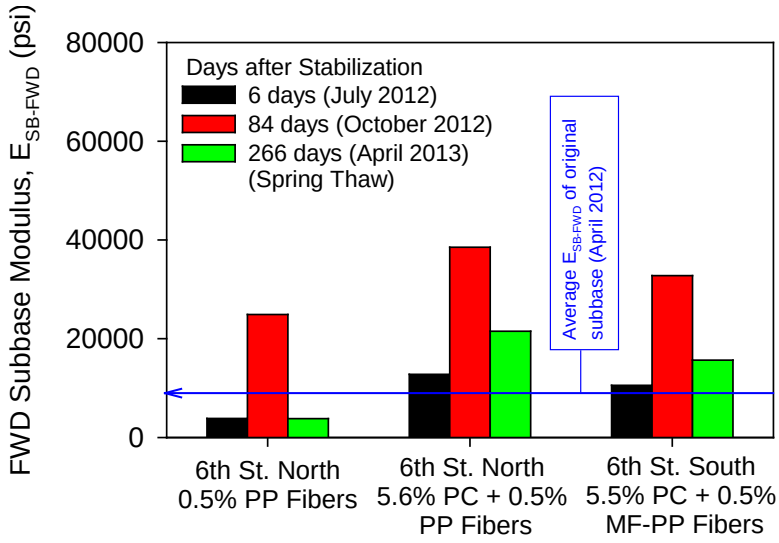

Figure 126. Average FWD subbase modulus (based on 10 tests on PC + fiber sections and 1 test on fiber only section) on 6th St. South and North sections

7th North-South: Bottom 6 inch subbase with 5% Cement Stabilization

Construction Observations

PC stabilized reclaimed subbase layer was conducted on 7th St. North and South test sections. The pavement foundation profiles are shown in Figure 127. The construction process involved: (1) excavating the existing subbase and subgrade material down to the desired elevation and loosely placing the reclaimed subbase material over the subgrade (Figure 128a,b); (2) distributing a target 5% PC on the subbase (Figure 128c); (3) mixing PC with the subbase layer using a soil reclaimer (Figure 128d); and (4) compacting the stabilized layer with a vibratory padfoot roller immediately behind the reclaimer (Figure 128e). Within one to three days of curing, a 6 in. crushed limestone MSB layer was placed over the stabilized subbase layer (Figure 128f) and compacted using a vibratory smooth drum roller.

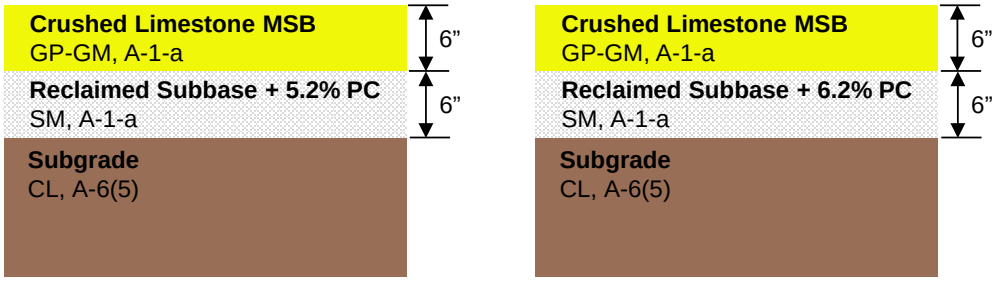

Figure 127. Pavement foundation profiles with (a) 5.2% PC stabilized reclaimed subbase on 7th St. South; and (b) 6.2% PC stabilized reclaimed subbase on 7th St. South

(a) (b)

(c) (d)

(e) (f)

Figure 128. Construction operations on 7th St.: (a) removing existing subbase layer down to subgrade elevation, (b) reclaimed subbase layer placed over subgrade (c) placing PC over reclaimed subbase, (d) moisture conditioning and mixing reclaimed subbase with PC, (e) compacting stabilized layer with padfoot roller, and (f) placing crushed limestone MSB layer over stabilized subbase

As-Constructed Test Results

RICM values (MDP*, CMV, and elevation) along 7th St. on compacted crushed limestone MSB layer are shown in Figure 129. RICM measurements were obtained in low amplitude mode (a = 0.85 mm, f = 30 Hz). FWD and LWD modulus measurements obtained from 20 test locations along 7th St. are also presented in Figure 129.

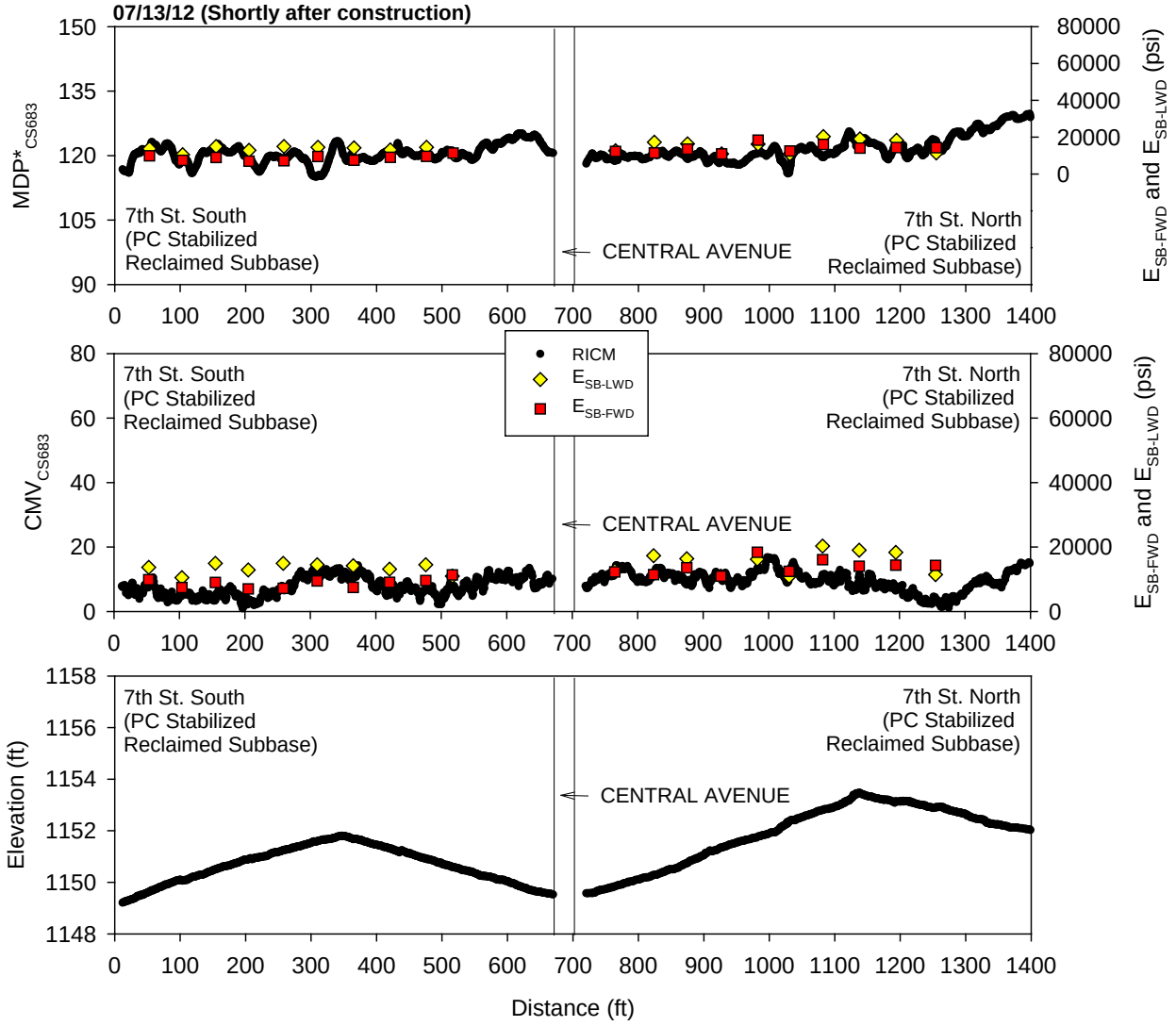

Figure 129. RICM, LWD, and FWD measurements on 7th St. shortly after construction (July 2012)

Performance Monitoring Results

CCV results obtained in low amplitude mode (a = 0.63 mm, f = 33 Hz) in comparison with $E_{SB\text{-}FWD}$ from October 2012 (about three months after construction) are shown in Figure 130. MDP^*_{CS683} and CMV_{CS683} results in comparison with $E_{SB\text{-}FWD}$ from April 2013 (during spring-

thaw) are shown in Figure 131. Similarly, results from the CS74 machine are shown in Figure 132. MDP^*_{CS683} and CMV_{CS683} from July 2012 and April 2013 are compared in Figure 133.

DCP-CBR and cumulative blows profiles from different testing times are shown in Figure 134 and Figure 135. DCP profiles obtained from different testing times from one selected test location each from 7th St. North and South test sections are presented in Figure 136. Average CBR_{MSB}, $CBR_{PC\text{-}Subbase}$ and CBR_{SG} from different testing times in each test section are shown in Figure 137 and Figure 138. Average $E_{SB\text{-}FWD}$ for each test section are shown in Figure 139.

$E_{SB\text{-}FWD}$ obtained on both 7th St. North and South showed lower values in April 2013 during spring-thaw than in October 2012. CBR_{MSB} and $CBR_{PC\text{-}Fiber\ Subbase}$ layers also showed lower values in April 2013 than in October 2012, but the values increased in May 2013. RICM measurements obtained in July 2012 and April 2013 were generally similar.

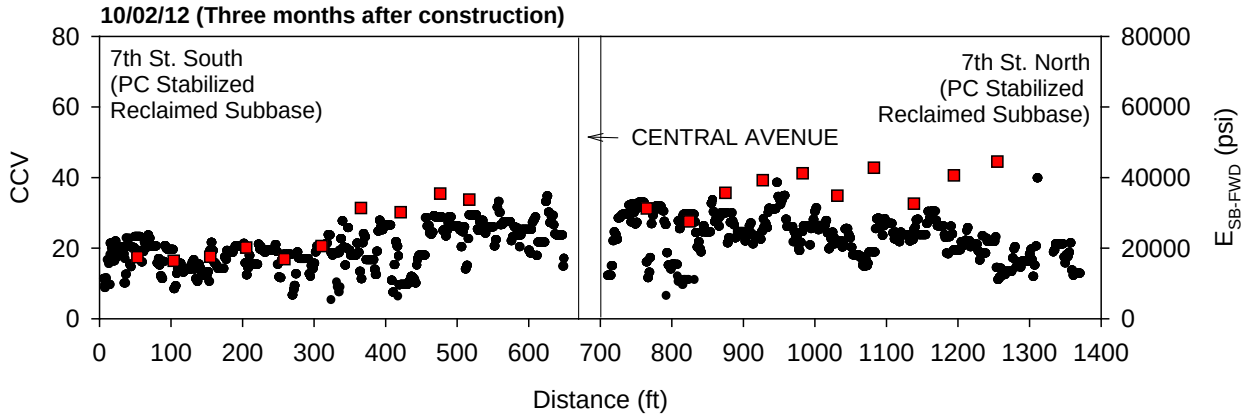

Figure 130. Sakai CCV and FWD modulus measurements on 7th St. three months after construction (October 2012)

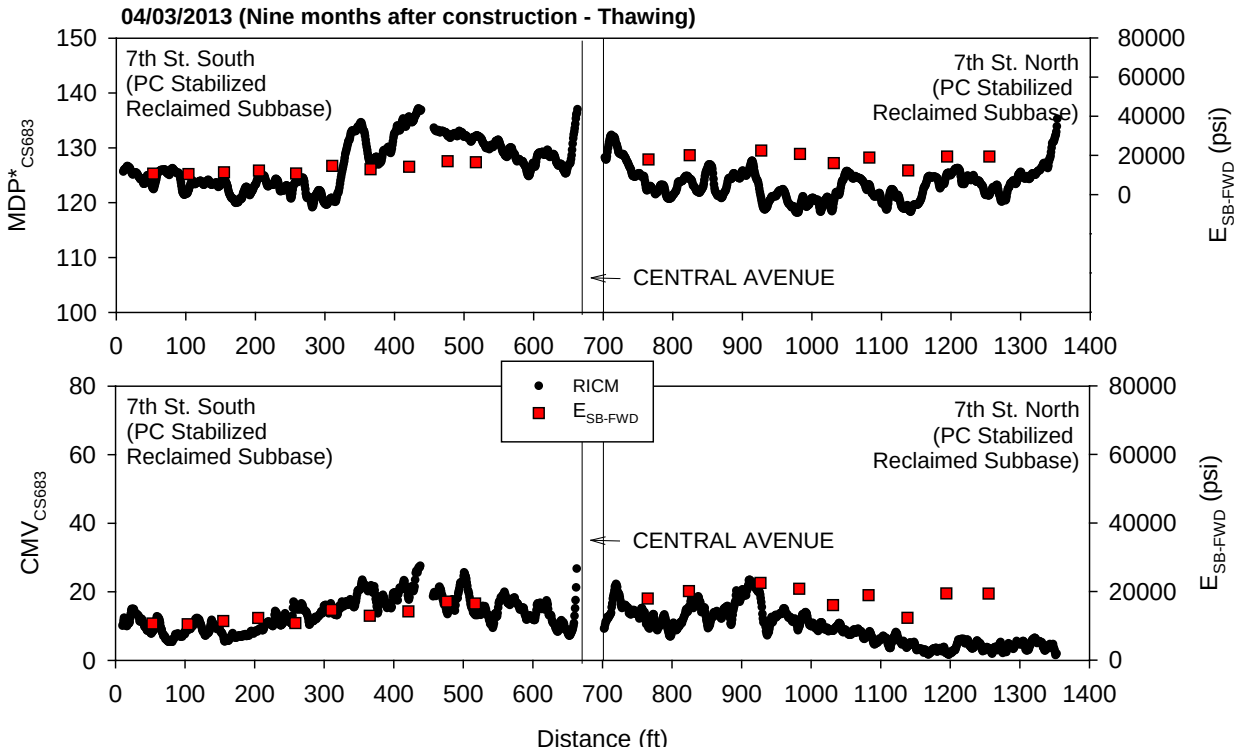

Figure 131. CS683 RICM and FWD modulus measurements on 7th St. nine months after construction during thawing (April 2013)

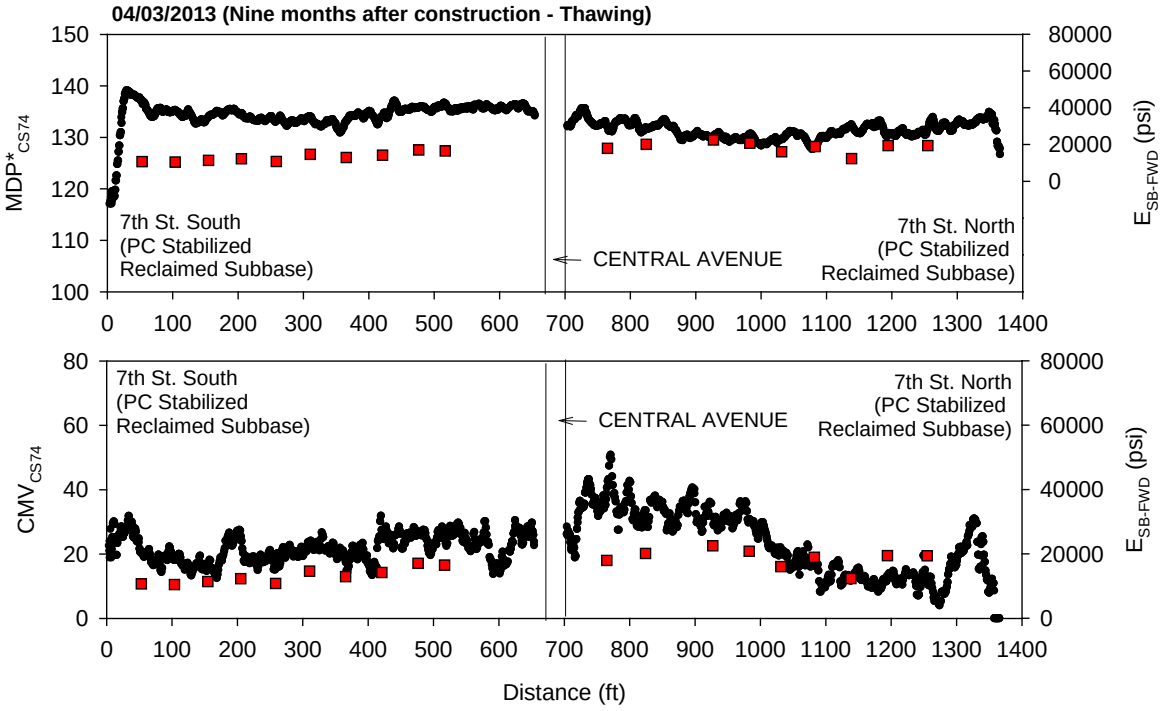

Figure 132. CS74 RICM and FWD modulus measurements on 7th St. nine months after construction during thawing (April 2013)

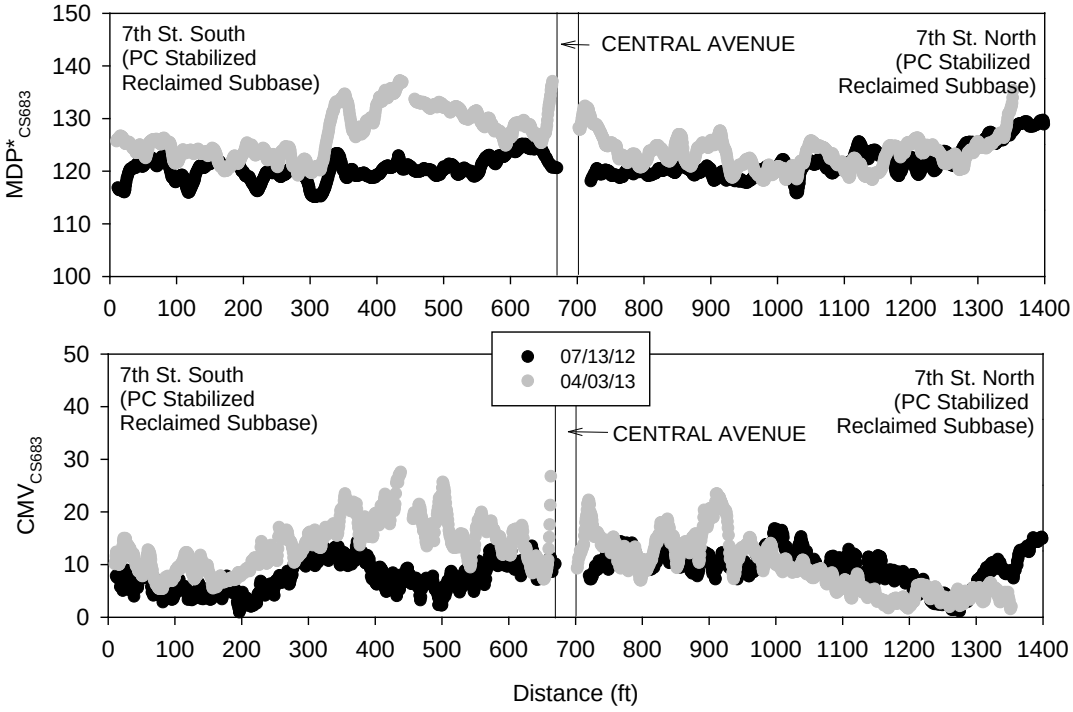

Figure 133. Comparison between CS683 RICM measurements on 4th St. shortly after construction and nine months after construction during thawing

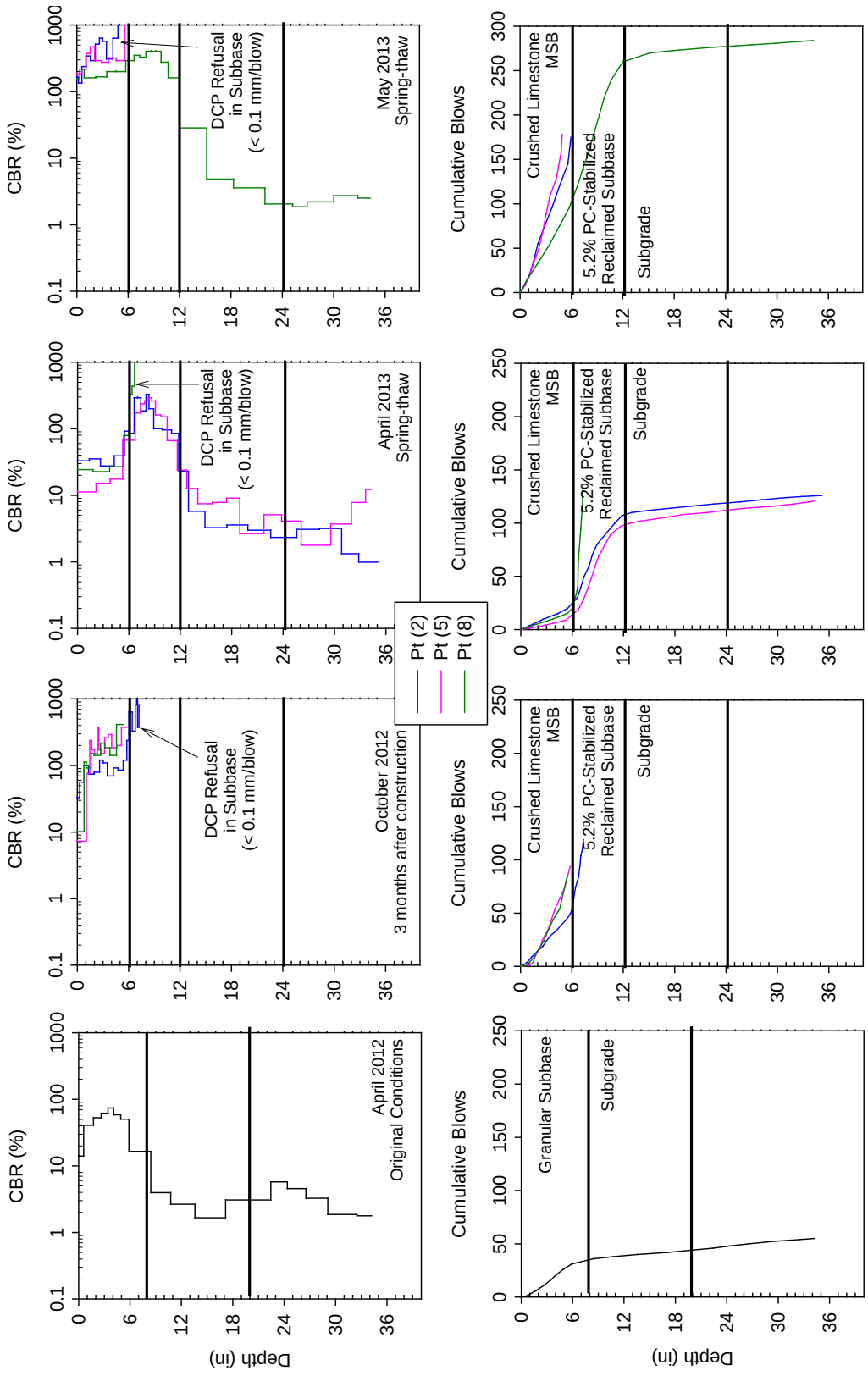

Figure 134. DCP test results from 7th St. South from different testing times

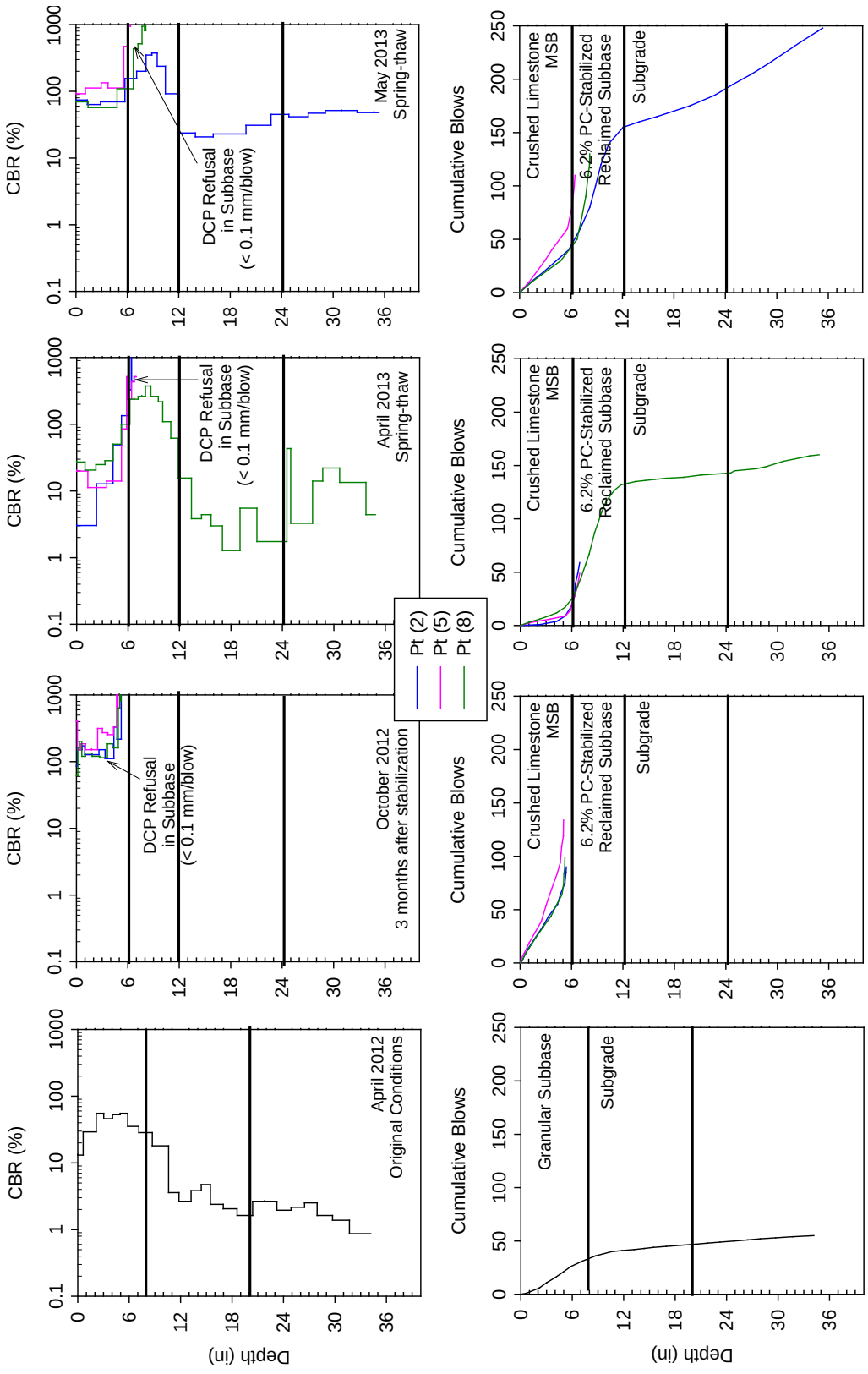

Figure 135. DCP test results from 7th St. North from different testing times

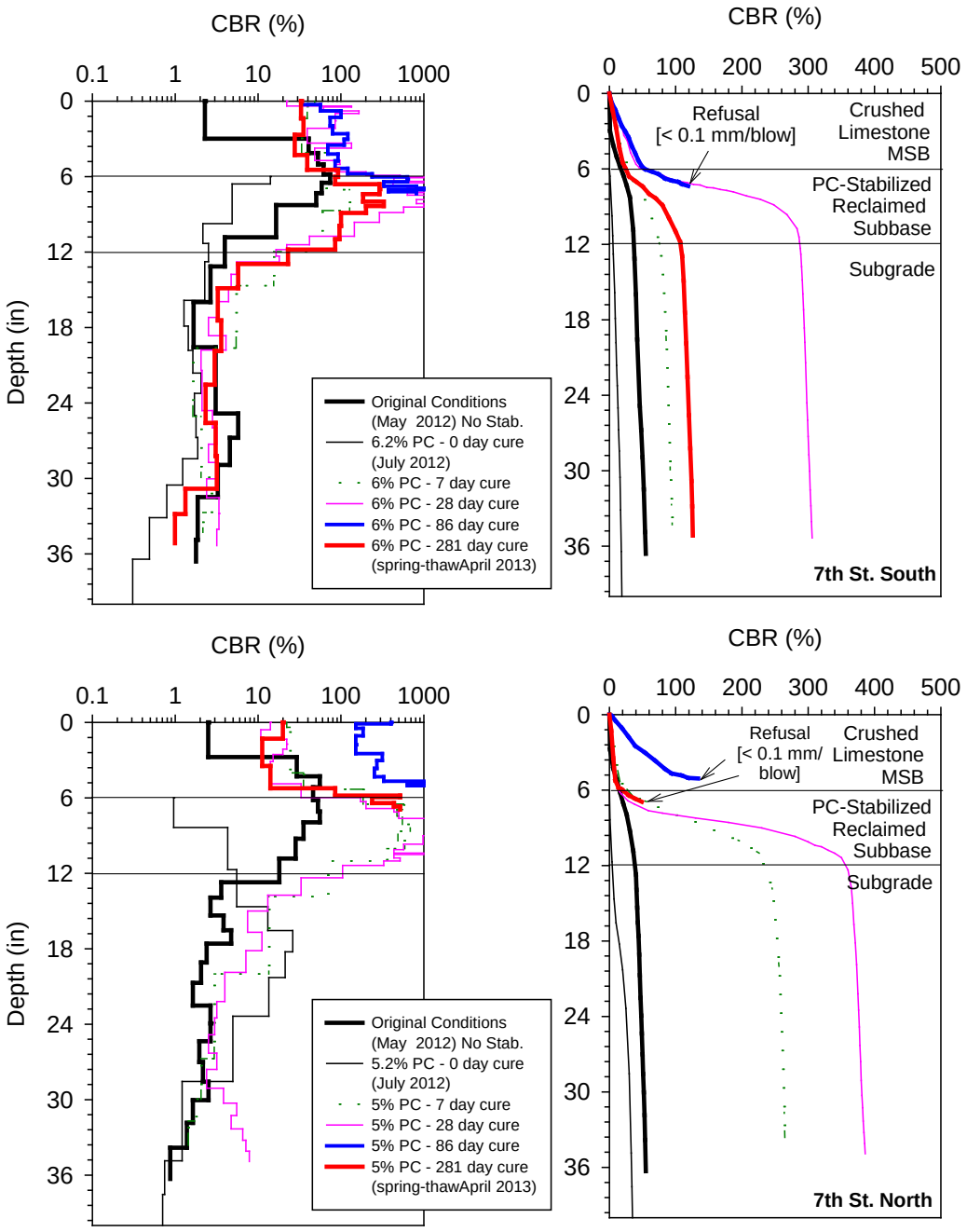

Figure 136. DCP test results from a selected test point each in 7th St. South and North at different curing times after construction

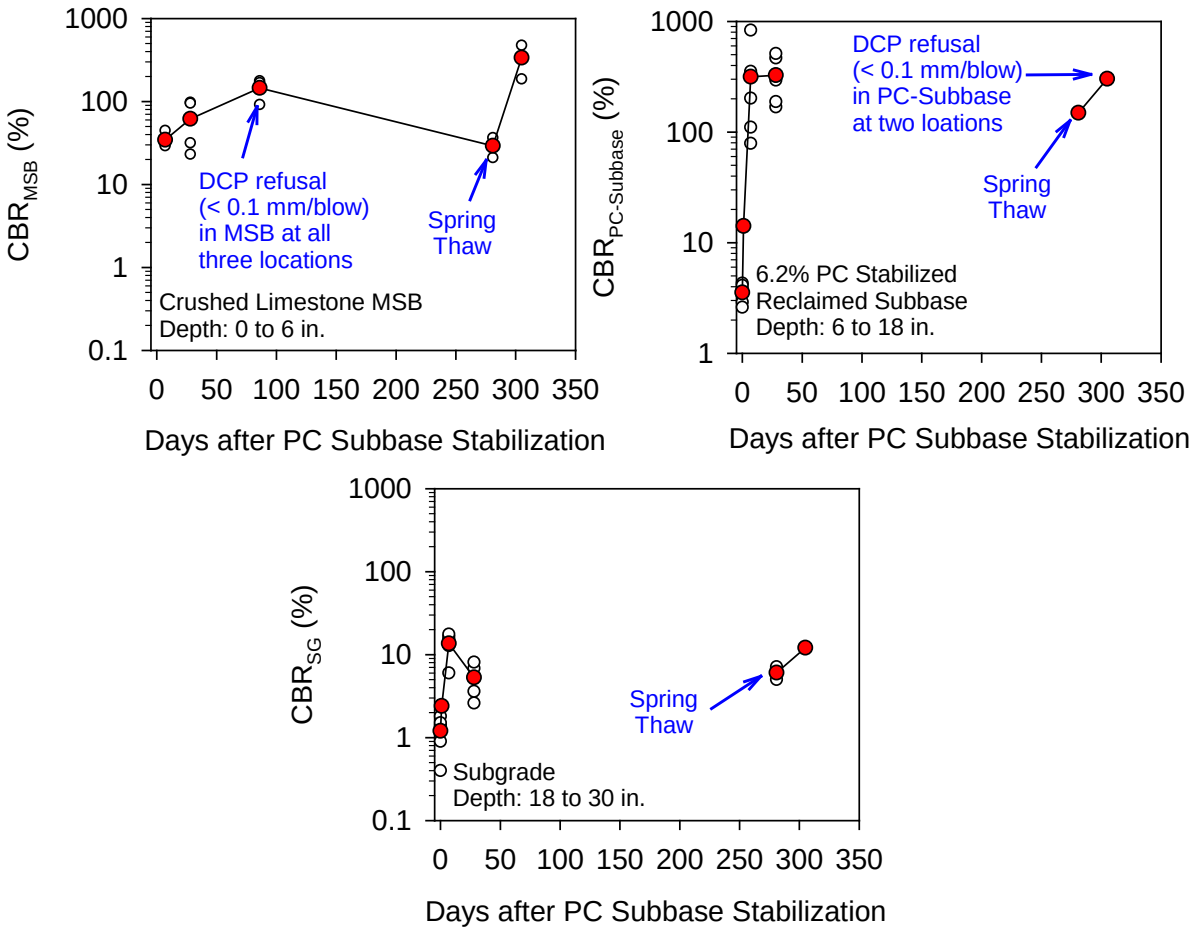

Figure 137. Average CBR (based on 3 tests) of MSB, PC stabilized reclaimed subbase, and unstabilized subgrade on 7th St. South

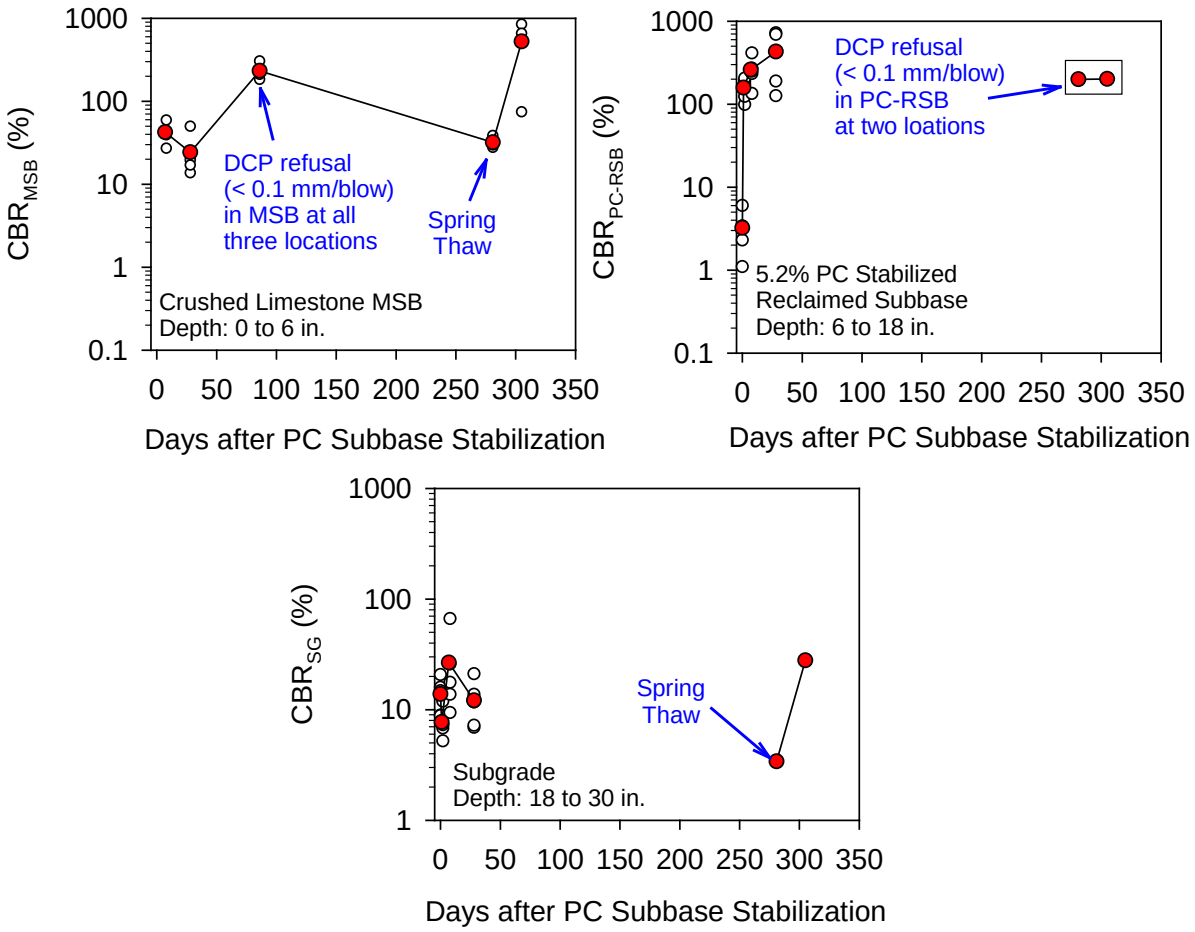

Figure 138. Average CBR (based on 3 tests) of MSB, PC stabilized reclaimed subbase, and unstabilized subgrade on 7th St. North

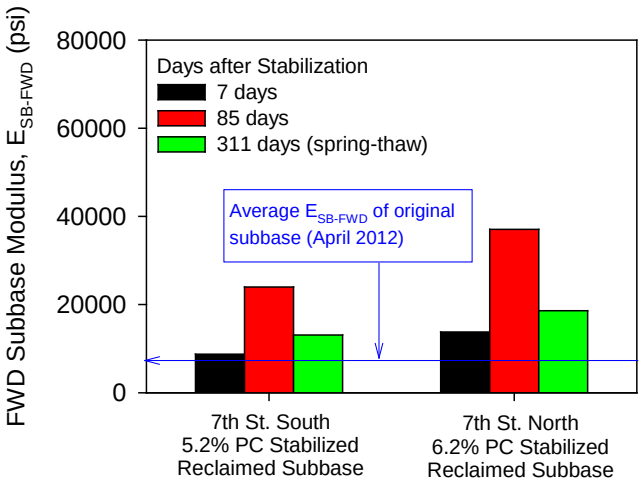

Figure 139. Average FWD subbase modulus (based on 10 tests) on 7th St. South and North sections

8th North-South: Compacted Subgrade (Control)

Construction Observations

The high-energy IR was used to rubblize and push down the chip seal coat and the existing granular subbase on 8th St. North and South test sections. The test sections were compacted using 20 IR passes with the high-energy impact roller at a nominal speed of 7 mph (on May 30, 2012), and then compacted using a vibratory smooth drum roller (on June 7, 2012). The chipseal surface after IR passes is shown in Figure 140.

DCP-CBR and cumulative blows with depth profiles seven test locations along 8th St. are shown in Figure 141 to Figure 144. . Results and field observations indicated that the chip seal coat surface was rubblized as expected. DCP test results at some locations indicated improvement in CBR with depth, while at other locations showed de-compaction at shallow depths. For example, at Pt (3) in Figure 142, the CBR from about 4 to 6 in. depth increased from an average of about 55 to 77 after 20 IR passes. On the other hand, at Pt (7) in Figure 144, the CBR values at almost all depths were lower after IR passes. Improvement of the underlying subgrade was not expected, as it is not possible under saturated conditions. Due to the limited scope on this project, potential advantages of the IR for earthwork compaction were not fully explored and warrant additional demonstration. However, this demonstration provided hands-on experience to researchers and practitioners with this technology.

Figure 140. Chipseal surface after IR passes on 8th St. North

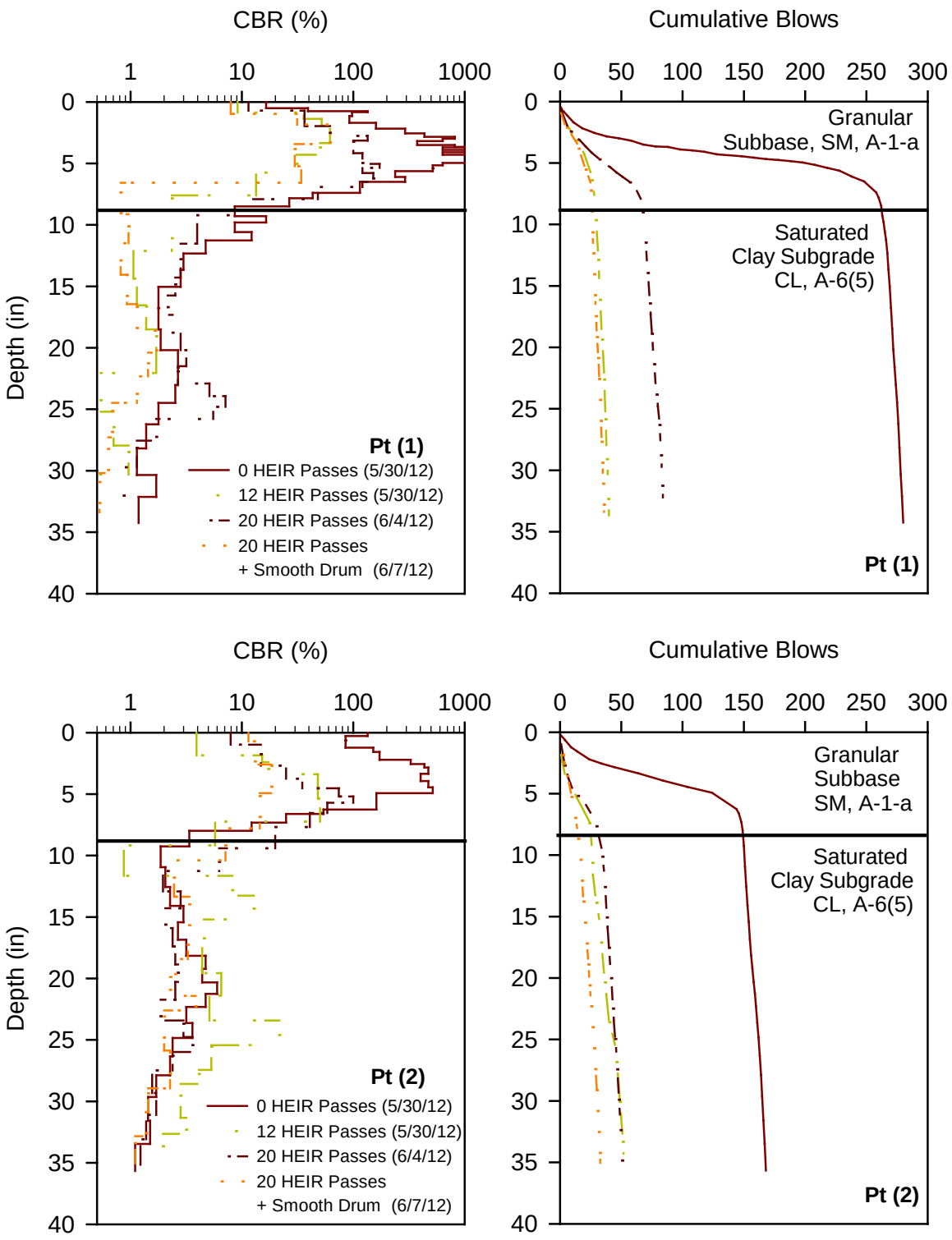

Figure 141. DCP test results from test points (1) and (2) on 8th St. before IR passes and after 12 and 20 IR passes, and after smooth drum roller passes

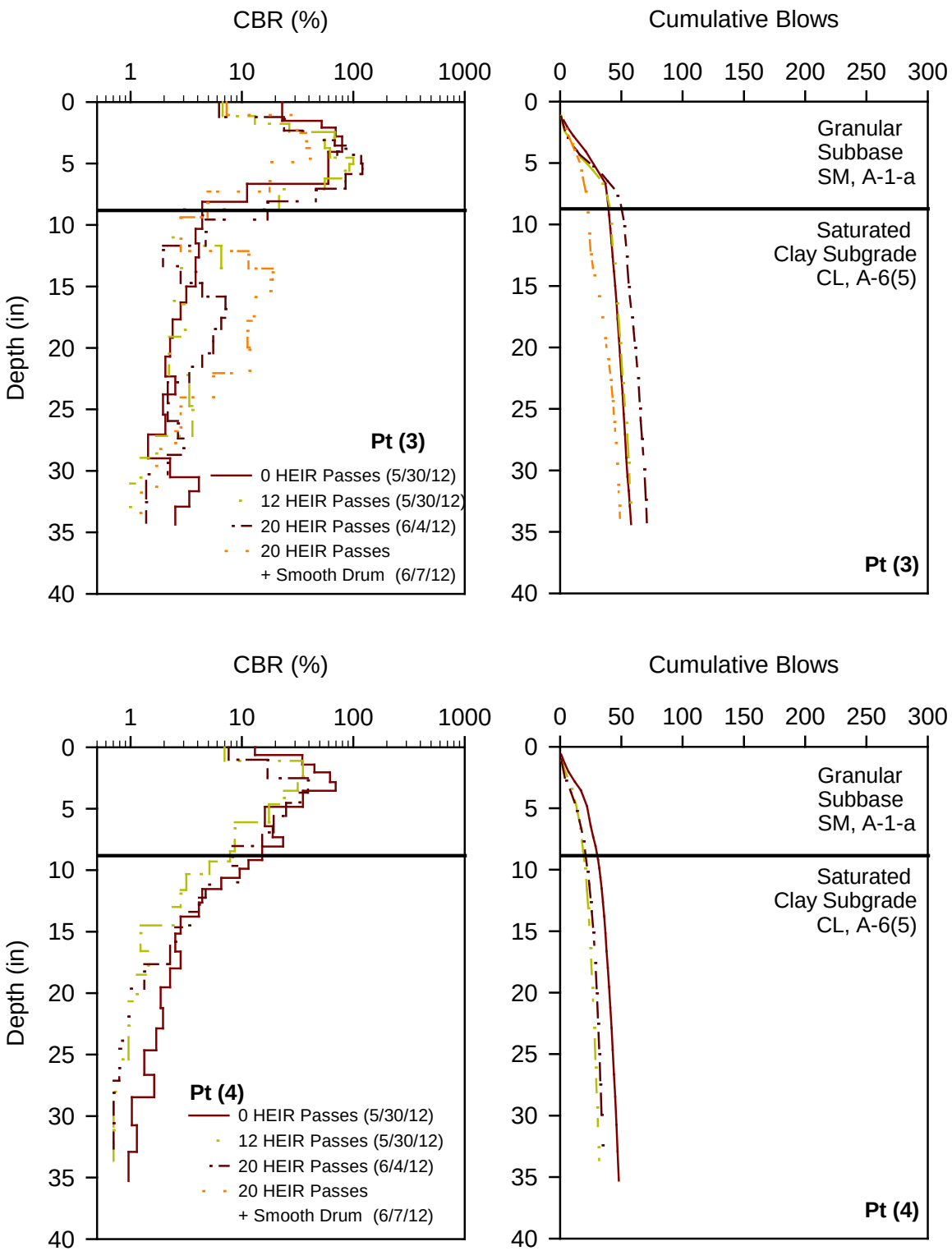

Figure 142. DCP test results from test points (3) and (4) on 8th St. before IR passes and after 12 and 20 IR passes, and after smooth drum roller passes

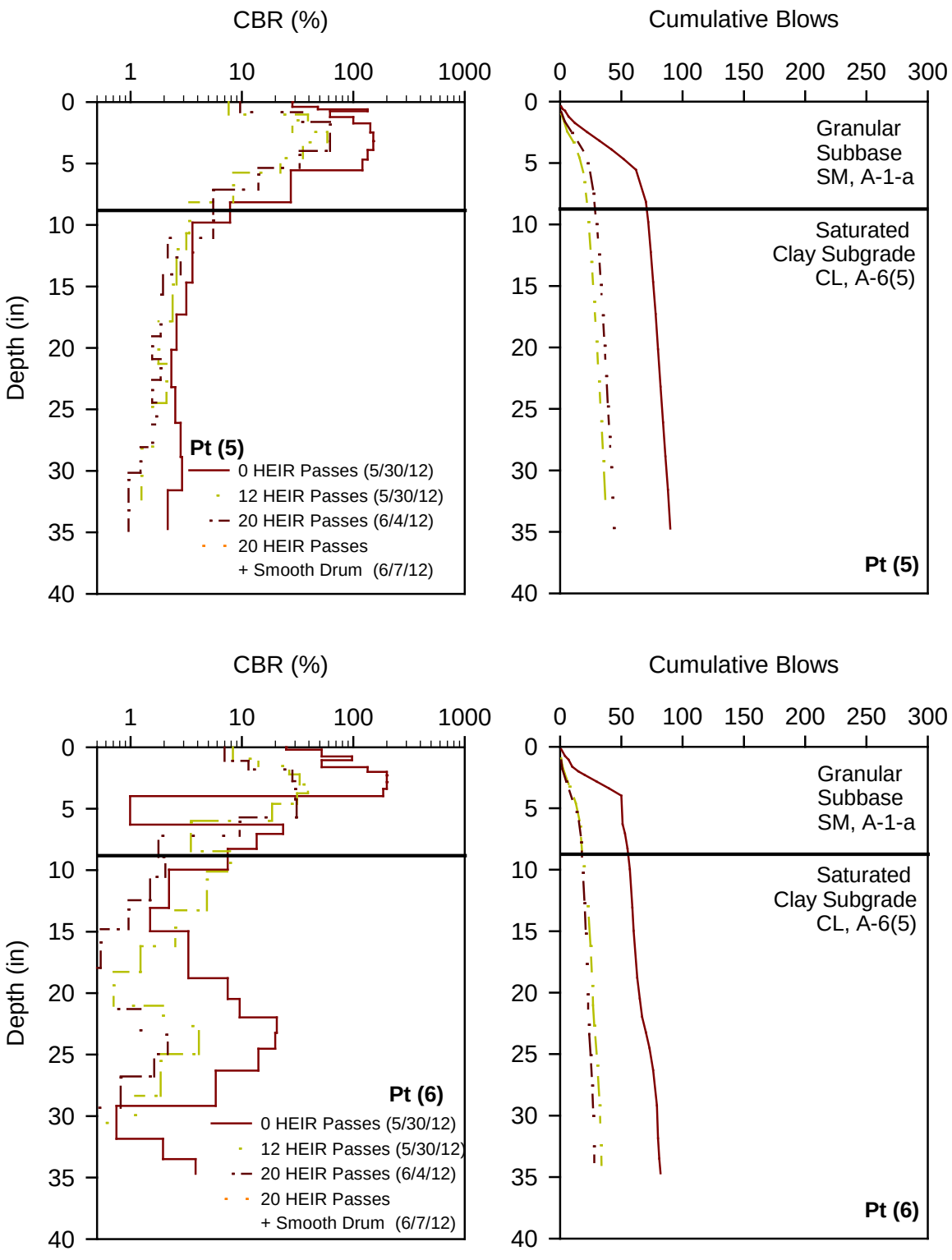

Figure 143. DCP test results from test points (5) and (6) on 8th St. before IR passes and after 12 and 20 IR passes, and after smooth drum roller passes

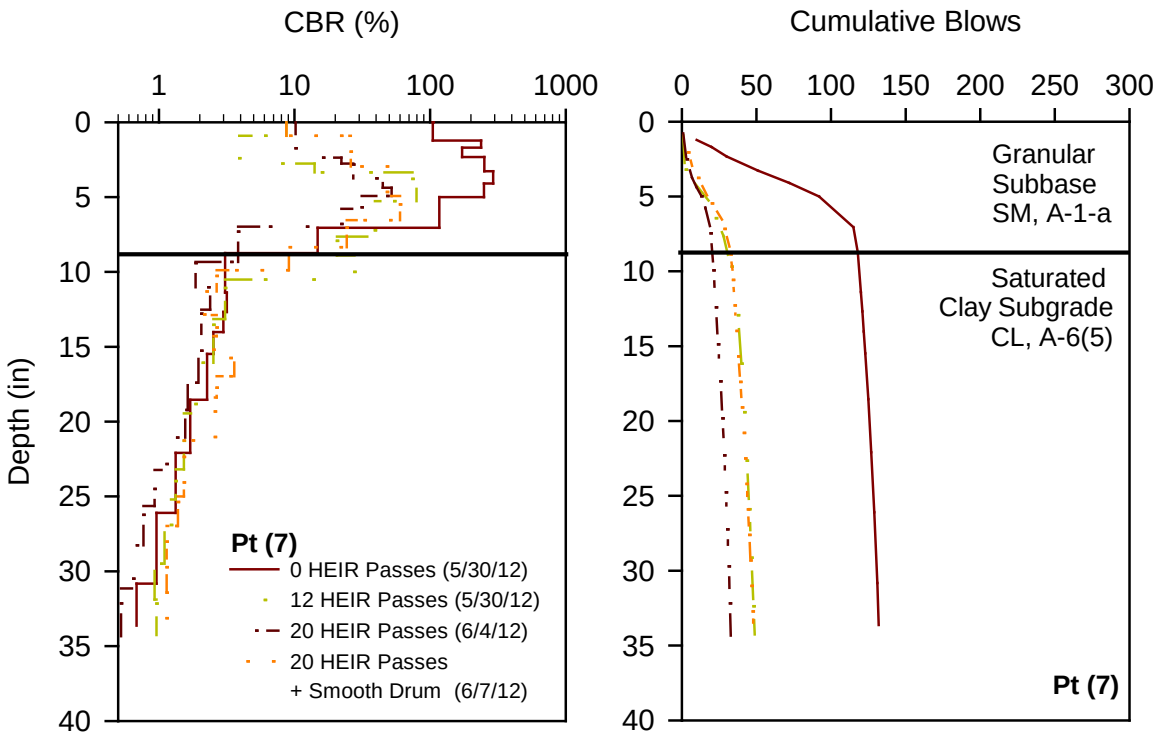

Figure 144. DCP test results from test point (7) on 8th St. before IR passes and after 12 and 20 IR passes, and after smooth drum roller passes

The 8th St. South and North test sections were converted to control test sections with "compacted" subgrade under IR passes. The pavement foundation profile on the test sections are shown in Figure 145. After IR and smooth drum roller passes, the rubblized chipseal surface and the subbase layer were excavated down to the desired subgrade elevation (Figure 146a,b). Then a 6 in. thick layer of crushed limestone MSB was placed and compacted over the subgrade (Figure 146c,d).

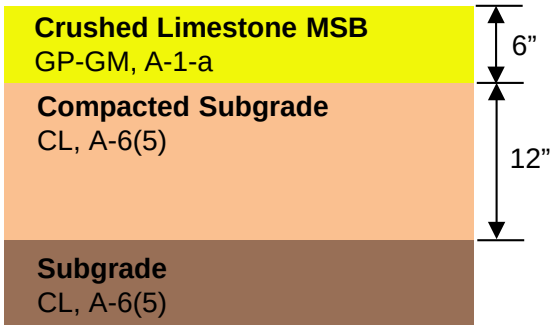

Figure 145. Pavement foundation profile on 8th St. North and South test sections

(a) (b)

(c) (d)

Figure 146. Construction operations on 8th St.: (a) existing subbase layer surface after IR passes, (b) excavating down to 6 in. below final grade to allow placement of MSB, (c) placement of crushed limestone MSB, and (d) 8th St. after placement and compaction of MSB

As-Constructed Test Results

RICM values (MDP*, CMV, and elevation) on compacted crushed limestone MSB layer are shown in Figure 147. RICM measurements were obtained in low amplitude mode (a = 0.85 mm, f = 30 Hz). FWD and LWD modulus measurements obtained from 20 test locations along 1st St. are also shown in Figure 147.

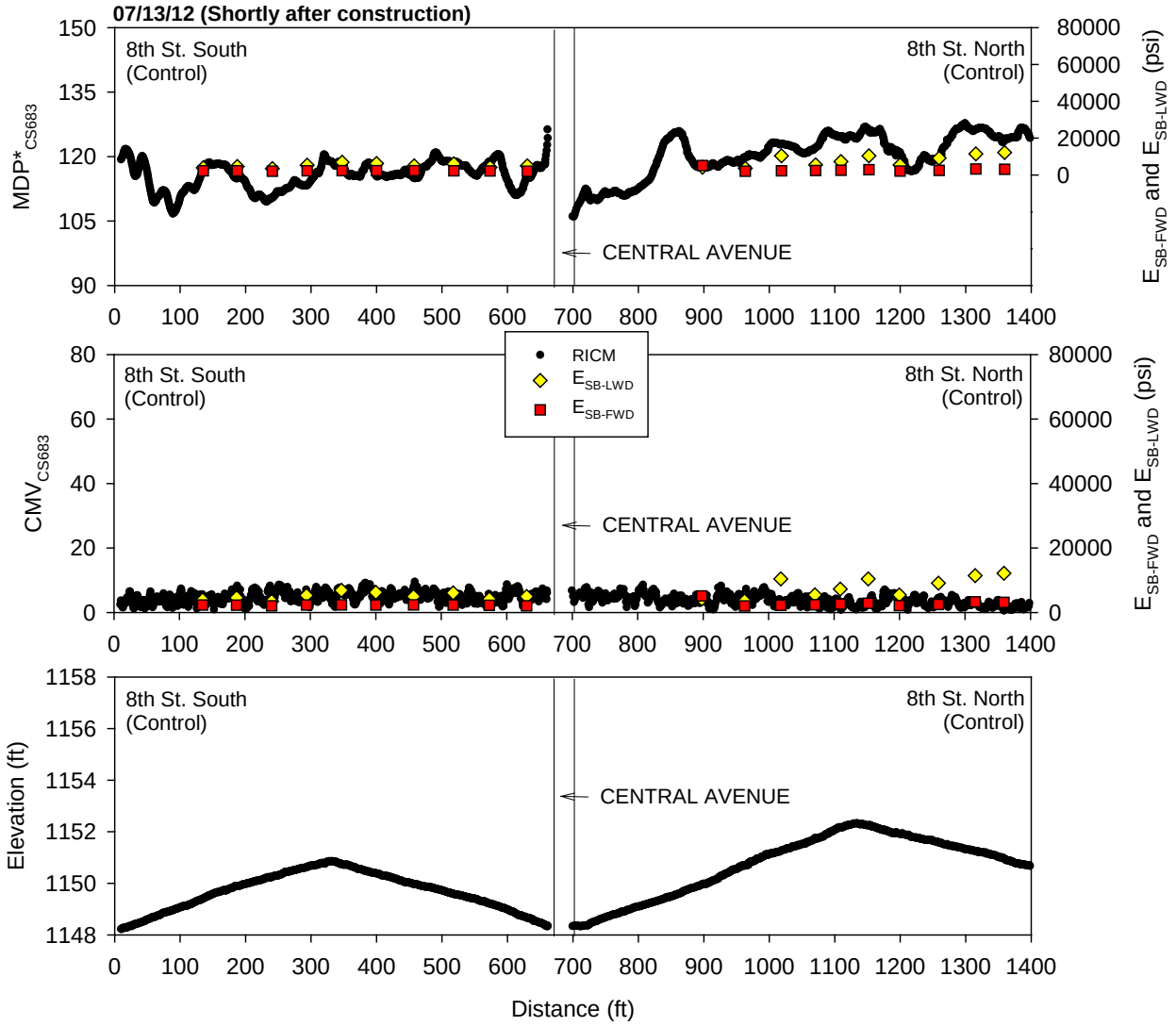

Figure 147. CS683 RICM, LWD, and FWD modulus measurements on 8th St. shortly after construction (July 2012)

Performance Monitoring Results

CCV results obtained in low amplitude mode (a = 0.63 mm, f = 33 Hz) in comparison with $E_{SB\text{-}FWD}$ from October 2012 (about three months after construction) are shown in Figure 148. MDP* and CMV results from the CS683 machine obtained in low amplitude mode (a = 0.85 mm, f = 30 Hz)) in comparison with $E_{SB\text{-}FWD}$ from April 2013 (during spring-thaw) are shown in Figure 149. Similarly, results from the CS74 machine obtained in low amplitude mode (a = 0.97 mm, f = 28 Hz) are shown in Figure 150. MDP* and CMV results obtained from the CS683 machine from July 2012 and April 2013 are compared in Figure 151.

DCP-CBR and cumulative blows profiles from different testing times are shown in Figure 152 and Figure 153. Average CBR_{MSB} and CBR_{SG} for each test section are shown in Figure 154. Average E_{SB-FWD} for each test section are shown in Figure 155.

CBR_{MSB} and CBR_{SG} showed lower values in April 2013 during spring-thaw compared to measurements in October 2012. The values increased slightly in May 2013. E_{SB-FWD} measurements were lower in April 2013 than in July and October 2012. There was no significant difference between RICM measurements obtained in July 2012 and April 2013.

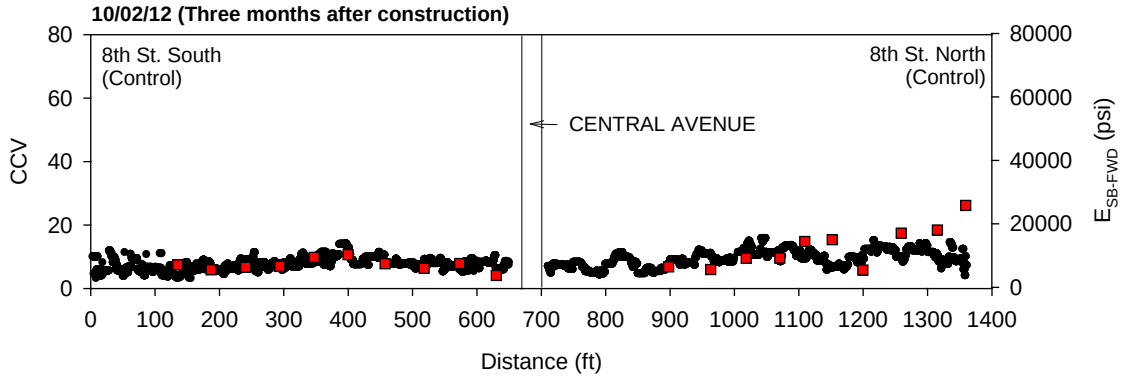

Figure 148. Sakai CCV and FWD modulus measurements on 8th St. three months after construction (October 2012)

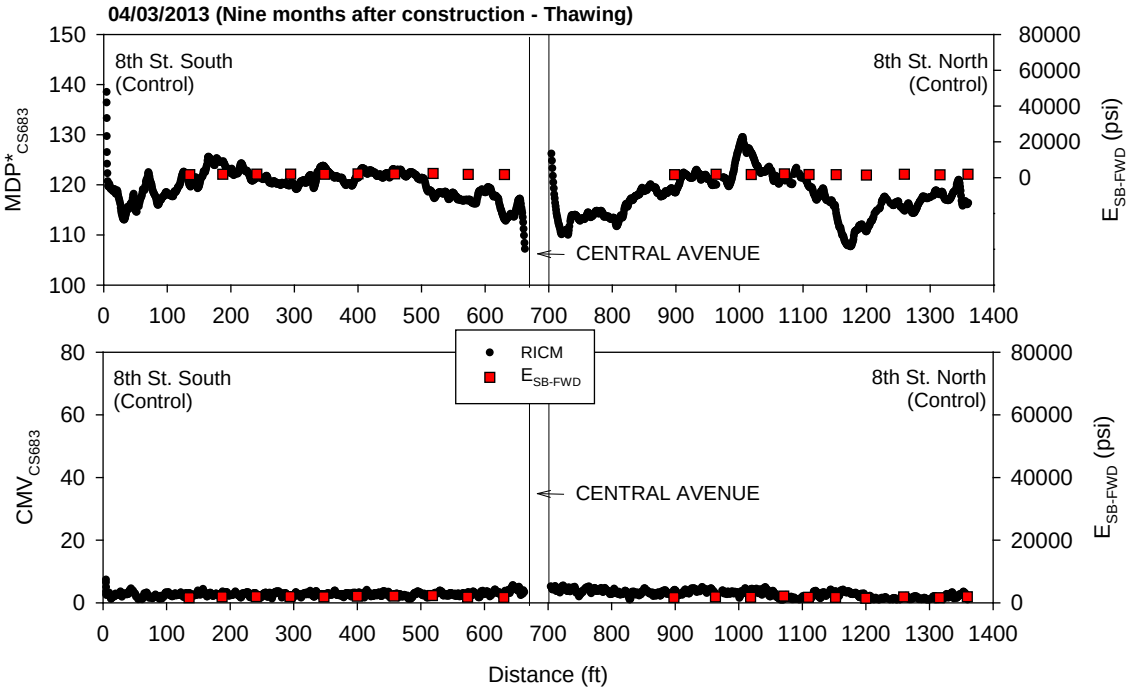

Figure 149. CS683 RICM and FWD modulus measurements on 8th St. nine months after construction during thawing (April 2013)

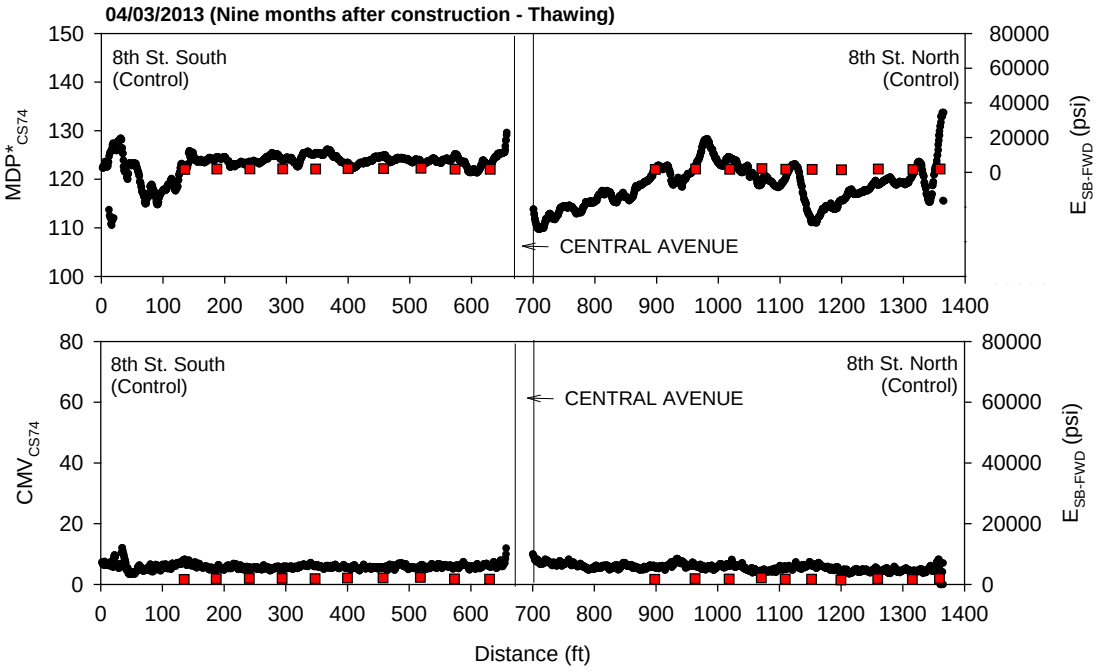

Figure 150. CS74 RICM and FWD modulus measurements on 8th St. nine months after construction during thawing (April 2013)

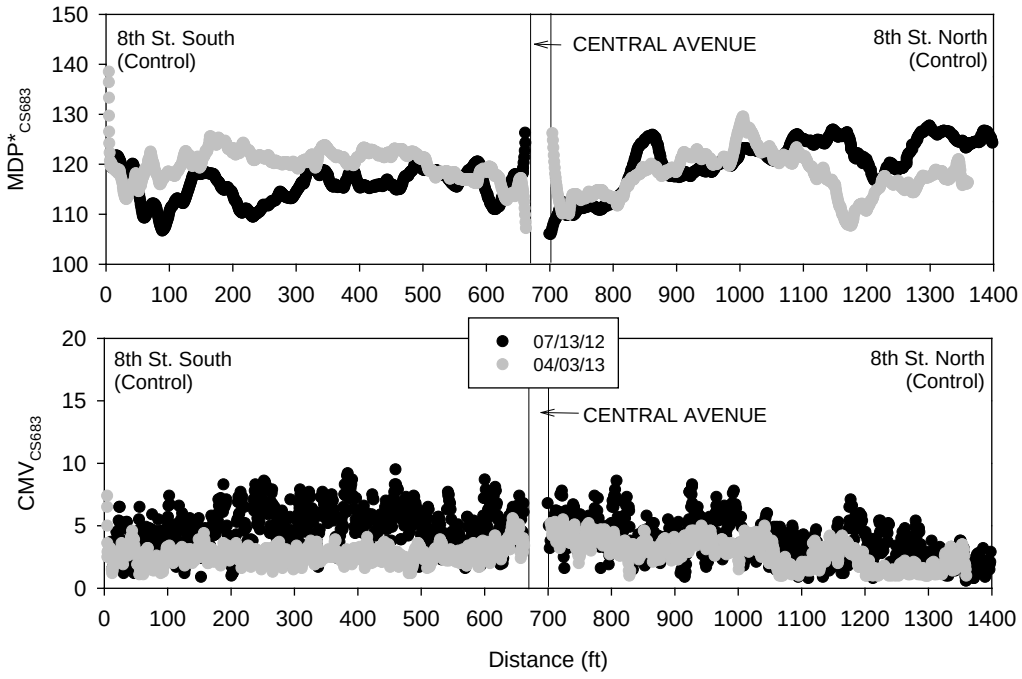

Figure 151. Comparison between CS683 RICM measurements on 8th St. shortly after construction and nine months after construction during thawing

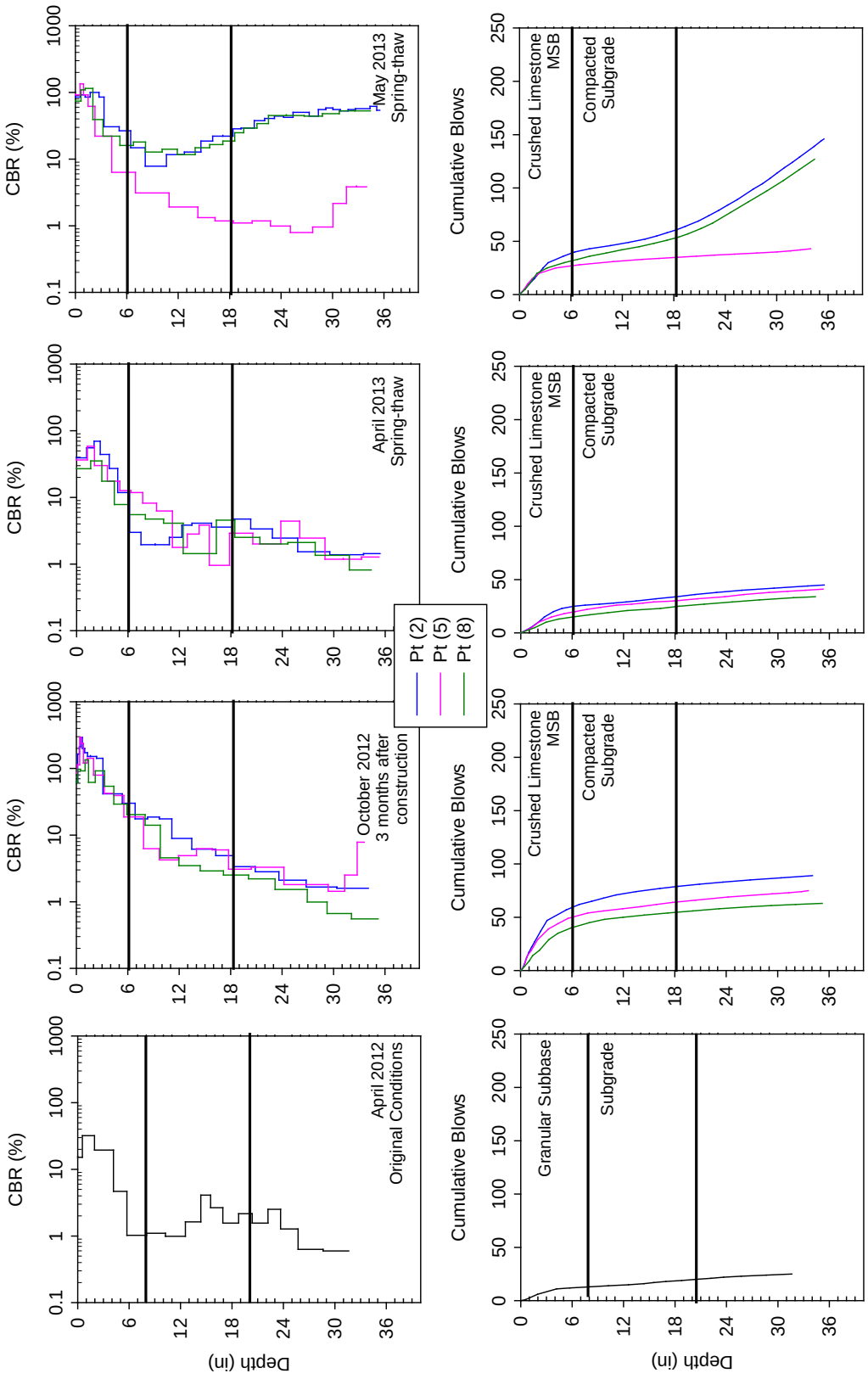

Figure 152. DCP test results from 8th St. South from different testing times

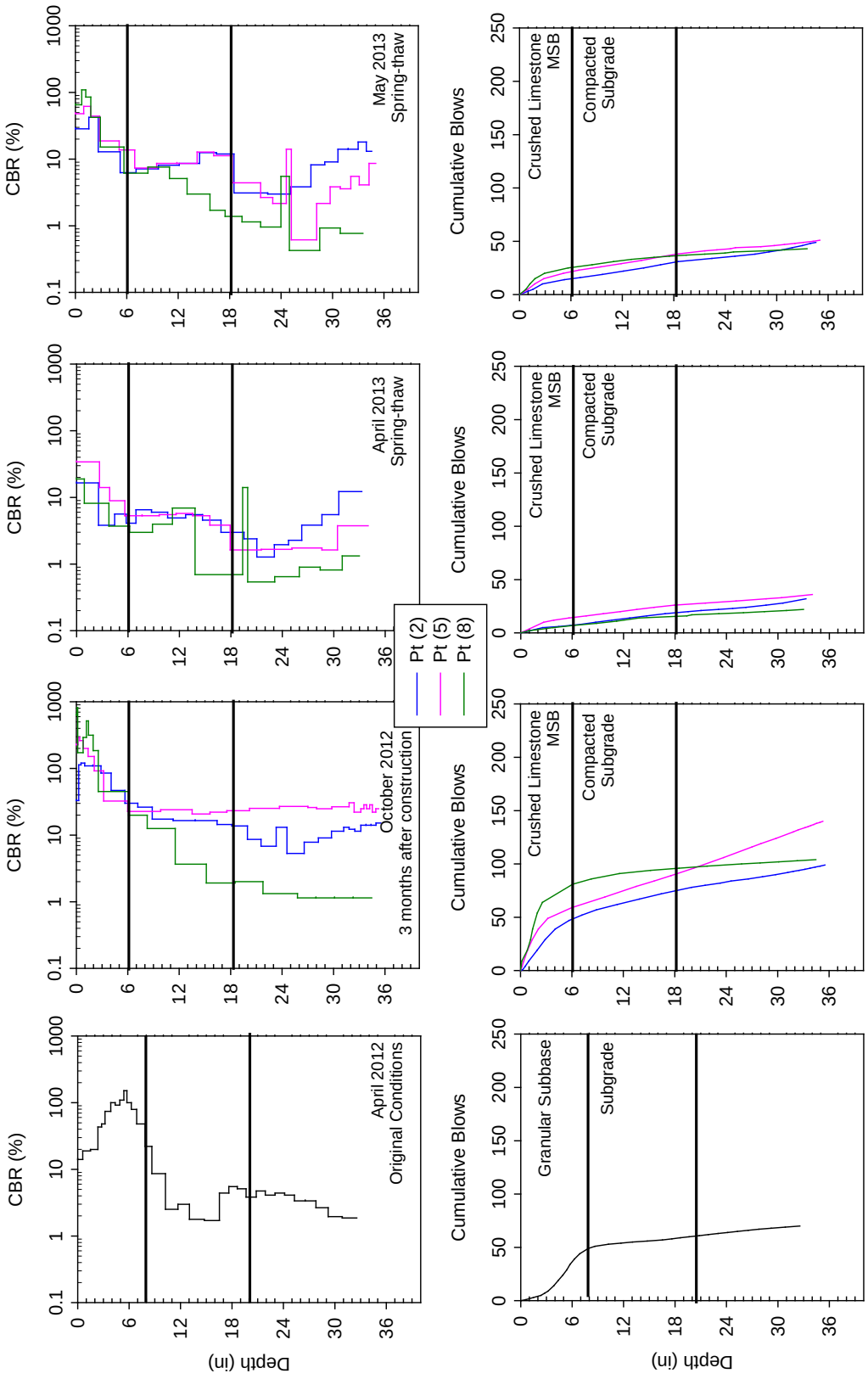

Figure 153**. DCP test results from 8th St. North from different testing times**

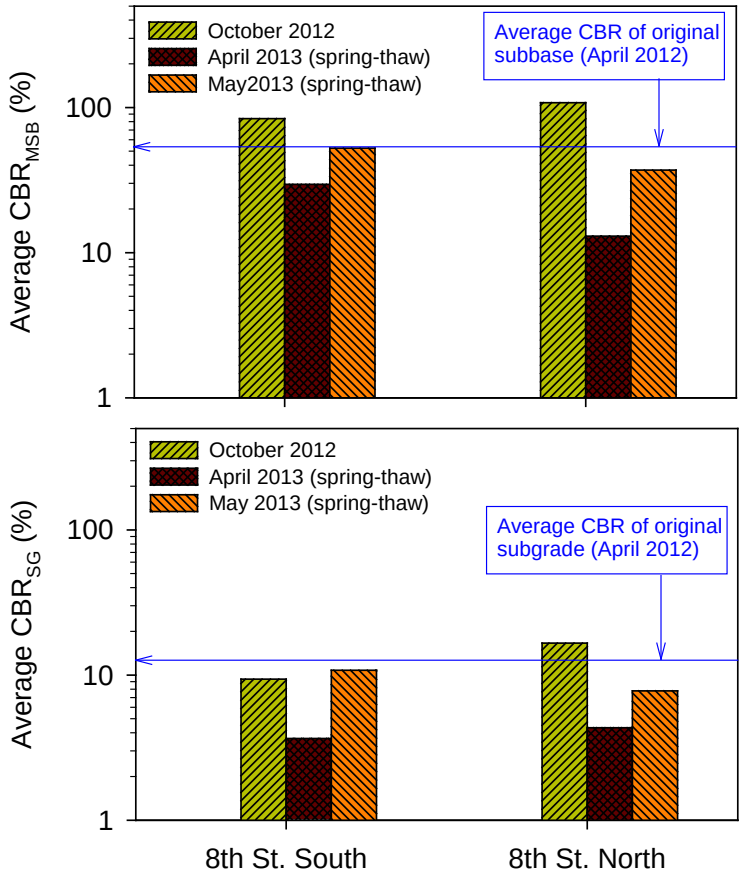

Figure 154. Average CBR (based on 2 to 3 tests) of MSB and subgrade layers on 8th St. South and North

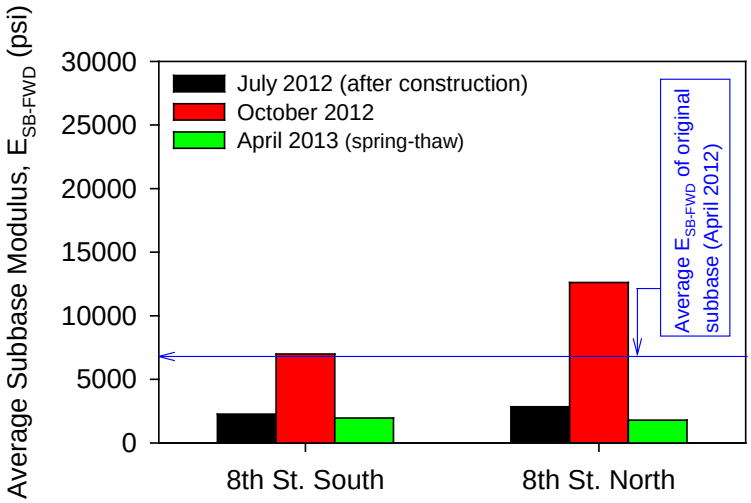

Figure 155. Average FWD subbase modulus (based on 10 tests) on 8th St. South and North sections

9th North-South: 6 inch Reclaimed Subbase

Construction Observations

The pavement foundation profile on 9th St. North and South is shown in Figure 156. Pictures during construction of the sections by removing the existing base down to the subgrade elevation, and placing the reclaimed subbase, and the crushed limestone MSB are shown in Figure 157.

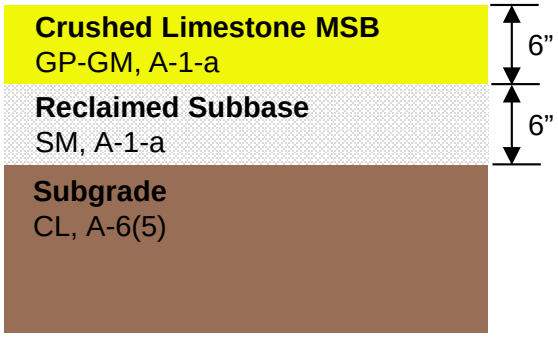

Figure 156. Pavement foundation profile on 9th St. South and North sections

(a) (b)

(c) (d)

(e) (f)

Figure 157. Construction operations on 9th St.: (a) scarifying and removing existing subbase, (b) excavating down to subgrade elevation, (c) placing relacimed subbase, (d) compacting reclaimed subbase layer, (e) placement of MSB layer, and (f) final compacted MSB layer

As-Constructed Test Results

FWD and LWD testing and RICM mapping was conducted on the crushed limestone MSB layer shortly after construction (July 2012). RICM values (MDP*, CMV, and elevation) along 1st St. on compacted crushed limestone MSB layer are shown in Figure 158. FWD and LWD modulus measurements obtained from 20 test locations along 1st St. are also shown in Figure 158.

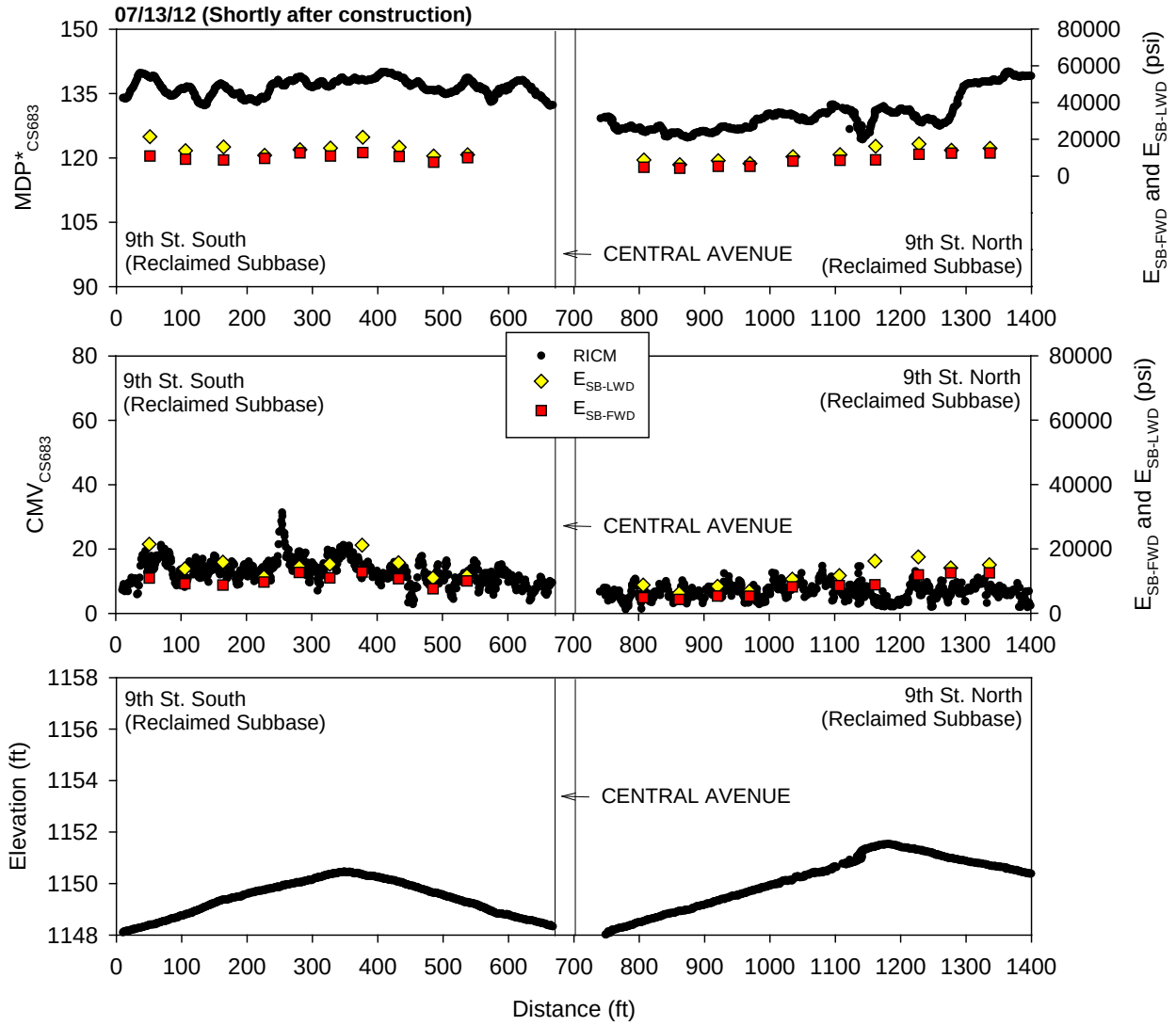

Figure 158. CS683 RICM, LWD, and FWD modulus measurements on 9th St. shortly after construction (July 2012)

Performance Monitoring Results

CCV results in comparison with $E_{SB\text{-}FWD}$ from October 2012 (about three months after construction) are shown in Figure 159. MDP* and CMV results from the CS683 machine in comparison with $E_{SB\text{-}FWD}$ from April 2013 (during thawing about nine months after construction)

are shown in Figure 160. Similarly, results from the CS74 machine are shown in Figure 161. MDP* and CMV results obtained from the CS683 machine from October 2012 and April 2013 are compared in Figure 162. DCP-CBR and cumulative blows profiles from different testing times are shown in Figure 163 and Figure 164. Average CBR_{MSB} and CBR_{SG} for each test section are shown in Figure 165. Average $E_{SB\text{-}FWD}$ for each test section are shown in Figure 166. CBR_{MSB} and CBR_{SG} showed the lowest values in May 2013, while $E_{SB\text{-}FWD}$ showed the lowest values in April 2013 when the foundation layers were partially thawed at the surface. MDP* and CMV measurements were also lower in April 2013 during thawing than in Ocotber 2012.

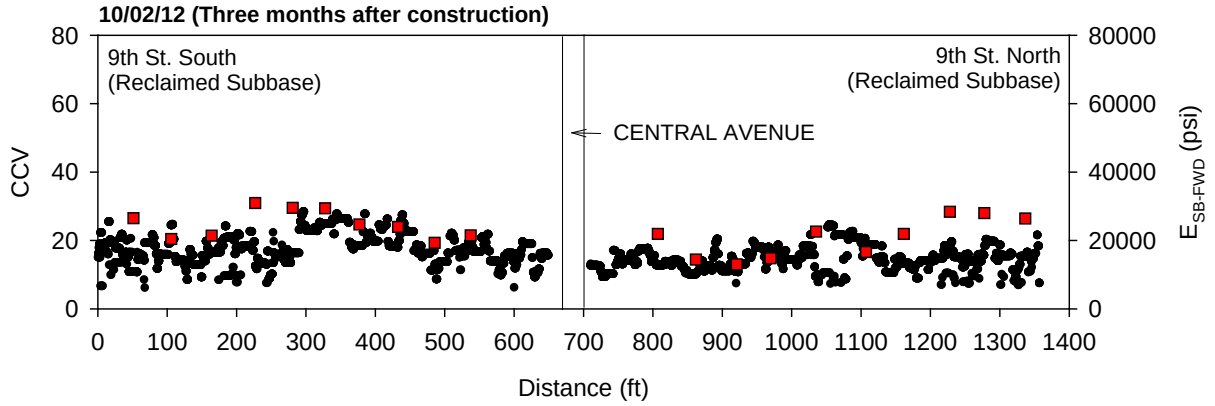

Figure 159. Sakai CCV and FWD modulus measurements on 9th St. three months after construction (October 2012)

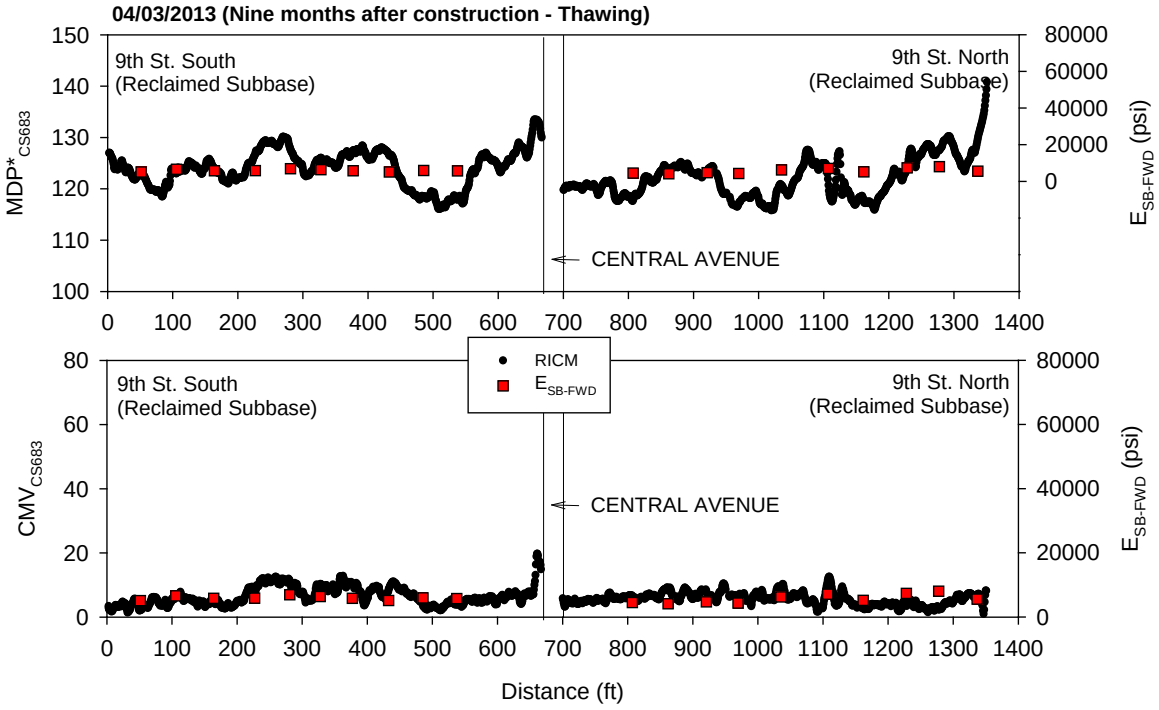

Figure 160. CS683 RICM and FWD modulus measurements on 9th St. nine months after construction during thawing (April 2013)

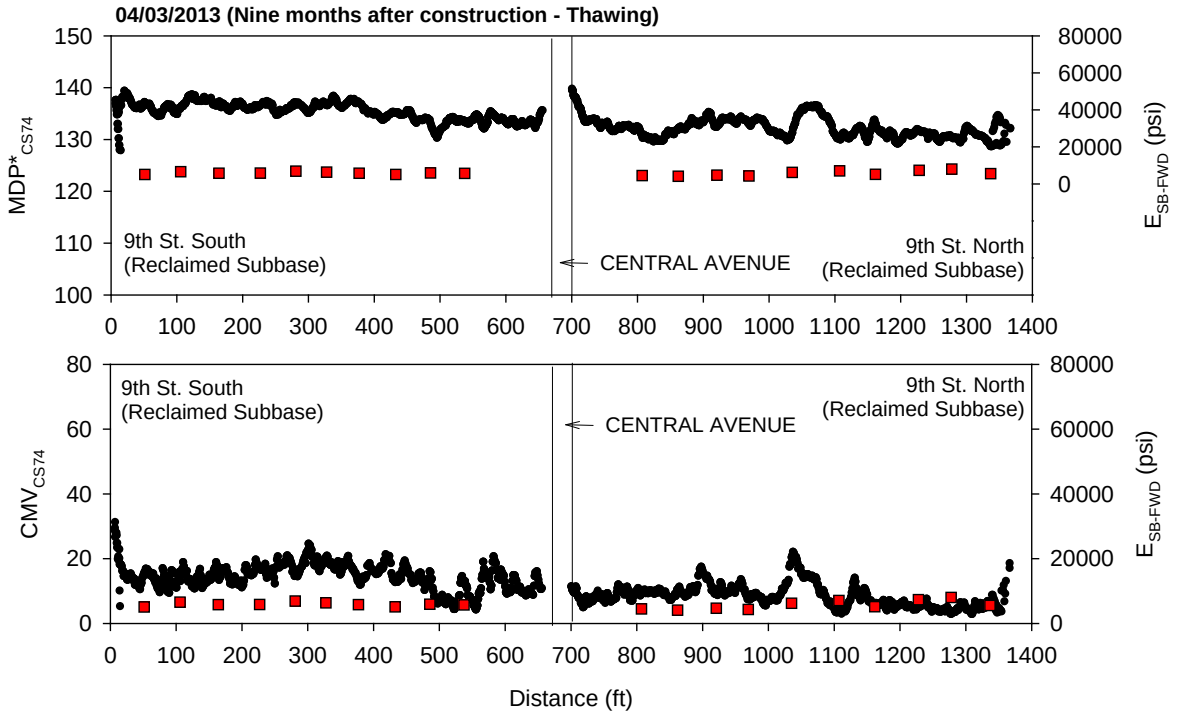

Figure 161. CS74 RICM and FWD modulus measurements on 9th St. nine months after construction during thawing (April 2013)

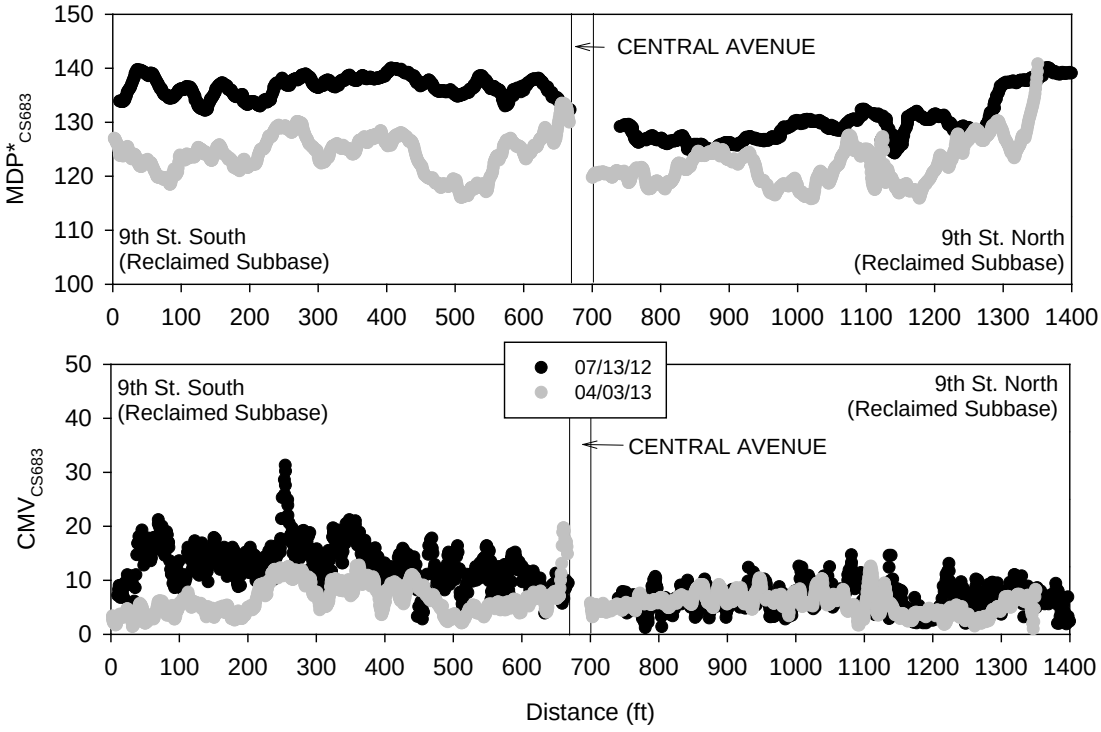

Figure 162. Comparison between CS683 RICM measurements on 9th St. shortly after construction and nine months after construction during thawing

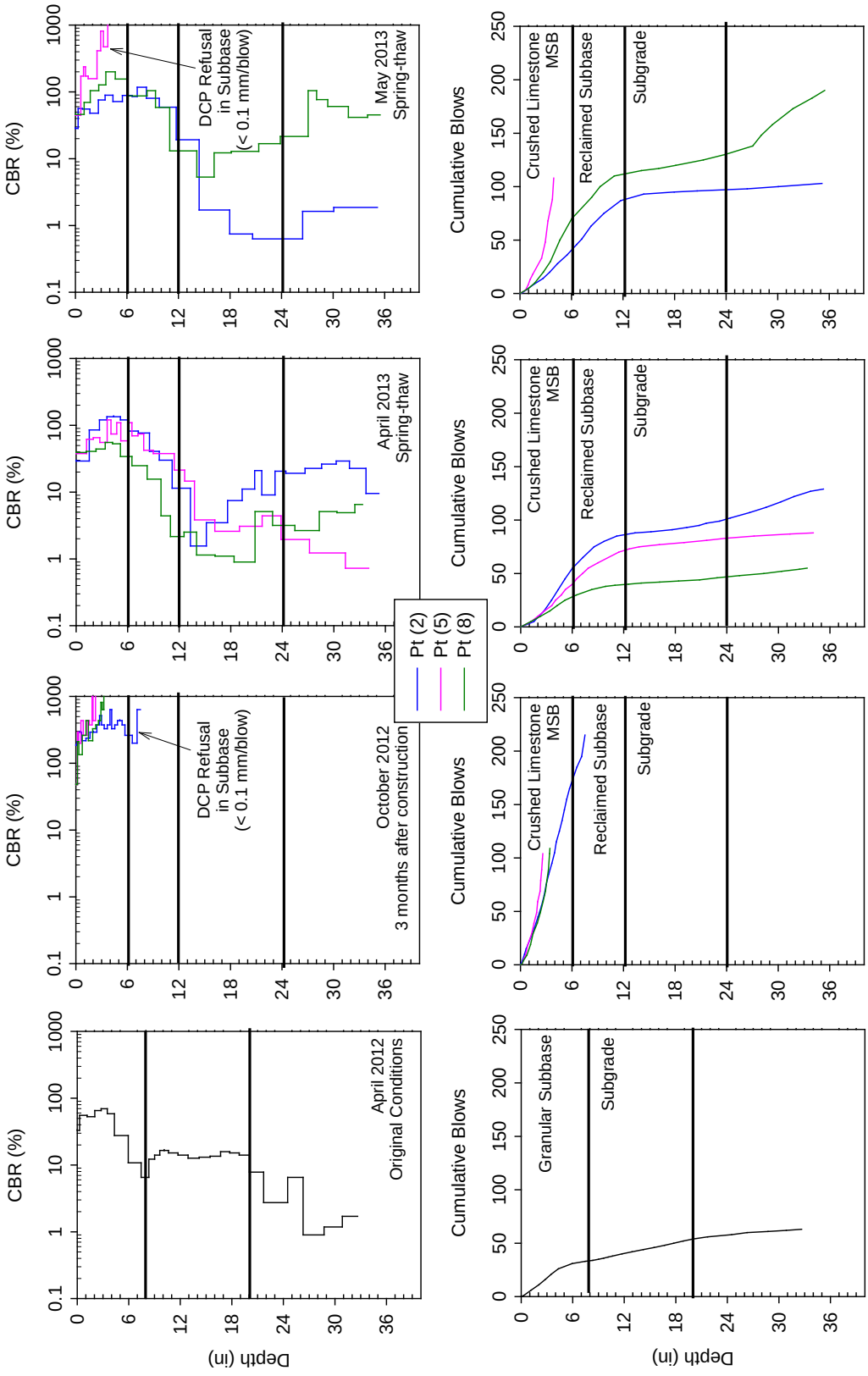

Figure 163. DCP test results from 9th St. South from different testing times

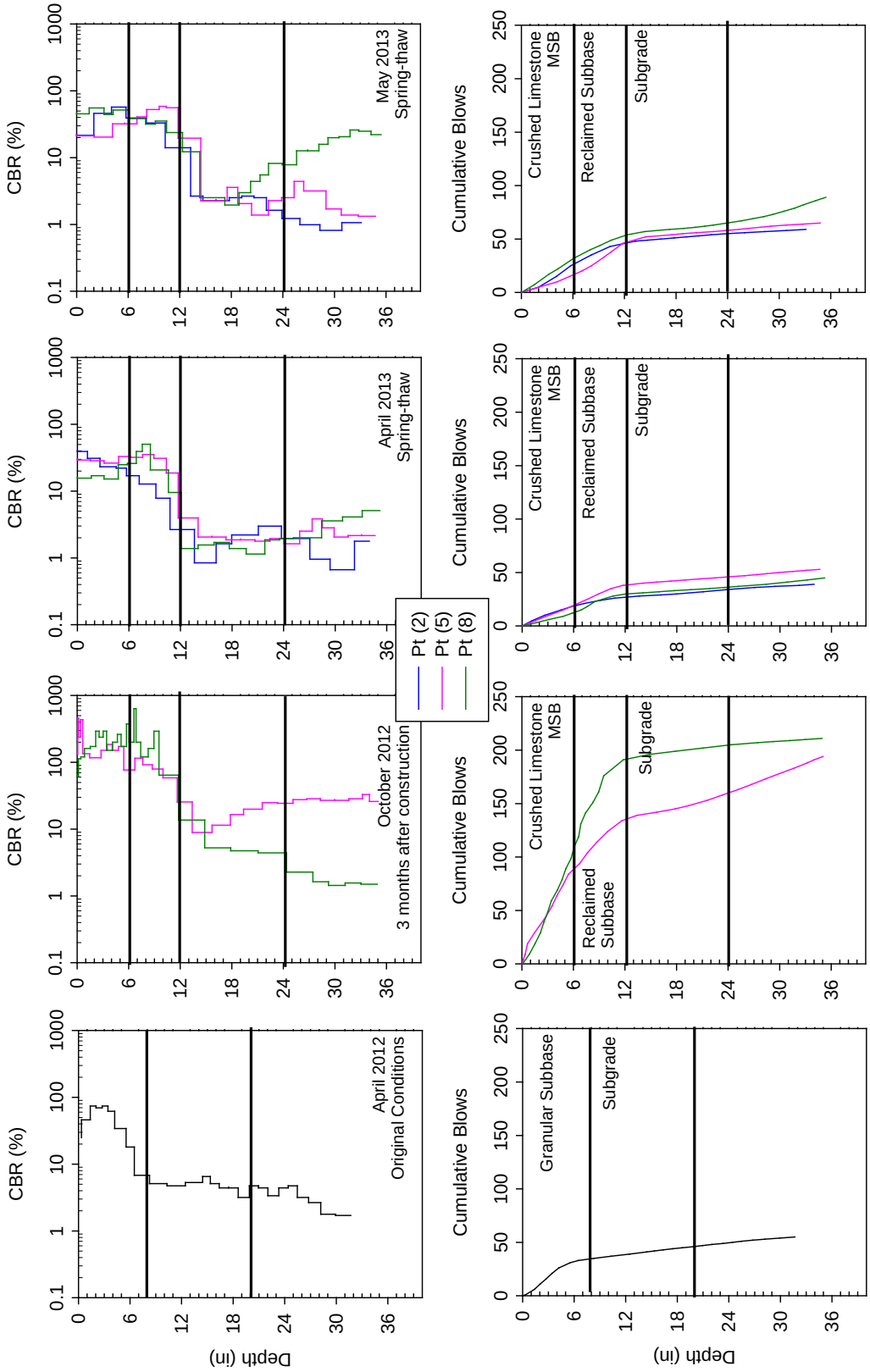

Figure 164. DCP test results from 9th St. North from different testing times

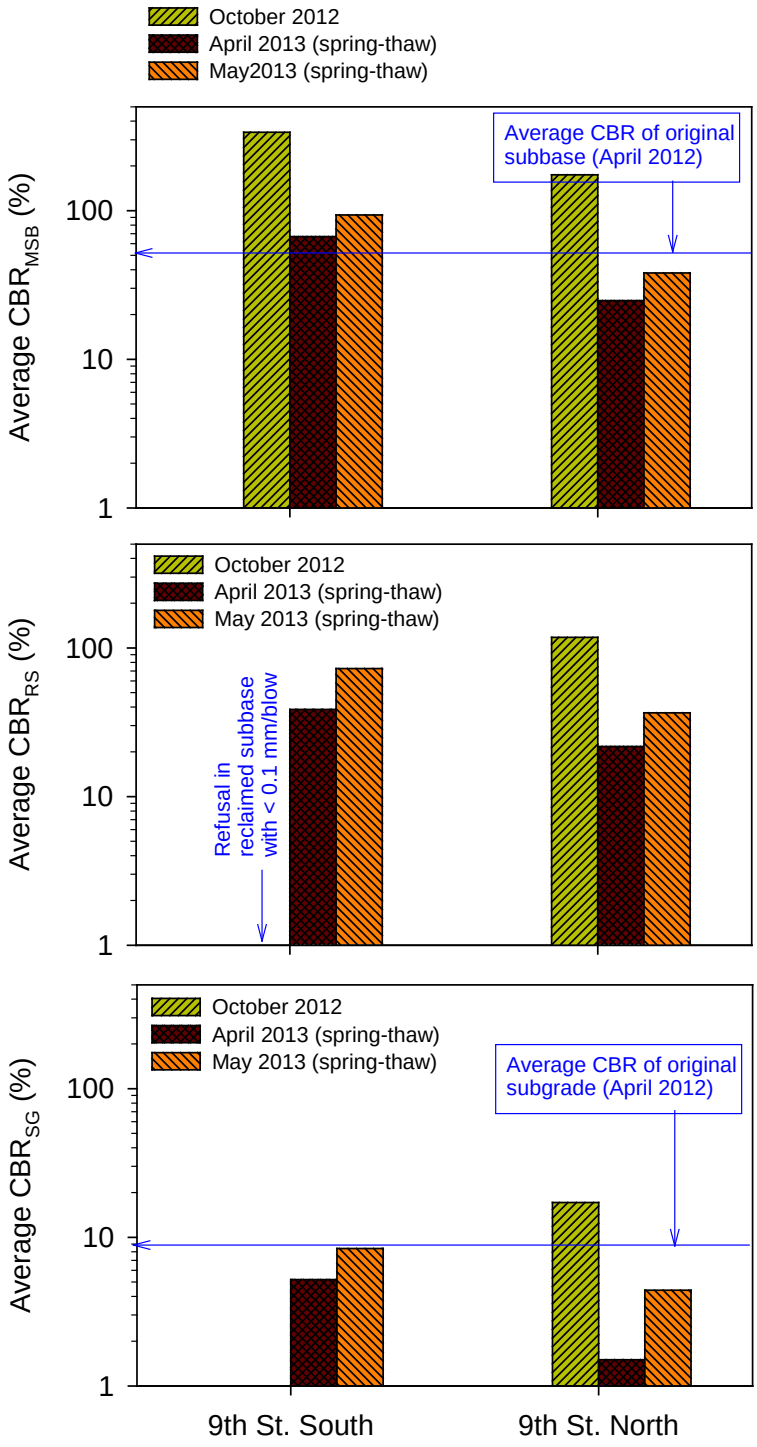

Figure 165. Average CBR (based on 2 to 3 tests) of MSB and subgrade layers on 9th St. South and North

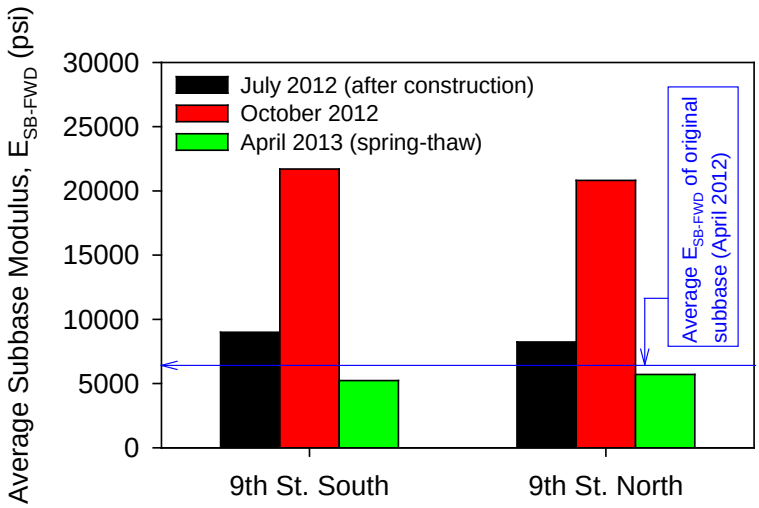

Figure 166. Average FWD subbase modulus (based on 10 tests) on 9th St. South and North sections

10th North-South: 12 inches of Compacted Subgrade and Control

Construction Observations

The pavement foundation profiles on 10th St. North and South is shown in Figure 167. The sections were constructed by removing the existing base down to the subgrade elevation, scarifying and compacting the subgrade on 10st. North, and placing and compacting the crushed limestone MSB on both north and south sections.

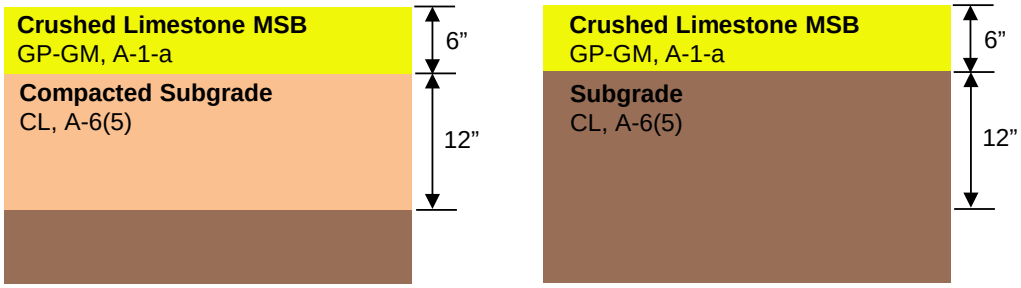

Figure 167. Pavement foundation profile on: (a) 10th St. North (compacted subgrade), and (b) 10th St. South (control)

As-Constructed Test Results

FWD and LWD testing and RICM mapping was conducted on the crushed limestone MSB layer shortly after construction (July 2012). RICM values (MDP*, CMV, and elevation) along 1st St.

on compacted crushed limestone MSB layer are shown in Figure 168. FWD and LWD modulus measurements obtained from 20 test locations along 1st St. are also shown in Figure 168.

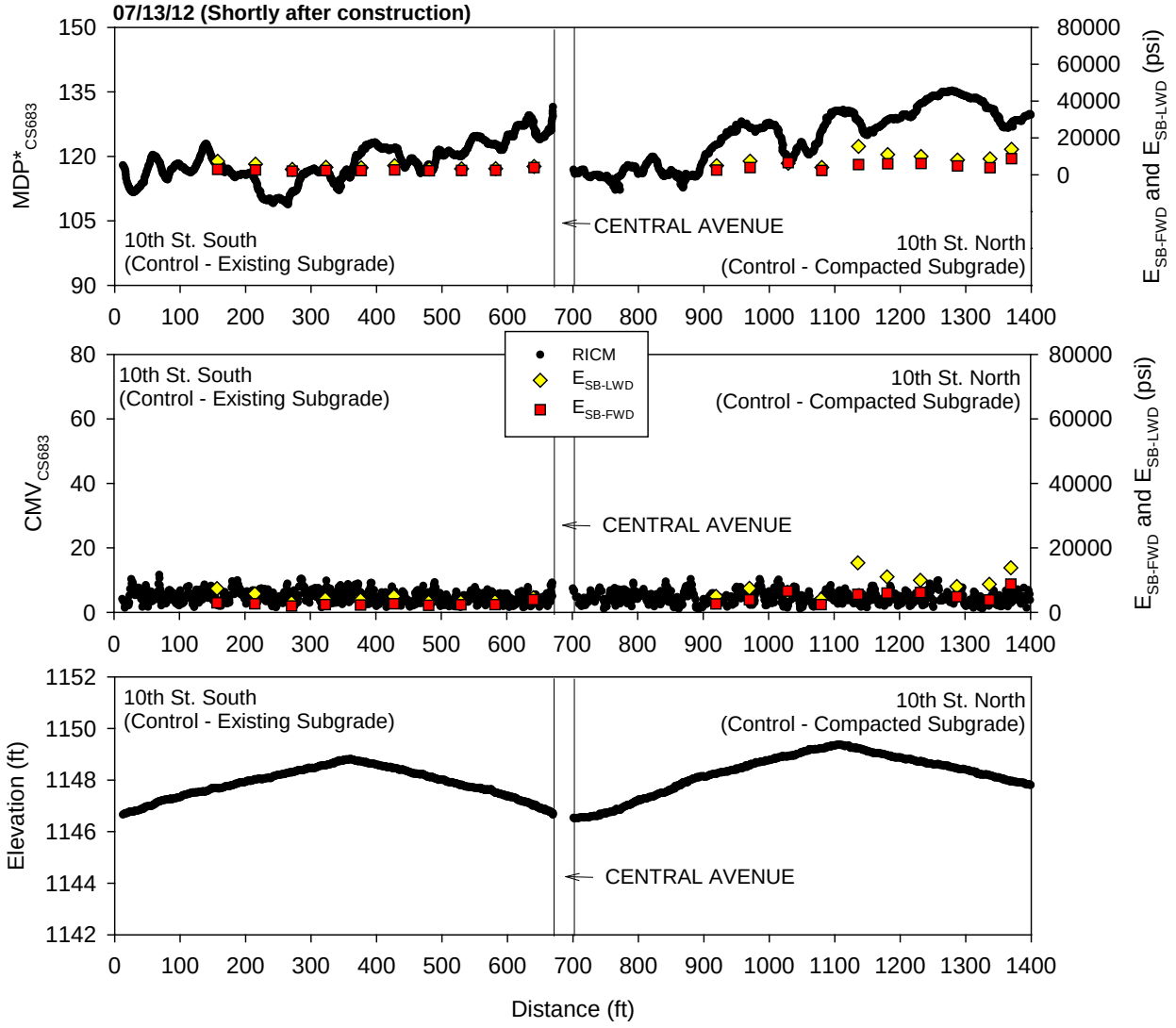

Figure 168. CS683 RICM, LWD, and FWD modulus measurements on 10th St. shortly after construction (July 2012)

Performance Monitoring Results

CCV results in comparison with $E_{SB\text{-}FWD}$ from October 2012 (about three months after construction) are shown in Figure 169. MDP* and CMV results from the CS683 machine in comparison with $E_{SB\text{-}FWD}$ from April 2013 (during thawing about nine months after construction) are shown in Figure 170. Similarly, results from the CS74 machine are shown in Figure 171. MDP* and CMV results obtained from the CS683 machine from October 2012 and April 2013 are compared in Figure 172. DCP-CBR and cumulative blows profiles from different testing times are shown in Figure 173 and Figure 174. Average CBR_{MSB} and CBR_{SG} for each test

section are shown in Figure 175. Average $E_{SB\text{-}FWD}$ for each test section are shown in Figure 176. CBR_{MSB} and CBR_{SG} showed the lowest values in May 2013, while $E_{SB\text{-}FWD}$ showed the lowest values in April 2013 when the foundation layers were partially thawed at the surface. MDP* and CMV measurements were also lower in April 2013 during thawing than in Ocotber 2012.

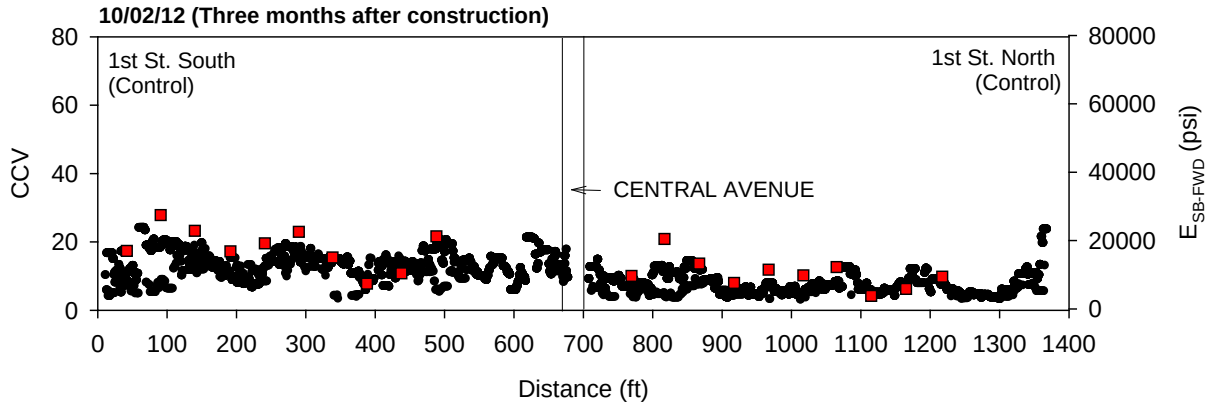

Figure 169. Sakai CCV and FWD modulus measurements on 10th St. three months after construction (October 2012)

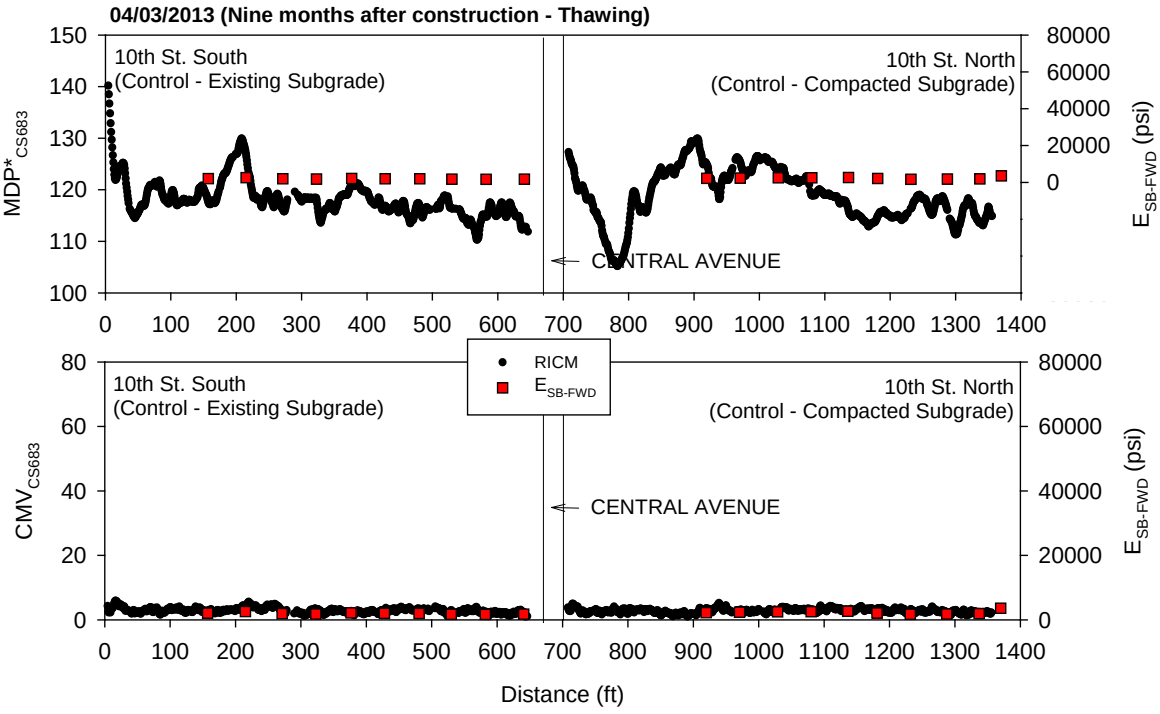

Figure 170. CS683 RICM and FWD modulus measurements on 10th St. nine months after construction during thawing (April 2013)

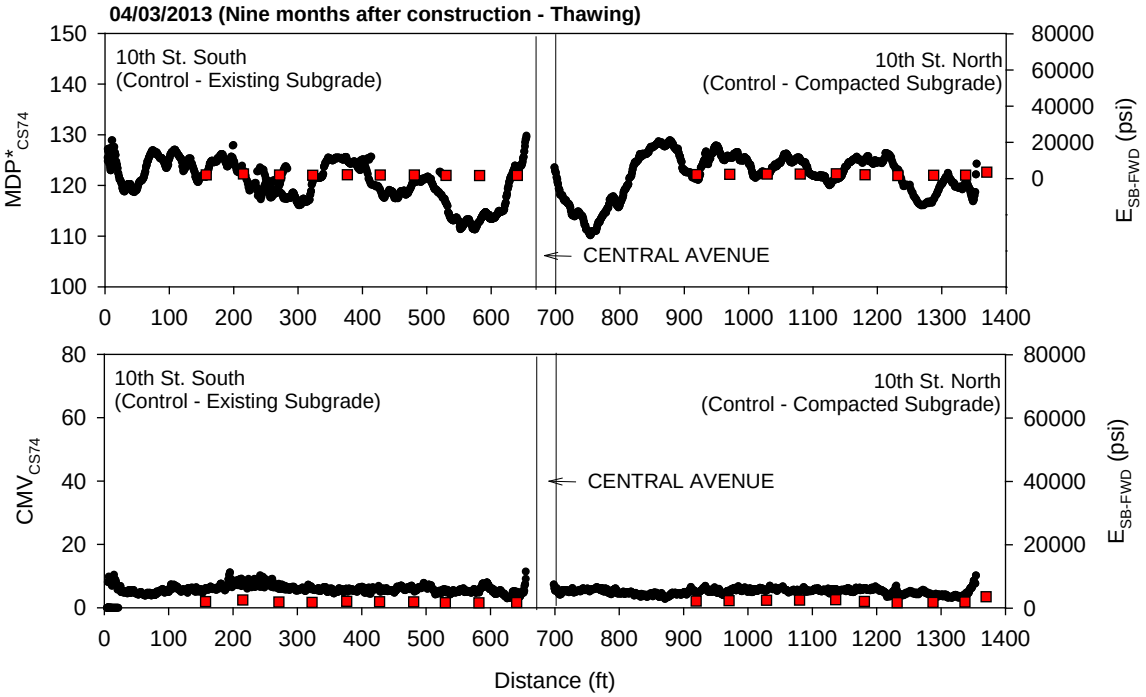

Figure 171. CS74 RICM and FWD modulus measurements on 10th St. nine months after construction during thawing (April 2013)

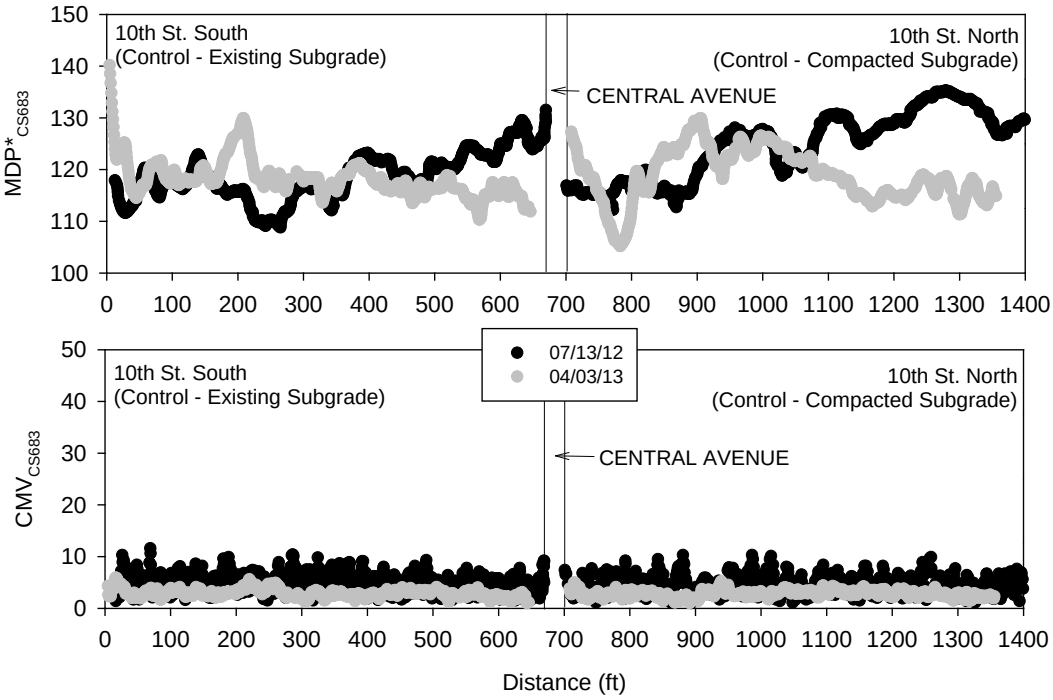

Figure 172. Comparison between CS683 RICM measurements on 10th St. shortly after construction and nine months after construction during thawing

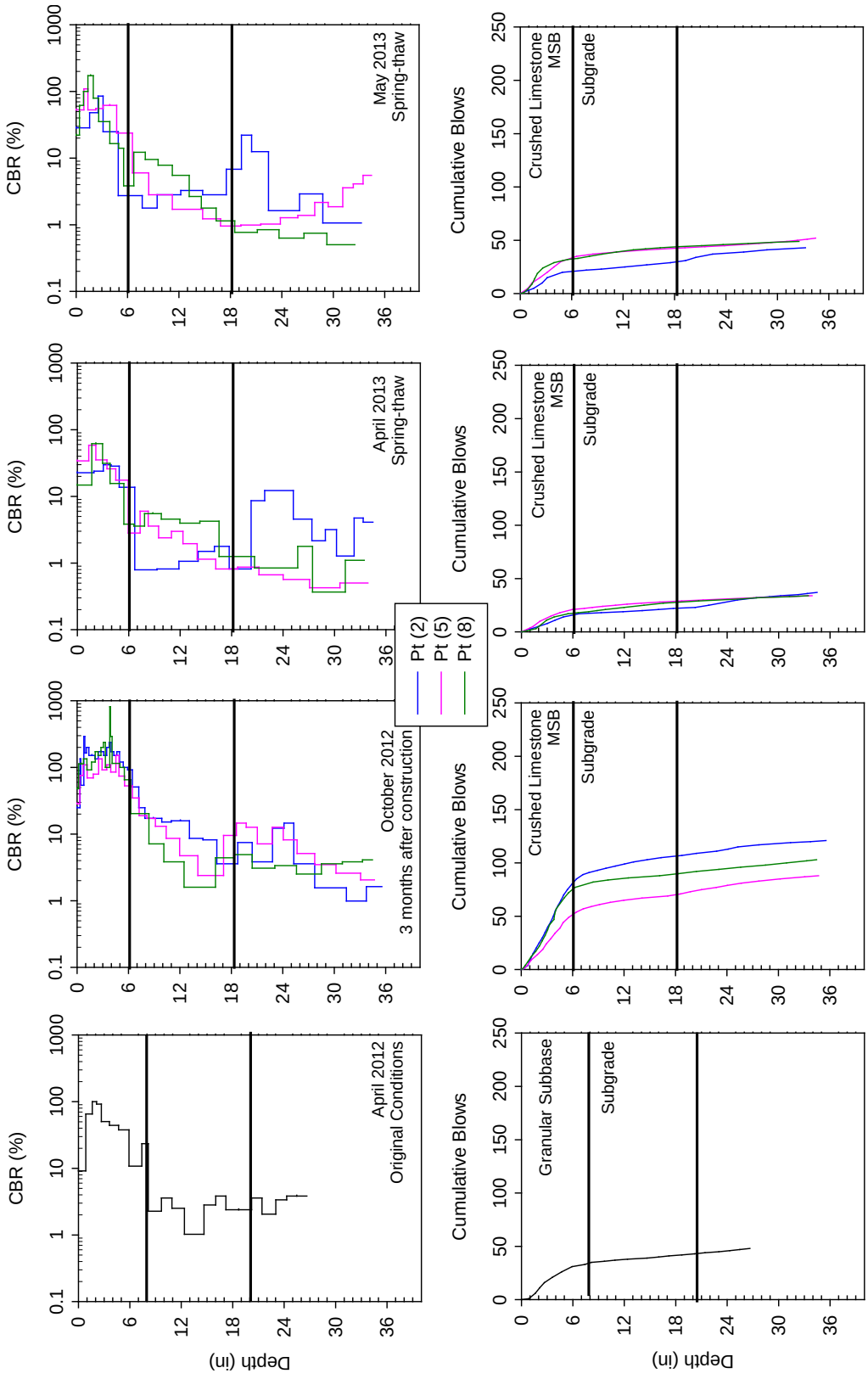

Figure 173. DCP test results from 10th St. South from different testing times

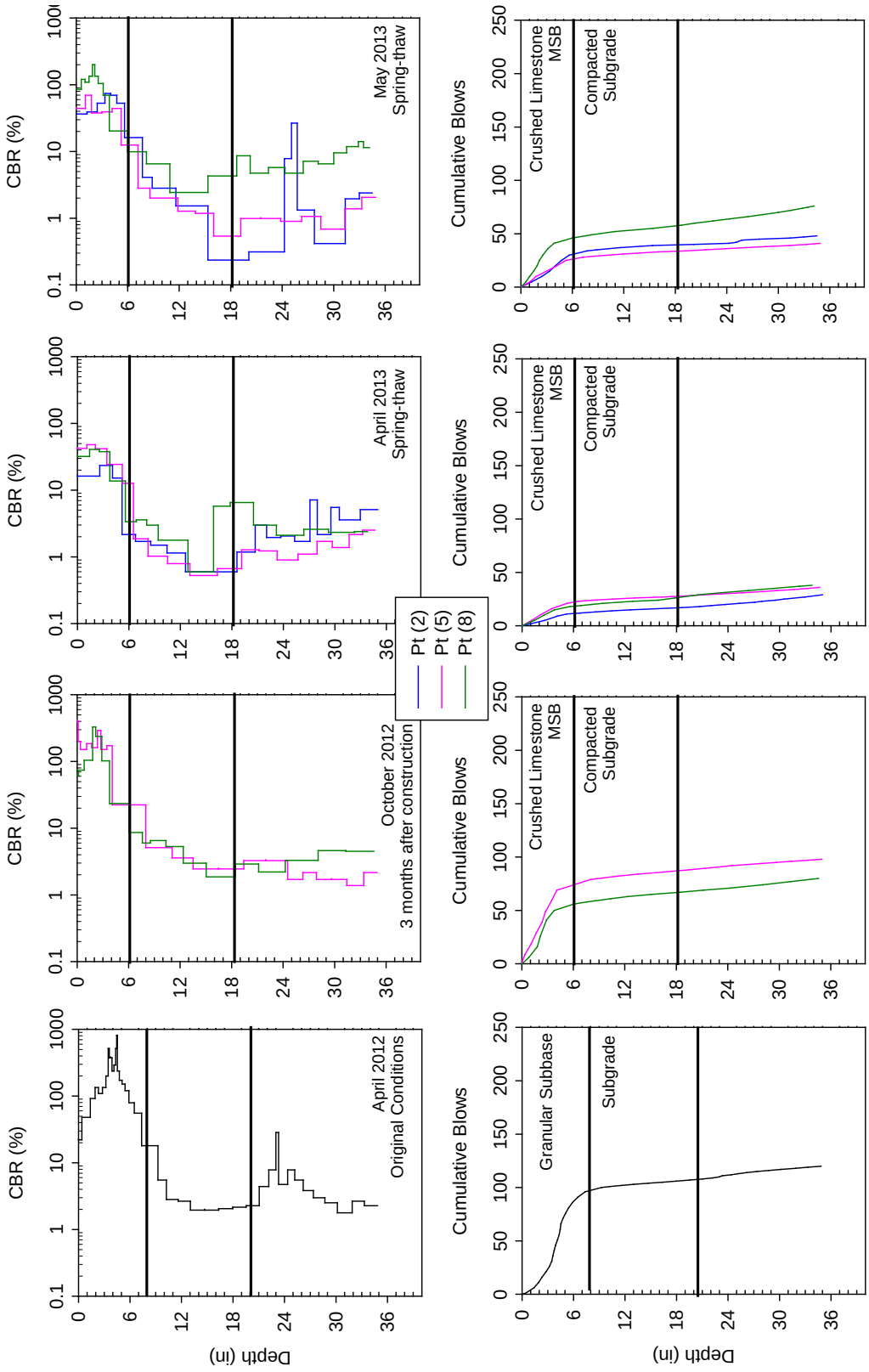

Figure 174. DCP test results from 10th St. North from different testing times

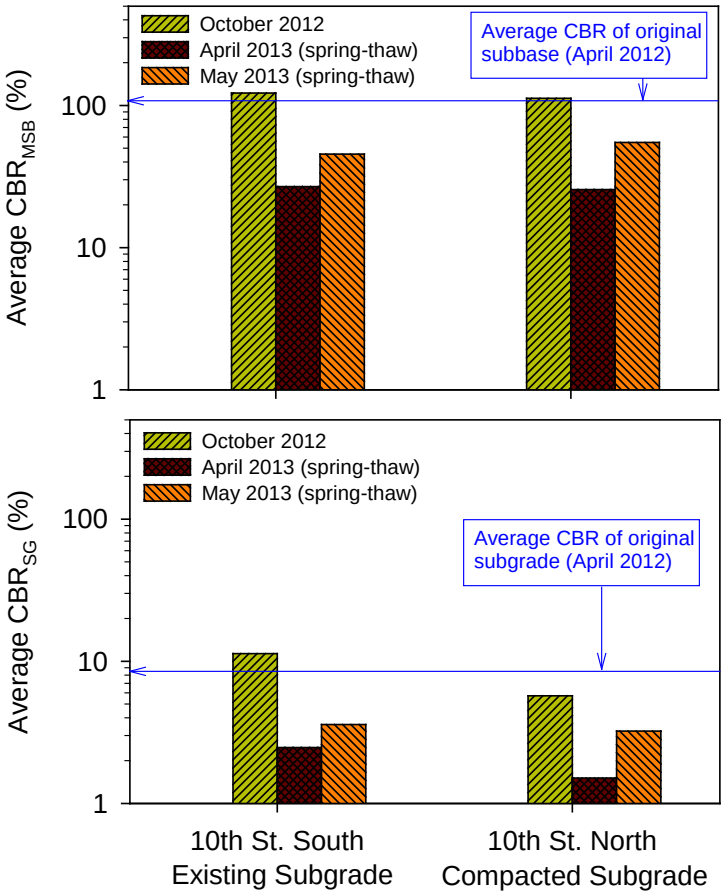

Figure 175. Average CBR (based on 2 to 3 tests) of MSB and subgrade layers on 10th St. South and North

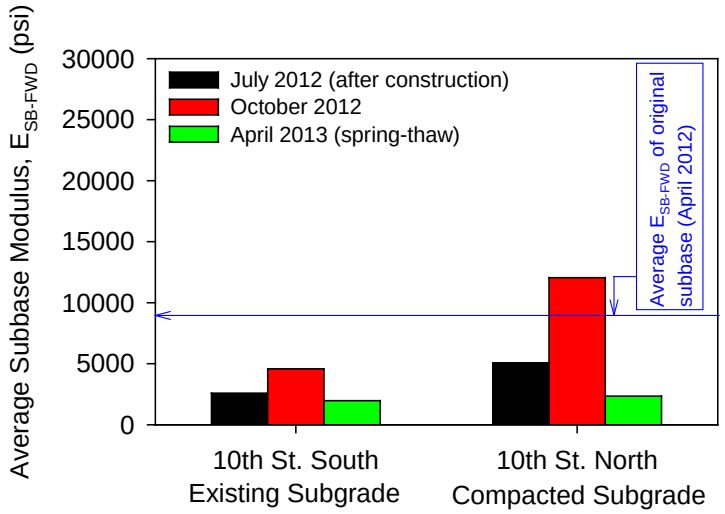

Figure 176. Average FWD subbase modulus (based on 10 tests) on 10th St. South and North sections

11th North: Subgrade + 10% Cement Stabilization

Construction Observations

The pavement foundation profile on 11th St. North is shown in Figure 177. Pictures from construction are shown in Figure 178.

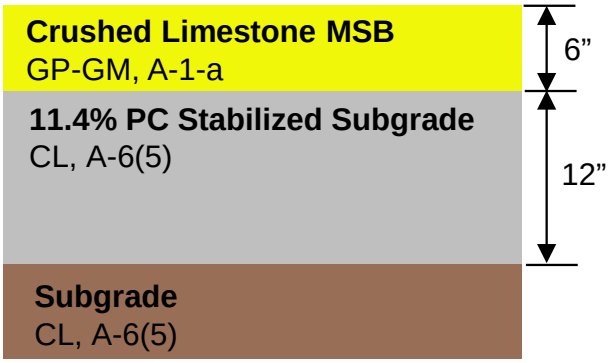

Figure 177. Pavement foundation profile on 11th St. North

(a) (b)

(c) (d)

(e) (f)

Figure 178. Construction operations on 11th St. North: (a) prepared subgrade for treatment, (b) placing PC over subgrade, (c) moisture conditioning and mixing PC with subgrade, (d) compacting stabilized layer with padfoot roller, (e) placing crushed limestone MSB, and (f) compacted MSB layer

As-Constructed Test Results

FWD and LWD testing and RICM mapping was conducted on the crushed limestone MSB layer shortly after construction (July 2012). RICM values (MDP*, CMV, and elevation) along 1st St. on compacted crushed limestone MSB layer are shown in Figure 179. FWD and LWD modulus measurements obtained from 20 test locations along 1st St. are also shown in Figure 179.

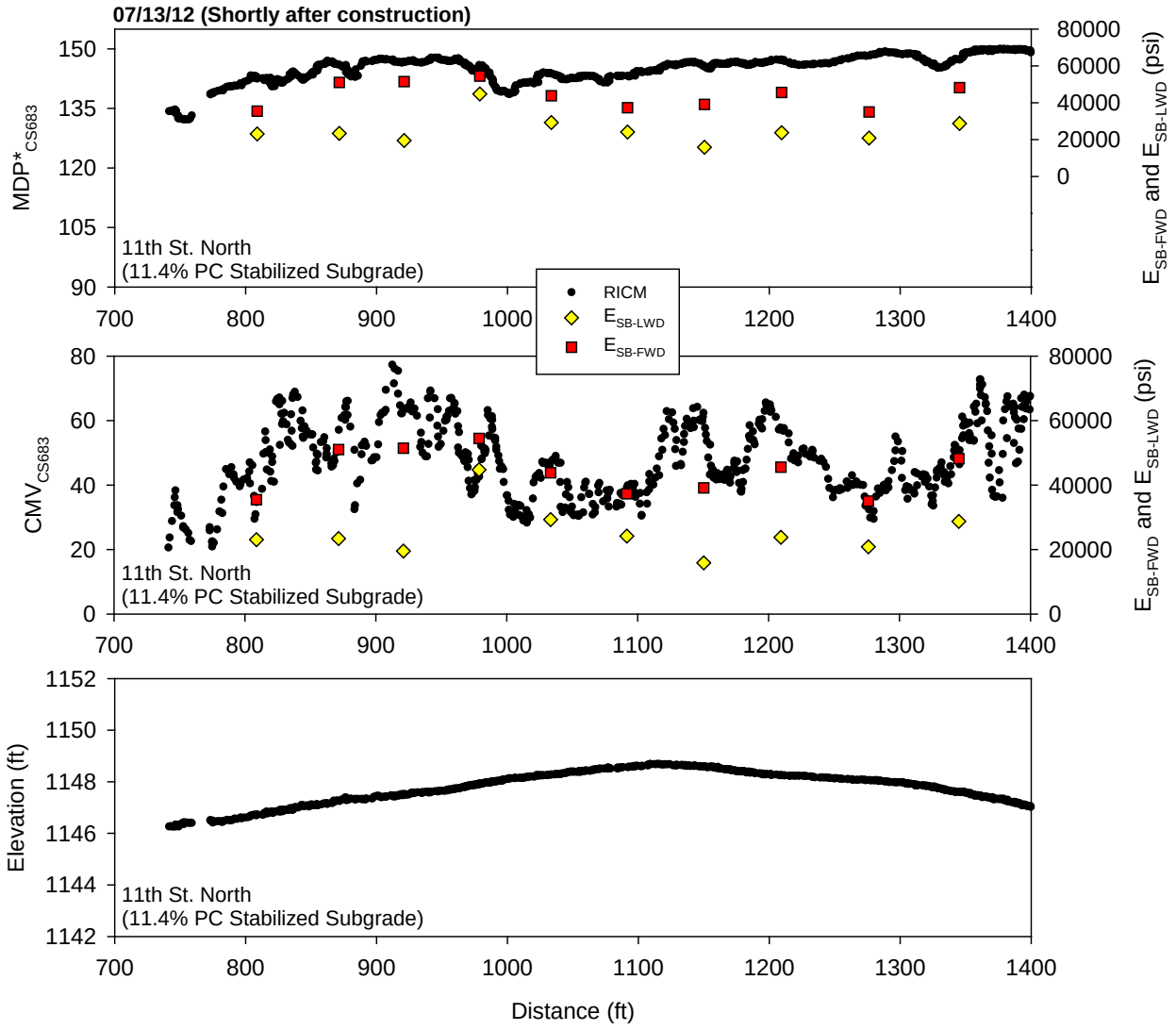

Figure 179. CS683 RICM, LWD, and FWD modulus measurements on 11th St. North shortly after construction (July 2012)

Performance Monitoring Results

CCV results in comparison with $E_{SB\text{-}FWD}$ from October 2012 (about three months after construction) are shown in Figure 180. MDP* and CMV results from the CS683 machine in comparison with $E_{SB\text{-}FWD}$ from April 2013 (during thawing about nine months after construction)

are shown in Figure 181. Similarly, results from the CS74 machine are shown in Figure 182. MDP* and CMV results obtained from the CS683 machine from October 2012 and April 2013 are compared in Figure 183. DCP-CBR and cumulative blows profiles from different testing times are shown in Figure 184 and Figure 185. Average CBR_{MSB} and CBR_{SG} for each test section are shown in Figure 186. Average $E_{SB\text{-}FWD}$ for each test section are shown in Figure 187. CBR_{MSB} and CBR_{SG} showed the lowest values in May 2013, while $E_{SB\text{-}FWD}$ showed the lowest values in April 2013 when the foundation layers were partially thawed at the surface. MDP* and CMV measurements were also lower in April 2013 during thawing than in Ocotber 2012.

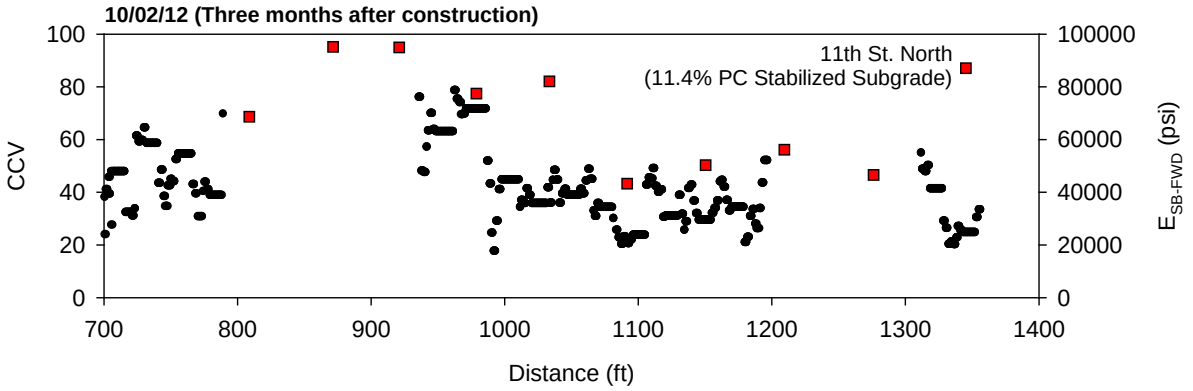

Figure 180. Sakai CCV and FWD modulus measurements on 11th St. North three months after construction (October 2012)

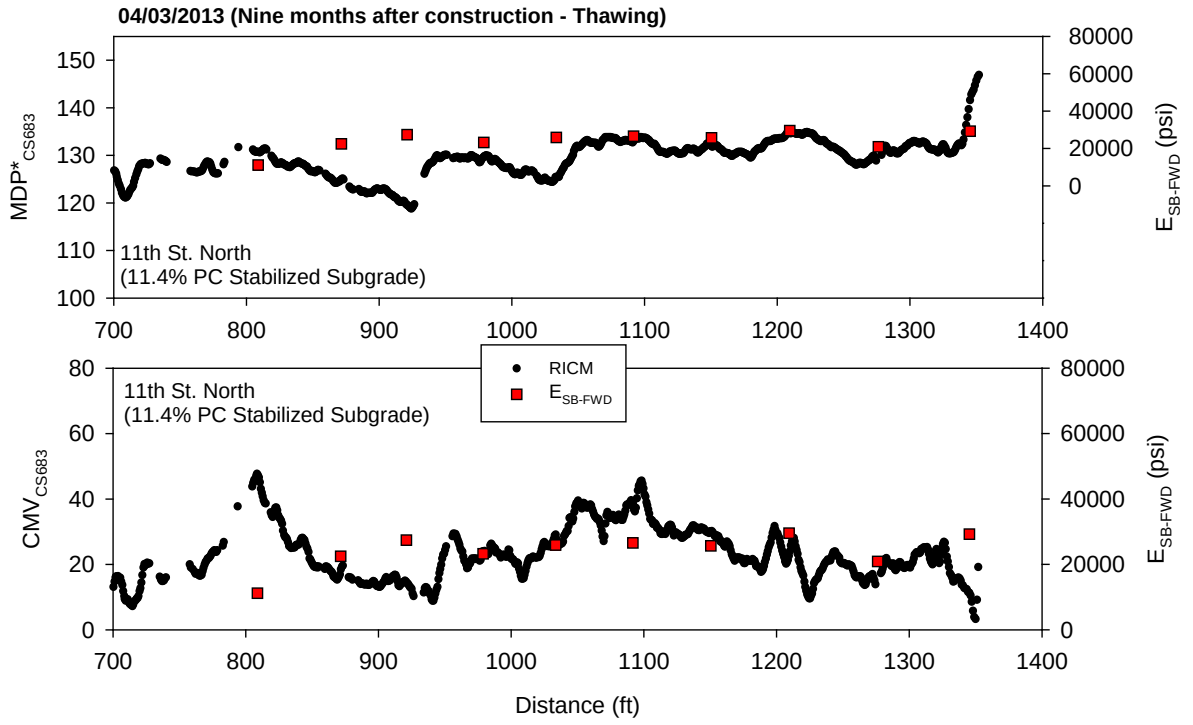

Figure 181. CS683 RICM and FWD modulus measurements on 11th St. North nine months after construction during thawing (April 2013)

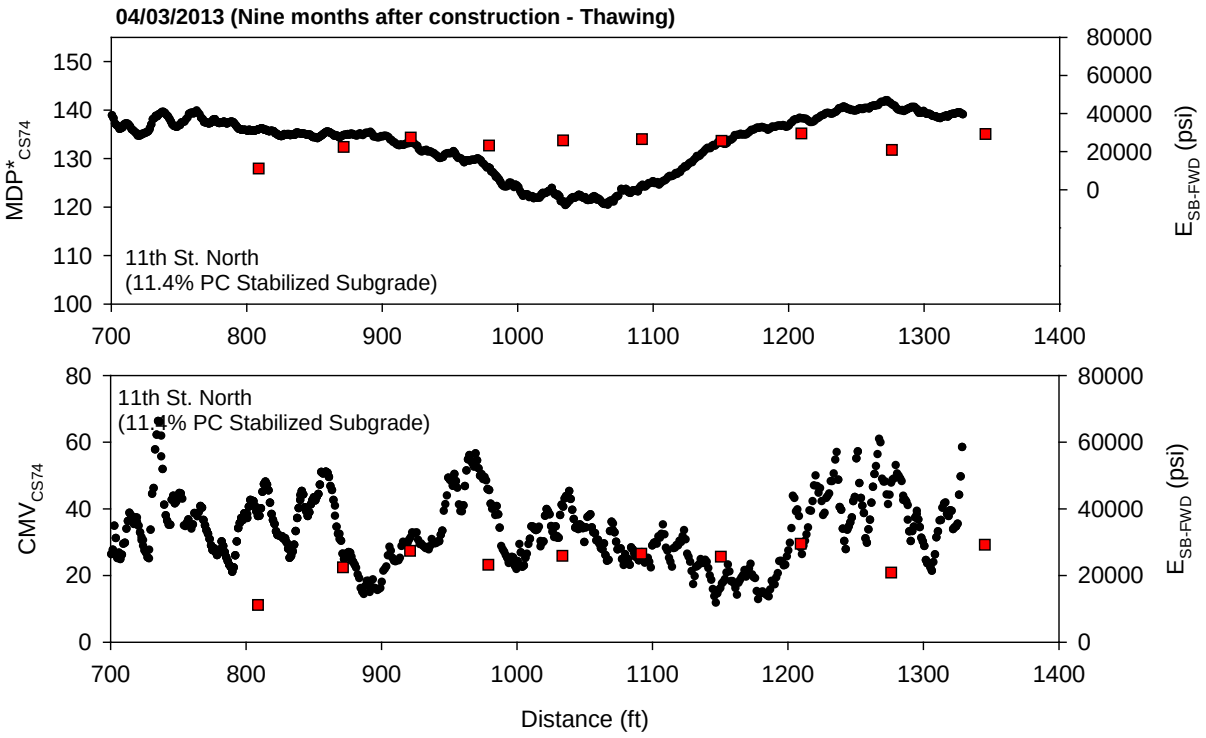

Figure 182. CS74 RICM and FWD modulus measurements on 11th St. North nine months after construction during thawing (April 2013)

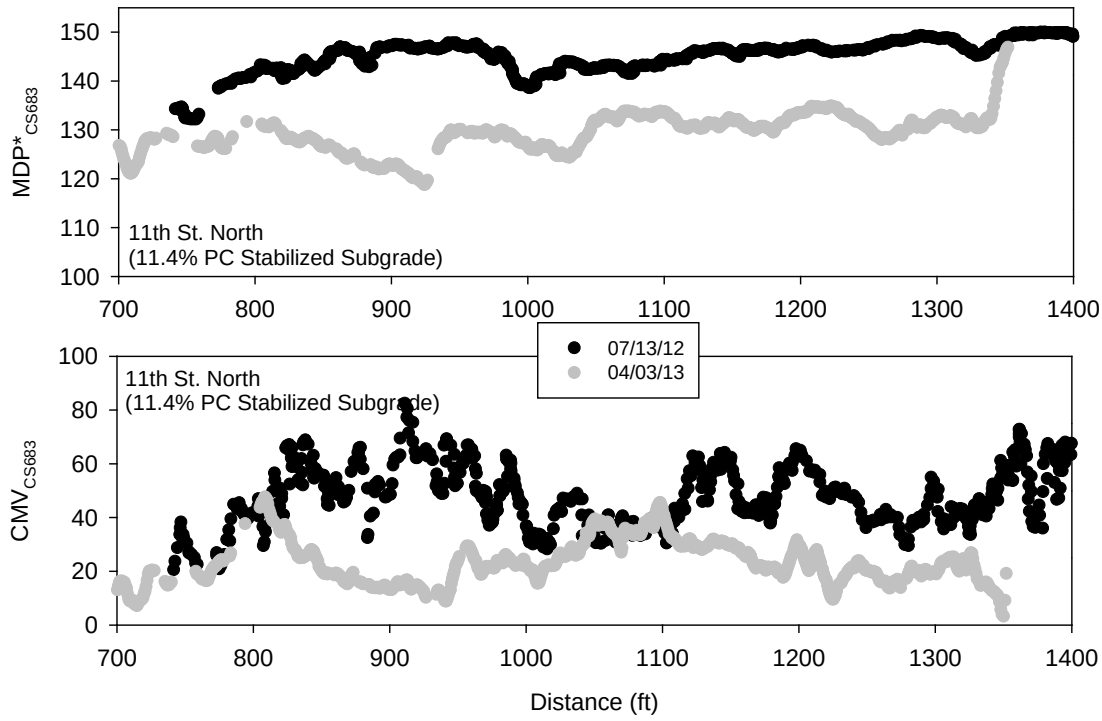

Figure 183. Comparison between CS683 RICM measurements on 11th St. North shortly after construction and nine months after construction during thawing

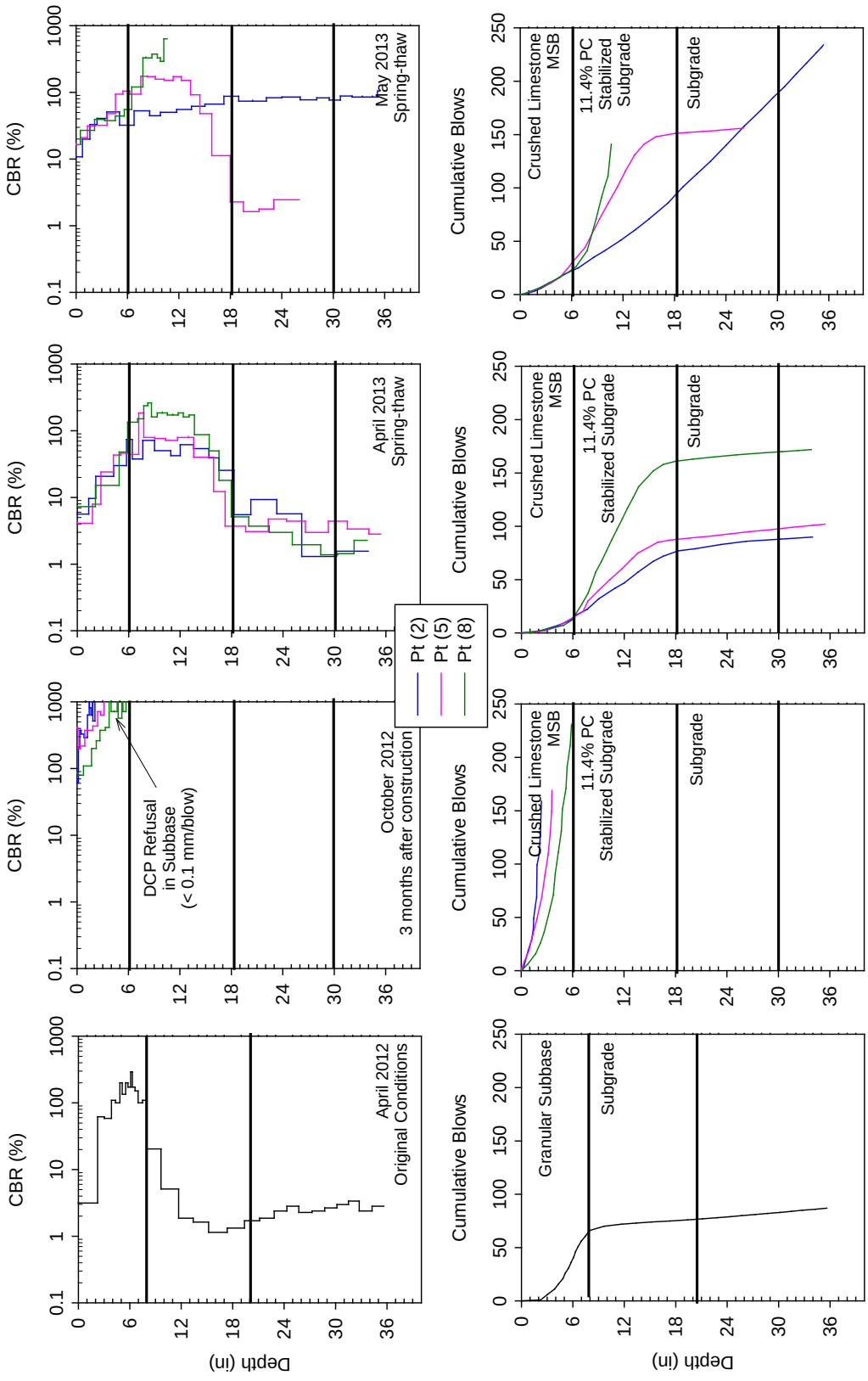

Figure 184. DCP test results from 11th St. North from different testing times

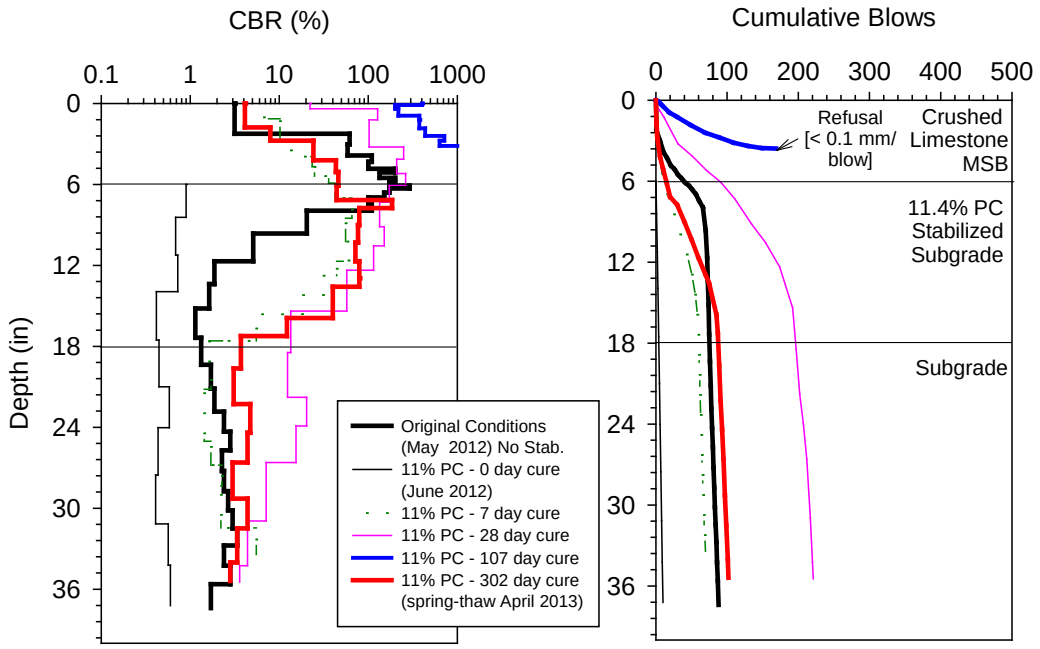

Figure 185. DCP test results at different times of curing at a selected test location on 11th St. North

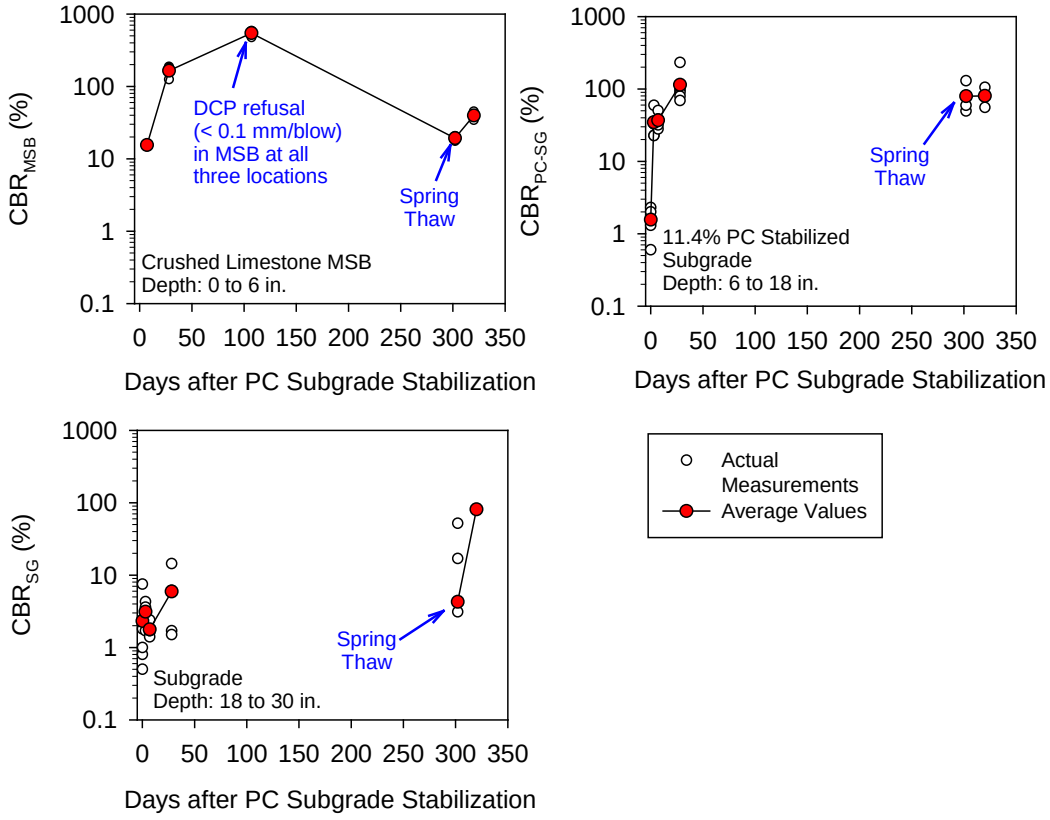

Figure 186. CBR mesaurements in MSB, stabilized subgrade, and unstabilized subgrade layers on 11th St. North

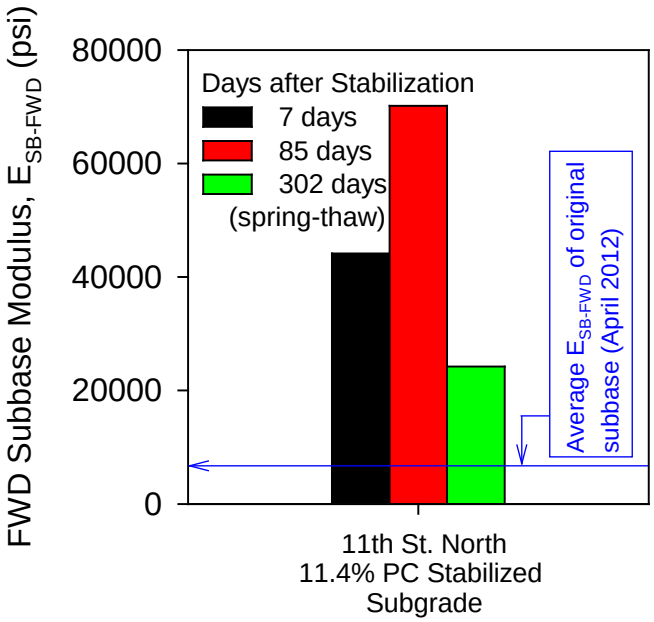

Figure 187. Average FWD subbase modulus (based on 10 tests) on 11th St. North

11th South: Subgrade + 20% Class-C Fly Ash

Construction Observations

The pavement foundation profile on 11th St. South is shown in Figure 188. Pictures from construction are shown in Figure 189.

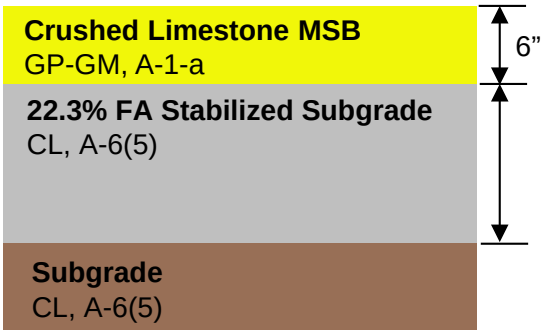

Figure 188. Pavement foundation profile on 11th St. South

(a) (b)

(c) (d)

(e) (f)

Figure 189. Construction operations on 11th St. South: (a) excavating existing subbase down to subgrade layer for treatment, (b) placing FA over subgrade, (c) and (d) moisture conditioning and mixing FA with subgrade, (e) placing crushed limestone MSB, and (f) compacted MSB layer

As-Constructed Test Results

FWD and LWD testing and RICM mapping was conducted on the crushed limestone MSB layer shortly after construction (July 2012). RICM values (MDP*, CMV, and elevation) along 1st St. on compacted crushed limestone MSB layer are shown in Figure 190. FWD and LWD modulus measurements obtained from 20 test locations along 1st St. are also shown in Figure 190.

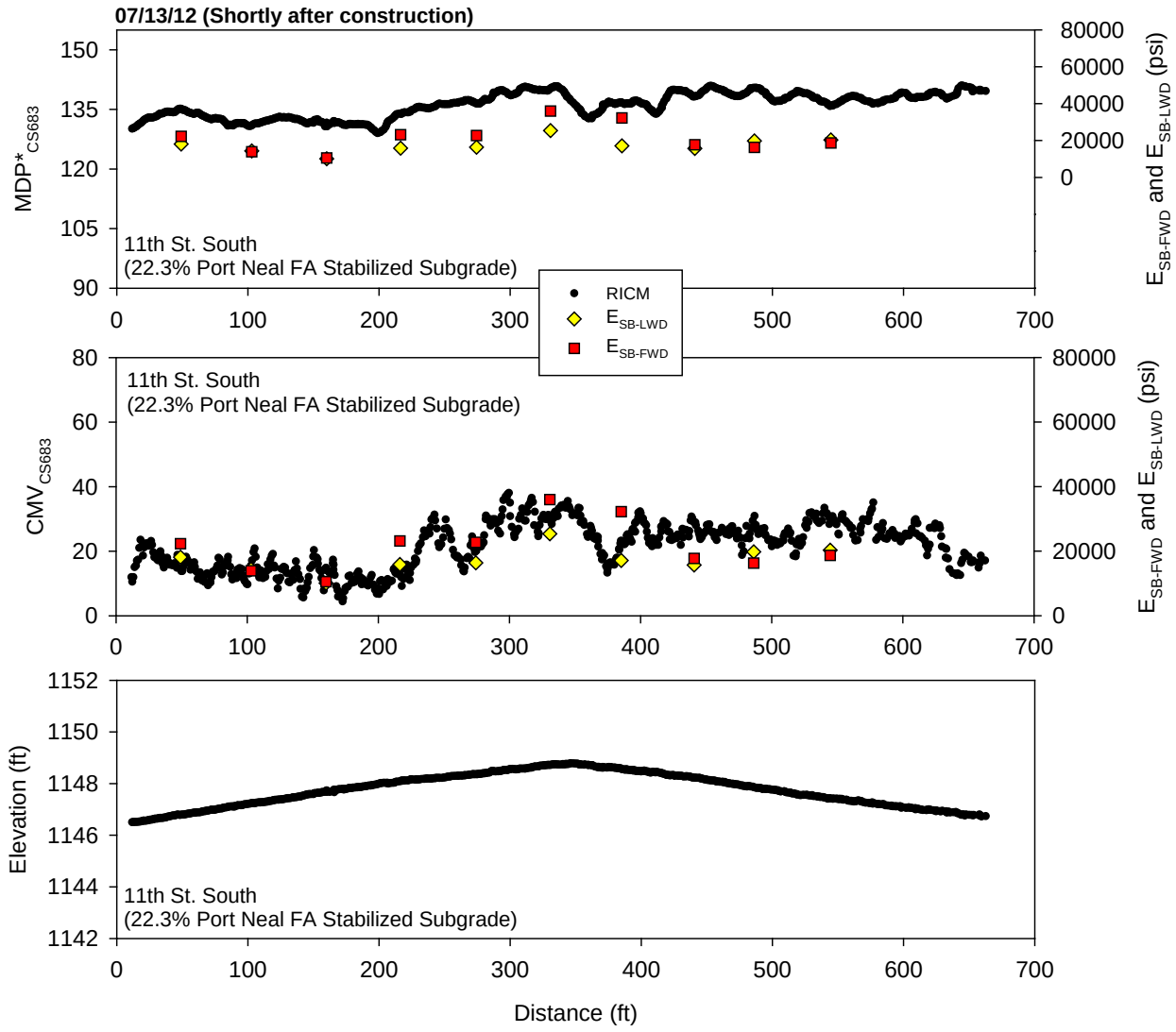

Figure 190. CS683 RICM, LWD, and FWD modulus measurements on 11th St. South shortly after construction (July 2012)

Performance Monitoring Results

CCV results in comparison with $E_{SB\text{-}FWD}$ from October 2012 (about three months after construction) are shown in Figure 191. MDP* and CMV results from the CS683 machine in comparison with $E_{SB\text{-}FWD}$ from April 2013 (during thawing about nine months after construction)

are shown in Figure 192. Similarly, results from the CS74 machine are shown in Figure 193. MDP* and CMV results obtained from the CS683 machine from October 2012 and April 2013 are compared in Figure 194. DCP-CBR and cumulative blows profiles from different testing times are shown in Figure 195 and Figure 196. Average CBR_{MSB} and CBR_{SG} for each test section are shown in Figure 197. Average $E_{SB\text{-}FWD}$ for each test section are shown in Figure 198. CBR_{MSB} and CBR_{SG} showed the lowest values in May 2013, while $E_{SB\text{-}FWD}$ showed the lowest values in April 2013 when the foundation layers were partially thawed at the surface. MDP* and CMV measurements were also lower in April 2013 during thawing than in Ocotber 2012.

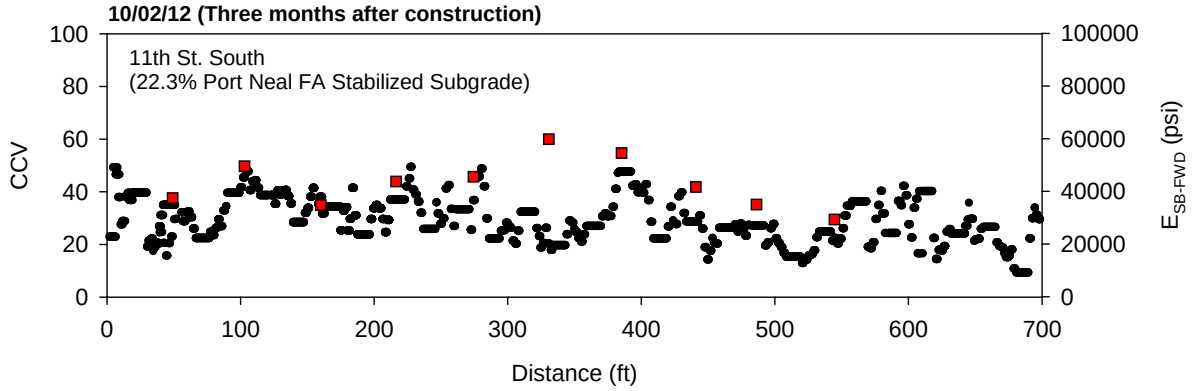

Figure 191. Sakai CCV and FWD modulus measurements on 11th St. South three months after construction (October 2012)

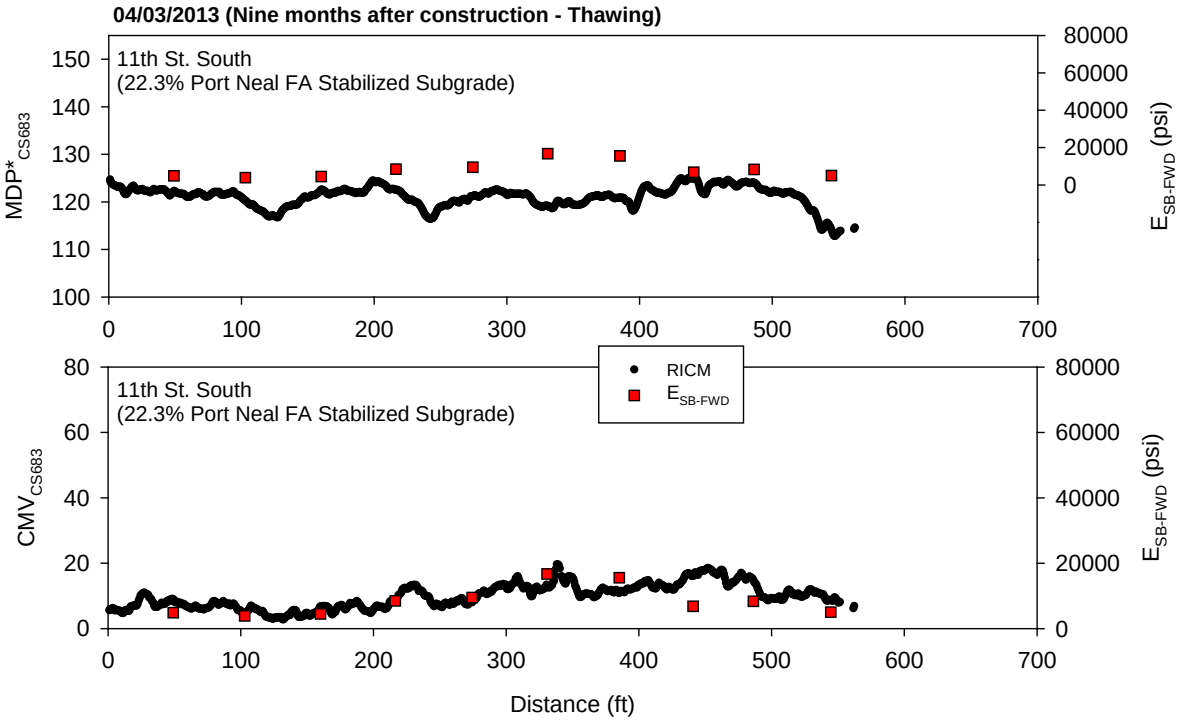

Figure 192. CS683 RICM and FWD modulus measurements on 11th St. South nine months after construction during thawing (April 2013)

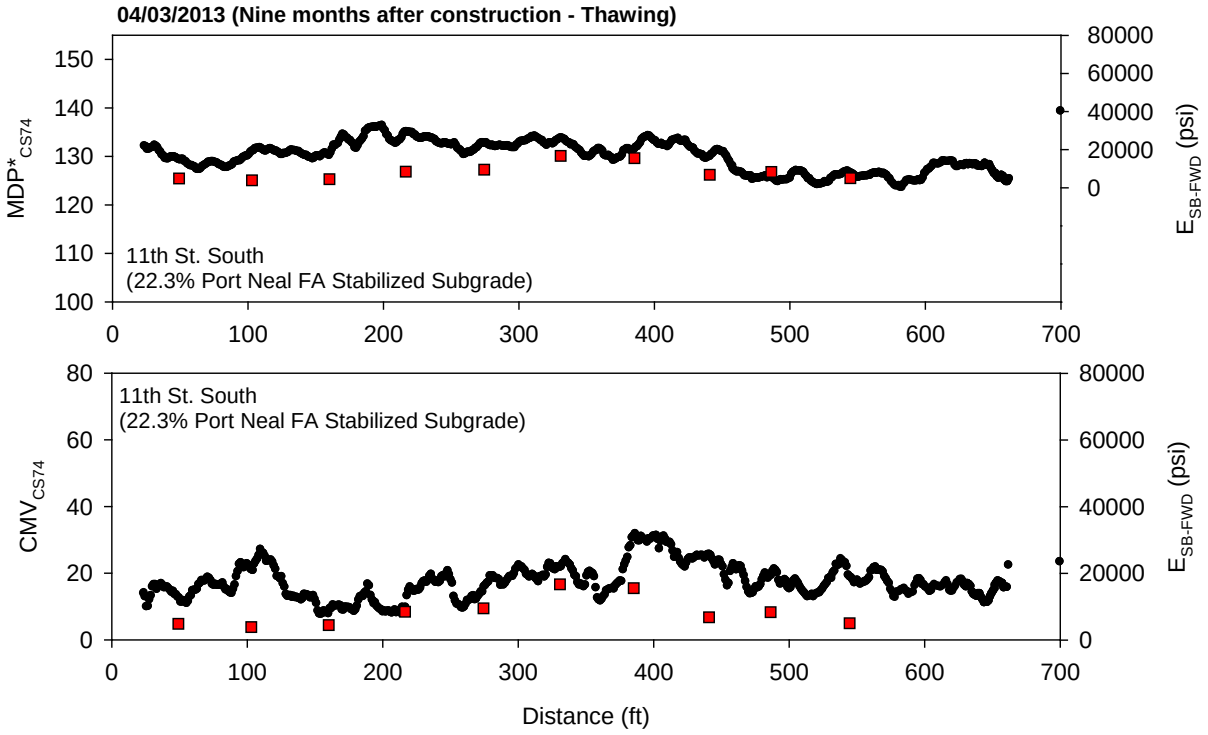

Figure 193. CS74 RICM and FWD modulus measurements on 11th St. South nine months after construction during thawing (April 2013)

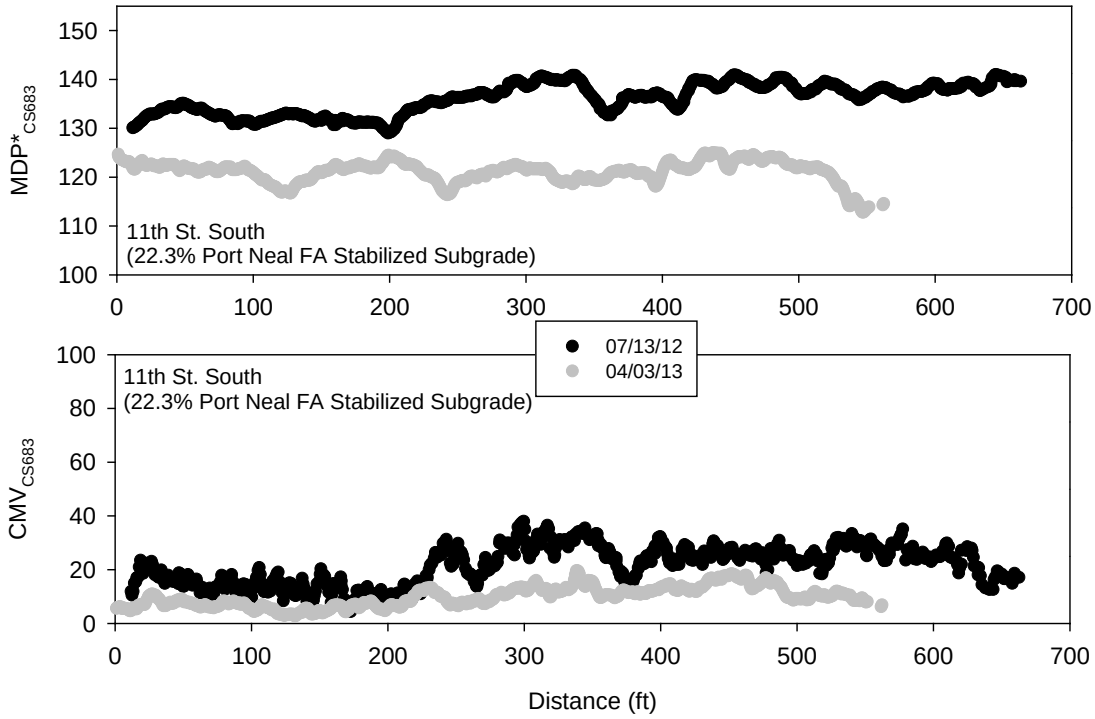

Figure 194. Comparison between CS683 RICM measurements on 11th St. South shortly after construction and nine months after construction during thawing

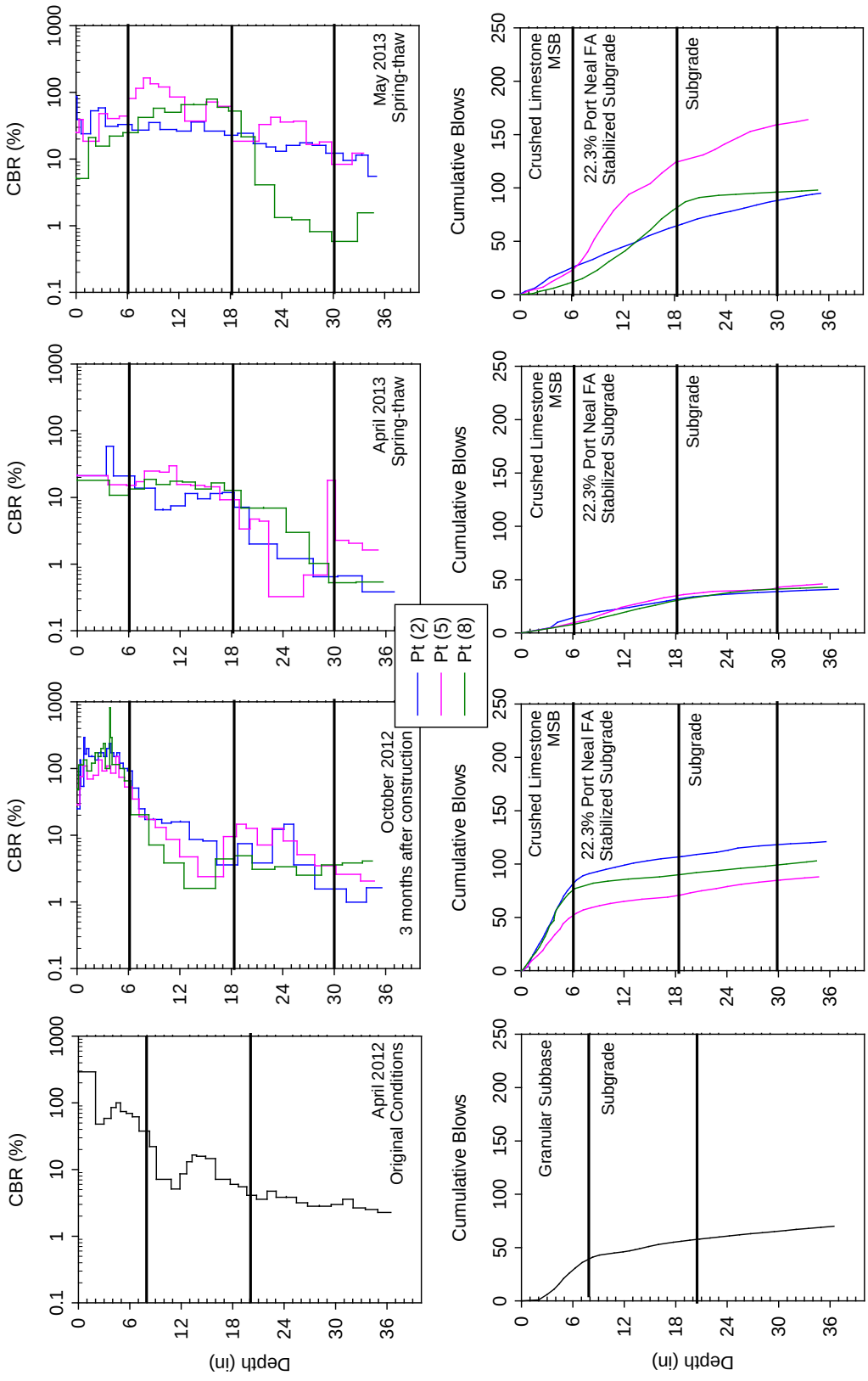

Figure 195. DCP test results from 11th St. South from different testing times

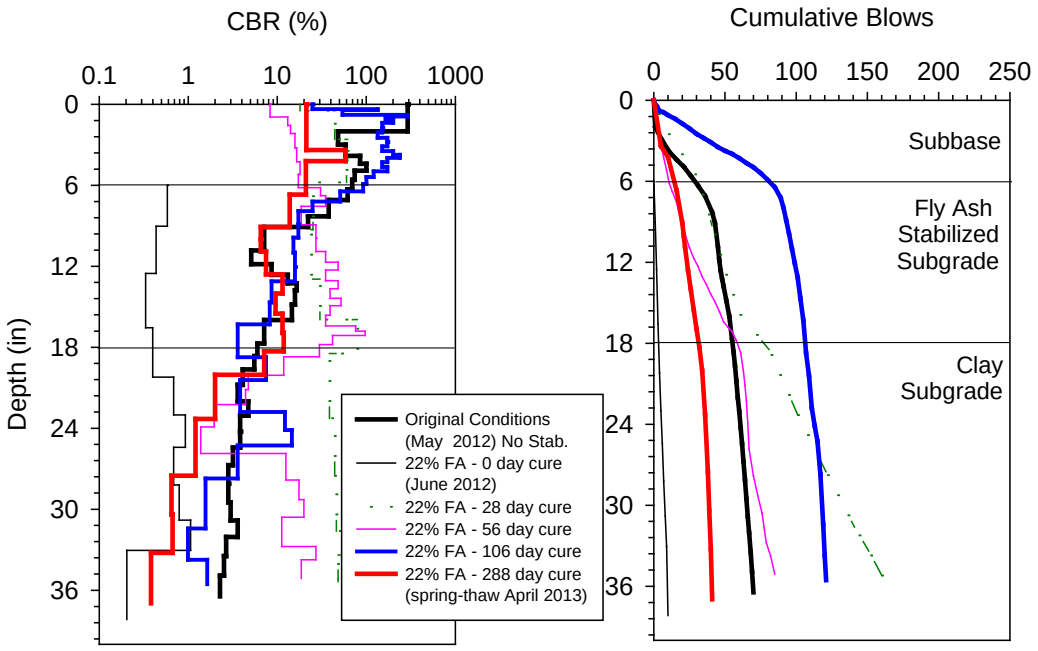

Figure 196. DCP test results at different times of curing at a selected test location on 11th St. South

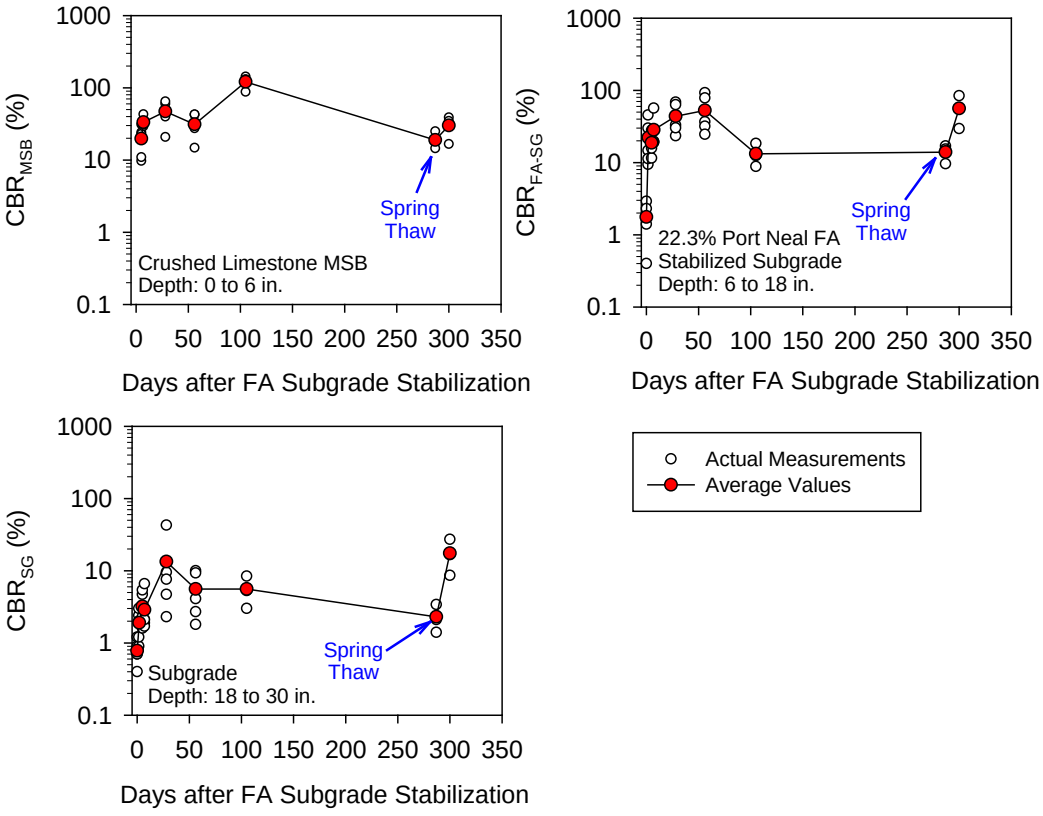

Figure 197. CBR mesaurements in MSB, stabilized subgrade, and unstabilized subgrade layers on 11th St. South

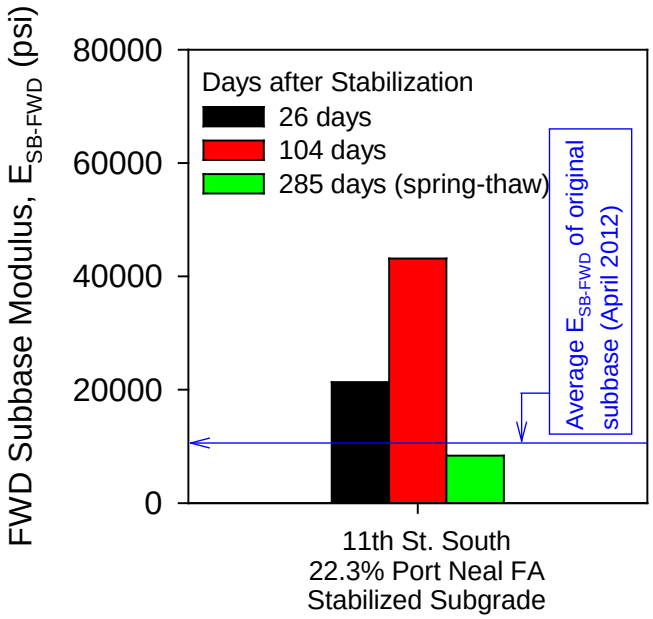

Figure 198. Average FWD subbase modulus (based on 10 tests) on 11th St. South

12th North: Subgrade + 15% Class-C Fly Ash

Construction Observations

The pavement foundation profile on 12th St. North is shown in Figure 199. Pictures from construction are shown in Figure 200.

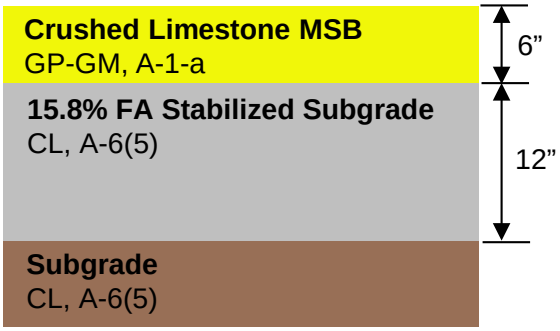

Figure 199. Pavement foundation profile on 12th St. North

(a) (b)

(c) (d)

(e)

Figure 200. Construction operations on 11th St. South: (a) prepared subgrade prior to treatment, (b) placing FA over subgrade, (c) moisture conditioning and mixing FA with subgrade, (d) compacting FA treated subgrade with padfoot roller, and (f) compacted MSB layer over FA treated subgrade

As-Constructed Test Results

FWD and LWD testing and RICM mapping was conducted on the crushed limestone MSB layer shortly after construction (July 2012). RICM values (MDP*, CMV, and elevation) along 1st St. on compacted crushed limestone MSB layer are shown in Figure 201. FWD and LWD modulus measurements obtained from 20 test locations along 1st St. are also shown in Figure 202.

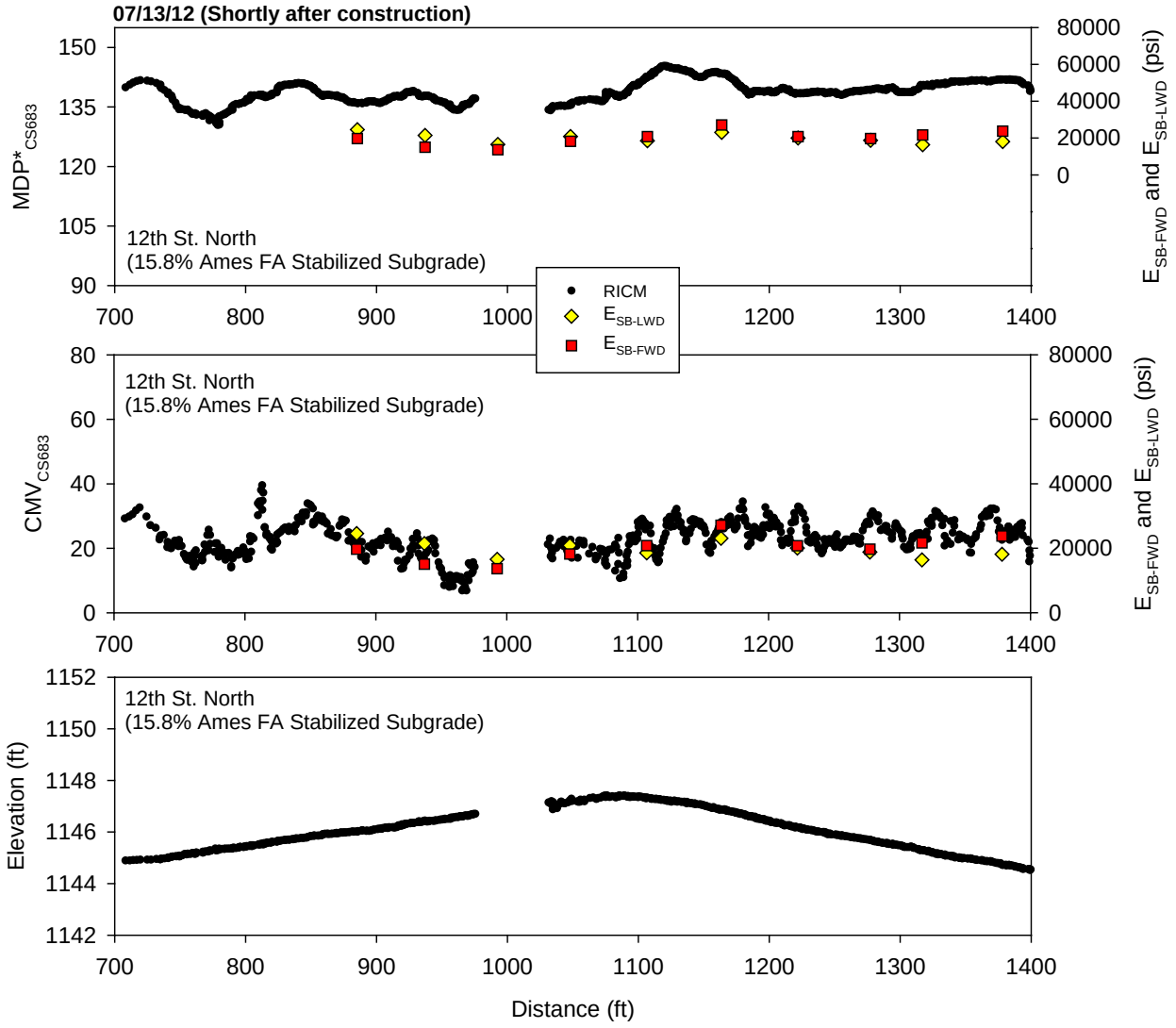

Figure 201. CS683 RICM, LWD, and FWD modulus measurements on 11th St. South shortly after construction (July 2012)

Performance Monitoring Results

CCV results in comparison with $E_{SB\text{-}FWD}$ from October 2012 (about three months after construction) are shown in Figure 202. MDP* and CMV results from the CS683 machine in comparison with $E_{SB\text{-}FWD}$ from April 2013 (during thawing about nine months after construction)

are shown in Figure 203. Similarly, results from the CS74 machine are shown in Figure 204. MDP* and CMV results obtained from the CS683 machine from October 2012 and April 2013 are compared in Figure 205. DCP-CBR and cumulative blows profiles from different testing times are shown in Figure 206 and Figure 207. Average CBR_{MSB} and CBR_{SG} for each test section are shown in Figure 208. Average $E_{SB\text{-}FWD}$ for each test section are shown in Figure 209. CBR_{MSB} and CBR_{SG} showed the lowest values in May 2013, while $E_{SB\text{-}FWD}$ showed the lowest values in April 2013 when the foundation layers were partially thawed at the surface. MDP* and CMV measurements were also lower in April 2013 during thawing than in Ocotber 2012.

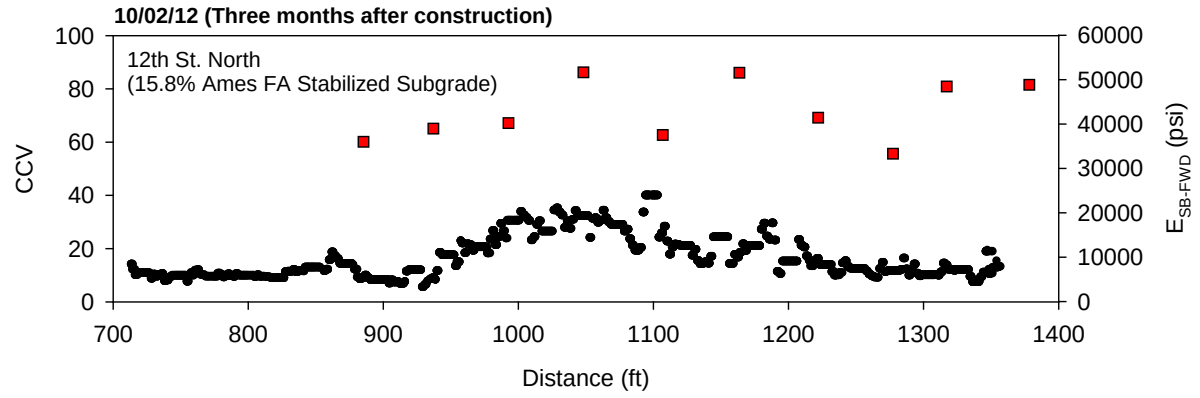

Figure 202. Sakai CCV and FWD modulus measurements on 11th St. South three months after construction (October 2012)

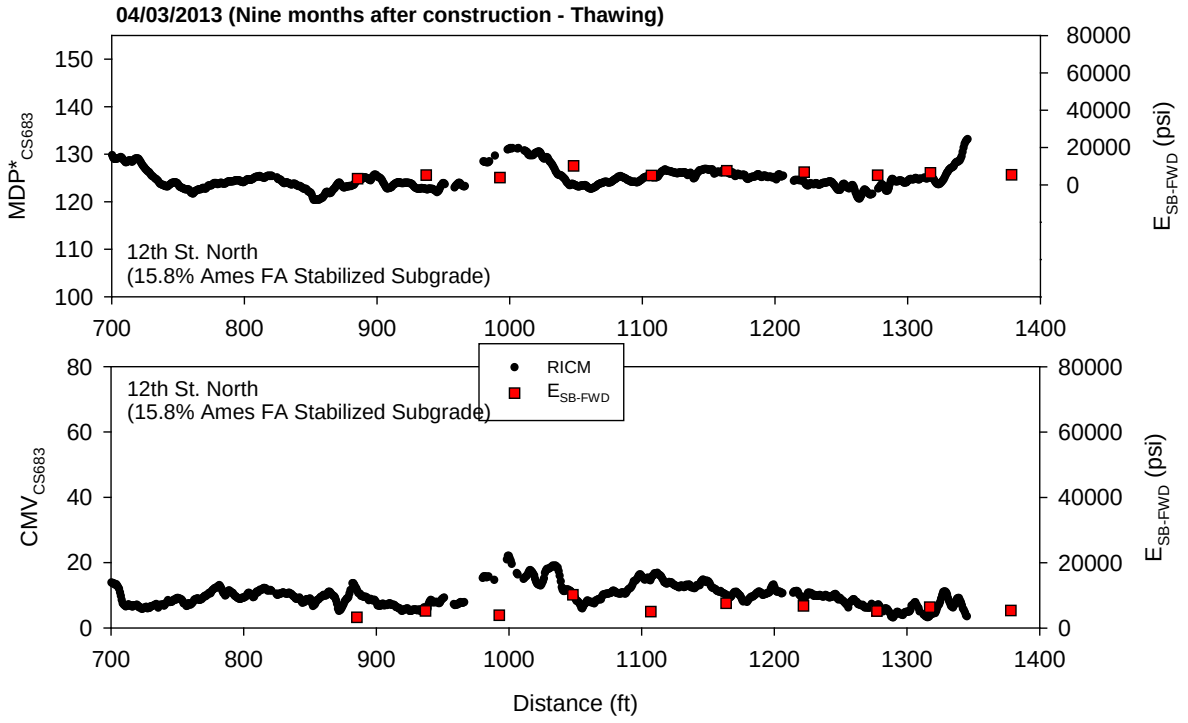

Figure 203. CS683 RICM and FWD modulus measurements on 12th St. North nine months after construction during thawing (April 2013)

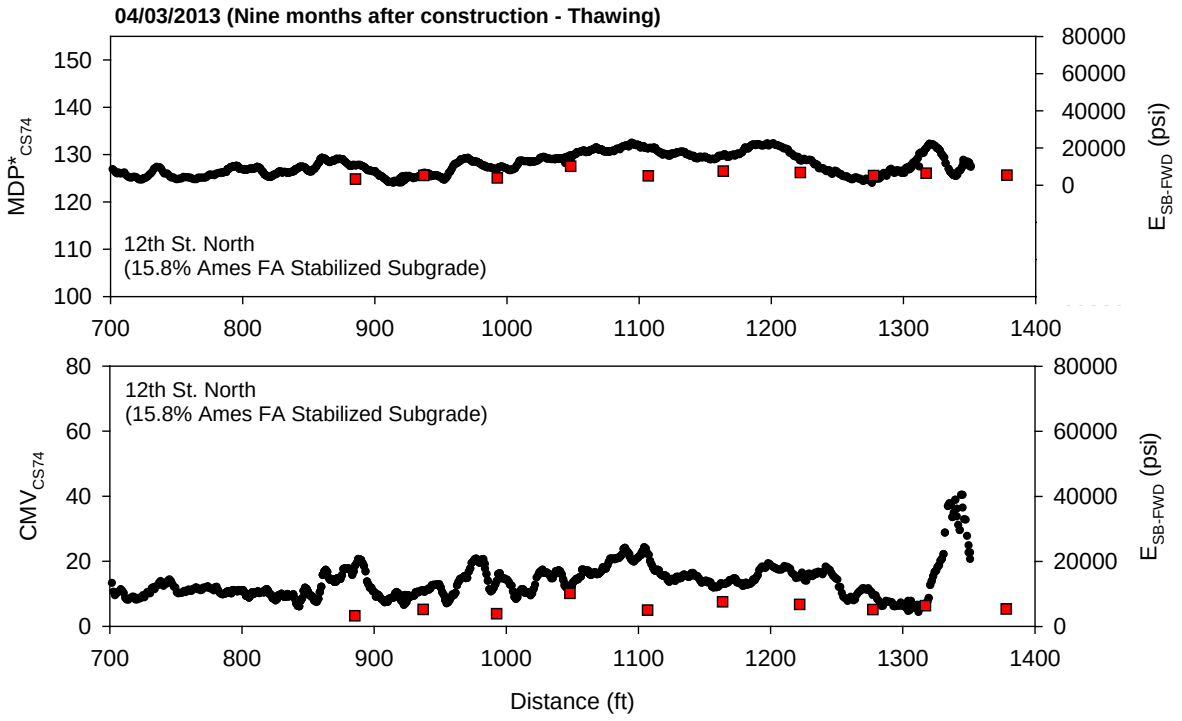

Figure 204. CS74 RICM and FWD modulus measurements on 12th St. North nine months after construction during thawing (April 2013)

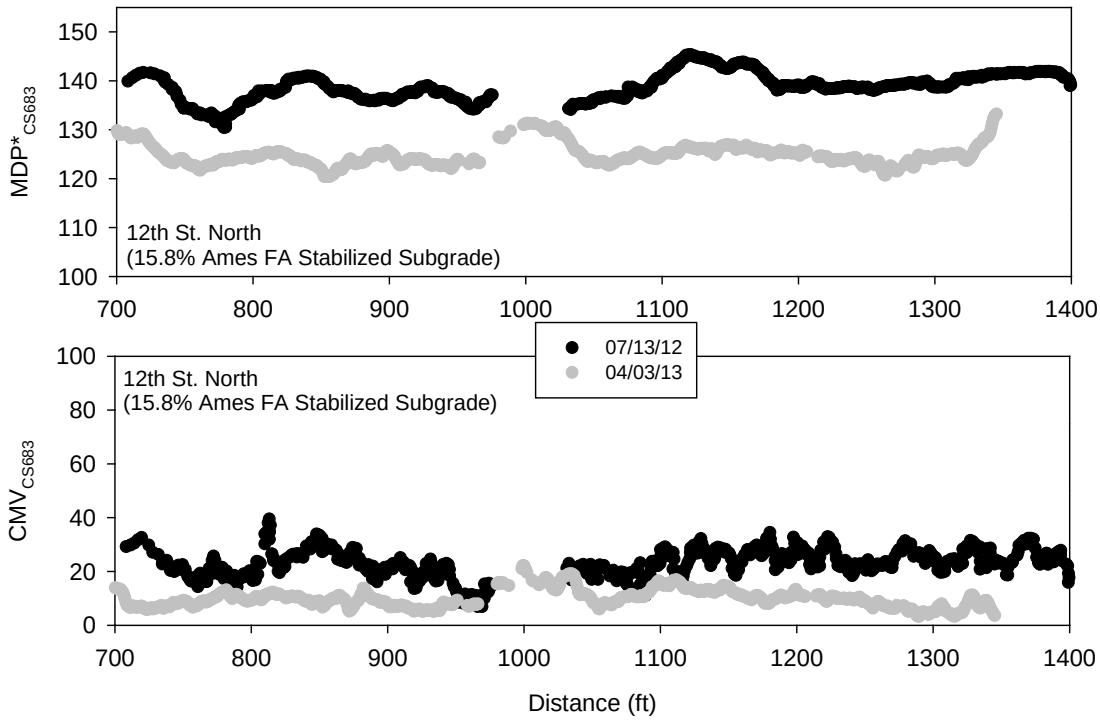

Figure 205. Comparison between CS683 RICM measurements on 12th St. North shortly after construction and nine months after construction during thawing

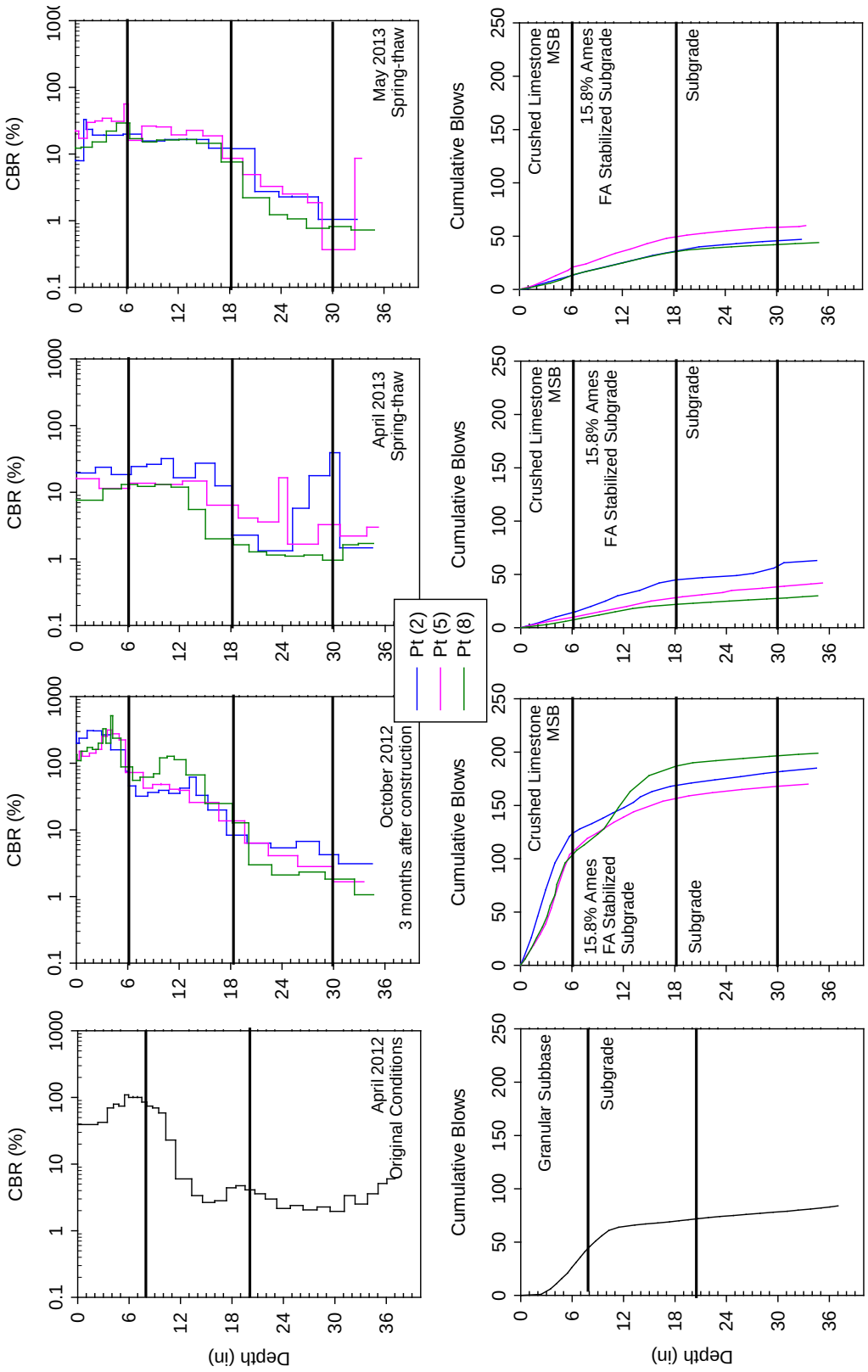

Figure 206. DCP test results from 12th St. North from different testing times

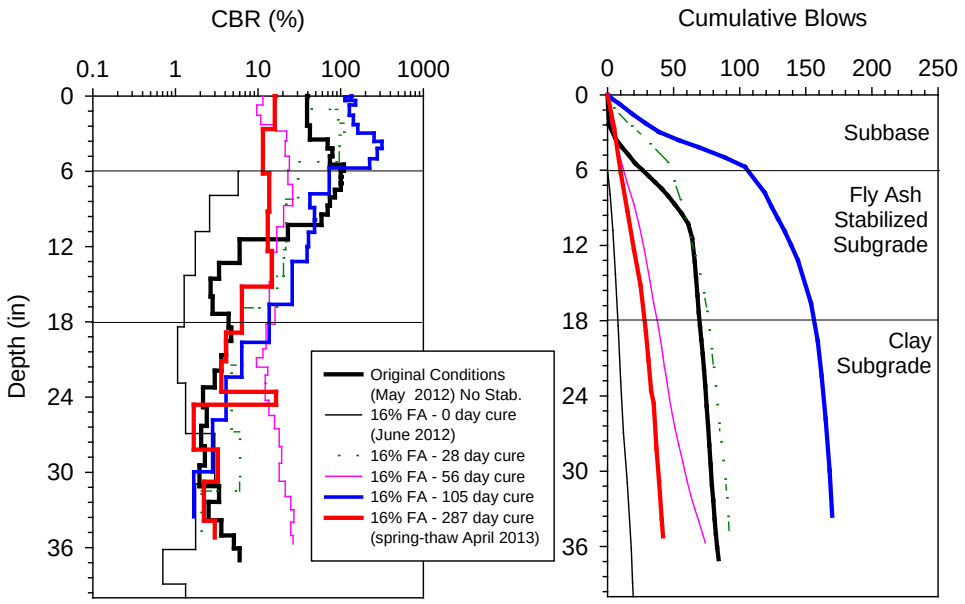

Figure 207. DCP test results at different times of curing at a selected test location on 12th St. North

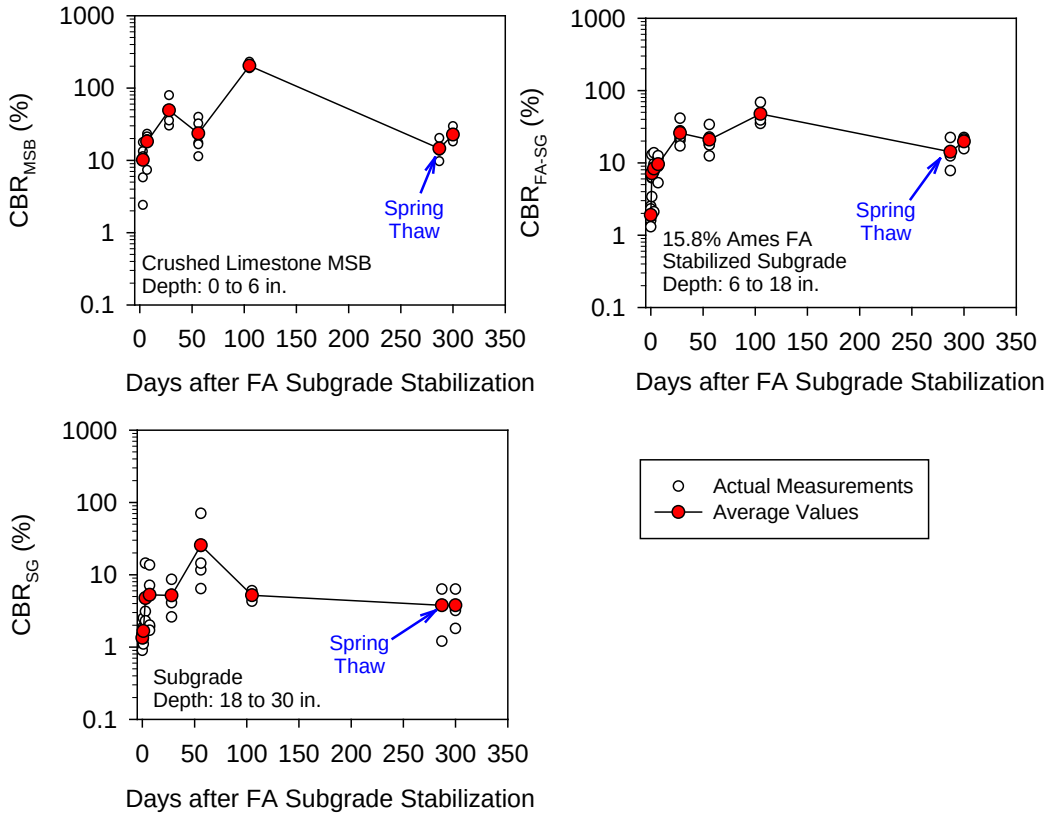

Figure 208. CBR measurements in MSB, stabilized subgrade, and unstabilized subgrade layers on 12th St. North

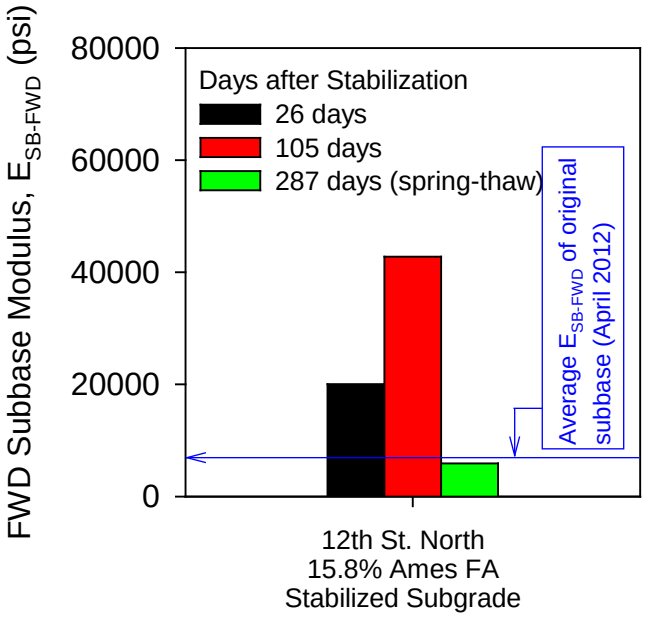

Figure 209. Average FWD subbase modulus (based on 10 tests) on 12th St. North

12th South: Subgrade + 10% Class-C Fly Ash

Construction Observations

The pavement foundation profile on 12th St. South is shown in Figure 210. Pictures from construction are shown in Figure 211.

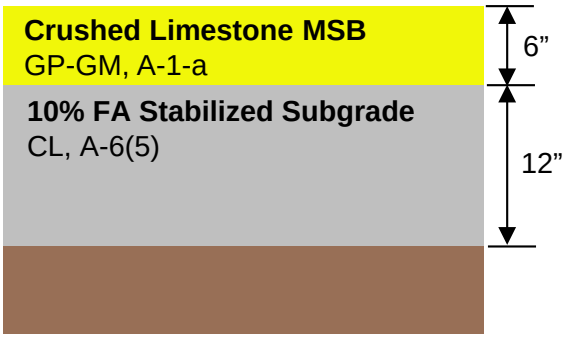

Figure 210. Pavement foundation profile on 12th St. South

(a) (b)

(c) (d)

(e)

Figure 211. Construction operations on 12th St. South: (a) prepared subgrade prior to treatment, (b) placing FA over subgrade, (c) moisture conditioning and mixing FA with subgrade and compacting with padfoot roller, (d) placing crushed limestone MSB layer over FA treated subgrade, and (f) compacted MSB layer

As-Constructed Test Results

FWD and LWD testing and RICM mapping was conducted on the crushed limestone MSB layer shortly after construction (July 2012). RICM values (MDP*, CMV, and elevation) along 1st St. on compacted crushed limestone MSB layer are shown in Figure 212. FWD and LWD modulus measurements obtained from 20 test locations along 1st St. are also shown in Figure 212.

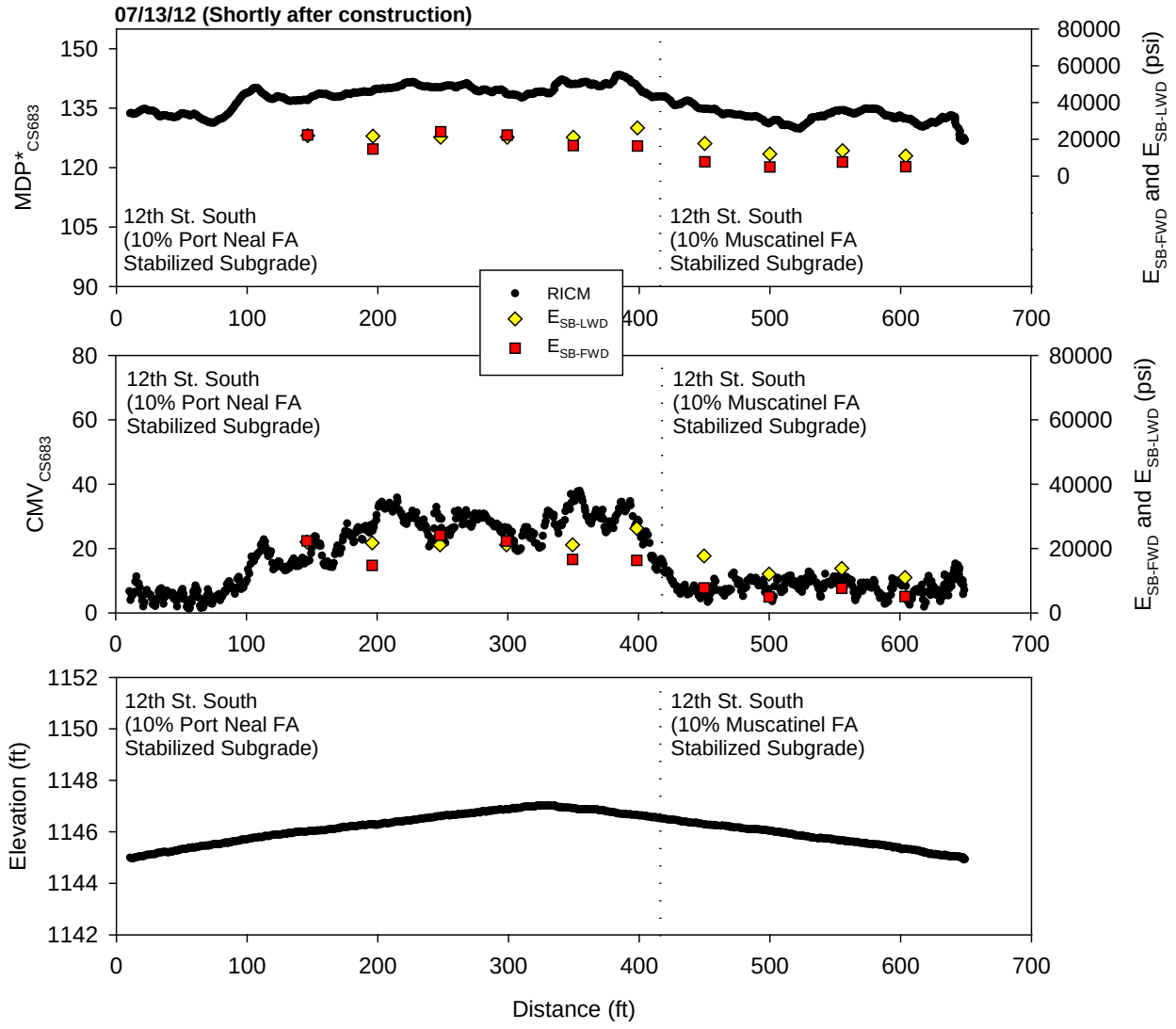

Figure 212. CS683 RICM, LWD, and FWD modulus measurements on 11th St. South shortly after construction (July 2012)

Performance Monitoring Results

CCV results in comparison with $E_{SB\text{-}FWD}$ from October 2012 (about three months after construction) are shown in Figure 212. MDP* and CMV results from the CS683 machine in comparison with $E_{SB\text{-}FWD}$ from April 2013 (during thawing about nine months after construction)

are shown in Figure 213. Similarly, results from the CS74 machine are shown in Figure **214**. MDP* and CMV results obtained from the CS683 machine from October 2012 and April 2013 are compared in Figure 215. DCP-CBR and cumulative blows profiles from different testing times are shown in Figure 217 and Figure 218. Average CBR_{MSB} and CBR_{SG} for each test section are shown in Figure 219. Average $E_{SB\text{-}FWD}$ for each test section are shown in Figure 220. CBR_{MSB} and CBR_{SG} showed the lowest values in May 2013, while $E_{SB\text{-}FWD}$ showed the lowest values in April 2013 when the foundation layers were partially thawed at the surface. MDP* and CMV measurements were also lower in April 2013 during thawing than in Ocotber 2012.

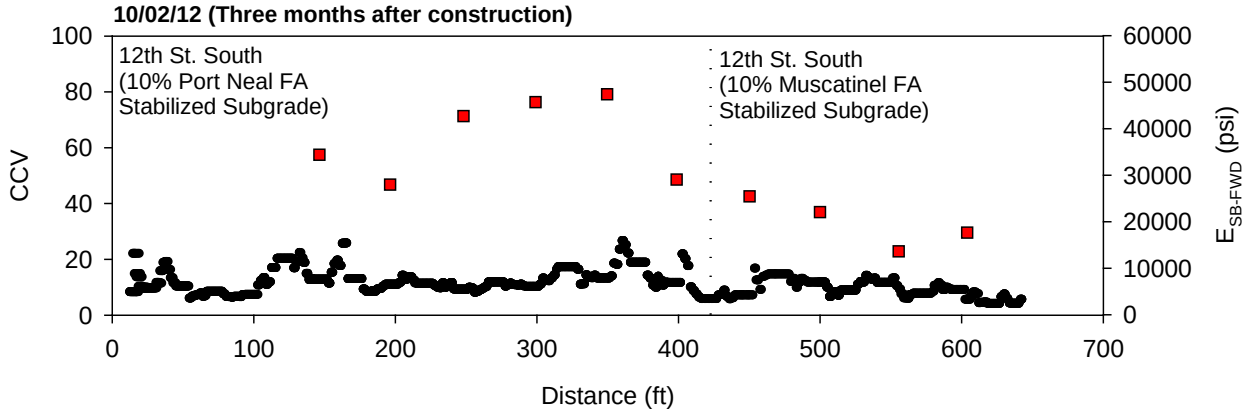

Figure 213. Sakai CCV and FWD modulus measurements on 11th St. South three months after construction (October 2012)

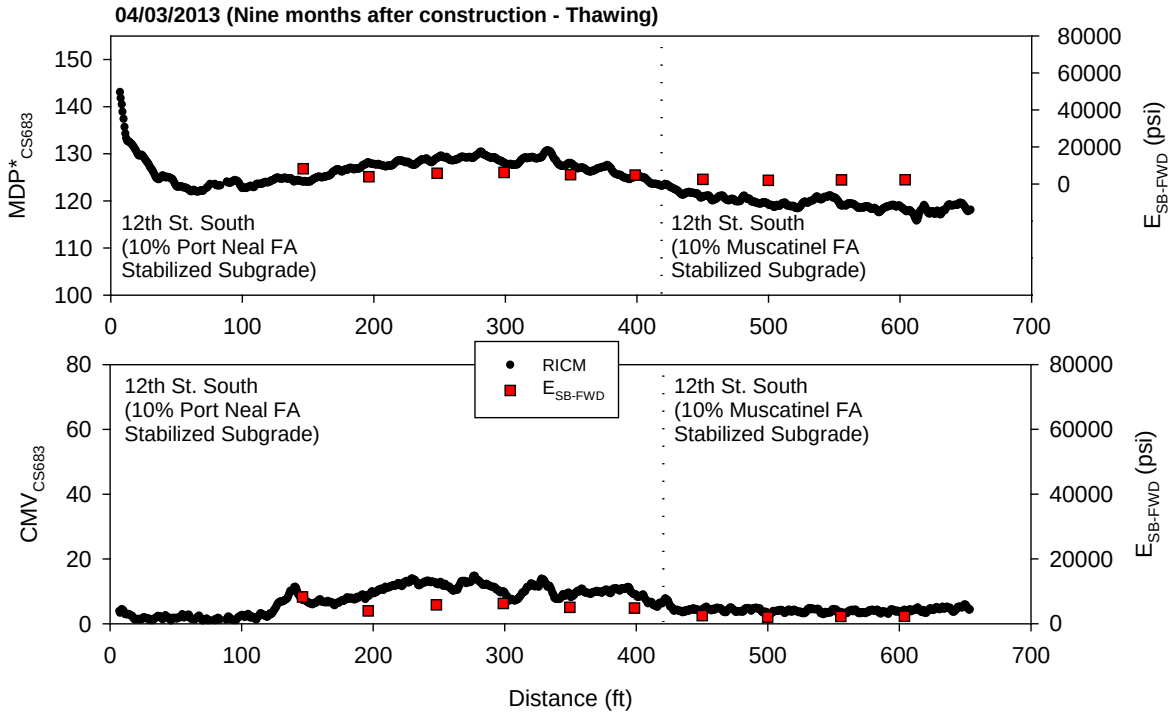

Figure 214**. CS683 RICM and FWD modulus measurements on 12th St. North nine months after construction during thawing (April 2013)**

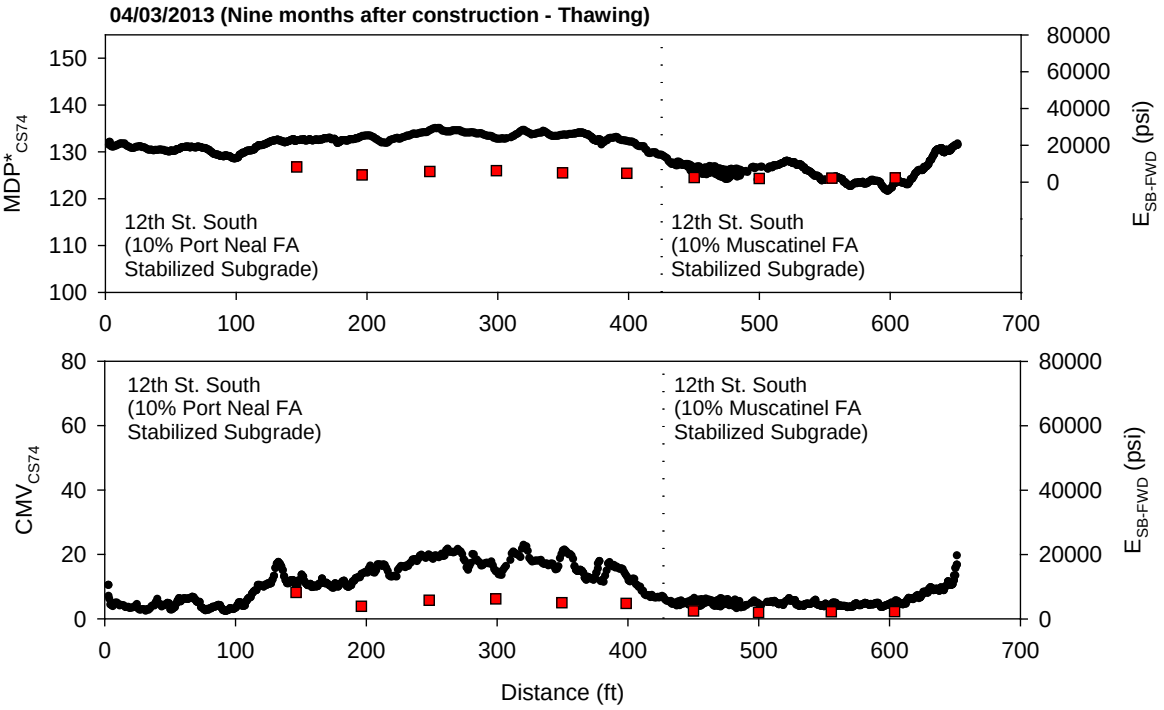

Figure 215. CS74 RICM and FWD modulus measurements on 12th St. North nine months after construction during thawing (April 2013)

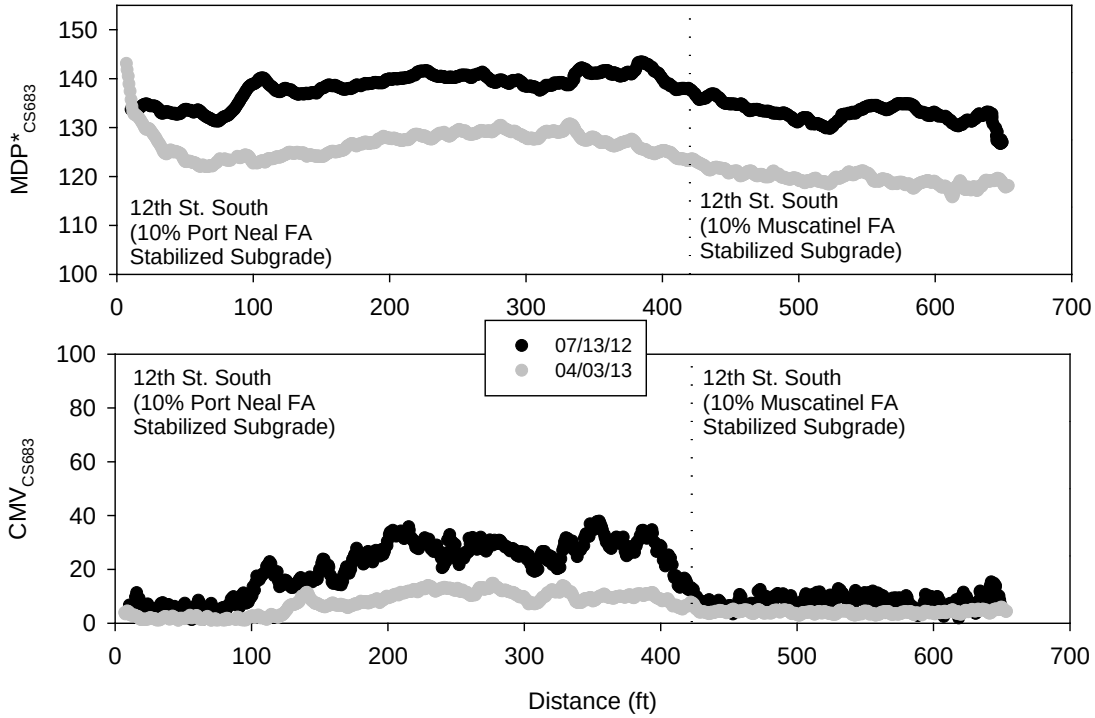

Figure 216. Comparison between CS683 RICM measurements on 12th St. North shortly after construction and nine months after construction during thawing

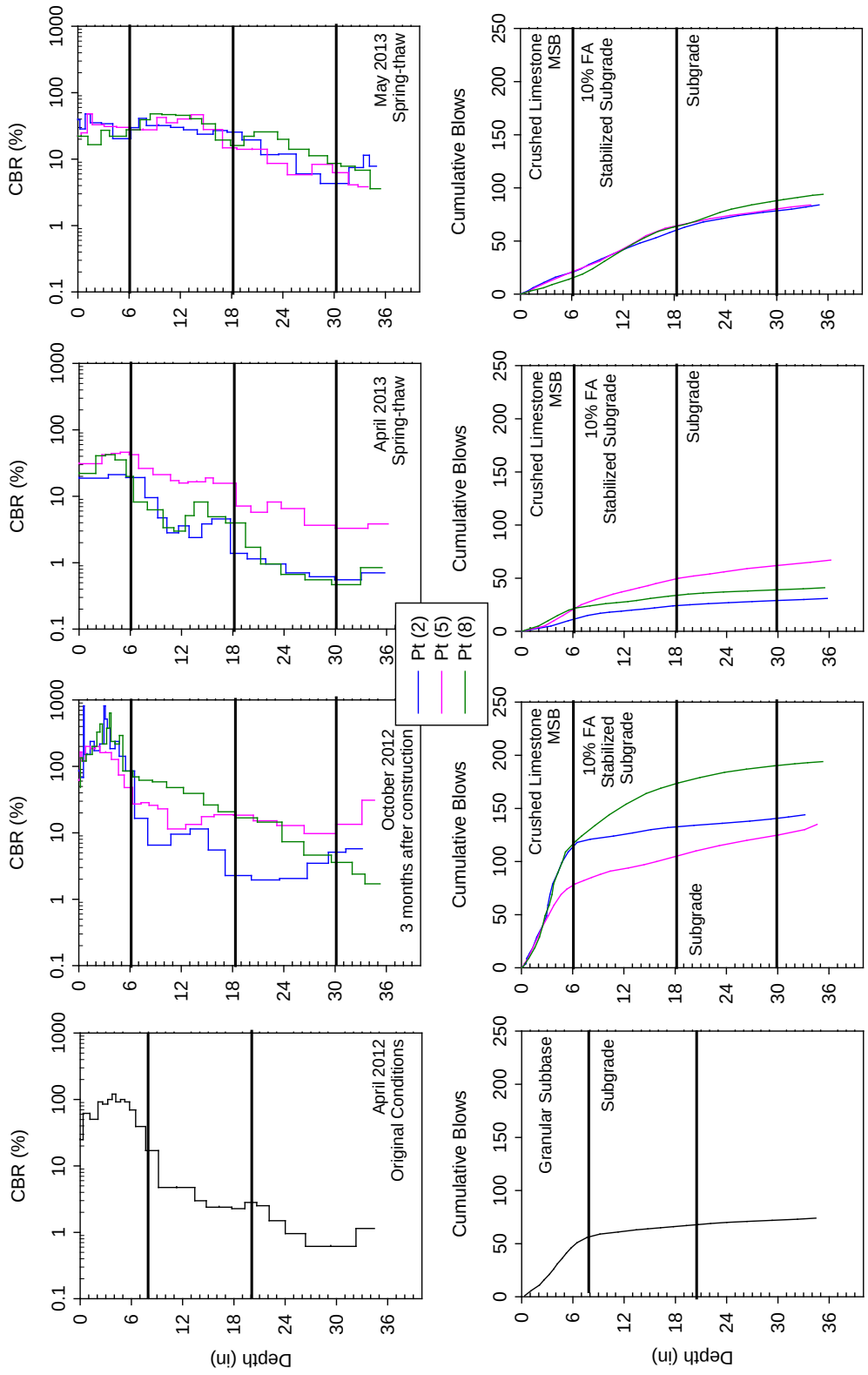

Figure 217. DCP test results from 12th St. South from different testing times (note: Pt (2) consists of Muscatine FA and Pts (5) and (8) consist of Port Neal FA)

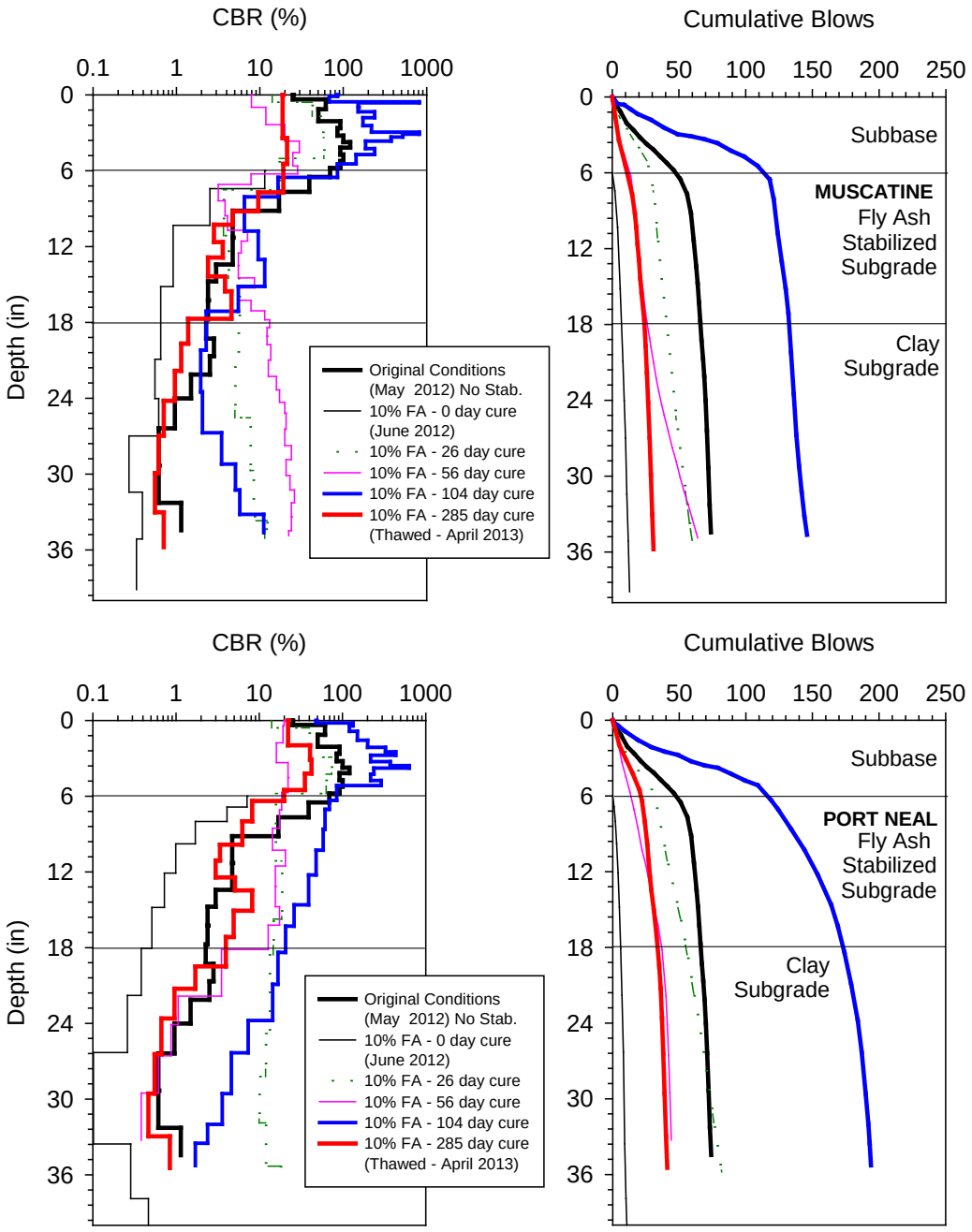

Figure 218. DCP test results at different times of curing at a selected test location on 12th St. North Muscatine and Port Neal FA stabilized sections

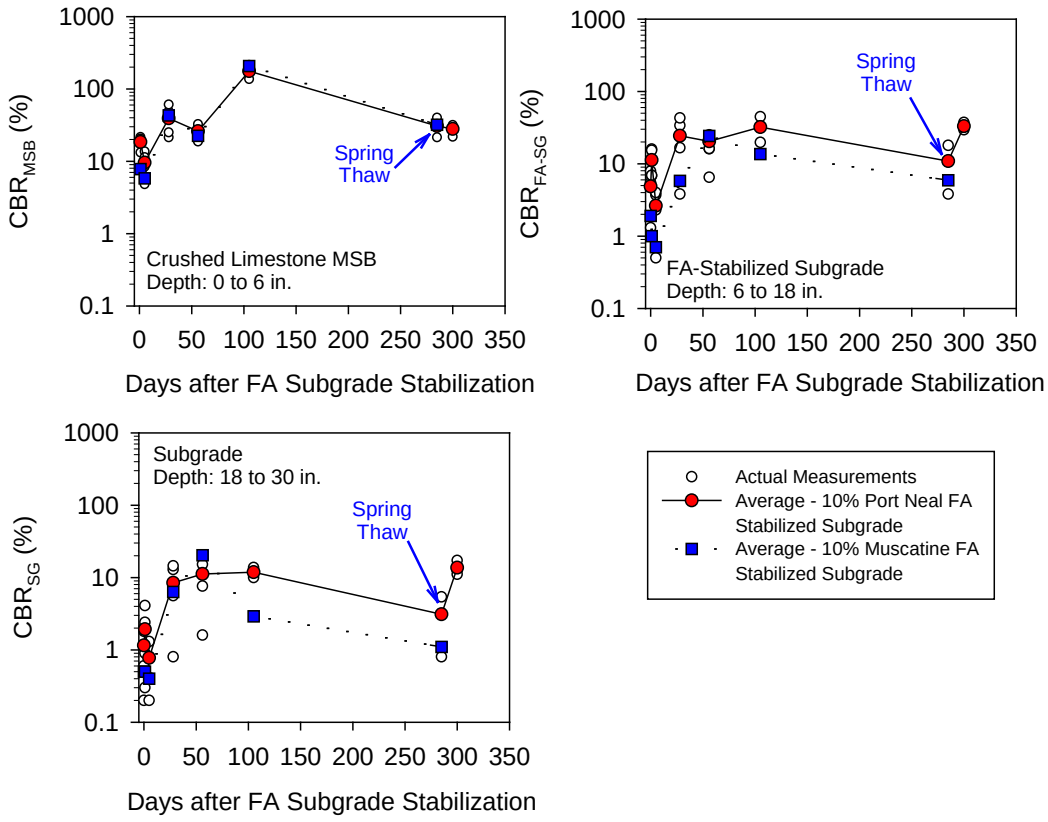

Figure 219. CBR mesaurements in MSB, stabilized subgrade, and unstabilized subgrade layers on 12th St. North

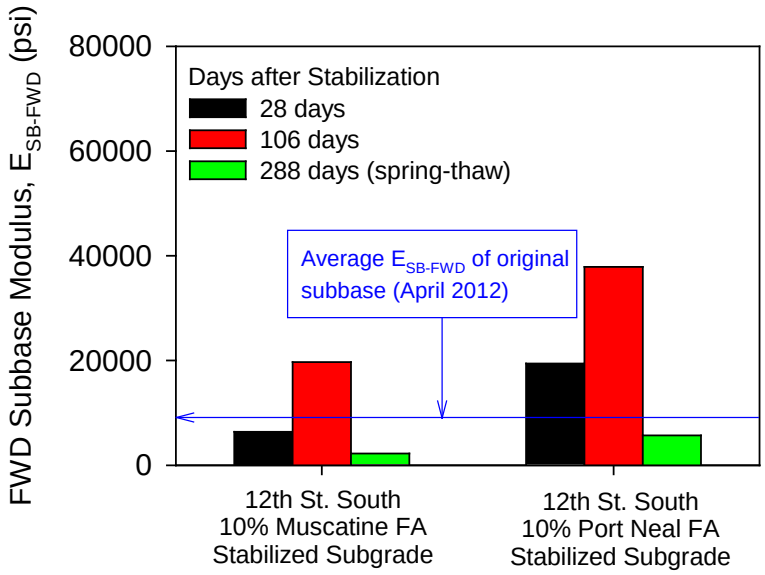

Figure 220. Average FWD subbase modulus (based on 10 tests) on 12th St. North

Project QA/QC Test Results versus Stiffness/Strength Based Measurements

Traditional nuclear gauge moisture-density testing has played an important role in earthwork quality assessment specifications in the U.S. for decades. This form of QC/QA can be effective, but has shortcomings due to regulations, test reproducibility, limited test frequency, and only serving as a surrogate to strength and stiffness design requirements. Figure 221 shows the QC agent and QA agent test results during foundation layer construction. Results show that the QC agent results all meet the minimum 95% criteria and ±2% moisture control criteria. In contrast, the QA agent results are much more variable on both accounts. At this point, one could only speculate about these differences. It is clear though that the nuclear density testing does not indicate the wide stiffness variations resulting from treatments and materials (see discussion in the following section of this chapter).

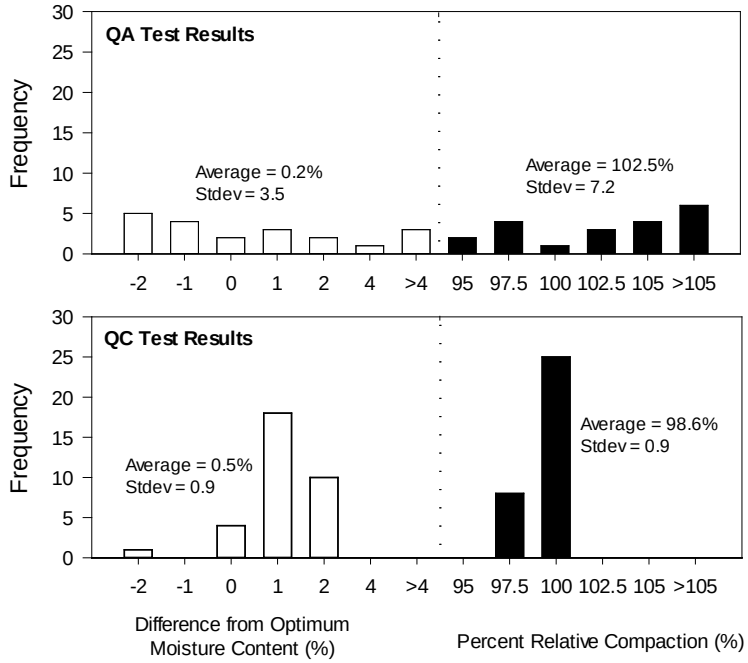

Figure 221. Comparison of nuclear density/moisture measurements for the QC and QA agents

The distinct advantage of FWD and LWD soil stiffness measurements on this project is the identification of variations in support values between different stabilization sections. The advantage of RICM measurements is that they are reported electronically on a near-continuous basis and are available to the contractor in real-time such that the construction process can be controlled around identifying “soft spots” that need remediation and achieving design target values. The primary weakness with soil stiffness assessment is that moisture control remains the critical factor in the construction process.

Summary of Foundation Layer Construction Costs

Figure 222 summarizes the combined material and installation costs for the test sections used on this project. The cost data was compiled from all six contractor bidders' unit prices as requested in the plans and specifications. Geosynthetics are at the low end of the cost range, chemical stabilization is at the intermediate range, and special products (fibers and geocell) are at the high end of the range. The quantities used on this project ranged from about 140 m^2 to 420 m^2.

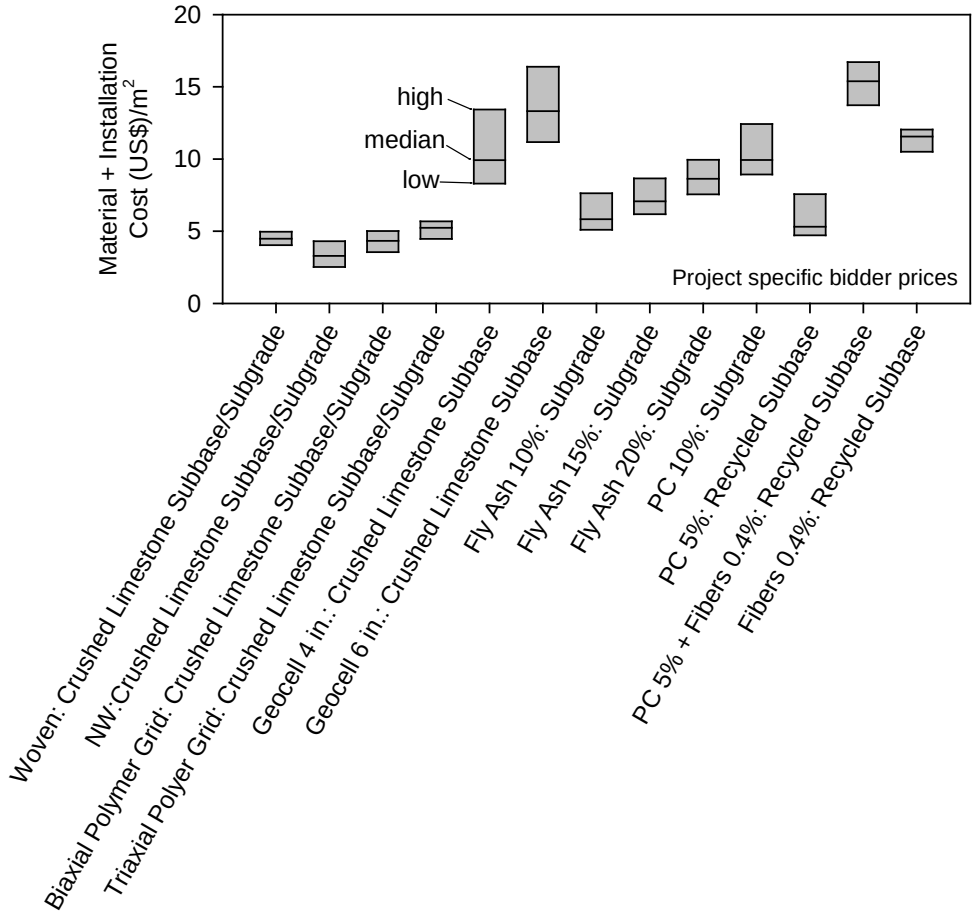

Figure 222. Bid prices for stabilization material + placement based on six bidders

CHAPTER 7: COMPARISONS OF PAVEMENT FOUNDATION LAYER PROPERTIES BETWEEN TEST SECTIONS

Measurement Influence Depth of Stiffness Measurements

To implement soil stiffness measurements, the assessment of measurement influence depth (MID) is needed so that the measurement value is assigned to a volume of soil beneath the test device. It has been demonstrated that RICM values are influenced by ground conditions to depths of about 0.3 m to more than 0.9 m (Floss et al., 1983; Mooney et al., 2010; Thompson and White, 2007; Vennapusa et al. 2012; White et al., 2009;). An influence zone can be defined as analogous to a strip footing where the depth of influence is proportional to the footing width and length. Complicating factors for determining influence depth include layered soft to stiff materials and setting a value for stress increase. In this report, the authors assigned MID based on a total vertical stress increase equal to 10 psi (1 psi = 6.89 kPa) as the defining value. This simple approach eliminates more complicated analyses that require assumptions for unknown parameters. The MID values are shown in Figure 223. Establishing MID values is important as part of understanding analyses of correlations between test devices and in determining remedial actions for areas of non-compliance—is it a shallow problem or an unstable deeper layer?

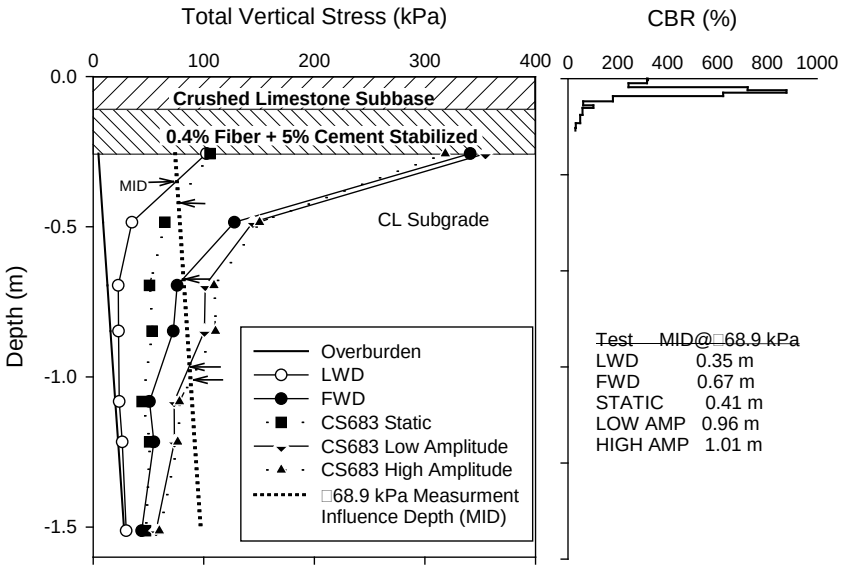

Figure 223. Measurement influence depth (MID) for LWD, FWD, and smooth drum roller using +10 psi criteria from piezoelectric earth pressure cells.

As Constructed Strength and Stiffness Properties Comparison between Test Sections

Figure 224 shows the summary results of the FWD and LWD measurements for each test section. The sections with fly ash and cement stabilized subgrade produced the highest stiffness values. Figure 225 shows the summary results of the CBR measurements for each layer within the test sections. Generally, CBR values within the test sections are consistent with the FWD and

LWD results. The exception however is the polymer grid test sections, which produced CBR values higher than most of the other test sections. The sections underlain by stiff layers (e.g., cement stabilized subgrade) produced the highest CBR values within the crushed limestone subbase layer.

Figure 226 establishes the correlations between FWD and LWD results. The correlation analysis indicates that LWD MID values are lower than FWD MID values, and that FWD MID values better reflect stiff underlying layers better than LWD measurements. Note that the FWD and LWD results from 11th St. show increased differences in moduli due to differences in the MID. 11st St. included a subgrade stabilized layer 305 mm below the surface.

Figure 227 summarizes RICM measurement results. RICM correlations analyses with FWD and LWD are presented in Figure 228. Results show that the CMV measurements are better correlated to FWD than LWD for the range of materials and conditions tested at this site. The FWD produced vertical stress conditions more similar to the roller in comparison with the LWD vertical stress profile (see Figure 223). Geospatially referenced maps of the CMV and $MDP*$ values for low amplitude vibratory operations are presented in Figure 229 and Figure 230. Note that the installation of the geosynthetic sections was to aid in control of rutting/permanent deformation and to provide a durable layer during spring thaw, because drawing conclusions of "effectiveness" solely based on as-constructed stiffness measurements would not necessarily be a complete assessment of the benefits of the products.

Table 15 and Table 16 summarizes the average values for the various measurements for each test section. The coefficients of variation (COV) values are also reported for each section. It is worth noting that the COV for CMV is in line with stiffness based values whereas the $MDP*$ is very low. Low COV values for $MDP*$ are attributed to a higher scaled value; lower sensitivity to variations in stiffness of underlying layers (i.e., lower MID) compared to the CMV measurements; and lower sensitivity to variations in stiffness for very stiff materials.

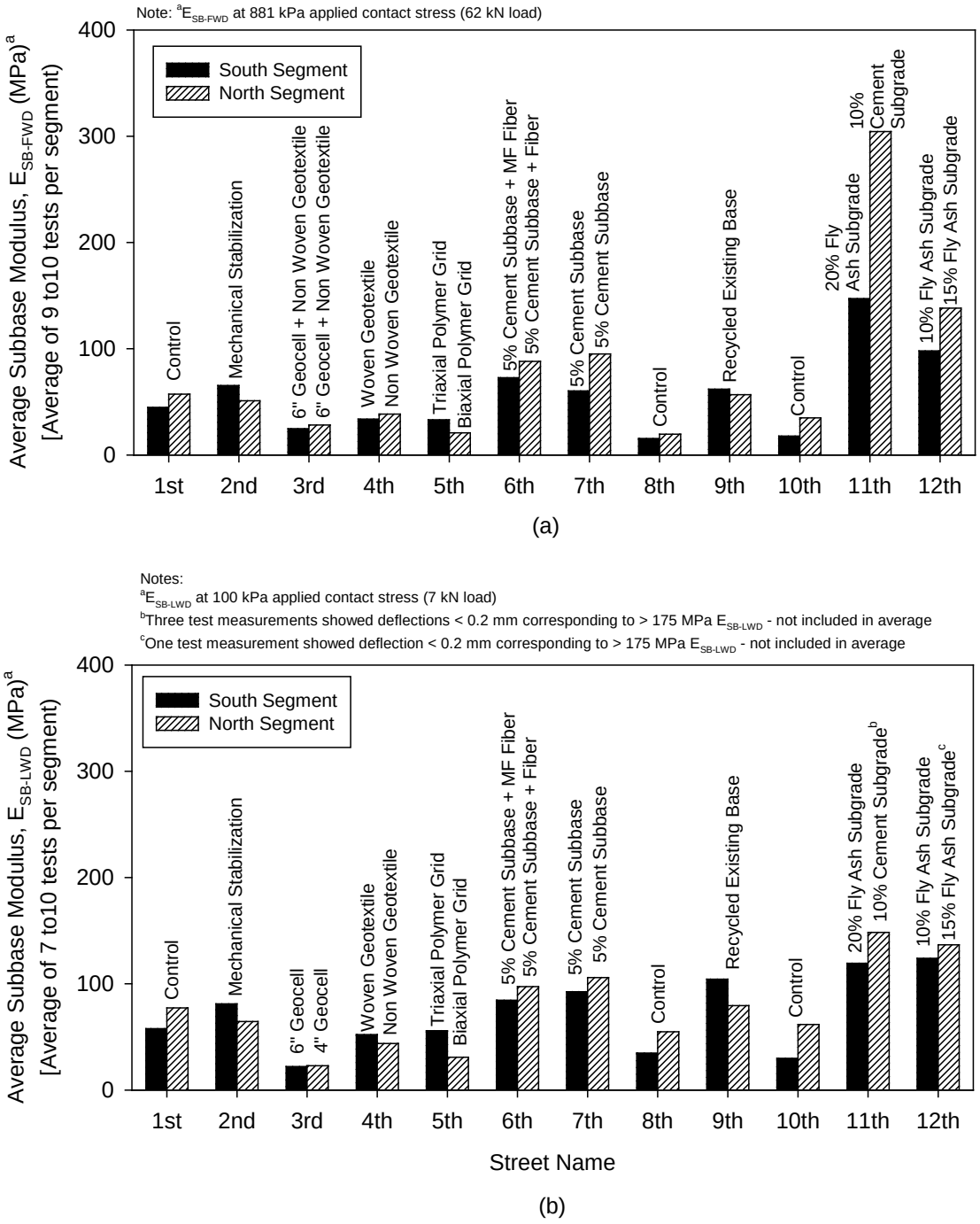

Figure 224. Average subbase elastic modulus measurements from (a) FWD tests and (b) LWD tests on each segment (As constructed properties – July 2012).

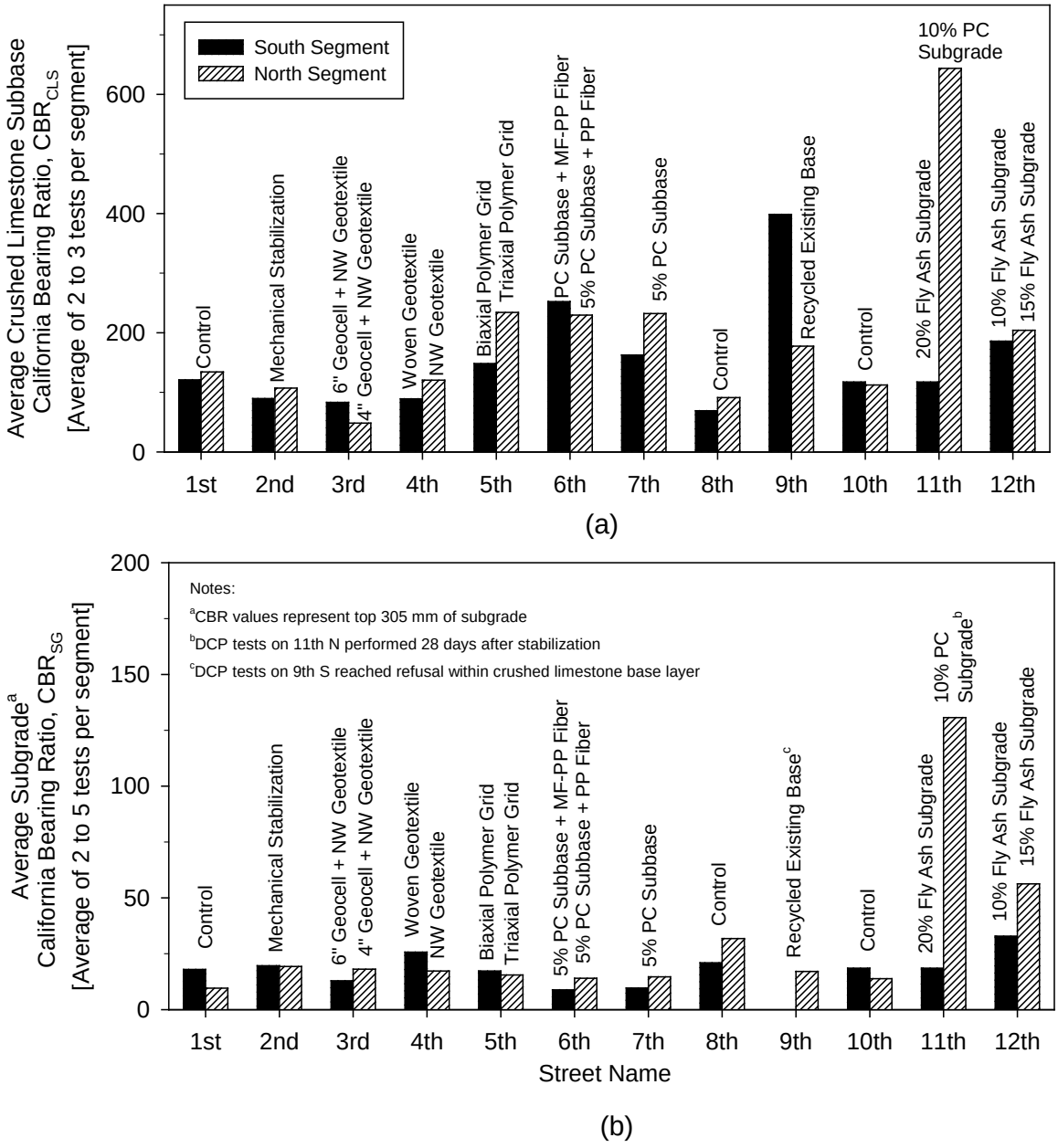

Figure 225. Average California bearing ratio from DCP tests within (a) crushed limestone subbase and (b) subgrade (As constructed properties – July 2012).

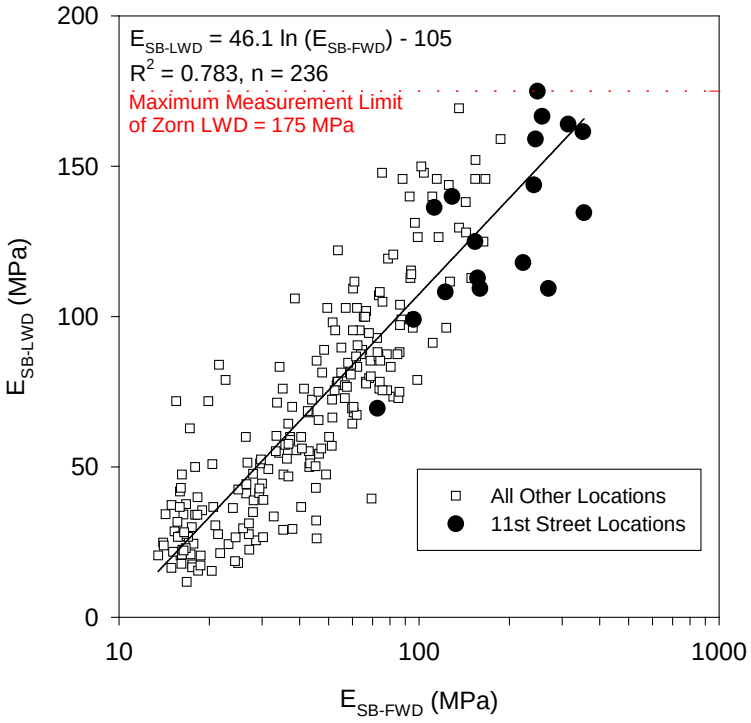

Figure 226. Correlations between subbase elastic modulus measurements from LWD and FWD tests (note log scale for FWD) that compare 11th St. with all other locations.

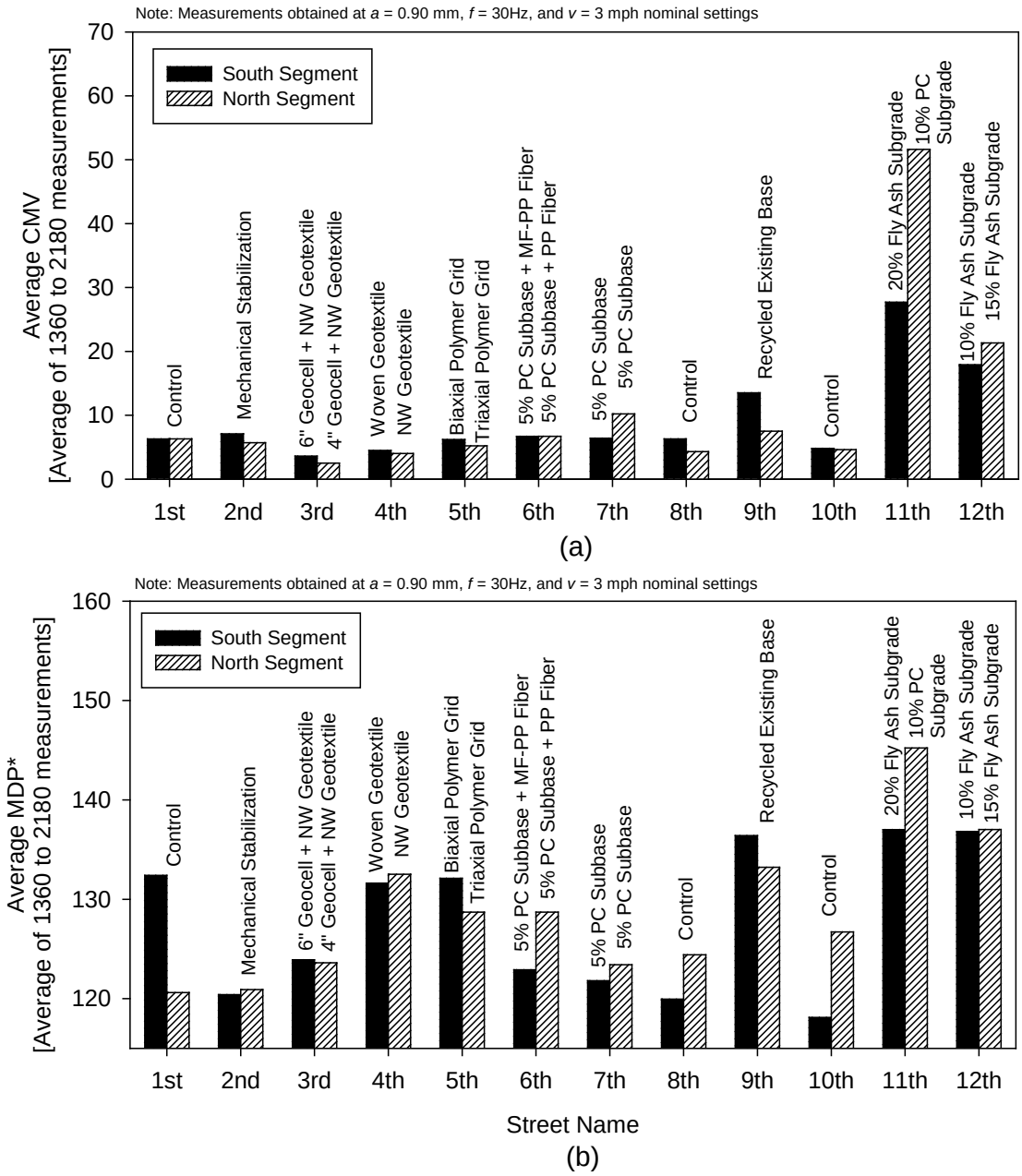

Figure 227. RICM results of each test segment: (a) average CMV and (b) average MDP* ((As constructed properties – July 2012).

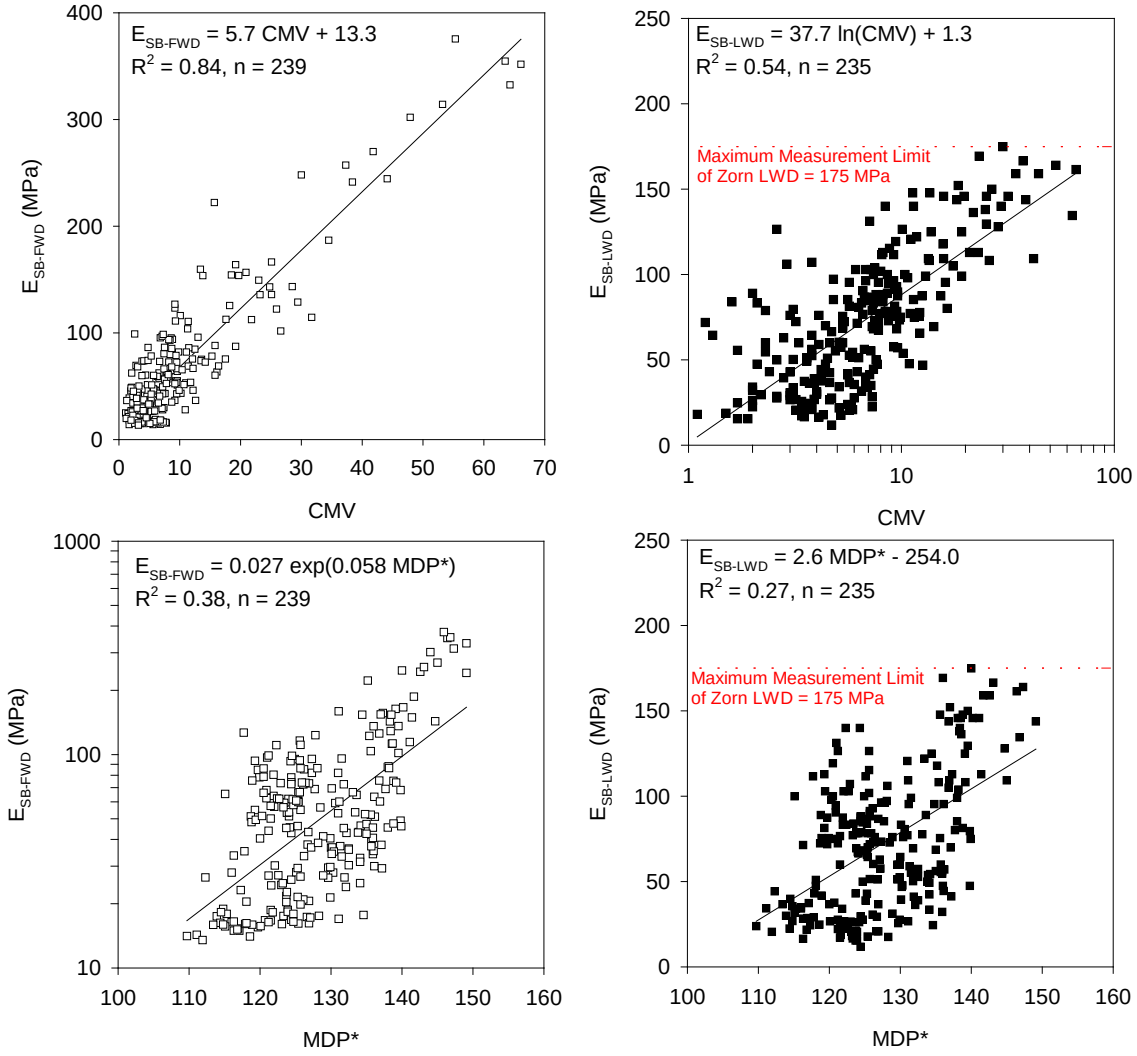

Figure 228. Correlations between (a) CMV and E_{SB-FWD}, (b) CMV and E_{SB-LWD}, (c) MDP* and E_{SB-FWD}, and (d) MDP* and E_{SB-LWD}.

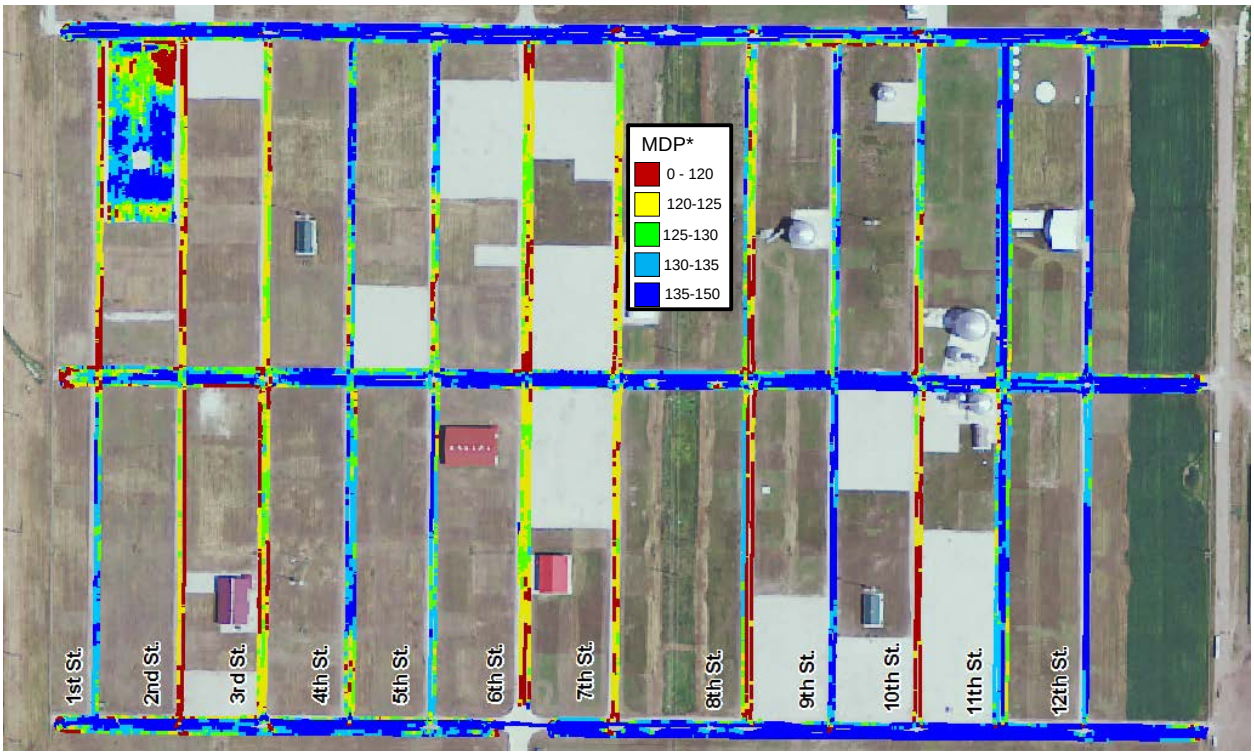

Figure 229. MDP*$_{CS683}$ map from July 2012

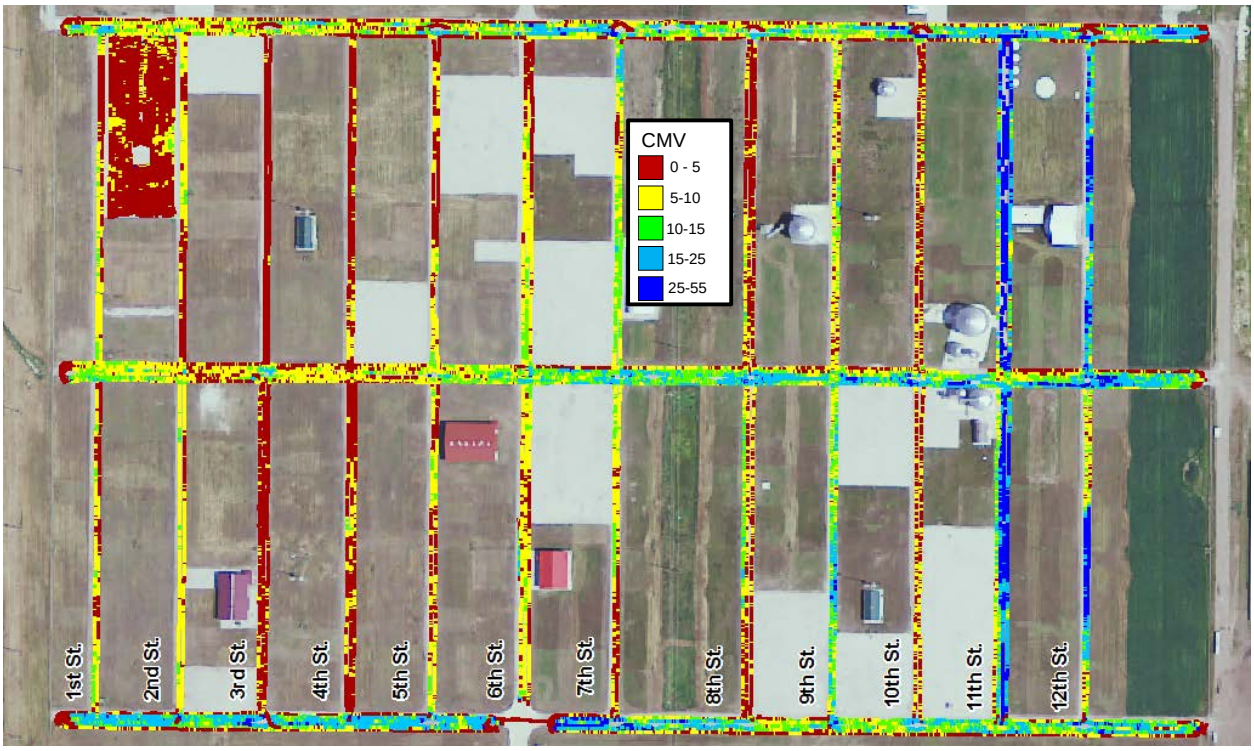

Figure 230. CMV$_{CS683}$ map from July 2012

Table 15. Summary statistics of in situ test measurements on each road segment (as-constructed properties – July 2012)

Street Name[fg]	Foundation Layer Description	$E_{SB\text{-}FWD}$[a] (MPa) [COV[b] %]	$E_{SB\text{-}LWD}$[a] (MPa) [COV[b] %]	CBR[c] in Crushed Limestone Subbase (%) [COV[b]%]	CBR[c] in Subgrade (%) [COV[b]%]	MDP*[d] [COV[b] %]	CMV[e] [COV[b] %]
1st S	Control	45 [24]	58 [25]	121 [25]	18 [21]	132 [3]	6 [48]
1st N	Control	57 [15]	77 [12]	134 [74]	10 [53]	121 [5]	6 [43]
2nd S	Mechanical Stabilization	65 [15]	81 [10]	90 [20]	20 [47]	120 [3]	6 [44]
2nd N	Mechanical Stabilization	51 [46]	64 [42]	107 [44]	19 [18]	121 [3]	7 [25]
3rd S	6 in. Geocell + NW Geotextile	25 [65]	22 [34]	83 [55]	13 [54]	124 [3]	3 [40]
3rd N	4 in. Geocell + NW Geotextile	28 [29]	23 [25]	48 [16]	18 [27]	124 [2]	4 [31]
4th S	Woven Geotextile	34 [19]	52 [30]	89 [65]	26 [52]	132 [4]	4 [43]
4th N	NW Geotextile	38 [39]	44 [42]	121 [23]	17 [36]	133 [4]	5 [42]
5th S	Biaxial Polymer Geogrid Geogrid	33 [28]	56 [28]	148 [34]	17 [42]	132 [4]	5 [42]
5th N	Triaxial Polymer	21 [39]	31 [44]	234 [38]	16 [42]	129 [6]	6 [39]
6th S	5% PC Subbase + MF-PP Fibers	73 [30]	84 [27]	252 [23]	9 15]	123 [3]	7 [43]
6th N	5% PC Subbase + PP Fibers	82 [32]	97 [18]	230 [24]	14 [91]	129 [6]	7 [33]

Notes:
[e]CMV = compaction meter value
[f]S = south
[g]N = north
[a]E = elastic modulus
[b]COV = coefficient of variation
[c]CBR = California bearing ratio
[d]MDP* = machine drive power
[h]Data not available

Table 16. Summary statistics of in situ test measurements on each road segment (as-constructed properties – July 2012) (continued)

Street Name[fg]	Foundation Layer Description	E_{SB-FWD}[a] (MPa) [COV[b]%]	E_{SB-LWD}[a] (MPa) [COV[b]%]	CBR[c] in Crushed Limestone Subbase (%) [COV[b]%]	CBR[c] in Subgrade (%) [COV[b]%]	MDP*[d] [COV[b]%]	CMV[e] [COV[b]%]
7th S	5% PC Subbase	60 [16]	93 [12]	163 [39]	10 [20]	122 [2]	10 [35]
7th N	5% PC Subbase	95 [16]	106 [23]	232 [28]	15 [44]	123 [2]	6 [44]
8th S	Control	16 [5]	35 [22]	69 [24]	21 [23]	120 [6]	4 [53]
8th N	Control	20 [32]	55 [40]	91 [34]	32 [4]	124 [5]	6 [56]
9th S	Recycled Existing Base	62 [18]	104 [24]	399 [20]	[h]	136 [1]	8 [41]
9th N	Recycled Existing Base	57 [39]	79 [35]	178 [15]	17 [38]	133 [3]	14 [35]
10th S	Control	18 [21]	30 [32]	117 [27]	19 [18]	118 [3]	5 [43]
10th N	Control	35 [39]	62 [41]	112 [22]	14 [25]	127 [5]	5 [40]
11th S	20% Fly Ash Subgrade	147 [37]	119 [23]	117 [27]	19 [18]	137 [2]	52 [21]
11th N	10% PC Subgrade	304 [16]	148 [14]	644 [32]	131 [7]	145 [2]	28 [39]
12th S	10% Fly Ash Subgrade	98 [52]	124 [25]	186 [24]	33 [57]	137 [3]	21 [31]
12th N	15% Fly Ash Subgrade	138 [19]	137 [14]	204 [11]	56 [38]	137 [3]	18 [66]

Notes:
[e]CMV = compaction meter value
[f]S = south
[g]N = north
[a]E = elastic modulus
[b]COV = coefficient of variation
[c]CBR = California bearing ratio
[d]MDP* = machine drive power
[h]Data not available

Before Freeze and After Freeze-Thaw Strength and Stiffness Properties Comparison between Test Sections

FWD and DCP testing evaluated test section pavement foundation stiffness in situ. Between 9 and 10 FWD tests at 15 m intervals were performed on each test section, and between 2 and 3 DCP tests at 46 m intervals were performed on each test section. Tests that were conducted during October 2012 represent never-frozen pavement foundation stiffness, and tests that were

conducted during April 2013 and May 2013 represent freeze-thaw pavement foundation stiffness. FWD and DCP testing that evaluated never-frozen pavement foundation stiffness was conducted on October 2–3, 2012 when local temperatures ranged from a minimum of 8 °C to a maximum of 27 °C (Weather Channel, 2016). FWD testing that evaluated freeze-thaw pavement foundation stiffness was conducted on April 3, 2013 when local temperatures ranged from a minimum of –4 °C to a maximum of 8 °C (Weather Channel, 2016). DCP testing that evaluated freeze-thaw pavement foundation stiffness was conducted on April 24–25, 2013 when local temperatures ranged from a minimum of –3 °C to a maximum 16 °C and on May 23–24, 2013 when local temperatures ranged from a minimum of 6 °C to a maximum of 22 °C (Weather Channel, 2016).

FWD Test Results

Figure 231 shows comparisons of average test section E_c values during October 2012 testing and April 2013 testing, and Table 17 reports average test section E_c values with respective coefficients of variation during October 2012 testing and April 2013 testing. October 2012 FWD testing yielded E_c values that ranged from about 37 MPa to 507 MPa. Test sections with PC stabilized subgrade (i.e., 11th North), fly ash stabilized subgrade (i.e., 11th South, 12th South, 12th North), or PC stabilized reclaimed gravel subbase (i.e., 6th South, 6th North, 7th South, and 7th North) produced the highest E_c values during October 2012 testing. Other test sections that produced comparatively higher E_c values during October 2012 testing included test sections with mechanically stabilized subgrade (i.e., 2nd South and 2nd North), compacted subgrade (i.e., 1st South, 1st North, and 10th North), or untreated reclaimed gravel subbase (i.e., 9th South and 9th North).

As shown in Figure 231, all test sections experienced reductions in E_c (by about 2 to 9 times on average) during the spring thaw in April 2013 to where E_c values ranged from about 11 MPa to 159 MPa. Test sections with PC stabilized subgrade (i.e., 11th North) or PC stabilized reclaimed gravel subbase (i.e., 6th South, 6th North, 7th South, and 7th North) produced the highest E_c values during April 2013 testing. Other test sections that produced comparatively higher E_c values during April 2013 testing included test sections with fly ash stabilized subgrade (i.e., 11th South, 12th South, 12th North) or untreated reclaimed gravel subbase (i.e., 9th South and 9th North).

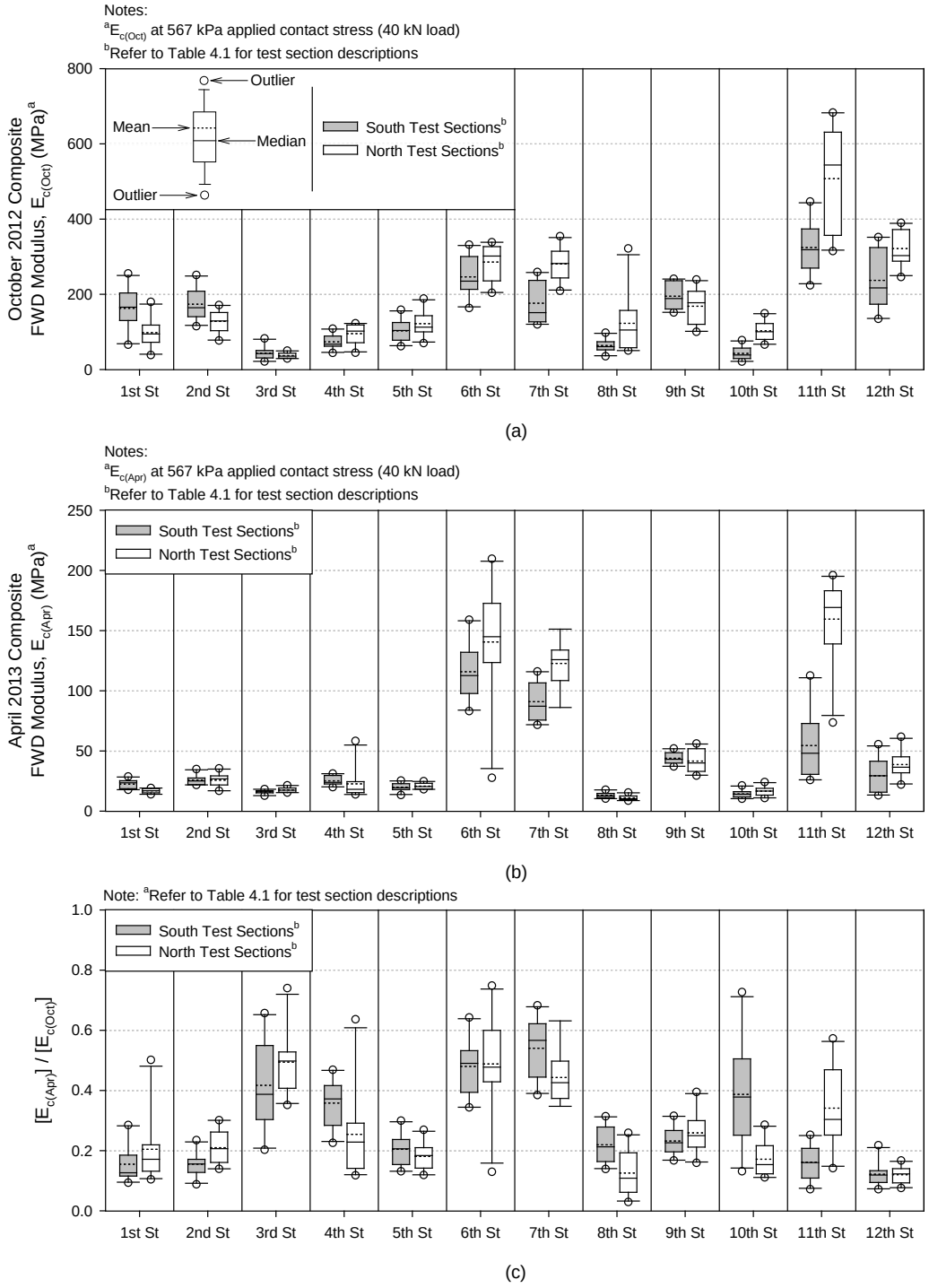

Figure 231. Average test section (a) composite moduli from October 2012 FWD testing, (b) composite modulit from April 2013 FWD testing, and (c) ratios of October 2012 to April 2013 FWD composite moduli

Table 17. Summary statistics of FWD testing on each test section (Fall 2012 vs. Spring 2013 testing)

		October 2012 Average Composite FWD Modulus, $E_{c(Oct)}$ (Mpa) [COV[a] (%)]	April 2013 Average Composite FWD Modulus, $E_{c(Apr)}$ (Mpa) [COV[a] (%)]	$E_{c(Apr)}$ / $E_{c(Oct)}$ [COV[a] (%)]
1st	South	163 [34]	22 [17]	0.15 [42]
	North	98 [39]	17 [11]	0.20 [57]
2nd	South	174 [24]	26 [16]	0.16 [25]
	North	128 [24]	26 [22]	0.21 [28]
3rd	South	44 [42]	16 [10]	0.42 [36]
	North	37 [19]	18 [12]	0.49 [21]
4th	South	74 [27]	25 [15]	0.36 [22]
	North	95 [28]	23 [58]	0.25 [60]
5th	South	103 [29]	20 [17]	0.20 [26]
	North	122 [28]	21 [12]	0.18 [26]
6th	South	246 [21]	116 [21]	0.48 [20]
	North	285 [17]	140 [35]	0.49 [34]
7th	South	176 [32]	91 [18]	0.54 [18]
	North	280 [16]	123 [16]	0.44 [20]
8th	South	63 [28]	13 [19]	0.22 [29]
	North	123 [66]	11 [19]	0.13 [59]
9th	South	195 [18]	44 [11]	0.23 [21]
	North	168 [29]	41 [23]	0.26 [27]
10th	South	43 [41]	14 [23]	0.39 [45]
	North	103 [27]	17 [23]	0.17 [35]
11th	South	324 [21]	54 [54]	0.16 [36]
	North	507 [28]	159 [23]	0.34 [39]
12th	South	237 [33]	29 [48]	0.12 [33]
	North	321 [15]	39 [29]	0.12 [23]

Notes: [a]COV = coefficient of variation

Figure 232 shows correlations between E_c in April 2013 [$E_{c(Apr)}$] and E_c in October 2012 [$E_{c(Oct)}$]. Because test sections with PC stabilization yielded both the highest $E_{c(Oct)}$ values and the highest $E_{c(Apr)}$ values, FWD test points on these test sections were plotted separately from test points on all other test sections. A power equation best fits the relationship between $E_{c(Apr)}$ and $E_{c(Oct)}$ for FWD test points with PC stabilization, and an exponential growth equation best fits the relationship between $E_{c(Apr)}$ and $E_{c(Oct)}$ for FWD test points without PC stabilization. $E_{c(Apr)}$ correlates well with $E_{c(Oct)}$ for both FWD test points with PC stabilization and FWD test points without PC stabilization. As evidenced by the 95% confidence intervals for the two correlations in Figure 232, $E_{c(Apr)}$ for FWD test points with PC stabilization will be predictably

greater (with statistical significance) than $E_{c(Apr)}$ for FWD test points without PC stabilization. These results suggest that PC stabilized pavement foundations are less susceptible to thaw-weakening than untreated pavement foundations or fly ash stabilized pavement foundations.

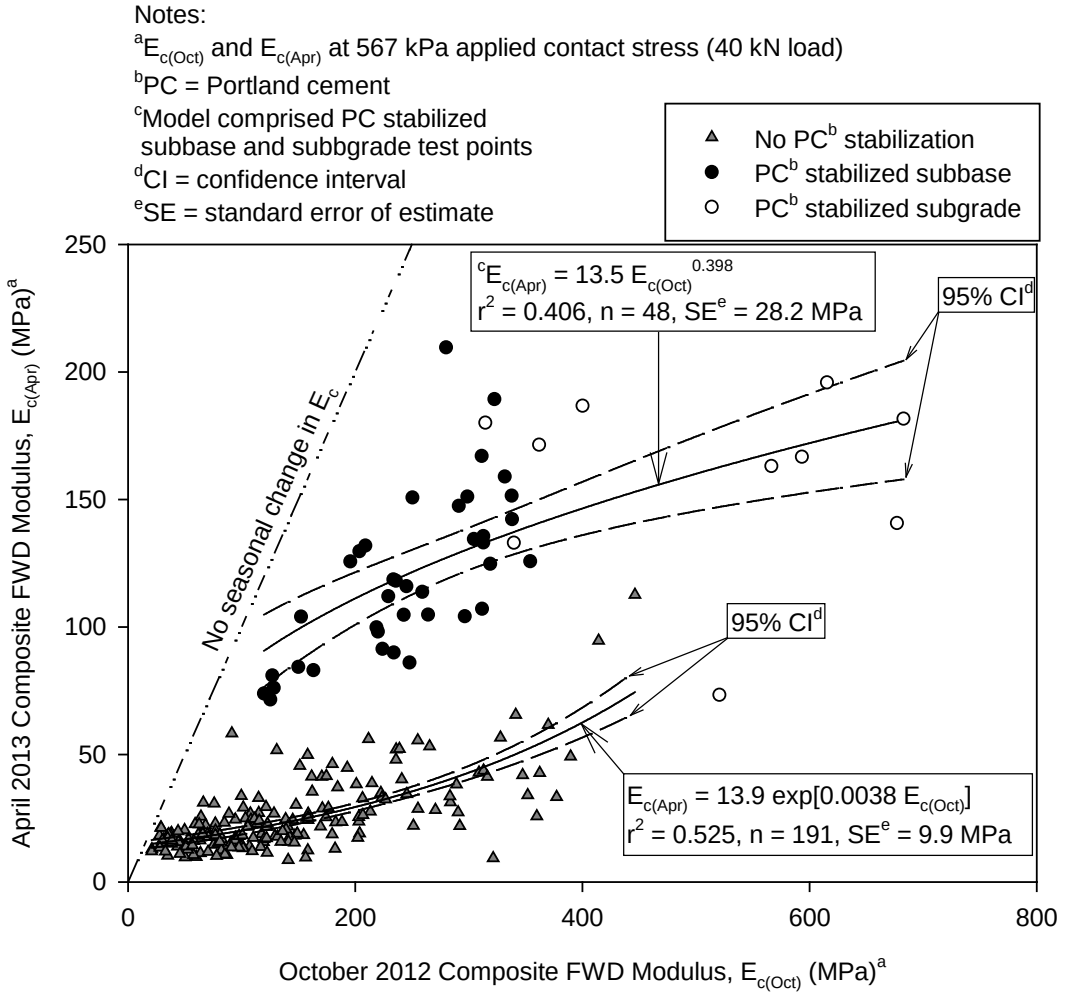

Figure 232. Correlations between April 2013 composite FWD moduli and October 2012 composite FWD moduli.

DCP Test Results

Figure 233a shows comparisons of average test section subbase CBR values during October 2012 DCP testing. With the exception of test sections on which all DCP tests reached refusal before penetrating the subbase layer, October 2012 DCP testing yielded average test section subbase CBR values that ranged from about 32% to 179%. In general, October 2012 DCP results show that test sections with stiff layers (e.g., PC stabilized subgrade) that underlay subbase layers tend to produce comparatively higher subbase CBR values. Figure 234a shows comparisons of average test section subgrade CBR values during October 2012 DCP testing. For test points at which DCP tests had penetrated the subbase layer, average test section subgrade CBR values

ranged from about 2.6% to 44% during October 2012 DCP testing. Test sections with fly ash stabilized subgrade (i.e., 11th South, 12th South, and 12th North) produced the highest subgrade CBR values during October 2012 DCP testing. The 6th North test section produced a relatively high average subgrade CBR value equal to approximately 33%; however, this average is the result of a single data point unlike all other test sections. Therefore the high subgrade CBR value on 6th North during October 2012 is likely an outlier in the data set. Results from different times are summarized in Table 18.

Figure 233b shows comparisons of average test section subbase CBR values during April 2013 DCP testing. April 2013 DCP testing yielded average test section subbase CBR values that ranged from about 12% to 96%. Not including test sections in which DCP tests reached refusal during October 2012 testing, the average subbase CBR value decreased for all test sections during April 2013 DCP testing (by about 1.2 to 12 times on average), except for the 1st North test section, which increased by a factor of about 1.3. Figure 234b shows comparisons of average test section subgrade CBR values during April 2013 DCP testing. April 2013 DCP testing yielded average test section subgrade CBR values that ranged from about 1.2% to 63%. Similar to subbase CBR results, subgrade CBR on test sections on which DCP tests penetrated the subbase layer decreased during April 2013 testing (by about 1.0 to 7 on average), except for the 1st South, 1st North, 2nd South, 2nd North, and 5th South test sections, which all experienced increases in subgrade CBR. There is no evident reason as to why subgrade CBR increased for multiple test sections during April 2013 testing; however, the authors hypothesize that these test sections were still partially frozen at the time of testing. Of the test sections that experienced decreased subgrade CBR values during April 2013 testing, test sections with PC stabilized subgrade (i.e., 11th North) and test sections with fly ash stabilized subgrade (i.e., 11th South, 12th South, and 12th North) produced the highest subgrade CBR values.

Because of the possibility that multiple test sections were still partially frozen during April 2013 DCP testing, additional DCP testing was performed in May 2013 to reassess the thaw-weakened CBR values for the test sections. Figure 233c shows comparisons of average test section subbase CBR during May 2013 DCP testing. May 2013 DCP testing yielded average test section subbase CBR values that ranged from about 21% to 268%. Not including test sections in which DCP tests reached refusal during October 2012 testing, average subbase CBR decreased (by about 1.1 to 8 on average), except for the 4th South, 6th North, 10th South, and 10th North test sections, which all experienced increases in subbase CBR. Most test sections produced increased subbase CBR values during May 2013 testing as compared with April 2013 testing, except for the 1st South, 1st North, 2nd South, 2nd North, and 12th South test sections, which all produced lower subbase CBR values. Test sections with PC stabilized subbase (i.e., 6th South, 6th North, 7th South, and 7th North) and the test section with woven geotextile (i.e., 4th South) produced the highest subbase CBR values during May 2013 testing. Because only these test sections have such markedly higher subbase CBR values during May 2013 testing than during April 2013 testing, these stabilization techniques (i.e., PC stabilized subbase and woven geotextiles) may hasten the rate for recovery from thaw-weakening for subbase materials. Figure 234c shows comparisons of average test section subgrade CBR during May 2013 DCP testing. May 2013 DCP testing yielded average test section subgrade CBR values that ranged from about 2.7% to 57%. Not including test sections in which DCP tests reached refusal during October 2012 testing, average

subgrade CBR decreased (by about 1.0 to 3 on average), except for the 1st South, 3rd South, 8th South, 10th South, 11th South, and 12th South test sections, which all experienced increases in subgrade CBR. Similar to test section subbase layers, most test sections produced increased subgrade CBR values during May 2013 testing than during April 2013 testing, except for the 1st South, 1st North, 2nd South, 2nd North, 3rd North, 5th South, and 11th North test sections, which all produced lower subgrade CBR values. Test sections with either PC stabilized subgrade (i.e., 11th North) or fly ash stabilized subgrade (i.e., 11th South, 12th South, and 12th North) yielded the highest subgrade CBR values during May 2013 DCP testing. The average subgrade CBR value for the PC stabilized subgrade test section remained relatively unchanged between April 2013 testing and May 2013 testing; however, average subgrade CBR for the fly ash stabilized subgrade test sections increased by about 1.4 to 3 times on average between April 2013 testing and May 2013 testing. Because the subgrade CBR values for fly ash stabilized subgrade are markedly higher during May 2013 testing than during April 2013 testing, fly ash stabilization may hasten the rate for recovery from thaw-weakening for cohesive subgrades.

Because multiple April 2013 DCP testing points seemed to have still been partially frozen at the time of testing and because multiple May 2013 DCP testing points seemed to have already began recovering from their initial thaw-weakened states at the time of testing, the authors combined the two data sets to best represent thaw-weakened CBR and PI values on the test sections. Therefore, for both subbase and subgrade layers at a particular data point, thaw-weakened layer CBR equals the minimum of April 2013 layer CBR and May 2013 layer CBR, and thaw-weakened layer PI equals the maximum of April 2013 layer PI and may 2013 layer PI. Figure 235a correlates the minimum of April 2013 and May 2013 subbase CBR values to October 2012 subbase CBR values. As evidenced by the position of the data points relative to the line of equality, test point subbase layers all experience reductions in CBR within the thaw-weakened state. However, the correlation between thaw-weakened subbase CBR and never-frozen (i.e., October 2012 DCP testing) subbase CBR is poor ($r^2 = 0.0662$) and lacks statistical significance so thaw-weakened subbase CBR is likely independent of never-frozen subbase CBR. Figure 235b correlates the minimum of April 2013 and May 2013 subgrade CBR values to October 2012 subgrade CBR values. Similar to test section subbase layers, the majority of test point subgrades layers experienced reductions in CBR within the thaw-weakened state as shown by data point position relative to the line of equality. Unlike test section subbase layers, however, thaw-weakened subgrade CBR has a respectable correlation ($r^2 = 0.3799$) with statistical significance to never-frozen subgrade CBR, so never-frozen subgrade CBR is likely an indicator of thaw-weakened subgrade CBR. Only one DCP test penetrated through a PC stabilized layer during October 2012 DCP test, so no conclusions on possible decreased susceptibility of PC stabilized pavements to thaw-weakening can made.

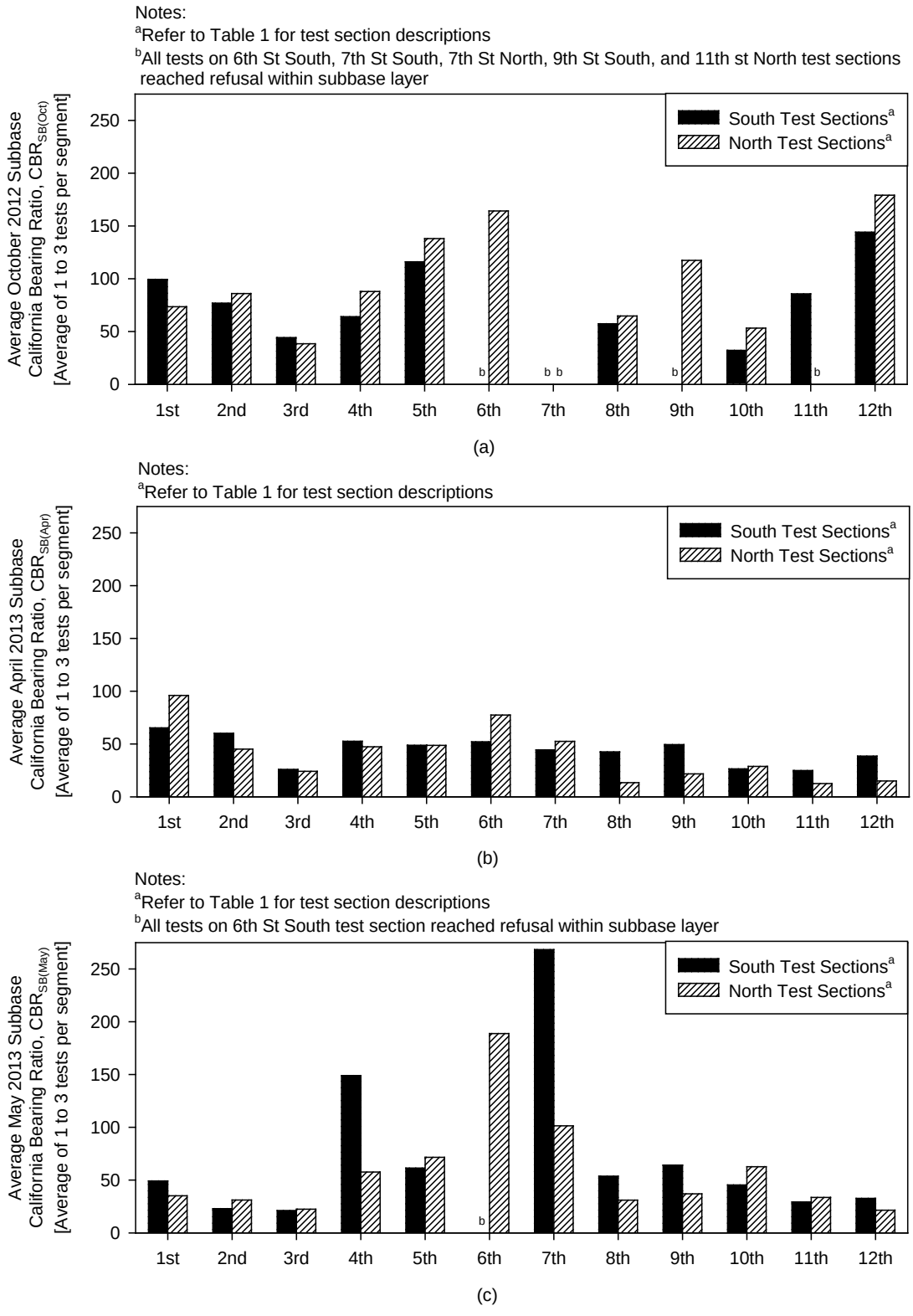

Figure 233. Average subbase layer California bearing ratio values from DCP testing during (a) October 2012, (b) April 2013, and (c) May 2013 for each test section

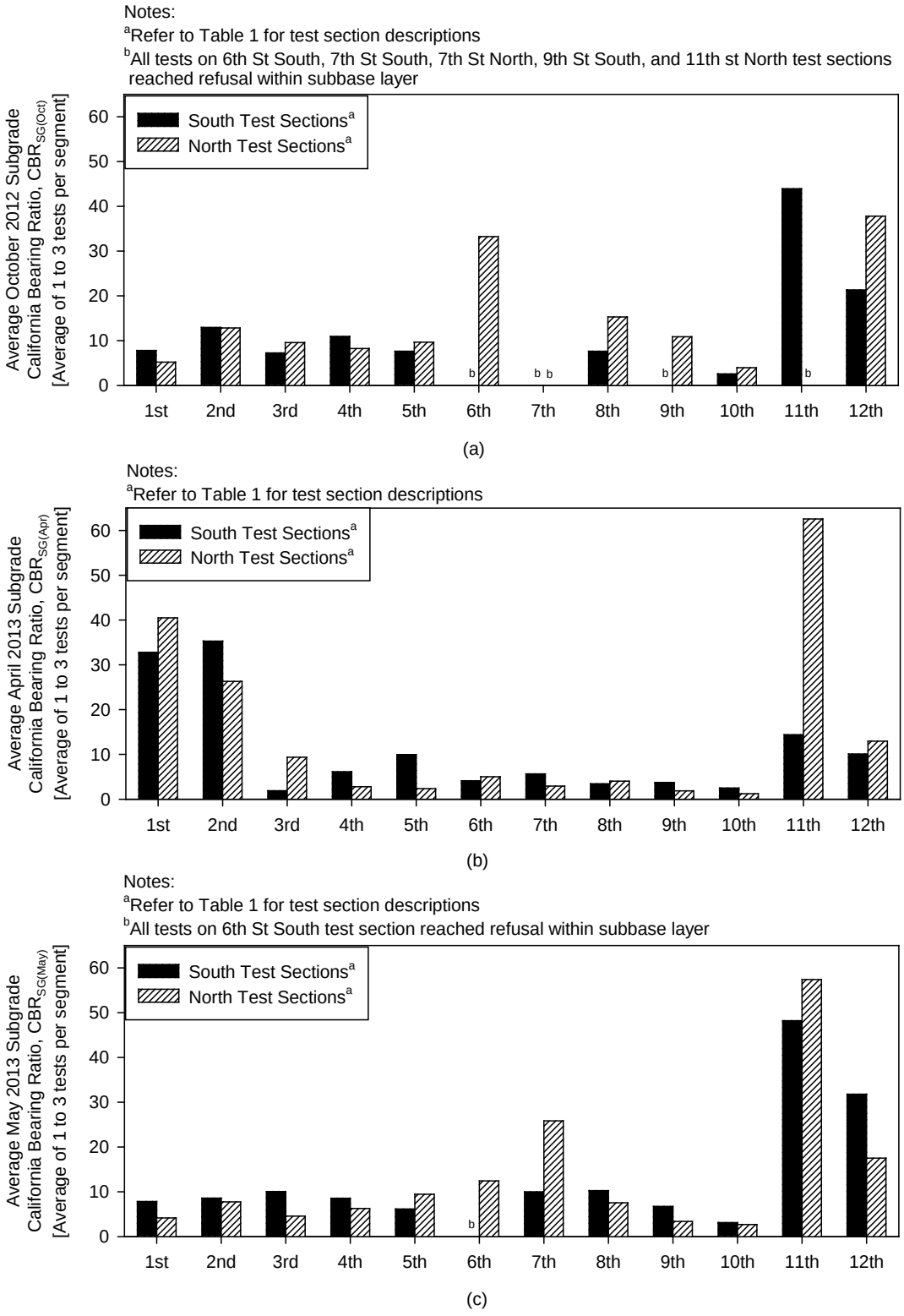

Figure 234. Average subgrade layer California bearing ratio values from DCP testing during (a) October 2012, (b) April 2013, and (c) May 2013 for each test section

Table 18. Summary statistics of DCP testing on each test section (Fall 2012 vs. Spring 2013 testing)

Test Section		October 2012 Testing		April 2013 Testing		May 2013 Testing	
		Average Subbase CBR, $CBR_{SB(Oct)}$ (%) [COV[a]]	Average Subgrade CBR, $CBR_{SG(Oct)}$ (%) [COV[a]]	Average Subbase CBR, $CBR_{SB(Apr)}$ (%) [COV[a]]	Average Subgrade CBR, $CBR_{SG(Apr)}$ (%) [COV[a]]	Average Subbase CBR, $CBR_{SB(May)}$ (%) [COV[a]]	Average Subgrade CBR, $CBR_{SG(May)}$ (%) [COV[a]]
1st	South	99 [20]	8 [57]	65 [16]	33 [50]	49 [14]	8 [19]
	North	73 [46]	5 [66]	96 [35]	40 [8]	35 [66]	4 [122]
2nd	South	77 [11]	13 [67]	60 [38]	35 [40]	23 [19]	9 [77]
	North	86 [48]	13 [30]	45 [53]	26 [49]	31 [8]	8 [5]
3rd	South	44 [38]	7 [92]	26 [50]	2 [29]	21 [36]	10 [63]
	North	38 [8]	10 [40]	24 [59]	9 [104]	22 [11]	5 [51]
4th	South	64 [93]	11 [47]	53 [20]	6 [53]	149 [22]	9 [18]
	North	88 [11]	8 [47]	47 [72]	3 [32]	58 [21]	6 [44]
5th	South	116 [33]	8 [61]	49 [12]	9 [57]	61 [21]	6 [90]
	North	138 [30]	10 [65]	49 [48]	2 [38]	72 [43]	9 [47]
6th	South	[b]	[b]	52 [[c]]	4 [[c]]	[b]	[b]
	North	164 [[c]]	33 [[c]]	77 [9]	5 [63]	189 [b]	12 [[c]]
7th	South	[b]	[b]	44 [51]	6 [13]	268 [b]	10 [[c]]
	North	[b]	[b]	52 [[c]]	3 [[c]]	101 [b]	26 [[c]]
8th	South	57 [10]	8 [44]	43 [33]	3 [16]	54 [7]	10 [64]
	North	65 [12]	15 [59]	13 [38]	4 [35]	31 [24]	8 [34]
9th	South	[b]	[b]	49 [39]	4 [54]	64 [5]	7 [114]
	North	117 [15]	11 [64]	22 [30]	2 [13]	37 [8]	3 [19]
10th	South	32 [57]	2.6 [31]	26 [11]	2 [69]	45 [18]	3 [36]
	North	53 [13]	4 [9]	29 [14]	1 [35]	63 [31]	3 [68]
11th	South	86 [39]	44 [5]	25 [27]	14 [20]	29 [51]	48 [39]
	North	[b]	[b]	12 [16]	63 [39]	34 [17]	57 [21]
12th	South	144 [19]	21 [73]	39 [33]	10 [79]	33 [31]	32 [10]
	North	179 [13]	38 [32]	15 [43]	13 [57]	22 [36]	18 [18]

Notes: [a]COV = coefficient of variation
[b]All DCP tests on test section reached refusal within subbase layer
[c]Test section contained only one data point (i.e., indeterminate coefficient of variation)

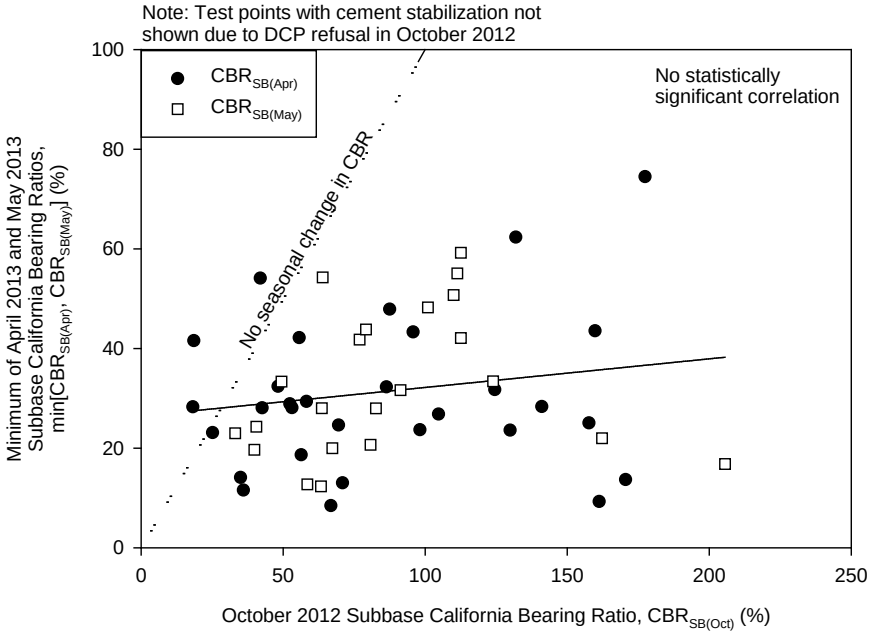

(a)

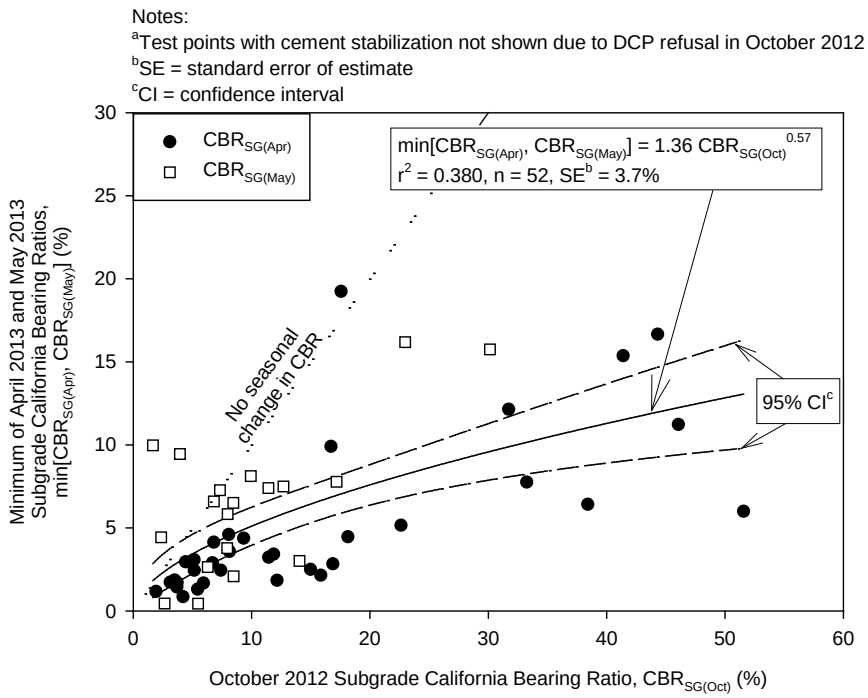

(b)

Figure 235. Correlations between (a) minimum of April 2013 and May 2013 subbase CBR values and October 2012 subbase CBR values and (b) minimum of April 2013 and May 2013 subgrade CBR values and October 2012 subgrade CBR values

Layer influence on overall pavement foundation stiffness

Herein, the results have been analyzed to determine which layer, subgrade or subbase, has greater influence on the overall pavement foundation stiffness during never-frozen and freeze-thaw conditions. E_c values from FWD testing represent overall pavement foundation stiffness, and subbase PI values and subgrade PI values represent subbase and subgrade layer stiffnesses, respectively. Figure 236a shows correlations between October 2012 E_c values and October 2012 subbase and subgrade PI values. During October 2012 testing (i.e., never frozen condition), both subbase PI values and subgrade PI values correlate well ($r^2 = 0.4059$ and $r^2 = 0.6882$, respectively) and with statistical significance to E_c values. Figure 236b shows correlations between April 2013 E_c values and the maximum of April 2013 and May 2013 PI values for subbase and subgrade layers. During April 2013 and May 2013 testing (i.e., freeze-thaw condition), subgrade PI values correlate well ($r^2 = 0.4844$) and with statistical significance to E_c values; however, subbase PI values do not correlate ($r^2 = 0.0513$) and without statistical significance to E_c values.

Table 19 reports the results of multivariable analyses that incorporate both subbase and subgrade layer PI values into models for predicting E_c for both October 2012 testing and April 2013 and May 2013 testing. 6th South and North, 7th South and North, and 9th South and North test sections were not included in the multivariable analysis because subbase layers on these test sections were nominally twice as thick as subbase layers on all other test sections, and influence of subbase thickness is beyond the scope of the multivariable analyses.

The October 2012 multivariable model for predicting E_c fits well (r^2 Adj. = 0.6978), and both subbase PI and subgrade PI model coefficients are statistically significant ($p < 0.0001$ and $p < 0.0001$, respectively). Sensitivity index for subbase PI equals 0.835, and sensitivity index for subgrade PI equals 0.165. In essence, during the never-frozen condition, subbase layer stiffness accounts for 83.5% of the overall pavement foundation stiffness and subgrade layer stiffness accounts for 16.5% of the overall pavement foundation stiffness.

Similar to the October 2012 multivariable model, the April 2013 and May 2013 multivariable model for predicting E_c fits well (r^2 Adj. = 0.6615). However, unlike the October 2012 multivariable model, the subgrade PI model coefficient is statistically significant ($p < 0.0001$) while the subbase PI model coefficient is not statistically significant ($p = 0.4799$). Because the subbase PI model coefficient is not statistically significant for the April 2013 and May 2013 multivariable model, overall pavement foundation stiffness is independent of subbase layer stiffness (i.e., subbase PI sensitivity index equals 0) and only subgrade layer stiffness accounts for the overall pavement foundation stiffness (i.e., subgrade PI sensitivity index equals 1).

Layered stress distribution in accordance with Burmister (1945) may explain why subbase stiffness has no effect on overall pavement foundation stiffness during the thaw-weakened condition. When a stiff layer overlies a soft layer (e.g., subbase over subgrade), the stiff layer acts as a reinforcing layer with a load-spreading effect. Load-spreading effectiveness depends on the ratio of the stiff layer elastic modulus to the soft layer elastic modulus. Because DCP testing showed that thaw-weakening causes reductions in not only test section subgrade stiffness but

also test section subbase stiffness, the insensitivity of overall pavement foundation stiffness to subbase stiffness during thaw-weakening may therefore be the result of reduced load-spreading effectiveness.

The subbase elastic moduli (E_{SB}) and subgrade layer elastic moduli (E_{SG}) were backcalculated for October 2012 and April 2013 FWD testing. Figure 237a shows boxplot comparisons of E_{SB} to E_{SG} ratios for October 2012 and April 2013 FWD testing. The average E_{SB} to E_{SG} ratio during October 2012 FWD testing equals about 7.6, and the average E_{SB} to E_{SG} ratio during April 2013 FWD testing equals about 1.6. A Welch's t test analysis (i.e., assumed unequal variances) showed with statistical significance ($p < 0.001$) that the average E_{SB} to E_{SG}ratio during October 2012 FWD testing does not equal the average E_{SB} to E_{SG}ratio during April FWD testing. Because the ratio of E_{SB} to E_{SG}decreases by about 4.6 times on average from the never-frozen condition to the thaw-weakened condition, the load-spreading effectiveness of test section subbase layers also decreases from the never-frozen condition to the thaw-weakened condition.

Ratios of σ_{SG} to σ_o for October 2012 and April 2013 testing were determined using the Burmister solution for stress distribution and values for E_{SB} and E_{SG} from FWD testing. Figure 237b shows boxplot comparisons of σ_{SG} to $\sigma_o$for October 2012 and April 2013 testing. The average σ_{SG} to σ_o ratio during October 2012 FWD testing equals about 0.406, and the average σ_{SG} to σ_o ratio during April 2013 FWD testing increased as compared with October 2012 testing (by about 1.5 times on average) to about 0.593. A Welch's t test analysis showed with statistical significance ($p < 0.001$) that the average σ_{SG} to σ_o ratio during October 2012 FWD testing does not equal the average σ_{SG} to σ_o ratio during April FWD testing. If the subbase load-spreading effect is ignored (i.e., applying the Boussinesq solution), then the ratio of σ_{SG} to σ_o equals about 0.638.

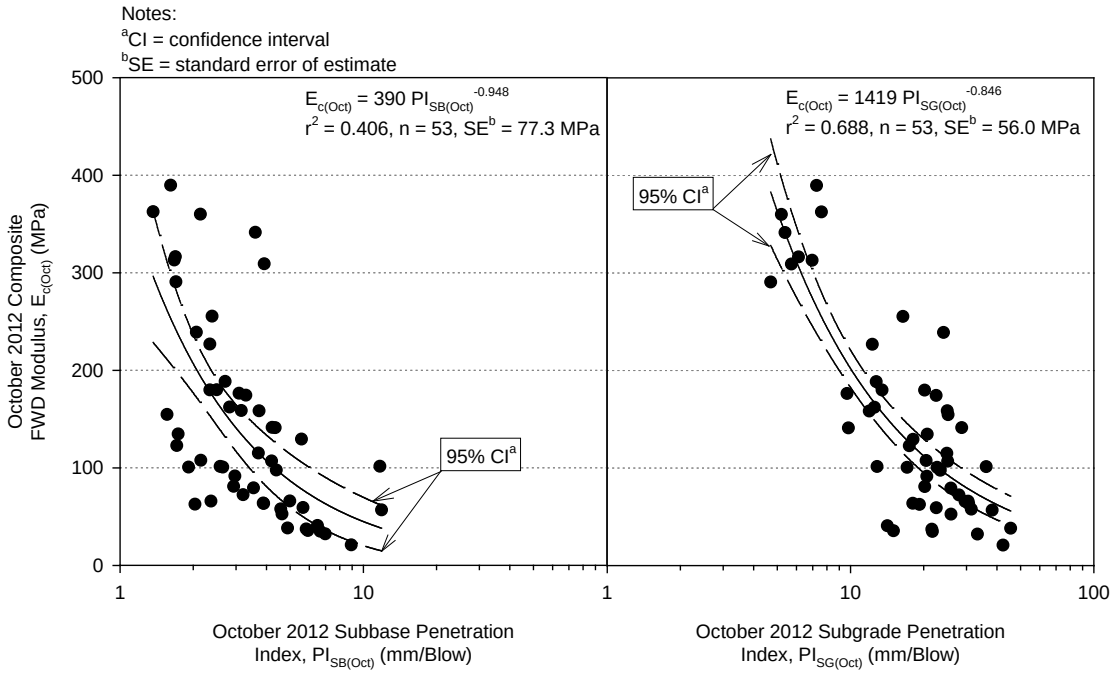

(a)

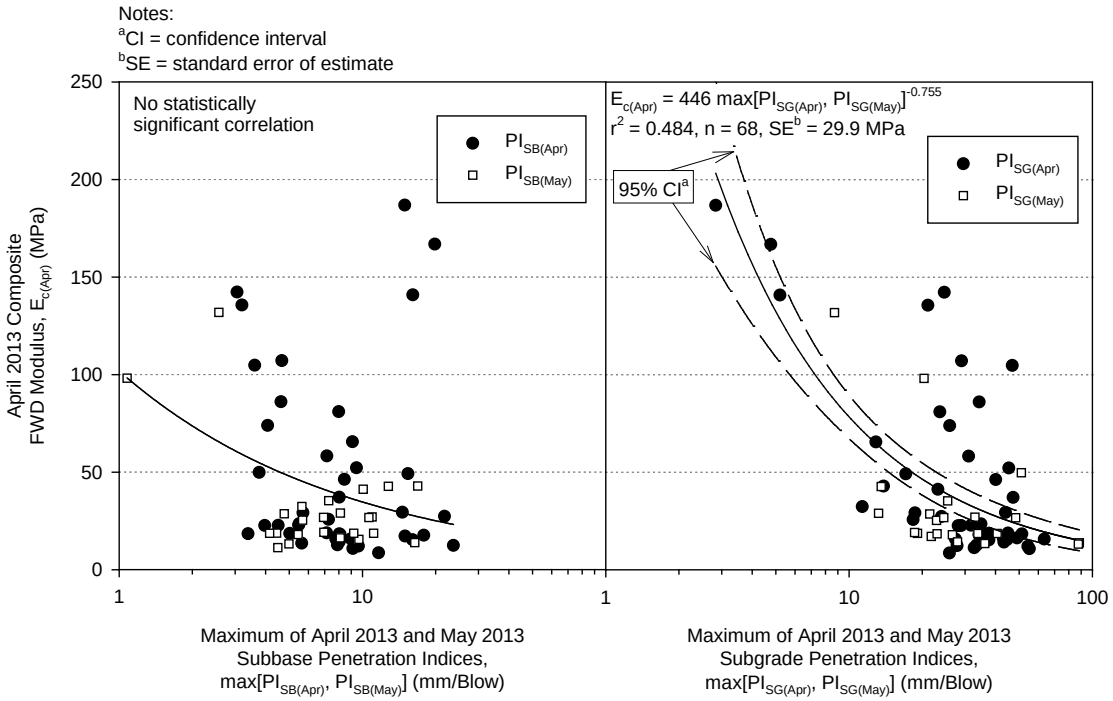

(b)

Figure 236. Correlations between (a) October 2012 FWD composite moduli and October 2012 subbase and subgrade CBR values and (b) April 2013 FWD composite moduli and minimum of April 2013 and May 2013 subbase and subgrade CBR values

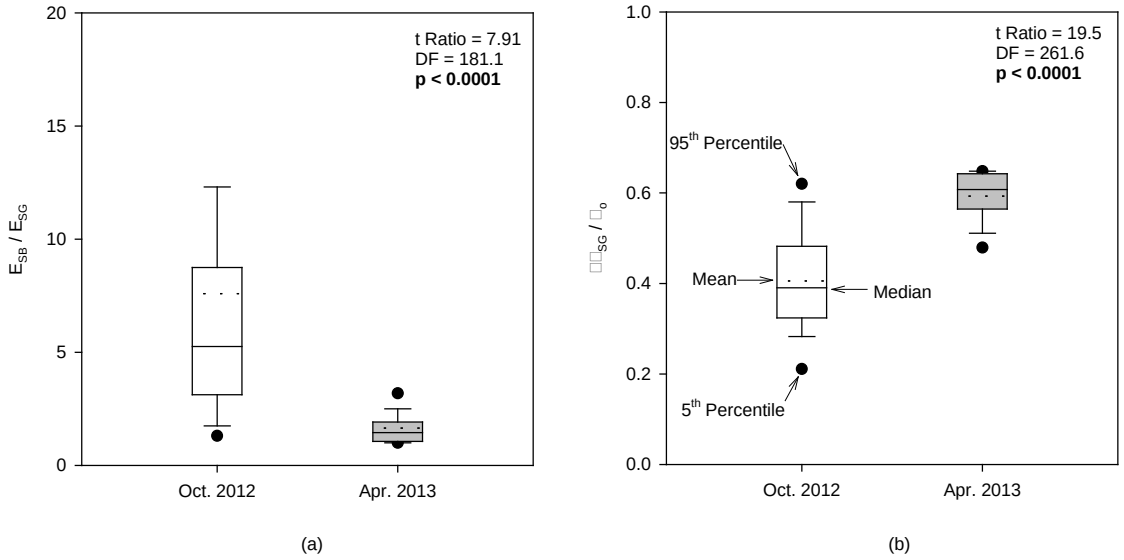

Figure 237. Comparisons between October 2012 and April 2013 (a) ratios of subbase to subgrade elastic moduli and (b) ratios of distributed stress on subgrade to applied surface stress

Table 19. October 2012 testing and April/May 2013 testing multivariable models for FWD composite moduli as functions of subbase and subgrade PI values

Multivariable Analysis[a]	Term	Estimate	Standard Error (MPa)	t Ratio	Prob. > t[b]	r^2 Adj
Oct. 2012	b_o	3.261	1.339	25.7	< **0.0001**	0.698
	b_1	-0.597	1.318	-5.0	< **0.0001**	
	b_2	-0.731	1.282	-6.8	< **0.0001**	
min[Apr. 2013,	b_o	2.435	1.511	13.6	< **0.0001**	0.662
May 2013]	b_1	0.078	1.295	0.7	0.478	
	b_2	-0.799	1.210	-9.6	< **0.0001**	

To quantitatively describe load-spreading effectiveness, the authors introduced the load-spreading effectiveness index (LEI) that is shown in the following equation:

$$LEI = \frac{\sigma_{SG(Bouss.)} - \sigma_{SG(Bur.)}}{\sigma_{SG(Bouss.)}},\ \sigma_{SG(Bouss.)} \geq \sigma_{SG(Bur.)} > 0$$

where LEI = load-spreading effectiveness index; $\sigma_{SG(Bouss.)}$ = distributed stress on subgrade using the Boussinesq solution; $\sigma_{SG(Bur.)}$ = distributed stress on subgrade using the Burmister solution. The lower limit for LEI is 0 (i.e., no load-spreading effect), and the upper limit for LEI is 1 (i.e., complete load-spreading effectiveness). Average test section subbase LEI equaled about 0.364 for October 2012 FWD testing, and average test section subbase LEI equaled about

0.070 for April 2013 FWD testing. As environmental test section condition transitioned from never-frozen to thaw-weakened, LEI decreased by about 5 times on average to the point where the load-spreading effect was nearly negligible. With decreased subbase load-spreading effectiveness, subgrade layers must endure higher levels of stress and therefore must experience greater amounts of deformation. Increased deformation from reduced subbase load-spreading effectiveness during thaw-weakening therefore results in the apparent softening of pavement foundations. So reduction of overall pavement foundation stiffness during thaw-weakening is likely the result of reduced load-spreading effectiveness, in addition to the saturation of unbound layers from freeze-thaw processes.

Summary

The following key findings from this comparison:

- Average test section composite elastic moduli (E_c) during October 2012 (i.e., never-frozen) FWD testing ranged from 37 MPa to 507 MPa. Test sections with Portland cement (PC) stabilized subgrade, fly ash stabilized subgrade, or PC stabilized reclaimed gravel subbase produced the highest E_c values. Test sections with mechanically stabilized subgrade, compacted subgrade, or untreated reclaimed gravel subbase produced comparatively high E_c values. Subbase and subgrade layer CBR values from DCP testing in October 2012 revealed test section stiffnesses that were consistent with FWD testing.
- Average test section composite elastic moduli (E_c) during April 2013 (i.e., thaw-weakened) FWD testing ranged from 11 MPa to 159 MPa. All test sections experience reductions in E_c values as conditions transitioned from never-frozen to thaw-weakened (by about 2 to 9 times on average). Test sections with PC stabilized subgrade or PC stabilized reclaimed gravel subbase produced the highest E_c values. Test sections with fly ash stabilized subgrade or untreated reclaimed gravel subbase produced relatively high E_c values as well. Similar to testing during the never-frozen condition, subbase and subgrade layer CBR values from DCP testing in April 2013 and May 2013 reflect FWD testing during April 2013.
- Correlations between thaw-weakened and never-frozen E_c values suggest that PC stabilized pavement foundations are less susceptible to thaw-weakening than untreated pavement foundations or fly ash stabilized pavement foundations. Because of a lack of data, DCP results could neither support nor oppose this claim. The authors recommend future research to investigate the claim further.
- There is no correlation between thaw-weakened and never-frozen subbase CBR values, so thaw-weakened subbase CBR is likely independent of never-frozen subbase CBR. However, there is a statistically significant correlation between thaw-weakened and never-frozen subgrade CBR values, so so never-frozen subgrade CBR is likely an indicator of thaw-weakened subgrade CBR.
- Never-frozen E_c correlated to both never-frozen subbase penetration index (PI) and never-frozen subgrade PI, while thaw-weakened E_c only correlated with thaw-weakened subgrade PI. Multivariable analyses that related E_c to subbase and subgrade layer PI showed with statistical significance that both subgrade and subbase layer stiffnesses account for overall pavement foundation stiffness during the never-frozen condition

(83.5% and 16.5%, respectively), while only subgrade layer stiffness account for overall pavement foundation stiffness during the thaw-weakened condition.

- Loss in subbase layer load-spreading effectiveness during thaw-weakening may explain why subbase layer stiffness does not contribute to overall pavement foundation stiffness during thaw-weakening. Application of Burmister stress distribution with backcalculated layer elastic moduli showed that the average distributed stress on the subgrade layer increased by about 1.5 times on average as conditions transitioned from never-frozen to thaw-weakened.
- The authors introduced the load-spreading effectiveness index (LEI), which ranges from 0 (no load-spreading effectiveness) to 1 (complete load-spreading effectiveness), to quantify the effectiveness of the subbase layer to distribute applied loading to the underlying subgrade layer. As conditions transitioned from never-frozen to thaw-weakened, subbase layer LEI decreased by about a factor of 5 from 0.364 to 0.070, so reduction of overall pavement foundation stiffness during thaw-weakening is likely the result of reduced load-spreading effectiveness.

Assessment of Drainage Properties

Drainage is an important component of pavement design and is critical in achieving good pavement performance. Pavement design engineers typically assume a minimum hydraulic conductivity value in design, primarily based on marginally accurate empirical relationships (see Zapata and Houston 2008, White et al. 2014) or limited laboratory testing. Virtually, no field verification is conducted to measure in situ hydraulic conductivity. Previous research has documented that the coefficient of variation (COV) of in situ hydraulic conductivity of pavement granular base layers can be in the range of 50% to 400% (see White et al. 2004, White et al. 2007). The lack of field verification during construction provide little confidence to the assumed design values and do not address the variability associated with this parameter.

Because aggregates can breakdown or degrade as a result of the compaction process, specifications for subbase placement typically restrict the number of roller passes and roller compaction effort. The Iowa DOT specification (Iowa DOT 2013) limits compaction to a maximum of three passes of a self-propelled non-vibratory steel or pneumatic roller. The roller compactive effort is required to be 150 to 200 pounds per lineal inch of contact surface. The underlying support conditions are not considered in the determination of the compaction limits.

Permeability Field Testing

To assess the influence of underlying support conditions, in situ APTs were conducted on three selected test sections (5th St. South, 8th St. South, and 11th St. North) surfaced with crushed limestone MSB layer. The support conditions consisted of PC stabilized subgrade with 11.4% PC (11th St. North), biaxial geogrid reinforcement at the subbase/subgrade interface (5th St. South), and compacted subgrade with no stabilization which served as a control (8th St. South). As indicated in the last chapter, MSB layer on all test sections were constructed in July 2012 and were compacted with vibratory smooth drum roller. Since construction, all test sections were

mapped using vibratory smooth drum intelligent compaction rollers for a total of 10 roller passes. APTs were conducted in a dense grid pattern at about 0.6 m to 1.0 m apart over a relatively small area (about 350 to 500 ft^2). K_{sat} results were used to conduct geostatistical semi-variogram analysis to quantify spatial variability and develop spatial contour maps for visualization. Samples of the subbase layer were obtained from a few test locations to conduct particle size analysis and compare with the variations observed in the K_{sat} values.

Photos taken while conducting APTs in these sections are shown in Figure 238. Representative DCP-CBR and cumulative blows with depth profiles from the three test sections from October 2012 and May 2013 testing are provided in Figure 239, for reference.

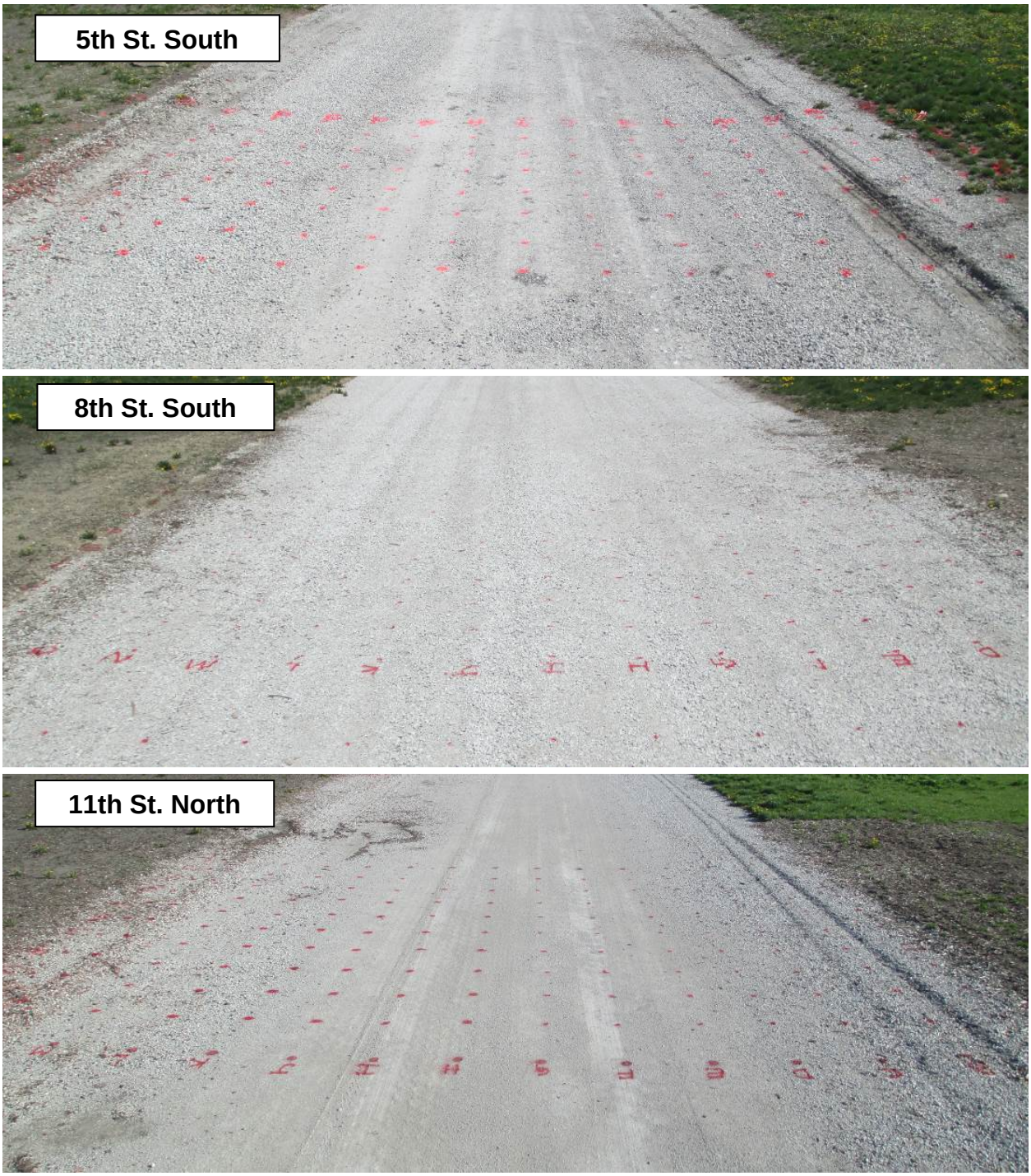

Figure 238. Photographs showing surface conditions during APT testing on the three test sections (May 2013)

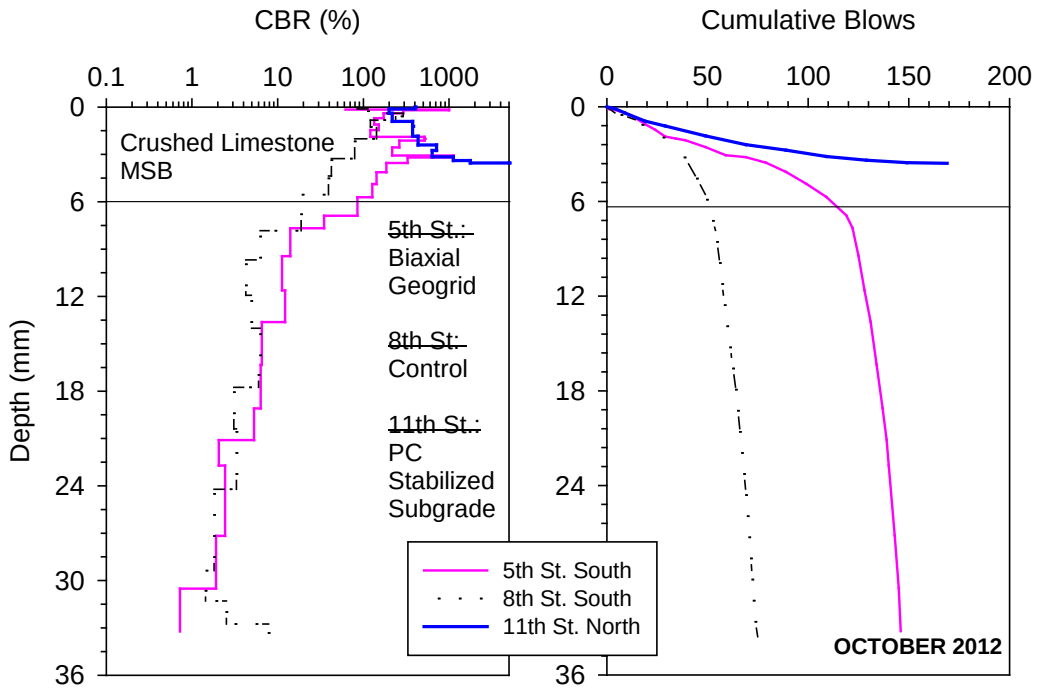

Figure 239. Representative DCP-CBR and cumulative blows profiles from the three test sections from October 2012 testing

Spatial Variability of Saturated Hydraulic Conductivity

Using the APT measurements obtained in a dense grid pattern from the test sections, the spatial variability of Ksat is quantified using geostatistical semivariogram analysis. The semivariogram $\gamma(h)$ is defined as one-half of the average squared differences between data values that are separated at a distance, h (Isaaks and Srivastava 1989). If this calculation is repeated for as many different values of h as the sample data will support, the result can be graphically presented as an experimental semi-variogram plot. Data points shown in Figure 240 are the experimental semi-variogram points for the three test sections. The K_{sat} values showed a skewed distribution, therefore, the data was transformed to determine log K_{sat} to determine the experimental semi-variogram (Clark and Harper 2002). A theoretical spherical variogram model was fit to the data, to define the spatial relationship between the values at specified distances. The mathematical expression to define the spherical model is shown as follows:

$$\gamma(h) = C_0 + C\left[\frac{3h}{2a} - \frac{h^3}{2a^3}\right] \text{ when } 0 < h < a \tag{9}$$

$$\gamma(h) = C_0 + C \text{ when } h > a \tag{10}$$

where, C_0 = nugget, $C + C_0$ = sill, a = range. The nugget is the value of semi-variogram on the y-axis, when h = 0. Nugget was observed as zero for the three test sections. Range is the distance at

which the semi-variogram reaches a plateau and sill is the semi-variogram at the range. The sill and range values are defined on Figure 242. More discussion on the theoretical models can be found elsewhere in the literature (e.g., Clark and Harper 2002, Isaaks and Srivastava 1989). For the results presented in this report the sill, range, and nugget values during theoretical model fitting were determined by checking the models for "goodness" using the modified Cressie goodness fit method (see Clark and Harper 2002) and cross-validation process (see Isaaks and Srivastava 1989). Comparatively, larger range and smaller sill values suggest greater spatial continuity or uniformity.

The range values were similar (varied between 10 and 13 ft) but the sill values were significantly different between the three test sections. The 8th St. South control section showed the lowest sill value (0.17) and the 5th St. South geogrid reinforced section showed the highest sill value (1.80). The average and COV of K_{sat} measurements are summarized in Figure 241 for the three sections. The COV values showed the same trend as the sill values with high COV on the 5th St. South section and low COV on the 8th St. South section.

In addition to quantifying spatial variability, semi-variogram can be used to predict values at unsampled locations based on values at sampled locations. Kriging is a stochastic interpolation procedure developed by Krige (1951), in which the variance of the difference between the predicted and "true" values is minimized using a semivariogram model. Kriging is used to create contour maps of K_{sat} values and are presented in the Figure 242.

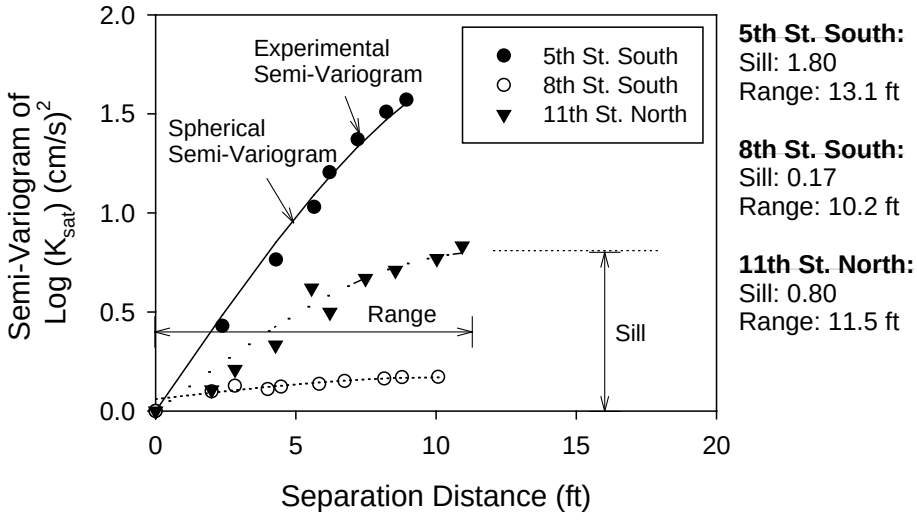

Figure 240. Semi-variograms of Log (K_{sat}) measurements on the three test sections

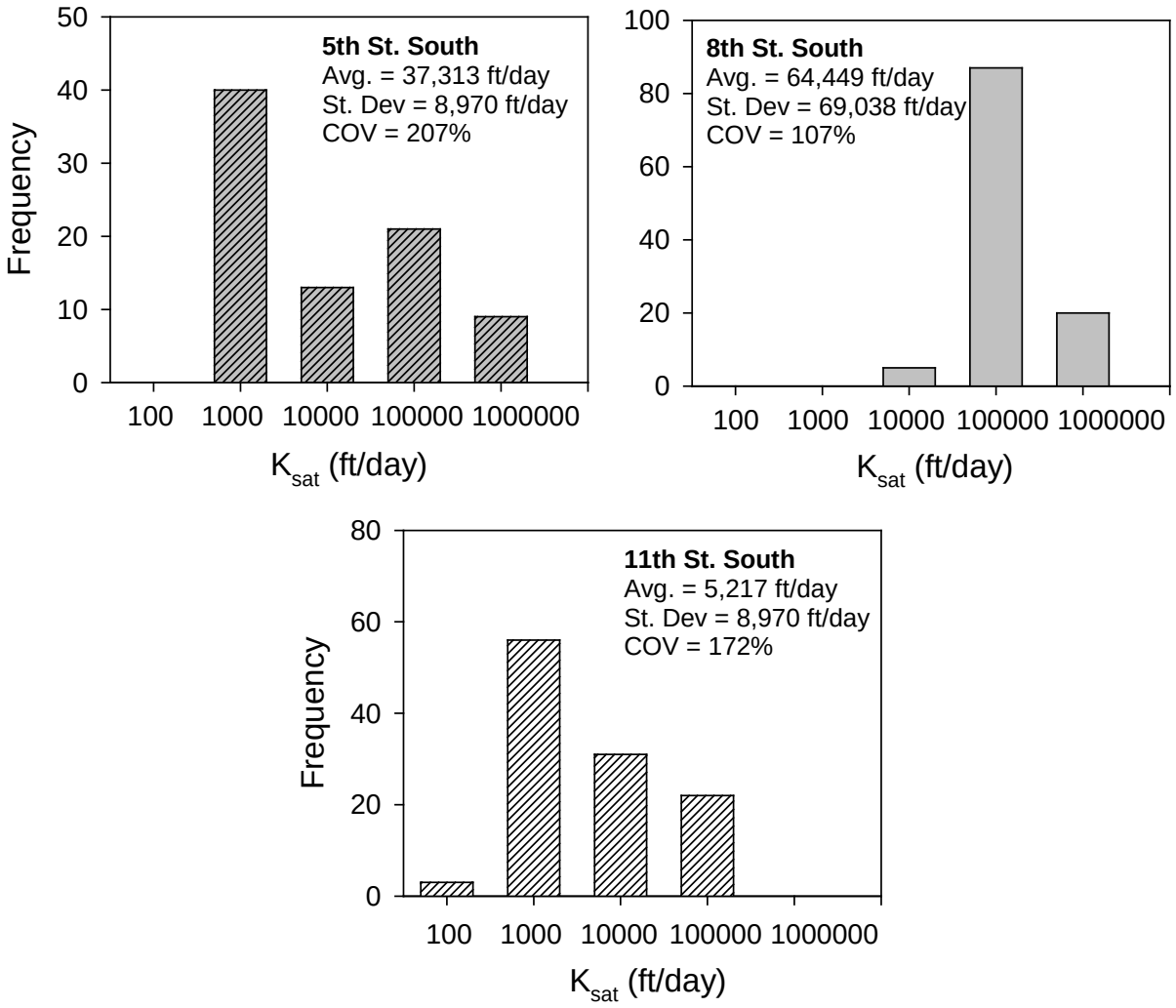

Figure 241. Histograms of K_{sat} measurements on the three test sections

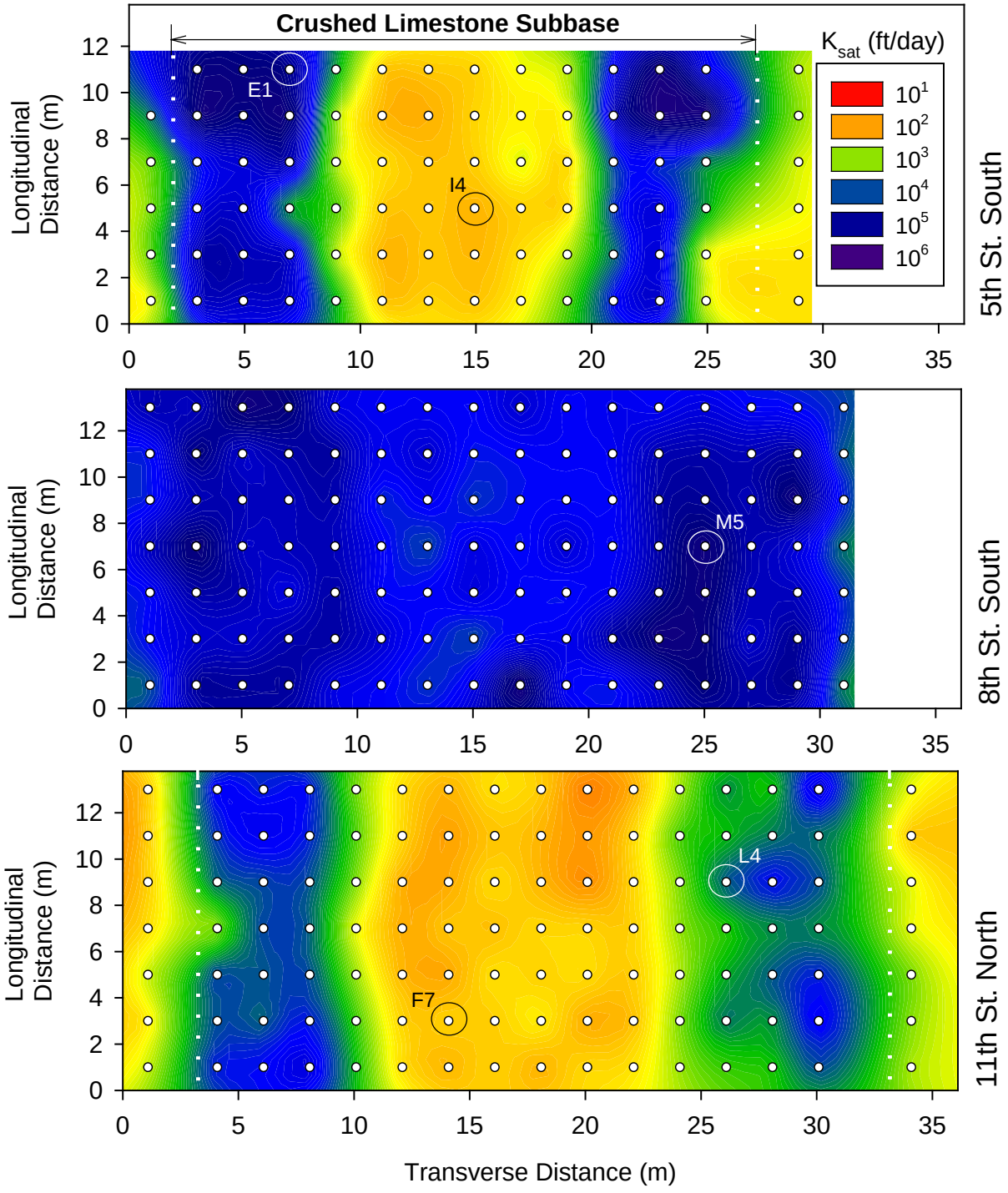

Figure 242. Kriged spatial contours of Ksat measurements on three test sections

Particle Size Analysis

Aggregate subbase material samples were obtained from 10 test locations in the three sections. Grain size distribution curves of five selected test locations with a circle around the test point in Figure 242 are provided in Figure 243. Pictures of these samples are shown in Figure 244. Comparison of grain size analysis results and gradation paramters with K_{sat} values at these test locations indicate that the K_{sat} values were lower at locations where the materials were relatively well-graded and contained high amount of fines content.

Relationship between percent passing the No. 200 (F_{200}), No. 100 (F_{200}), and No. 40 (F_{200}) sieves and Ksat, is provided in Figure 245. Similarly, relationship between gradation parameter D_{30} (i.e., particle diameter corresponding to 30% passing) and K_{sat} is provided in Figure 246. Statistically signinficant relationship with an exponential trend was observed between these gradation parameters and K_{sat}.

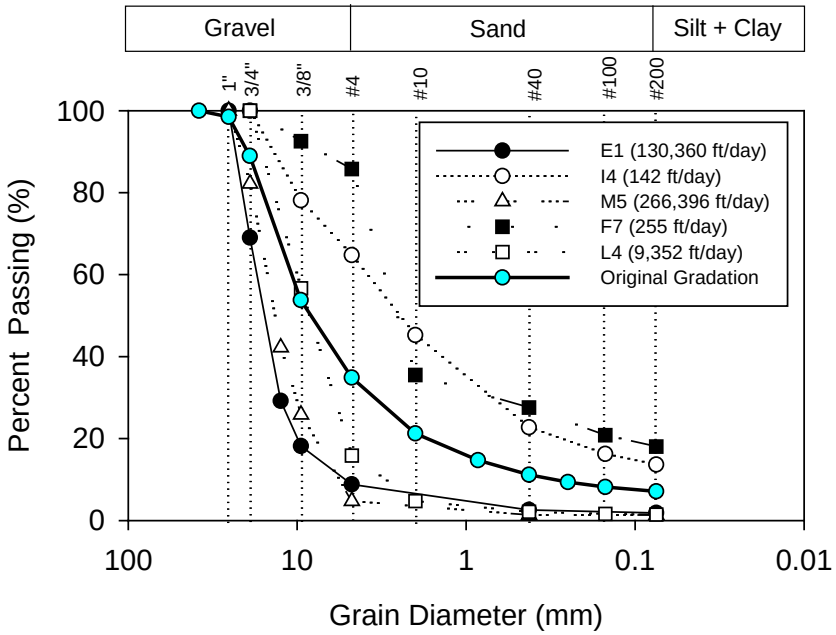

Figure 243. Particle size analysis of samples collected from different test locations

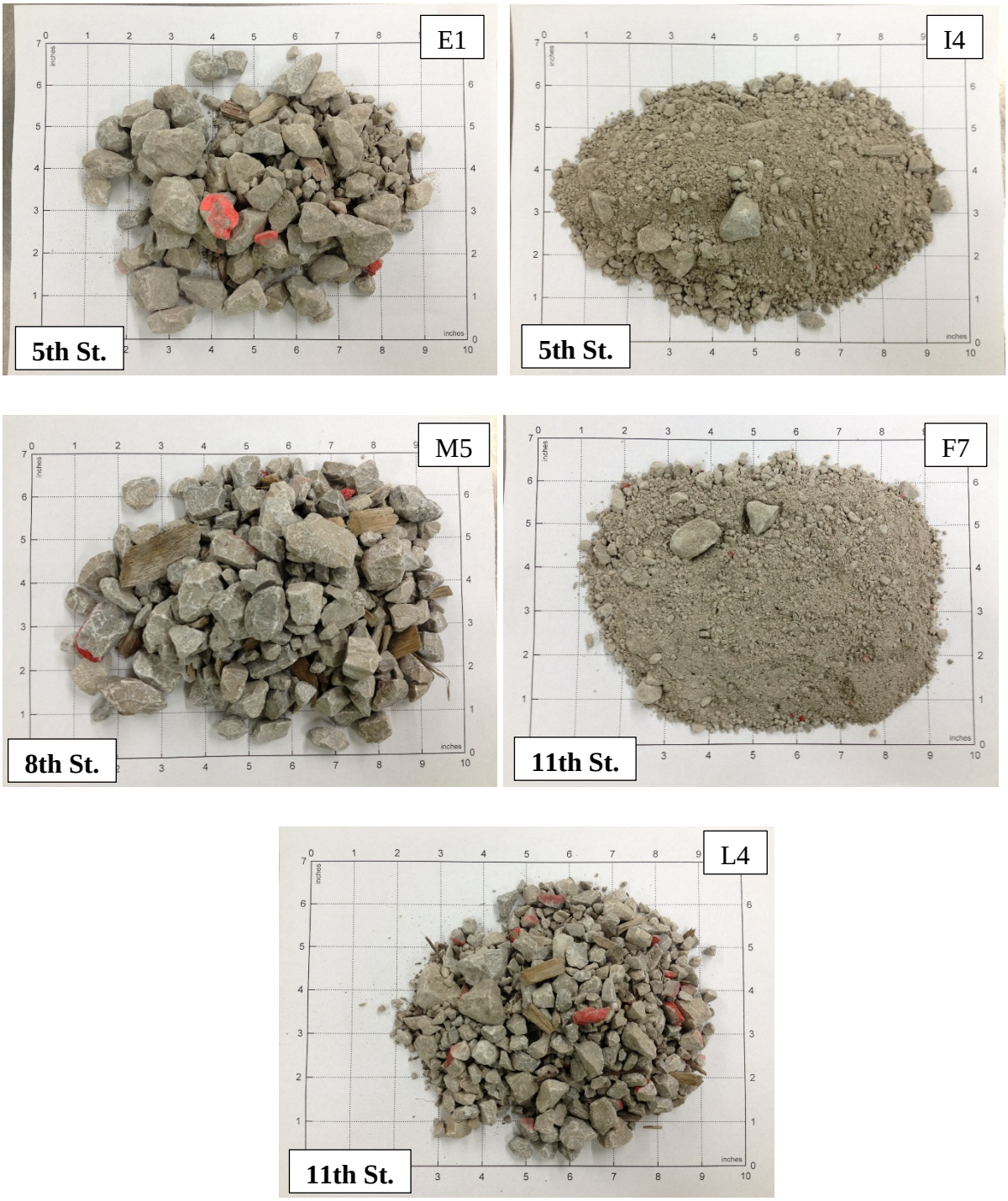

Figure 244. Pictures of samples collected from the three test sections

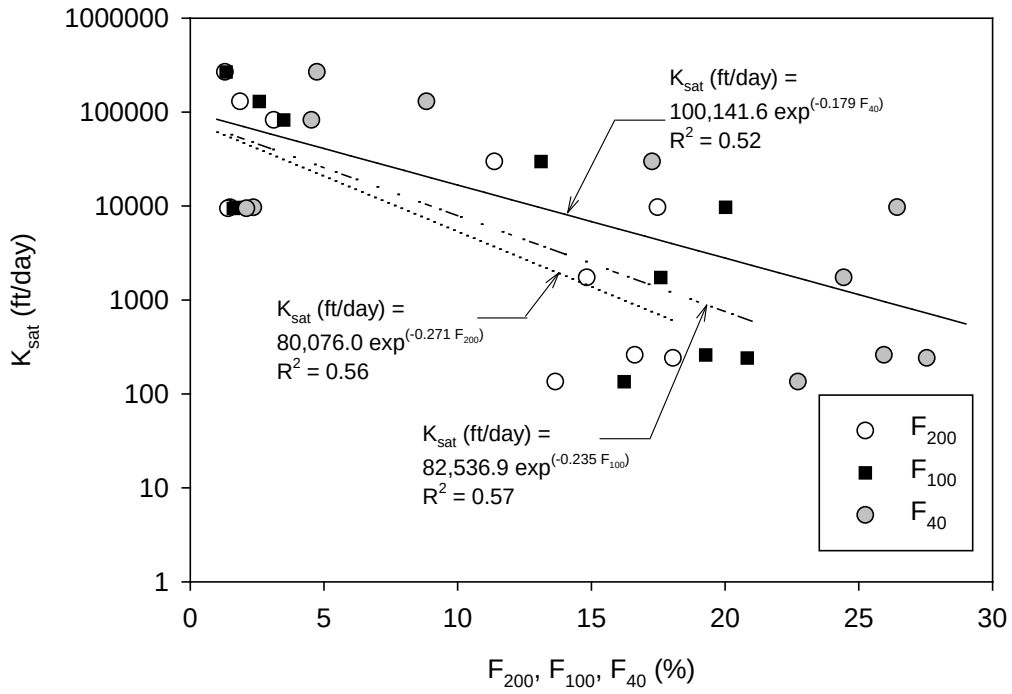

Figure 245. Relationship between percent fines passing No. 200, No. 100, and No. 40 sieves and K_{sat}

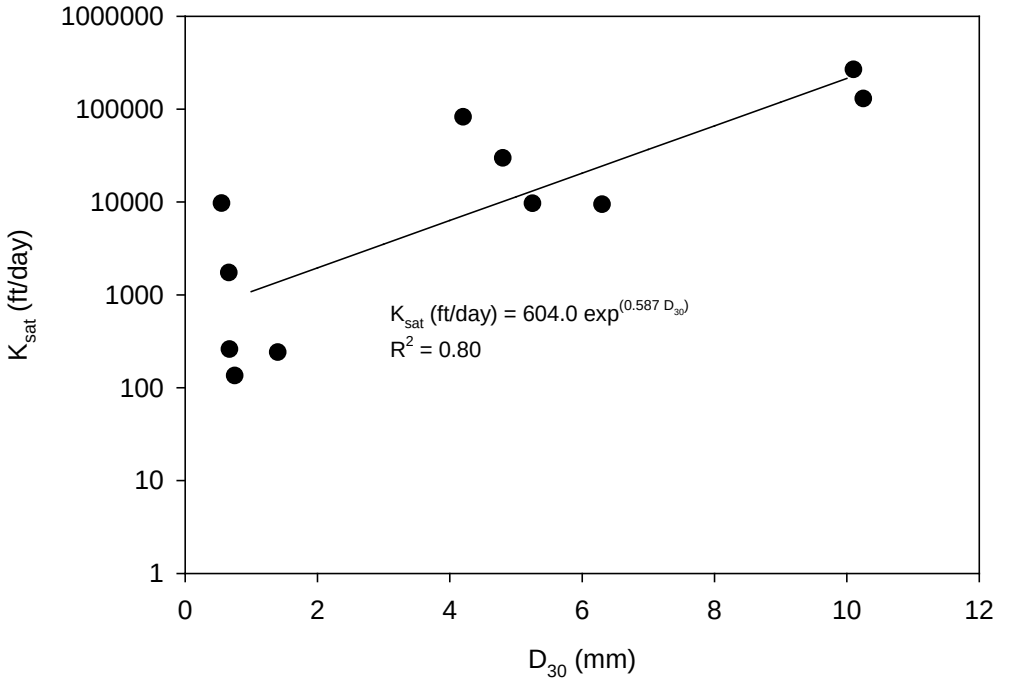

Figure 246. Relationship between D_{30} and K_{sat}

Summary

The findings presented above show relationships between in situ hydraulic conductivity, foundation support conditions, and gradation of the subbase material. The subbase layer for each of the three test sections was compacted with a vibrator smooth drum roller, which contributed to the aggregate degradation. Degradation varied, however, between sections and appears to be linked to the foundation support conditions. The section with the highest support values (i.e, high CBR values) was the cement stabilized subgrade showed the highest degradation of the aggregate subbase and the lowest hydraulic conductivity. The control section yielded the lowest support values, but the highest hydraulic conductivity. The geogrid reinforced aggregate section provided high support conditions and intermediate hydraulic conductivity values. The results demonstrate that the performance of pavement foundation sections from a stiffness and drainage perspective are variable and require detailed testing to fully characterize the behavior. By better characterizing the engineering properties, it is envisioned that construction specifications could be shifted from prescriptive (i.e., limits on roller passes, etc.) to performance specifications.

CHAPTER 8: PAVEMENT CONSTRUCTION, TESTING, AND RICM DATA ANALYSIS

Description of Surface Layer Details in Each Section

Phase II construction, which occurred in summer 2013, involved placing a 102 mm thick asphalt base course layer and a 51 mm thick asphalt surface course layer. Test section surface and base course layer asphalt mixes comprised different combinations of either warm mix or hot mix binder and either low or high absorption aggregate. Table 20 details the binder and aggregate types used in the test section asphalt pavement layers. All test section asphalt pavement layers were compacted using a Hamm HD+ 120 VV dual smooth-drum vibratory roller equipped with RICM technology (Figure 247).

Statistical Methods for Analysis

Statistical methods used in this report include the first-order, variance-based sensitivity analyses of multivariable models and the comparison of measurement method agreement. Statistical significance in this study was based on an alpha value of 0.05 (i.e., 95% confidence).

First-order, variance-cased sensitivity analysis

The authors of this report developed multivariable models to empirically predict HMV measurements from subbase FWD composite moduli [$E_{FWD(SB)}$] and asphalt pavement moduli (E_{AP}). First-order, variance-based sensitivity analyses of the multivariable models assessed the sensitivity of HMV measurements to changes $E_{FWD(SB)}$ and E_{AP}. Per Sobol' (1990), the influences of $E_{FWD(SB)}$ and E_{AP} on HMV measurements were quantified using sensitivity indices (S) that are calculated from following equations:

$$S_i = \frac{V_i}{V_Y} \tag{5.6}$$

$$V_Y = \sum_{i=1}^{N} V_i \tag{5.7}$$

where S_i = sensitivity index of i^{th} independent variable; V_i = partial variance of i^{th} independent variable; V_Y = total unconditional variance; and N = number of independent variables. The summation of all sensitivity indices for a given model must equal unity (Sobol', 1990); therefore the authors interpreted sensitivity index for each independent variable as the percent influence of the independent variable on the predicted dependent variable.

Table 20. Descriptions of test section pavement cross-sections

Pavement Layers by Test Section		Layer Description
TS-W	Asphalt Surface Course	51 mm warm mix asphalt binder with low absorption aggregate
	Asphalt Base Course	102 mm warm mix asphalt binder with low absorption aggregate
	Subbase Layer	152 mm modified subbase[a] underlain by woven geotextile fabric
	Subgrade Layer	Natural subgrade[b]
TS-NW	Asphalt Surface Course	51 mm warm mix asphalt binder with low absorption aggregate
	Asphalt Base Course	102 mm warm mix asphalt binder with low absorption aggregate
	Subbase Layer	152 mm modified subbase[a] underlain by non-woven geotextile fabric
	Subgrade Layer	Natural subgrade[b]
TS-BX	Asphalt Surface Course	51 mm warm mix asphalt binder with low absorption aggregate
	Asphalt Base Course	102 mm warm mix asphalt binder with low absorption aggregate
	Subbase Layer	152 mm modified subbase[a] underlain by biaxial polymer geogrid
	Subgrade Layer	Natural subgrade[b]
TS-TX	Asphalt Surface Course	51 mm warm mix asphalt binder with low absorption aggregate
	Asphalt Base Course	102 mm warm mix asphalt binder with low absorption aggregate
	Subbase Layer	152 mm modified subbase[a] underlain by triaxial polymer geogrid
	Subgrade Layer	Natural subgrade[b]
TS-PCSB	Asphalt Surface Course	51 mm hot mix asphalt binder with high absorption aggregate
	Asphalt Base Course	102 mm hot mix asphalt binder with low absorption aggregate
	Subbase Layer	152 mm modified subbase[a] underlain by152 mm reclaimed subbase[c] stabilized with 5% Portland cement
	Subgrade Layer	Natural subgrade[b]
TS-NSG	Asphalt Surface Course	51 mm warm mix asphalt binder with high absorption aggregate
	Asphalt Base Course	102 mm hot mix asphalt binder with low absorption aggregate
	Subbase Layer	152 mm modified subbase[a]
	Subgrade Layer	Natural subgrade[b]
TS-CSG	Asphalt Surface Course	51 mm warm mix asphalt binder with high absorption aggregate
	Asphalt Base Course	102 mm hot mix asphalt binder with low absorption aggregate
	Subbase Layer	152 mm modified subbase[a]
	Subgrade Layer	305 mm compacted subgrade[b] underlain by natural subgrade[b]
TS-FASG	Asphalt Surface Course	51 mm warm mix asphalt binder with high absorption aggregate
	Asphalt Base Course	102 mm warm mix asphalt binder with low absorption aggregate
	Subbase Layer	152 mm modified subbase[a]
	Subgrade Layer	305 mm compacted subgrade[b] stabilized with 20% fly ash underlain by natural subgrade[b]
TS-PCSG	Asphalt Surface Course	51 mm warm mix asphalt binder with high absorption aggregate
	Asphalt Base Course	102 mm warm mix asphalt binder with low absorption aggregate
	Subbase Layer	Synthetic subsurface drainage layer[d] underlain by 152 mm modified subbase[a]
	Subgrade Layer	305 mm compacted subgrade[b] stabilized with 10% Portland cement underlain by natural subgrade[b]

[a]Modified subbase classifies as GP-GM (A-1-a)
[b]Compacted/natural subgrade classifies as CL [A-6(5)]
[c]Reclaimed subbase classifieds as SM (A-1-a)
[d]Synthetic subsurface drainage layer included in northernmost 175 m portion of 205 m long test section

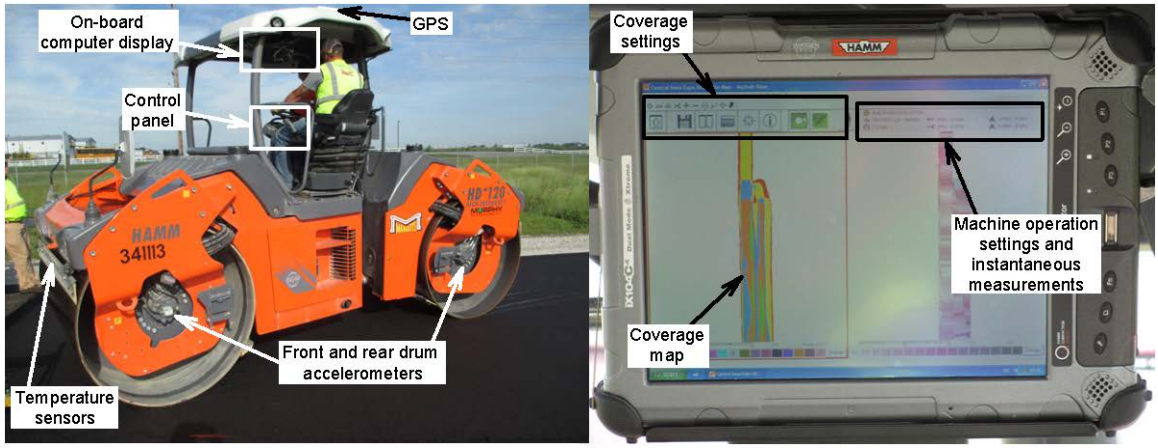

Figure 247. (a) Hamm HD+ 120 VV dual smooth-drum vibratory roller used to compact test section asphalt base course and surface course layers; (b) on-board computer that recorded RICM measurements, which the operator viewed in real time

Agreement between Different Measurement Methods

Comparisons between two indirect methods of measurement are oftentimes misleading because both methods are expected to generate measurement error, so Bland & Altman (1999) recommend comparing measurement agreement instead of correlating measurements with one another. Bland Altman plots graphically represent measurement agreement by plotting difference in measurements versus average of measurements, and measurement agreement limits quantify measurement agreement. If the difference in measurements distributes uniformly, then the measurement agreement limits are calculated from equation 5.8.

$$AL = \bar{d} \pm sZ_{\alpha/2} \tag{5.8}$$

where AL = agreement limits; $\bar{d}$ = mean of difference in measurements; s = standard deviation of difference in measurements; and $Z_{\alpha/2}$ = two-tailed standard score for a given alpha value. Bland & Altman (1999) detail a regression-based approach for calculating agreement limits when the difference in measurements distributes nonuniformly.

Influence of Underlying Layer on HMV

Figure 248 presents boxplot comparisons of HMV_{SB} and final pass HMV_{BC} and HMV_{SC} for each test section along the centerline, and Table 21 summarizes the average and coefficient of variation values for the HMV_{SB} and final pass HMV_{BC} and HMV_{SC} measurements by test section. On average, HMV_{SB} ranges from 7 to 67, HMV_{BC} ranges from 8 to 24, and HMV_{SC} ranges from 21 to 48.

Test section pavement foundations ranged from soft to very stiff, as evidenced by average FWD moduli measured on top of subbase layers [$E_{FWD(SB)}$] (Table 21). Average $E_{FWD(SB)}$ values on stiff pavement foundation test sections (TS-PCSB, TS-FASG, and TS-PCSG) ranged from 280 to 507 MPa, and average $E_{FWD(SB)}$ values on soft pavement foundation test sections (TS-W, TS-NW, TS-BX, TS-TX, TS-CSG, and TS-NSG) ranged from 43 MPa to 122 MPa.

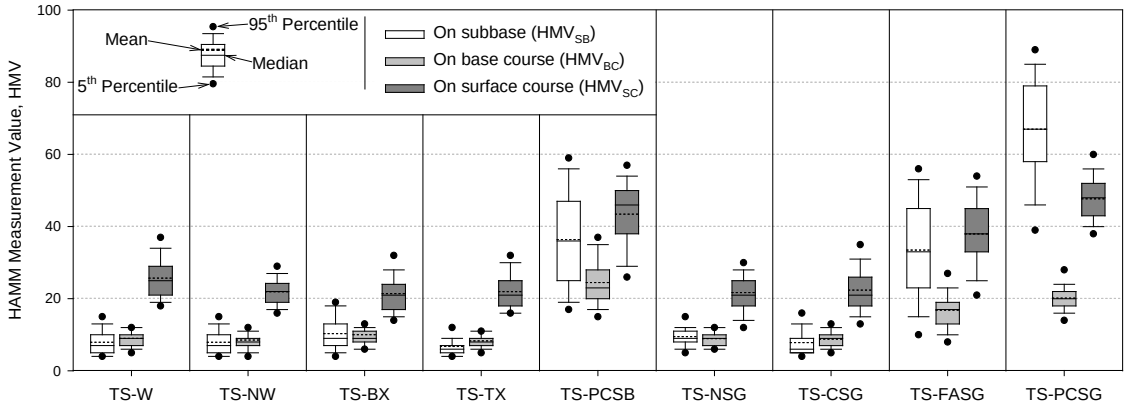

Figure 248. Comparisons of pre-construction HMV measured on subbase, final pass HMV measured on base course, and final pass HMV measured on surface course along centreline each test section

Table 21. Summary Statistics of RICM and FWD Measurements on Each Test Section

Test Section	Average HMV on Subbase, HMV_{SB} [COV (%)]	Average HMV on Base Course, HMV_{BC} [COV (%)]	Average HMV on Surface Course, HMV_{SC} [COV (%)]	Average E_{FWD} on Subbase, $E_{FWD(SB)}$ (MPa) [COV (%)]	Average E_{FWD} on Surface Course, $E_{FWD(SC)}$ (MPa) [COV (%)]	Average Asphalt Pavement Modulus, E_{AP} (MPa) [COV (%)]
TS-W	8 [43]	9 [36]	26 [22]	74 [27]	277 [19]	7077 [76]
TS-NW	7 [23]	9 [69]	22 [21]	95 [28]	268 [33]	3755 [80]
TS-BX	10 [48]	10 [95]	21 [26]	103 [29]	219 [16]	1537 [64]
TS-TX	7 [37]	8 [64]	22 [25]	122 [28]	215 [16]	994 [64]
TS-PCSB	36 [38]	24 [26]	43 [21]	280 [16]	594 [14]	3429 [33]
TS-NSG	9 [36]	9 [58]	22 [35]	43 [41]	181 [19]	7140 [109]
TS-CSG	8 [48]	9 [26]	22 [29]	103 [27]	248 [18]	2773 [98]
TS-FASG	33 [42]	17 [33]	38 [27]	324 [21]	478 [21]	1252 [39]
TS-PCSG	67 [23]	20 [22]	48 [13]	507 [28]	415 [17]	385 [32]

In general, stiff pavement foundation test sections differed from soft pavement foundation test sections in that the stiff pavement foundation test sections yielded significantly higher HMV_{SB}, HMV_{BC}, and HMV_{SC} measurements. On stiff pavement foundation test sections, average HMV_{SB} ranged from 33 to 67, average HMV_{BC} ranged from 17 to 24, and HMV_{SC} ranged from 38 to 48; and, on soft pavement foundation test sections, average HMV_{SB} ranged from 7 to 10, average

HMV_{BC} ranged from 8 to 10, and HMV_{SC} ranged from 21 to 26. Therefore, HMV measured during asphalt pavement construction reflects the stiffness of underlying pavement foundation.

Table 22 summarizes statistical comparisons between HMV_{SB}, HMV_{BC}, and HMV_{SC} by test section. In general, HMV measurements on soft pavement foundation test sections increase with each additional layer (i.e., $HMV_{SC} > HMV_{BC} > HMV_{SB}$). However, stiff pavement foundation layer HMV decreases from subbase to base course (i.e., $HMV_{SB} > HMV_{BC}$) and then increases from base course to surface course (i.e., $HMV_{SC} > HMV_{BC}$). TS-PCSG [average $E_{FWD(SB)}$ equalled 507 MPa] was an exception in that HMV_{SB} significantly exceeded both HMV_{BC} and HMV_{SC}.

Table 22. Statistical comparisons of HMVSB, HMVBC, and HMVSC on each test Section

Test Section	HMV value Comparison	Mean Difference	Standard Error Difference	Mean Difference 95% Confidence Limits Lower Bound	Upper Bound	p Value[a]
TS-W	$HMV_{SC} - HMV_{SB}$	17.79	0.14	17.46	18.12	**< 0.0001**
	$HMV_{SC} - HMV_{BC}$	16.71	0.17	16.31	17.11	**< 0.0001**
	$HMV_{BC} - HMV_{SB}$	1.08	0.16	0.70	1.46	**< 0.0001**
TS-NW	$HMV_{SC} - HMV_{SB}$	14.71	0.15	14.35	15.07	**< 0.0001**
	$HMV_{SC} - HMV_{BC}$	13.39	0.18	12.99	13.81	**< 0.0001**
	$HMV_{BC} - HMV_{SB}$	1.31	0.16	0.94	1.68	**< 0.0001**
TS-BX	$HMV_{SC} - HMV_{SB}$	11.13	0.22	10.62	11.64	**< 0.0001**
	$HMV_{SC} - HMV_{BC}$	11.401	0.26	10.81	12.01	**< 0.0001**
	$HMV_{BC} - HMV_{SB}$	-0.28	0.24	-0.85	0.29	0.492
TS-TX	$HMV_{SC} - HMV_{SB}$	15.21	0.14	14.88	15.55	**< 0.0001**
	$HMV_{SC} - HMV_{BC}$	13.64	0.18	13.22	14.06	**< 0.0001**
	$HMV_{BC} - HMV_{SB}$	1.57	0.16	1.19	1.95	**< 0.0001**
TS-PCSB	$HMV_{SC} - HMV_{SB}$	7.08	0.37	10.84	12.97	**< 0.0001**
	$HMV_{SC} - HMV_{BC}$	18.99	0.49	17.84	20.13	**< 0.0001**
	$HMV_{BC} - HMV_{SB}$	-11.91	0.45	-12.97	-10.84	**< 0.0001**
TS-NSG	$HMV_{SC} - HMV_{SB}$	12.22	0.21	11.72	12.72	**< 0.0001**
	$HMV_{SC} - HMV_{BC}$	12.78	0.23	12.25	13.30	**< 0.0001**
	$HMV_{BC} - HMV_{SB}$	-0.55	0.22	-1.06	-0.04	**0.032**
TS-CSG	$HMV_{SC} - HMV_{SB}$	14.56	0.15	14.21	14.92	**< 0.0001**
	$HMV_{SC} - HMV_{BC}$	13.59	0.18	13.16	14.01	**< 0.0001**
	$HMV_{BC} - HMV_{SB}$	0.98	0.16	0.601	1.34	**< 0.0001**
TS-FASG	$HMV_{SC} - HMV_{SB}$	4.45	0.38	3.60	5.39	**< 0.0001**
	$HMV_{SC} - HMV_{BC}$	21.15	0.41	20.20	22.11	**< 0.0001**
	$HMV_{BC} - HMV_{SB}$	-4.45	0.38	-5.39	-3.60	**< 0.0001**
TS-PCSG	$HMV_{SC} - HMV_{SB}$	-19.30	0.47	-20.41	-18.19	**< 0.0001**
	$HMV_{SC} - HMV_{BC}$	27.55	0.57	26.21	28.88	**< 0.0001**
	$HMV_{BC} - HMV_{SB}$	-46.85	0.48	-47.97	-45.73	**< 0.0001**

Note: [a]Emboldened p values indicate statistical significance

Differences in HMV_{SB}, HMV_{BC}, and HMV_{SC} were all statistically significant across the test sections, except the comparison of HMV_{SB} and HMV_{BC} on TS-BX (p = 0.49). Additional t testing showed that HMV_{SB} on TS-BX was significantly greater than HMV_{SB} on all other soft pavement foundation test sections (all p values were less than 0.0001), even though $E_{FWD(SB)}$ on TS-BX

(equaled 103 MPa) was not substantially greater than all other soft pavement foundation $E_{FWD(SB)}$ values. Therefore, the biaxial polymer geogrid underlying the TS-BX subbase may have influenced HMV measurements on that test section.

Figure 249 presents a scatterplot matrix for associations between spatially paired HMV_{SB}, final pass HMV_{BC}, and final pass HMV_{SC} measurements across the test sections. In general, HMV_{SB}, HMV_{BC}, and HMV_{SC} all positively correlated with one another. Because HMV_{SB} did not distribute normally (skewed right), nonlinear equations best fit the associations between HMV_{SB} and HMV_{BC} ($r^2 = 0.55$) and between HMV_{SB} and HMV_{SC} ($r^2 = 0.58$). The distributions for both HMV_{BC} and HMV_{SC} were approximately normal, so a linear equation best fit the association between HMV_{BC} and HMV_{SC} ($r^2 = 0.52$). Results from the regression analyses are consistent with findings from White and Vennapusa (2008) and further demonstrate how underlying layers influence HMV measured during asphalt pavement construction.

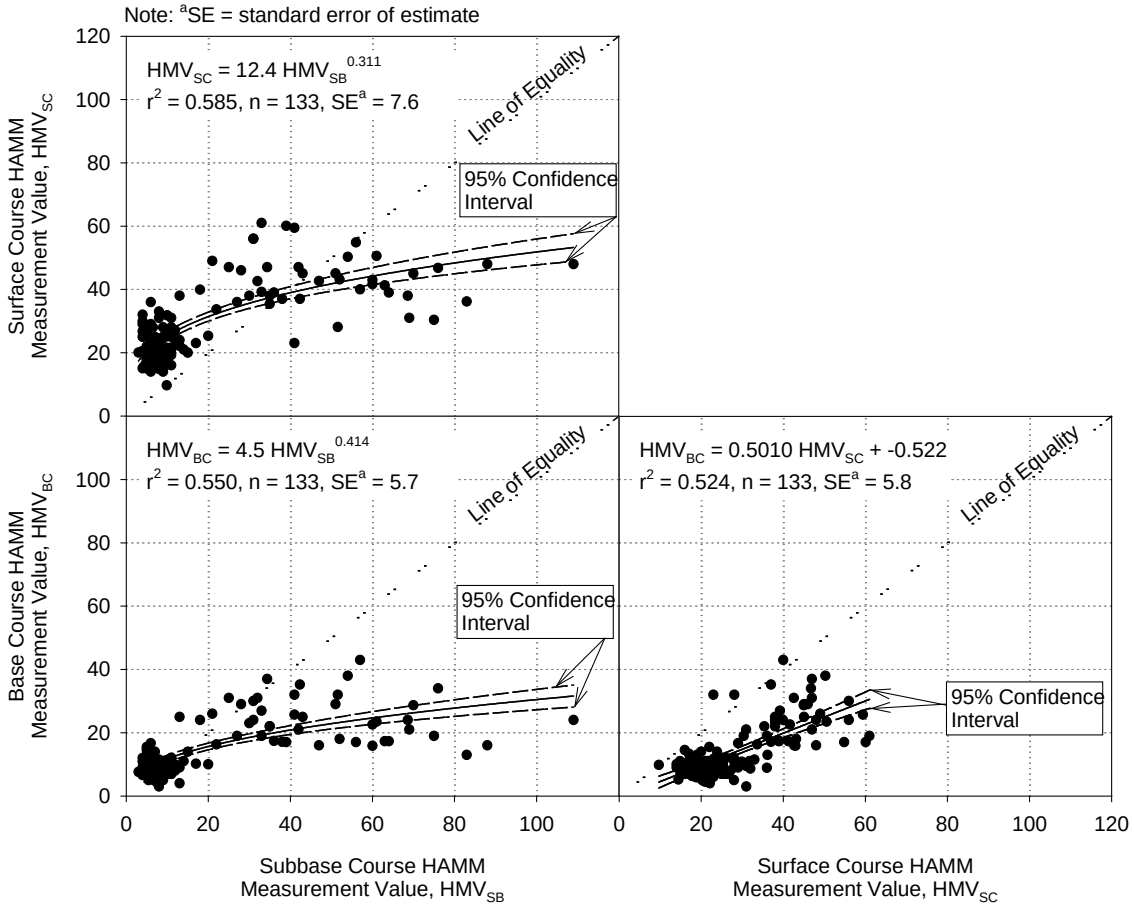

Figure 249. Scatter plot matrix for correlations between subbase HMV, asphalt base course HMV, and surface course HMV

Comparisons between RICM and QC spot test methods

During asphalt base course layer construction, RC_{NG} and T_{FLIR} in situ spot measurements with increasing roller pass number were obtained at a single location within each test section. The in situ testing process was repeated for asphalt surface course layer construction, although tests were conducted at separate locations within the test sections. GPS coordinates were obtained for each in situ spot test location to spatially pair RC_{NG} and T_{FLIR} measurements with RICM data.

Comparison of HMV with Nuclear Density Gauge Relative Compaction

Figure 250 presents asphalt base and surface course RC_{NG} and HMV measurements with increasing roller pass number for all of the test sections combined. For both base course and surface course asphalt layers, RC_{NG} increased with increasing roller pass number. Hyperbolic models best fit the associations between base course RC_{NG} [$RC_{NG(BC)}$] and roller pass number (r^2 = 0.83) and between surface course RC_{NG} [$RC_{NG(SC)}$] and roller pass number (r^2 = 0.90).

Although asphalt layers quite evidently densify with additional compactive effort, there is little to no change in HMV with increasing roller pass numbers. No statistically significant correlation exists between HMV_{BC} and number of roller passes, and a slight correlation exists between HMV_{SC} and number of roller passes (r^2 = 0.16). Interpretation of Figure 250 suggests that HMV measurements do not strongly associate with RC_{NG}, so the authors used data from all test sections to conduct regression analyses (Table 5.5) between HMV_{BC} and $RC_{NG(BC)}$ and between HMV_{SC} and $RC_{NG(SC)}$, and, as suspected, neither regression analysis yielded a statistically significant correlation.

However, Vennapusa et al. (2013) noted that relative compaction and RICM measurements do not correlate well with one another when data sets comprise heterogeneous underlying layer conditions (e.g., data combined from multiple test locations). Therefore, regression analyses between $RC_{NG(BC)}$ and HMV_{BC} and between $RC_{NG(SC)}$ and HMV_{SC} by test section are summarized in Table 23. On the sole basis of r^2 value, the majority of regression analyses did not yield statistically significant correlations; however, r^2 values for certain test sections were considerably large (e.g., r^2 equalled 0.89 for TS-PCSB base course). Despite the occasional large r^2 value, F-tests indicated that only one of the correlations (TS-PCSG) was statistically significant because, in general, the test section regression analyses had insufficient amounts of degrees of freedom. So, neither base course nor surface course HMV adequately predicts its respective RC_{NG}, even after data sets representing the entire project site were separated and grouped together by test section.

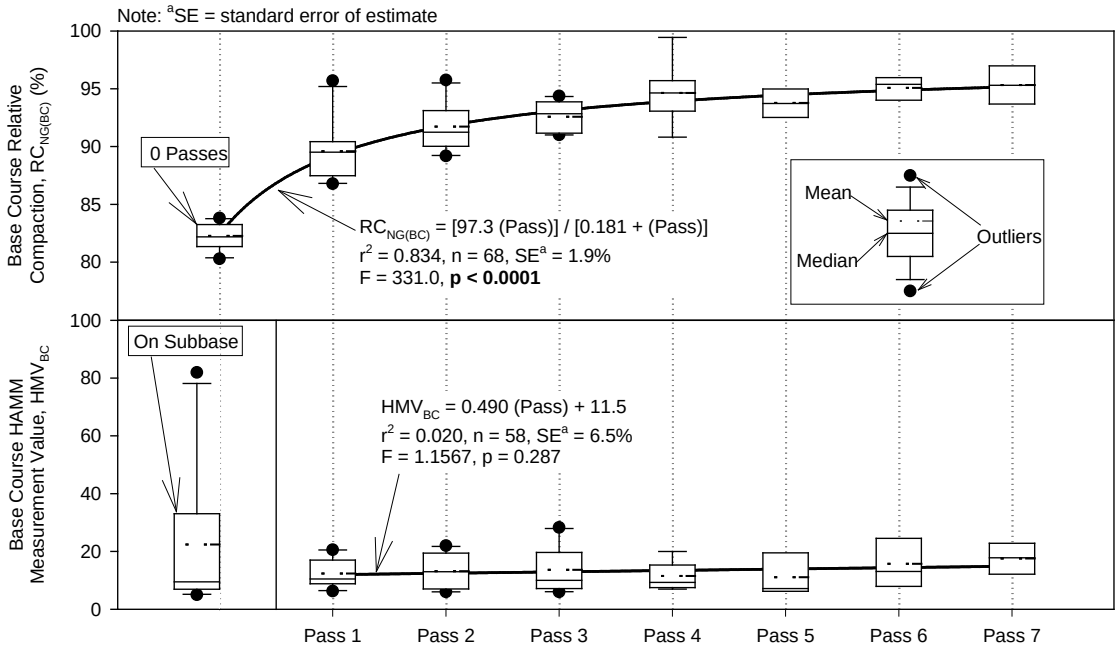

(a)

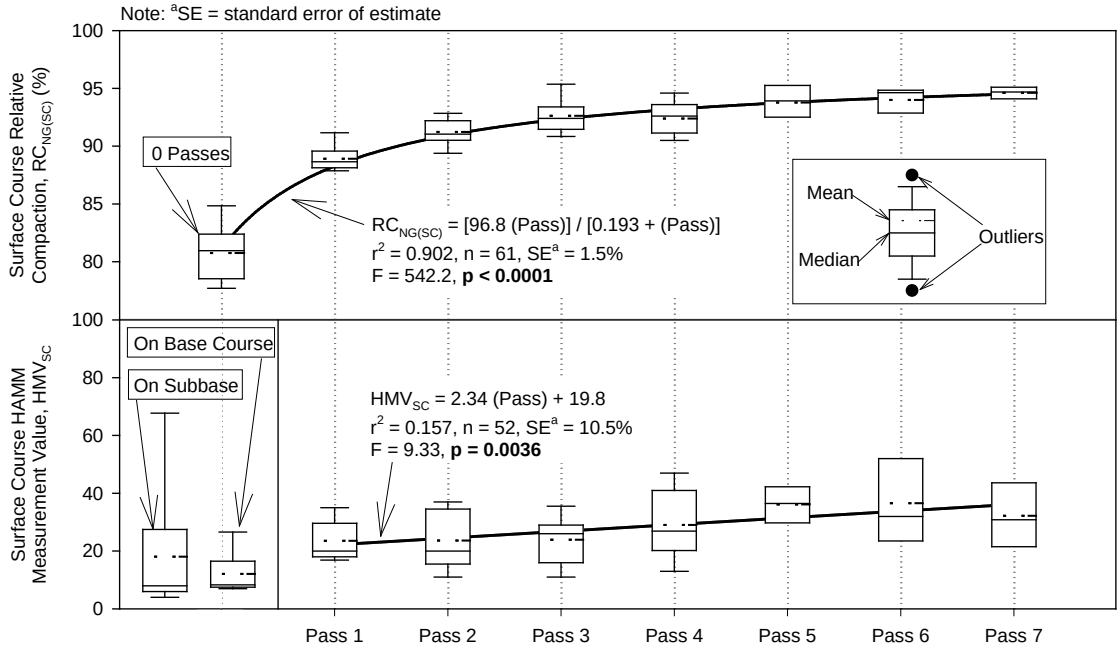

(b)

Figure 250. Comparison of relative compaction with HMV with increasing roller pass number for (a) asphalt base course layer and (b) asphalt surface course layer

Table 23. Correlations of RCNG(BC) with HMVBC and RCNG(SC) with HMVSC for each test section and combined test sections

		Estimated Parameters					
Asphalt Layer	Test Section	a	b	n	r^2	F Ratio	p value[b]
Base Course[a]	All test sections	1.952	0.015	54	0.054	2.98	0.090
	TS-W	2.096	-0.148	4	0.850	11.35	0.078
	TS-NW	1.958	0.003	7	0.007	0.03	0.861
	TS-BX	1.934	0.034	6	0.099	0.44	0.544
	TS-TX	1.973	-0.014	5	0.006	0.02	0.904
	TS-PCSB	1.445	0.409	3	0.886	7.75	0.220
	TS-NSG	1.992	-0.023	5	0.050	0.16	0.717
	TS-CSG	1.933	0.043	9	0.115	0.91	0.372
	TS-FASG	1.976	-0.006	7	0.001	0.01	0.945
	TS-PCSG[c]	1.839	0.114	8	0.368	3.49	0.111
Surface Course[d]	All test sections	1.948	0.013	60	0.049	3.01	0.088
	TS-W	1.830	0.093	4	0.697	4.61	0.165
	TS-NW	1.956	0.010	5	0.011	0.03	0.868
	TS-BX	1.982	-0.017	4	0.607	3.09	0.221
	TS-TX	1.526	0.309	4	0.427	1.49	0.346
	TS-PCSB	1.931	0.025	11	0.054	0.52	0.490
	TS-NSG	1.992	-0.023	5	0.050	0.16	0.717
	TS-CSG	1.967	0.052	9	0.000	0.00	0.958
	TS-FASG	1.979	-0.007	8	0.002	0.01	0.912
	TS-PCSG[c]	1.887	0.051	8	0.775	20.67	**0.004**

[a]$\log[RC_{NG(BC)}] = a + b \log(HMV_{BC})$
[b]Emboldened p values indicate statistical significance
[c]Testing conducted on portion of test section with synthetic subsurface drainage layer
[d]$\log[RC_{NG(SC)}] = a + b \log(HMV_{SC})$

Comparison between Roller-Integrated Temperature Sensor and FLIR Thermal Camera Asphalt Surface Temperature Measurements

According to West et al. (2010); mix temperature is one of the primary factors affecting asphalt pavement compactability. Asphalt mix temperature must be high enough for the binder to act as a lubricant, thereby facilitating the movement of aggregates in a dense configuration. In addition, asphalt mixes become stiffer and more resistant to compaction with decreasing mix temperature (Roberts et al. 1996). Therefore, control of asphalt mix temperature is critical to the construction of quality pavements.

Figure 251a presents the Bland Altman plot comparing asphalt surface temperatures measured from the roller-integrated temperature sensors (T_{Roller}) and from the FLIR thermal camera (T_{FLIR}). There was an apparent relationship between temperature measurement difference and average temperature measurement, so the authors logarithmically transformed the temperature measurement data as recommended by Bland and Altman (1999). Despite the logarithmic

transformation, the relationship remained (r^2 = 0.38) so the authors used the regression-based approach detailed by Bland and Altman (1999) to develop the agreement interval. In general, T_{Roller} measurements tended to be lower than T_{FLIR} measurements with the measurement discrepancy increasing in magnitude with decreasing temperature.

Figure 251b presents the results of the agreement comparison as a plot of T_{Roller} versus T_{FLIR}. Consistent with the Bland Altman plot, T_{Roller} and T_{FLIR} values seem to be approximately equal to one another at warm FLIR temperatures (T_{FLIR} equals about 90 to 110 °C), but T_{FLIR} tended to be increasingly greater than T_{Roller} with decreasing FLIR temperature. The upper agreement limit intersects the line of equality (i.e., $T_{Roller} = T_{FLIR}$) at T_{FLIR} equal to 87.4 °C, so T_{Roller} and T_{FLIR} values are in agreement with another when FLIR temperature exceeds 87.4 °C (zone of agreement). T_{Roller} and T_{FLIR} values are not in agreement when FLIR temperature is less than 87.4 °C (zone of disagreement). Average T_{Roller} to T_{FLIR} ratios ranged from 0.8 to 1.0 within the zone of agreement and from 0.7 to 0.8 within the zone of disagreement. Therefore, the roller-integrate temperatures sensors in this study adequately measured asphalt surface temperature at high temperatures (greater than 87.4 °C), but underestimated asphalt surface temperature at low temperatures (less than 87.4 °C).

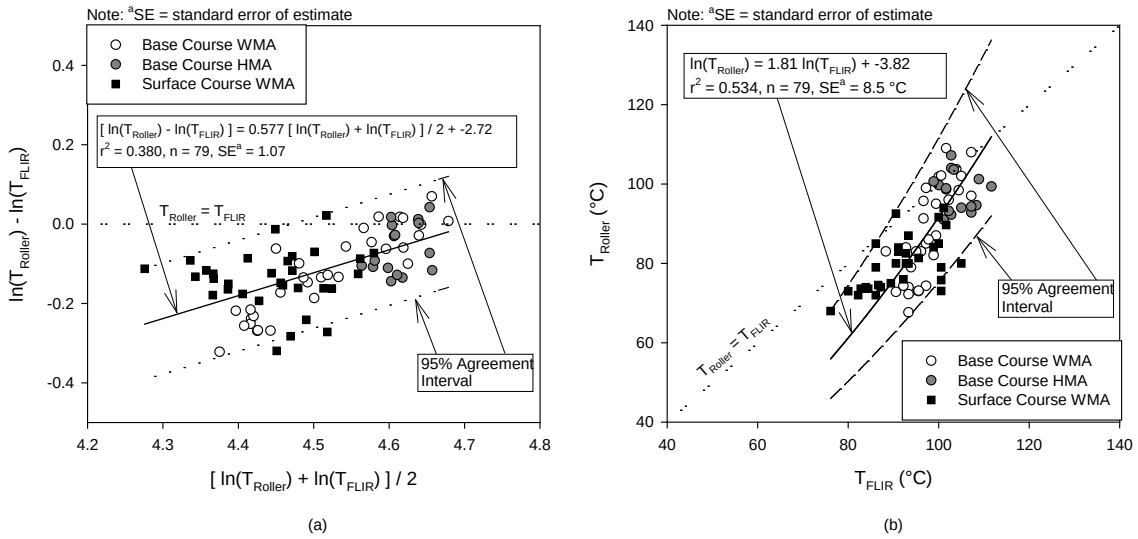

Figure 251. Comparison of roller-integrated temperature sensor and FLIR thermal camera for measuring asphalt mix temperature during compaction; (a) logarithmically transformed Bland-Altman plot, (b) correlation between roller-integrated temperature sensor and FLIR thermal camera measurements

Regression Analyses between HMV and QA Properties

The overseeing transportation agency used relative compaction determined from core samples as acceptance criteria. Immediately after asphalt pavement placement, transportation agency technicians extracted core samples from both base course and surface course layers. For both base and surface course layers, technicians extracted one or two core samples from each of the test sections. Authors of the study conducted 10 FWD tests on each test section subbase layer

before and after asphalt pavement placement. GPS coordinates were obtained for the locations of each core sample and FWD test to spatially pair with RICM data.

Comparison of HMV with Asphalt Core Relative Compaction

Figure 252a presents comparisons between base course core relative compaction [$RC_{Core(BC)}$] and HMV_{SB}, HMV_{BC}, and HMV_{SC} measurements, and Figure 252b presents comparisons between surface course core relative compaction [$RC_{Core(SC))}$] and HMV_{SB}, HMV_{BC}, and HMV_{SC} measurements. Neither $RC_{Core(BC)}$ nor $RC_{Core(SC)}$ correlated with statistical significance to any HMV measurement. Because only 1 or 2 core samples were extracted from each test section, the authors did not perform regression analyses between RC_{Core} and HMV measurement by test section. Despite the lack of regression analyses by test section, the comparisons between RC_{Core} and HMV measurements are consistent with comparisons between RC_{NG} and HMV measurements that the authors discussed earlier in this report. Therefore, results from this study suggest that asphalt pavement relative compaction does not correlate with RICM measurements.

Comparison of HMV with FWD Measurements

Figure 253a presents regression analyses between FWD modulus measured on test section subbase layers [$E_{FWD(SB))}$] and HMV_{SB}, HMV_{BC}, and HMV_{SC} measurements, and Figure 253b presents regression analyses between FWD modulus measured on test section surface course layers [$E_{FWD(SC)}$] and HMV_{SB}, HMV_{BC}, and HMV_{SC}. $E_{FWD(SB)}$ correlated with statistical significance to all HMV measurements—HMV_{SB} (r^2 = 0.79), HMV_{BC} (r^2 = 0.39), and HMV_{SC} (r^2 = 0.50). In addition, $E_{FWD(SC)}$ correlated with statistical significance to all HMV measurements—HMV_{SB} (r^2 = 0.55), HMV_{BC} (r^2 = 0.62), and HMV_{SC} (r^2 = 0.60).

The strong correlations between HMV measurements and FWD moduli are consistent with previous studies that report RICM measurements typically correlating well with stiffness measurements. Simple linear models best fit all associations between FWD moduli and HMV measurements, except for the association between $E_{FWD(SC)}$ and HMV_{SB}, which followed a nonlinear model. The nonlinear relationship between $E_{FWD(SC)}$ and HMV_{SB}, which is similar to the relationships between HMV_{BC} and HMV_{SB} and between HMV_{SC} and HMV_{SB} that were reported earlier in this report, may be the result of load spreading in layered systems (Burmister, 1945). This hypothesis, however, is a mere conjecture that requires additional research to validate or reject.

Figure 253c presents regression analyses between asphalt pavement (i.e., combined base and surface courses) modulus (E_{AP}) and HMV_{SB}, HMV_{BC}, and HMV_{SC}. Although this study has already shown that HMV measurements correlate quite well with stiffness measurements, none of the HMV measurements correlated with E_{AP} (r^2 values ranged from 0.01 to 0.07). However, an F-test indicated that the association between E_{AP} and HMV_{SB} was statistically significant (p value equalled 0.01). This unexpected statistically significant association may be due to the fact that $E_{FWD(SB)}$, which strongly correlates with HMV_{SB}, was used to calculate E_{AP}.

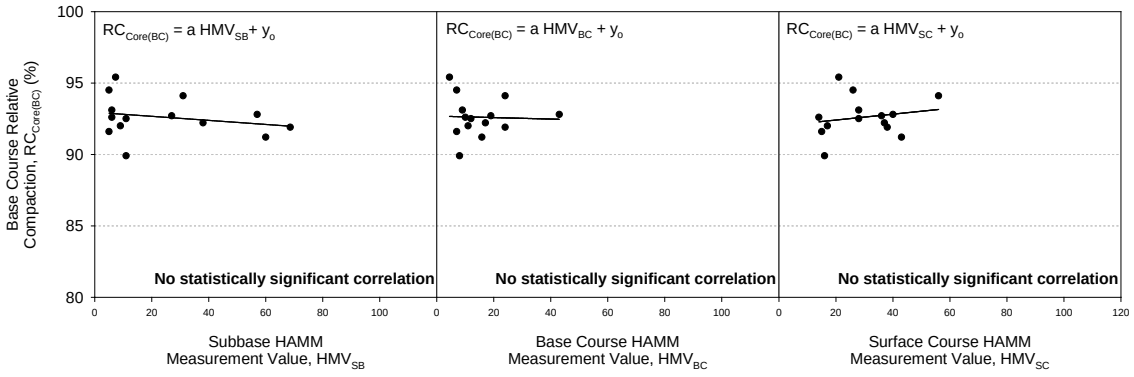

(a)

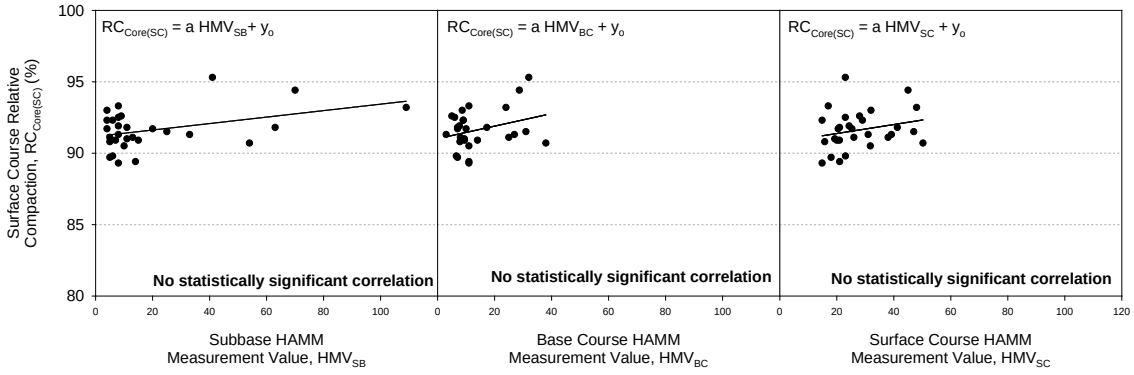

(b)

Figure 252. Correlations of subbase HMV, asphalt base course HMV, and asphalt surface course HMV with relative compaction values for (a) asphalt base course and (b) asphalt surface course

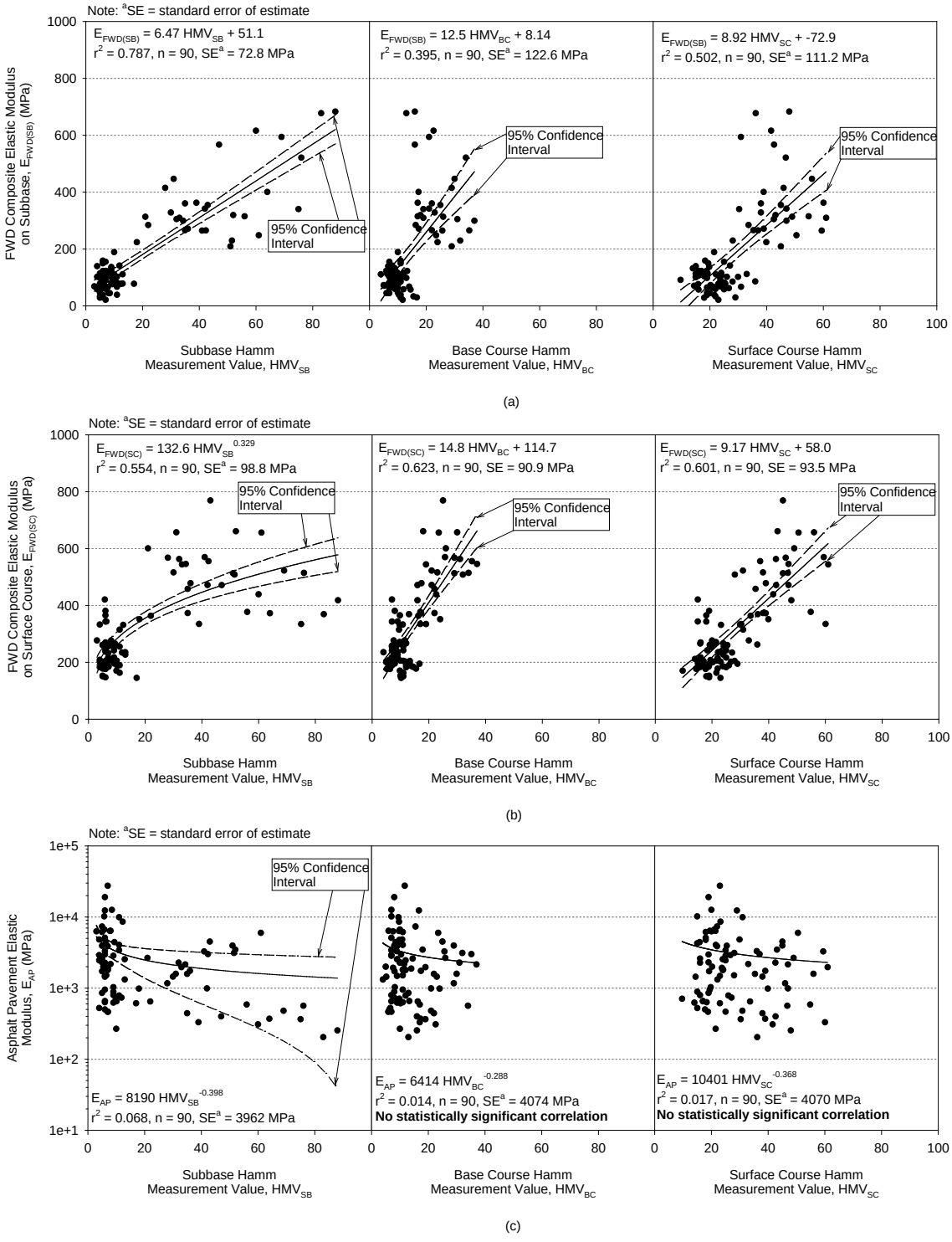

Figure 253. Correlations of subbase HMV, asphalt base course HMV, and asphalt surface course HMV with (a) E_{FWD} on subbase, (b) E_{FWD} on asphalt surface course, and (c) asphalt pavement elastic modulus

Implications for RICM in HMA Construction Practice

Results from this report have indicated with statistical significance that HMV does not correlate with asphalt pavement relative compaction, which is consistent with previous RICM studies. The lack of correlations between RICM measurements and relative compaction poses an obstacle for implementing RICM for QC and QA because many asphalt pavement contractors in the United States currently use relative compaction measurements for QC. However, the presence of this obstacle attests more so to the necessity of a paradigm shift end-result to performance-related construction specifications than to the limitations of RICM.

According to Epps et al. (2002), asphalt pavement performance is governed by the prevalence of fatigue cracking and rutting in pavement wheel paths, which are both related to in situ strains and therefore asphalt pavement modulus. In this study, FWD tests showed that average test section asphalt pavement moduli (E_{AP}) ranged from 385 to 7,140 MPa, even though RC_{Core} values ranged from 90% to 95% and 89% to 95%, respectively. Due to this observed discrepancy between RC_{Core} and E_{AP}, the authors contend that relative compaction is not a good indicator of asphalt pavement modulus and therefore not a good indicator of pavement performance.

As discussed earlier in this report, HMV values strongly correlate with performance-related QA measurements (i.e., FWD modulus), so the QC applicability for RICM technologies in asphalt pavement construction is quite promising. However, there is a caveat to the relationship between RICM measurements and stiffness because of the degree to which underlying layer stiffness affects RICM measurements during asphalt pavement construction. This study compared asphalt base and surface course HMV with asphalt pavement layer elastic modulus, but found no statistically significant correlations. However, when these correlations are expanded to account for pavement foundation elastic modulus [i.e., $E_{FWD(SB)}$] in addition to asphalt pavement modulus, then asphalt pavement elastic modulus becomes a statistically significant predictor of HMV.

Table 5.6 presents results from multivariable analyses relating E_{AP} and $E_{FWD(SB)}$ together with HMV_{BC} and HMV_{SC} measurements. In both multivariable models, E_{AP} and $E_{FWD(SB)}$ are statistically significant predictors of HMV. For the multivariable model predicting HMV_{BC} (r^2 adj = 0.46), E_{AP} sensitivity index equaled 0.036 and $E_{FWD(SB)}$ sensitivity index equaled 0.964, so E_{AP} accounts for 3.6% of HMV_{BC} and $E_{FWD(SB)}$ accounts for 96.4% of HMV_{BC}. For the multivariable model predicting HMV_{SC} (r^2 adj = 0.58), E_{AP} sensitivity index equaled 0.019 and $E_{FWD(SB)}$ sensitivity index equaled 0.981, so E_{AP} accounts for 1.9% of HMV_{SC} and $E_{FWD(SB)}$ accounts for 98.1% of HMV_{SC}. Therefore, RICM systems can potentially be used as QC for asphalt pavement layer modulus, provided that the composite modulus of the pavement foundation is known.

Table 24. Multivariable models for HMVBC and HMVSC as functions of EFWD(SB) and EAP

Multivariable Analysis	Term	Estimate	Standard Error	t Ratio	p Value	r^2 Adj
HMV_{BC}[a]	b_o	-1.079	1.94	-3.76	**0.0003**	0.462
	b_1	0.616	1.17	8.85	< **0.0001**	
	b_2	0.269	1.13	5.13	< **0.0001**	
HMV_{SC}[b]	b_o	-0.173	1.53	-0.94	0.352	0.579
	b_1	0.489	1.11	10.93	< **0.0001**	
	b_2	0.171	1.08	5.07	< **0.0001**	

Notes: [a]$\log(HMV_{BC}) = b_o + b_1 \log(E_{FWD(SB)}) + b_2 \log(E_{AP})$
[b]$\log(HMV_{BC}) = b_o + b_1 \log(E_{FWD(SB)}) + b_2 \log(E_{AP})$
[c]Emboldened p values indicate statistical significance

Summary and Key Conclusions

The key findings from the Phase II pavement construction data analysis are as follows:

- In general, HMV values during asphalt pavement construction are higher when placing asphalt over stiff pavement foundations. All HMV measurements correlated with statistical significance to one another.
- For asphalt construction over soft pavement foundations, HMV increased with each additional pavement layer. For asphalt construction over stiff foundations in general, pavement foundation HMV was greater than base course HMV, and base course HMV was less than surface course HMV.
- Asphalt pavement surface temperature measurements from the RICM temperature sensors were in agreement with FLIR thermal camera temperatures at higher temperatures (greater than 87.4 °C), but tended to underestimate pavement surface temperatures at lower temperatures (less than 87.4 °C).
- Asphalt pavement relative compaction from neither nuclear density gauge tests nor pavements cores correlated with HMV measurements. However, falling weight deflectometer (FWD) measurements strongly correlate with HMV measurements.
- Based on multivariable analyses, RICM systems can potentially be used as QC for asphalt pavement layer modulus, provided that the composite modulus of the pavement foundation is known.

CHAPTER 9: ESTIMATING INDIVIDUAL LAYER PROPERTIES FROM FWD AND DCP TESTING ON PAVEMENT

The mechanistic empirical pavement design guide (MEPDG) emphasizes the importance of proper characterization of pavement foundation layer mechanistic properties for pavement analysis, design, and construction quality control/assurance (AASHTO 2008). Resilient modulus (Mr) for unbound foundation layers and elastic modulus (E) for bound foundation layers is a required input in the design and it has a significant effect on the computed pavement responses (Rao et al. 2012). Determining Mr through laboratory testing following AASHTO T-307 (AASHTO 2000) or NCHRP 1-28A (Andrei et al. 2004) testing protocols is suggested in the design guide for Level 1 analysis on newly constructed foundation layers. For rehabilitation projects, back-calculated moduli values from falling weight deflectometer (FWD) testing per ASTM D4694-09 (ASTM 2009) is the preferred method. For Level 2 analysis on new and rehabilitated projects, empirical relationships are used to determine the moduli values from California bearing ratio (CBR) values, penetration resistance (PR) values determined from dynamic cone penetrometer (DCP) tests, and R-values (NCHRP 2004).

Use of FWD in estimating the modulus has advantages of being relatively rapid and non-destructive, and many state agencies are currently equipped with the test devices (Alavi et al. 2008). To determine layer moduli values, FWD data analysis requires either forward- or back-calculations. Forward-calculations involve using deflection basin measurements in closed-loop equations. Back-calculations involve selecting initial moduli values for each layer and modifying them in an iterative process until the predicted deflection basin matches the measured deflection basin. Many forward- and back-calculation methods have been documented in the literature over the past three decades and each method has its own advantages and disadvantages (Smith et al. 2007, Stubstad et al. 2007).

Despite significant research and development over the past four decades on back-calculation analysis programs, many researchers have expressed challenges associated with the analysis procedures. The MEPDG (AASHTO 2008) acknowledges these challenges and states that: *"Backcalculation programs that use this iterative technique do not result in a unique solution or set of layer moduli. As such, determining a set of elastic layer moduli to match a measured deflection basin that deviates from elastic theory, for whatever reason, may become difficult and frustrating. . . . There are forward calculation programs that do result in unique layer moduli, but these have not been commonly used and are restricted to three layer structures."*

Stubstad et al. (2006) stated that "*a serious drawback to [back-calculation] is that one or more of the many input assumptions . . . may be incorrect and therefore may not apply to the actual pavement system. . . . forward calculation is easy to understand and use, whereas back-calculation is presently more of an art than a science"*.

Because of these challenges there is a need to properly understand the limitations and characterize differences in different calculation methods using FWD data. This can be done by statistically comparing moduli values estimated from the different calculation procedures over a wide range of support conditions and assessing the standard error associated with the estimates.

Estimating modulus using DCP measurements with empirical relationships also presents uncertainty due to variations in material types and conditions, differences in test and analysis methods, and the prediction errors observed within those correlations. Review of literature indicates that, correlations have been developed using various methods including laboratory cyclic triaxial (or resilient modulus) tests, FWD, static or cyclic plate load tests, and laboratory or field small-strain wave propagation tests (Chen et al. 2005; George and Uddin 2000; Heukelom and Klomp 1962; Mohammad et al. 2007; Powell et al. 1984). Correlation studies that involved FWD tests to determine moduli values have made use of different calculation procedures, which makes direct comparison difficult. It is believed that the limitations (i.e., standard error in estimates) are often overlooked as part of the pavement design process. This is because it is often difficult to determine the errors or they are not reported. Further, the design mechanism itself does not conveniently allow for introducing measurement error into the process.

This study was undertaken with the goal of assessing the uncertainties involved in estimating the asphalt pavement and foundation layer moduli values using FWD and DCP. Testing was conducted on 16 test sections in Iowa with varying pavement ages, support conditions, and foundation layer thicknesses. Moduli values of asphalt, subgrade, and intermediate base layers were determined from FWD data using forward-calculations recommended by Stubstad et al. (2007) and back-calculations using Engineering Research Institute data analysis (ERIDA) software. DCP tests were used to determine layer thicknesses used in the FWD data analysis and correlate with FWD back-calculated and forward-calculated moduli values.

Forward Calculation Methods

AASHTO Method for Subgrade Modulus Determination

AASHTO (1993) presents closed-form equations based on Boussinesq solutions to determine subgrade moduli values. The original Boussinesq equations relating vertical deflection, applied stress, and elastic modulus for load applied at the surface of a half-space elastic, homogenous, and isotropic material are expressed as:

$$E = (1 - v^2)Pf/(\pi a d_o) \text{ for uniformly distributed load at } r = 0 \quad (1)$$

$$E = (1 - v^2)P/(\pi r d_r) \text{ for point load on the surface at any } r \quad (2)$$

where, E = Elastic modulus (MPa), P = applied load (N), r = distance of deflection reading d_r from center of load (mm), d_r = peak deflection at a distance r from the center of the load (mm), d_o = peak deflection at the center of the loading plate (mm), v = Poisson's ratio, and f = shape factor that depends on the rigidity of the plate and the material type (i.e., cohesive or granular or mixed) and varies between $\pi/2$ to 8/3, depending on the anticipated stress distribution (Vennapusa and White 2009).

Eq.1 uses peak deflection directly beneath the loading plate, which is a composite deflection measure of all layers within the measurement influence depth, and therefore represents a composite modulus. Ullitdtz (1987) determined that the *E* values calculated using Eq. 2 represent the subgrade modulus, provided the distance *r* is sufficiently large such that there is no influence of deformation of the layers above the subgrade. AASHTO (1993) describes a relationship to determine the minimum distance *r*, based on Odemark's method of equivalent layer thickness (Odemark 1949) combined with the Boussinesq's solutions. The MET method is described in detail in Ullidtz (1987).

Ullitdz (1987) reported that if *E* values determined from Eq. 1 and 2 are plotted against distance *r*, using peak deflections obtained at various distances away from the plate, one of the following two trends are generally observed: (1) modulus decreases with increasing distance and then levels off after a certain distance or (2) modulus initially decreases and then increases after a certain distance. The first type of trend represents a linear elastic subgrade and the lowest modulus value can be used as the subgrade modulus value. The second type of trend represents a non-linear subgrade indicating stress-dependency. For this case, according to Salt (1998) the lowest modulus value calculated can be used as the subgrade modulus value. Ullidtz (1987) proposed a stress-dependent non-linear model to address this case, but it requires an iterative procedure to determine the curve fitting parameters in the non-linear model. Some software programs (e.g. ELMOD developed by Dynatest, Inc.) currently use the nonlinear model in subgrade analysis.

Hogg Model for Subgrade Modulus Determination

The Hogg model is described in detail by Stubstad et al. (2007). Hogg et al. (1944) developed the original model based on a hypothetical two-layer pavement system. This model simplifies multilayered elastic systems to calculate subgrade stiffness, and elastic modulus under a surface load. The Hogg model as modified by Wiseman and Greenstein (1983) was used in this study. The model consists of a series of equations to compute subgrade layer modulus as follows:

$$E = I\frac{(1+v)(3-4v)}{2(1-v)}\left(\frac{S_0}{S}\right)\left(\frac{p}{\Delta_0 l}\right) \tag{3}$$

$$l = y_0\frac{r_{50}}{2} + [(y_0 r_{50})^2 - 4mar_{50}]^{1/2} \qquad if\ \frac{a}{l} < 0.2, then\ l = (y_0 - 0.2m)r_{50} \tag{4}$$

$$r_{50} = r\frac{\left(\frac{1}{\alpha}\right)^{\frac{1}{\beta}} - B}{\left[\frac{1}{\alpha}\left(\frac{d_0}{d_r} - 1\right)\right]^{\frac{1}{\beta}} - B} \tag{5}$$

$$\left(\frac{S_0}{S}\right) = 1 - \overline{m}\left(\frac{a}{l} - 0.2\right) \qquad if\ \frac{a}{l} < 0.2, then\ \frac{S_0}{S} = 1 \tag{6}$$

where, S_0 = theoretical point load stiffness; S = pavement stiffness calculated as P/d_0 (area loading); P = applied load; d_0 = deflection at center of load plate; d_r = deflection at offset

distance *r*; *r* = distance from center of load plate; r_{50} = offset distance where $\Delta_r/\Delta_0 = 0.5$; *l* = characteristic length; α, β, and *B* = curve fitting coefficients (Table 1); y_0 and *m* = characteristic length coefficients (Table 1); and $\overline{m}$ = stiffness ratio coefficient (Table 1).

The Hogg model described by Wiseman and Greenstein (1983) included three cases: Cases I and II are used for finite elastic layer with an effective thickness which is assumed to be 10 times the characteristic length *l* and Case III is an infinite elastic foundation. The difference between Cases I and II are the assumed Poisson's ratio which is 0.5 for Case I and 0.4 for Case II. According to Stubstad et al (2007), Case II is typically used in calculating subgrade layer moduli and provides conservative values. In this study, Case II is assumed and the model coefficients are summarized in Table 1.

Table 25. Hogg model coefficients (modified from Stubstad et al. 2007)

Parameter	Coefficient	Values
Assumed depth to hard bottom	*h/l*	10
Poisson's ratio	*v*	0.40
"Influence" factor	*I*	0.1689
For $\Delta_r/\Delta_0 > 0.43$	α	0.3804
$r_{50} = f(\Delta_r/\Delta_0)$	β	1.8246
	B	0
For $\Delta_r/\Delta_0 < 0.43$	α	4.3795E-04
$r_{50} = f(\Delta_r/\Delta_0)$	β	4.9903
	B	3
$l = f(r_{50},a)$	y_0	0.603
	m	0.108
$(S/S_0) = f(a/l)$	$\overline{m}$	0.208

AREA Forward Calculation Method for Asphalt Surface Layer Modulus Determination

The AREA method was defined in Hoffman and Thompson (1981) and is commonly used in rigid pavement analysis. Stubstad et al. (2007) proposed a simple set of equations using the AREA method for determining asphalt surface layer moduli values based on calibrations carried out with multi-layered elastic analysis programs. The procedure requires calculation of AREA factor (AF), composite modulus using Eq.1, and normalized surface layer thickness to the loading plate. The following equations are used to calculate asphalt pavement modulus:

$$E_{AC} = \left[E_0 * AF_{AC} * k_3^{\left(\frac{1}{AF_{ac}}\right)}\right] / k_3^2 \quad (7)$$

$$AF = \left[(k_2 - 1)/(k_2 - \frac{A_{12}}{k_1})\right]^{1.35} \quad (8)$$

$$A_{12} = 2 * [2 + 3\left(\frac{d_8}{d_0}\right) + \left(\frac{d_{12}}{d_0}\right)] \quad (9)$$

where, E_{AC} = modulus of the asphalt layer, E_0 = composite modulus of the entire pavement system calculated using Eq.1, *AF* = AREA factor, k_1 = 6.85, k_2 = 1.752, k_3 = thickness ratio of upper layer thickness / load plate diameter = h_1 / (2**a*), h_1 = thickness of the asphalt layer, A_{12} = AREA beneath the first 305 mm (12 in.) of the deflection basin, d_0 = deflection measured at the center of the loading plate, d_8 = deflection measured at 203 mm (8 in.) away from the center of the plate, and d_{12} = deflection measured at 305 mm (12 in.) from the center of the plate.

According to Stubstad et al. (2007), these equations work well for typical pavement materials and modular ratios when the underlying materials are unbound. It is also noted therein that this approach is not totally rigorous but is rather empirical in nature.

Dorman and Metcalf Forward Calculation Method for Base Layer Modulus Determination

Stubstad et al. (2007) proposed using the Dorman and Metcalf (1965) method to determine modulus intermediate (base) layer between the bound surface and unbound subgrade layers. Equation 10 is used to calculate the base layer modulus:

$$\mathrm{E_{Base}} = 0.86 \times \mathrm{h_2^{0.45}} \times \mathrm{E_{SG}} \quad (10)$$

where, E_{Base} = base layer modulus (psi), h_2 = Thickness of the base layer (in.), and E_{SG} = Subgrade modulus (psi).

According to Stubstad et al. (2007), the above method provides reasonable and realistic base course modulus.

ERIDA Back-Calculation Method

ERIDA back-calculation software is provided by Engineering Research International, Inc. (2009). This method assumes that the surface load is uniformly distributed over a circular area; all layers are homogenous, isotropic, and linearly elastic; upper layers extend horizontally to infinity; and bottom layer is a semi-infinite half-space. ERIDA uses the ELSYM5 calculation routine in analyzing pavement deflections. Details of ELSYM5 calculation routine are provided in Ahlbornm (1972). The process requires inputting a seed (or initial) modulus for each layer, the lower and upper bounds of modulus for each layer, Poisson's ratio of each layer, and thickness of each layer. Calcuations are initiaited using an iterative approach where the layer moduli are repeatedly adjusted until a suitable match between the calculated and measured deflection basin is found. The program computes the root mean square error (RMSE) between the measured and the calculated deflection values and runs the iterations until the lowest RMSE is achieved. Review of literature indicated that acceptable errors in back-calculation vary from 2% to 10% (AASHTO 2008; Engineering and Research International Inc. 2009). AASHTO (2008) indicates that RMSE > 3% generally implies that the modulus values calculated are questionable. Irwin

(2002) indicated that although RMSE is advisable to check the deflection basin fit, it does not assure that the back-calculated modulus values are "correct."

DCP Testing and Empirical Relationships to Determine Modulus

Many researchers have developed empirical relationships to estimate modulus values for foundation layers from PR and CBR measurements. A summary of those relationships is provided in Table 2 along with the statistical parameters (i.e., standard error (SE), coefficient of determination (R^2)) associated with the relationships and their validity ranges. The R^2 values of the relationships ranged from about 0.4 to 0.9. In those relationships, the procedures used to determine the modulus values included both laboratory and field testing methods. FWD was the most commonly used method to determine the modulus values using back-calculation analysis.

Various different back-calculation analysis procedures were used in developing the empirical relationships. Figure 254 shows the upper and lower bound relationships between PR and E or Mr values as summarized in Table 26. The bounds suggest that the predicted moduli values can have an error of ± 50 to 335 MPa if PR value is between 2 and 10 mm/blow, and ± 10 to 50 MPa if PR value is > 10 mm/blow. Relationships derived from this study are also included in Figure 254, and will be discussed later in this report. In MEDPG, the empirical relationship provided by Powell et al. (1984) between CBR and E is used as default, where CBR are estimated from DCP-PR values using Eq.11. The Powell et al. (1984) equation is presented in Figure 254 for reference, by converting CBR to PR. The E value determined from Powell et al. (1984) equation is assumed to be same as Mr in MEPDG (NCHRP 2004).

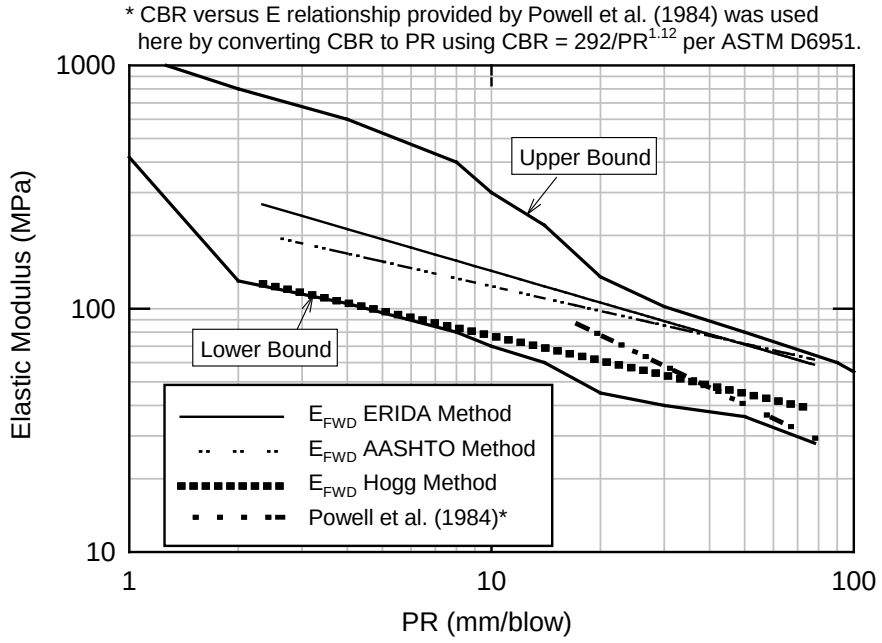

Figure 254. Upper and lower bounds of relationships between PR and subgrade/base layer modulus along with relationships observed in this study

Table 26. Empirical relationships to determine modulus

Reference	Material	Prediction Equation	Relationship Statistics	Test Method[b]	Data validity range
Heukelom and Klomp (1962)	Not indicated	E (MPa) = 9.81 (CBR)	R^2 = 0.89 SE = 59.4	E is calculated from shear wave velocity, three-layer elastic systems , and stiffness measurements[c]	CBR= 2 to 200 E = 34 to 1,960 MPa
Powell et al. (1984)	Subgrade materials[a]	E (MPa) = 17.6 (CBR)$^{0.64}$	Not provided	Laboratory traixial and CBR tests	CBR = 2 to 12 E = no range provided
Pen (1990)	Subgrade[a]	E (MPa) = 1780 (PR)$^{-0.89}$	R^2 = 0.56	E is back-calculated from FWD test using PHONIX program	PR = 12 to 70 mm/blow E = 30 to 250 MPa
		E (MPa) = 4594 (PR)$^{-1.17}$	R^2 = 0.81	E is back-calculated from FWD test using PEACH program	PR = 12 to 70 mm/blow E = 30 to 250 MPa
	Granular base[a]	E (MPa) = 419 (P)$^{-0.85}$	R^2 = 0.73		PR = 1.5 to 10 mm/blow E = 60 to 300 MPa
De Beer (1990)	Granular base and subbase, and subgrade materials[a]	Log (E) (MPa) = 3.05–1.07 log(PR)	R^2 = 0.76 SE = 0.209	E is back-calculated from FWD test using ELSYM5 program	PR = 0.6 to 25 mm/blow E = 25 to 3,980 MPa
AASHTO (1993)	Fine-grained subgrade[a]	E (MPa) = 10.34 (CBR)	Relationship based on Heukelom and Klomp (1962) limiting CBR to < 10		Soaked CBR < 10
Chen et al. (1999)	Lean clay to silt subgrade	E (MPa) = 338 (PR)$^{-0.39}$	R^2 = 0.42 SE = 30.5	E is back-calculated from FWD test using EVERCALC program	PR = 10 to 60 mm/blow E = 62 to 288 MPa
George and Uddin (2000)	Coarse grained sand soil	M_r (MPa) = 235.3 (PR)$^{-0.48}$	R^2 = 0.4 SE = 18.5	M_r determined using laboratory resilient modulus test per AASHTO TP46 on recompacted samples obtained from field	PR = 2.8 to 73 mm/blow M_r = 30 to 160 MPa
	Fine grained sand soil	M_r (MPa) = 532.1 (PR)$^{-0.492}$	R^2 = 0.4 SE = 35.3	M_r determined using laboratory resilient modulus test per AASHTO TP4 on Shelby tube samples obtained from field	PR = 3.8 to 253 mm/blow M_r = 35 to 275 MPa
Konard and Lachance (2001)d	Granular base/subbase and granular subgrade	Log (E) (MPa) = –0.884 log(PR) + 2.906	R^2 = 0.92	E is back-calculated from static plate load test using VIEWBACK program	PR = 4 to 11 mm/blow E = 100 to 226 MPa
Nazzal (2003)	Cement treated, lime treated, untreated clay, granular subgrade	Ln (E) (MPa) = 2.35+5.21/ln(PR)	R^2 = 0.91 SE = 0.2	E is back-calculated from FWD test using ELMOD 4.0 program provided by Dynatest, Inc.	PR = 5 to 67 mm/blow E = 30 to 240 MPa

Reference	Material	Prediction Equation	Relationship Statistics	Test Method[b]	Data validity range
George (2004)	Medium clay and sand	$E\ (MPa) = 21.83\ (CBR)^{0.478}$	Not provided	M_r determined using laboratory resilient modulus test per AASHTO TP46	Not provided
Chen et al. (2005)	Granular base, chemically stabilized/treated subgrades, and natural subgradea	$E\ (MPa) = 537.76\ (PR)^{-0.6645}$	$R^2 = 0.86$	E is back-calculated from FWD test using MODULUS program	PR = 0.1 to 60 mm/blow
Mohammad et al. (2007)	A-4, A-6, A-7-5, and A-7-6	$M_r\ (MPa) = 151.8/(PR)^{1.096}$	$R^2 = 0.91$ SE = 6.1	M_r determined using laboratory resilient modulus test per AASHTO T294	PR = 9 to 65 mm/blow M_r = 7.6 to 91.4 MPa
Vennapusa et al. (2012)	Well-graded sand, poorly graded sand, and clayey sand	$E\ (MPa) = 1519\ (PR)^{-0.11}$	$R^2 = 0.79$ SE = 39.5	E is back-calculated from FWD test using EVERCALC program	PR = 4 to 18 mm/blow E = 60 to 400 MPa
This Study [e]	Poorly-graded crushed limestone subbase, silty sand subbase, cement treated silty sand subbase, glacial till subgrade, and cement/fly ash treated subgrade	$E\ (MPa) = 73.28\text{-}0.15(PR)$	$R^2 = 0.04$ SE = 12.2	E is back-calculated from FWD using the ERIDA program (see text for details)	PR = 23 to 78 mm/blow
		$E\ (MPa) = 323.03(PR)^{-0.3724}$	$R^2 = 0.54$ SE = 56.2		PR = 2 to 78 mm/blow
		$E\ (MPa) = 86.11\text{-}0.14(PR)$	$R^2 = 0.0114$ SE = 22.0	E is back-calculated using AASHTO forward calculation method (see text for details)	PR = 23 to 78 mm/blow
		$E\ (MPa) = 253.94(PR)^{-0.3044}$	$R^2 = 0.38$ SE = 56.4		PR = 2 to 78 mm/blow
		$E\ (MPa) = 53.16\text{-}0.11(PR)$	$R^2 = 0.03$ SE = 9.8	E is back-calculated using Hogg model forward calculation method (see text for details)	PR = 23 to 78 mm/blow
		$E\ (MPa) = 152.35(PR)^{-0.3024}$	$R^2 = 0.50$ SE = 26.5		PR = 2 to 78 mm/blow

Note: PR determined using DCP described in ASTM D6951, unless otherwise indicated.
a Type of material is not indicated.
b PR is determined from DCP tests and therefore is not repeated in the column, while E and CBR are determined from various test and analysis procedures as indicated.
c The type of stiffness method used is not indicated.
d PR determined using a larger DCP than described in ASTM D6951, with a 63.5 kg hammer dropped over a height of 760 mm and 51 mm diameter tip.
e The relationships developed using PR of the weakest 75 mm of subgrade are summarized in this report.
E = elastic modulus, M_r = resilient modulus, SE = standard error, PR = penetration resistance, CBR = California bearing ratio, R^2 = coefficient of determination.

Field Data Analysis

FWD data was used to calculate the composite moduli values using Eq.1, and are reported as $E_{FWD\text{-}Composite}$. Forward- and back-calculation of FWD deflection basin data was performed to determine the subgrade, asphalt surface, and intermediate base layer moduli values, using the procedures described earlier in this report. Subgrade modulus calculated using the AASHTO method are reported as $E_{FWD\text{-}AASHTO\text{-}SG}$ values (Eq.2). Subgrade modulus calculated using the Hogg method (Case II) are reported as $E_{FWD\text{-}Hogg\text{-}SG}$ values (Eq.3). The asphalt surface layer modulus calculated using the AREA method are reported as $E_{FWD\text{-}AREA\text{-}Asphalt}$ values (Eq.7). The intermediate base layer modulus calculated using $E_{FWD\text{-}AASHTO\text{-}SG}$ and $E_{FWD\text{-}Hogg\text{-}SG}$ as E_{SG} values in Eq.10 and are reported as $E_{FWD\text{-}AASHTO\text{-}Base}$ and $E_{FWD\text{-}Hogg\text{-}Base}$, respectively. The back-calculated layer moduli values obtained using ERIDA software are reported as $E_{FWD\text{-}ERI\text{-}Asphalt}$ for asphalt layer modulus, $E_{FWD\text{-}ERI\text{-}Base}$ for base layer modulus, and $E_{FWD\text{-}ERI\text{-}SG}$ for subgrade layer modulus.

For all pavement sections, the multiple base/subbase layers were combined into one base layer to simplify the analysis into a three-layer system. This decision was made after reviewing the DCP-PR profiles from the Boone test sections, which showed that the base/subbase layers yielded similar PR values compared to the underlying subgrade layer. Representative PR profiles from selected test sections at the Boone expo site are shown in Figure 255. Some test points on 7th street and 11th street north reached refusal (i.e., < 2 mm after 5 blows, per ASTM D6951-03) within the chemically stabilized subbase/subgrade layers. PR from those test points were not determined for this study.

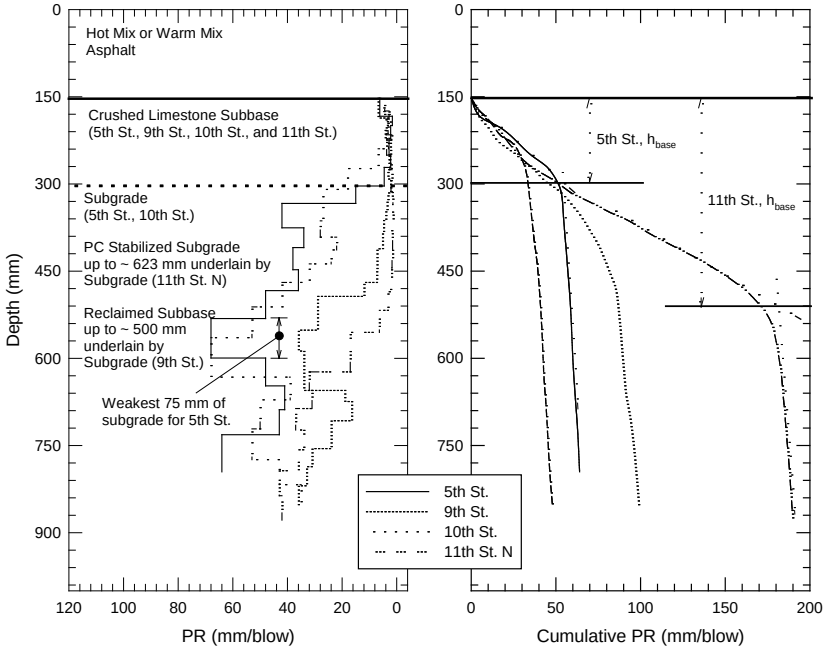

Figure 255. Representative PR profiles from DCP test at Boone Expo test sections: (left) showing different foundation support conditions, (right) showing base layer determination

On the 11th street north section with PC or FA stabilized subgrade between the MSB and subgrade layers, the calculations showed unreasonably high moduli values using the ERIDA back-calculation method when the MSB and stabilized subgrade layers were analyzed as separate layers (four-layer system). As the MSB and the PC stabilized subgrade layers showed similar PR values (see Figure 255 for 11th St. N section results), the two layers were combined and analyzed as a single base layer (three-layer system) in both forward- and back-calculations.

Layer thicknesses from the Boone expo sections were obtained from DCP testing as illustrated in Figure 255. The base layer thickness was determined as the depth from the bottom of the asphalt layer to the intersection of the tangents of the upper and lower portions of the cumulative blows with depth curve.

In both forward- and back-calculations, a Poisson's ratio of 0.45 was assumed for subgrade and 0.4 for base and 0.35 for asphalt layers. In back-calculation analysis, RMSE $\leq$ 3.0 was used as the criteria in determining the layer moduli values, in accordance with AASHTO (2008). This criteria could not be achieved for a few data points, so those data points were excluded.

In determining the PR of each layer, the thickness of each layer divided by the cumulative blows needed for the cone tip to reach that depth was used. This procedure was straight-forward for base layer, where the thickness was easily distinguishable. For the subgrade, the PR values varied with depth (Figure 255). Therefore, PR representing the average of the top 300 mm of the subgrade and PR representing the weakest 75 mm thickness within the DCP penetration depth were calculated for comparison with the modulus values. The weakest layer approach was found to work well in correlating with FWD back-calculated modulus of subgrade reaction values in a recent study conducted by White and Vennapusa (2014).

Results and Discussion

Average composite FWD moduli values from all test sections are shown in Figure 256 which ranged between 300 to 950 MPa. Tests from multiple testing times on Hamilton County test sections indicated that the composite moduli values decreased during the spring thaw time, as expected.

Figure 257 shows the average base and subgrade layer moduli values, calculated using the forward- and back-calculation methods from each test section and the testing time. Statistical regression analysis between the forward and back-calculated subgrade moduli values from all test points are shown in Figure 258. Similarly, regression analysis results for base layer and surface layer moduli values are shown in Figure 259 and Figure 260, respectively.

On average, the AASHTO method produced the highest and the Hogg method produced the lowest subgrade moduli values. The back-calculation method produced average subgrade moduli values that are in between the two forward-calculation methods. Stubstad et al. (2006) indicated that Hogg method typically produces conservative (lower) subgrade moduli values, which is also the case for the results presented herein. The R^2 values of the regression relationships between

the subgrade moduli values estimated from the three methods ranged from 0.85 to 0.95. On average, the AASHTO and ERIDA methods produced subgrade moduli values that are about 1.3 and 1.5 times higher than the Hogg method.

Base layer modulus calculations showed significant variations between the forward- and back-calculation methods. On average, the base layer moduli values calculated based on the subgrade moduli values form the Hogg method produced the lowest moduli values. Regression relationships between the forward- and back-calculated moduli values yielded low R^2 values (< 0.3) and high SE values (> 120 MPa). The R^2 value for the two forward-calculation methods was high (> 0.90) and about the same as in the case of subgrade modulus calculations. This was expected because the same Dorman and Metcalf method was followed in calculating the base layer moduli for both cases.

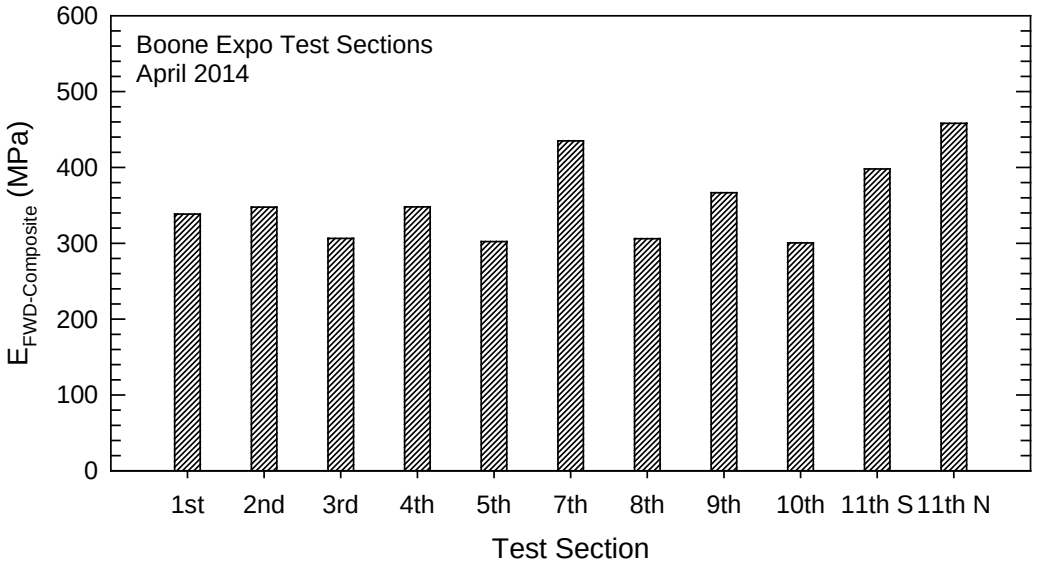

Figure 256. Composite FWD modulus measurements on different test sites at different testing times in (a) Hamilton County, and (b) Boone Expo

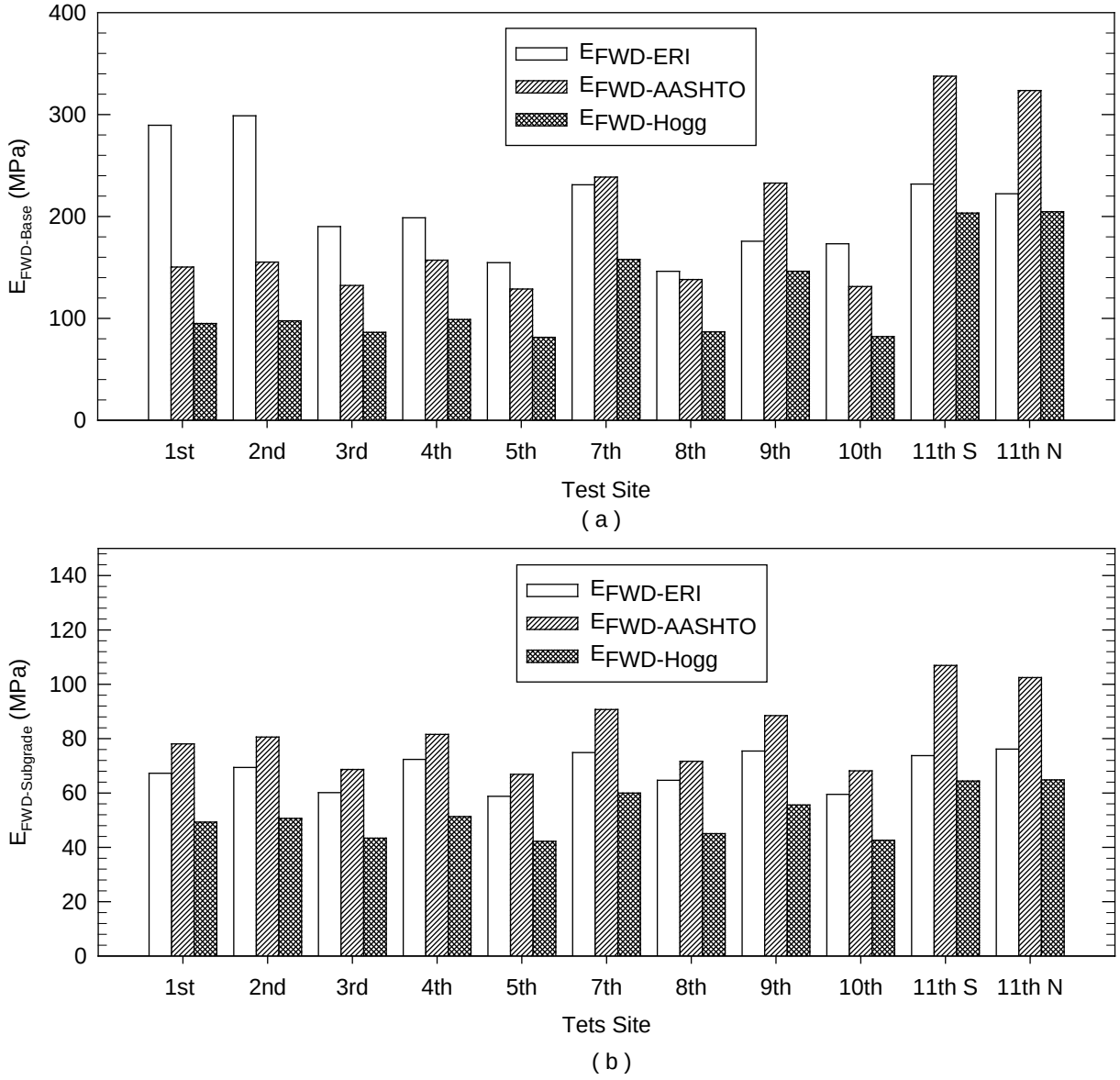

Figure 257. Average (a) base and (b) subgrade layer modulus calculated from each method for Boone County test section

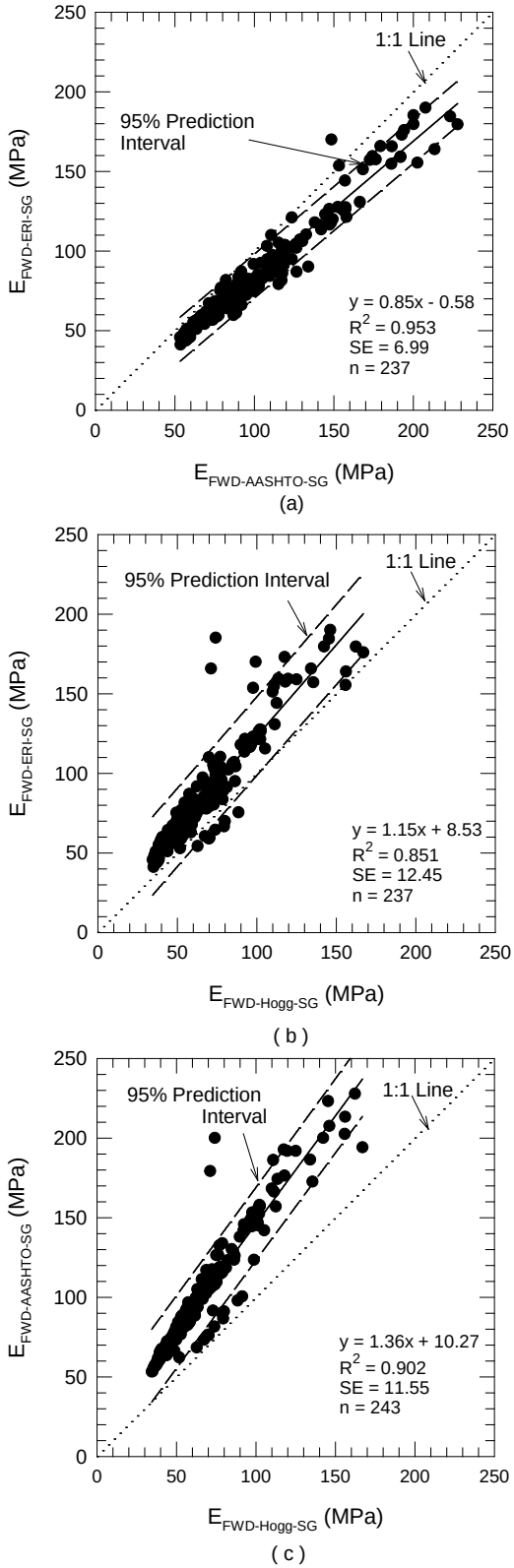

Figure 258. Comparison of subgrade layer modulus between each method

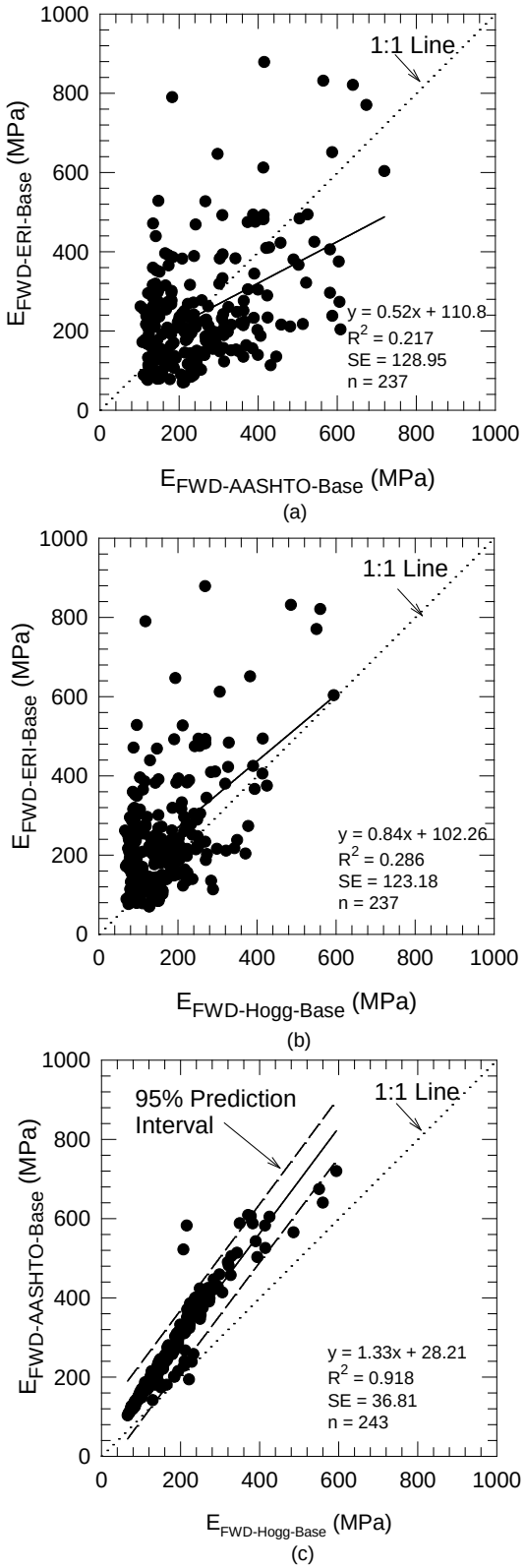

Figure 259. Comparison of base layer modulus between each method

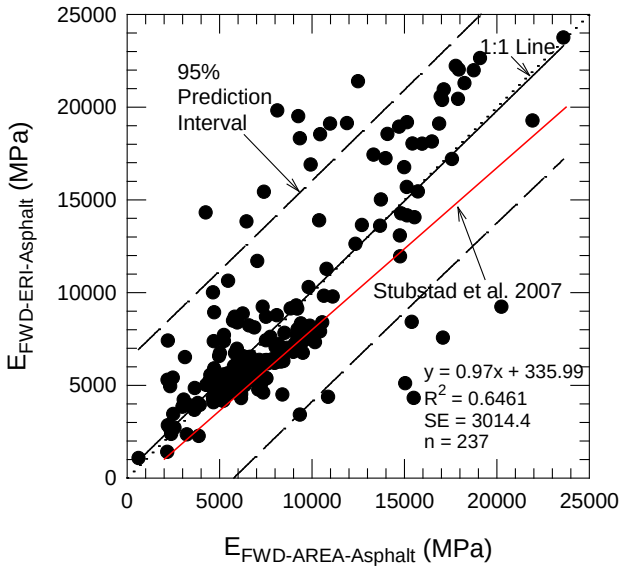

Figure 260. Comparison of asphalt surface layer modulus values predicted using back-calculation and forward-calculation

In asphalt layer modulus calculations, the regression analysis between the back-calculated and forward-calculated methods yielded a best fit line close to the 1:1 line with $R^2 = 0.65$ and SE of about 3,000 MPa. Regression equation presented in Stubstad et al. (2007) comparing back- and forward-calculation methods based on 1,300 test points obtained from long term pavement performance test sections is also shown in Figure 260, for reference. It must be noted that the back-calculated values presented in Stubstad et al. (2007) used MODCOMP back-calculation program.

Figure 10 shows the relationships between PR and base and subgrade layer moduli values, based on testing conducted at the Boone Expo test site. Figure 261 (a), (b), (c) shows the PR values of the subgrade using the 75 mm thick weakest portion of subgrade, and Figure 261 (d), (e), (f) shows PR values of the subgrade using the top 300 mm subgrade. The data included PR values ranging between 2 and 78 mm/blow.

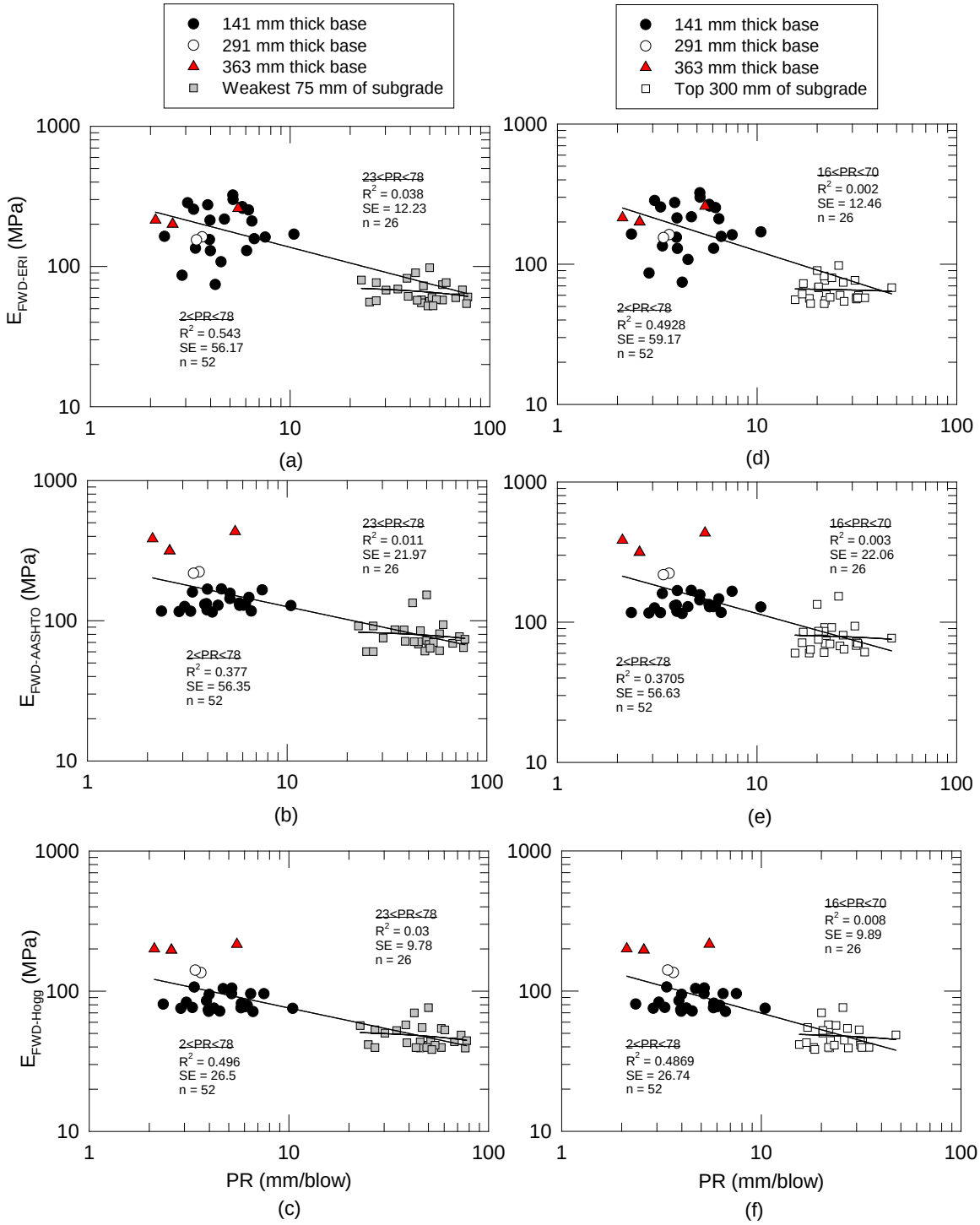

Figure 261. Correlations between: (a) $E_{FWD\text{-}ERI}$ and weakest subgrade PR; (b) $E_{FWD\text{-}AASHTO}$ and weakest subgrade PR; (c) $E_{FWD\text{-}Hogg}$ and weakest subgrade PR; (d) $E_{FWD\text{-}ERI}$ and top 300 mm subgrade PR; (e) $E_{FWD\text{-}AASHTO}$ and top 300 mm subgrade PR; (f) $E_{FWD\text{-}Hogg}$ and top 300 mm subgrade PR.

The relationships between PR and moduli values yielded non-linear exponential relationships, similar to presented by others as summarized in Table 26. The forward-calculation methods yielded slightly higher R^2 values and lower SE values, compared to the back-calculation method. The PR values determined from the weakest 75 mm of the subgrade produced slightly higher R^2 values (R^2 = 0.57 to 0.59) than with PR values determined from the top 300 mm of the subgrade (R^2 = 0.46 to 0.54). When only data from the subgrade with PR > 23 mm/blow are considered, the SE of the estimates reduced to < 20 MPa, although the R^2 values are also low (< 0.1).

Summary

Many highway agencies currently use FWD testing as part of routine testing of pavements in situ. Different agencies use different back- or forward-calculation procedures to determine layer moduli values. Many agencies also rely on empirical relationships in determining the design moduli values. This study attempts to point out the statistical uncertainties associated with the values determined from the different procedures and empirical relationships. Key findings from the result and analysis presented in this study are as follows:

The AASHTO and Hogg forward-calculation methods and ERIDA back-calculation program produced subgrade moduli values that are strongly correlated with R2 between 0.85 and 0.95 and SE < 13 MPa. However, the AASHTO and ERIDA methods produced subgrade moduli values that are about 1.3 and 1.5 times higher than the Hogg method.

Base layer modulus calculations showed significant variations between the forward- and the back-calculation methods Regression relationships between the two methods yielded low R2 values (< 0.3) and high SE values (> 120 MPa).

Regression analysis between the back- and forward-calculated asphalt layer moduli values yielded a linear relationship that is close to the 1:1 line with R2 = 0.65. However, there was significant scatter in the data with a SE of about 3,000 MPa.

Numerous regression relationships have been documented in the literature between DCP test measurements and moduli values and are summarized herein. Upper and lower bounds are presented based on the available relationships. The bounds suggest that the predicted moduli values can have an error of ± 50 to 335 MPa if PR value is between 2 and 10 mm/blow, and ± 10 to 50 MPa if PR value is > 10 mm/blow.

New relationships between PR and moduli values calculated from three forward and back calculation methods for a PR range of 2 and 78 mm/blow are presented herein. PR values determined from the weakest 75 mm of the subgrade showed slightly higher R2 values when compared to PR values for the top 300 mm of the subgrade.

The relationships presented in this study indicated that for if PR data between 2 to 78 mm are considered, the SE of the estimate ranged from 24 to 60 MPa, depending on the modulus

calculation method. The SE of the estimate decreased to < 20 MPa, when PR data from only subgrade are considered.

CHAPTER 10: PAVEMENT AND STABILIZED FOUNDATION LAYER ASSESSMENT WITH GPR

Increasingly, non-destructive testing methods are being applied to assess pavement system conditions. According to the mechanistic empirical pavement design guide (AASHTO 2008), ground penetrating radar (GPR) surveys of existing pavements is a key assessment method for pavement rehabilitation design. Although primarily used for thickness determination, GPR scans are also used to identify defects (e.g., voids, stripping within the asphalt layer, weak bonds between pavement layers) within the pavement layers and beneath the pavement layer; determine depth and alignment of reinforcement in pavements; and determine air void content and density of asphalt layers (Al-Qadi et al. 2003, Al-Qadi and Lahouar 2005, Al-Qadi et al. 2010, Lahouar and Al-Qadi 2008, Evans et al. 2008, Plati et al. 2012, Goel and Das 2008, Poikajarvi et al. 2012, Moropoulou et al. 2002, Loizos and Plati 2007). Conducting GPR scans has the advantage of being rapid and less expensive compared to conducting test pits or borings to evaluate existing pavement conditions and it can provide continuous measurements along a pavement alignment. Validation of the GPR results, however, limits broader application of this technology, especially for pavement foundation layer assessment.

Dielectric properties of the pavement and foundation layer materials are key input parameters in determining layer thickness using GPR. The dielectric properties of layers are either assumed based on published typical values, determined from field calibrations (Al-Qadi and Lahouar 2005), or measured directly using independent test devices (Loizos and Plati 2007). Field calibration and direct measurement methods have proved successful for asphalt materials, although some studies have shown that variations in asphalt moisture content can affect the results (Al-Qadi et al. 2010, Lahouar and Al-Qadi 2008, Loizos and Plati 2007, Al-Qadi et al. 2003). For the underlying pavement foundation layer materials, however, the dielectric properties can vary significantly because of moisture and material property variations (e.g., clay content, moisture content, chemical stabilizer content, partially frozen/thawed, etc.). Previous research (Al-Qadi et al. 2003, Grote et al. 2005) has demonstrated that GPR data can be used to detect moisture variations within the foundation layers, but very limited data exists for stabilized foundation layers.

This study was undertaken with two objectives. The first objective was to evaluate the use of ground-coupled GPR to determine the asphalt and pavement foundation layer thicknesses, where an independent dielectric property measurement was used as an input. The second objective is to assess if ground-coupled GPR can be used to detect moisture variations and effects of freezing/thawing in the unstabilized and stabilized subbase, and subgrade layers beneath the pavement.

In this study, the pavement thicknesses were measured from pavement cores and using a magnetic imaging tomography (MIT) gauge, and foundation layer thicknesses were measured using dynamic cone penetrometer (DCP). A laboratory experimental plan was designed to evaluate dielectric properties of chemically stabilized and unstabilized foundation materials in frozen and unfrozen conditions. To the authors' knowledge, this is the first study to document

dielectric properties of chemically stabilized materials and dielectric properties of pavement foundation layer materials in frozen and unfrozen conditions.

Thickness Determination using GPR

To determine thickness using GPR, the dielectric constant of the material is needed. The material dielectric constants can be estimated based on GPR signals or directly measured using hand-held test devices. There are two common ways to estimate dielectric constants of materials from GPR signals. One is to use the peak amplitude signals from each layer from a GPR scan in reference to the amplitude signal from a reflective metal surface, and the other is to use the two-way travel time in conjunction with known thickness values. The first method is applicable for air-coupled antennas (Cao et al. 2008, Al-Qadi et al. 2003), which were not used in this study and is therefore not described here. The two-way travel time method, which is applicable for ground-coupled antennas, was used in this study. According to Loken (2007), the two-way travel time method is not influenced by the errors associated with signal attenuations as with air-coupled methods.

The interval of time that it takes for the wave to travel from the transmitter to the receiver is called the two-way travel time. Using the two-way travel times between the different amplitude peaks observed in a wiggle scan, and known layer thickness values, the dielectric constant values can be determined using Eq.1 (Davis and Annan, 1989):

$$\varepsilon = \left(\frac{ct_i}{2h_i}\right)^2 \quad (1)$$

where, c = speed of light in air (0.30m/ns), ε = dielectric constant or relative electrical permittivity, h_i = individual layer thickness, and t_i = time travel in each individual layer.

Irrespective of the two test methods described above, a field calibration is first required wherein dielectric constant of the material is determined using direct thickness measurements. Using air-coupled GPR antennas, some previous studies (Al-Qadi et al. 2003, Irwin et al. 1989, Lalague et al. 2014) have documented average errors of about 6 to 10% when no core calibration was performed versus 1 to 5% when core calibration was performed. Some researchers [20, 23] have indicated that calibrating GPR data with at least 3 cores when compared to 1 core can substantially reduce the error.

As an alternative to field calibration, dielectric properties of the materials can be determined independent of GPR using hand-held test devices. However, there is no widely accepted method in terms of what test device should be used. Loizos and Plati (2007) used a hand-held Percometer device in determining dielectric properties of asphalt materials. They found that the location where the dielectric properties were measured (i.e., at the surface or in the middle or at multiple locations on a core), influenced the results. A dielectric probe manufactured by Adek, Ltd. was used by Saarenketo and Scullion (1995). In this study, a GS3 sensor manufactured by Decagon

Devices, Inc. was used to measure dielectric properties of asphalt and foundation layer materials. Details of GS3 are provided later in this chapter.

Moisture Content Determination in Foundation Layers

Moisture content influences the dielectric properties of the materials because the water dielectric constant is much higher (81) than that of air (1) or soil materials (4 to 20). Therefore, high dielectric constants of materials can be attributed to high moisture values (Loken, 2007).

Halabe et al. (1989) used the complex refractive model (CRM) to evaluate relationships between dielectric properties of a material mixture, its volumetric ratios, and dielectric properties of its components. Using the CRM, the gravimetric moisture contents of granular base materials can be obtained using Eq. 2 (Halabe et al. 1989):

$$w = (\sqrt{\varepsilon_b} - 1 - \frac{1-n}{\sqrt{\varepsilon_s}-1})/(\sqrt{\varepsilon_b} - 1 - \frac{1-n}{\sqrt{\varepsilon_s}-22.2}) \quad (2)$$

where, w = moisture content determined as fractional weight of water to total weight; ε_s = dry aggregate dielectric constant; ε_b = base layer dielectric constant determined using the two-way travel time method (Eq.1); and n = porosity = fractional volume of voids (air + water) to total volume.

To determine moisture contents from Eq. 2, the porosity of the material has to be either measured or assumed. Maser and Scullion (1992) used Eq. 2 by measuring the dry unit weight of granular base material at one location for calibration and then used the same constant value to estimate moisture content at other locations. Comparison between the measured and the predicted moisture contents in their study resulted in root mean squared error of < 2%.

Scullion et al. (1995) reported a procedure that involved developing a laboratory relationship between gravimetric moisture content and dielectric constant, to estimate moisture contents in situ from GPR scans. Results from their study indicated that the relationship between dielectric content of the mixtures increased with increasing moisture content (as expected), and the relationships were unique for each material type.

Grote et al. (2005) used field GPR scans to estimate the dielectric properties of the foundation layers from the two-way travel time method and then estimated material volumetric moisture contents based on laboratory relationships. Site and material specific relationships between volumetric moisture content and dielectric properties were used in their study for some materials. For materials where those relationships were not available, a third-order polynomial equation developed by Topp et al. (1980) based on tests conducted over a wide range of material types (sandy loam to clay loam to organic soil to glass beads) as shown in Eq. 3 was used:

$$\theta_v = 4.3 \times 10^{-6}\varepsilon^3 - 5.5 \times 10^{-4}\varepsilon^2 + 2.92 \times 10^{-2}\varepsilon - 0.053 \quad (3)$$

where, θ_v = volumetric moisture content; and ε = material dielectric constant.

Field and Laboratory Testing Methods

Field and Laboratory GPR Surveys

A GPR manufactured by Geophysical Survey Systems, Inc. (GSSI) was used in this study. GPR surveys were conducted on field test sections in March (winter/frozen ground) and September (fall) of 2014. A ground-coupled 900 MHz antenna setup with SIR-20 data acquisition system was used Figure 262. Based on the manufacturer recommendations, the following scan settings were used: (a) range = 15 ns; (b) frequency of scans = 64 Hz; and (c) number of samples per scan = 512.

For in situ GPR scanning, a survey encoder was used to connect the GPR device with a calibrated survey wheel to measure distance. For GPR scanning conducted in the laboratory box study, scans were performed in point-mode setting (i.e., data is collected only over a single point).

Pavement Coring

Iowa Department of Transportation (Iowa DOT) performed pavement coring at 58 locations in April 2014. The core thicknesses were measured in accordance with ASTM D3549. The core thicknesses are reported in this chapter as h_{core}.

MIT Gauge Scanning

The working principle of the MIT gauge is described in detail in Grove et al. (2012) and is manufactured by the MIT Measurement and Testing Technology (MIT Mess- und Prüftechnik) in Dresden, Germany. In brief, the MIT gauge generates a variant magnetic field that creates an eddy current in a metal reflector that is placed beneath the pavement. This eddy current will generate an induced magnetic field inside the metal reflector that can be detected by a sensor in the MIT gauge. Based on a calibration between the intensity of the induced magnetic field for a given type of reflector and the distance between the sensor and the metal reflector, the pavement thickness is calculated. The calibration is unique to the type of metal reflector used. Grove et al. (2012) showed that the differences between the MIT gauge thickness measurements and core thickness measurements was 2 mm or less, based on 106 data points collected over 12 project sites.

A picture of the MIT gauge used in this study is shown in Figure 262. In this study, 0.6 mm thick galvanized sheet metal circular discs supplied by the manufacturer were used. The metal discs were placed beneath the pavement at 109 selected locations that were marked with global positioning system (GPS).

Field DCP Testing

DCP tests were conducted in the foundation layers shortly after the pavement cores were removed and at various test locations prior to paving (Figure 262). Tests were done at a total of 100 locations in accordance with ASTM D6951. Penetration resistance (PR) and cumulative blows versus depth plots were generated at each test point to determine the base layer thickness as illustrated in Figure 262. The base layer thickness was determined as the depth from the bottom of the asphalt layer to the inflection point of the tangent of the lower portion of the cumulative blows with depth curve.

Figure 262. (a) Test setup using GS3 sensor and GPR antenna in laboratory box study; (b) MIT gauge; (c) GPR setup with a scanning survey wheel setup in situ; and (d) DCP testing of the foundation layer through a pavement core

Dielectric Constant Determination

Dielectric constant of asphalt and foundation layer materials were directly measured using a GS3 sensor manufactured by Decagon Devices, Inc. (Figure 262) and was also estimated using the

two-way travel time method per Eq.1. The dielectric constant measured with the GS3 is reported as ε_{GS3} while the dielectric constant estimated from Eq.1 is reported as ε_{GPR}.

The GS3 device uses capacitance/frequency domain technology to measure soil dielectric constant. The device uses an epoxy body and consists of three stainless steel needles, and has a thermistor to measure temperature. It uses an electromagnetic field to measure the dielectric permittivity of the surrounding medium (Decagon 2015). The sensor supplies a 70 MHz oscillating wave to the sensor prongs that charges according to the dielectric properties of the material. According to the manufacturer, the sensor has a measurement influence depth of about 10 cm (Decagon 2015).

The GS3 sensor was used for measurement of laboratory compacted specimens and in field on the asphalt layers. The laboratory compacted specimens for foundation materials were prepared by compacting materials in accordance with ASTM D698 at various target moisture contents, to assess relationships between gravimetric moisture content (w) and ε_{GS3}. Laboratory testing was conducted on the following materials: loess, subgrade glacial till, CLS, reclaimed subbase (RSB), and Portland cement (PC) and fly ash (FA) treated glacial till subgrade. A nominal 10% PC and 20% FA (by dry weight of soil) was used for treatment, to match with field conditions. All compacted specimens, except the FA and PC treated subgrade samples, were tested immediately after compaction and after freezing for about 48 hours at about -16^{o}C. The PC and FA treated subgrade samples were tested at various times after compaction up to about 7 days to assess the influence of curing (i.e., time dependent formation of cementitious reaction products that hold water) on ε_{GS3} measurements.

Laboratory Box Testing

Laboratory box testing was conducted in this study to evaluate the GS3 device by comparing ε_{GPR} and ε_{GS3} results for various materials compacted at different target moisture contents. A repeatability study on the two-way travel time method to estimate the ε_{GPR} was also conducted as part of the box study. The materials included Iowa loess, concrete sand, CLS, and cold mix asphalt (CMA).

The materials were compacted in a 762 mm × 304.8 mm × 381 mm wooden box. A metal plate was placed at the bottom of the box as a reflection surface for GPR scans. Tests were conducted on uniform single layer of material with Iowa loess and concrete sand and two- and three-layered structures with loess, CLS, and CMA. The layers were compacted in thin layers (< 30 mm thick) using a hand tamper.

GPR scan and GS3 sensor measurements were simultaneously obtained on the different materials. The two- and three-layered structures were tested at room temperature and after freezing in a temperature chamber for 48 hours (at about -18^{o}C) to assess the influence of frozen versus unfrozen conditions.

Asphalt Layer Thickness Determination In Situ

Asphalt layer thicknesses were determined from core measurements and using the MIT gauge. GPR scanning data was used to estimate the asphalt layer thicknesses at the core and MIT test locations for comparison with the measured thicknesses, using three procedures.

The first procedure involved the following steps: (1) measure ε_{GS3} from one location in each asphalt mixture type and assume the same at all core locations in the test sections with the same mixture type; (2) convert ε_{GS3} to ε_{GPR} using a relationship developed from the laboratory box study; (3) determine the two-way travel time from the GPR scan at each core location for the asphalt layer; and (4) use the two-way travel time and ε_{GPR} in Eq.1 to estimate the asphalt layer thickness (h_{GPR1}).

The second procedure involved the following steps: (1) determine two way travel times at each core location in sections with same asphalt mixture type; (2) use Eq.1 and h_{core} at each location to calculate ε_{GPR}; (3) average those values for each asphalt mixture; (3) using the two-way travel time at each location and the average ε_{GPR}, estimate the asphalt layer thickness (h_{GPR2}). This procedure was used herein to assess the advantage of using average data (from multiple samples) over single point data as described below in the third procedure.

The third procedure involved the following steps: (1) determine two-way travel time from the GPR scan at one random core location for each asphalt mixture type; (2) use Eq.1 and the measured h_{core} at the location to determine ε_{GPR} and assume it's the same at all core locations in the test sections with the same mixture type; and (3) determine two-way travel time at the remaining core locations use in Eq.1 to estimate the asphalt layer thickness (h_{GPR3}).

Results and Discussion

Laboratory Box Study Results

GPR scanning test results on two- and three-layered systems at room temperature and after freezing are presented in Figure 263. Moisture contents of the CLS and loess layers are noted in Figure 263. Comparison of results at room temperature and after freezing indicated different two-way travel times. For example, the two-way travel time to the metal sheet was about 8 ns at room temperature, while it was about 6 ns after freezing. In the frozen condition, the CLS/loess layer interface is not as well defined as when not frozen.

Results from the box study comparing ε_{GPR} and ε_{GS3} are shown in Figure 264, which yielded a linear regression relationship with coefficient of determination (R^2) = 0.95 and standard error (SE) = 1.3. As shown the ε_{GS3} values are lower than ε_{GPR} values. The reasons for this difference is attributed to the differences in the measurement influence depths and the measurement errors associated with the two methods. ε_{GPR} represents an average value for the full depth of each layer, while ε_{GS3} only represents the surrounding medium in the depth of penetration.

The repeatability of the two-way travel time method to determine ε_{GPR} was evaluated by obtaining repeated measurements on two-layer and three-layer structures. The results are summarized in Table 3, which indicated that the measurement error of ε_{GPR} was < 0.1 for all materials and the percentage error relative to the average value was < 1.5%. The CLS and loess layers showed different dielectric constant values in two-layer and three-layer systems. The reason for this is attributed to differences in the material moisture contents.

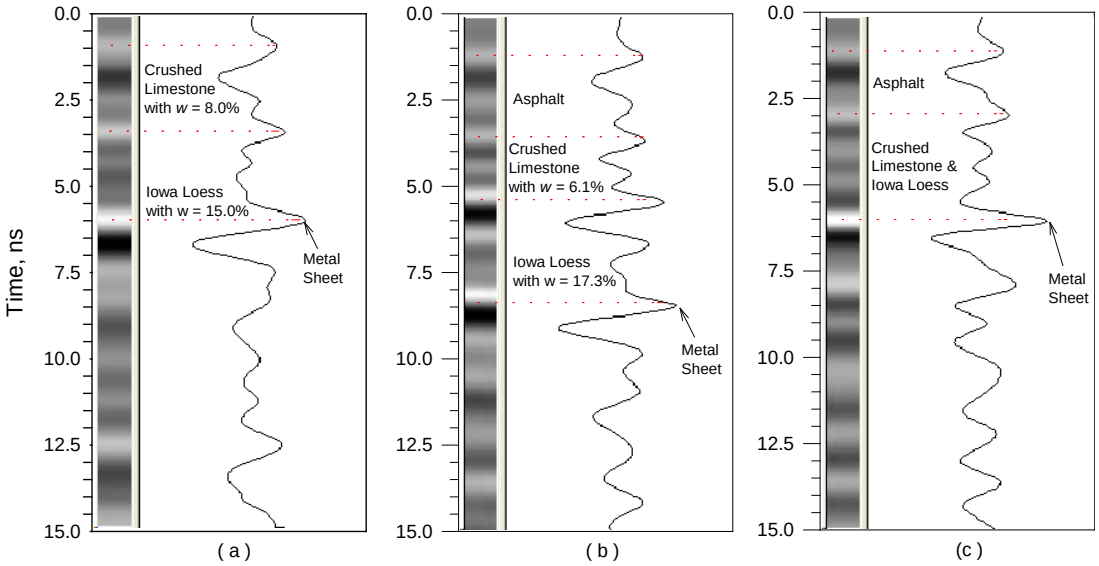

Figure 263. Results of laboratory box study with (a) two layered profile at room temperature, (b) three layered profile at room temperature, and (c) three layered profile frozen at -17.8°C for 48 hours.

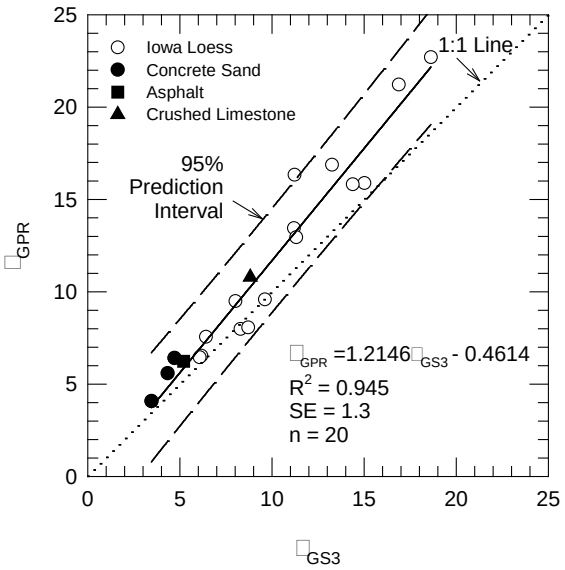

Figure 264. Comparison of dielectric constant values determined from GPR (ε_{GPR}) and GS3 sensor (ε_{GS3}).

Laboratory Dielectric Constant Measurements on Compacted Specimens

Results showing ε_{GS3} versus gravimetric moisture content (determined on batched materials) immediately after compaction and after freezing are shown in Figure 265. The results indicated that ε_{GS3} values increased with increasing gravimetric moisture content for all materials, as expected, and the relationship between ε_{GS3} and moisture content is unique for each material type. When frozen, the ε_{GS3} values ranged between 4 and 6 for all materials. This is expected because the dielectric constant in the ice phase of frozen water is about 3.2 (Hallikainen 1977).

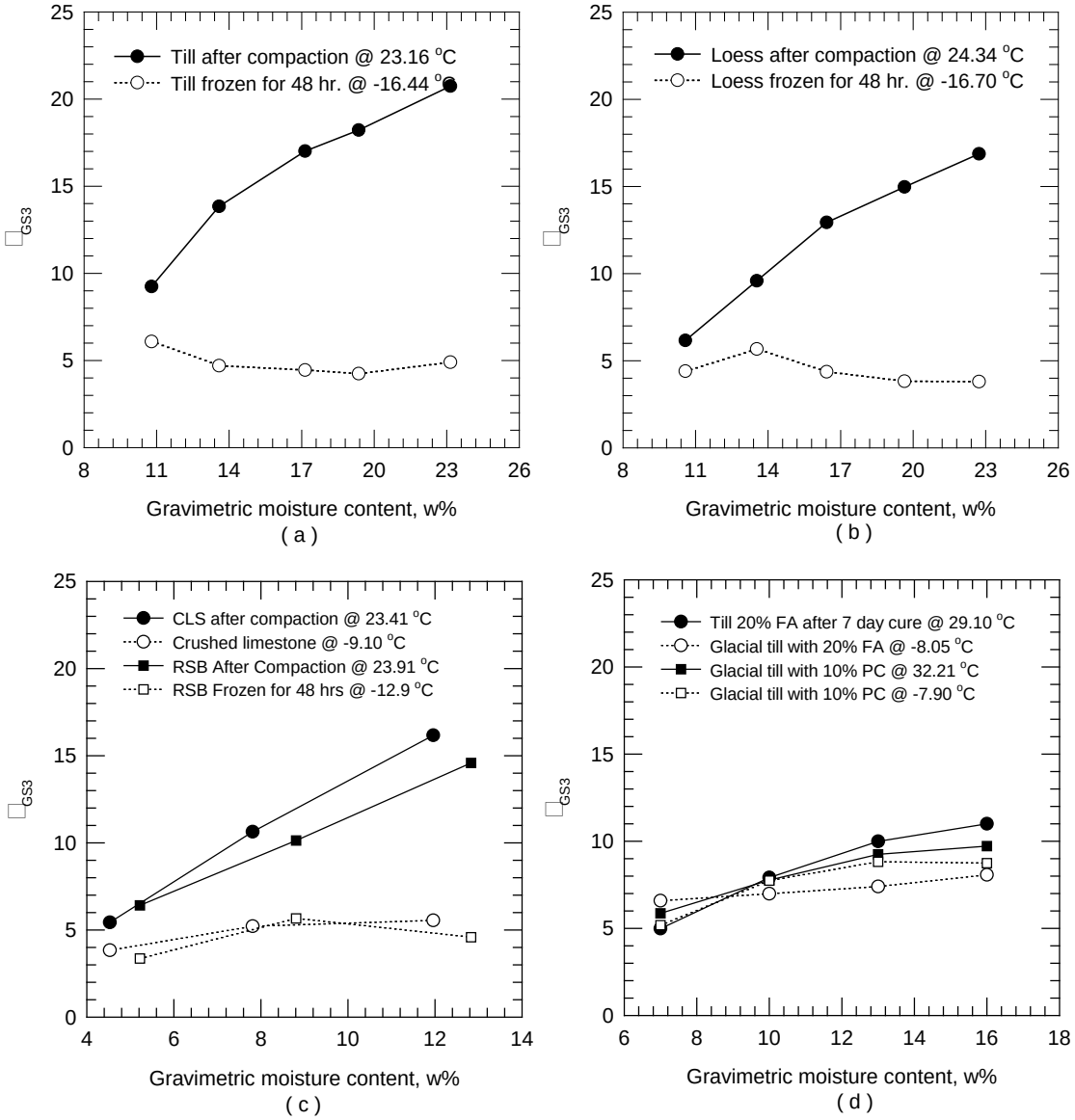

Figure 265. ε_{GS3} versus gravimetric moisture content on: (a) glacial till subgrade, (b) Iowa loess, (c) CLS and RSB, and (d) glacial till treated with PC and FA.

Figure 266 shows ε_{GS3} versus curing time for chemically stabilized specimens compacted at different moisture contents. ε_{GS3} increased with increasing moisture content and decreased with curing time up to about 12 hours and then stayed relatively constant. The changes in ε_{GS3} with curing time is attributed to the hydration process where the amount of free water decreases with curing. This was also observed by others that investigated the concrete hydration and curing process (Makul 2013).

The PC and FA stabilized subgrade produced lower dielectric constant values compared to unstabilized subgrade. For example, at about 16% gravimetric moisture content, the ε_{GS3} of the unstabilized subgrade was 16 while ε_{GS3} of the PC and FA stabilized subgrade was about 10.

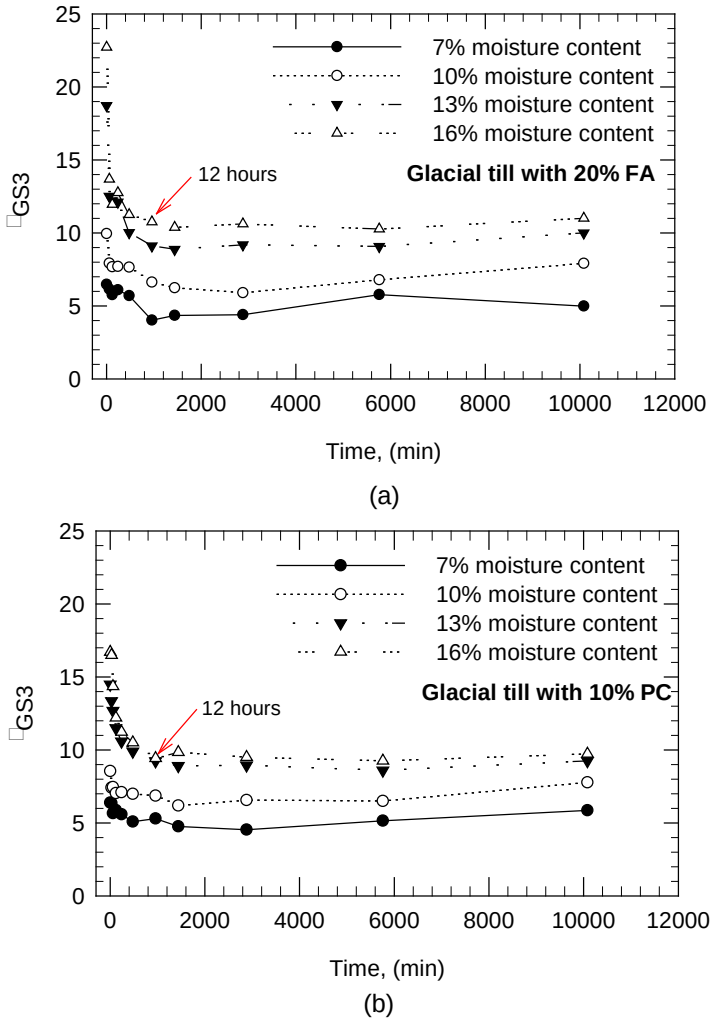

Figure 266. ε_{GS3} on chemically stabilized till subgrade at different moisture contents after different curing times: (a) stabilized with 20% FA and (b) stabilized with 10% PC.

Field Test Results

Results of GPR scans for a portion of a test section from the two testing times are shown in Figure 267. Ground temperatures are presented in Figure 268, which indicates the foundations layers were frozen in March up to a depth of about 1.3 m below the pavement surface. GPR scans obtained during March did not show a transition between subbase and subgrade layers. This confirmed the laboratory box study results.

The measured (h_{core}) and estimated (h_{GPR1}, h_{GPR2}, h_{GPR3}) asphalt layer thicknesses are compared in Figure 269. Comparison between the average measured and estimated thickness values for each asphalt mixture type and the average percentage error of the estimates relative to the average measured values are summarized in Table 27. The percentage error is calculated as the ratio of the root mean square error relative to h_{core} and the average h_{core}.

The h_{GPR1} values estimated using the ε_{GS3} values produced an average error of about 11%. The estimated h_{GPR2} and h_{GPR3} values produced values closer to the 1:1 line when compared with the measured values. The error values ranged between 2.7 and 8.6% for h_{GPR3}, depending on the core sample selected in the analysis. The average error reduced to about 3.7% for h_{GPR3}, when average ε_{GPR} was used for each material type. This suggests that if calibration is performed with more number of samples, the error in the predicted values can potentially be minimized. The percentage error values reported herein are similar to reported by others with air-coupled antennas (Al-Qadi et al. 2003).

Comparison between asphalt layer thickness measured using the MIT gauge and GPR (h_{GPR2}) is presented in Figure 270. h_{GPR2} was chosen here for comparison as the data was close to the 1:1 line when compared with h_{core} (Figure 269). Results indicated that MIT gauge thickness measurements were on average about 9% higher (i.e., about 15 mm) than estimated with GPR. The 15 mm error measured from testing on asphalt cores in this study is higher than reported in Grove et al. (2012) study which was 2 mm from testing on concrete cores. A thorough future evaluation with a direct comparison between core thickness and MIT gauge is warranted.

GPR scans from September 2014 identified the bottom of the granular base layer (CLS or CLS+RSB layer). On 9th St. test sections where CLS and RSB constitute the subbase layers, a clear transition between the two layers could not be identified in the GPR scans, and is therefore analysed as a single layer. This is attributed to the similar dielectric properties of the two materials as identified in the laboratory testing. The analysis herein is focused only on the CLS and RSB layers, as no transitions were identified in the layers beneath the RSB layers.

Thickness determination of foundation layers from GPR scans was not possible as the laboratory testing showed strong influence of moisture content on dielectric properties of the subbase layer material. The thickness of the base layers (h_{base}) determined from DCP tests and the two-way travel times were used to determine ε_{GPR} of the subbase material. Volumetric moisture contents were determined using ε_{GPR} and Eq. 3 for comparison between the test sections. The purpose of this analysis was to assess variations in the subbase layer moistures between the various test

sections. The average ε_{GPR} and volumetric moisture content values determined from DCP test locations are shown in Figure 271.

Results indicated that on average, the volumetric moisture contents in the subbase layer varied from about 6% to 25%. The 8th St. test section showed the lowest values. Field permeability test results documented earlier in Chapter 7 on 8th St. South section indicated that the CLS layer on this street yielded high saturated hydraulic conductivity and less non-uniformity (Average = 22.7 cm/s and coefficient of variation = 107%), compared to testing performed on 11th St. South section (Average = 1.8 cm/s and coefficient of variation = 172%) and 5th St. South section (Average = 13.2 cm/s and coefficient of variation = 207%). The 8th St. section consisted of more open-graded materials with less segregation and particle degradation compared to 11th St. and 5th St. sections.

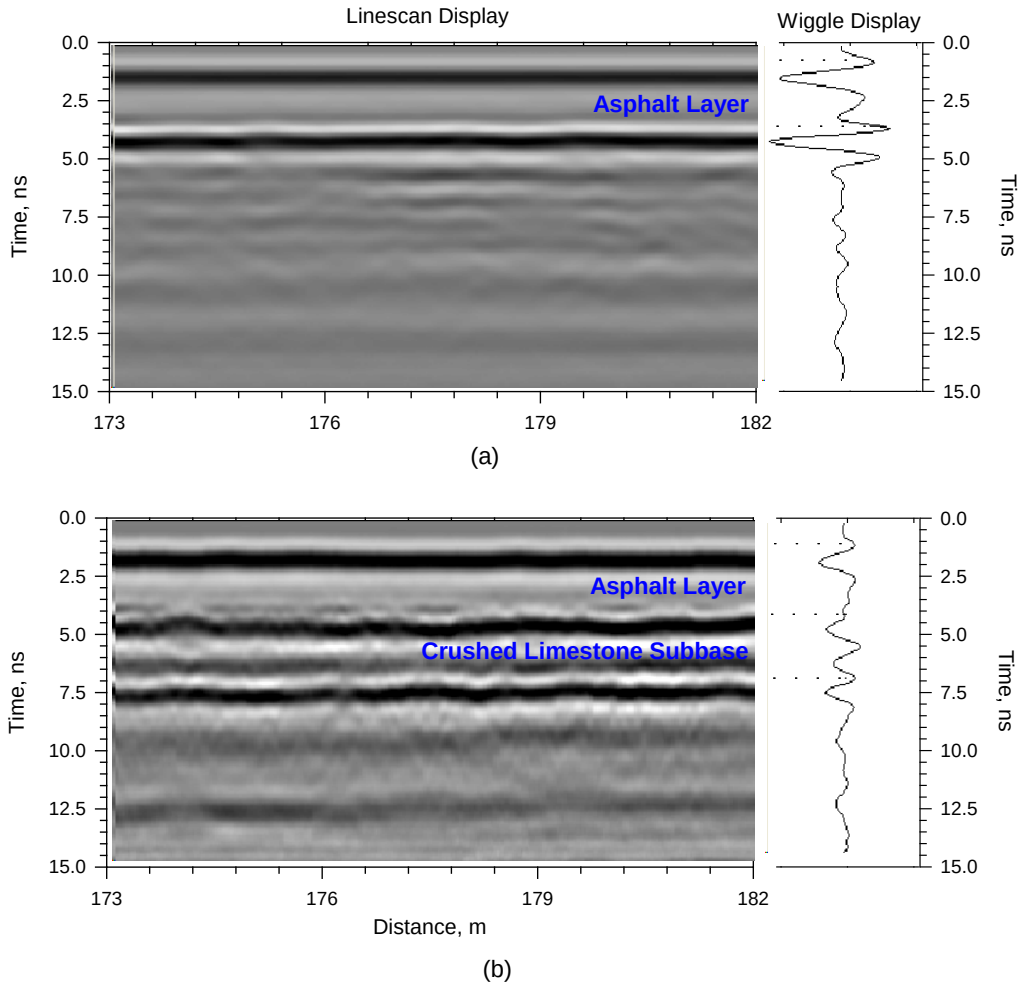

Figure 267. In situ GPR scans on 10th St. South section (a) on 03/12/14, (b) on 09/16/14.

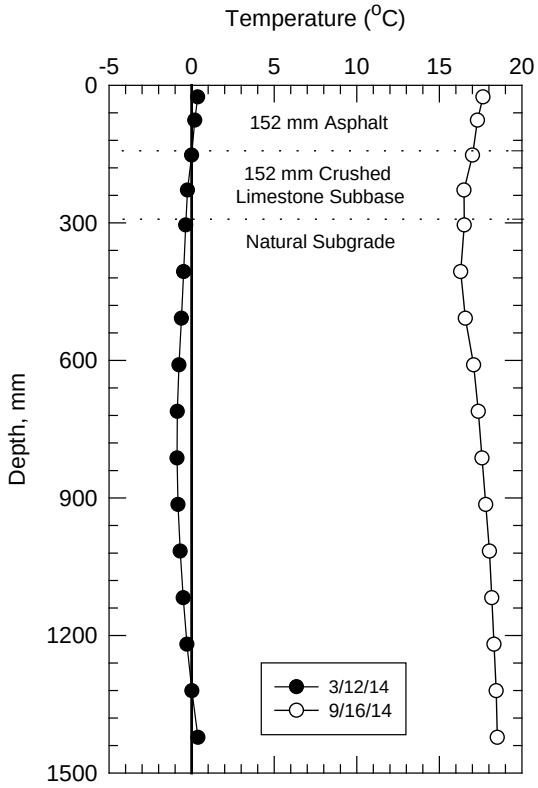

Figure 268. In situ ground temperatures during the two testing times.

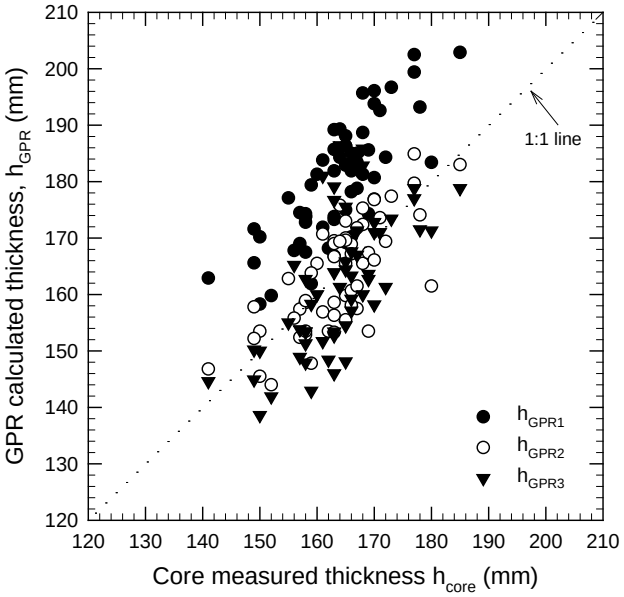

Figure 269. GPR estimated h_{GPR} versus core measured asphalt layer thickness h_{core}.

Table 27. Comparison between average asphalt thicknesses measured from core and different predicted from GPR scans and percentage errors in predictions.

Street	Asphalt layer description	No. of Measurements	Average h_{core} (mm)	h_{GPR1} Average (mm)	h_{GPR1} Error[e] (%)	h_{GPR2} (mm) Average (mm)	h_{GPR2} (mm) Error[e] (%)	h_{GPR3} (mm) Average (mm)	h_{GPR3} (mm) Error[e] (%)
1st / 2nd	50 mm HMA[a] surface with LAA[c] and 102 mm HMA[a] base with LAA[c]	16	163.3	178.8	10.3	163.2	3.6	156.3-175.6	3.9-8.5
3rd S. / 4th	50 mm WMA[b] surface with LAA[c] and 102 mm WMA[b] base with LAA[c]	10	165.5	183.5	11.3	165.5	2.7	160.9-175.6	2.7-5.1
7th / 8th	50 mm HMA[a] surface with HAA[d] and 102 mm HMA[a] base with LAA[c]	16	165.4	182.2	11.1	165.1	5.3	155.7-184.0	5.3-8.6
9th S. / 10th	50 mm WMA[b] surface with HAA[d] and 102 mm HMA[a] base with LAA[c]	11	160.1	173.9	9.5	159.8	3.8	151.0-169.9	4.8-7.2
11th	50 mm WMA[b] surface with HAA[d] and 102 mm WMA[b] base with LAA[c]	5	163.8	181.6	11.4	163.7	3.1	157.2-172.7	3.4-6.3

[a] Hot mix asphalt.
[b] Warm mix asphalt.
[c] Low absorbed aggregate.
[d] High absorbed aggregate.
[e] Error (%) = 100 x (root mean squared error in reference to h_{core})/Average h_{core}.

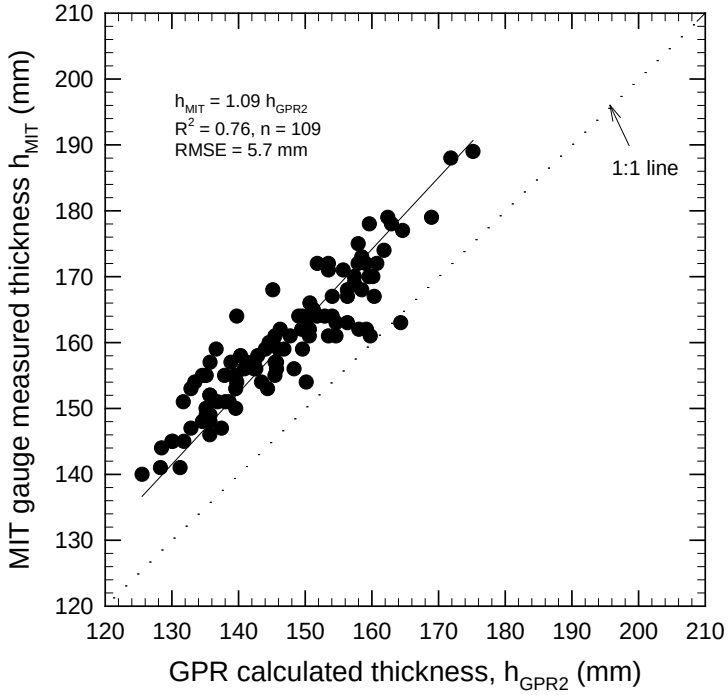

Figure 270. GPR versus MIT gauge measured asphalt layer thickness.

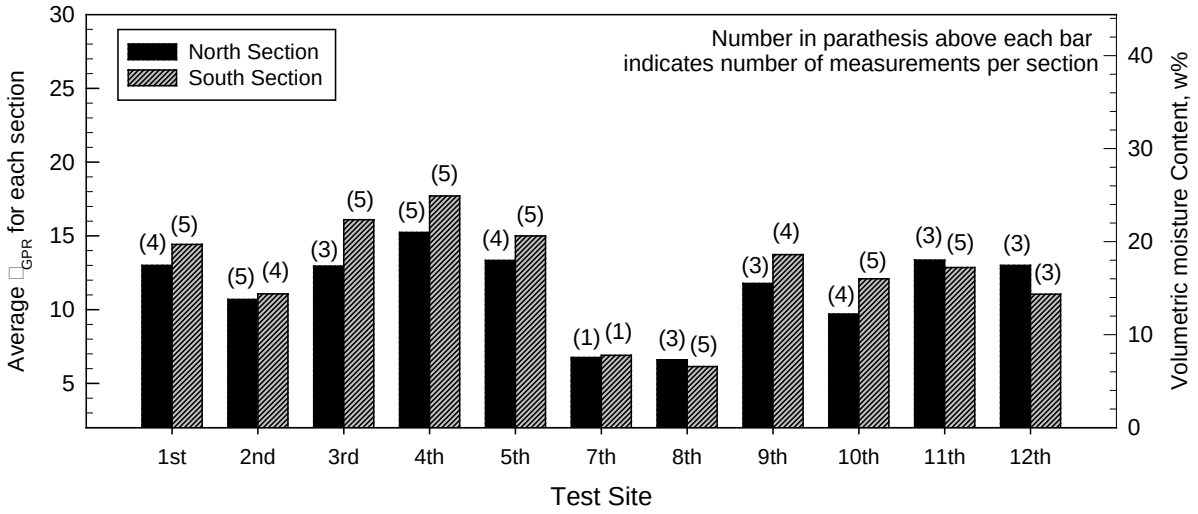

Figure 271. Estimated average in situ base layer ε_{GPR} and volumetric moisture content for each street based on DCP measurements.

Summary

Following are key findings and conclusions from this study:

- The dielectric properties obtained from the independent dielectric measurement gauge used in this study correlated strongly with the values back-calculated from GPR and yielded R2 = 0.945 with a standard error of 1.3.

- A new database of dielectric properties of subgrade and base layer materials and chemically stabilized subgrade materials at different moisture contents is provided in this report. Results indicated that the dielectric properties are sensitive to moisture content, as expected, and are sensitive to curing times for chemically stabilized soil due to the hydration process. PC and FA stabilized subgrade materials produced lower dielectric values than unstabilized subgrade materials.
- GPR surveys conducted during frozen condition did not properly differentiate variations in the foundation layers because of similar dielectric properties of those materials in a frozen condition. This was verified by conducting a simple laboratory box study with compacted pavement and foundation layers in frozen and unfrozen conditions.
- The estimated asphalt thicknesses (hGPR1) using the □GS3 values produced an average error of about 11% (Table 4). The estimated values (hGPR2 and hGPR3) were close to the 1:1 line when compared with the measured values, when □GPR was used. The error values ranged between 2.7 and 8.6% hGPR3, depending on the core sample selected in the analysis (Table 4). The average error reduced to 3.7% for hGPR3, when average □GPR (based on multiple cores for each material type) was used in the analysis. These errors are similar to reported by others in the literature with air-coupled GPR antennas.
- Comparison between asphalt thickness measured using the MIT gauge and GPR (hGPR2) indicated that the MIT gauge measurements were on average about 9% higher than estimated with GPR.
- GPR data was used to estimate volumetric moisture content of the granular subbase material. Results indicated that on average, the volumetric moisture contents in the subbase layer varied from about 6 to 25%. The variations are attributed to material segregation and degradation, and variations in aggregate gradations and permeability between the test sections.

CHAPTER 11: TEMPERATURE MONITORING RESULTS AND ANALYSIS

In seasonal frost areas, freeze-thaw and frost penetration depth have been reported as contributors to accelerated pavement problems (Cassagrande et al. 1931; Chamberlain 1986; DeGaetano et al. 2001). Estimating freezing depth has gained great importance for pavement design and maintenance. Several researchers have investigated various empirical and numerical methods to predict frost penetration in pavement systems (Aldrich and Paynter 1953; DeGaetano et al. 2001; Jumikis 1955; McCracken 1988).

Stefan (1890) presented an equation based on Fourier's law to calculate the rate of ice formation. There are critical assumptions and limitations associated with the Stefan equation. However, civil engineers used the equation for predicting frost penetration into bare ground, and later, they improved the Stefan equation (Aldrich and Paynter 1953; Andersland and Ladanyi 2004). Several simplified models have been developed, but model results indicate significant uncertainties (Baladi and Rajaei 2015; Yoder and Witczak 1975). The modified Berggren equation is widely used in civil engineering (Bianchini and Gonzalez 2012). For this model, a modified factor that was determined empirically was included in the Stefan equation to overcome the limitation of neglecting soil volumetric heat. (Aldrich and Paynter 1953; Freitag and McFadden 1997). Several computer programs and methodologies were developed for calculating heat transfer in multi-layer conditions, including pavements (Aitken and Berg 1968; Bianchini and Gonzalez 2012). However, limited research has been performed to evaluate the modified Berggren based methods by comparing the predicted results to actual in situ measurements.

In this study, pavement temperature sensors were installed at three locations in the state of Iowa. The principal objectives of this research are to determine the actual frost penetrations from in situ pavement temperature measurements, to estimate the frost penetrations with the traditional modified Berggren and other simplified empirical models, and to compare the predicted results to the actual measurements.

Seasonal Frost Penetration Estimations

Climatic influences have been taken into consideration in recent pavement design guides (AASHTO 1993; AASHTO 2008). In seasonal frost areas, the design of mechanistic parameters of roadbeds (e.g., resilient modulus and modulus of subgrade reaction) was modified using values determined under different seasonal conditions (AASHTO 1993; AASHTO 2008). However, frost penetration depth is still a key factor and needs to be verified if pavements have the potential to undergo freezing and thawing. From historical weather station data, frost depth maps are available for the United States (DeGaetano et al. 2001). The frost depths were determined from one to two hundred year return periods for bare soil, bare soil with snow cover, and turf. The average maximum frost penetration depths in Iowa ranged from 100 to 120 cm using pavement temperature data. Andersland and Ladanyi (2004) reported the 0°C isotherm value as an approach for analyzing temperature variations in pavement structures for lengths of freezing and thawing periods in different layers. Frozen zones versus time can be estimated from

the 0°C isothermal depth. Determination of the 0°C isotherm depth also represent the maximum frost penetration depth.

Hoover et al. (1962) investigated pavement freeze-thaw conditions over three winters (1957 through 1960) on US Highway 117 in Jasper County, Iowa using the modified Berggren equation. Seven thawing periods during the 1957–1958 winter and nine during the 1959–1960 winter were documented (Hoover et al. 1962). During the 1958–1959 winter, a large continuous frozen zone and several smaller, thawed zones were observed at shallow depths for short times within the frozen period. Hoover et al. (1962) also estimated that there were 11 freeze-thaw cycles based on air temperature data, but only one freeze-thaw cycle at the 0.4 m depth. The maximum frost penetration reached around 1.05 m during the three winters. New empirical and numerical models were developed to estimate frost penetrations based on air temperature data (see Table 27). However, each model had particular limitations and assumptions, which led to variations in the estimated results. The simultaneous heat and water (SHAW) model is a one-dimensional model that is able to simulate heat and water movement in freezing and thawing soils (Flerchinger et al. 1998).

Table 28. Models for predicting frost penetrations using air temperature data

Key Equation	Measurements	Initial Assumptions	Limitations	Reference
$X = \sqrt{\frac{48k(FI)}{L}}$	ɣ and ω – assumed or measured in lab; T – measured in field (air or surface); n – assumed based on literature values or measured in situ. (or measure soil thermal properties directly in situ)	Air T equals surface T; isothermal boundary T is 0°C; surface T is constant. The soil is semi-infinite, uniform and isotropic; Surface temperature changes to below 0°C suddenly and keeps constant.	Overestimate X due to neglecting volumetric heat effect.	Stefan (1889) Freitag and McFadden (1997)
$X = \lambda\sqrt{\frac{48kn(FI)}{L}}$		Homogeneous soil; ground is bare soil with single layer (weighted soil properties if multi-layer).	Does not consider the movement of water in freezing soil; ground is one-dimensional.	Aldrich and Paynter (1953) Aitken and Berg (1968)
$FI = \frac{d_i L_i}{24n\lambda_i^2} \times R$		Surface temperature changes to below 0°C suddenly and keeps constant;		Bianchini and Gonzalez (2012)
$X = a(FI)^b$	T - measured in field (air or surface)	Bare single layer soil; temperature is the only significant influence on X.	Empirical correlations based on local data.	Rajaei and Baladi (2015)

Note: Equations are in US units. *X*: frost penetration depth; *k*: thermal conductivity; *FI*: Freezing Index; *n*: factor transfers air FI to surface FI; *L*: latent heat; λ: correction coefficient; *d*: layer depth; *R*: thermal resistance; ɣ: dry unit weight; ω: moisture content; T: temperature; a, b: constant; C: volumetric heat capacity; v_0: absolute value of the difference between the mean annual temperature below the ground surface and 0°C; v_s: absolute value of the difference between the mean annual ground surface temperature and 0°C.

The Stefan equation was originally created for calculating the growth rate of ice sheets (Bianchini and Gonzalez 2012; Freitag and McFadden 1997; Stefan 1889). This model assumes that the amount of heat flux flow through an existing ice sheet was equal to the amount of latent heat generated from the formation of new ice. The Stefan equation was then applied to solve the soil-ice problem. An equation was developed based on the Fourier's law, which is used to calculate the thickness of an ice sheet or a frozen soil layer. The equation was a function of freezing index (FI), thermal conductivity (k), and latent heat (L) (Freitag and McFadden 1997). However, the three principal assumptions lead to significant influences on the calculations: the air temperature was the same as the ground surface temperature; the temperature at the isothermal boundary was 0ºC; and the soil profile was homogeneous and isotropic (Jumikis 1955).

Weaknesses on applying the Stefan equation have been reported (Aldrich and Paynter, 1953; Bianchini and Gonzalez, 2012; Nixon and McRobert 1973). First, there is a possible misuse of the FI term. In accordance with the process of deducing this equation, the FI term was obtained by integrating the temperature difference between the frozen soil and the freezing temperature (0°C) (Bianchini and Gonzalez 2012). Even when the temperature is measured near the interface of the frozen soil and air, it still shows a significant difference between this temperature and the air temperature. This led to inclusion of an n-factor used to transfer the air FI term to the ground surface FI term (Hanson et al. 2010). Andersland and Ladanyi (2004) summarized the freezing and thawing n-factors of different types of ground (e.g., the freezing n is 0.25–0.95 for concrete pavement). Limited research has focused on determining this factor, although investigators have reported different assumed n values for different areas (Brown 1963). However, it can be inferred that local environmental conditions such as wind speed, radiation, and moisture content influence n-factor values (Andersland and Ladanyi 2004; Khoshkhoo et al. 2015).

Due to the original assumption (Jumikis 1955), the sensible heat released from ice formation was not taken into consideration. As the ice mass increases, the volumetric heat of the frozen soil layer increases. The sensible heat generated near the frozen surface increases as ice forms, while the equation only accounts for latent heat. This weakness leads to an overestimation of the frozen soil thickness (Aitken and Berg 1968; Freitag and McFadden 1997). For the purpose of reducing influences from these weaknesses, the modified Berggren equation was developed (Jumikis 1955; MIT 1957).

Aldrich and Paynter (1953) modified the Stefan equation to become the modified Berggren equation by introducing a correction coefficient, λ. This coefficient can be calculated through a semi-empirical correlation accounting for both the latent heat and the sensible heat (Braley and Connor 1989). Computer programs were developed to determine λ through transcendental equations, especially to iterate the λ values of multilayered ground and to estimate frost penetration depth (Bianchini and Gonzalez 2012; USDA and USDAF 1988). However, manual computation of λ is only accessible through an empirical correlation in terms of fusion parameter μ and thermal ratio α, where μ is the parameter accounting for sensible heat (Aldrich and Paynter 1953). Hoover et al. (1962) applied the modified Berggren equation to estimate historical frost penetration depths, and Orakoglu et al. (2016) used it to estimate maximum frost penetration depths. Averaged soil properties corresponding to assumed frost penetration depths were used to determine λ and soil thermal properties for the study reported by Orakoglu et al. (2016).

Following Braley and Connor (1989), Bianchini and Gonzalez (2012) reported an improved method for predicting multi-layered frost penetration using air FI values based on the modified Berggren equation. A computer program named "Pavement-Transportation Computer Assisted Structural Engineering" (PCASE) was developed based on this calculation process. The basic theory of this method is to calculate the portion of FI that is required to penetrate a specific thickness of ground layer. After the sum of the FI of each calculated layer becomes equal to the surface FI, it indicates that the final depth in the lowest layer represents the calculated frost penetration depth (Bianchini and Gonzalez 2012). A minor weakness of this method and also the previous average method is that the dry unit weights and moisture contents of each layer need to be assumed if measurements are not available in order to determine the latent heat and thermal conductivity. These assumptions increase the uncertainty of the results (Orakoglu et al. 2016). The default values of moisture content and dry unit weight in PCASE for the US moist-cold zone are summarized in Table 28.

Table 29. Default moisture contents and dry unit weights for the moist-cold zone in PCASE

	Moisture Content (%)	Dry Unit Weight (kg/m^3)
Asphalt Cement Concrete	0.5	2243
Portland Cement Concrete	0.5	2323
Base Coarse	5	2243
Subbase Coarse	8	2082
Subgrade (clay/silt)	16 – 21	1522 – 1682

In Situ Measurements

In Situ Pavement Temperature Monitoring

Thermocouples were installed at three locations in the state of Iowa, central Iowa Expo (Expo – 1) site 1, central Iowa Expo (Expo – 2) site 2, and the US Highway 30 (US 30) site during construction. The pavement structures differ at the three locations. At the Expo sites, thermocouples were installed in each pavement layer and solar powered data acquisition systems were set-up at the testing locations (Figure 272). Temperature data were monitored every minute, and the data were collected before winter freezing initiated until spring thaw occurred.

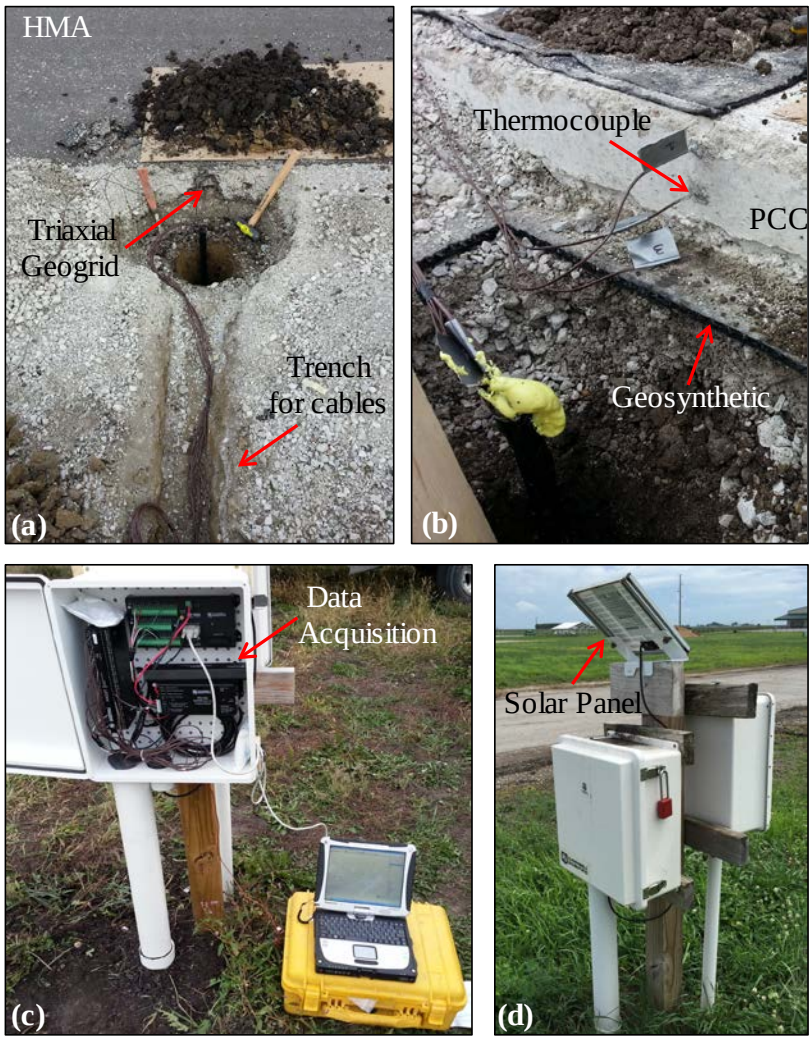

Figure 272. Installing thermocouples in pavements at (a) the Expo – 1 site and (b) Expo – 2 site, (c) collecting data at site, and (d) data acquisition system

At the expo sites, a total of 32 thermocouples were installed in October 2013 at Expo – 1 which had a HMA surface and at Expo – 2 which had a PCC surface (16 thermocouples each street), and two thermocouples were also placed near the ground surface to monitor the air temperature. Thermocouple 1 is placed 2.54 cm below the surface, and thermocouple 2 is 5.08 cm below the first thermocouple. Temperature data from thermocouple 1 were used to approximate boundary condition. Thermocouples 2 to 5 are 7.62 cm vertically apart from each other, and thermocouples below thermocouple 5 are spread by 10.16 cm. There is a modified subbase layer (MSB) under the 15 cm thick pavement layer at both streets, and a layer of geosynthetic was placed at Expo – 2 between the PCC and MSB layer. A layer of triaxial geogrid was used at Expo – 1 at the bottom of MSB. Another 15 cm thick subbase layer was stabilized with portland cement and fibers at Expo – 2 above the natural subgrade. The detailed thermocouple layout and pavement profiles at the Expo site are shown in (Figure 273).

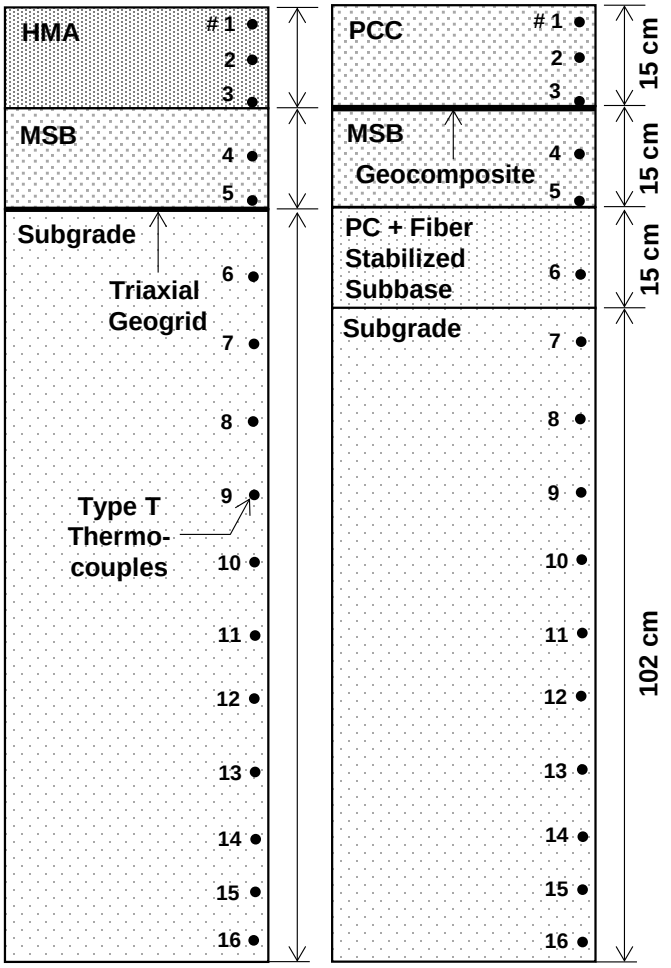

Figure 273. Pavement profiles with thermocouples at Expo – 1 (left) and Expo – 2 (right)

Thermocouple temperature sensors were installed at about mile 143.68 on US30 eastbound lane in July 2011. A nominal 25 cm thick jointed plain concrete pavement (JPCP) was placed on a 40 cm thick modified subbase (MSB) that was over the natural existing subgrade. Sensors were installed vertically from about 0.4 m to about 1.6 m below pavement surface. No sensor was installed within the 25 cm thick PCC layer and the upper 15 cm thick MSB layer. All vertical sensors were located at the center line. A pavement and foundation layer cross-section along with the temperature sensor locations was shown in Johnson (2012).

Frost Penetration Depth

The number of freeze-thaw cycles with depth calculated for each year from 2013 to 2016 from the temperature monitoring data at both Expo sites are presented in Figure 274. The cycles were determined using ±0.5ºC as boundary values, which means temperature dropped below -0.5 ºC and later increased higher than 0.5 ºC was defined as one freeze-thaw cycle. This approach effectively neglected some cycles that the temperature slightly varied around 0 ºC (such as from -0.1 ºC to 0.1 ºC), which may not significantly influence pavement conditions. Freeze-thaw cycles decreased with depth as expected. The number of freeze-thaw cycles in air were between 41 and

65 and decreased to about 3 to 11 cycles near the bottom of the pavement. Although there were differences in the number of freeze-thaw cycles between PCC and HMA layers, the numbers of freeze-thaw cycles became more similar as depth increased. From the bottom of the MSB layer at a depth of about 40 cm, less than 3 cycles were found at both locations. The deepest freeze-thaw cycle during the monitored years was observed between 120 to 140 cm. This finding indicated that the maximum frost penetration was within this range at the Expo sites.

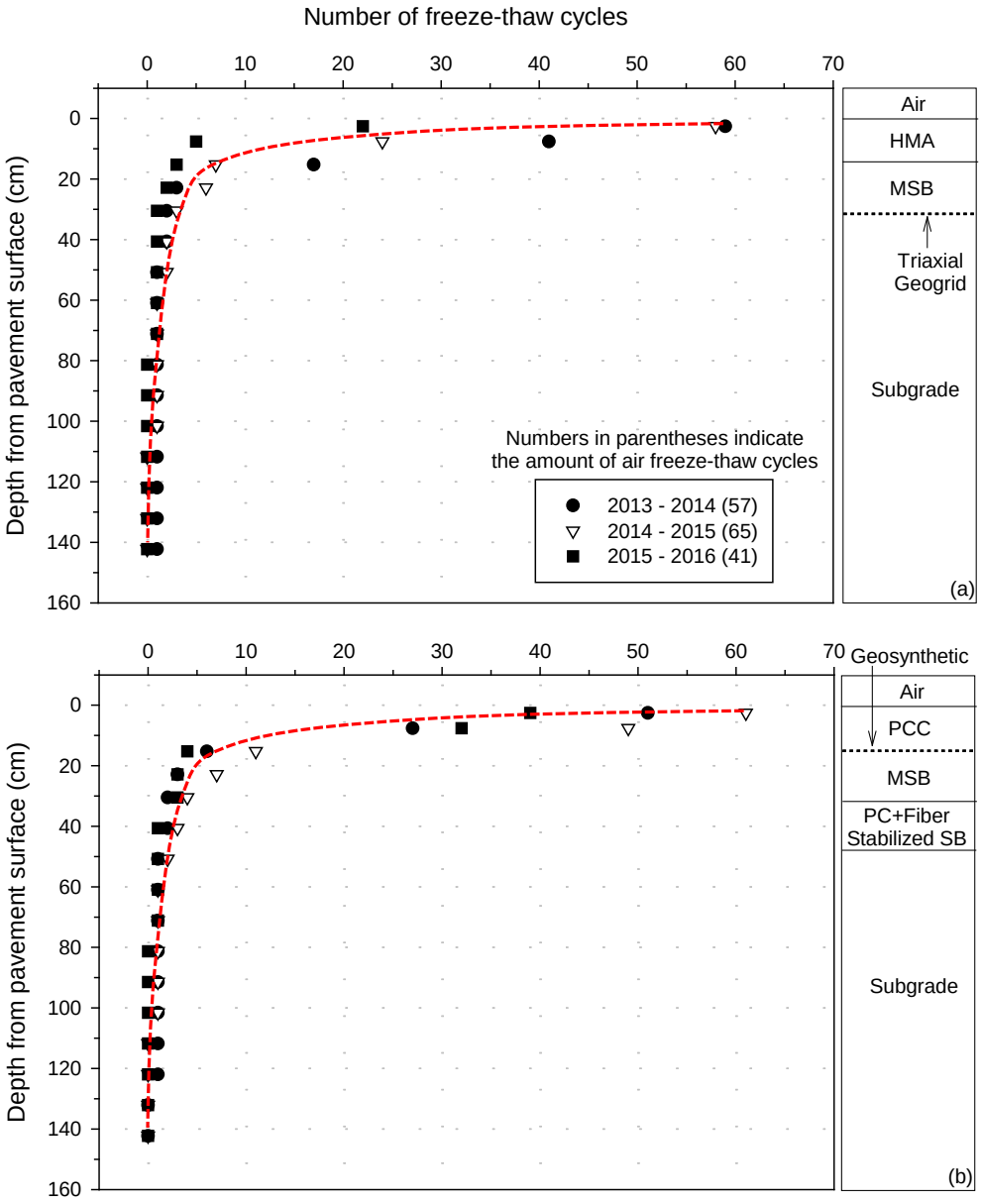

Figure 274. Freeze-thaw cycles at depth of (a) Expo – 1 and (b) Expo – 2

In accordance with the isothermal figure in Andersland and Ladanyi (2004), the dates of 0ºC at each depth were determined during both the freezing and thawing periods. Connecting these 0ºC points provided the estimated isotherm lines (Figure 275). The upper areas of the isothermal

lines were so called “frost zones”, which indicated the length of freezing periods at different depths. The lowest point of the isothermal line was the maximum frost penetration of the year. Results in Figure 275 show a relatively large frost zone during the 2013–14 winter, two separated medium frost zones during the 2014–15 winter, and a smaller zone for the 2015–16 winter for each street. In general, differences of 2 to 13 cm were found between the maximum frost penetrations at Expo sites for each year. The 2013–14 winter at Expo – 1 presented the largest value of 145 cm for frost penetration. The warmer winter of 2015–16 at Expo sites indicated around 70 cm maximum frost penetration, which was a value within the literature reported range for the 2014–15 winter (DeGaetano et al. 2001).

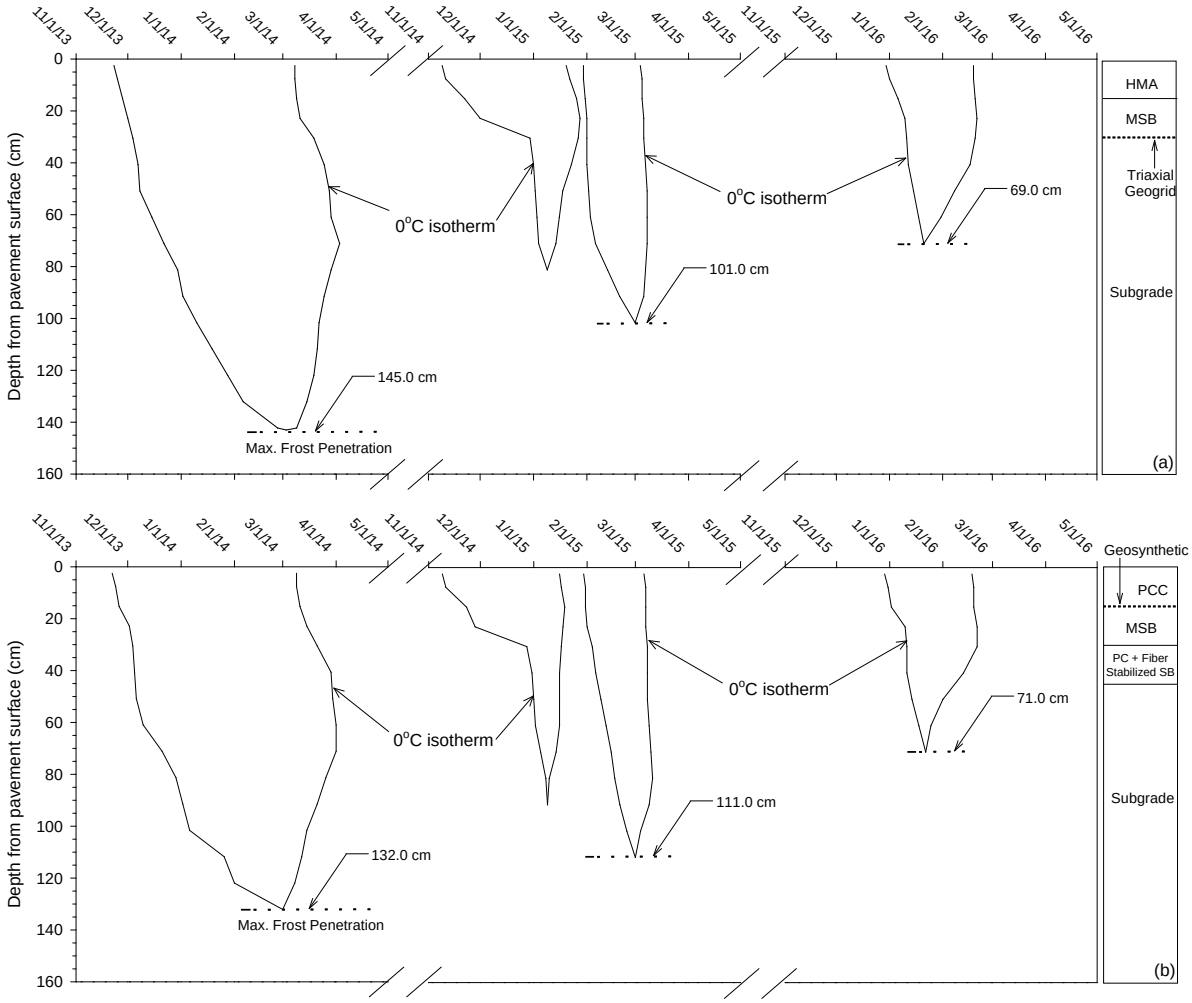

Figure 275. Frost zones from 2013 to 2016 at (a) Expo – 1 and (b) Expo – 2

The maximum frost penetrations from 2011 to 2016 at the US 30 site were also determined based on the in situ measurements. Although the US 30 site was only about 11 km away from the Expo site, significant differences were noticed between the maximum frost penetrations for these locations in the same year (Table 30).

Table 30. Summary of maximum frost penetration depths at a nearby US 30 site and the Expo sites

	US 30 (cm)	Expo – 1 (cm)	Expo – 2 (cm)
2011–12	54	–	–
2012–13	72	–	–
2013–14	102	145	132
2014–15	73	101	111
2015–16	57	69	71

Note: – indicates that data were not available.

Simplified Empirical Correlations

Numerous empirical models have been developed to predict frost penetration with only the freezing index. Most of these models average the soil thermal properties, which indicates that the ground was treated as bare soil with a single layer. Local weather station data provided the air temperature recording (RWIS 2016). In this study, the models by Chisholm and Phang (1983) and Rajaei and Baladi (2015) were selected to evaluate the accuracy of applying these models to this project data. The Chisholm and Phang (1983) model (Equation 1 in metric units) is based on Ontario weather history, and the Rajaei and Baladi (2015) model (Equation 2 for clayey soils and Equation 3 for sandy soils) is based on Michigan weather history. Air FI is the only input for frost penetration prediction.

$$X = 4.31\sqrt{1.8FI + 32} - 32.79 \quad (1)$$

$$X = 4.0388 \times (1.8FI + 32)^{0.4896} \quad (2)$$

$$X = 3.3787 \times (1.8FI + 32)^{0.5423} \quad (3)$$

The Frost penetrations of the three locations in this study were estimated with Equations 1, 2, and 3 (Figure 276). In comparison with the 11 actual measurements, predicted results showed wide variations. In general, the Rajaei and Baladi (2015) model overestimated actual values, and the Chisholm and Phang (1983) model underestimated actual values. The differences between the penetration results from these two models were around 35 to 50 cm, and it was difficult to summarize a particular relationship between FI and the actual frost penetrations. This finding indicates that estimating frost penetrations through these simplified models provided various results. As these models were developed empirically based on local data, many other factors such as soil type, thermal properties, climatic conditions, layer conditions may influence predictions.

Results from this study showed that the frost penetrations were different between two adjacent roads with different pavement surfaces and layer conditions. Also, significant differences were found between frost penetrations between sites with different water conditions. Therefore, it is recommended that improving the frost penetration prediction models still needs numerical analysis based on ground heat transfer. Even though at times the modified Berggren equation

applied in PCASE showed estimations approximating the actual measurements, the model ignored the influence of water movement to heat transfer during freezing and thawing, which may essentially affect predicted penetrations (Jury and Horton 2004).

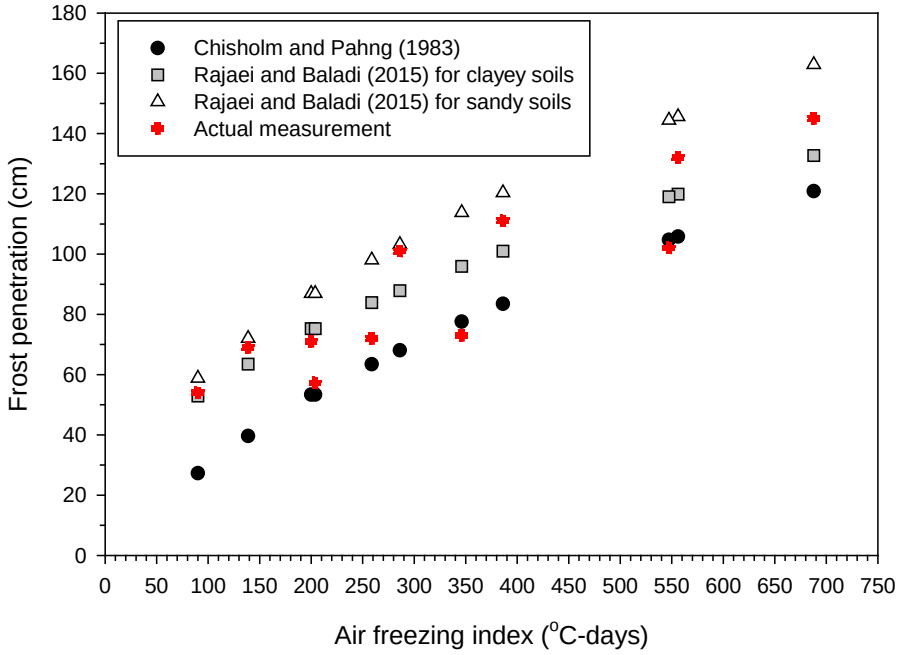

Figure 276. Comparisons between results correlated from empirical models and actual measurements

Frost Penetration Estimations Using Modified Berggren Equation

A principal objective of this study is to estimate the maximum frost penetration using the modified Berggren model. PCASE is the computer program used to implement the modified Berggren model. Because the modified Berggren model is an energy balance based model, some parameters used in the model can be determined from in situ measurements, but some soil properties used to estimate soil thermal properties must be assumed. The following sections discuss the specific procedures for estimating the frost penetrations in terms of air temperature data and soil properties.

Determination of n-factor and Freezing Index

Annual air freezing index (FI) was calculated for each test location. At the Expo sites, annual surface FI was calculated from the first subsurface thermocouple data, which were assumed to represent the surface temperature condition. The n-factor is used to relate air FI to surface FI was determined from the measured results. The reason for determining the n-factor was to compare the actual field measurements to the default values that were used in the computer program. Results from the Expo sites showed that the n-factor had a range between 0.41 and 0.72 for the HMA surface, while the value was around 0.6 for the PCC surface (Table 31). Because the US

30 site did not have a shallow sensor, the average n value from the Expo PCC surface was used to relate the air FI to the surface FI at the US 30 site.

Table 31. Measured n-factor for HMA and PCC pavement surfaces

	2013–14	2014–15	2015–16	Average
Expo – 1 (HMA)	0.72	0.49	0.41	0.54
Expo – 2 (PCC)	0.59	0.65	0.61	0.62

The air FI and surface FI are summarized in Table 32. During the same season, air FI at the different locations had slight differences, however differences between the surface FI values were relatively large. This indicated that the ground surface energy balance was influenced by multiple factors, such as the wind speed, snow cover, and radiation. It was difficult to determine a constant n-factor value for a particular ground surface type. However, as seen from the Stefan equation (see Equation 4 in metric units), the n-factor has a significant influence on the calculated results.

Table 32. Summary of air and surface freezing index

Freezing Index (°C-days)	2011–12		2012–13		2013–14		2014–15		2015–16	
	Air	Surface	Air	Surface	Air	Surface	Air	Surface	Air	Surface
US 30	146	90	423	259	892	547	565	346	333	205
Expo – 1	–	–	–	–	948	688	589	286	339	139
Expo – 2	–	–	–	–	948	556	589	386	339	204

Note: – indicates data were not available.

$$X = \sqrt{172800 \frac{knFI}{L}} \quad (4)$$

where, X is the frost penetration depth, k is soil thermal conductivity, FI is the annual air freezing index, and L is the soil latent heat.

Predicting Multi-Layer Frost Penetration in PCASE

The modified Berggren equation (Equation 5) added a factor, λ, into the Stefan equation to account for the volumetric heat. For manual calculations, the new factor λ can be estimated empirically from the thermal ratio (α) and the fusion parameter (μ). The α is a function of mean annual temperature (v_0) and average freezing temperature (v_s), and μ is a function of volumetric heat capacity (C), latent heat (L), and v_s.

$$X = \lambda\sqrt{172800\frac{knFI}{L}} \tag{5}$$

However, for computer calculations such as in PCASE, another method to determine λ is used (Bianchini and Gonzalez, 2012). A transcendental equation in terms of exponential relationships between soil thermal properties (C, k, and L) was used to calculate a constant γ. This constant was originally used to describe the relationship between permafrost soil thawing depth and time (t) (Equation 6). As FI is also a time dependent factor (FI is equal to v_s times t), the modified Berggren equation can be converted to Equation 8 based on a mathematical relationship between λ and γ (Equation 7).

$$X = \gamma\sqrt{t} \tag{6}$$

$$\lambda = \gamma\sqrt{\frac{2L}{Cv_s}} \tag{7}$$

$$X = \gamma\sqrt{345600\frac{knFI}{Cv_s}} \tag{8}$$

After applying the modified factor λ, the modified Berggren equation is considered to overcome the weakness of neglecting sensible heat during ice formation. However, another need is to learn how to apply the modified Berggren equation to solve multi-layer soil conditions, such as the pavement structures in this study. Bianchini and Gonzalez (2012) reported a solution and stated that the fundamental mechanism of the solution was to "compute the required FI for the freezing front to penetrate each layer" in accordance with the work by Zarling et al. (1989). Bianchini and Gonzalez (2012) treated FI as heat energy and calculated the amount of energy (FI) needed to freeze a layer with particular thickness. When the sum of FI for all layers equals the surface FI, the total thickness of all accounted layers represents the freezing front depth, which is the frost penetration. Therefore, Bianchini and Gonzalez (2012) converted Equation 2 into a FI expression (Equation 9), and modified the equation based on the thermal physics (Equation 10).

$$FI = \frac{D^2L}{172800\lambda^2nk} \tag{9}$$

$$FI = \frac{DL}{172800\lambda^2n}\left(\sum_{N=1}^{i-1} R_N + \frac{R_i}{2}\right) \tag{10}$$

where, D is the layer thickness, L is the layer latent heat, k is thermal conductivity, n is the FI transfer factor, N is the number of layers, and R is the thermal resistance (equal to D divided by k).

In PCASE, the US continent is classified into four typical areas: moist-cold, moist-hot, dry-cold, and dry-moist (Bianchini and Gonzalez, 2012). The PCASE contains a database with air FI collected from weather stations all over the USA. A default value of n-factor for particular

ground surface type was set in the system (0.75 for PCC and 0.7 for ACC), and these values cannot be changed by users. Default and changeable dry unit weights and moisture contents for typical soils were also provided in PCASE for estimating soil thermal properties. The pavement layer conditions of the Expo sites were input, and default soil properties were applied. Weather stations with similar air FI to locations in this study were selected to calculate the frost penetrations with the PCASE n-factor first. However, because the in situ measured n-factors differ from the default values, weather stations with similar surface FI were then selected for comparison as well. In other words, another approach to estimate the frost penetration based on surface FI in PCASE was performed by avoiding using the default n-factors. The calculated results of frost penetration are summarized in Table 33. Results indicate differences between air FI based and surface FI based frost penetration values, primarily due to the different n values. In general, the frost penetration depths based on surface FI were smaller than those based on air FI. The HMA pavement of 2014–15 showed the largest difference of about 23 cm between the two estimations. This finding indicates that the n-factor has significant influence on the modified Berggren equation estimated frost penetrations.

Table 33. Summary of PCASE frost penetration results at the Expo site

Frost penetration based on air FI (cm)			
	2013–14	**2014–15**	**2015–16**
Expo – 1	107	85	53
Expo – 2	117	94	62
Frost penetration based on surface FI (cm)			
	2013–14	**2014–15**	**2015–16**
Expo – 1	109	62	38
Expo – 2	102	82	56

In order to evaluate the estimated frost penetrations from PCASE, a figure was drawn to compare estimates with the actual measurements (Figure 277). Significant underestimations occurred for PCASE results. For both HMA and PCC pavements, the PCASE results were about 20% lower than the actual measurements. A possible reason for these underestimations might be the foundation layer stabilizations and drainage used at these two pavement sites. For the modified Berggren equation, decreasing the water content results in deeper frost penetration estimates. Stabilizations and drainage systems tend to reduce moisture contents of foundation layers. However, the default soil properties used in PCASE did not change even though the actual stabilization and drainage information was input into the system, which probably resulted in an overestimation of model moisture contents and/or an underestimation of the unit weights.

At the US 30 site, no particular treatment or stabilization was applied on the JPCP. Default soil properties were used for this location. Due to the lack of sensor near the pavement surface to estimate surface FI, the average measured n-factor value for the PCC surface of Expo – 2 was used for this location. Differences of 5 to 23 cm are estimated for the air FI and surface FI based results (Table 34). However, the estimated frost penetrations were less than 5% different from the in situ measurements at this site (Figure 278). The frost penetration depths calculated based on surface FI were similar to actual frost penetration depths. This result indicates that estimations

using the measured n-factor value results in higher accuracy than using default n-factor values in PCASE.

In order to determine if modifications on soil properties can improve PCASE estimation accuracy, the moisture contents and dry unit weights of each soil layer were changed based on laboratory Proctor test results (optimum moisture content and maximum dry unit weight). Some adjusted values were larger and some were smaller than the default values in PCASE. PCASE estimates with adjusted values showed significant improvement on the differences between estimated and measured frost penetrations (Figure 279). For the US 30 site, changes in soil properties did not have much influence on the estimations. The estimated results of four of the five seasons maintained high accuracy. For the Expo sites, using either or both air FI and surface FI with modified soil properties provided frost penetration estimates similar to in situ measurements. Besides the n-factor and soil properties, several other factors may also influence the output, such as the unchangeable mean annual temperature and length of the frost season.

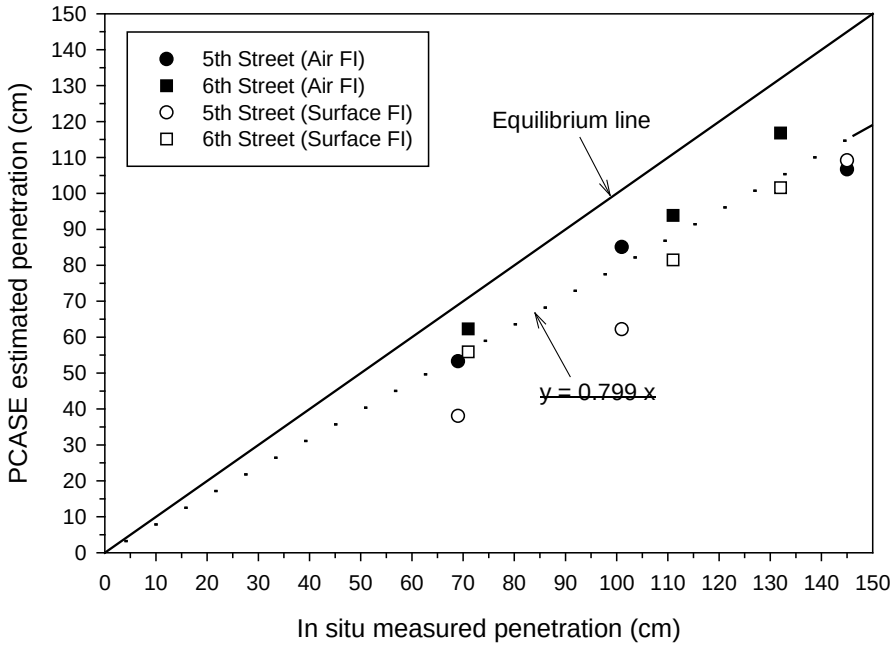

Figure 277. Comparison between estimated and measured frost penetrations at the Expo site

Table 34. Summary of PCASE frost penetration results at US 30 site

	2011–12	2012–13	2013–14	2014–15	2015–16
Based on air FI (cm)	33.0	73.7	116.8	96.5	68.6
Based on surface FI (cm)	55.8	68.6	102.9	78.7	61.0

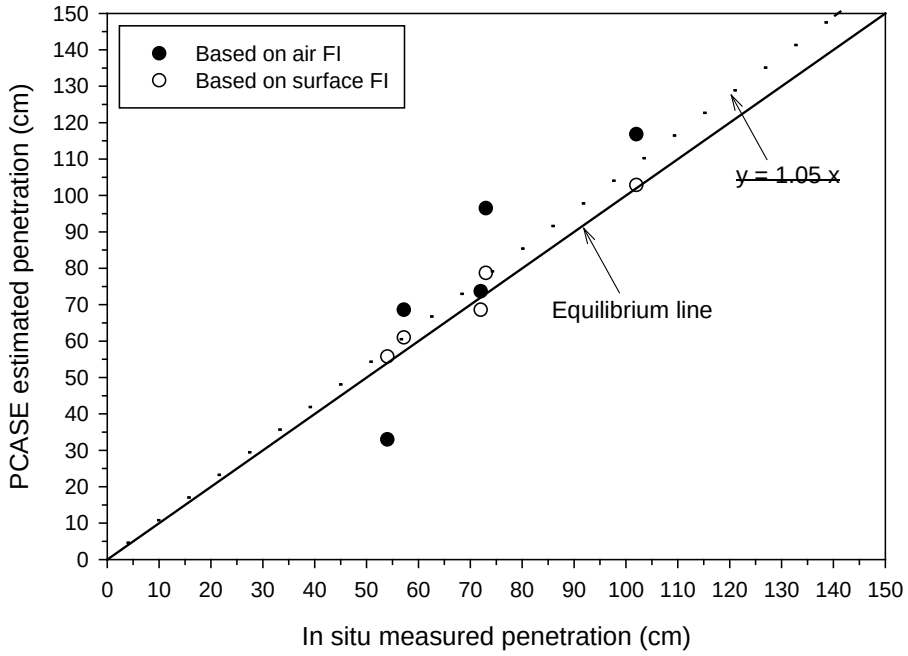

Figure 278. Comparison between estimated and measured frost penetrations at US 30 site

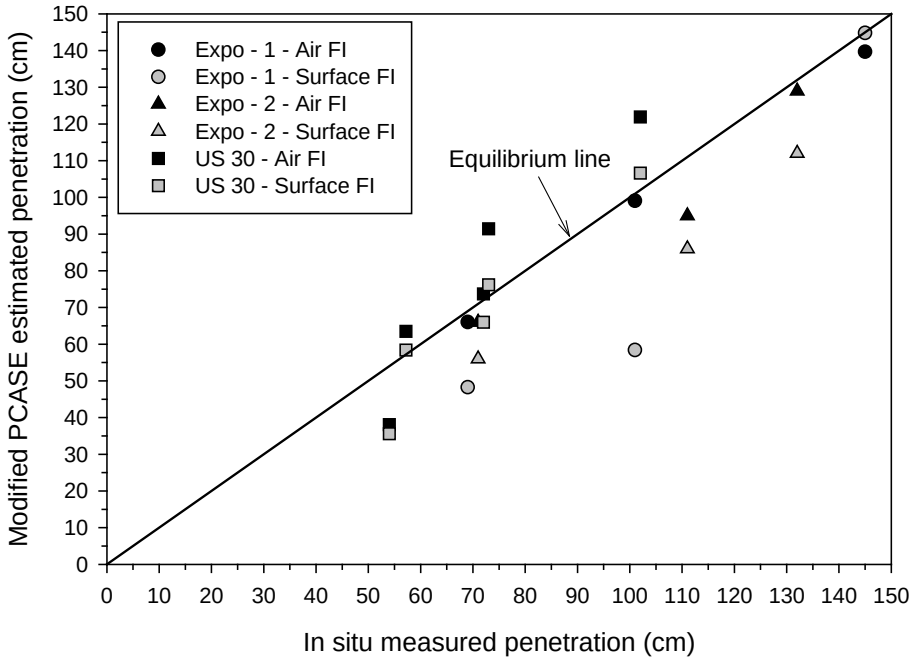

Figure 279. Comparison between estimated and measured frost penetrations after modifying soil properties

Summary

In this study, pavement and foundation temperatures were recorded at three locations in central Iowa. Air and surface temperatures were used to estimate the seasonal frost penetrations in accordance with three simplified empirical models and the modified Berggren equations applied in PCASE. The estimated results were compared to in situ measurements to evaluate the accuracy of these models. Based on the study findings, the following conclusions have been drawn:

- From field measurements, the maximum frost penetration at central Iowa reached 145 cm. However, during the same winter, locations showed differences between maximum frost penetrations despite the close distance between tested sites. Different pavement types and foundation conditions influenced the measured frost penetration depths;
- Frost penetration depth estimates with the three simplified empirical equations did not match well the measured frost penetration depths;
- The modified Berggren equation used in PCASE is able to predict frost penetration in multi-layer pavements based on freezing index and soil properties. Using default values for soil properties in PCASE resulted in about 20% underestimation of the frost penetration depths;
- When using tested values for moisture contents and dry unit weights, calculations with the modified Berggren equation in PCASE provided more accurate results of predicted frost penetrations than using default soil properties values. However, the n-factor was found to have a significant influence on the accuracy of estimations, although it is difficult to determine the precise value of n at every specific location. Empirical values of n-factor may not be broadly applicable to each particular site;
- Stabilization and drainage systems utilized in foundation layers may have affected the frost penetration estimations. The possible causes may be that stabilization and drainages lead to changes in soil densities, pore conditions, and water contents.

CHAPTER 12: KEY FINDINGS AND RECOMMENDATIONS

Significant findings from the Phase I testing were as follows:

- Cost, average stiffness values, and COV were reported for all of the pavement foundation sections. Analysis of this data is useful to optimize pavement foundation design.
- Comparison between LWD and FWD measurements indicated that both provided statistically related moduli measurement values, but LWD measurements does not always reflect stiff underlying layers as measured with the FWD. The measurement influence depth is greater for the FWD compared to the LWD, because of the higher stresses that can applied with the FWD.
- The RICM values (CMV and MDP* measured with Caterpillar IC roller and CCV measured with Sakai roller) provided near-continuous electronic records of ground stiffness and showed variations between the test sections and locations of lower stiffness materials within sections. The CMV and CCV values correlated better with FWD values than MDP* values. CMV values correlated better to FWD values than LWD values.
- The QC/QA nuclear density testing showed that this approach to quality assessment can lead to shortcomings (including lack of reproducibility and infrequent testing) and does not capture the wide range in stiffness values measured from the other devices.
- Shortly after construction and after spring thaw, test sections with mechanical stabilization (TS-MS) with in situ mixing of recycled aggregate with existing subgrade versus over excavation (TS-OE) and replacement produced comparatively higher elastic moduli values than control (TS-C) sections. There was no statistical evidence to suggest that TS-OE pavement foundation performed better than the TS-MS pavement foundation, or vice versa, shortly after construction. However, after spring-thaw, results showed that the TS-OE pavement foundation performed better than the TS-MS foundation.
- Laboratory freeze-thaw testing showed that the mechanically stabilized subgrade used in this study exhibits strength and stiffness behavior similar to the on-site recycled material at optimum environmental conditions. During thaw-weakening conditions, the mechanically stabilized subgrade exhibits strength and stiffness behavior similar to the subgrade.
- Average FWD composite elastic moduli values from each test section during October 2012 (i.e., never-frozen) ranged from 37 MPa to 507 MPa. Test sections with Portland cement (PC) stabilized subgrade, fly ash stabilized subgrade, or PC stabilized reclaimed gravel subbase produced the highest moduli values. Test sections with mechanically stabilized subgrade, compacted subgrade, or untreated reclaimed gravel subbase produced comparatively higher moduli values than control test sections with no subgrade compaction or other treatment.
- Average FWD composite elastic moduli during April 2013 (i.e., thaw-weakened) ranged from 11 MPa to 159 MPa. All test sections experienced reductions in moduli values as conditions transitioned from never-frozen to thaw-weakened (by about 2 to 9 times on average). Test sections with PC stabilized subgrade or PC stabilized reclaimed gravel subbase produced the highest moduli values. Test sections with fly ash stabilized subgrade or untreated reclaimed gravel subbase produced relatively high moduli values as well.

- Correlations between thaw-weakened and never-frozen elastic moduli values suggest that PC stabilized pavement foundations are less susceptible to thaw-weakening than untreated pavement foundations or fly ash stabilized pavement foundations.
- Elastic moduli values determined FWD in never-frozen condition showed statistically significant relationships with both subbase and subgrade layer penetration index (*PI*) values from DCP tests at that time. But, FWD elastic moduli values after thawing showed strong correlation with the subgrade PI, but not with the subbase layer PI at that time. This emphasizes the importance of subgrade support on the composite response on top of the subbase layer.
- Laboratory freeze-thaw durability tests showed that subgrade stabilized with fly ash exhibits improvements with increasing fly ash content up to 15% with decreasing level of frost-heave and thaw-weakening susceptibility. Greater improvement was related to shorter fly ash set time. Subgrade and subbase stabilized with cement showed low to negligible frost susceptibility. For subbase, the addition of fibers increased the pre-test and post-test (saturated) CBR values slightly. Comparatively, the addition of cement reduced the heave rates and increased the CBR values significantly. Results also indicated that curing time and compaction delay influence the freeze-thaw performance of chemically stabilized soils.
- To achieve very low thaw-weakening susceptibility, the heave rate has to be controlled to less than 4 mm/day per ASTM D5918. The current ASTM classification does not distinguish classifications with CBR values greater than 20. A proposed classification for chemically stabilized soils identifies thaw-susceptibility as negligible for post-test CBR values ≥ 100. The advantage of this rating is it provides additional criteria for rating freeze-thaw susceptibility for stabilized soils with post-test CBR values greater than 20. It is difficult to predict the post-tests CBR values from the pre-test measurements for chemically stabilized soils due to time-dependent strength gain and supports the need to perform the freeze-thaw tests and monitoring the influence of curing time for stabilized soils.
- GPT tests were conducted to rapidly determine field saturated hydraulic conductivity of granular base layer and its relationship with different foundation support conditions and gradation of the subbase. Testing was focused on three test sections, where the subbase layer for was compacted with a vibrator smooth drum roller, which contributed to the aggregate degradation. Degradation varied, however, between sections and appears to be linked to the foundation support condition. The section with the highest support values (i.e, high CBR and elastic moduli values) consisted of cement stabilized subgrade, but it showed the highest degradation of the aggregate subbase and the lowest hydraulic conductivity. The control section (with only granular subbase over uncompacted subgrade) yielded the lowest support values, but the highest hydraulic conductivity. The geogrid reinforced aggregate section provided comparatively better support conditions than the control section and intermediate hydraulic conductivity values.

Significant findings from the Phases II and III testing were as follows:

- In general, HMV values during asphalt pavement construction were higher when placing asphalt over stiff pavement foundations. All HMV measurements correlated with statistical significance to HMV measurements obtained on the foundation layer.
- For asphalt construction over softer pavement foundations, HMV increased with each additional pavement layer. For asphalt construction over stiff foundations, in general, the pavement foundation HMV was greater than base course HMV, and base course HMV was less than surface course HMV.
- Asphalt pavement surface temperature measurements from the roller temperature sensors were in agreement with thermal camera temperatures at higher temperatures (greater than 87.4 °C), but tended to underestimate pavement surface temperatures at lower temperatures (< 87.4 °C).
- Asphalt pavement relative compaction from neither nuclear density gauge tests nor pavements cores correlated with HMV measurements. However, falling weight deflectometer (FWD) measurements strongly correlate with HMV measurements.
- Based on multivariable analyses, RICM systems can potentially be used as QC for asphalt pavement layer modulus, provided that the composite modulus of the pavement foundation is a known target value.
- Comparison of three different forward and back-calculation procedures for FWD data analysis has indicated significant differences in the estimated moduli values for the asphalt, base, and subgrade layers. Standard errors of the estimated values were in the range of 13 MPa for subgrade, over 120 MPa for base layer, and over 3,000 MPa for asphalt layer.
- Numerous regression relationships have been documented in the literature between DCP test measurements and moduli values and are summarized herein. Upper and lower bounds are presented based on the available relationships. The bounds suggest that the predicted moduli values can have an error of ± 50 to 335 MPa if DCP penetration resistance (PR) values are between 2 and 10 mm/blow, and ± 10 to 50 MPa if PR value is > 10 mm/blow.
- New relationships between PR and moduli values calculated from three forward and back calculation methods for a PR range of 2 and 78 mm/blow are presented herein. PR values determined from the weakest 75 mm of the subgrade showed slightly higher R^2 values when compared to PR values for the top 300 mm of the subgrade.
- The relationships presented in this study indicated that for if PR data between 2 to 78 mm are considered, the SE of the estimate ranged from 24 to 60 MPa, depending on the modulus calculation method. The SE of the estimate decreased to < 20 MPa, when PR data from only subgrade are considered.
- A new database of dielectric properties of subgrade and base layer materials and chemically stabilized subgrade materials at different moisture contents are provided in this study. Results indicated that the dielectric properties are sensitive to moisture content, as expected, and are sensitive to curing times for chemically stabilized soil due to the hydration process. PC and FA stabilized subgrade materials produced lower dielectric values than unstabilized subgrade materials.
- GPR surveys conducted during frozen condition did not properly differentiate variations in the foundation layers because of similar dielectric properties of those materials in a frozen condition. This was verified by conducting a simple laboratory box study with compacted pavement and foundation layers in frozen and unfrozen conditions.

- The estimated asphalt thicknesses using the actual measured dielectric properties from the GS3 device values produced an average error of about 11%. The estimated values asphalt thicknesses were close to the 1:1 line when compared with the measured values, when dielectric properties backcalculated from GPR were used. The average error reduced to about 3.7% with that process and the errors are similar to reported by others in the literature with air-coupled GPR antennas.
- Comparison between asphalt thickness measured using the MIT gauge and GPR indicated that the MIT gauge measurements were on average about 9% higher than estimated with GPR.
- GPR data was used to estimate volumetric moisture content of the granular subbase material. Results indicated that on average, the volumetric moisture contents in the subbase layer varied from about 6 to 25%. The variations are attributed to material segregation and degradation, and variations in aggregate gradations and permeability between the test sections, as documented in the Phase I portion of this study with GPT measurements.
- Air and surface temperatures were used to estimate the seasonal frost penetrations in accordance with three simplified empirical models and the modified Berggren equations in this study. The estimated results were compared to in situ measurements to evaluate the accuracy of these models. These comparisons showed that the frost penetration depth estimates from the three empirical models did not match well the measured frost penetration depths. When using tested values for moisture contents and dry unit weights, calculations with the modified Berggren equation provided more accurate results of predicted frost penetrations than using default soil property values. However, the n-factor used in the estimations was found to have a significant influence on the accuracy of estimations, although it is difficult to precisely determine the value of n at every specific location.

This project generated significant and important information regarding the mechanistic properties for pavement foundation support for a range of foundation improvement/ stabilization methods. The test sections at the Central Iowa Expo facility are unique in terms of the range of technologies used and for the fact that the performance data particularly isolates the influence of the seasonal changes without any loading. Some significant lessons learned from this project and the limitations of the findings are identified below, to identify the path forward for the Iowa DOT with implementation of the findings into the design and construction practice and future research/testing on these test sections.

- Traditional nuclear gauge moisture-density testing has played an important role in earthwork quality assessment specifications in the U.S. for decades. This form of QC/QA can be effective, but has shortcomings due to regulations, test reproducibility, limited test frequency, and only serving as a surrogate to strength and stiffness design requirements. Results from this study showed that all the QC agent test results met the target moisture and density criteria, while the QA agent results are much more variable on both accounts. At this point, one could only speculate about these differences. It is clear though that the nuclear density testing does not indicate the wide stiffness variations resulting from treatments and materials.

- The distinct advantage of the strength/stiffness related measurements used at this site (i.e., DCP, FWD, and LWD) is that they identified the variations in support values between different stabilization sections. While these measurements were critical in identifying the relative differences in the strength/stiffness properties between the test sections, they all produced different measurement values that can potentially be used to *estimate* the mechanistic input parameters used in the pavement design process. However, the following limitations of these test measurements must be realized:
    - Thus far, however, there is no supporting evidence that these measurements can be reliably used to predict the key mechanistic input parameters used in design (i.e., resilient modulus (M_r) and modulus of subgrade reaction (*k*-value)) with high statistical confidence.
    - Empirical relationships have been published between DCP or CBR measurements and M_r and *k*-values, but all these relationships produce significantly different numbers and therefore present significant uncertainty in selecting an appropriate value in design. Local or regional correlations can be more reliable, but can be very time consuming to generate.
    - In situ M_r is commonly predicted from non-destructive surrogate tests including the FWD or LWD, but the elastic moduli values calculated from these test devices based on elastic deformations are often confused with resilient modulus values which is based on resilient (i.e., recoverable) deformations. One of the major limitations of these non-destructive surrogate tests is the lack of a conditioning stage prior to testing. During pavement construction, pavement foundation materials are subjected to relatively high loads from construction traffic and compaction equipment. In response to these loads, aggregate particles rearrange themselves resulting in higher density and stiffness. For this reason, it is important to apply conditioning load cycles prior to testing to determine in situ resilient modulus. Once surface paving is complete, the pavement foundation below is confined by the overlying pavement layers. The response of a pavement foundation to subsequent repeated traffic loading is both nonlinear and stress-dependent and therefore the effect of confinement is an important condition to consider in a field based M_r test.
    - FWD testing provides an estimate of the modulus of the asphalt layer, but is not the same as the stress and frequency dependent dynamic modulus value used in the design for the asphalt layer.
- The results documented herein demonstrated the importance of support conditions on the overall composite response at the surface under loading. Improved support at the subgrade level with cement stabilization provided the best response to loading at the surface, followed by cement stabilization at the granular base layer level. The geosynthetic stabilized test sections, although did not show as high of moduli values as cement stabilized test sections, past experience has showed that geosynthetic reinforcement can provide better resistance against permanent deformation/rutting under traffic loading than sections without reinforcement. This aspect was not evaluated at this site and must be evaluated in future testing.
- Although cement stabilization method provided improved support conditions than in sections without stabilization, stabilization did not improve uniformity. The coefficient of variation of moduli values in the cement stabilized sections were higher than in the

sections without stabilization, and this is related to lack of construction process control with the stabilization process.

Based on the lessons learned and the limitations identified above, the following are recommended for considerations by the Iowa DOT for future testing and evaluation at this site:

- Evaluate new in situ testing technologies that provide a direct measurement of the M_r and *k*-values of the foundation layers, and stress and frequency dependent dynamic modulus of the asphalt layers. The objective of such testing and evaluation should be to generate typical foundation input parameter values that can be used in future design by the Iowa DOT.
- Evaluate the test sections over the long-term (10+ years) and/or with accelerated pavement testing (trafficking or accelerated loading) to evaluate the influence of the foundation layers on the permanent deformation behavior at the surface.
- Evaluate the condition of the temperature monitoring sensors and continue the monitoring to generate frost-depth penetration data over longer period.

REFERENCES

AASHTO (1993). *AASHTO guide for design of pavement structures*, American Association of State Highway and Transportation Officials, Washington, D.C.

AASHTO (2000). Standard method of test for determining the resilient modulus of soils and aggregate materials, *AASHTO T-307*, American Association of State Highway and Transportation Officials, Washington, D.C.

AASHTO (2008). *Mechanistic-empirical pavement design guide: A manual of practice*, American Association of State Highway Officials and Transportation Officials, Washington, D.C.

Ahlbornm, G. (1972). ELSYM5, Computer program for determining stresses and deformations in five layered systems, University of California, Berkeley, CA.

Aitken, G.W., and Berg, R.L., 1968. Digital Solution of Modified Berggren Equation to Calculate Depths of Freeze or Thaw in Multilayered Systems. Special Report, SR 122. CRREL. U.S. Army.

Al-Qadi IL, Lahouar S, Loulizi A. (2003). "Successful application of ground-penetrating radar for quality assurance-quality control of new pavements" *Transportation Research Record*, Journal of the Transportation Research Board, No. 1861, 86-97.

Al-Qadi IL, Lahouar S, Loulizi A. (2003). "GPR: From the state-of-the-art to the state-of-the-practice." In: *International Symposium of Non-Destructive Testing in Civil Engineering.* Proceedings BB85-CD; 2003 September 16-19; Berlin. Germany: The German Society for Non-Destructive Testing (DGZfp).

Al-Qadi I, Lahouar S. (2005). "Measuring layer thicknesses with GPR–Theory to practice," *Construction and Building Materials.* Vol. 19, 763-772.

Al-Qadi IL, Leng Z, Lahouar S, Baek J. (2010). "In-place hot-mix asphalt density estimation using ground-penetrating radar." Transportation Research Record: Journal of the Transportation Research Board, Vol. 2152, 19-27.

Al-Refeai, T. O. (1991). "Behavior of granular soils reinforced with discrete randomly oriented inclusions," *Geotext. Geomembr*., 10, 319– 333.

Alavi, S., LeCates, J. F., and Tavares, M. P. (2008). "Falling weight deflectometer usage." *NCHRP Synthesis 381,* National Cooperative Highway Research Program, Transportation Research Board, Washington, DC.

Aldrich, H., and Paynter, H., 1953. Analytical Studies of Freezing and Thawing of Soils. Technical Report No. 42. U.S. Army Corps of Engineers.

Andersland, O. B., and Ladanyi, B., 2004. Frozen Ground Engineering. The American Society for Civil Engineers.

Andrei, D., Witczak, M. W., Schwartz, C. W., and Uzan, J. (2004). "Harmonized resilient modulus test method for unbound pavement materials." *Transportation Research Record: Journal of the Transportation Research Board*, 1874, 29–37.

Andrawes, K. Z., McGown, A., Mashhour, M. M., and Wilson-Fahmy, R. F. (1980). "Tension resistant inclusions in soils." *Journal of the Geotechnical Engineering Division*, ASCE, 10(12), 1313–1326.

Austroads (1998). "Guide to stabilisation in roadworks." Austroads, Sydney, A4, New Zealand.

Bathurst, R.J., Karpurapu, R. (1993). "Large-scale triaxial compression testing of geocell reinforced granular soils," *Geotechnical Test. J.*, 16 (3), 296–303

Baladi, G., and Rajaei, P., 2015. Predictive Modeling of Freezing and Thawing of Frost-Susceptible Soils. Final Report, RC-1619. Michigan Department of Transportation.

Benson, C. H., and Khire, M. V. (1994). “Reinforcing sand with strips of reclaimed high-density polyethylene.” *Journal of Geotechnical Engineering*, ASCE, 120(5), 838–855.

Berg, K. C. (1998). "Durability and strength of activated reclaimed Iowa Class C fly ash aggregate in road bases." M.S. Thesis, Department of Civil Engineering, Iowa State University, Ames, Iowa.

Berg, R. R., Christopher, B. R., and Perkins, S. (2000). "Geosynthetic Reinforcement of the Aggregate Base/Subbase Courses of Pavement Structures." Geosynthetic Materials Association, Roseville, MN.

Bin-Shafique, S., Rahman, K., Yaykiran, M., and Azfar, I. (2010). “The long-term performance of two fly ash stabilized fine-grained soil subbases,” *Resources, Conservation and Recycling*, 54(10), 666–672.

Bland J.M, Altman D.G. (1999). “Measuring agreement in method comparison studies,” *Statistical Methods in Medical Research*, Vol. 8, 135-160.

Bolander, P. (1999). "Laboratory Testing of Nontraditional Additives for Dust Abatement and Stabilization of Roads and Trails," Transportation Research Record No. 1652, Volume 2, Washington, D.C.

Bouazza, A., and D. L. Avalle. 2006. “Verification of the effects of rolling dynamic compaction using a continuous surface wave system.” *Australian Geomechanics*, Vol. 41, No. 2, pp. 101-108.

Bianchini, A., and Gonzalez, C., 2012. Pavement-Transportation Computer Assisted Structural Engineering (PCASE) Implementation of the Modified Berggren (ModBerg) Equation for Computing the Frost Penetration Depth within Pavement Structures. TR-12-15. Geotechnical and Structural Laboratory. U.S. Army Corps of Engineers.

Braley, W., and Connor, B., 1989. Berg2 Micro-computer Estimation of Freeze and Thaw Depths and Thaw Consolidation. Alaska Department of Transportation and Public Facilities, Fairbanks, Alaska.

Brown, R.J.E., 1963. Relation between mean annual air and ground temperatures in the permafrost region of Canada. Proceedings: Permafrost International Conference. November, 1963. Ottawa, Canada.

Burmister, D.M. (1945). The general theory of sresses and displacements in layered systems: I. Journal of Applied Physics, 16(89), 89–94.

Bushman, W. H., Freeman, T. E., and Hoppe, E. J. (2005). "Stabilization techniques for unpaved roads." *Transportation Research Record*, Journal of the Transportation Research Board, 1936, 26-33.

Cassagrande, A., Taber, S., and Watkins, W., (1931). “Discussion of Frost Heaving,” *Highway Research Board*, 165-177.

Castedo, L. H., and Wood, L. E. (1983). "Stabilization with foamed asphalt of aggregates commonly used in low-volume roads." *Transportation Research Record*, Journal of the Transportation Research Board, 898, 297-302.

Chamberlain, E.J., 1986. Evaluation of Selected Frost-Susceptibility Test Methods. U.S. Army Cold Regions Research and Engineering Laboratory. CRREL Report 86-14.

Chen, J., Hossain, M., and LaTorella, T. M. (1999). "Use of falling weight deflectometer and dynamic cone penetrometer in pavement evaluation." *Transportation Research Record: KonJournal of the Transportation Research Board*, 1655, 145-151.

Chen, D.-H., Lin, D.-F., Liau, P.-H., and Bilyeu, J. (2005). "A correlation between dynamic cone penetrometer values and pavement layer moduli." *Geotechnical Testing Journal*, 28(1), 42-49.

Chisholm, R. A., and Phang, W. A., 1983. Measurement and prediction of frost penetration in highway. Journal of Transportation Research Board, No 918, Transportation Research Board of the National Academies, Washington D.C., 1983, pp. 1-10.

Christopher, B. R., Schwartz, C., and Boudreau, R. (2005). "Geotechnical Aspects of Pavements." FHWA NHI-05-037, National Highway Institute, Federal Highway Administration, U.S. Dept. of Transportation, Washington, D.C.

Chu, T.Y. Davidson, D.T, Goecker, W.L. and Moh, Z.C. (1955). "Soil stabilization with Lime-Fly ash Mixtures: Preliminary Studies with Silty and Clayey Soils," *Highway Research Board Bulletin 108*, Washington, D.C, pp102–112.

Clark, I., Harper, W. (2002). *Practical Geostatistics 2000*, 3rd Reprint, Ecosse North America LLC, Columbus, Ohio.

Clyne, T. R., V. R. Voller, and B. Birgisson. (2001). "Evaluation of a Field Permeameter to Measure Saturated Hydraulic Conductivity of Base/Subgrade Materials." Report MN-RC-2001-19. Minnesota Department of Transportation, St. Paul, MN.

Clegg, B., and A. R. Berrangé. 1971. "The development and testing of an impact roller," *Transactions of the South African Institution of Civil Engineers.* Vol. 13, No. 3, pp. 65-73.

Collings, D., Lindsay, R., and Shunmugam, R. (2004). "LTPP Exercise on a Foamed Bitumen Treated Base - Evaluation of Almost 10 Years of Heavy Trafficking on MR504 in Kwazulu-Natal." *Proc., 8th Conference on Asphalt Pavements for Southern Africa (CAPSA'04)*, Document Transformation Technologies.

Collins, R. W. (2011). "Stabilization of marginal soils using geofibers and nontraditional additives." MS Thesis, University of Alaska, Fairbanks, Alaska.

Consoli, N.C., Prietto, P.D.M., Ulbrich, L.A. (1998). "Influence of fiber and cement addition on behavior of sandy soil," *Journal of Geotechnical and Geoenvironmental Engineering*, 124 (12), 1211-1214.

Consoli, N. C., Vendruscolo, M. A., Prietto, P. D. M. (2003). "Behavior of plate load tests on soil layers improved with cement and fiber," *Journal of Geotechnical and Geoenvironmental Engineering*, 129 (1), 96-101.

Consoli, N.C., Vendruscolo, M.A., Fonini, A., Dalla Rosa, F. (2009). "Fiber reinforcement effects on sand considering a wide cementation range," *Geotextiles and Geomembranes*, 27 (3), 196-203.

Consoli, N.C., Cruz, R.C., Floss, M.F., Festugato, L. (2010). "Parameters controlling tensile and compressive strength of artificially cemented sand," *Journal of Geotechnical and Geoenvironmental Engineering*, 136 (5), 759-763.

Consoli, N. C., F. Zortea, M. de Souza, and L. Festugato. (2011). "Studies on the dosage of fiber-reinforced cemented soils." *Journal of Materials in Civil Engineering*, Vol. 23, No. 12, 1624–1632.

Cook, D. (2002)., "Tree sap helps hold roadside shoulders," *Better Roads*, Vol. 72, No. 5, James Informational Media, Des Plaines, IL.

Davis JL, Annan AP. (1989). "Ground-penetrating radar for high-resolution mapping of soil and rock stratigraphy," *Geophysical Prospecting*; 37(5), 531-551.

Daniels JJ. (1989). “Fundamentals of ground penetrating radar,” In: *Symposium on the Application of Geophysics to Engineering and Environmental Problems*. Proceedings; 1989 March 13-16: Environment and Engineering Geophysical Society.

DeBeer, M. (1990). "Use of the dynamic cone penetrometer (DCP) in the design of road structures." *Geotechnics in the African Environment,* Blight et al. (Eds), Balkema, Rotterdam, 167-176.

Decagon. (2015). GS3 Water Content, EC and Temperature Sensors Operator's Manual. Pullman Washington (USA): Decagon Devices, Inc.

DeGaetano, A.T., Cameron, M.D., and Wilks, D.S., 2001. Physical simulation of maximum seasonal soil freezing depth in the united states using routine weather observations. J. Appl. Meteor., 40:546-555.

Dempsey, B. J.; Thompson, M. R. (1973). “Vacuum Saturation Method for Predicting Freeze-Thaw Durability of Stabilized Materials,” *Highway Research Record*, No. 442, 44–57

Dorman, G. M., and Metcalf, C. T. (1965). "Design curves for flexible pavements based on layered system theory." *Highway Research Record*, 71, 69–84.

Doré, G., and Zubeck, H.K. (2009). Cold regions pavement engineering. Reston, VA: ASCE Press.

Engineering and Research International Inc. (2009). *ERI data analysis users guide: version 7*, Engineering and Research International, Inc., Savoy, IL.

Epps, J.A., Hand, A., Seeds, S., Schulz, T., Alavi, S., Ashmore, C., Monismith, C.L., Deacon, J.A., Harvey, J.T., & Leahy, R. (2002). Recommended performance-related specification for hot-mix asphalt construction: Results of the Westrack project (NCHRP 455). Washington, D.C.: National Cooperative Highway Research Program.

Evans, R., Frost, M., Stonecliffe-Jones, M., Dixon, N. (2008). “A review of pavement assessment using ground penetrating radar (GPR),” In: Rogers CDF, Chignell RJ, editors. 12th *International Conference on Ground Penetrating Radar*. Proceedings; 2008 June 16-19; Birmingham. UK.

Flerchinger, G. N., W. P. Kustas, and M. A. Weltz. 1998. Simulating surface energy fluxes and radiometric surface temperatures for two arid vegetation communities using the SHAW model. J. Appl. Meteor. 37:449–460. Link

Fletcher, C. S., and Humphries, K. (1991). “California bearing ratio improvement of remolded soils by the addition of polypropylene fiber reinforcement.” *Transportation Research Record*, 1295, Transportation Research Board, Washington, D.C., 80–86

Floss, R., N. Gruber, and J. Obermayer. (1983). “A dynamical test method for continuous compaction control,” *Proceedings of the 8th European Conference on Soil Mechanics and Foundation Engineering*, Rathmayer, H.G., and K. H. O. Saari, Eds., Helsinki, pp. 25–30.

Freitag, D.R., and McFadden, T., 1997. Introduction to Cold Regions Engineering. The American Society for Civil Engineers.

Freitag, D.R. (1986). “Soil randomly reinforced with fibers.” Journal of geotechnical Engineering, ASCE, Vol. 112, No. 8, pp. 823-826.

George, K. P. (2004). "Prediction of resilient modulus from soil index properties." *Final Report FHWA/MS-DOT-RD-04-172*, Mississippi Department of Transportation, Jackson, MS.

George, K. P., and Uddin, W. (2000). "Subgrade characterization for highway design." *Final Report FHWA/MS-DOT-RD-00-131*, Mississippi Department of Transportation, Jackson, MS.

Giroud, J. P., and Han, J. (2004a). "Design Method for Geogrid-Reinforced Unpaved Roads. I. Development of Design Method." *Journal of Geotechnical and Geoenvironmental Engineering*, 130(8), 775-786.

Giroud, J. P., and Han, J. (2004b). "Design Method for Geogrid-Reinforced Unpaved Roads. II. Calibration and Applications." *Journal of Geotechnical and Geoenvironmental Engineering*, 130(8), 787-797.

Goel, A., Das, A. (2008). "Nondestructive testing of asphalt pavements for structural condition evaluation: a state of the art," *Nondestructive Testing and Evaluation*, Vol. 23:121-140.

Gopalakrishnan, K., Ceylan, H., and Kim, S. H. (2010). "Biofuel Co-Product Uses for Pavement Geo-Materials Stabilization." IHRB Project TR-582, Institute of Transportation, Iowa State University, Ames, Iowa.

Gray, D. H., and Ohashi, H. (1983). "Mechanics of fiber reinforcement in sand." J*ournal of Geotechnical Engineering*, 109(3), 335-353.

Grogan, W.P., and Johnson, W.G. (1993). "Stabilization of high plasticity clay and silty sand by inclusion of discrete fibrillated polypropylene fibers for use in pavement subgrades." Tech. Rep. CPAR-GL-93-3.

Grote K, Hubbard S, Harvey J, Rubin Y. (2005). "Evaluation of infiltration in layered pavements using surface GPR reflection techniques," *Journal of Applied Geophysics*. Vol. 57:129-153.

Grove J, Jones K, Ye D, Gudimettla J. Nondestructive tests of thickness measurements for concrete pavements. Transportation Research Record: Journal of the Transportation Research Board. 2012;2268:61-67.

GSSI. GSSI handbook for RADAR inspection of concrete. Salem, New Hampshire (USA): Geophysical Survey Systems, Inc; 2006.

Gullu, H. and Khudir, A., (2014). "Effect of freeze-thaw cycles on unconfined compressive strength of fine-grained soil treated with jute fiber, steel fiber and lime." *J. Cold Reg. Sci. Technol.*, 106-107 (2014):55-65.

Halabe UB, Maser K, Kausel E. (1989). "Condition assessment of reinforced concrete using EM waves," Cambridge, Massachusetts (USA): Massachusetts Institute of Technology, 1989.

Hallikainen, M. (1977). "Dielectric properties of NaCl ice at 16GHz," Report No. S-1107; Espoo. Finland: Helsinki University of Technology, Radio Laboratory.

Henry, K. S. (1996). "Geotextiles to mitigate frost effects in soils: A critical review." *Transportation Research Record: Journal of the Transportation Research Board*, 1534, 5-11.

Henry, K. S., Olson, J. P., Farrington, S. P., and Lens, J. (2005). "Improved performance of unpaved roads during spring thaw." ERDC/CRREL TR-05-01, Engineer Research and Development Center Cold Regions Research and Engineering Laboratory, Hanover, New Hampshire.

Heukelom, W., and Klomp, A. (1962). "Dynamic testing as a means of controlling pavements during and after construction." *Proceedings of the International Conference on the Structural Design of Asphalt Pavements*, University of Michigan, Ann Arbor, MI, 667-679.

Hicks, R. G. (2002). "Alaska soil stabilization design guide." FHWA-AK-RD-01-6B, State of Alaska Department of Transportation and Public Facilities, Fairbanks, Alaska.

Hirai, H. (2004). Settlements and stresses of multi-layered grounds and improved grounds by equivalent elastic method. International Journal for Numerical and Analytical Methods in Geomechanics, 32(5), 523–557.

Hoffman, M. S., and Thompson, M. R. (1981). "Mechanistic interpretation of nondestructive pavement testing deflections." *Transportation Engineering Series No. 32*, University of Illinois at Urbana-Champaign, IL.

Hogg, A. H. A. (1944). "Equilibrium of a thin plate on an elastic foundation of finite depth." *The London, Edinburgh, and Dublin Philosophical Magazine and Journal of Science*, 35(243), 265–276.

Hoover, J. M., Huffman, R. T., and Davidson, D. T., 1962. Soil stabilization field trials, primary Highway 117, Jasper County, Iowa. The Forty First Annual Meeting of the Highway Research Board, NAS-NRC, Washington D.C., January 1962.

Hoover, J. M., Pitt, J. M., Handfelt, L. D., and Stanley, R. L. (1981). "Performance of soil-aggregate-fabric systems in frost-susceptible roads, Linn County, Iowa." *Transportation Research Record: Journal of the Transportation Research Board*, 827, 6-14.

Hoover, J. M., Moeller, D. T., Pitt, J. M., Smith, S. G., and Wainaina, N. W. (1982). "Performance of randomly oriented, fiber-reinforced roadway soils: A laboratory and field investigation." Iowa Highway Research Board Project HR-211, Engineering Research Institute, Iowa State University, Ames, Iowa.

Hopkins, T. C., Beckham, T. L., and Hunsucker, D. Q. (1995). "Modification of highway soil subgrades." Report KTC 94-11, Kentucky Transportation Center, University of Kentucky, Lexington, KY.

Iowa DOT. (2016). “Section 2115. Modified Subbase,”. Ames, Iowa: Iowa Department of Transportation.

Iowa DOT. (2013). “Section 2111. Granular Subbase,” Iowa Department of Transportation General Specifications, Ames, Iowa..

Irwin, L. H. (2002). "Backcalculation: An overview and perspective." Pavement Evaluation Conference, Roanoke, Virginia, USA.

Irwin HL, Yang W, Stubstad R. (1989). “Deflection reading accuracy and layer thickness accuracy of pavement layer moduli.” Nondestructive Testing of Pavements and Backcalculation of Pavement Layer Moduli. ASTM STP1026:229-44.

Isaaks, E.H., Srivastava, R.M. (1989) *An introduction to applied geostatistics*. Oxford University Press, New York.

Jumikis, A.R., 1955. The Frost Penetration Problem in Highway Engineering. Rutgers University Press.

Jury, W.A., and Horton, R., 2004. Soil Physics. Sixth Edition. Wiley.

Johnson, A. Freeze-thaw performance of pavement foundation materials. Master of Science, Iowa State University, Ames, Iowa, 2012.

Kaniraj, S.R., and V.G. Havanagi. (2001). “Behavior of cement stabilized fiber-reinforced fly ash-soil mixtures.” *Journal of Geotechnical and Geoenvironmental Engineering*, Vol. 127, No. 7, 574–584.

Kendall, M., Baker, B., Evans, P., and Ramanujan, J. (2001). "Foamed Bitumen Stabilization - The Queensland Experience." *Proc., 20th Australian Road Research Board (ARRB) Conference*, Sydney, Australia.

Kettle, R. J., and McCabe, E. Y. (1985). "Mechanical Stabilization for the Control of Frost Heave." *Canadian Journal of Civil Engineering*, 12, 899-905.

Khoshkhoo, Y., Jansson, P.E., Irannejad, P., Khalili, A., and Rahimi, H., 2015. Calibration of an energy balance model to simulate wintertime soil temperature, soil frost depth, and snow depth for a 14 year period in a highland area of Iran. Cold Regions Science and Technology. 119, 47-60.

Khoury, N., and Zaman, M. M. (2007). "Environmental Effects on Durability of Aggregates Stabilized with Cementitious Materials." *Journal of Materials in Civil Engineering*, 19(1), 41-48.

Konard, J. M., and Lachance, D. (2001). "Use of in situ penetration tests in pavement evaluation." *Canadian Geotechnical Journal*, 38(5), 924-935.

Krige, D.G. (1951). "A statistical approach to some mine valuations and allied problems at the Witwatersrand," M.S. Thesis, University of Witwatersrand, Johannesburg, South Africa.

Lahouar S, Al-Qadi IL. (2008). "Automatic detection of multiple pavement layers from GPR data," *NDT & E International*, Vol. 41:69-81.

Lalague A, Lebens MA, Hoff I, (2014). "Accuracy of ground penetrating radar in pavement thickness evaluation - impact of interpretation errors," In: *Transport Research Arena: Transport Solutions from Research to Deployment*. Proceedings; 2014 April 14-17; Paris. France: Institut Francais des Sciences et Technologies des Transports, de l'Aménagement et des Réseaux (IFSTTAR).

Lalagüe A, Hoff I, Accuracy of ground penetrating radar in bituminous pavement thickness evaluation. 2010; In: Transport Research Arena 2010. Proceedings; Brussels, Belgium: 2014.

Latha, G.M., Murthy, V.S. (2007). "Effects of reinforcement form on the behavior of geosynthetic reinforced sand," *Geotextiles and Geomembranes*, 25(1), 23-32.

Loizos A, Plati C. (2007). "Accuracy of pavement thicknesses estimation using different ground penetrating radar analysis approaches," *NDT & E International*. Vol. 40:147-57.

Loken MC. (2007). "Use of ground penetrating radar to evaluate Minnesota roads." St. Paul, Minnesota (USA): Minnesota Department of Transportation.

Makul N. (2013). "Dielectric permittivity of various cement-based materials during the first 24 hours hydration." *Open Journal of Inorganic Non-Metallic Materials*; Vol. 3; 53-57.

Maser K, Scullion T. (1992). "Influence of asphalt layering and surface treatments on asphalt base layer thickness computations using radar". Report No. TX-92-1923-1; College Station, Texas (USA): Texas Transportation Institute.

McCracken, J. K. (2008). "Seasonal Analysis of the Response of Jointed Plain Concrete Pavements to FWD and Truck Loads", MS Thesis, University of Pittsburg, Pittsburg, PA.

Mengelt, M., Edil, T. & Benson, C. (2000). "Reinforcement of Flexible Pavements with Geocells," *Geo Engineering Report No. 00-04*. Department of Civil and Environmental Engineering, University of Wisconsin-Madison, Madison, WI, USA.

Michalowski, R. L., and Cerma ´k, J. (2002). ''Strength anisotropy of fiber-reinforced sand.'' *Comput. Geotech*., Vol. 29, pp. 279–299.

Mohammad, L. N., Herath, A., Gaspard, K., Abu-Farsakh, M. Y., and Gudishala, R. (2007). "Prediction of resilient modulus of cohesive subgrade soils from dynamic cone penetrometer test parameters." *Journal of Materials in Civil Engineering*, 19(11), 986-992.

Mooney, M., R. Rinehart, D. J. White, P. Vennapusa, N. Facas, and O. Musimbi. (2010). *Intelligent Soil Compaction Systems*, NCHRP Report 676, National Cooperative Highway Research Program, Washington, D.C.

Moropoulou A, Avdelidis NP, Koui M, Aggelopoulos A, Karmis P. (2002). “Infrared thermography and ground penetrating radar for airport pavements assessment,” *Nondestructive Testing and Evaluation*. Vol. 18:37-42.

Muthen, K. M. (1999). "Foamed Asphalt Mixes - Mix Design Procedure." CR-98/077, CSIR Transportek, Pretoria, South Africa.

Nazzal, M. M. (2003). "Field evaluation of in-situ test technology for QC/QA procedures during construction of pavement layers and embankments.” Master of Science, The Department of Civil and Environmental Engineering, Louisiana State University, Baton Rogue, LA.

NCHRP (2004). "Guide for mechanistic-empirical design of new pavement and rehabilitated pavement structures." Final Report, National Cooperative Highway Research Program, Transportation Research Board, Washington, D.C.

Nixon, J.F., and McRoberts, E.C. (1973). “A study of some factors affecting the thawing of frozen soils,” *Canadian Geotechnical Journal*. 10:439-452.

Odemark, N. (1949). Undersökning av elasticitetsegenskaperna hos olika jordarter samt teori för beräkning av beläggningar enligt elasticitetsteorin (Meddelande 77). Stockholm: Statens Väginstitut.

Orakoglu, M., Liu, J., and Tutumluer, E. (2016). “Frost depth prediction for seasonal freezing area in Eastern Turkey,” *Cold Regions Science and Technology*, Vol. 124, 118-126.

Parsons, R., and Milburn, J. (2003). Engineering Behavior of Stabilized Soils. *Transportation Research Record*, 1837, 20–29.

PCA (1995). "Soil-Cement Construction Handbook." Portland Cement Association, Skokie, Illinois.

Pen, C. K. (1990). "An assessment of the available methods of analysis for estimating the elastic moduli of road pavements." *Proceedings of the Third International Conference on Bearing Capacity of Roads and Airfields*, Norwegian Institute of Technology, Trondheim, Norway.

Plati, C., Loizos, A. (2012). “Using ground-penetrating radar for assessing the structural needs of asphalt pavements,” *Nondestructive Testing and Evaluation*. Vol. 27, 273-284.

Poikajärvi J, Peisa K, Herronen T, Aursand PO, Maijala P, Narbro A. (2012). “GPR in road investigations – equipment tests and quality assurance of new asphalt pavement.” *Nondestructive Testing and Evaluation*, Vol. 27:293-303.

Pokharel, S.K. (2010). “Experimental study on geocell-reinforced bases under static and dynamic loading.” Ph.D. Dissertation, Dept. of Civil, Environmental, and Architectural Engineering, University of Kansas, Kansas.

Powell, W., Keller, G. R., and Brunette, B. (1999). "Applications for geosynthetics on forest service low-volume roads." *Transportation Research Record: Journal of the Transportation Research Board*, 1999, 113-120.

Powell, W. D., Potter, J. F., Mayhew, H. C., and Nunn, M. E. (1984). "The structural design of bituminous roads." Transport and Road Research Laboratory, London.

Rao, C., Tutus-Clover, L., Bhattacharya, B., Darter, M. I., Stanley, M., and Von Quintus, H. L. (2012). "Estimation of key PCC, base, subbase, and pavement engineering properties from routine tests and physical characteristics." *Final Report FHWA-HRT-12-030*, Federal Highway Administration, McLean, VA.

Rea, C., and Mitchell, J.K. (1978). “Sand reinforcement using paper grid cells.” *Proc., ASCE Spring Convention and Exhibit*, Symposium on Earth Reinforcement, Pittsburg, Pennsylvania.

Roberts, F.L., Kandal, P.S., Brown, E.R., Lee, D., and Kennedy, T.W. (1996). Hot mix asphalt materials, mixture design, and construction (2nd Ed.). Auburn, Alabama: National Center for Asphalt Technology.

Rollings, M. P., and Rollings, R. S. (1996). *Geotechnical Materials in Construction*, McGraw-Hill, New York, NY.

RWIS, 2016. Iowa State Environmental Mesonet, RWIS Soil Probe Download. Iowa State University, Department of Agronomy. Road Weather Information System. http://www.rwisonline.com/scanweb/swlogin.asp. Accessed December, 2016.

Saarenketo T, Scullion T. (1995). "Using electrical properties to classify the strength properties of base course aggregates," College Station, Texas (USA): Texas Transportation Institute.

Sadek, S., Najjar, S. S., and Freiha, F. (2010). "Shear strength of fiber-reinforced sands." *Journal of Geotechnical and Geoenvironmental Engineering*, ASCE, 136(3), 490–499.

Salour, F., and Erlingsson, S. (2012). "Pavement Structural Behavior during Spring Thaw - Interpretation of FWD measurements by monitoring environmental data from county road 126 at Torpsbruk." 2009/0572-29, Swedish National Road and Transport Research Institute (VTI), Linkoping, Sweden.

Salt, G. (1998). "Pavement deflection measurement and interpretation for the design of rehabilitation treatments." *Research Report 117*, New Zealand Transport Agency, New Zealand.

Sandström Å., and C. B. Pettersson. Intelligent Systems for QA/QC in Soil Compaction. In *Proceedings of the Transportation Research Board Annual Meeting.* CD-ROM. Transportation Research Board of the National Academies, Washington, D. C., 2004.

Santoni, R. L., and S. L. Webster. (2002). "Airfields and road construction using fiber stabilization of sands." *Journal of Transportation Engineering*, Vol. 127, No. 2, 96–104.

Scherocman, J., Rakowski, S., and Uchiyama, K. (2007). "Intelligent compaction, does it exist?" 2007 Canadian Technical Asphalt Association (CTAA) Conference, Victoria, BC, July.

Scullion T, Chen Y, Lau CL. (1995). COLORMAP-user's Manual with Case Studies. Report No. FHWA/TX-96/1341-1; College Station, Texas: Texas Transportation Institute.

Simonsen, E., and Isacsson, U. (1999). Thaw weakening of pavement structures in cold regions. Cold Regions Science and Technology, 29(2), 135–151.

Smith, K. D., Wade, M. J., and Bruinsma, J. E. (2007). "Using falling weight deflectometer data with mechanistic-empirical design and analysis." *Draft Interim Report*, Federal Highway Administration Office of Acquisition Management, Washington D.C.

Sobol', I.M. (1990). On sensitivity estimation for nonlinear mathematical models. Matematicheskoe modelirovanie, 2(1), 112–118.

Stefan, J. (1890). Ueber die verdampfung und die auflösung als vorgänge der diffusion. Annalen der Physik. Vol. 277, Iss. 12(1890), 725–747. DOI: 10.1002/andp.18902771206.

Stubstad, R. N., Jiang, Y. J., and Lukanen, E. O. (2006). "Guidelines for review and evaluation of backcalculation results." *Final Report FHWA-RD-05-152*, Federal Highway Administration, Washington, D.C.

Stubstad, R., Jiang, Y. J., and Lukanen, E. (2007). "Forward calculation of pavement moduli with load-deflection data." *Transportation Research Record: Journal of the Transportation Research Board*, 2005, 104-111.

Terrel, R. L., Epps, J. A., Barenberg, E. J., Mitchell, J., and Thompson, M. R. (1979). “Soil Stabilization in pavement Structures - A User Manual.” FHWA Research Report No. FHWA-IP-80-2, WA.

Topp GC, Dadvis JL, Annan AP. (1980). “Electromagnetic determination of soil water content: measurements in coaxial transmission lines,” *Water Resour Res.* Vol. 16, 574-582.

Thompson, M., and White. D. J. (2007). “Field Calibration and Spatial Analysis of Compaction Monitoring Technology Measurements. In *Transportation Research Record: Journal of the Transportation Research Board,* No. 2004, Transportation Research Board of the National Academies, Washington, D.C. pp. 69–79.

Thompson, M., and D. J. White. (2008). “Estimating Compaction of Cohesive Soils from Machine Drive Power,” *ASCE Journal of Geotechnical and Geoenvironmental Engineering*, Vol. 134, No. 12, pp. 1771–1777.

Ullidtz, P. (1987). Pavement Analysis, Developments in Civil Engineering Series, Elsevier, New York.

USDA and USDAF (1988). *Arctic and Subarctic Construction Calculation Methods for Determination of Depths of Freeze and Thaw in Soils*. Technical Manual, 5-852-6. Departments of the Army and the Air Force.

Vennapusa, P. K. R., and White, D. J. (2009). "Comparison of light weight deflectometer measurements for pavement foundation materials." *Geotechnical Testing Journal*, 32(3), 239-251.

Vennapusa, P., D. J. White, and H. Gieselman. (2009). “Influence of Support Conditions on Roller-Integrated Machine Drive Power Measurements for Granular Base.” Presented at 2009 *International Foundation Congress and Equipment Expo*, Orlando, FL.

Vennapusa, P. K. R., White, D. J., Siekmeier, J., and Embacher, R. A. (2012). "In situ mechanistic characterisations of granular pavement foundation layers." *International Journal of Pavement Engineering*, 13(1), 52-67.

Vennapusa, P.K.R., White, D.J., and Schram, S. (2013). Roller-integrated compaction monitoring for hot-mix asphalt overlay construction. Journal of Transportation Engineering, 139(12), 1164–1173.

Von Quintus, H. L., and Simpson , A. L. (2002). "Back-calculation of layer parameters for LTPP test sections, Volume II: layered elastic analysis for flexible and rigid pavements." Final Report FHWA-RD-01-113, Federal Highway Administration, McLean, Virginia.

Weather Channel, The (2016). [Average monthly temperatures for Boone, Iowa] Weather History for KBNW. Retrieved from http://www.wunderground.com/history/airport/KBNW/2016/01/25/DailyHistory.html?req_city=Boone&req_state=IA&reqdb.zip=50036&reqdb.magic=1&reqdb.wmo=99999.

Webster, S. L. (1979). “Investigation of beach sand trafficability enhancement using sand grid confinement and membrane reinforcement concepts.” Report GL-79-20 (1), U.S. Army Engineer Waterways Experiment Station, Vicksburg, Mississippi.

Webster, S. L. (1981). “Investigation of beach sand trafficability enhancement using sand-grid confinement and membrane reinforcement concepts-Report 2.” U.S. Army Engineer Waterways Experiment Station, Vicksburg, Mississippi.

Welch, B. L. The Generalization of `Student's' Problem when Several Different Population Variances are Involved. Biometrika, Vol. 34, No. 1/2, 1947, pp. 28-35.

West, R.C., Watson, D.E., Turner, P.A., and Casola, J.R. (2010). Mixing and compaction temperatures of asphalt binders in hot-mix asphalt (NCHRP 648). Washington, D.C.: National Cooperative Highway Research Program.

Wiseman, G., and Greenstein, J. (1983). "Comparison of methods of determining pavement parameters from deflection bowl measurements." *Proceeding of the 7th Asian Regional Conference on Soil Mechanics and Foundation Engineering*, Haifa, Israel, 158-165.

White, D. J., Vennapusa, P. Jahren. C. T. (2004). "Determination of the Optimum Base Characteristics for Pavements," Final Report, Iowa DOT Project TR–482, Center for Transportation Research and Education Project 02-119, Iowa State University, Ames, IA.

White, D. J., D. Harrington, and Z. Thomas (2005a). "Fly Ash Soil Stabilization for Non-Uniform Subgrade Soils, Volume I: Engineering Properties and Construction Guidelines." IHRB Project TR-461; FHWA Project 4. Iowa State University, Ames, Iowa

White, D. J., Jaselskis, E. Schaefer, V. and Cackler, T. (2005b). "Real-time Compaction Monitoring in Cohesive Soils from Machine Response." *Transportation Research Record*, Journal of the Transportation Research Board, No. 1936, pp. 173–180.

White, D. J., Mekkawy, M. M., Jahren, C. T., Smith, D., and Suleiman, M. T. (2007). "Effective Shoulder Design and Maintenance." IHRB Project TR-531, Center for Transportation Research and Education, Iowa State University, Ames, Iowa.

White, D.J., Vennapusa, P., Suleiman, M.T., Jahren, C.T. (2007). "An in situ test device for rapid determination of permeability of granular bases," *Geotechnical Testing Journal*, Vol. 30(4): 282-291.

White, D. J., and M. Thompson. (2008). "Relationships Between In Situ and Roller-Integrated Compaction Measurements for Granular Soils." *ASCE Journal of Geotechnical and Geoenvironmental Engineering*, Vol. 134, No. 2, pp. 1763–1770.

White, D.J., and Vennapusa, P. (2008). Accelerated implementation of intelligent compaction monitoring technology for embankment subgrade soils, aggregate base, and asphalt pavement materials (TPF-5(128)). Washington, D.C.: Federal Highway Administration.

White, D. J., P. Vennapusa, J. Zhang, H. Gieselman, and M. Morris. (2009). *Implementation of Intelligent Compaction Performance Based Specifications.* Final Report MN/RC 2009-14, Minnesota Department of Transportation, St. Paul, MN.

White, D. J., P. Vennapusa, J. Han, B. Christopher, H. Gieselman, S. Wang, W. Riko, P. Becker, D. Horhota, S. Pokharel, and J. Thakur. (2011a). "Compaction "Roadeo" Field Demonstration Project Report: Roller-Integrated Compaction Monitoring and Subgrade Geosynthetic Reinforcement," In *SHRP2R02: Geotechnical Solutions for Soil Improvement, Rapid Embankment Construction, and Stabilization of the Pavement Working Platform*. Transportation Research Board of the National Academies, Washington, D.C.

White, D. J., P. Vennapusa, and H. Gieselman. (2011b). "Field Assessment and Specification Review for Roller-Integrated Compaction Monitoring Technologies," Special Issue: Advances in Instrumentation and Monitoring in Geotechnical Engineering, *Advances in Civil Engineering Journal*, Vol. 2011, Article ID 783836, Hindawi Publishing Corporation.

White, D.J., Vennapusa, P., Zhao, L. (2014) "Verification and repeatability analysis for the in situ air permeameter test," Geotechnical Testing Journal, Vol. 37, 365-376.

White, D. J., and Vennapusa, P. K. R. (2014). "Optimizing pavement base, subbase, and subgrade layers for cost and performance of local roads." Final Report, Iowa Department of Transportation, Ames, IA.

Willett DA, Rister B. (2002). “Ground penetrating radar pavement layer thickness evaluation,” Lexington, Kentucky (USA): Kentucky Transportation Center/

Yoder, E.J., and Witczak, M.W. (1975). *Principles of Pavement Design*. Second Edition. John Wiley & Sons.

Yuu, J., Han, J., Rosen, A., Parsons, R.L., and Leshchinsky, D. (2008). “Technical review of geocell-reinforced base courses over weak subgrade.” *Proc., First Pan American Geosynthetics Conference & Exhibition*, Cancún, Mexico.

Zapata, C. E., Houston, W. N. (2008) “Calibration and validation of the enhanced integrated climatic model for pavement design.” NCHRP Report 602, Transportation Research Board, Washington, DC.

Zarling, J. P., Braley, W. A., and Pelz., C., (1989). “The modified Berggren method – A review,” *Proceedings of the Fifth International Conference*, Cold Regions Engineering. 267-273. New York, NY: ASCE.

Zhang, Y. Frost-heave and thaw-weakening of pavement foundation materials. Master of Science, Iowa State University, Ames, Iowa, 2013.

Zorn, G. Operating Manual: Light Drop-Weight Tester ZFG2000, Zorn Stendal, Germany, 2003.

APPENDIX A: CPT LOCATIONS AND RESULTS

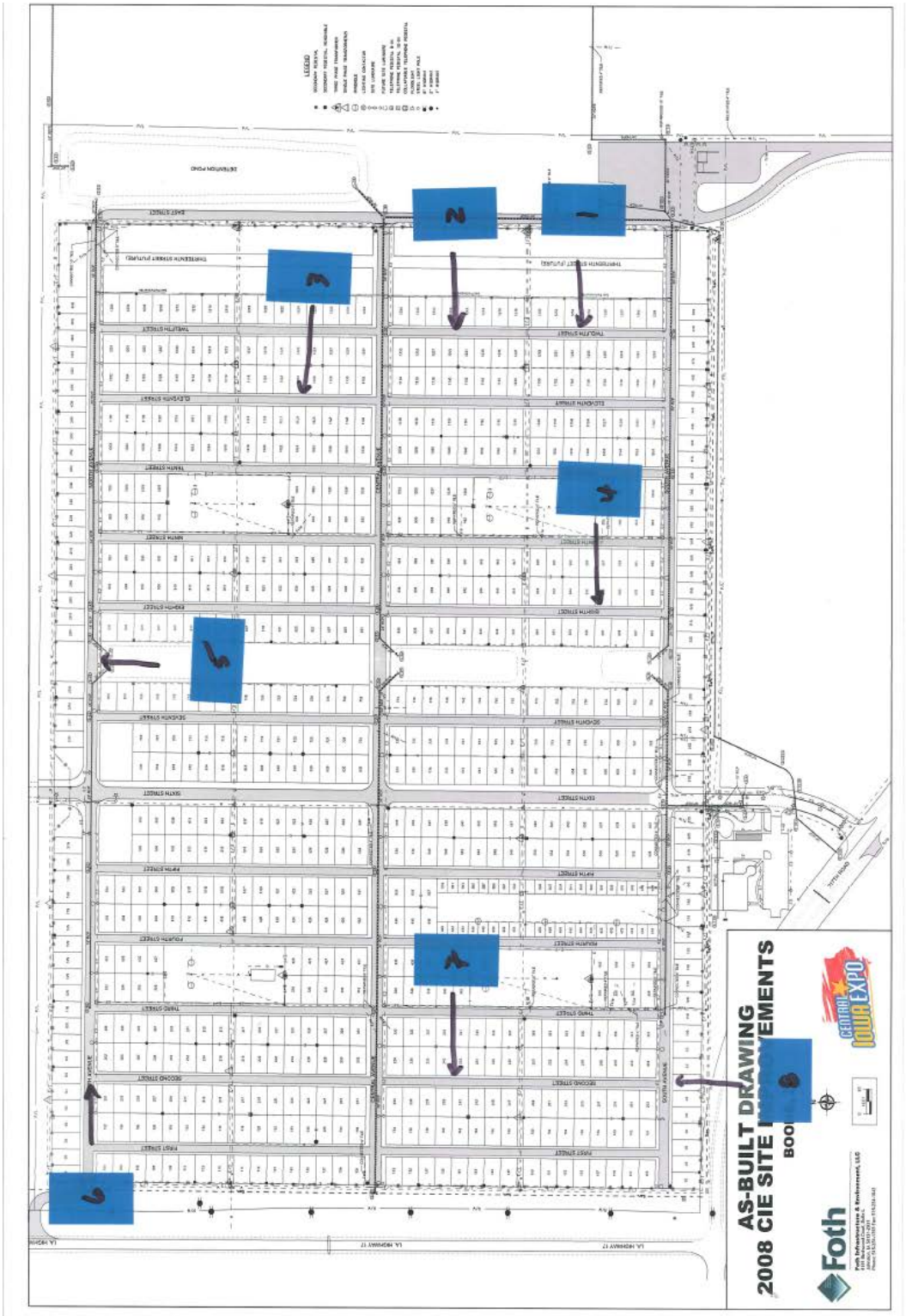

Figure A1. Map of CPT locations

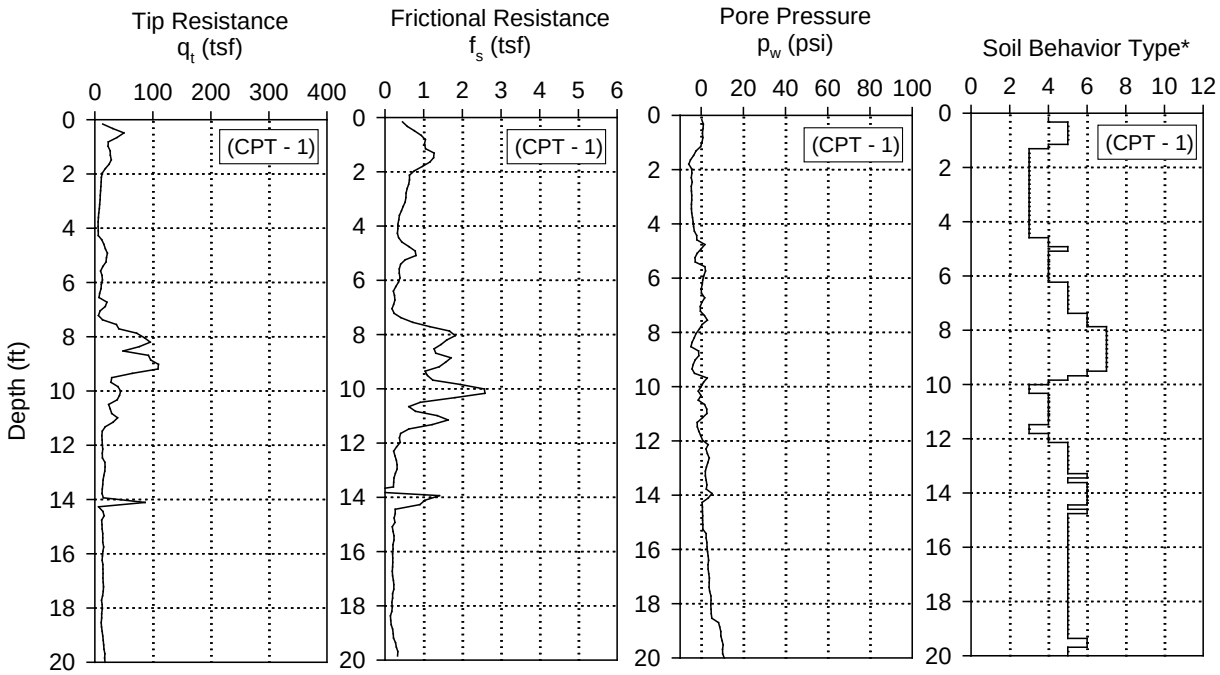

*Soil Behavior Type (Robertson and Campanella 1986): 1 - sensitive fine grained, 2 - organic material, 3 - clay, 4 - silty clay to clay, 5 - clayey silt to silty clay, 6 - sandy silt to clayey sitl, 7 - silty sand to sandy silt, 8 - sand to silty sand, 9 - sand, 10 - gravelly sand to sand, 11 - very stiff fine grained, 12 - sand to clayey sand

Figure A2. CPT results from test location 1

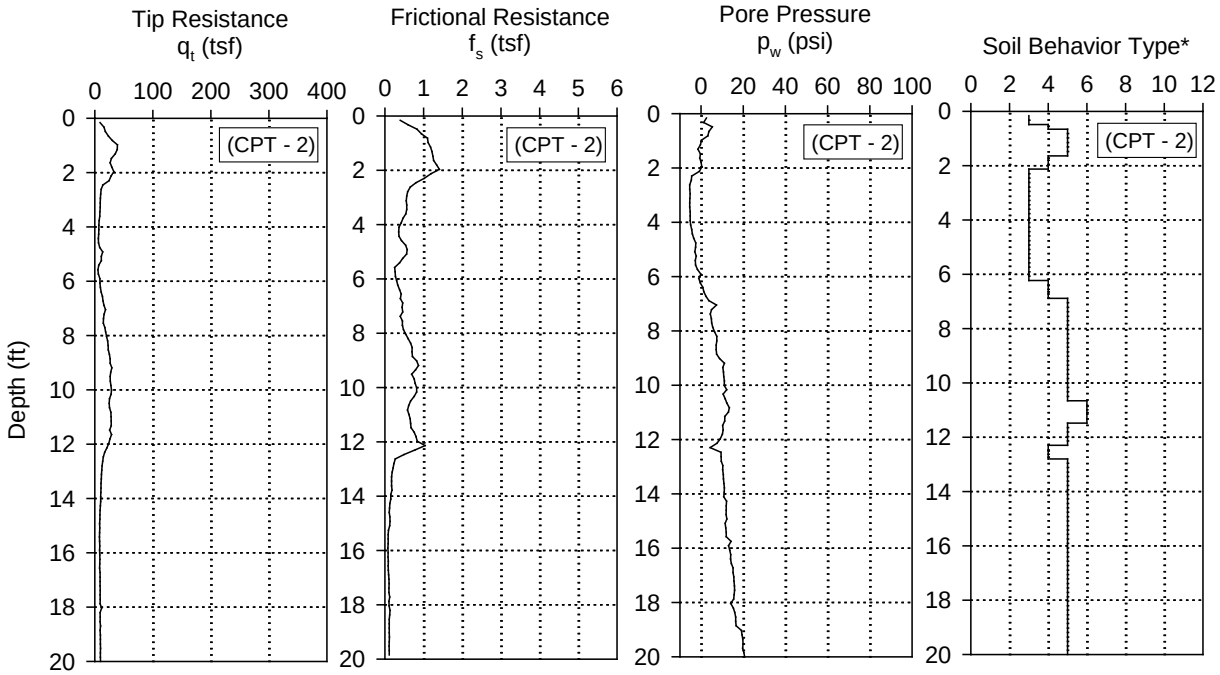

*Soil Behavior Type (Robertson and Campanella 1986): 1 - sensitive fine grained, 2 - organic material, 3 - clay, 4 - silty clay to clay, 5 - clayey silt to silty clay, 6 - sandy silt to clayey sitl, 7 - silty sand to sandy silt, 8 - sand to silty sand, 9 - sand, 10 - gravelly sand to sand, 11 - very stiff fine grained, 12 - sand to clayey sand

Figure A3. CPT results from test location 2

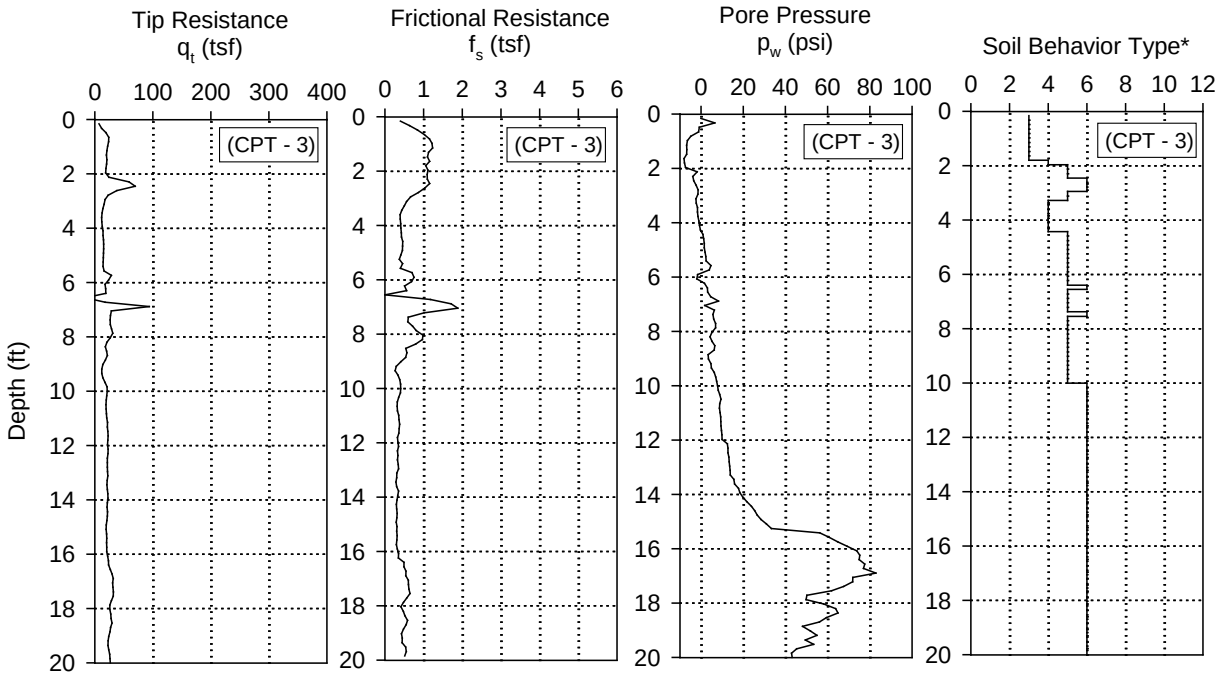

*Soil Behavior Type (Robertson and Campanella 1986): 1 - sensitive fine grained, 2 - organic material, 3 - clay, 4 - silty clay to clay, 5 - clayey silt to silty clay, 6 - sandy silt to clayey sitl, 7 - silty sand to sandy silt, 8 - sand to silty sand, 9 - sand, 10 - gravelly sand to sand, 11 - very stiff fine grained, 12 - sand to clayey sand

Figure A4. CPT results from test location 3

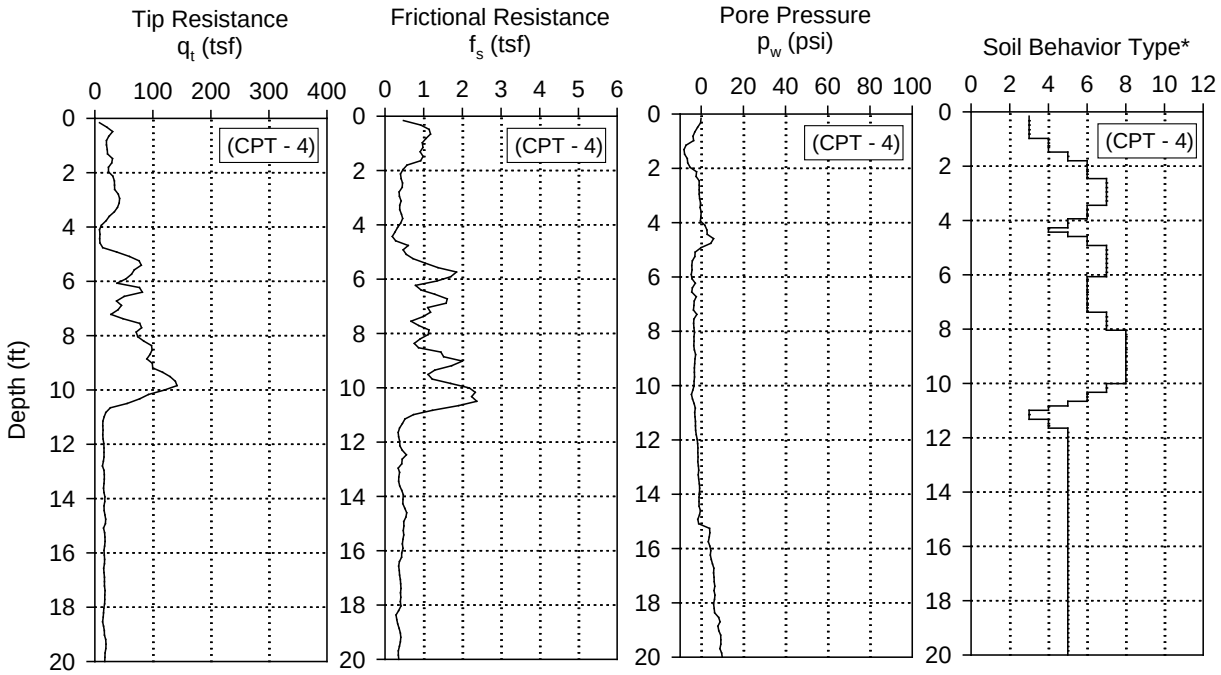

*Soil Behavior Type (Robertson and Campanella 1986): 1 - sensitive fine grained, 2 - organic material, 3 - clay, 4 - silty clay to clay, 5 - clayey silt to silty clay, 6 - sandy silt to clayey sitl, 7 - silty sand to sandy silt, 8 - sand to silty sand, 9 - sand, 10 - gravelly sand to sand, 11 - very stiff fine grained, 12 - sand to clayey sand

Figure A5. CPT results from test location 4

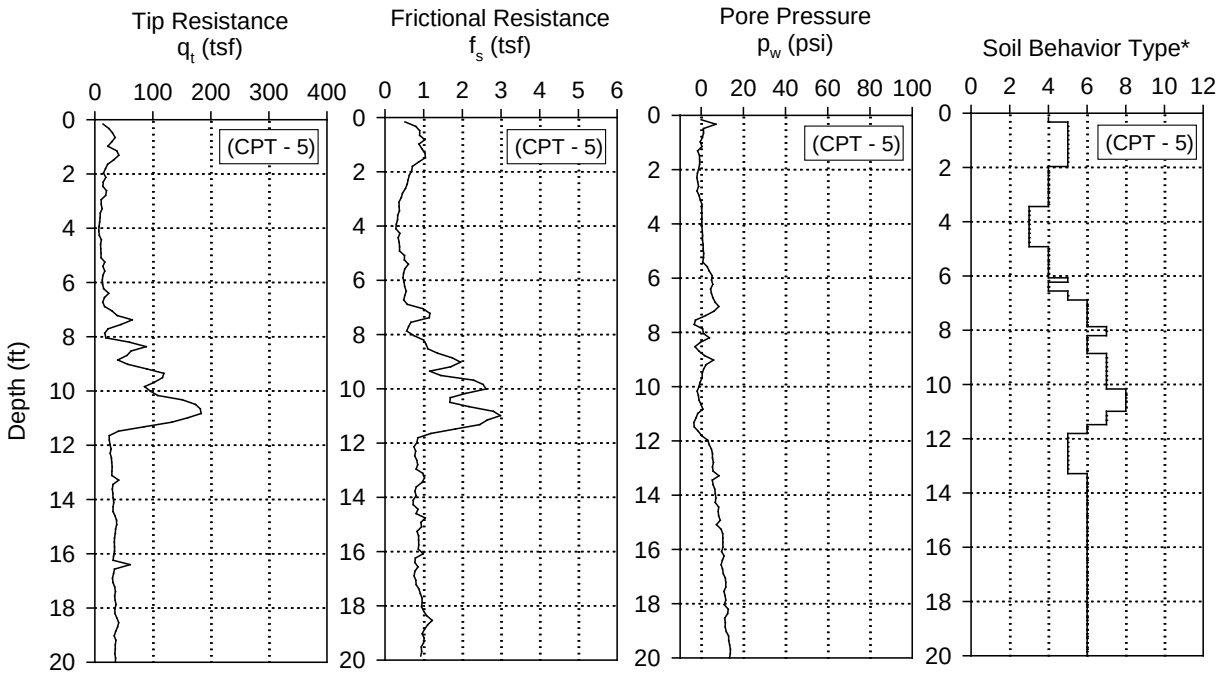

*Soil Behavior Type (Robertson and Campanella 1986): 1 - sensitive fine grained, 2 - organic material, 3 - clay, 4 - silty clay to clay, 5 - clayey silt to silty clay, 6 - sandy silt to clayey sitl, 7 - silty sand to sandy silt, 8 - sand to silty sand, 9 - sand, 10 - gravelly sand to sand, 11 - very stiff fine grained, 12 - sand to clayey sand

Figure A6. CPT results from test location 5

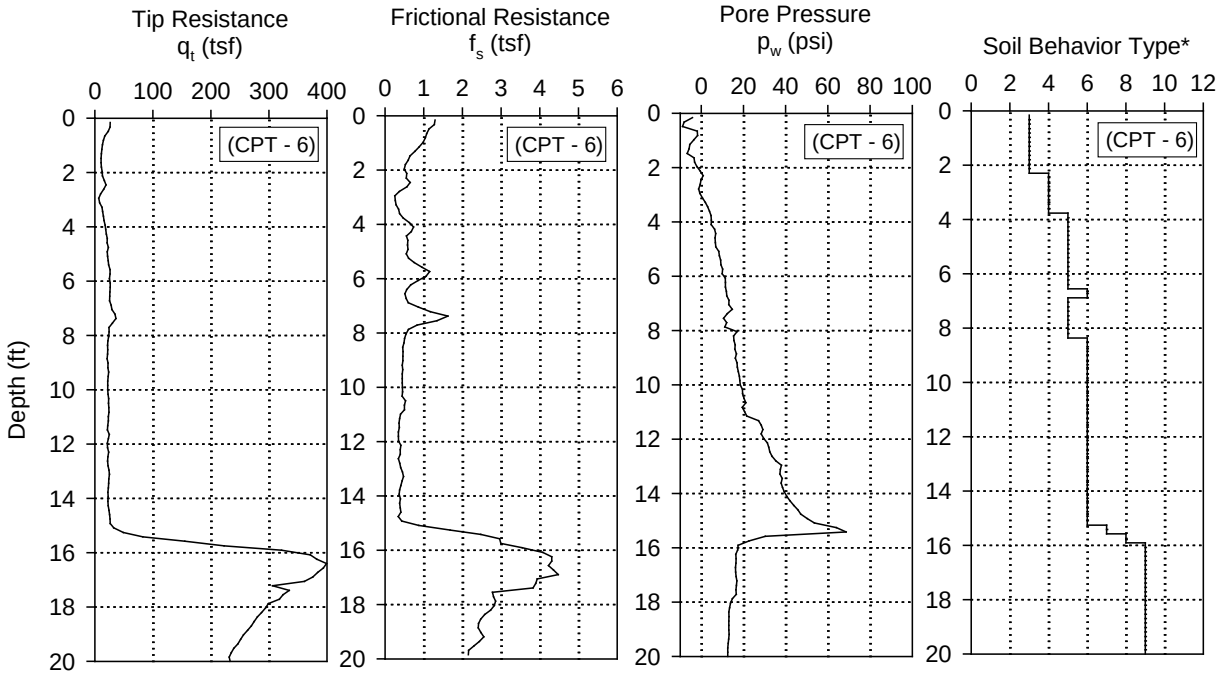

*Soil Behavior Type (Robertson and Campanella 1986): 1 - sensitive fine grained, 2 - organic material, 3 - clay, 4 - silty clay to clay, 5 - clayey silt to silty clay, 6 - sandy silt to clayey sitl, 7 - silty sand to sandy silt, 8 - sand to silty sand, 9 - sand, 10 - gravelly sand to sand, 11 - very stiff fine grained, 12 - sand to clayey sand

Figure A7. CPT results from test location 6

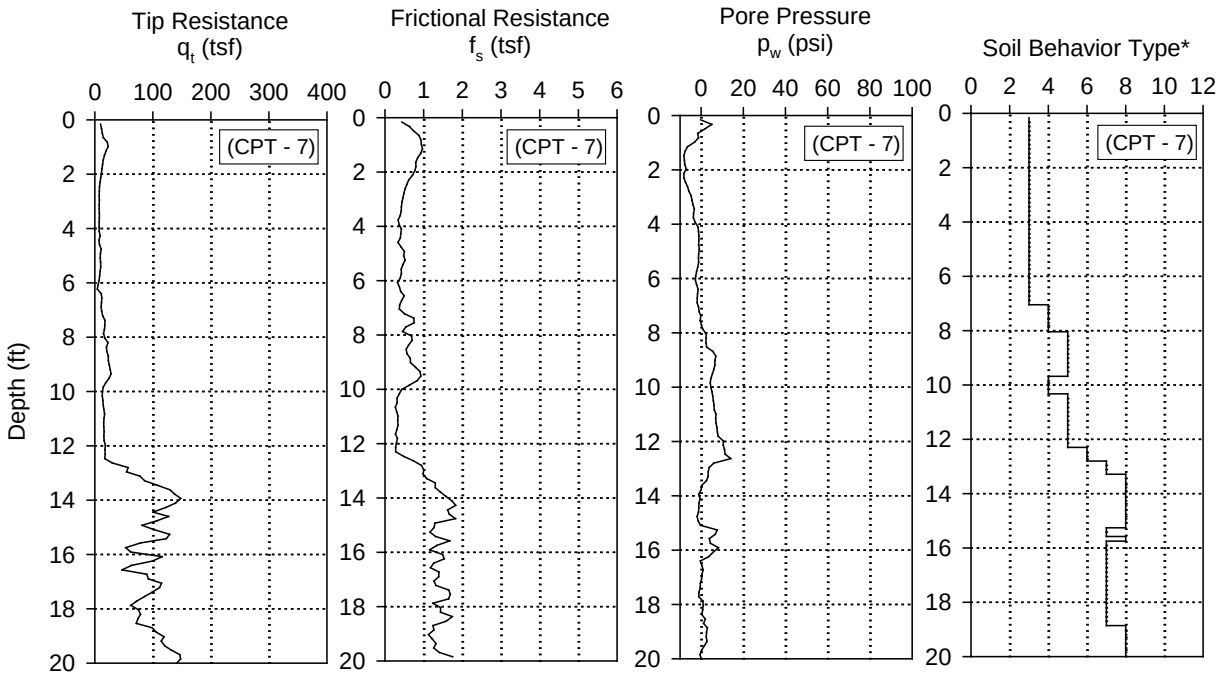

*Soil Behavior Type (Robertson and Campanella 1986): 1 - sensitive fine grained, 2 - organic material, 3 - clay, 4 - silty clay to clay, 5 - clayey silt to silty clay, 6 - sandy silt to clayey sitl, 7 - silty sand to sandy silt, 8 - sand to silty sand, 9 - sand, 10 - gravelly sand to sand, 11 - very stiff fine grained, 12 - sand to clayey sand

Figure A8. CPT results from test location 7

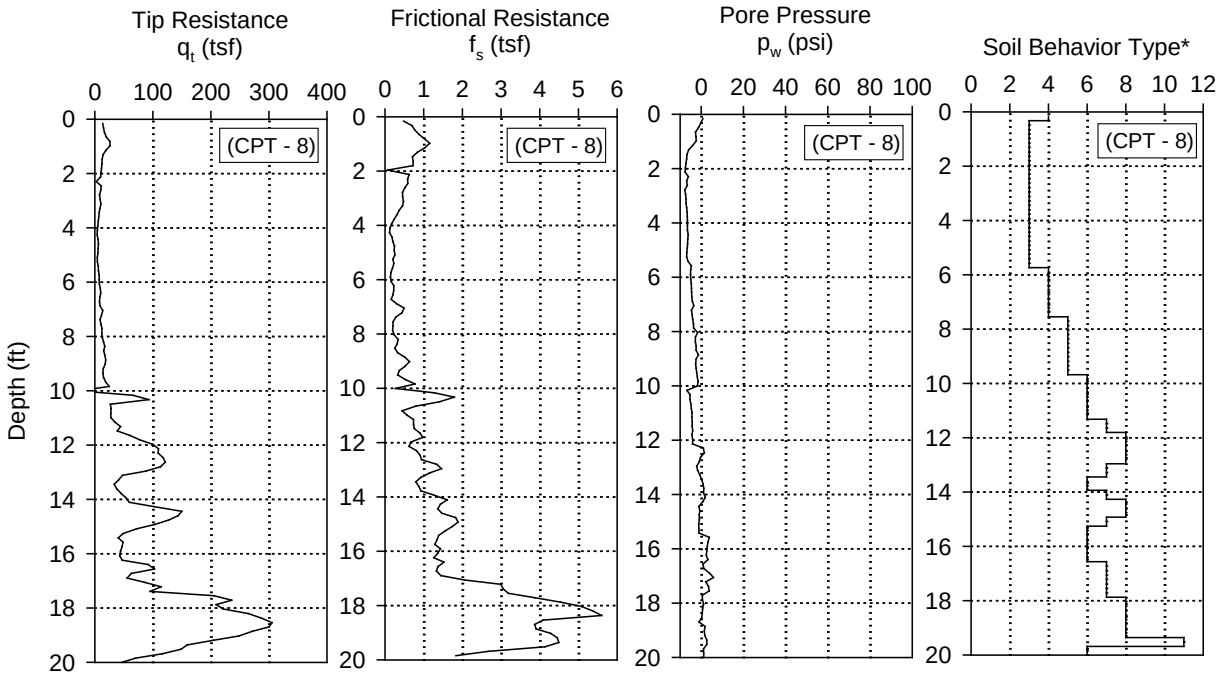

*Soil Behavior Type (Robertson and Campanella 1986): 1 - sensitive fine grained, 2 - organic material, 3 - clay, 4 - silty clay to clay, 5 - clayey silt to silty clay, 6 - sandy silt to clayey sitl, 7 - silty sand to sandy silt, 8 - sand to silty sand, 9 - sand, 10 - gravelly sand to sand, 11 - very stiff fine grained, 12 - sand to clayey sand

Figure A9. CPT results from test location 8